2015-ENAM-0027

École doctorale n° 432 : Science des Métiers de l'ingénieur

Doctorat ParisTech

T H È S E

pour obtenir le grade de docteur délivré par

l'École Nationale Supérieure d'Arts et Métiers

Spécialité " Automatique "

présentée et soutenue publiquement par

Zhongkai CHEN

le 8 octobre 2015

Optimized Walking of an 8-link 3D Bipedal Robot

Directeur de thèse : **Gabriel ABBA**
Co-encadrement de la thèse : **Nafissa LAKBAKBI ELYAAQOUBI**

Jury

M. Pierre RIEDINGER, Professeur, Université de Lorraine	Président
Mme. Christine CHEVALLEREAU, Directrice de Recherche, CNRS	Rapporteur
M. Jessy GRIZZLE, Professeur, University of Michigan	Rapporteur
M. Philippe FRAISSE, Professeur, Université Montpellier 2	Rapporteur
Mme. Nafissa LAKBAKBI ELYAAQOUBI, Maître de conférence, ENIM	Examinateur
M. Gabriel ABBA, Professeur, ENIM	Examinateur

T H È S E

Arts et Métiers ParisTech - Campus de Metz
Laboratoire de Conception, Fabrication et Commande

CONTENTS

List of Figures 4

List of Tables 14

Acknowledgement 15

1. Introduction 17
- 1.1 Motivation 17
- 1.2 Current Developments of Bipedal Robots 18
  - 1.2.1 Bipedal Robots in Asia 18
  - 1.2.2 Bipedal Robots in Europe 20
  - 1.2.3 Bipedal Robots in North America 21
- 1.3 Control Approaches in Bipedal Walking 22
  - 1.3.1 Actuated Quasi-Static Walking 22
  - 1.3.2 Unactuated/Actuator-Assisted Dynamic Walking 24
  - 1.3.3 Actuated Dynamic Walking 24
- 1.4 Energy Optimal Gaits of Bipedal Robots 27
- 1.5 Elastic Coupling 29
- 1.6 Thesis Contribution 31
- 1.7 Thesis Outline 32

2. Methodology 35
- 2.1 Lagrangian Mechanics 35
  - 2.1.1 Kinetic Energy 35
  - 2.1.2 Potential Energy 36
  - 2.1.3 Obtaining Dynamic Model 37
  - 2.1.4 Calculating External Forces 37
- 2.2 Feedback Linearization 38
  - 2.2.1 Single-input, Single-output Systems 39
  - 2.2.2 Multiple-input, Multiple-output Systems 40
- 2.3 Hybrid System Stability 43
  - 2.3.1 Autonomous Systems with Impulse Effects 43
  - 2.3.2 Poincaré Map 44
  - 2.3.3 Restricted Poincaré Map 45
- 2.4 Parametric Optimization 47
  - 2.4.1 Constrained Optimization 47
  - 2.4.2 Sequential Quadratic Programming 50

2.5 Conclusion 51

3. Underactuated Planar Bipedal Robots with Point Feet 53
3.1 Robot Structure and Hypotheses 54
3.2 Dynamic Model of Walking 56
3.2.1 Swing Phase Model 57
3.2.2 Impact Model 58
3.2.3 Hybrid Model 60
3.2.4 Point-foot Contact Model 60
3.3 Feedback Control Design 60
3.3.1 Controlled Outputs 60
3.3.2 Swing Phase Control 62
3.3.3 Stability Analysis 64
3.4 Optimization of Walking Motion 66
3.4.1 Parameterization of h_d 66
3.4.2 Optimization Criterion 68
3.4.3 Constraints 69
3.4.4 Optimization Realization 70
3.5 Results and Analysis 72
3.6 Conclusion 78

4. Elastic Couplings for the 5-link Planar Biped 79
4.1 Modeling of Elastic Couplings 79
4.2 Optimal Walking with Elastic Couplings 81
4.2.1 2D Coupling Case I 81
4.2.2 2D Coupling Case II 89
4.3 Discussion 95
4.4 Conclusion 98

5. Underactuated 3D Bipedal Robots with Massless Line Feet 99
5.1 Robot Structure and Hypotheses 101
5.2 Dynamic Model of Walking 102
5.2.1 Swing Phase Model 105
5.2.2 Impact Model 105
5.2.3 Hybrid Model 108
5.2.4 Line-foot Contact Model 109
5.3 Feedback Control Design 110
5.3.1 Controlled Outputs 110
5.3.2 Swing Phase Control 111
5.3.3 Stability Analysis 112
5.4 Optimization of Walking Motion 113
5.4.1 Parameterization of h_d 113
5.4.2 Optimization Criterion 117
5.4.3 Constraints 117
5.4.4 Optimization Realization 118

5.5 Results And Analysis . . . 119
5.5.1 Analysis of the Starting Point . . . 120
5.5.2 3D Optimization Case I . . . 121
5.5.3 3D Optimization Case II . . . 128
5.6 Conclusion . . . 135

6. Elastic Couplings for Underactuated 3D Bipedal Robots . . . 137
6.1 Modeling of Elastic Couplings . . . 137
6.2 Optimal Walking with Elastic Couplings . . . 139
6.2.1 3D Coupling Case I . . . 139
6.2.2 3D Coupling Case II . . . 145
6.2.3 3D Coupling Case III . . . 152
6.3 Discussion . . . 160
6.4 Conclusion . . . 162

7. Conclusions and Future Work . . . 163
7.1 Conclusions . . . 163
7.2 Future Work . . . 165

8. Résumé en français . . . 167
8.1 Introduction . . . 167
8.2 Méthodologie . . . 176
8.3 Robot bipède 2D avec des pieds ponctuels . . . 180
8.4 Couplages élastiques pour le robot 2D . . . 186
8.5 Robot bipède 3D avec des pieds à contact linéique . . . 191
8.6 Couplages élastiques pour le robot 3D . . . 199
8.7 Conclusion et perspectives . . . 204

Bibliographie . . . 207

Appendix 223

A. Supplementary Charts for Chapter 3 . . . 225

B. Supplementary Charts for Chapter 4 . . . 229
B.1 2D Coupling Case I . . . 229
B.2 2D Coupling Case II . . . 233

C. Supplementary Charts for Chapter 5 . . . 237
C.1 3D Optimization Case I . . . 237
C.2 3D Optimization Case II . . . 241

D. Supplementary Charts for Chapter 6 . . . 247
D.1 3D Coupling Case I . . . 247
D.2 3D Coupling Case II . . . 251
D.3 3D Coupling Case III . . . 255

LIST OF FIGURES

1.1 Asian bipedal robots. 19
1.2 European bipedal robots. 20
1.3 Bipedal robots in North America. 21

2.1 Geometric interpretation of a Poincaré return map $P : \mathcal{S} \to \mathcal{S}$ for a system with impulse effects. 45

3.1 Definitions of joints and links of the 5-link planar robot 56
3.2 The generalized coordinates and the length information of the 5-link planar robot 57
3.3 The geometric interpretation of the controlled outputs. 61
3.4 Feedback loop of the control law that renders $\mathcal{Z}$ forward invariant and attractive. 64
3.5 A typical 5-degree Bézier curve. 66
3.6 The posture parameters of the 5-link planar biped. 68
3.7 The nonlinear inequality optimization constraints for the 5-link planar biped. 70
3.8 Optimization process using `fmincon` 71
3.9 The zero dynamics of the 5-link planar biped walking at 0.7m/s . . . 72
3.10 The energy cost curves of the 5-link planar biped and its actuators at different walking speeds. 73
3.11 The optimized postural parameters of the 5-link biped at different speeds. 73
3.12 The step duration and step frequency of the 5-link biped at different speeds. 74
3.13 The stick charts of the 5-link biped walking at various speeds. 74
3.14 The angle curves of joints and outputs of the 5-link planar biped walking at 0.7 m/s and 1.5 m/s. 75
3.15 The angular velocity curves of joints of the 5-link planar biped walking at 0.7 m/s and 1.5 m/s. 75
3.16 The torque curves of the actuated joints of the 5-link planar biped walking at 0.7 m/s and 1.5 m/s. 76
3.17 The mechanical output powers of the actuators of the 5-link planar biped walking at 0.7 m/s and 1.5 m/s (two steps) with solid lines representing stance joint angles, dashed lines representing swing joint angles, and green dashed lines representing the jumps caused by the impact 76

3.18 The ground reaction forces of the 5-link planar biped walking at 0.7 m/s and 1.5 m/s. 77
3.19 The trajectories of the hip and the CoM of the 5-link planar biped walking at 0.7 m/s and 1.5 m/s. 77
3.20 The trajectories of the swing foot of the 5-link planar biped walking at 0.7 m/s and 1.5 m/s. 78

4.1 2D Coupling Cases of the 5-link planar biped. 80
4.2 The swing leg transformed into a compound pendulum. 81
4.3 The relation among the stiffness k_s, the walking speed and the energy cost of the 5-link planar robot for *2D Coupling Case I* 82
4.4 The optimized energy cost curve with optimized k_s and the cost curves with different fixed k_s of the 5-link planar biped for *2D Coupling Case I* 82
4.5 The stick charts of the 5-link planar biped walking at different speeds for *2D Coupling Case I* with different fixed k_s 83
4.6 The stick charts of the 5-link planar biped walking at different speeds for 2D Coupling Case I with $k_s = k_{opt}$ 84
4.7 The energy costs of the actuators of the 5-link planar biped at different walking speeds for 2D Coupling Case I with $k_s = k_{opt}$. 84
4.8 The evolution of posture parameters at different walking speeds of the 5-link planar biped for *2D Coupling Case I* with $k_s = k_{opt}$ 85
4.9 The step frequencies and reference step frequencies of the 5-link planar robot for *2D Coupling Case I* 85
4.10 The angle curves of the joints and outputs of the 5-link planar biped walking at 0.7 m/s and 1.5 m/s for *2D Coupling Case I* with $k_s = k_{opt}$ 86
4.11 The angular velocity curves of the joints of the 5-link planar biped walking at 0.7 m/s and 1.5 m/s for *2D Coupling Case I* with $k_s = k_{opt}$. 87
4.12 The torque curves of the actuated joints and springs of the 5-link planar biped walking at 0.7 m/s and 1.5 m/s for *2D Coupling Case I* with $k_s = k_{opt}$ 87
4.13 The mechanical output powers of the actuators of the 5-link planar biped walking at 0.7 m/s and 1.5 m/s (two steps) for *2D Coupling Case I* with $k_s = k_{opt}$ (Solid lines represents stance joint angles, dashed lines represents swing joint angles, and green dashed lines represents the jumps caused by the impact.) 88
4.14 The ground reaction forces acting on the 5-link planar biped walking at 0.7 m/s and 1.5 m/s during the swing phase for *2D Coupling Case I* with $k_s = k_{opt}$ 88
4.15 The trajectories of the hip and the CoM of the 5-link planar biped walking at 0.7 m/s and 1.5 m/s for *2D Coupling Case I* with $k_s = k_{opt}$. 89
4.16 The trajectories of the swing foot of the 5-link planar biped walking at 0.7 m/s and 1.5 m/s for *2D Coupling Case I* with $k_s = k_{opt}$. 89
4.17 The energy costs of the 5-link planar biped and the actuators at different walking speeds for *2D Coupling Case II* with $k_s = k_{opt}$ and $\varphi_s = \varphi_{opt}$. 90

4.18 The evolution of posture parameters of the 5-link planar biped at different walking speeds for *2D Coupling Case II* with $k_s = k_{opt}$ and $\varphi_s = \varphi_{opt}$. 90
4.19 The stiffness k_s, unloaded position φ_s, step frequency f_{step} and reference step frequency f^*_{step} of the 5-link planar biped for *2D Coupling Case II*. 91
4.20 The stick charts of the 5-link planar biped walking at different speeds for *2D Coupling Case II* with $k_s = k_{opt}$ and $\varphi_s = \varphi_{opt}$. 91
4.21 The angle curves of the joints and outputs of the 5-link planar biped walking at 0.7 m/s and 1.5 m/s for *2D Coupling Case II* with optimized k_s and φ. 92
4.22 The angular velocity curves of the joints of the 5-link planar biped walking at 0.7 m/s and 1.5 m/s for *2D Coupling Case II* with $k_s = k_{opt}$ and $\varphi_s = \varphi_{opt}$. 92
4.23 The torque curves of the joints and springs of the 5-link planar biped walking at 0.7 m/s and 1.5 m/s for *2D Coupling Case II* with $k_s = k_{opt}$ and $\varphi_s = \varphi_{opt}$. 93
4.24 The mechanical output powers of the actuators of the 5-link planar biped walking at 0.7 m/s and 1.5 m/s (two continuous steps) for *2D Coupling Case II* with $k_s = k_{opt}$ and $\varphi_s = \varphi_{opt}$ (Solid lines represents stance joint angles, dashed lines represents swing joint angles, and green dashed lines represents the jumps caused by the impact.) 93
4.25 The ground reaction forces on the 5-link planar biped walking at 0.7 m/s and 1.5 m/s for *2D Coupling Case II* with $k_s = k_{opt}$ and $\varphi_s = \varphi_{opt}$. 94
4.26 The trajectories of the hip and the CoM of the 5-link planar biped at 0.7 m/s and 1.5 m/s for *2D Coupling Case II* with $k_s = k_{opt}$ and $\varphi_s = \varphi_{opt}$. 94
4.27 The trajectories of the swing foot of the 5-link planar biped walking at 0.7 m/s and 1.5 m/s for *2D Coupling Case II* with $k_s = k_{opt}$ and $\varphi_s = \varphi_{opt}$. 94
4.28 The comparisons of the spring stiffness and maximum deflection between *2D Coupling Case I* and *II* 95
4.29 The phase plots of the 5-link planar biped in the three different cases at 0.7 m/s. (Solid lines represent stance joint angles, dashed lines represent swing joint angles, and black arrows represent the jumps caused by the impact.) 97

5.1 The definitions of the joints and links of the 8-link 3D biped. 103
5.2 The generalized coordinates of the 8-link 3D biped with the left foot serving as the stance foot. 104
5.3 The analysis of the swing foot of the 8-link 3D biped at the impact. . 106
5.4 The line-foot contact model of the 8-link 3D biped. 109
5.5 The posture parameters of the 8-link 3D biped with the pelvis marked in red 114

5.6 The inverse kinematics of the 8-link 3D biped. 115
5.7 The starting point ϑ_0 for optimizing the 8-link 3D biped 119
5.8 The stick chart of the 3D biped by directly applying the optimized parameters of the planar biped walking at 1.5m/s. 120
5.9 The ZMP range of the 3D biped by directly applying the optimized parameters of the planar biped walking at 1.5m/s. 120
5.10 The evolution of the zero dynamics of the 8-link 3D biped walking at $0.7m/s$ for *3D Optimization Case I*. 121
5.11 The energy costs of the 8-link 3D biped and its actuators and the percentages of contribution at different speeds for *3D Optimization Case I* 122
5.12 The optimized posture parameters of the 8-link 3D biped at different speeds for *3D Optimization Case I* with the stance ankle being the origin and the sagittal parameters being the same with the parameters shown in Figure 3.11 122
5.13 The step duration and step frequency of the 8-link 3D biped at different speeds for *3D Optimization Case I* 123
5.14 The stick charts of the 8-link 3D biped walking at various speeds for *3D Optimization Case I* 123
5.15 The angle charts of the joints and outputs of the 8-link 3D biped walking at 0.7 m/s and 1.5 m/s for *3D Optimization Case I* 124
5.16 The angular velocity charts of the joints of the 8-link 3D biped walking at 0.7 m/s and 1.5 m/s for *3D Optimization Case I* 125
5.17 The torque charts of the actuators of the 8-link 3D biped walking at 0.7 m/s and 1.5 m/s for *3D Optimization Case I* 125
5.18 The mechanical output powers of the actuators of the 8-link 3D biped walking at 0.7 m/s and 1.5 m/s (two steps) for *3D Optimization Case I* (Dashed lines represent swing joint angles, and green dashed lines represent the jumps caused by the impact. On the left side, solid lines represent stance joint angles.) 126
5.19 The ground reaction forces and torques of the 8-link 3D biped walking at 0.7 m/s and 1.5 m/s for *3D Optimization Case I* 127
5.20 The trajectories of the pelvis center and the CoM of the 8-link 3D biped walking at 0.7 m/s and 1.5 m/s for *3D Optimization Case I*. . . 127
5.21 The trajectories of the swing ankle and the footprint of the 8-link 3D biped walking at 0.7 m/s and 1.5 m/s for *3D Optimization Case I* . . 128
5.22 The energy costs of the 8-link 3D biped and its actuators and the percentages of contribution at different speeds for *3D Optimization Case II* 129
5.23 The optimized posture parameters of the 8-link 3D biped at different speeds for *3D Optimization Case II* with the stance ankle being the origin. 129
5.24 The step duration and step frequency of the 8-link 3D biped at different speeds for *3D Optimization Case II* 130

5.25 The stick charts of the 8-link 3D biped walking at various speeds for *3D Optimization Case II* 130
5.26 The angle charts of the joints and outputs of the 8-link 3D biped walking at 0.7 m/s and 1.5 m/s for *3D Optimization Case II* 131
5.27 The angular velocity charts of the joints of the 8-link 3D biped walking at 0.7 m/s and 1.5 m/s for *3D Optimization Case II* 132
5.28 The torque charts of the actuators of the 8-link 3D biped walking at 0.7 m/s and 1.5 m/s for *3D Optimization Case II* 132
5.29 The mechanical output powers of the actuators of the 8-link 3D biped walking at 0.7 m/s and 1.5 m/s (two steps) for *3D Optimization Case II* (Dashed lines represent swing joint angles, and green dashed lines represent the jumps caused by the impact. On the left side, solid lines represent stance joint angles.) 133
5.30 The ground reaction forces, torques and the ZMP curves of the 8-link 3D biped walking at 0.7 m/s and 1.5 m/s for *3D Optimization Case II* 134
5.31 The trajectories of the pelvis center and the CoM of the 8-link 3D biped walking at 0.7 m/s and 1.5 m/s for *3D Optimization Case II* . . 134
5.32 The trajectories of the swing ankle and the footprint of the 8-link 3D biped walking at 0.7 m/s and 1.5 m/s for *3D Optimization Case II* . 135

6.1 Coupling cases of the 8-link 3D biped 138
6.2 The energy costs and percentages of contribution of the 8-link 3D biped and its actuators at different speeds for *3D Coupling Case I* . . 139
6.3 The optimized posture parameters of the 8-link 3D biped at different speeds for *3D Coupling Case I* with the stance ankle being the origin. 140
6.4 The step frequency and the spring stiffness of the 8-link 3D biped at different speeds for *3D Coupling Case I*. 140
6.5 The stick charts of the 8-link 3D biped walking at various speeds for *3D Coupling Case I* 141
6.6 The angle charts of the joints and output variables of the 8-link 3D biped walking at 0.7 m/s and 1.5 m/s for *3D Coupling Case I* 141
6.7 The angular velocity charts of the joints of the 8-link 3D biped walking at 0.7 m/s and 1.5 m/s for *3D Coupling Case I* 142
6.8 The torque charts of the actuators of the 8-link 3D biped walking at 0.7 m/s and 1.5 m/s for *3D Coupling Case I* 142
6.9 The mechanical output powers of the actuators of the 8-link 3D biped walking at 0.7 m/s and 1.5 m/s (two steps) for *3D Coupling Case I* (Dashed lines represent swing joint angles, and green dashed lines represent the jumps caused by the impact. On the left side, solid lines represent stance joint angles.) 143
6.10 The ground reaction forces and torques of the 8-link 3D biped walking at 0.7 m/s and 1.5 m/s for *3D Coupling Case I* 144
6.11 The trajectories of the pelvis center and the CoM of the 8-link 3D biped walking at 0.7 m/s and 1.5 m/s for *3D Coupling Case I* 144

6.12 The trajectories of the swing ankle and the footprint of the 8-link 3D biped walking at 0.7 m/s and 1.5 m/s for *3D Coupling Case I* 145
6.13 The energy costs of the 8-link 3D biped and its actuators at different speeds for *3D Coupling Case II* 146
6.14 The optimized posture parameters of the 8-link 3D biped at different speeds for *3D Coupling Case II* with the stance ankle being the origin 146
6.15 The step frequency and the spring stiffness of the 8-link 3D biped at different speeds for *3D Coupling Case II* 147
6.16 The stick charts of the 8-link 3D biped walking at various speeds for *3D Coupling Case II* 147
6.17 The angle charts of the joints and output variables of the 8-link 3D biped walking at 0.7 m/s and 1.5 m/s for *3D Coupling Case II* 148
6.18 The angular velocity charts of the joints of the 8-link 3D biped walking at 0.7 m/s and 1.5 m/s for *3D Coupling Case II* 149
6.19 The torque charts of the actuators of the 8-link 3D biped walking at 0.7 m/s and 1.5 m/s for *3D Coupling Case II* 149
6.20 The mechanical output powers of the actuators of the 8-link 3D biped walking at 0.7 m/s and 1.5 m/s (two steps) for *3D Coupling Case II* (Dashed lines represent swing joint angles, and green dashed lines represent the jumps caused by the impact. On the left side, solid lines represent stance joint angles.) 150
6.21 The ground reaction forces and torques of the 8-link 3D biped walking at 0.7 m/s and 1.5 m/s for *3D Coupling Case II* 151
6.22 The trajectories of the pelvis center and the CoM of the 8-link 3D biped walking at 0.7 m/s and 1.5 m/s for *3D Coupling Case II* 151
6.23 The trajectories of the swing ankle and the footprint of the 8-link 3D biped walking at 0.7 m/s and 1.5 m/s for *3D Coupling Case II* 152
6.24 The energy costs and percentages of contribution of the 8-link 3D biped and its actuators at different speeds for *3D Coupling Case III* . 153
6.25 The optimized posture parameters of the 8-link 3D biped at different speeds for *3D Coupling Case III* with the stance ankle being the origin 153
6.26 The step frequency and the spring stiffness of the 8-link 3D biped at different speeds for *3D Coupling Case III* 154
6.27 The stick charts of the 8-link 3D biped walking at various speeds for *3D Coupling Case III* 154
6.28 The angle charts of the joints and output variables of the 8-link 3D biped walking at 0.7 m/s and 1.5 m/s for *3D Coupling Case III* 155
6.29 The angular velocity charts of the joints of the 8-link 3D biped walking at 0.7 m/s and 1.5 m/s for *3D Coupling Case III* 156
6.30 The torque charts of the actuators of the 8-link 3D biped walking at 0.7 m/s and 1.5 m/s for *3D Coupling Case III* 156

6.31 The mechanical output powers of the actuators of the 8-link 3D biped walking at 0.7 m/s and 1.5 m/s (two steps) for *3D Coupling Case III* (Dashed lines represent swing joint angles, and green dashed lines represent the jumps caused by the impact. On the left side, solid lines represent stance joint angles.) 157
6.32 The ground reaction forces and torques of the 8-link 3D biped walking at 0.7 m/s and 1.5 m/s for *3D Coupling Case III* 158
6.33 The trajectories of the pelvis center and the CoM of the 8-link 3D biped walking at 0.7 m/s and 1.5 m/s for *3D Coupling Case III* 159
6.34 The trajectories of the swing ankle and the footprint of the 8-link 3D biped walking at 0.7 m/s and 1.5 m/s for *3D Coupling Case III* 159
6.35 The phase plots of the 8-link 3D biped in three different cases at 0.7 m/s (Solid lines represent stance joint angles except for the lumber joint, dashed lines represent swing joint angles, and black arrows represent the jumps caused by the impact. Note that the evolution of the swing ankle during the step is unknown.) 161

A.1 The angle curves of joints and outputs of the 5-link planar biped walking at $0.3\,m/s$ and $1.1\,m/s$. 225
A.2 The angular velocity curves of joints of the 5-link planar biped walking at $0.3\,m/s$ and $1.1\,m/s$. 225
A.3 The torque curves of the actuated joints of the 5-link planar biped walking at $0.3\,m/s$ and $1.1\,m/s$. 226
A.4 The mechanical output powers of the actuators of the 5-link planar biped walking at $0.3\,m/s$ and $1.1\,m/s$ (two steps) with solid lines representing stance joint angles, dashed lines representing swing joint angles, and green dashed lines representing the jumps caused by the impact 226
A.5 The ground reaction forces of the 5-link planar biped walking at $0.3\,m/s$ and $1.1\,m/s$. 227
A.6 The trajectories of the hip and the CoM of the 5-link planar biped walking at $0.3\,m/s$ and $1.1\,m/s$. 227
A.7 The trajectories of the swing foot of the 5-link planar biped walking at $0.3\,m/s$ and $1.1\,m/s$. 227

B.1 The angle curves of the joints and outputs of the 5-link planar biped walking at $0.3\,m/s$ and $1.1\,m/s$ for *2D Coupling Case I* with $k_s = k_{opt}$ 229
B.2 The angular velocity curves of the joints of the 5-link planar biped walking at $0.3\,m/s$ and $1.1\,m/s$ for *2D Coupling Case I* with $k_s = k_{opt}$.230
B.3 The torque curves of the actuated joints and springs of the 5-link planar biped walking at $0.3\,m/s$ and $1.1\,m/s$ for *2D Coupling Case I* with $k_s = k_{opt}$ 230

B.4 The mechanical output powers of the actuators of the 5-link planar biped walking at $0.3\,m/s$ and $1.1\,m/s$ (two steps) for *2D Coupling Case I* with $k_s = k_{opt}$ (Solid lines represent stance joint angles, dashed lines represent swing joint angles, and green dashed lines represent the jumps caused by the impact.) 231
B.5 The ground reaction forces acting on the 5-link planar biped walking at $0.3\,m/s$ and $1.1\,m/s$ during the swing phase for *2D Coupling Case I* with $k_s = k_{opt}$ 231
B.6 The trajectories of the hip and the CoM of the 5-link planar biped walking at $0.3\,m/s$ and $1.1\,m/s$ for *2D Coupling Case I* with $k_s = k_{opt}$. 232
B.7 The trajectories of the swing foot of the 5-link planar biped walking at $0.3\,m/s$ and $1.1\,m/s$ for *2D Coupling Case I* with $k_s = k_{opt}$. 232
B.8 The angle curves of the joints and outputs of the 5-link planar biped walking at $0.3\,m/s$ and $1.1\,m/s$ for *2D Coupling Case II* with optimized k_s and φ. 233
B.9 The angular velocity curves of the joints of the 5-link planar biped walking at $0.3\,m/s$ and $1.1\,m/s$ for *2D Coupling Case II* with $k_s = k_{opt}$ and $\varphi_s = \varphi_{opt}$. 233
B.10 The torque curves of the joints and springs of the 5-link planar biped walking at $0.3\,m/s$ and $1.1\,m/s$ for *2D Coupling Case II* with $k_s = k_{opt}$ and $\varphi_s = \varphi_{opt}$. 234
B.11 The mechanical output powers of the actuators of the 5-link planar biped walking at $0.3\,m/s$ and $1.1\,m/s$ (two continuous steps) for *2D Coupling Case II* with $k_s = k_{opt}$ and $\varphi_s = \varphi_{opt}$ (Solid lines represent stance joint angles, dashed lines represent swing joint angles, and green dashed lines represent the jumps caused by the impact.) 234
B.12 The ground reaction forces on the 5-link planar biped walking at $0.3\,m/s$ and $1.1\,m/s$ for *2D Coupling Case II* with $k_s = k_{opt}$ and $\varphi_s = \varphi_{opt}$. 235
B.13 The trajectories of the hip and the CoM of the 5-link planar biped at $0.3\,m/s$ and $1.1\,m/s$ for *2D Coupling Case II* with $k_s = k_{opt}$ and $\varphi_s = \varphi_{opt}$. 235
B.14 The trajectories of the swing foot of the 5-link planar biped walking at $0.3\,m/s$ and $1.1\,m/s$ for *2D Coupling Case II* with $k_s = k_{opt}$ and $\varphi_s = \varphi_{opt}$. 235

C.1 The angle charts of the joints and outputs of the 8-link 3D biped walking at $0.3\,m/s$ and $1.1\,m/s$ for *3D Optimization Case I* 237
C.2 The angular velocity charts of the joints of the 8-link 3D biped walking at $0.3\,m/s$ and $1.1\,m/s$ for *3D Optimization Case I* 238
C.3 The torque charts of the actuators of the 8-link 3D biped walking at $0.3\,m/s$ and $1.1\,m/s$ for *3D Optimization Case I* 238

C.4 The mechanical output powers of the actuators of the 8-link 3D biped walking at $0.3\,m/s$ and $1.1\,m/s$ (two steps) for *3D Optimization Case I* (Dashed lines represent swing joint angles, and green dashed lines represent the jumps caused by the impact. On the left side, solid lines represent stance joint angles.) 239
C.5 The ground reaction forces and torques of the 8-link 3D biped walking at $0.3\,m/s$ and $1.1\,m/s$ for *3D Optimization Case I* 240
C.6 The trajectories of the pelvis center and the CoM of the 8-link 3D biped walking at $0.3\,m/s$ and $1.1\,m/s$ for *3D Optimization Case I*. . . 240
C.7 The trajectories of the swing ankle and the footprint of the 8-link 3D biped walking at $0.3\,m/s$ and $1.1\,m/s$ for *3D Optimization Case I* . . 241
C.8 The angle charts of the joints and outputs of the 8-link 3D biped walking at $0.3\,m/s$ and $1.1\,m/s$ for *3D Optimization Case II* 241
C.9 The angular velocity charts of the joints of the 8-link 3D biped walking at $0.3\,m/s$ and $1.1\,m/s$ for *3D Optimization Case II* 242
C.10 The torque charts of the actuators of the 8-link 3D biped walking at $0.3\,m/s$ and $1.1\,m/s$ for *3D Optimization Case II* 242
C.11 The mechanical output powers of the actuators of the 8-link 3D biped walking at $0.3\,m/s$ and $1.1\,m/s$ (two steps) for *3D Optimization Case II* (Dashed lines represent swing joint angles, and green dashed lines represent the jumps caused by the impact. On the left side, solid lines represent stance joint angles.) 243
C.12 The ground reaction forces and torques of the 8-link 3D biped walking at $0.3\,m/s$ and $1.1\,m/s$ for *3D Optimization Case II* 244
C.13 The trajectories of the pelvis center and the CoM of the 8-link 3D biped walking at $0.3\,m/s$ and $1.1\,m/s$ for *3D Optimization Case II*. . 244
C.14 The trajectories of the swing ankle and the footprint of the 8-link 3D biped walking at $0.3\,m/s$ and $1.1\,m/s$ for *3D Optimization Case II* . 245

D.1 The angle charts of the joints and output variables of the 8-link 3D biped walking at $0.3\,m/s$ and $1.1\,m/s$ for *3D Coupling Case I* 247
D.2 The angular velocity charts of the joints of the 8-link 3D biped walking at $0.3\,m/s$ and $1.1\,m/s$ for *3D Coupling Case I* 248
D.3 The torque charts of the actuators of the 8-link 3D biped walking at $0.3\,m/s$ and $1.1\,m/s$ for *3D Coupling Case I* 248
D.4 The mechanical output powers of the actuators of the 8-link 3D biped walking at $0.3\,m/s$ and $1.1\,m/s$ (two steps) for *3D Coupling Case I* (Dashed lines represent swing joint angles, and green dashed lines represent the jumps caused by the impact. On the left side, solid lines represent stance joint angles.) 249
D.5 The ground reaction forces and torques of the 8-link 3D biped walking at $0.3\,m/s$ and $1.1\,m/s$ for *3D Coupling Case I* 250
D.6 The trajectories of the pelvis center and the CoM of the 8-link 3D biped walking at $0.3m/s$ and $1.1m/s$ for *3D Coupling Case I* 250

D.7 The trajectories of the swing ankle and the footprint of the 8-link 3D biped walking at $0.3\,m/s$ and $1.1\,m/s$ for *3D Coupling Case I* 251
D.8 The angle charts of the joints and output variables of the 8-link 3D biped walking at $0.3\,m/s$ and $1.1\,m/s$ for *3D Coupling Case II* 251
D.9 The angular velocity charts of the joints of the 8-link 3D biped walking at $0.3\,m/s$ and $1.1\,m/s$ for *3D Coupling Case II* 252
D.10 The torque charts of the actuators of the 8-link 3D biped walking at $0.3\,m/s$ and $1.1\,m/s$ for *3D Coupling Case II* 252
D.11 The mechanical output powers of the actuators of the 8-link 3D biped walking at $0.3\,m/s$ and $1.1\,m/s$ (two steps) for *3D Coupling Case II* (Dashed lines represent swing joint angles, and green dashed lines represent the jumps caused by the impact. On the left side, solid lines represent stance joint angles.) 253
D.12 The ground reaction forces and torques of the 8-link 3D biped walking at $0.3\,m/s$ and $1.1\,m/s$ for *3D Coupling Case II* 254
D.13 The trajectories of the pelvis center and the CoM of the 8-link 3D biped walking at $0.3\,m/s$ and $1.1\,m/s$ for *3D Coupling Case II* 254
D.14 The trajectories of the swing ankle and the footprint of the 8-link 3D biped walking at $0.3\,m/s$ and $1.1\,m/s$ for *3D Coupling Case II* 255
D.15 The angle charts of the joints and output variables of the 8-link 3D biped walking at $0.3\,m/s$ and $1.1\,m/s$ for *3D Coupling Case III* . . . 255
D.16 The angular velocity charts of the joints of the 8-link 3D biped walking at $0.3\,m/s$ and $1.1\,m/s$ for *3D Coupling Case III* 256
D.17 The torque charts of the actuators of the 8-link 3D biped walking at $0.3\,m/s$ and $1.1\,m/s$ for *3D Coupling Case III* 256
D.18 The mechanical output powers of the actuators of the 8-link 3D biped walking at $0.3\,m/s$ and $1.1\,m/s$ (two steps) for *3D Coupling Case III* (Dashed lines represent swing joint angles, and green dashed lines represent the jumps caused by the impact. On the left side, solid lines represent stance joint angles.) 257
D.19 The ground reaction forces and torques of the 8-link 3D biped walking at $0.3\,m/s$ and $1.1\,m/s$ for *3D Coupling Case III* 258
D.20 The trajectories of the pelvis center and the CoM of the 8-link 3D biped walking at $0.3\,m/s$ and $1.1\,m/s$ for *3D Coupling Case III* . . . 258
D.21 The trajectories of the swing ankle and the footprint of the 8-link 3D biped walking at $0.3\,m/s$ and $1.1\,m/s$ for *3D Coupling Case III* . . . 259

LIST OF TABLES

3.1 Model Parameters of the 5-link planar robot 57

5.1 The model parameters for the 8-link 3D biped. 103

ACKNOWLEDGEMENT

> Thank the flame for its light, but do not forget the lampholder standing in the shade with constancy of patience.
>
> Rabindranath Tagore

I am glad and relieved that this PhD project has finally come to fruition. Frankly, this thesis would not have been possible without the guidance and the help of several individuals to whom I owe a great debt of gratitude.

First and foremost, my utmost gratitude to my thesis director Dr. Gabriel Abba. If it were not for his timely help, I would not have been able to submit my CSC scholarship documents on time. I am also grateful for his constructive advises that illuminates my research directions in times of difficulty.

I would also like to express my gratitude to my thesis co-director Dr. Nafissa Lakbakbi Elyaaqoubi for her patience and kindness in proofreading this manuscript and helping me prepare my thesis defense.

Besides my advisor, I would like to thank the rest of my thesis committee: Dr. Pierre Riedinger, Dr. Christine Chevallereau, Dr. Jessy W. Grizzle and Dr. Philippe Fraisse for their encouragement, insightful comments, and hard questions. Dr. Christine Chevallereau has helped me a lot ever since the beginning of this research work. There are no words to express my gratitude. Dr. Philippe Fraisse has proposed to cooperate in testing my control methods and configurations of elastic couplings on the real humanoid robot HOAP. I am very grateful for this proposal.

I am thankful to Dr. Fabian Bauer, Dr. Ryan Sinnet and Dr. Robert D. Gregg for the precious insights concerning the SQP algorithm and the Routhian reduction.

My sincere thanks also goes to the China Scholarship Council (CSC) for the PhD scholarship, without which I would not obtain the PhD degree in France.

I take this opportunity to record my sincere gratitude to my fellow labmates in the LCFC: Jinna Qin, Guochao Gu, Thanh Hung Nguyen, Mathieu Hobon, Simon Jung, Fan Li, Catalina Gutierrez, Bruno Kaici, Philippe Mayer, François Cristofari, Peng Wang, Ke Wang, Qing Xia, Jianjie Zhang, for the stimulating discussions and for all the fun we have had in the last three years. Jinna Qin, Guochao Gu and Thanh Hung Nguyen were very supportive in helping me adapt to life in France with limited knowledge of French. Catalina Gutierrez, Bruno Kaici, Philippe Mayer and François Cristofari showed me the rhythm and excitement of working in France. Fan Li is a living manual of "A Chinese student in France", and he speaks French better than me. He and Peng Wang, Qing Xia, Jianjie Zhang prepared the traditional buffet after my thesis defense.

I am indebted to my friends of the Metz-Borny church: Mrs. Cardon, Mrs. Levalois, Mr. Sabot, Mr. and Mrs. Vanzo, Mr. and Mrs. Leuba, Mr. and Mrs. Fernandes, Mr. and Mrs. Gustin, Mr. and Mrs. Gentner and the others, for helping me overcome the language barrier and teaching me the culture of France and Christianity.

I also thank my other young friends in France: Sandrine Meyer, Emmy Dreyfuss, Jonathan Fleurent, Marie-Hélène Dintinger, Diego Ippolito, Olivier Igout, Chloé Jupiter, Damaris Jupiter, David Brázda, David Ferris, Samuel Genay, Josué Rinder, Shizhe Yu and the others for filling my leisure time with fun and laughter and sharing precious moments together.

Last but not the least, I would like to thank my family: my parents Peiling Jiang and Huafang Chen and my sister Xiao Chen for supporting me spiritually throughout my life.

1. INTRODUCTION

> The artisan who wants to do his work
> well must first of all sharpen his tools.
>
> Confucius

1.1 Motivation

Like other legged robots, bipedal robots have the potential to outperform wheeled machines in coping with complex terrains. In addition, according to some biology studies, the efficiency of bipedalism is superior to any other forms of legged locomotion, which allows our ancestors to hunt animals in a long "marathon" [1]. However, compared with human beings, most actuated bipedal robots are energy inefficient. This greatly limited the potential applications of bipedal robots, and up till now no full-size bipedal robots have been mass produced for purposes other than entertainment, advertising, or education. As such, it is of great importance to study optimal gaits, mechanical configurations and control methods that can improve the status quo of bipedal robotics.

A previous PhD project from Hobon [2] concerns the gait optimization of a 7-link planar bipedal robot composed of a torso, two thighs, two shins and two feet. This robot model is featured with rolling knees similar to human knees, and the simulation results have demonstrated the advantages of having such knees over traditional cylindrical knees [3, 4]. Based on the experience gathered from optimizing this 7-link robot, the initial goal of this PhD project is threefold: (1) to include more DOFs, bodies and structures in a bipedal robot model; (2) to study optimal gaits in 3D space with corresponding control methods; and (3) to study relations between the optimization results from planar bipeds and 3D bipeds.

The research topic of this thesis has drawn inspiration from the optimization and experiment results about the French planar bipedal robot RABBIT in Grenoble [5] as well as the pioneering work in [6, 7]. This robot is purposefully underactuated (point feet) so that the ZMP principle does not apply. The control of this robot is realized based on feedback linearization and hybrid zero dynamics [8]. The experiment [5] and optimization [8] results have demonstrated great potential in achieving dynamic walking with these methods. Since optimization results concerning underactuated bipeds in 3D space are relatively rare, we are determined to incorporate the idea in studying optimal gaits of our 3D biped.

1.2 Current Developments of Bipedal Robots

The idea of designing bionic machines has a fascinating history that dates back thousands of years. Ancient machines such as the mechanical knight designed by Leonardo da Vinci around the year 1495 and the mysterious wooden ox created by Zhuge Liang in 231 have intrigued many historians and craftsmen generation after generation. Nevertheless, these early attempts were all limited by low technological capability before the industrial revolution. The modern history of bipedal robotics started in late 1960s, and the major achievements have come from three continents: Asia, North America and Europe.

1.2.1 Bipedal Robots in Asia

In Asia, Ichiro Kato and his team pioneered the study of bipedal robotics at Waseda University with the robot WL-1 in 1967. Two years later, they created the bipedal robot WL-3, which is capable of providing some human-like motions in both the swing phase and the stance phase. The first climax came in 1973 when the world's first full-scale anthropomorphic robot WABOT-1 was created at Waseda. Like many early bipedal robots, this hydraulically powered robot also has disproportionately large feet for stability considerations, but it is still able to walk several steps in slow static equilibrium [9]. At that period, people usually evaluate the performance of bipedal robots by how long they take to complete a single step. For instance, the robot WL-5, which is used as the lower limbs of WABOT-1, needs 45 seconds to walk a single step, while the later version WL10-RD managed to reduce this number substantially to 1.3 seconds [10]. The latest bipedal robot from Waseda is WABIAN-2, which has 41 DOFs and the joints designed in reference to human ones. In addition, this robot is also known for its bionic feet featured with passive toe joints and human-like arches [11, 12].

Apart from Waseda University, Japanese companies like Honda and Kawada Industries are equally renowned for their cutting-edge bipedal robots. Honda started developing humanoid robots in 1986, and after E-series (E0-E6) and P-series (P1-P4), they successfully increased walking speed from 0.07 m/s to 0.44 m/s by the world famous humanoid robot ASIMO with 34 DOFs [13], which is well recognized for being the first humanoid robot capable of walking and running autonomously. The latest version of ASIMO is able to walk at 0.75 m/s and run at 2.5 m/s. During this evolution process from E0 to ASIMO, the P2 biped was also worth mentioning for being the world's first self-regulating biped with three types of controllers respectively responsible for ground reaction force control, ZMP control and foot landing position control [14]. Kawada started their activities in robotics in 1997 with the humanoid robot H6. In 2000, Kawada was awarded the contract of the Humanoid Robotics Project (HRP) funded by Japanese government for development of general domestic helper robots [15]. In the following years, they successively developed HRP-2 (30 DOFs) [16, 17, 18], HRP-3 (36 DOFs) [19] and HRP-4 (42 DOFs) [20]. The important features of HRP-2 include collision avoidance [21], running capability [18] and the ability to lie down and get up [16]. HRP-4 is featured with lightweight

(39kg for a height of 1.80m) and slim body [20] and the capability to updating walking trajectories according to external disturbances [22].

Despite Japan's leading position of bipedal robotics research, other Asian countries like Korea and China have been catching up over the past few years. In Korea, the research in bipedal robotics engineering has accelerated since 2000 under the leadership of Korea Advanced Institute of Science and Technology (KAIST). After the prototypes KHR-0 to KHR-2, the complete humanoid robot KHR-3 was built in 2005. This robot is named Hubo, and its improved version Jaemi HUBO (KHR-4) with capabilities of walking at 0.42 m/s and running 1 m/s was unveiled in 2008 [23]. In China, the Beijing Institute of Technology recently has developed three different models of the BHR (Beijing Humanoid Robot). One of them is the BHR-2 [24], which stands 158cm tall and features 32 degrees of freedom and capability to perform Chinese martial arts.

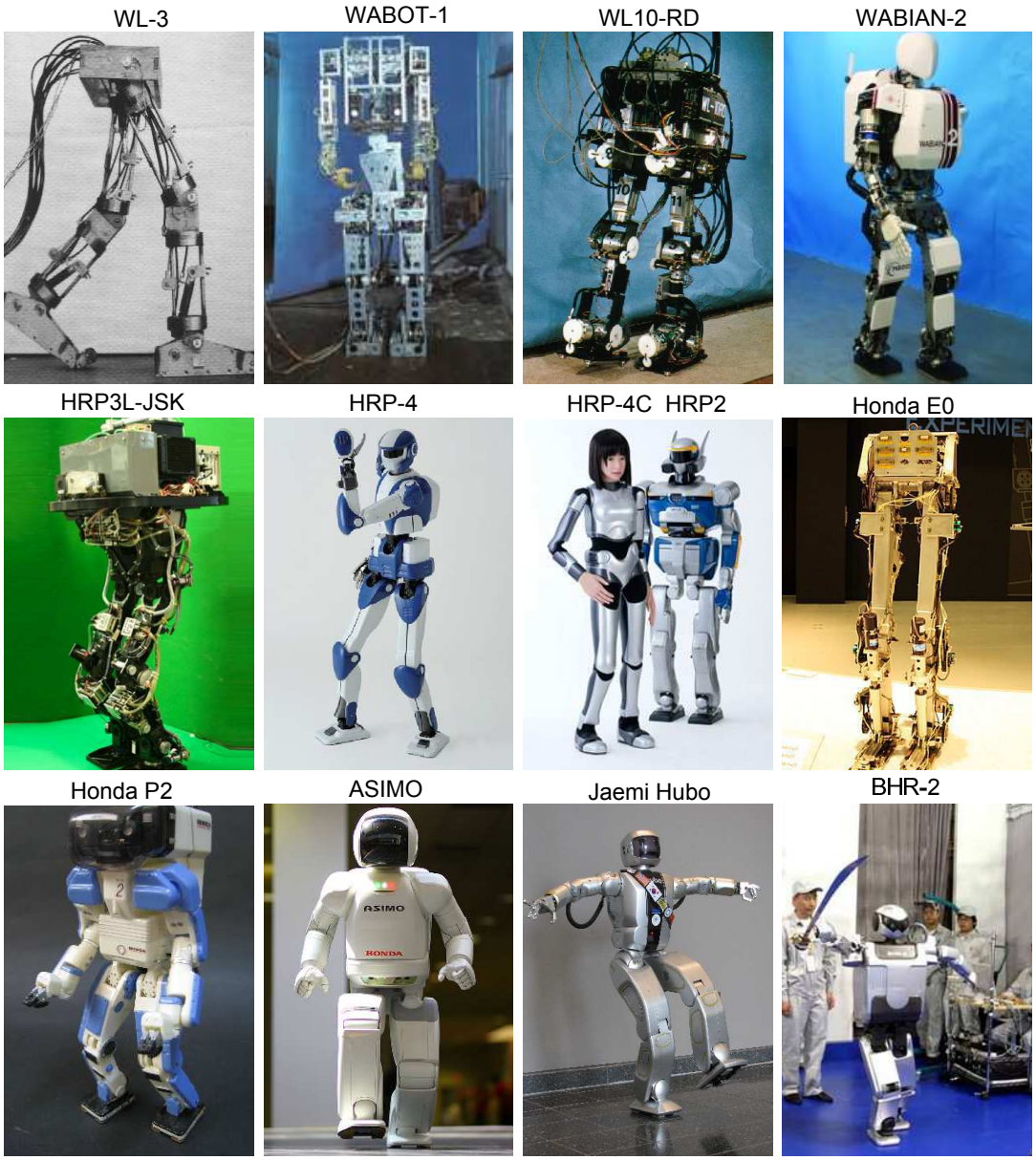

Fig. 1.1: Asian bipedal robots.

1.2.2 Bipedal Robots in Europe

Unlike Asia, Europe has many countries participating in research projects of bipedal robots. Here we list some special bipedal robots from these projects. Developed in Germany, the robot LOLA, with the walking speed exceeding 0.83 m/s, might be the most impressive humanoid robot in Europe. The distinguishing characteristics of LOLA include the redundant kinematic structure with 7-DOF legs, the extremely lightweight construction (55kg for a height of 1.80m) and the modular joint design using brushless motors [25]. The DLR-Biped walker is also an interesting bipedal robot in Germany. Designed for providing domestic services, this robot differentiate itself from competitors for its multi-task balancing control [26] and torque controlled joints [27]. In France, Nao is surely the best-known and most influential humanoid robot, and it has a large variety of sensors such as ultrasonic sensors and directional microphones integrated in a 58 cm height body. Despite its limited height, it has also been used in studying walking motions [28]. As for full scaled bipedal robots, the BIP-2000 [29] is also noteworthy because of its anthropomorphic structure and screw-nuts with satellite rollers transmitters [30]. From a research point of view, the 5-link planar bipedal robot RABBIT developed in Grenoble has undoubtedly an important position in the history of bipedal robots. As an underactuated biped with point feet, this robot is capable of walking at 1.0 m/s under the controller based on hybrid zero dynamics and virtual constraints, which is fundamentally different from ZMP-based control methods [5]. In addition this robot is also capable of achieving periodic steps with asymptotic stability.

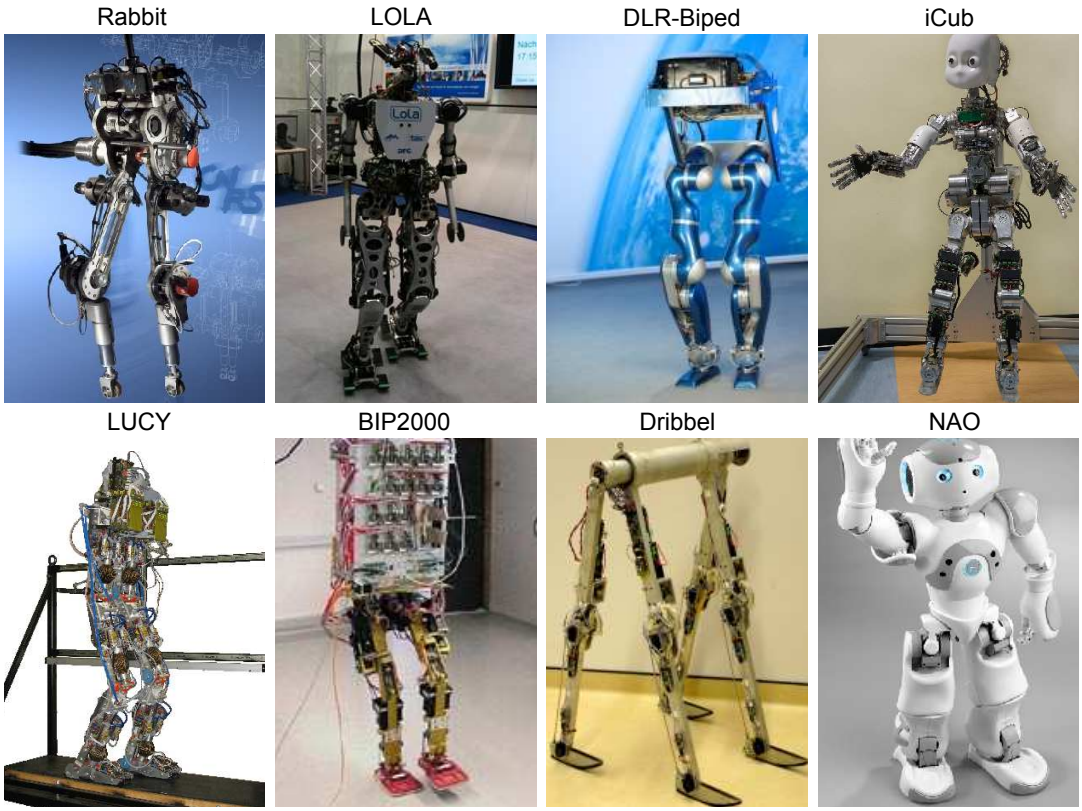

Fig. 1.2: European bipedal robots.

Other interesting European bipedal robots are: the Italian robot iCub (featured with open-source software and cognitive power) [31, 32], the Belgian robot LUCY (featured with pneumatic artificial muscles) [33], the Dutch robot Dribbel (featured with energy efficient knee locking mechanism).

1.2.3 *Bipedal Robots in North America*

In North America, Marc Raibert is the first scientist who bring about a remarkable breakthrough in legged robotics. He designed a sequence of active hopping robots, with one, two or four legs with impressive results, and the bipedal version built in 1989 can even perform a flip [34]. In 1990s, McGeer undertook another pioneering work to design passive bipedal robots. Beginning from designing passive compass robots, he managed to realize a passive bipedal robot with knees [35]. In addition, he also popularized the application of Poincaré maps in analyzing orbital stability among roboticists. Following this track, Steven H. Collins and his team successfully developed a 3D passive biped by attaching counter-swinging arms rigidly to their opposing legs [36].

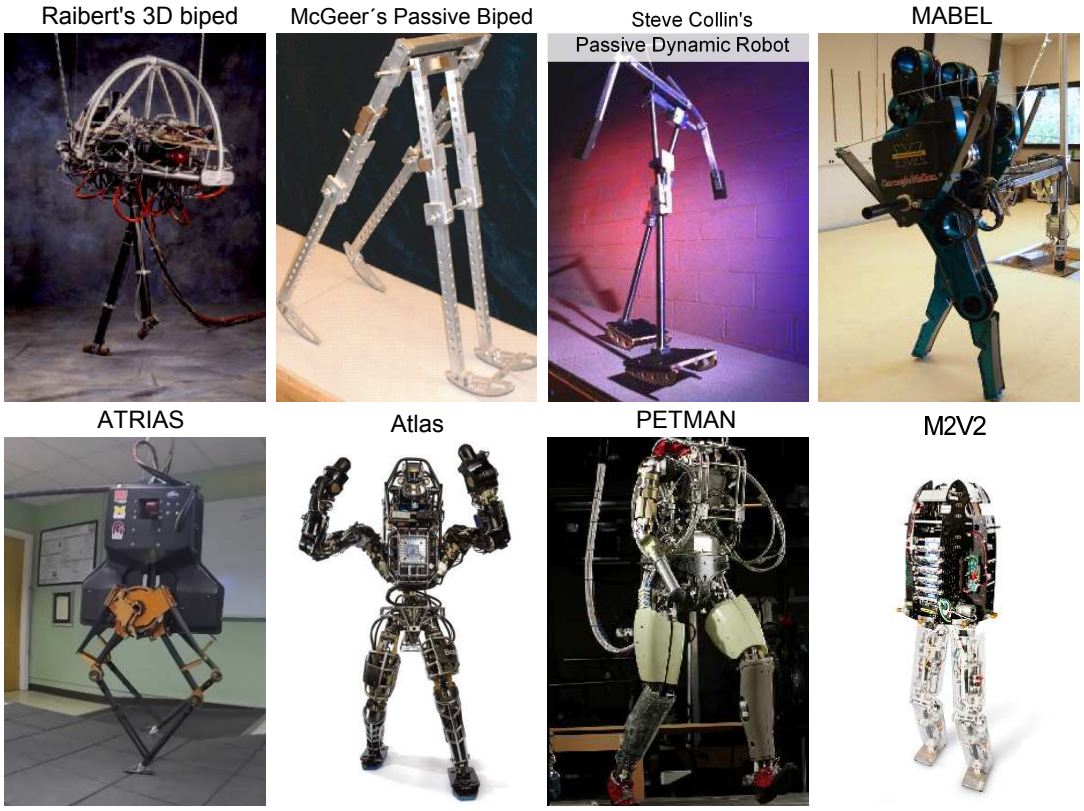

Fig. 1.3: Bipedal robots in North America.

In the past decade, more researchers have been participating in designing innovative bipedal robots. Following the planar biped RABBIT in France, MABEL and ATRIAS are respectively designed and realized at University of Michigan and Oregon State University. MABEL is still a planar biped, but it can run at 3 m/s continuously and has additional elastic components [37, 38]. ATRIAS is a prototype underactuated human-scale bipedal robot that can walk and run in 3D space

[39, 40]. Based on the idea of capture point, the bipedal robot M2V2 is also worth mentioning for its straight-legged gait and push recovery capability [41, 42]. Last but not least, Boston Dynamics, the famous company known for the development of the quadruped robot BigDog, have also in recent years built PETMAN and Atlas, and both of them have impressive balancing ability [43].

1.3 Control Approaches in Bipedal Walking

Despite years of research with various perspectives from passive walkers with simple mechanical designs to sophisticated multifunctional humanoids, the study of bipedal walking is still a challenging task questioning from time to time our capabilities of truly reproducing nature for the benefit of human beings. Generally speaking, the control problem of bipedal robots stands out from classical control problems in our textbooks mainly because of two inherent characteristics of bipedal locomotion: limited foot-ground interaction and discretely changing dynamics. In order to tackle these challenges, researchers have mainly worked on three types of walking: (1) actuated quasi-static walking, (2) unactuated/actuator-assisted dynamic walking, and (3) actuated dynamic walking. This classification might not be exhaustive, and boundaries among these three types might not be decisive either, but it nevertheless represent some of the dominant research directions of bipedal walking.

1.3.1 Actuated Quasi-Static Walking

Many sophisticated humanoid robots nowadays such as HRP-4 [20] and Honda ASIMO [13] have entertained people with their extensive integration of cutting-edge technologies and amazing built-in artificial intelligence, but fundamentally, the bipedal walking that they have so far demonstrated is not quite dynamic, especially when compared with human walking. Rather, the nature dynamics of these robots is overridden by "quasi-static" equilibrium conditions based on the zero moment point (ZMP) [44]. The ZMP condition states that as long as the ZMP of a robot remains strictly within the support convex hull of the ground contact area, then the robot cannot fall by tipping over a point or edge on the boundary of the support convex hull. For researchers studying quasi-static walking, this condition should always be respected, despite the fact for dynamic walking the ZMP condition is usually violated for some portion of the step cycle (think about the motion of heel strike in human walking).

Owing to its simplicity, the ZMP has inspired several variants including the FRI (Foot Rotation Index) [45] and the CoP (Center of Pressure) [46]. Based on the quasi-static ZMP criterion, the corresponding control strategies can achieve walking by planning the motion of a biped's CoM (Center of Mass) such that the ZMP remains strictly within the convex hull of the ground contact area and then idealizing the contact of the bipedal robot with the ground as a rigid connection to implement various trajectory tracking techniques. Therefore, this method is highly dependent on the measurement precision of a biped's CoM, of which a recent study concerning statically equivalent serial chains can be found in [47].

Historically, the ZMP condition is also closely related to several simplifications based on inverted pendulum models concerning the control of a biped's CoM. Among these simplifications, the first and perhaps most simple one is the Linear Inverted Pendulum Model (LIPM), where the ZMP can be expressed explicitly via a linear ordinary differential equation related to the dynamics of the robot's CoM. This simplification of bipedal robot models requires some assumptions including representing a robot as a point mass with massless telescopic legs. Besides, the height of the CoM is also assumed constant throughout a step [48]. Historically, the ZMP control method and the LIPM have been tightly combined, and the benefit of this combination is that the researchers can save a lot of troubles in learning nonlinear control theory and can conduct experiments about human-robot interaction, anthropomorphic hardware and online gait synthesis in a heuristic fashion. The widespread successful examples in implementing this method include HRP-4 [20], ASIMO [13], LOLA [25], BIP-2000 [29], Hubo [23], BHR-2 [24] and so on. Despite these remarkable progresses, the inherent limitations in adopting this simplification becomes more and more recognized. Apart from impinging energy efficiency with unnatural shuffling motions and flexed knees [49], gaits designed using this method often involves many trials, and successes on one robot might not be fully transferable to another. Besides, impacts are generally neglected in this method, and thus the swing foot is required to impact the ground with minimal velocity, which is hard to achieve on rough terrain. Furthermore, from the standpoint of control theory, meeting the ZMP condition is not sufficient for asymptotic stability of a periodic walking motion [50].

In order to counterbalance the limitations of the LIPM model, roboticists have many several variants of inverted pendulum models. In the Gravity Compensated LIPM [51], an additional point mass is added to the swing foot for improving modeling accuracy. In the Three-Mass Linear Inverted Pendulum Model (3MLIPM) proposed for improving the dynamic performance of bipedal walking, the precision of LIPM is improved by using three masses to represent a torso and two legs [52]. According to some studies, the requirement of constant CoM height dictated by the LIPM can also be relaxed to form a nonlinear inverted pendulum model [53]. Throughout the literature, adding a flywheel to the inverted pendulum is also proposed and has been used for posture control [54], error compensation [55] and so on. In addition, the application of the inverted pendulum model with an additional flywheel also generated the idea of the capture point[1], which is widely used nowadays to achieve push recovery and improve walking robustness [56, 57, 58].

Despite the advancements in ZMP related methods, they are still far away from producing truly dynamic gaits. However, in the humanoid applications requiring fast motion planning [59] , obstacle avoidance, interaction with complex environments [60, 61] and special body movements [62], ZMP control strategies still play an irreplaceable role.

[1] A point on the ground where a biped must step to so as to achieve a complete stop.

1.3.2 Unactuated/Actuator-Assisted Dynamic Walking

Unactuated dynamic walking refers to the walking demonstrated by passive bipedal robots. These bipeds do not incorporate any actuators, and the locomotion they produce is purely from the interaction between their mechanical structures and the environment, which makes them highly dynamic and energy efficient. In the simulation studies of passive bipeds, the stability of candidate walking gaits is numerically verified by estimating the eigenvalues of the Jacobian linearization of the Poincaré map, but this stability test has no relation with the generation of passive gaits. The pioneering work in this direction is presented by McGeer [63, 35], where he realized a passive compass robots and a passive bipedal robot with knees. Based on his study, a carefully tuned 3D passive biped is later created by attaching counter-swinging arms rigidly to their opposing legs [36]. This biped is capable of walking down a particular fixed slope from a specific initial configuration, but its gait is very sensitive to perturbations. Some studies even show that by adopting collisionless gait, passive bipedal robots can walk with no energy consumption [64, 65].

Actuator-assisted dynamic walking is realized by adding a reduced set of actuators to passive bipeds so that gait-related energetic losses can be compensated by these actuators. Starting from the 3D passive walker [36], a similar 3D walker featured minimal actuation was later constructed [66]. This biped was able to walk stably on flat ground at 0.44 m/s with an energy cost similar to that of a human. Another minimally actuated biped named Denise was built at Delft University of Technology, which installed pneumatically powered actuators called McKibben muscles [67]. Both of these robots have no sensors except one in each foot, and the control programs are very simple. When these robots step down, the motor in the other foot is briefly activated to provide a small push off [68]. The stability characteristics of these robots were further analyzed in [69] where a planar biped named Mike is tested to demonstrate a simple rule "You will never fall forward if you put your swing leg fast enough in front of your stance leg. In order to prevent falling backward the next step, the swing leg shouldn't be too far in front." The result shows that this simple control law can dramatically enlarge the basin of attraction of a passive walker. Additional work was later done concerning the rejection of small disturbances [70] and realizing locally stable gaits with purely reflexive control [71].

Despite the advancements of unactuated/actuator-assisted dynamic walking, the inherent shortcoming of these methods have long been recognized. With no actuators or minimal actuators, the autonomy of these bipeds is highly limited, and it is impossible for them to climb stairs, pause, turn or run. Therefore, the main contributions of these researches are mostly theoretical rather than practical.

1.3.3 Actuated Dynamic Walking

Actuated dynamic walking is difficult to realize because it is nonlinear, nominally unstable, multi-input multi-output (MIMO) and exhibit time variant and hybrid dynamics (during support exchange). Because of energy efficiency concerns, these robots are required to embrace ballistic momentum and gravitational potential en-

ergy to minimize the energy consumption of their actuators. As such, the ZMP-based tracking methods are generally incapable of producing dynamic gaits. This motivates researchers to propose different methods to achieve actuated dynamic walking.

In the work described by [72], the authors recommended virtual model control for realizing bipedal locomotion. The idea of this method is to calculate actuator forces by the imaginary interaction between virtual components and a robot system. In a similar effort, state-dependent control torques are calculated via virtual passive elements (i.e., angular springs and dampers with fixed equilibrium points) and then transformed to actuator torques utilizing the Gauss principle of least constraint [73, 74]. The simulation and experiment results from these studies have demonstrated impressive capabilities of handling slopes and reducing energy consumption for planar bipeds. There are also researchers attempting to apply machine learning techniques such as neural network [75, 76], but the extent of dynamic walking produced by neuronal controllers is unclear and follow-up studies towards this direction are scarce.

In recent years, many researchers have tried to study hybrid systems where continuous dynamics and discrete events are closely intertwined. The related studies and applications are wide spread [6, 77, 78]. The challenging tasks concerning hybrid systems include the strategies of overcoming the curse of dimensionality [79], the analysis of stability [80], the search of optimal control laws [81] and so on. In the notable work of [6], a 3-link planar biped with one degree of underactuation (point feet) was utilized to demonstrate the idea of realizing asymptotically stable walking using techniques of zero dynamics in conjunction with a finite-time controller. The reason of considering point feet is to facilitate the study of underactuated phases in an anthropomorphic walking gait (during the rotations of stance toe or stance heel). This method was also implemented in a 5-link planar biped with one degree of underactuation [7], and later it was extended in [82, 5], where the notions of hybrid zero dynamics (HZD) and virtual constraints are explained in detail. For planar bipeds, the major advantages of using hybrid zero dynamics are that hybrid invariance[2] can be easily achieved and that the stability of planar bipeds can be validated by calculating the restricted scalar Poincaré map[3] [83] in closed form [84]. As a result, optimization can be performed directly on the parameters of the controller with respect to some optimization criteria (such as energy consumption) to simultaneously determine a periodic dynamic walking and a controller that achieves it. The experimental validation of hybrid zero dynamics for planar bipeds was successfully obtained from the bipedal robot RABBIT [5, 85] and more recently the robot MABEL [37]. In addition, this method has also been enriched adding features like locked knees [86], rotating feet [50, 87], impulsive foot action [88] and torque saturation [89].

Compared with the situation of planar bipeds, the study of zero dynamics and

[2] The notion of hybrid invariance is used for ensuring the periodicity of each step, and the detailed explanation is given in Section 2.3.

[3] The notion of restricted Poincaré map is also explained in Section 2.3.

virtual constraints in 3D bipeds is still in the beginning stage. In the recent work [90], virtual constraints are proven to be capable of stabilizing a large class of periodic orbits of a bipedal robot. In the groundbreaking work of [91], the asymptotically stable walking of a 5-link 3D biped with passive point feet[4] is realized through three strategies including imposing a stability condition for optimization, using an event-based controller and selecting appropriate outputs. The stability of the walking gait is evaluated with the linearization of the restricted Poincaré map of dimension three. Among these three strategies, the idea of designing event-based controllers was later extended to control a 3D bipedal walker named Atrias [40] in the notable work [39], where a time-invariant one-step hybrid control scheme is proposed on the basis of right-left symmetry, linear matrix inequalities (LMIs), and robust optimal control (ROC).

Another interesting approach for extending the method of hybrid zero dynamics and virtual constraints is called functional Routhian reduction. This method has proved to be helpful in achieving quasi-3D walking in a number of bipeds in the simulation [92, 93] and the experiment [94]. The basic idea of this method is to decouple the sagittal and coronal dynamics of a 3D bipedal robot so that control design can be conducted using existing methods for control of planar bipeds and, at the same time, the 3D biped can be stabilized in an upright configuration in the coronal plane. The main limitation of this method, though, is that the "almost-cyclic" condition [92] required by the reduction eliminates the possibility for decouple coronal DOFs other than the one located at the ankle joint. In addition, this method requires 3D bipedal robots to be fully actuated, which somehow counteracts the benefit in trying to find walking motions for underactuated planar bipedal robots. Besides, it is also questionable whether the benefit of high energy efficiency can remain once the reduction control is performed.

Additional advancements for 3D bipeds with non-trivial feet include the regulation of ZMP [95], steering control [96], foot rotation [97] and so on. In the interesting study [98], a simplifying assumption of the coronal plane being fully actuated and the sagittal plane being underactuated was made to analyze stability and stability basins. Despite these efforts in studying hybrid zero dynamics of 3D bipeds, there are still many challenges confronting roboticists. One of them is to obtain optimal walking motions, since the dynamic property of enforcing virtual constraints depends largely on whether the energy cost function is truly minimized during the design process of virtual constraints. (Dictating position-level information or cancelling the natural dynamics is generally believed to be energetically expensive among bipedal roboticists.) However, the complexity of obtaining optimal motions arises significantly when one tries to extend the method of zero dynamics to fit into the scenario where 3D bipedal robots with point feet and two or more degrees of underactuation become objects of research. In comparison to the 2D case, hybrid invariance is no longer easy to achieve, and the only known method is to use a deadbeat hybrid extension. In addition, the resulting restricted Poincaré map is no

[4] The yaw rotation of the stance point feet is inhibited, and therefore the mention of "point feet" can be viewed as an approximation.

longer scalar either; instead, it is of dimension three or higher. Furthermore, the conditions for asymptotic stability now depend on the particular selection of the virtual constraints [99, 91]. These difficulties might bring a negative effect on the quality of the optimized motions.

In conclusion, the method of virtual constraints and hybrid zero dynamics is a powerful tool in studying actuated dynamic walking of bipedal robots. As the efforts in utilizing hybrid zero dynamics to control 3D bipeds are still confronted with many difficulties, it would be helpful to know whether other options are available and whether the quality of optimized motions can be further improved in this direction.

1.4 Energy Optimal Gaits of Bipedal Robots

One of the key challenges in robotic bipedal locomotion is finding control parameters that fulfill a certain objective, in terms of motion velocity, while minimizing the energy needed to produce a gait. Due to the unpredictable effects and correlations among the gait parameters, gait optimization is an open and non-trivial problem of which analytical results are scarce and limited to only some simple cases [100]. In most cases, numerical solutions is the only option, and some of the early attempts can be dated back to 1970s [101].

Roughly speaking, finding numerical solutions of optimal gaits is a constrained optimization problem which involves the selection of optimization parameters, objective functions, optimization algorithms and optimization constraints. Up till now, researchers have tested many combinations.

To begin with, the choice of optimization parameters is not unique, and the torques, the Cartesian coordinates and joint coordinates can all be used to parameterize gaits. For instance, in the early work [102], piecewise constant torques are chosen as the optimization parameters. However, when the torques are treated as optimized variables, it is necessary to solve the inverse dynamic problem to find the joint coordinates so as to verify whether the gaits generated are cyclic or not. In the early days of bipedal robotics, the Cartesian coordinates of the hip, swing foot and the trunk angle were also used as optimization parameters [103], but one shortcoming of this method is that one has to inverse the geometric robot model to define the joint reference trajectories. Due to these problems, these two choices are superseded by joint coordinates of which the evolution can be defined as polynomials [103], cubic splines [104], Bézier curves [84], Fourier expansions [105], canonical human walking functions [106, 107], etc.

The criteria of minimal energy can be different also. Apart from using pure mechanical energy [65], the energy cost can also be defined as the integral of the absolute value of the work of external forces and torques [108]. However, this definition has no relation with real energy consumption of specific actuators. A more popular cost function is given in [102] where the torque cost is defined as the integral of the norm of the torque for a displacement of one meter. This definition has considered the fact that, in DC motors (or brushless motors), most part of the energy consumption is due to the Joule effect, which is roughly proportional to the square

of the current going through its coil, and the current is in turn proportional to the torque exerted by this motor. If more detailed information of specific actuators are provided, it is also possible to define more accurate cost functions [109].

Most optimization algorithms used in the past for gait optimization can be broadly categorized into gradient-based methods and direct search methods. The different between them depends on whether derivative information is required. In the notable work of [110], three direct search algorithms are tested including Nelder and Mead, Genetic, and Simulated Annealing for obtaining energy efficient gaits. The additional applications of these methods can be found in [4, 111, 112]. Although these methods are very flexible because of their good tolerance to the presence of noise in the function and constraints, they are, like most direct search algorithms, computationally expensive. For instance, in most genetic algorithms, multiple sets of parameters from the population must be evaluated for each iteration, and therefore the number of evaluations required is usually impractical, especially for complex 3D bipeds. In order to increase rate of convergence, many researchers have tried gradient-based methods such as the sequential quadratic programming (SQP) method [84, 113, 114, 115], the augmented Lagrangian method [116], and the (nonlinear) interior point method [117]. Among them, SQP is the most popular one which has been used in gait optimization of both planar bipeds [84, 113, 115] and 3D bipeds [114, 118]. Other algorithms available for gait optimization include direct shooting algorithm [102], particle swarm algorithm [119], etc.

The constraints in gait optimization include conditions such as joint limitations, gait stability, unilateral ground contact, average walking velocity, periodicity and so on. For traditional gait optimization based on open-loop trajectories of time-polynomials, the stability verification is not included in the optimization process. However, for bipeds with one degree of underactuation, it is possible to verify the stability by replacing time with a scalar path parameter in joint trajectories [115] or using the method of virtual constraints [84]. A positive byproduct of these methods is that the equality constraint of periodicity is no longer required, which is crucial for improving the performance of optimization program. Another interesting constraint is the friction constraint. For most studies on optimal gaits of 3D bipeds [114], this constraint is usually simplified by neglecting possible yaw motion of the stance foot (feet). The reason behind this simplification is that in order to calculate maximum vertical torque preventing yaw motion, it is necessary to calculate the pressure distribution of the normal force acting on the foot, which is extremely difficult. In this thesis, we will provide a simplified model that can include this constraint (Section 5.2.4).

Because of limited computing power, almost all the early attempts of gait optimization are conducted on the models of planar bipeds, and some of them even contain certain simplifications of dynamic model [102]. Up until now, different cases have been studied concerning energy optimal gaits for planar bipedal robots, and the list includes, but is not limited to, feet rotation [120], point feet [115], segmented torso [121], four-bar knees [3], rolling knees [3] and swinging arms [122]. With the development of computing resources, there are more and more gait optimization

results obtained from the models of 3D bipedal robots [114]. The special cases also include point feet [123], toe rotation [118], swinging arms [124], etc. However, in comparison to 2D cases, the optimization results for 3D bipeds are usually limited in quality and quantity. For instance, in most cases, researchers need to use interpolation methods to illustrate the variation of energy cost at various walking speeds [123], and in some other cases, results are provided for only one walking speed [124]. Besides, there are few studies that deal with the relation between planar bipeds and corresponding 3D bipeds with similar model parameters. These problems will be touched upon in this thesis.

1.5 Elastic Coupling

Certainly, when it comes to energy efficiency, it is always appealing to add passive components like elastic couplings. This applies not only to bipedal robots but also to all the legged robot [125, 126, 127, 128]. In fact, most biological systems are more energy efficient than active legged robots, largely due to their elastic muscles and tendons [129]. According to [130], these elastic structures in biological legged systems mainly serve three purposes: (1) to act as an elastic boundary layer for damping impacts; (2) to function as a pogo stick for redirecting the vertical movement of mass center; (3) to serve as return spring for buffering energy during the redirection of the swing leg. By fully exploiting natural dynamics and utilizing elastic components in accordance to (2) and (3), biological systems like humans can move in resonance and reduce energy consumption [131, 132]. Since achieving human-like energy efficient walking motions has long been pursued by many bipedal roboticists, it should be interesting to apply this biological method to the design of bipedal robots.

Indeed, the application of elastic components in bipedal robots dates back at least to 1980s when Marc Raibert and his team built a planar running biped with pneumatic springs for recycling the energy of the vertical vibration of the mass center [133]. Similar methods have also been applied to the recent planar biped MABEL, of which the energy efficiency during running is greatly enhanced by adding differentials to its drivetrain for creating virtual compliant legs [37]. However, these examples only demonstrate the benefit of elastic couplings serving as pogo sticks, and the general idea behind them can be analyzed using the spring-loaded inverted pendulum (SLIP) model [134].

For bipedal walking, the energy-saving benefits of parallel knee compliance in the bipedal robot ERNIE was studied in [135], but knee joints are not the most interesting places to place elastic components. During walking, the vertical movement of the mass center is quite limited, and thus the major purpose of having elastic couplings for walking bipeds is to accelerate and decelerate the torsional vibration of the swing leg, which is also observed in human beings [136, 137]. Nevertheless, elastic couplings acting as return springs were initially only used to improve passive dynamic running [138, 139], and it is only later that they were applied in form of a

hip spring to a 3D passive dynamic walker to stabilize lateral motion [70]. Gradually, this research direction began to catch roboticists's attention.

For instance, hip springs began to be used to adjust step frequency [140] and to estimate energy efficient speed–step length relationship [141]. According to [142], the impact energy losses during step-to-step transitions are the major cause for metabolic energy consumption of human walking. Some researchers also attempted to use elastic couplings to realize passive bipedal robots with collisionless gait and thus create walking motions that consume no energy [64, 65]. By properly adjusting the stiffness of the hip spring, it is possible to obtain an optimal step length with minimum impact losses at a specific speed. Aside from influencing step frequency and energy efficiency, hip springs are also used to prevent passive bipeds from falling forward [140] and ensure ground clearance [143]. One study on a five-link passive biped with knees and upper body even reveals that erect body posture for passive bipeds is only possible with torsional springs properly placed in the hip joints [144].

Nevertheless, these studies are only valid for passive biped robots walking in a highly controlled environment, which makes it difficult to apply these results to any autonomous humanoid robots. For actuated bipedal robots, some researchers have tried to mimic passive bipeds by applying virtual forces generated by virtual springs and dampers [73, 72]. However, it is questionable whether the proposed virtual passive components can be replaced by physical passive components so as to recycle energy. Besides, it is computationally expensive to evaluate the energy criterion at a given speed since the lack of periodicity condition in these methods naturally forces researchers to simulate dozens of steps for obtaining average speed and average energy criterion. There are also some control designs for compliant bipedal robots using heuristic approaches such as machine learning techniques [145] or posture-based state machines [146], but the experimental results thereby obtained cannot truly demonstrate the benefit of elastic components since heuristic approaches are usually incapable of fully exploit the natural dynamics of bipedal robots. All things considered, it seems that optimizing a single periodic step is a viable approach in analyzing the energy benefit of adding elastic components to bipedal robots.

Currently, the research in this direction is mostly limited to planar bipeds. Based on the application of predefined time-based reference trajectory, the optimal walking of 3-link compass gait biped has already been presented [147, 148]. However, bipeds with kneeless legs are far away from humanoid robots, and the elastic couplings therein analyzed are optimized only for one specific speed whereas a real robot needs to be energy efficient at different speeds. Similar studies have also been conducted for a 7-link robot composed of a torso, two thighs, two shins and two feet [149] and, in this case, springs are added to the hip, knee and ankle joints of the robot. Nevertheless, the impactless model used therein for the instantaneous double support phase cannot represent the foot strike situation in real robots or human beings. Intuitively, all of us have the impression that the faster we walk, the harsher our foot strike becomes. Apart from all these deficiencies, all the above optimization results are obtained by optimizing parameters of predefined time-based reference trajectories, and therefore the stability condition is not considered in these

methods. In order to ensure the stability of optimized gait, a recent study based on feedback linearization and virtual constraints has been conducted on the elastic couplings of a 3-link planar biped [150] and a 5-link planar biped [109]. Although the results delivered from this study are comprehensive and cover different combinations of torsion springs, the study is still limited to planar bipeds, and the definition of criterion is also too specific to be compared with other optimization results.

Although the results presented herein are only theoretical, there are already some published studies concerning the realization of elastic couplings in physical bipedal robots with viable control methods [151, 152]. As mathematical control techniques for utilizing elastic couplings become ever more sophisticated, the hardware technologies must grow as well. In order to improve the energy efficiency of bipeds at different speeds, some researchers have been studying possible ways to modify spring stiffness and unloaded position with power on. Up till now, some compliant actuators with tunable elastic elements have already been developed, such as the MACCEPA [153, 154] and the Jack Spring^{TM} [155], which allow adjustment of the unloaded position of a series elastic element. Another method is to modify the spring stiffness by adjusting the pre-tension of a system with non-linear springs. This approach has been used in the VSSEA (Variable Stiffness SEA) [156] and the AMASC [157]. (2004). Recently, a MACCEPA-based Series-Parallel Elastic Actuator has been proposed [158], which has greatly reduced torques or forces acting on the motor by its parallel configuration.

In conclusion, based on the current literature and technology advancement, it should be interesting to investigate the benefit of adding elastic couplings to hip joints in both planar and 3D bipedal robots.

1.6 Thesis Contribution

The contributions of this thesis are:

1. The extension of the control method [84] for 2D bipedal walking to 3D scenarios.

2. The impact model and contact model for 3D bipedal robots with massless line feet.

3. The "Symmetry Outputs" for achieving better geometric interpolation of posture control and swing leg advancement.

4. The comparison of optimized gaits between a planar biped and a 3D biped with same model parameters in the sagittal plane.

5. The method of using optimized parameters from the planar biped as a starting point or as the sagittal parameters to facilitate the optimization of the corresponding 3D biped.

6. The detailed studies concerning the elastic couplings at the hip joint for both planar and 3D biped.

1.7 Thesis Outline

The remainder of this thesis proceeds as follows:

Chapter 2 gives a brief explanation of four foundations of calculating optimal stable gaits for both 2D and 3D bipedal robots. These four foundations are: (1) the Lagrange method and additional equations for calculating external forces and torques; (2) the method of feedback linearization and the concept of zero dynamics; (3) the stability analysis using restricted Poincaré map; and (4) the concept of parametric optimization and sequential quadratic programming. These contents are rephrased and tailored to suit the purpose of this thesis, and for more detailed information, one can refer to [8, 159, 160, 161, 162].

Chapter 3 presents the hypotheses, modeling, controlling and optimizing of an underactuated 5-link planar bipedal robot composed of a torso, two thighs and two shins. This work is, to some extent, based on the previous theoretical work in [8], but we have adopted fixed base models and posture parameters to achieve coherence with Chapter 5. In addition, we also introduced the "Symmetry Outputs" to facilitate the geometric interpolation of the control method [121]. The gait optimization results of this robot is provided at the end of this chapter.

Chapter 4 provides the applications of elastic couplings in our 5-link planar biped. We have tried two different ways of adding torsion springs to the hip joints: either by connecting one thigh to another or via connecting two thighs respectively to the torso. The corresponding optimization results of these two coupling cases are presented and compared with those in Chapter 3, which indicates that both spring configurations can significantly reduce the energy cost of the 5-link planar biped. The results also show that the desired step frequency in two coupling cases is close to twice of the natural frequency of the pendulum formed by the swing leg.

Chapter 5 presents the central work of this thesis concerning the hypothesis, modeling, controlling and optimizing of an underactuated 8-link 3D bipedal robot composed of a torso, a pelvis, two thighs, two shins and two massless line feet. Although the method we use in this Chapter stems from the published work in [84] for planar bipeds, we have made important adaptations regarding robot hypotheses, line-foot impact model, line-foot contact model, optimization parameters and optimization constraints so that this method can also fit into the scenario of 3D biped cases. As a byproduct of our methods, the gait optimization results from 2D bipeds and 3D bipeds are no longer isolated. Indeed, we have divided our optimization parameters into sagittal parameters and coronal parameters so that the optimized parameters from the 2D biped can be used as a starting point for the gait optimization of the corresponding 3D biped. Furthermore, the optimization is performed for two different optimization cases. In the Optimization Case I, we optimize only the coronal parameters and use the corresponding optimized parameters from the 5-link planar biped as the sagittal parameters. In the Optimization Case II, we optimize all the parameters. The results indicate that the optimization performance of Case II is

always better than those from Case I and that Case I is only effective at high speeds.

Chapter 6 provides the applications of elastic couplings in our 8-link 3D biped. The torsion springs are added to the 3D biped in three different ways: (1) to the sagittal plane; (2) to the coronal plane, (3) to both the sagittal and coronal plane. By comparing the first two cases, we can conclude that the elastic couplings in the sagittal plane play a much more important role in recycling energy than the couplings in the coronal plane. However, the maximum energy criterion in the third case drops even further if elastic couplings are added in both planes, indicating that the elastic couplings in the coronal plane cannot be neglected.

Chapter 7 concludes the thesis with a discussion and suggestions for future work.

2. METHODOLOGY

This chapter serves a compact explanation of the theories concerning Lagrangian mechanics(Section 2.1), feedback linearization(Section 2.2), hybrid system stability(Section 2.3) and numerical optimization(Section 2.4). The applications of these theories in the later chapters includes: (1) generating dynamical models for different bipedal robots, (2) implementing nonlinear control law using virtual constraints, (3) analyzing the stability of given walking trajectories, and (4) obtaining optimized walking trajectories with satisfactory energy efficiency or other quadratic criteria. In the following sections, they will be briefly reviewed respectively.

2.1 Lagrangian Mechanics

The Euler-Lagrange approach has been widely applied ever since its discovery in 1750s by Euler and Lagrange during their studies of the tautochrone problem. Compared with the Newton-Euler formulation, it is capable of treating a multi-link robot as a whole instead of treating each link of the robot in turn. Using Euler-Lagrange approach, we can derive dynamical models in a straightforward manner.

An M-DOF robot with general coordinates $q \in \mathcal{Q}$ and configuration space $\mathcal{Q} \subset \mathbb{R}^M$ can be described by elements $(q, \dot{q})$ of the tangent bundle $\mathcal{TQ} \subset \mathbb{R}^{2M}$. If the robot only has rigid links and ideal elastic components that can only exert conservative forces, the Lagrangian function $\mathcal{L}$ of the robot can be defined as:

$$\mathcal{L}(q, \dot{q}) = \mathcal{K}(q, \dot{q}) - \mathcal{V}_g(q) - \mathcal{V}_e(q) \tag{2.1}$$

where $\mathcal{K}$ is the kinetic energy, $\mathcal{V}_g$ is the gravitational potential energy and $\mathcal{V}_e$ is the elastic potential energy. By applying the least action principle [163], the Euler-Lagrange equation of motion can be formulated as:

$$\frac{d}{dt}\frac{\partial \mathcal{L}}{\partial \dot{q}} - \frac{\partial \mathcal{L}}{\partial q} = \tau \tag{2.2}$$

where τ is an $M \times 1$ vector containing joint torques.

2.1.1 Kinetic Energy

The kinetic energy of a rigid body is composed of two parts: the translational energy contributed by its entire mass and the rotational kinetic energy about its CoM (Center of Mass). Thus for a N-link robot, its kinetic energy is given by:

$$\mathcal{K} = \frac{1}{2}\sum_{i=1}^{N} m_i v_i^\top v_i + \frac{1}{2}\sum_{i=1}^{N} \omega_i^\top \mathcal{I}_i \omega_i \tag{2.3}$$

where for the i-th link m_i is its mass, v_i and ω_i are its linear and angular velocities, and $\mathcal{I}_i$ is its matrix of moment of inertia at the CoM. For planar robots, ω_i is a scalar, and $\mathcal{I}_i$ equals to the corresponding moment of inertia I_i in the link attached frame. If robots move in a 3D space, v_i and ω_i will be 3×1 vectors and $\mathcal{I}_i$ will be 3×3 matrix equaling to:

$$\mathcal{I}_i = R_i^0 I_i R_i^{0\top} \tag{2.4}$$

where R_i^0 is the rotation matrix of the link i relative to the inertial reference frame and the moment of inertia I_i in the link attached frame is given by:

$$I_i = \begin{bmatrix} I_{ixx} & I_{ixy} & I_{ixz} \\ I_{ixy} & I_{iyy} & I_{iyz} \\ I_{ixz} & I_{iyz} & I_{izz} \end{bmatrix} \tag{2.5}$$

The diagonal element of the matrix I_i, I_{ixx}, I_{iyy}, I_{izz}, are named as the Principal Moment of Inertia, while the off-diagonal terms I_{ixy}, I_{ixz} and I_{iyz} are called Cross Products of Inertia. If the mass distribution of the body is symmetric regarding the link attached frame then the cross products of inertia equal to zero.

The linear and angular velocities of the CoM of the link i can be further expressed in terms of the Jacobian matrix and the derivatives of the joint variables:

$$v_i = J_{v_i}(q)\dot{q} \tag{2.6}$$

$$\omega_i = J_{\omega_i}(q)\dot{q} \tag{2.7}$$

with J_{v_i} and J_{ω_i} being the Jacobian matrices. Then from (2.3) it follows that the overall kinetic energy equals:

$$\mathcal{K} = \frac{1}{2}\dot{q}^\top \sum_{i=1}^{N} [m_i J_{v_i}(q)^\top J_{v_i}(q) + J_{\omega_i}(q)^\top \mathcal{I}_i(q) J_{\omega_i}(q)]\dot{q} \tag{2.8}$$

2.1.2 *Potential Energy*

When considering rigid dynamics, the potential energy is equivalent to gravitational potential energy [164]. For the i-th link, this potential energy can be calculated by assuming that the mass of the entire link is concentrated at its CoM (Center of Mass) and is formulated as:

$$\mathcal{V}_{gi} = m_i g_e^\top r_{ci}(q) \tag{2.9}$$

where g_e is the vector of gravity acceleration near Earth's surface, r_{ci} represents the coordinates of the CoM of link i. According, the overall gravitational potential energy is:

$$\mathcal{V}_g = \sum_{i=1}^{N} \mathcal{V}_{gi} = \sum_{i=1}^{N} m_i g_e^\top r_{ci}(q) \tag{2.10}$$

If the robot contains ideal elastic components, the overall potential energy should include elastic potential energy. For a single linear elastic coupling, the elastic potential energy is given by:

$$\mathcal{V}_{ei} = \frac{1}{2} k_{ei}(\varphi_{ei}(q) - \varphi_{ei}^*)^2 \tag{2.11}$$

where φ_{ei}^* represents the unloaded position, $\varphi_{ei} - \varphi_{ei}^*$ describes the deflection as a function of q, and k_{ei} is the stiffness. The overall elastic potential energy is then obtained by:

$$\mathcal{V}_e = \sum_{i \in \mathcal{C}_{set}} \mathcal{V}_{ei} = \frac{1}{2} \sum_{i \in \mathcal{C}_{set}} k_{ei}(\varphi_{ei}(q) - \varphi_{ei}^*)^2 \tag{2.12}$$

where $\mathcal{C}_{set}$ is the index set of all the applied elastic couplings.

2.1.3 Obtaining Dynamic Model

Using (2.8), (2.10), (2.12) and (2.2), the Euler-Lagrange equations can be written in matrix form as:

$$D(q)\ddot{q} + C(q, \dot{q})\dot{q} + G(q) = \tau + \tau_e \tag{2.13}$$

where the $M \times M$ matrix $D(q)$ is the inertia matrix, C is the $M \times 1$ vector of Coriolis terms and centrifugal terms, $G(q)$ is the $M \times 1$ vector of gravity terms, τ is the $M \times 1$ vector of external forces, τ_e is the $M \times 1$ vector of forces caused by elastic couplings. Among them, $D(q)$ and $G(q)$ are respectively given by:

$$D(q) = \sum_{i=1}^{N} [m_i J_{v_i}(q)^\top J_{v_i}(q) + J_{\omega_i}(q)^\top \mathcal{I}_i J_{\omega_i}] \tag{2.14}$$

$$G(q) = \frac{\partial \mathcal{V}_g}{\partial q} \tag{2.15}$$

Assuming there is no coupling in the transmission matrix, the rotors' inertias can be included in the dynamic model by replacing the D matrix can with D^*:

$$\begin{cases} (D(q))_{jk}^* = (D(q))_{jk} & j \neq k \\ (D(q))_{jk}^* = (D(q))_{jk} + I_{aj} & j = k \text{ and } q_j \text{ is actuated} \end{cases} \tag{2.16}$$

where $1 \leq j, k \leq M$ and I_{aj} is the reflected rotor inertia of q_j on the joint side. For the rest of the thesis, we will omit $*$ and assume that the motor inertia are included in $D(q)$. Using d_{jk} for representing the entry of the matrix $D(q)$, the entry c_{jk} of the $M \times M$ matrix $C(q, \dot{q})$ is given by:

$$c_{jk} = \frac{1}{2} \sum_{i=1}^{M} \left[\left(\frac{\partial d_{jk}}{\partial q_i} + \frac{\partial d_{ji}}{\partial q_k} - \frac{\partial d_{ik}}{\partial q_j} \right) \dot{q}_i \right] \tag{2.17}$$

Then the elastic torque vector τ_e is given by:

$$\tau_e = -\frac{\partial \mathcal{V}_e}{\partial q} = -\sum_{i \in \mathcal{C}_{set}} k_{ei}(\varphi_{ei}(q) - \varphi_{ei}^*) \frac{\partial \varphi_{ei}}{\partial q} \tag{2.18}$$

2.1.4 Calculating External Forces

Assuming the robot studied has only one base joint connecting the robot and the ground, we may need to calculate the external force F_{ext} and torque Γ_{ext} acting on this joint. The external force F_{ext} equals to the sum of the external forces F_i acting on the CoMs of each link of the robot, with the equation written as:

$$F_{ext} = \sum_{i=1}^{N} F_i \tag{2.19}$$

where F_i can be calculated using Newton's second law:

$$F_i = \frac{d(m_i v_i)}{dt} + m_i g_e = m_i \dot{v}_i + m_i g_e \tag{2.20}$$

with $\dot{v}_i$ given by:

$$\begin{aligned} \dot{v}_i &= \frac{d(J_{v_i}(q)\dot{q})}{dt} \\ &= J_{v_i}(q)\ddot{q} + \frac{\partial(J_{v_i}(q)\dot{q})}{\partial q}\dot{q} \end{aligned} \tag{2.21}$$

Γ_{ext} can be calculated by combining the external torques Γ_i and the additional torques $r_{ci} \times F_i$ caused by moving F_i to the base joint and then summing them up:

$$\Gamma_{ext} = \sum_{i=1}^{N}(\Gamma_i + r_{ci} \times F_i) \tag{2.22}$$

where Γ_i can be calculated using Newton's second law for rotation [159]:

$$\Gamma_i = \frac{d(\mathcal{I}_i \omega_i)}{dt} = \mathcal{I}\dot{\omega}_i + \omega_i \times \mathcal{I}\omega_i \tag{2.23}$$

with $\dot{\omega}_i$ being:

$$\dot{\omega}_i = \frac{d(J_{\omega_i}(q)\dot{q})}{dt} = J_{\omega_i}(q)\ddot{q} + \frac{\partial(J_{\omega_i}(q)\dot{q})}{\partial q}\dot{q} \tag{2.24}$$

2.2 Feedback Linearization

Feedback linearization is a common approach for controlling nonlinear systems. The central idea is to algebraically transform nonlinear systems into equivalent linear ones so that nonlinear systems can also adopt linear control methods [160]. A typical nonlinear system formulated by:

$$\dot{x} = f(x) + g(x)u \tag{2.25}$$

$$y = h(x) \tag{2.26}$$

where x is an $n \times 1$ state vector, u is an $m \times 1$ input vector, and y is an $m \times 1$ vector of controlled output, $f(x)$ is an $n \times 1$ vector of nonlinear functions, $h(x)$ is an $m \times 1$ vector of nonlinear functions, and $g(x)$ is an $n \times m$ matrix of nonlinear functions.

The feedback linearization can generate a linear model that is an exact representation of the original nonlinear model, and this procedure is based on two operations: nonlinear coordinate transformations and nonlinear state feedback [165]. The premises for this approach are that the coordinate transformation must be a diffeomorphism. That is, the transformation must not only be invertible, but both the transformation and its inverse must be smooth so that differentiability in the original coordinate system is preserved in the new coordinate system [160]. After feedback linearization, the input-output system is linear and can be expressed as:

$$\dot{\eta} = A_s\eta + B_s v_s \tag{2.27}$$

$$\gamma_s = C_s\eta \tag{2.28}$$

where η is a $\varrho\times 1$ vector of transformed state variable with ϱ being the relative degree, v_s is an $m \times 1$ vector of transformed input, γ_s is an $m \times 1$ vector of transformed output, and the matrices A_s, B_s, and C_s are similarly to their counterparts in a linear state-space system. If $\varrho < n$, an additional $n - \varrho$ state variables are required to complete the coordinate transformation.

The input-output linearization is one of the approaches to realize feedback linearization. The objective is to linearize the map between the transformed input v_s and the actual output y [161]. After that, one can adopt a linear controller for the linearized input-output model represented by (2.27) and (2.28) with $\varrho \leq n$ and $\gamma_s = y$. However, there is a subsystem that typically is not linearized,

$$\dot{\xi} = \Upsilon(\eta, \xi) \tag{2.29}$$

where ξ is an $(n-\varrho)\times 1$ vector of transformed state variables and Υ is an $(n-\varrho)\times 1$ vector of nonlinear functions.

In some general cases, one can achieve the control objectives by adopting a nonlinear static state feedback control law of the form,

$$u = \alpha_s(x) + \beta_s(x)v_s \tag{2.30}$$

where α_s is an $m \times 1$ vector of nonlinear functions and β_s is an $m \times m$ matrix of nonlinear functions. We start first with the input-output linearization approach for single-input, single-output (SISO) system where $m = 1$ to facilitate explanation of the basic concepts, and then we will extend the approach to multiple-input, multiple-output (MIMO) systems.

2.2.1 *Single-input, Single-output Systems*

For a SISO system, $m = 1$ and by taking the first derivative of y we have:

$$\dot{y} = \frac{\partial h}{\partial x}\dot{x} = L_f h + L_g h u \tag{2.31}$$

where L_f and L_g are notations for Lie derivatives, of which the calculation is given in (3.28) and (3.27). If $L_g h = 0$, we can keep taking derivatives of y until u appears. Thus we will end up with the relative degree ϱ of $y = h(x)$ and the following equations:

$$\begin{aligned}
y &= h(x) = L_f^0 h \\
\dot{y} &= L_f h + L_g h u = L_f^1 h\,, \quad L_g h = 0 \\
\ddot{y} &= L_f^2 h + L_g L_f h u = L_f^2 h\,, \quad L_g L_f h = 0 \\
&\vdots \\
y^{\varrho} &= L_f^{\varrho} h + L_g L_f^{\varrho-1} h u = v_s\,, \quad L_g L_f^{\varrho-1} h \neq 0
\end{aligned} \tag{2.32}$$

If we define η coordinates as $\eta = [\eta_1, \eta_2, ..., \eta_\varrho]^\top$ and $\xi = [\xi_1, \xi_2, ..., \xi_{n-\varrho}]^\top$ with items given by:

$$\eta_k = \Phi_k(x) = L_f^{k-1} h(x)\,, \quad 1 \leq k \leq \varrho \tag{2.33}$$

$$\xi_k = \Phi_{\varrho+k}(x)\,, \quad 1 \leq k \leq n - \varrho \tag{2.34}$$

then $[\eta^\top, \xi^\top]^\top = \Phi(x)$ are valid diffeomorphism of the state vector x. As a result, the nonlinear system can be transformed into normal form expressed as:

$$\begin{aligned} \dot{\eta}_1 &= \eta_2 \\ \dot{\eta}_2 &= \eta_3 \\ &\vdots \\ \dot{\eta}_\varrho &= \beta_s(\eta,\xi) + \alpha_s(\eta,\xi)u \\ \dot{\xi} &= = \Upsilon(\eta,\xi) \\ y &= \eta_1 \end{aligned} \tag{2.35}$$

From (2.32), we have $L_g L_f^{\varrho-1} h \neq 0$. By specifying the nonlinear static state feedback control law in (2.30) as:

$$\begin{aligned} u &= (\alpha_s(\eta,\xi))^{-1}(v_s - \beta_s(\eta,\xi)) \\ &= (L_g L_f^{\varrho-1} h(x))^{-1}(v_s - L_f^{\varrho} h(x)) \end{aligned} \tag{2.36}$$

we have $\dot{\eta}_\varrho = v_s$, and thus the map between the transformed input v_s and the output y is exactly linear. With this condition satisfied, we can move on to design a linear state feedback control law for stabilizing the η subsystem. A typical feedback control law is formulated as:

$$\begin{aligned} v_s &= -\kappa_\varrho \eta_\varrho - \kappa_{\varrho-1}\eta_{\varrho-1} - \cdots - \kappa_1 \eta_1 \\ &= -\kappa_\varrho L_f^{\varrho-1} h(x) - \kappa_{\varrho-1} L_f^{\varrho-2} h(x) - \cdots - \kappa_1 h(x) \end{aligned} \tag{2.37}$$

where κ_ϱ, $\cdots$, κ_1 are related to the pole placement design. Combining (2.36) and (2.37), we can formulate the complete static state feedback control law as:

$$u = (L_g L_f^{\varrho-1} h(x))^{-1}(-L_f^{\varrho} h(x) - \kappa_\varrho L_f^{\varrho-1} h(x) - \kappa_{\varrho-1} L_f^{\varrho-2} h(x) - \cdots - \kappa_1 h(x)) \tag{2.38}$$

By properly choosing controller tuning parameters κ_i, the state variables η converge exponentially to zero, the equation (2.29) as $t \to \infty$ becomes:

$$\dot{\xi} = \Upsilon(\mathbf{0}_{\varrho\times 1}, \xi) \tag{2.39}$$

Equation (2.39) is known as the zero dynamics, which can be viewed as the nonlinear analog of linear system zeros.

2.2.2 *Multiple-input, Multiple-output Systems*

A robot system is usually a MIMO system, and thus it is necessary to extend the input-output linearization approach to cover this scenario. This extension is often named input-output decoupling because the input-output decoupling problem is to find (if possible) a diffeomorphism and a state feedback control law satisfying the following requirements: (1) the map between the transformed input v_s and controlled output y is linear; (2) the i-th output variable y_i is decoupled from all input variables v_{sj} for $i \neq j$.

It is practical to rewrite the MIMO nonlinear system as:

$$\dot{x} = f(x) + \sum_{j=1}^{m} g_j(x)u_j \tag{2.40}$$

$$y_i = h_i(x)\,, \quad i = 1, 2, \cdots, m \tag{2.41}$$

The nonlinear system is said to have vector relative degree $\{\varrho_1, \varrho_2, \cdots, \varrho_m\}$ at the point x_0 if:

1. $L_{g_j} L_f^k h_i(x) = 0$ for all $1 \leq i, j \leq m$, for all $k < \varrho_i - 1$, and for all x in a neighborhood of x_0;

2. The $m \times m$ decoupling matrix

$$A_d(x) = \begin{bmatrix} L_{g_1} L_f^{\varrho_1 - 1} h_1(x) & \cdots & L_{g_m} L_f^{\varrho_1 - 1} h_1(x) \\ \vdots & \ddots & \vdots \\ L_{g_1} L_f^{\varrho_m - 1} h_m(x) & \cdots & L_{g_m} L_f^{\varrho_m - 1} h_m(x) \end{bmatrix} \tag{2.42}$$

   is nonsingular at the point x_0.

The integer ϱ_i is the smallest relative degree of the i-th output variable with respect to any of the m input variables. Actually, nonsingularity of the decoupling matrix $A_d(x)$ can be interpreted as the MIMO generalization of the condition $L_g L_f^{\varrho - 1} h(x) \neq 0$ in a SISO system. It is a necessary and sufficient condition for adopting static state feedback to solve the input-output decoupling control problem.

The sum of the elements of vector relative degree is given by: $\varrho = \varrho_1 + \cdots + \varrho_m$. Since $A_c(x)$ is nonsingular, the diffeomorphism $[\eta^\top, \xi^\top]^\top = \Phi(x)$ can be realized by defining the first ϱ coordinates as:

$$\eta_k^i = \Phi_k^i(x) = L_f^{k-1} h_i(x) \tag{2.43}$$

with $1 \leq k \leq r_i$ and $1 \leq i \leq m$. According to [160], it is possible to find $n - \varrho$ additional coordinates $\xi^\top = [\Phi_{\varrho+1}(x), \cdots, \Phi_n(x)]$ such that

$$\Phi^\top(x) = [\Phi_1^1(x), \cdots, \Phi_{\varrho_1}^1(x), \cdots, \Phi_1^m(x), \cdots, \Phi_{\varrho_m}^m(x), \Phi_{\varrho+1}(x), \cdots, \Phi_n(x)] \tag{2.44}$$

is invertible at the point x_0. The normal form attained from this diffeomorphism is:

$$\begin{aligned} \dot{\eta}_1^i &= \eta_2^i \\ \dot{\eta}_2^i &= \eta_3^i \\ &\vdots \\ \dot{\eta}_{\varrho_i}^i &= \beta_{si}(\eta, \xi) + \sum_{j=1}^{m} \alpha_{sij}(\eta, \xi) u_j \\ \dot{\xi} &= \Upsilon(\eta, \xi) + \sum_{j=1}^{m} p_{sj}(\eta, \xi) u_j \\ y &= \eta_1^i \end{aligned} \tag{2.45}$$

for $1 \leq i \leq m$. The functions $\alpha_{sij}(\eta, \xi)$ are elements of the decoupling matrix A_d expressed using the transformed coordinates, and the function β_{si} are defined as:

$$\beta_{si}(\eta, \xi) = L_f^{\varrho_i} h_i[\Phi^{-1}(\eta, \xi)] \tag{2.46}$$

The vector Υ is defined as in the SISO case, and the vectors $p_{sj}(\eta, \xi)$ are given by:

$$p_{sj}(\eta, \xi) = \begin{bmatrix} L_{gj}\Phi_{\varrho+1}[\Phi^{-1}(\eta, \xi)] \\ \vdots \\ L_{gj}\Phi_n[\Phi^{-1}(\eta, \xi)] \end{bmatrix} \tag{2.47}$$

Combining all the ϱ_i-th equations in the normal form, we have:

$$\begin{bmatrix} \dot{\eta}^1_{\varrho_1} \\ \vdots \\ \dot{\eta}^m_{\varrho_m} \end{bmatrix} = \beta_s(\eta, \xi) + A_d(\eta, \xi)u \tag{2.48}$$

Assuming the decoupling matrix is nonsingular, the static feedback control law which enables input-output decoupling is:

$$u = A_d^{-1}(\eta, \xi)[v_s - \beta_s(\eta, \xi)] \tag{2.49}$$

where v_s is the $m \times 1$ transformed input vector. Influenced by this control law, the equations listed in (2.48) now becomes:

$$\begin{bmatrix} \dot{\eta}^1_{\varrho_1} \\ \vdots \\ \dot{\eta}^m_{\varrho_m} \end{bmatrix} = \begin{bmatrix} v_{s1} \\ \vdots \\ v_{sm} \end{bmatrix} \tag{2.50}$$

As a result, the input-output map is linearized and decoupled, and it can be formulated as:

$$\begin{aligned} \dot{\eta}^i_1 &= \eta^i_2 \\ \dot{\eta}^i_2 &= \eta^i_3 \\ &\vdots \\ \dot{\eta}^i_{\varrho_i} &= v_{si} \\ y &= \eta^i_1 \end{aligned} \tag{2.51}$$

where $1 \leq i \leq m$. As in the case of SISO nonlinear system, each input variable v_{si} can be chosen as:

$$\begin{aligned} v_{si} &= -\kappa^i_{\varrho_i}\eta^i_{\varrho_i} - \kappa^i_{\varrho_i-1}\eta^i_{\varrho_i-1} - \cdots - \kappa^i_1\eta^i_1 \\ &= -\kappa^i_{\varrho_i}L_f^{\varrho_i-1}h(x) - \kappa^i_{\varrho_i-1}L_f^{\varrho_i-2}h(x) - \cdots - \kappa^i_1 h(x) \end{aligned} \tag{2.52}$$

When expressed in the original coordinates, the decoupling control law becomes:

$$u = -A_d^{-1}(x)\beta_s(x) - A_d^{-1}(x)v_s \tag{2.53}$$

where $\beta_s(x) = [L_f^{\varrho_1}h_1(x), \cdots, L_f^{\varrho_m}h_m(x)]^\top$ and $v_s = [v_{s1}, \cdots, v_{sm}]^\top$.

In general, the input-output linearization control law provides only partial linearization of the closed-loop nonlinear system. The subsystem that is not linearized can be expressed as:

$$\dot{\xi} = \Upsilon(\eta, \xi) - P_s(\eta, \xi)A_d^{-1}(\eta, \xi)\beta_s(\eta, \xi) + P_s(\eta, \xi)A_d^{-1}(\eta, \xi)v_s \tag{2.54}$$

where $P_s = [p_{s1}, \cdots, p_{sm}]$. The above system can be written as $\dot{\xi} = \tilde{\Upsilon}(\eta, \xi)$, and the zero dynamics $\dot{\xi} = \tilde{\Upsilon}(\mathbf{0}_{\varrho\times 1}, \xi)$ are obtained by setting $\eta(t) = 0$. If the vector fields $g_1(x)$, $g_2(x)$, $\cdots$, $g_m(x)$ are involutive, we can choose the additional coordinates ξ such that $L_{g_j}\Phi_{\varrho+i}(x) = 0$ for all $i \leq i \leq n - \varrho$ and for all $1 \leq j \leq m$. In this case, $A_d(x)$ can also be simply written as $L_g L_f^{\varrho-1} h(x)$. Accordingly, we have $\dot{\xi} = \Upsilon(\eta, \xi)$ with the zero dynamics being $\dot{\xi} = \Upsilon(\mathbf{0}_{\varrho\times 1}, \xi)$ similar to the case of SISO systems.

2.3 Hybrid System Stability

A hybrid system[1] is defined as a dynamic system that exhibits both continuous and discrete dynamic behavior. Systems with impulse effects are categorized as a special class of hybrid systems consisting of an ordinary differential equation (ODE), a switching surface, and a re-initialization rule. For bipedal walking, we are mainly interested in determining the existence and stability properties of periodic orbits of such systems. The classical method serving this purpose involves Poincaré sections and Poincaré return maps. The method of Poincaré sections can provide necessary and sufficient conditions for the existence and stability of qualified periodic orbits, but it is impossible to analytically determine the return map for a typical system while available numerical methods based on estimating eigenvalues are usually computationally intensive. Because of this, restricted Poincaré maps are studied to simplify the stability analysis.

2.3.1 Autonomous Systems with Impulse Effects

By using feedback control laws such as the one defined in (2.53), the nonlinear system previous defined in (2.25) can be viewed as an autonomous nonlinear system:

$$\dot{x} = f(x) \tag{2.55}$$

defined on some state space $\mathcal{X}$. If the system has impulse effects, we can further define a co-dimensional one surface $\mathcal{S} \subset \mathcal{X}$ at which the autonomous system undergo a discrete transition. This transition can be modeled as an instantaneous re-initialization $\Delta : \mathcal{S} \to \mathcal{X}$ that calculates new initial state as a function of the point at which the impulse occurs. Thus, the combined system is written as:

$$\Sigma : \begin{cases} \dot{x} = f(x) & x^- \notin S \\ x^+ = \Delta(x^-) & x^- \in S \end{cases} \tag{2.56}$$

According to [83], the system (2.56) is said to be of (differentiability) class C^1 if the following hypotheses are satisfied:

[1] There are other definitions of hybrid systems such as those combining neural nets and fuzzy logic. Therefore, we sometimes use the term "hybrid dynamic system" in order to be more specific.

HSH1) $\mathcal{X} \subset \mathbb{R}^n$ is open and connected;

HSH2) $f : \mathcal{X} \to \mathbb{R}^n$ is of class C^1;

HSH3) S is nonempty and there exists a differentiable function $H : \mathcal{X} \to \mathcal{X}$ such that $\mathcal{S} = \{x \in \mathcal{X} | H(x) = 0\}$ is non-empty and $\forall x \in \mathcal{S}$, $\frac{\partial H}{\partial x}|_x \neq 0$;

HSH4) $\Delta : S \to \mathcal{X}$ is of class C^1.

HSH5) $\Delta(\mathcal{S}) \cap \mathcal{S} = \emptyset$.

Roughly speaking, a solution $\varphi(t)$ of (2.56) is specified by the differential equation (2.55) until its state "impacts" the hyper surface $\mathcal{S}$ at some time t_I when the impact model Δ simplifies the impact event as a instantaneous discontinuity in the state trajectory. After that, the impact model provides the new initial condition from which the differential equation (2.55) evolves until its state impacts $\mathcal{S}$ again. In the light of this, $\mathcal{S}$ is sometimes called the impact surface. To avoid confusions, the impact event is described by the state x^- "just before impact" at time t_I^- and the state x^+ "just after impact" at time t_I^+. A function $\varphi : [t_0, t_f) \to \mathcal{X}$, $t_f \in \mathbb{R} \cup \{\infty\}$, $t_f > t_0$ is a solution of (2.56) if:

(i) $\varphi(t)$ is right continuous on $[t_0, t_f)$;

(ii) left and right limits exist at each point $t \in [t_0, t_f)$, denoted by $\varphi^-(t) = \lim_{\tau \nearrow t} \varphi(\tau)$ and $\varphi^+(t) = \lim_{\tau \searrow t} \varphi(\tau)$;

(iii) there exists a closed discrete subset $\mathcal{T} \subset [t_0, t_f)$ called impact times such that

- *(a)* for every $t \notin \mathcal{T}$, $\varphi(t)$ is differentiable, $\frac{d\varphi(t)}{dt} = f(\varphi(t))$ and $\varphi(t) \notin \mathcal{S}$;
- *(b)* for $t \in \mathcal{T}$, $\varphi^-(t) \in \mathcal{S}$ and $\varphi^+(t) = \Delta(\varphi^-(t))$.

A solution $\varphi(t)$ of (2.56) is periodic if there exists a finite $T > 0$ such that $\varphi(t + T) = \varphi(t)$ for all $t \in [t_0, \infty)$. A set $\mathcal{O} \subset \mathcal{X}$ is a periodic orbit of (2.56) if $\mathcal{O} = \{\varphi(t) | t \geq t_0\}$ for some periodic solution $\varphi(t)$. An orbit is considered nontrivial if it contains more that one point. If a periodic solution has an impact event, then the corresponding periodic orbit $\mathcal{O}$ is not closed, and its set closure is denoted as $\bar{\mathcal{O}}$. The stability of orbits in the sense of Lyapunov, asymptotic stability and exponential stability is defined in [166]. A periodic orbit $\mathcal{O}$ is transversal to $\mathcal{S}$ if its closure intersects $\mathcal{S}$ in exactly one point, and for $\bar{x} = \bar{\mathcal{O}} \cap \mathcal{S}$, $L_f H(\bar{x}) = \frac{\partial H}{\partial x}(\bar{x}) f(\bar{x}) \neq 0$.

2.3.2 *Poincaré Map*

The first recurrence map or Poincaré map is widely used to analyze the stability of periodic orbits with impact events. It is defined as the intersection of a periodic orbit in the state space with a certain lower-dimensional subspace, called the Poincaré section, transversal to the flow of the system. For studying periodic orbits with impact events, it is natural to choose $\mathcal{S}$ as the Poincaré section. Let $\phi(t, x_0)$ denote

the maximal solution of (2.55) with initial condition x_0 at time $t_0 = 0$. The time-to-impact function $T_I : \mathcal{X} \cup \infty$ is defined by:

$$T_I(x_0) = \begin{cases} \inf\{t \geq 0 | \phi(t, x_0) \in \mathcal{S}\} & \text{if } \exists t \text{ such that } \phi(t, x_0) \in S \\ \infty & \text{otherwise} \end{cases} \tag{2.57}$$

The Poincaré return map, $P : \mathcal{S} \to \mathcal{S}$ is then defined as:

$$P(x) = \phi(T_I \circ \Delta(x), \Delta(x)) \tag{2.58}$$

Theorem 2.1: If a system (2.56) is of class C^1 and has a periodic orbit $\mathcal{O}$ with $x^* = \bar{\mathcal{O}} \cap \mathcal{S}$ a singleton and $L_f H(x^*) \neq 0$, then the following statements are equivalent:

1. x^* is an exponentially stable fixed point of P;
2. $\mathcal{O}$ is an exponentially stable periodic orbit.

The proof of this theorem is given in [83]. For a class C^1 hybrid system, P is differentiable at x^*, and T_I is also proven to be differentiable at each point of $\tilde{\mathcal{S}} = \{x \in \mathcal{S} | T_I(x) < \infty \text{ and } L_f H(P(x)) \neq 0\}$ [167]. In addition, the differentiability of Δ and f proves that P is differentiable on $\tilde{S}$. Hence, we can now check exponential stability of orbits by linearizing P at x^* and calculating corresponding eigenvalues.

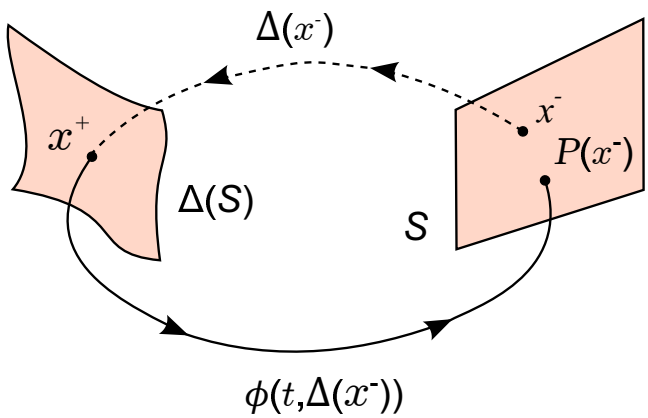

Fig. 2.1: Geometric interpretation of a Poincaré return map $P : \mathcal{S} \to \mathcal{S}$ for a system with impulse effects.

2.3.3 *Restricted Poincaré Map*

Consider a nonlinear system with impulse effects that depends on a real parameter $\epsilon > 0$:

$$\Sigma^\epsilon : \begin{cases} \dot{x} = f^\epsilon(x), & x^- \notin \mathcal{S} \\ x^+ = \Delta(x^-), & x^- \in \mathcal{S} \end{cases} \tag{2.59}$$

and suppose that for each value of $\epsilon > 0$, hypotheses HSH1-HSH5 are met. We further denote a solution of $\dot{x} = f^\epsilon(x)$ as $\phi^\epsilon(t, x_0)$, the time-to-impact function as T_I^ϵ, and the Poincaré map as $P^\epsilon : \mathcal{S} \to \mathcal{S}$. In addition, suppose that the following structural hypotheses hold [83]:

HS1) there exist global coordinates $x = [\eta^\top, \xi^\top]^\top$ for $\mathcal{X} \subset \mathbf{R}^n$, such that $\xi \in \mathbb{R}^{n-\varrho}$, and $\eta \in \mathbb{R}^\varrho$, $1 < \varrho < n$, in which f^ϵ has the form:

$$f^\epsilon(x) = f^\epsilon(\eta, \xi) = \begin{bmatrix} f^\epsilon_{1:\varrho}(\eta) \\ f^\epsilon_{\varrho+1:n}(\eta, \xi) \end{bmatrix} \tag{2.60}$$

HS2) for $\mathcal{Z} = \{[\eta^\top, \xi^\top]^\top \in \mathcal{X} | \eta = 0\}$, $\mathcal{S} \cap \mathcal{Z}$ is a $(n - \varrho - 1)$-dimensional, C^1-embedded submanifold of $\mathcal{Z}$ satisfying:

$$\Delta(\mathcal{S} \cap \mathcal{Z}) \subset \mathcal{Z} \tag{2.61}$$

HS3) (2.59) has a periodic orbit $\mathcal{O}$ that is contained in $\mathcal{Z}$ and hence the orbit is independent of ϵ;

HS4) $x^* = \bar{\mathcal{O}} \cap \mathcal{S} \cap \mathcal{Z}$ is a singleton;

HS5) $L_{f^\epsilon} H(x^*) \neq 0$;

HS6) $f^\epsilon_{1:\varrho}(\eta) = A(\epsilon)\eta$, and $\lim_{\epsilon \searrow 0} e^{A(\epsilon)} = 0$

Hypotheses HS1 and HS6 guarantee that the set $\mathcal{Z}$ is invariant under the continuous part of the model so that if $x_0 \in \mathcal{Z}$ then for all t in its maximal domain of existence, $\phi^\epsilon(t, x_0) \in \mathcal{Z}$. Hypothesis HS2 implies that $\mathcal{Z}$ remains invariant after the impact event, and therefore the solution of (2.56) satisfying $x_0 \in \mathcal{Z}$ implies $\varphi(t, x_0) \in \mathcal{Z}$ on its domain of existence. Hypotheses HS1 and HS2 suggest that the restriction of Σ^ϵ to the manifold $\mathcal{Z}$ is a well-defined system $\Sigma_\mathcal{Z}$ with impulse effects and restricted dynamics:

$$\Sigma_\mathcal{Z} : \begin{cases} \dot{z} = f_\mathcal{Z}(z), & z \notin \mathcal{S} \cap \mathcal{Z} \\ z^+ = \Delta_\mathcal{Z}(z^-), & z \in \mathcal{S} \cap \mathcal{Z} \end{cases} \tag{2.62}$$

where $z = [0_{1\times\varrho}, \xi^\top]^\top$, $f_\mathcal{Z}(z) = f^\epsilon(z)$, and $\Delta_\mathcal{Z} = \Delta(z)$. The invariance of $\mathcal{Z}$ also yields:

$$P^\epsilon(\mathcal{S} \cap \mathcal{Z}) \subset \mathcal{S} \cap \mathcal{Z} \tag{2.63}$$

From Hypothesis HS3, $\mathcal{O}$ is a periodic orbit of restriction dynamics independent of ϵ. Accordingly, $\phi_\mathcal{Z} = \phi^\epsilon|\mathcal{Z}$, $T_{I,\mathcal{Z}} = T^\epsilon_I|_\mathcal{Z}$ and $P^\epsilon|_\mathcal{Z}$ are also independent of ϵ, and hence:

$$t^* = T^\epsilon_I(\Delta(x^*)) = T_{I,\mathcal{Z}}(\Delta_\mathcal{Z}(x^*)) \tag{2.64}$$

is independent of ϵ. On the basis of (2.63), the restricted Poincaré map, $\rho : \mathcal{S} \cap \mathcal{Z} \to \mathcal{S} \cap \mathcal{Z}$, can be defined as:

$$\rho(z) = \phi_\mathcal{Z}(T_{I,\mathcal{Z}}(\Delta_\mathcal{Z}(z)), \Delta_\mathcal{Z}(z)) \tag{2.65}$$

and is independent of ϵ. According to HS4, x^* is a fixed point of P^ϵ and ρ, and from HS5, the orbit is transversal to $\mathcal{S}$, and hence also to $\mathcal{S} \cap \mathcal{Z}$. Hypothesis HS6 requires the dynamics transversal to $\mathcal{Z}$ to be sufficiently contracting. When $\eta(t) \neq 0$, the impact map may increase the norm of η at each impact. Hypothesis HS6 provides control to make $\eta(t)$ converge to zero during the continuous phase so that for a

complete cycle including an impact event and a continuous phase, the solution may converge to the periodic orbit.

Theorem 2.2: Under Hypotheses HSH1-HSH5, and HS1-HS6, there exists $\bar{\epsilon} > 0$ such that for $0 < \epsilon < \bar{\epsilon}$ the following statements are equivalent:

1. x^* is an exponentially stable fixed point of ρ;
2. x^* is an exponentially stable fixed point of P^ϵ.

The proof of this theorem is given in [83]. This theorem suggests that, for sufficiently small, positive ϵ, an exponentially stable periodic orbit of the restriction dynamics is also an exponentially stable periodic orbit of the full-dimensional model.

2.4 Parametric Optimization

Optimization is an important tool in decision science as well as in the analysis of physical systems. To apply it, we must first recognize the objective which is a quantitative measure of the performance of the system under study. The objective depends on certain characteristics of the system, named parameters. Depending on whether the parameters are continuous or discrete, optimization can be divided into continuous optimization and discrete optimization. In this thesis, the optimization we care about is continuous. By judging whether there are constraints on the parameters or not, we can further classify the continuous optimization into two categories: constrained optimization and unconstrained optimization. For our purpose, we will only focus on constrained optimization using sequential quadratic programming.

2.4.1 Constrained Optimization

Mathematically speaking, the goal of constrained optimization is to minimize a function subject to constraints on its variables. A typical optimization can be written as:

$$\min_{\vartheta \in \mathbb{R}^{n_\vartheta}} \hbar(\vartheta) \text{ subject to } \begin{cases} c_i(\vartheta) = 0, & i \in \mathcal{E}_{set} \\ c_i(\vartheta) \leq 0, & i \in \mathcal{I}_{set} \end{cases} \tag{2.66}$$

where ϑ is the vector of parameters, $\hbar$ is the positive-definite objective function of ϑ that we want to minimize, $\mathcal{E}_{set}$ and $\mathcal{I}_{set}$ are finite sets of indexes ($\mathcal{I}_{set} \cap \mathcal{E}_{set} = \emptyset$), and c_i with $i \in \mathcal{E}_{set}$ or $i \in \mathcal{I}_{set}$ are scalar-valued functions representing respectively the equality constraints or the inequality constraint. For convenience, it is assumed that $\mathcal{I}_{set} = \{1, 2, \cdots, n_\mathcal{I}\}$ and $\mathcal{E}_{set} = \{n_\mathcal{I} + 1, n_\mathcal{I} + 2, \cdots, n_\mathcal{E}\}$ with $n_\mathcal{I}$ and $n_\mathcal{E}$ representing the total numbers of set elements. If we define $\Omega_{set} = \{\vartheta | c_i(\vartheta) = 0, i \in \mathcal{E}_{set}; c_i(\vartheta) \leq 0, i \in \mathcal{I}_{set}\}$ to be the feasible set of points ϑ that satisfy the constraints, we can also rewrite (2.66) more compactly as:

$$\min_{\vartheta \in \Omega_{set}} \hbar(\vartheta) \tag{2.67}$$

A vector ϑ^* is a local solution of the problem (2.66) if $\vartheta^* \in \Omega_{set}$ and there is a neighborhood $\mathcal{N}_{set}$ of ϑ^* such that $\hbar(\vartheta) \geq \hbar(\vartheta^*)$ for $\vartheta \in \mathcal{N}_{set} \cap \Omega_{set}$. If we have

$\hbar(\vartheta) > \hbar(\vartheta^*)\ \forall\vartheta \in \mathcal{N}_{set} \cap \Omega_{set}$ with $\vartheta \neq \vartheta^*$, then the solution is considered a strict local solution.

In constrained optimization, the general approach is to transform the problem into an easier subproblem that can be solved and then used as the basis of an iterative process. Early methods usually involve the conversion of the constrained problem to a basic unconstrained problem using a penalty function for constraints. In this way, the constrained problem is solved using a sequence of parameterized unconstrained optimizations, which in the limit converge to the constrained problem. Nowadays these methods are considered relatively inefficient and have been replaced by methods focusing on solving the Karush-Kuhn-Tucker (KKT) equations [162].

In general, we can define the Lagrangian for the constrained optimization problem (2.66) as:

$$\mathcal{L}(\vartheta, \lambda) = \hbar(\vartheta) - \sum_{i \in \mathcal{E}_{set} \cup \mathcal{I}_{set}} \lambda_i c_i(\vartheta) \tag{2.68}$$

At a feasible point ϑ, the inequality constraints $i \in \mathcal{I}_{set}$ is said to be active if $c_i(x) = 0$ and inactive if $c_i(x) < 0$. The active set $\mathcal{A}_{set}(\vartheta)$ at any feasible ϑ is the union of $\mathcal{E}_{set}$ and the indexes of the active inequality constraints, namely $\mathcal{A}_{set}(\vartheta) = \mathcal{E}_{set} \cup \{i \in \mathcal{I}_{set} | c_i(\vartheta) = 0\}$. Given the point ϑ^* and the corresponding active set $\mathcal{A}_{set}(\vartheta^*)$, the linear independence constraint qualification (LICQ) holds if the set of active constraint gradients $\{\nabla c_i(\vartheta^*), i \in \mathcal{A}_{set}(\vartheta^*)\}$ is linearly independent. If this condition is satisfied, none of the active constraints gradients can be zero, and we can further state the following optimality conditions for a general nonlinear programming problem (2.66). These conditions are called KKT conditions or first-order necessary conditions (FONC) since they concern the properties of the gradients of the objective and constraints functions.

Theorem 2.3 (FONC): Suppose that ϑ^* is a local solution of (2.66) and that the LICQ holds at ϑ^*. Then there exists a Lagrange multiplier vector λ^* with components λ_i^*, $i \in \mathcal{E}_{set} \cup \mathcal{I}_{set}$ such that the following conditions are satisfied at (ϑ^*, λ^*) [162]:

$$\nabla_\vartheta \mathcal{L}(\vartheta^*, \lambda^*) = 0\,, \tag{2.69a}$$

$$c_i(\vartheta^*) = 0\,, \quad \text{for all } i \in \mathcal{E}_{set}\,, \tag{2.69b}$$

$$c_i(\vartheta^*) \leq 0\,, \quad \text{for all } i \in \mathcal{I}_{set}\,, \tag{2.69c}$$

$$\lambda_i^* \geq 0\,, \quad \text{for all } i \in \mathcal{I}_{set}\,, \tag{2.69d}$$

$$\lambda_i^* c_i(\vartheta^*) = 0\,, \quad \text{for all } i \in \mathcal{E}_{set} \cup \mathcal{I}_{set}\,. \tag{2.69e}$$

We move on to define the linearized feasible set as:

$$\mathcal{F}_{set} = \left\{ d : \begin{array}{ll} d^\top \nabla c_i(\vartheta) = 0 & \forall i \in \mathcal{E}_{set} \\ d^\top \nabla c_i(\vartheta) \geq 0 & \forall i \in \mathcal{A}_{set}(\vartheta) \cap \mathcal{I}_{set} \end{array} \right\} \tag{2.70}$$

For a point ϑ^* satisfying $\nabla_\vartheta \mathcal{L}(\vartheta^*, \lambda^*) = 0$ with some λ^*, we have:

$$\nabla \hbar(\vartheta^*) = \sum_{i \in \mathcal{A}_{set}(\vartheta^*)} \lambda_i^* \nabla c_i(\vartheta^*) \tag{2.71}$$

If ϑ^* is a local solution, then the following condition should hold:

$$d^\top \nabla \hbar(\vartheta^*) = \sum_{i \in \mathcal{A}_{set}(\vartheta^*)} \lambda_i^* d^\top \nabla c_i(\vartheta^*) \geq 0, \quad \forall d \in \mathcal{F}_{set}(\vartheta^*) \tag{2.72}$$

For $d^\top \nabla \hbar(\vartheta^*) \geq 0$ with $d \in \mathcal{F}_{set}(\vartheta^*)$, it is clear that moving along d away from ϑ^* will increase the objective function value. However, we can no longer make the same judgment if $d^\top \nabla \hbar(\vartheta^*) = 0$. In this case, we need to check the second order conditions.

Assuming that $\hbar$ and all c_i are twice continuously differentiable, we define the critical cone $\mathcal{C}(\vartheta^*, \lambda^*)$ as follows for some Lagrange multiplier λ^* satisfying the KKT conditions:

$$\mathcal{C} = \left\{ d : \begin{array}{ll} d^\top \nabla c_i(\vartheta) = 0 & \forall i \in \mathcal{E}_{set} \\ d^\top \nabla c_i(\vartheta) = 0 & \forall i \in \mathcal{A}_{set}(\vartheta^*) \cap \mathcal{I}_{set} \text{ with } \lambda_i^* > 0, \\ d^\top \nabla c_i(\vartheta) \geq 0 & \forall i \in \mathcal{A}_{set}(\vartheta^*) \cap \mathcal{I}_{set} \text{ with } \lambda_i^* = 0. \end{array} \right\} \tag{2.73}$$

In this way, we have:

$$d^\top \nabla \hbar(\vartheta^*) = \sum_{i \in \mathcal{A}_{set}(\vartheta^*)} \lambda_i^* d^\top \nabla c_i(\vartheta^*) = 0, \quad \forall d \in \mathcal{C}(\vartheta^*, \lambda^*) \tag{2.74}$$

which means that the critical cone $\mathcal{C}(\vartheta^*, \lambda^*)$ contains directions from $\mathcal{F}_{set}(\vartheta^*)$ for which it is not known whether $\hbar$ will increase or decrease from the corresponding first order information alone.

In order to know more about the behavior of $\hbar$, we can first define second-order necessary conditions (SONC) rendering the curvature of the Lagrangian nonzero along directions in $\mathcal{C}(\vartheta^*, \lambda^*)$.

Theorem 2.4 (SONC): Suppose that ϑ^* is a local solution of the constrained problem (2.66) and that the LICQ holds at ϑ^*. Let λ^* be the Lagrange multiplier vector for which the KKT conditions (2.69) are satisfied, and let the critical cone $\mathcal{C}(\vartheta^*, \lambda^*)$ defined as above [162]. Then we have:

$$d^\top \nabla_{\vartheta\vartheta} \mathcal{L}(\vartheta^*, \lambda^*) \geq 0, \quad \forall d \in \mathcal{C}(\vartheta^*, \lambda^*) \tag{2.75}$$

The second-order sufficient conditions (SOSC) is similar to the necessary conditions, but it differs in that the constraint qualification is no longer required, and the inequality is replaced by a strict inequality.

Theorem 2.5 (SOSC): Suppose for some feasible point $\vartheta^* \in \mathbb{R}^{n_\vartheta}$ there exists a Lagrange multiplier vector λ^* such that the KKT conditions (2.69) are satisfied [162]. Suppose also that:

$$d^\top \nabla_{\vartheta\vartheta} \mathcal{L}(\vartheta^*, \lambda^*) > 0, \quad \forall\, d \in \mathcal{C}(\vartheta^*, \lambda^*),\, d \neq 0 \tag{2.76}$$

Then ϑ^* is a strict local solution for (2.66).

In constrained optimization we are often confronted with the conflicting goals of reducing the objective function and satisfying the constraints. Therefore, we need

to define merit functions that can measure the balance between these two goals. A typical merit function is defined as:

$$\mathcal{M}(\vartheta, \mu) = \hbar(\vartheta) + \sum_{i \in \mathcal{E}_{set}} \mu_i |c_i(\vartheta)| + \sum_{i \in \mathcal{I}_{set}} \mu_i \max(0, c_i(\vartheta)) \tag{2.77}$$

where μ is the penalty parameter which determines the weight that we assign to constraint satisfaction relative to minimization of the objective. In some practical algorithms, μ is updated iteratively. The optimization algorithms that implement this merit function ensure that the value of $\mathcal{M}(\vartheta, \mu)$ in each optimization step is reducing.

2.4.2 *Sequential Quadratic Programming*

The sequential quadratic programming (SQP) approach is one of the most effective methods for nonlinearly constrained optimization. The method is based on the work of [168, 169, 170]. Given the problem description in (2.66), the principal idea of SQP is to formulate a quadratic programming (QP) subproblem based on a quadratic approximation of the Lagrangian function (2.68):

$$\min \tfrac{1}{2} d^\top \mathcal{H}_k d + \nabla \hbar_k^\top d \tag{2.78a}$$

$$\text{subject to } \nabla c_i(\vartheta_k)^\top d + c_i(\vartheta_k) = 0, \quad i \in \mathcal{E}_{set}, \tag{2.78b}$$

$$\nabla c_i(\vartheta_k)^\top d + c_i(\vartheta_k) \leq 0, \quad i \in \mathcal{I}_{set}. \tag{2.78c}$$

We first assume that $\mathcal{H}_k = \nabla^2_{\vartheta\vartheta} \mathcal{L}(\vartheta_k, \lambda_k)$. If all the constraints are equality constraints, we can apply a Newton-Lagrange method. By specializing the KKT conditions to the equality-constrained case, we obtain a system defined by:

$$\mathcal{N}(\vartheta, \lambda) = \begin{bmatrix} \nabla \hbar(\vartheta) - \nabla c(\vartheta) \lambda \\ c(\vartheta) \end{bmatrix} = 0 \tag{2.79}$$

If $\nabla c(\vartheta^*)$ has full rank, any solution (ϑ^*, λ^*) of the equality-constrained problem satisfies (2.79), and one approach for solving the nonlinear equations(2.79) is Newton's method.

Assuming (ϑ_k, λ_k) is an iterate, the Jacobian of (2.79) at (ϑ_k, λ_k) is given by:

$$J_{\mathcal{N}} = \begin{bmatrix} \mathcal{H}_k & -\nabla c(\vartheta_k, \lambda_k) \\ \nabla c(\vartheta_k, \lambda_k)^\top & 0 \end{bmatrix} \tag{2.80}$$

By solving the KKT system:

$$\begin{bmatrix} \mathcal{H}_k & -\nabla c_k \\ \nabla c_k^\top & 0 \end{bmatrix} \begin{bmatrix} \vartheta_{k+1} - \vartheta_k \\ \lambda_{k+1} - \lambda_k \end{bmatrix} = \begin{bmatrix} -\nabla \hbar_k + \nabla c_k \lambda_k \\ -c_k \end{bmatrix} \tag{2.81}$$

we can calculate the next iterate $(\vartheta_{k+1}, \lambda_{k+1})$. For practical SQP algorithms, $\mathcal{H}_k$ is usually estimated using Broyden–Fletcher–Goldfarb–Shanno (BFGS) algorithm, and the methods similar to the one given by (2.81) is used to produce a vector d_k which forms a new iterate $\vartheta_{k+1} = \vartheta_k + \alpha_k d_k$. The step length α_k is then determined in order to produce a sufficient decrease in a merit function such as (2.77). This

iterative process ends when the convergence test involving (2.69), (2.75), (2.76) or other conditions is satisfied.

The major advantage crucial for applying this algorithm in generating walking trajectories is its robustness to invalid results. During its iterations, the SQP algorithm can attempt to take a step that fails. This happens when the objective function or the nonlinear constraint function cannot provide valid value, i.e., the value is complex, infinite or not available. In this case, the algorithm attempts to take a smaller step.

2.5 Conclusion

In this chapter, four foundations of optimized control of bipedal walking are discussed in sequential order. To begin with, the Lagrange method and additional equations for calculating external forces and torques[2] are introduced for establishing the dynamic models of bipedal robots with rigid bodies, ideal springs, torque actuators and non-parallel structures. Then the method of feedback linearization is introduced to realize nonlinear control of bipedal robots and asymptotically forcing the robot system to evolve on a predefined zero dynamics surface. For the bipedal robots studied herein, it is convenient to realize hybrid invariance[3] and thus create hybrid zero dynamics. Thereafter, the stability of periodic gaits can be equivalently ensured by calculating the restricted Poincaré map about the evolution of hybrid zero dynamics with reduced dimensions. Finally, the general concept of parametric optimization and the method of sequential programming are explained briefly, and they will be later used for calculating optimized gaits.

[2] In the following chapters, these torques and forces are considered as ground reaction forces and torques.

[3] The method of achieving hybrid invariance is introduced in Chapter 3.

3. UNDERACTUATED PLANAR BIPEDAL ROBOTS WITH POINT FEET

This chapter focuses on modeling, controlling and optimizing an underactuated 5-link planar bipedal robot with point feet, which is fundamental to the development of similar planar robots consisting of more links.

Theoretically, all these robots consist of rigid links connected via frictionless revolute joints to form different kinematic chains in the sagittal plane. It is further assumed that two identical subchains (legs with point feet) connect at a common point called the hip, and during walking the point foot of the stance leg is underactuated. The idea of designing this type of robots started nearly two decades ago from a planar bipedal robot named "RABBIT" in Grenoble [5]. Over the years similar robots have been built such as AMBER [106] and MABEL [171]. For our 5-link robot, the model parameters we choose is estimated from the humanoid robot HRP-4 [172]. This process involves proportionally creating virtual anthropomorphic structures with different assumed morphologies with only two input parameters (the total mass and the height) and then obtaining model parameters including masses, lengths, moments of inertia and positions of CoMs from these generated virtual structures [173, 174].

For the walking, each step is simplified into two successive phases of single support and double support with two different models to form the hybrid model of the robot during a complete step. Thereafter, the gait control can be realized by applying holonomic constraints defined as functions of robot state [115, 84]. To achieve this, a within-step controller based on feedback linearization is adopted based on the ideas explained in Section 2.2. Using feedback linearization, we can create a two dimensional zero dynamics of the full hybrid model, which enables us to analyze the stability of the hybrid zero dynamics using a scalar LTI return map. If the hybrid zero dynamics is proven to be exponentially stable, then from Theorem 2.2 in Section 2.3 the evolution of the full hybrid dynamics is also exponentially stable, meaning that the stable walking of the underactuated bipedal robot is achieved.

In order to parameterize the hybrid zero dynamics and calculate optimized walking motions with satisfactory energy efficiency, it is of great importance to define satisfactory controlled outputs. For our planar biped, we seek to define outputs that can contain obvious geometric interpretations. Many researchers have delved into biped robots with similar intentions. For instance, Ferreira et al. [175] have studied the support vector regression based on ZMP (Zero moment point) theory, but ZMP cannot apply to robots without nontrivial feet. Yang et al. [176] have suggested using truncated Fourier series (TFS) formulation for biped robot balancing control. Our work has drawn inspiration from the paper of Grizzle et al. [6],

where they have proposed a feedback design to realize both posture control and swing leg advancement by specifying a constant value to the absolute torso angle and command the swing leg to behave as the mirror image of the stance leg. For 5-link robot, they also proposed a similar method by commanding the hip to remain roughly centered between two feet and at a nearly constant height [7]. In the light of these previous works, we attempt to propose an output vector named the "Symmetry Outputs". Our outputs, however, diverges from these preexisting works in three important ways: (a) we do not seek to control the position of the hip; (b) the angle of the bisector of the virtual swing and stance legs regarding the vertical position is defined to describe the mirror-like behavior of the virtual swing leg; (c) the swing knee angle and the stance knee angle are included in the symmetry outputs.

For the optimization of underactuated walking, we first define the desired outputs using both Bézier coefficients and postural parameters to achieve hybrid invariance. Subsequently, the cost function based on the energy consumption of DC motors or brushless motors is proposed, and the constraints ensuring valid walking motions are listed. The optimization is realized by using the SQP algorithm provided by the `fmincon` function in MATLAB® optimization toolbox (R2010a). By running optimization with symmetry outputs at different walking speeds from 0.2 m/s to 1.5 m/s, we have attained various data of optimal walking including the curves of angles and torques, and we have also proved that the walking generated by the optimization program is exponentially stable.

This chapter is organized as follows. Section 3.1 lists all the hypotheses concerning planar bipedal robots with point feet. Section 3.2 delineates the 5-link robot model treated in this chapter. Section 3.3 introduces the symmetry outputs together with the feedback design using optimized Hybrid Zero Dynamics (HZD). Section 3.4 addresses the details of the optimization program including the parameterization of holonomic constraints, the definition of the criterion and the constraints, and the optimization algorithm. Section 3.5 presents the optimized walking data with a speed ranging from 0.2 m/s to 1.5 m/s. Finally, a conclusion is given in Section 3.6

3.1 Robot Structure and Hypotheses

In this thesis, a planar biped is a bipedal robot with motions taking place only in the sagittal plane, and it consists of two kinematic subchains named legs and another subchain named torso, all connected at a common point called hip. When there is only one of two legs contacting the ground, the contacting leg is named the stance leg and the other is named swing leg. The parts of legs can be named separately in the same way. A foot is defined as the end of a leg, whether it is a body or not. The single support phase is defined to be the phase of locomotion where only one foot is in contact with the ground. Conversely, the double support phase is the phase where both feet are on the ground. Walking is then considered as alternating phases of single and double support, with the requirement that the robot's CoM monotonically moving along the walking direction. With these in mind, we can revisit the hypotheses originally listed in [84] and rephrase them in the context

of our robot to achieve logical completion and to provide comparison with similar hypotheses for 3D biped in later chapters.

Planar Robot Hypotheses: The planar robot is assumed to be:

HPR1) comprised of N rigid links connected by $(N-1)$ frictionless revolute joints, and each link has nonzero mass;

HPR2) planar, with motion constrained to the sagittal plane;

HPR3) bipedal, with two symmetric legs connected at a common point called the hip, and both legs are terminated in point feet;

HPR4) underactuated at the stance point foot connecting the stance leg and the ground;

HPR5) independently actuated at the other $(N-1)$ joints;

HPR6) the model is expressed in $(N-1)$ relative angular coordinates $(q_2, \cdots, q_N)$ plus one absolute angular coordinate q_1.

Note that the properties of the robot are independent of the choice of coordinate, and *HPR6* is used only to facilitate the calculation of zero dynamics.

Planar Robot Gait Hypotheses: The controller of the robot is required to insure robot motion satisfying the following properties:

HPG1) there are alternative phases of single support and double support;

HPG2) during the single support phase, the stance foot lies on the ground and does not slide on the ground;

HPG3) the double support phase is instantaneous and can be modeled as a rigid contact;

HPG4) in steady state, two continuous steps are symmetric with respect to the two legs;

HPG5) in each step, only the stance foot contacts the ground, and the swing foot starts from the position strictly behind the stance foot and lands on the position strictly in front of the stance foot at the impact;

HPG6) walking takes place on a horizontal surface.

Planar Robot Impact Hypotheses: An impact occurs at the double support phase when the swing foot hits the ground. The impact model is based on the following assumptions:

HPI1) the impact occurs when the swing foot contacts the ground, and the swing foot neither slips nor rebounds;

HPI2) at the impact, the stance foot is raised from the ground without interaction;

HPI3) the impact happens instantaneously;

HPI4) the external forces acting on the swing foot during the impact can be represented by impulses;

HPI5) there may be an instantaneous change of the velocities, but the configuration remain unchanged;

HPI6) all the actuators are not capable of generate impulses and thus they are ignored during impact.

3.2 Dynamic Model of Walking

This section develops a mathematical model for a 5-link bipedal robot conforming to Hypotheses *HPR1-HPR6*, *HPG1-HPG6* and *HPI1-HPI6*. As illustrated in Figure 3.1, the planar robot analyzed in this chapter is modeled as a tree structure with two identical legs and a torso all connected at a single point called hip. It contains five links: a torso, two thighs and two shins. The end of each shin is considered as a point foot.

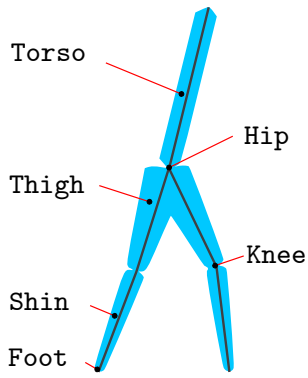

Fig. 3.1: Definitions of joints and links of the 5-link planar robot

As depicted in Figure 3.2, the generalized coordinate vector describing the biped in the sagittal plane is defined as $q_e = [x_{st}, z_{st}, q_1, q_2, q_3, q_4, q_5]^\top$. It contains two coordinates (x_{st}, z_{st}) in the coordinate frame $o_g x_g z_g$ describing the position of the stance foot and an angle vector with five coordinates $q = [q_1, q_2, q_3, q_4, q_5]^\top$ for the orientation of legs and torsos. Using q, the absolute angle of the swing tibia q_6 is given by:

$$q_6 = q_1 + q_2 + q_3 - q_4 - q_5 \tag{3.1}$$

which is used with (x_{sw}, z_{sw}) for calculating the impact model. We assume that the positive angles are clockwise. In reference to the humanoid robot HRP-4, the total mass is 39 kg and the total height is 1.5 m [172]. The reflected motor inertias on the joint sides of all the actuated joints are 0.8 kgm^2. The rest of the model parameters

are extracted from proportional virtual anthropomorphic structures automatically generated using the total mass and the total height[173, 174]. All the other parameters are listed in Table 3.1. Among them, the CoMs of the thighs and the torso are measured in reference to the hip, and the CoMs of the shins are located by their distances from the knees.

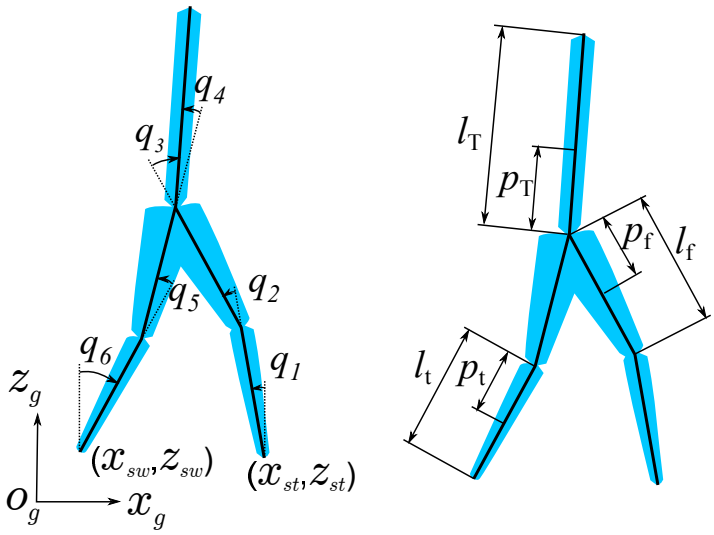

Fig. 3.2: The generalized coordinates and the length information of the 5-link planar robot

Tab. 3.1: Model Parameters of the 5-link planar robot

Model Parameters	Torso(T)	Thigh(f)	Shin(t)
Mass,$m_*(kg)$	26.675	3.9360	2.227
Length,$l_*(m)$	0.693	0.404	0.404
Inertia,$I_*(m^2kg)$	0.984	0.054	0.030
Center of Mass,$p_*(m)$	0.217	0.174	0.174

3.2.1 *Swing Phase Model*

The swing phase model is used to simulate the bipedal robot behavior when one of the two feet in contact with the ground. As the gait is assumed to be symmetric according to Hypothesis *HPG4*, it does not matter which leg end is pinned, and the swapping of the legs can be handled by the impact model. Let $\mathcal{Q}$ denote the 5-dimensional configuration space of the robot during the single support phase and let $q \in \mathcal{Q}$ be the set of generalized coordinates with $q = [q_1, q_2, q_3, q_4, q_5]^\top$. Using the Lagrange method described in Section 2.1, the dynamic model during the swing phase can be easily obtained:

$$D(q)\ddot{q} + C(q, \dot{q}) + G(q) = Bu = \begin{bmatrix} 0_{1\times 4} \\ I_{4\times 4} \end{bmatrix} u \tag{3.2}$$

where the matrix D is the (5×5) inertia matrix, C is the (5×1) vector of Coriolis and centrifugal terms, G is the (5×1) vector of gravity terms, and B is the (5×4)

matrix mapping the joint torques $u = [u_2, u_3, u_4, u_5]^\top$ to generalized forces. The matrix D also contains rotor inertia estimated from a previous publication [8]. Let $x = [q^\top, \dot{q}^\top]^\top$ be the state variables of the robot and $\mathcal{TQ} = \{x = (q^\top, \dot{q}^\top)^\top | q \in \mathcal{Q}, \dot{q} \in \mathbb{R}^N\}$ be the state space. The swing phase model can also be written in state space form:

$$\begin{aligned} \dot{x} &= \begin{bmatrix} \dot{q} \\ D^{-1}(q)[-C(q,\dot{q})\dot{q} - G(q) + Bu] \end{bmatrix} \\ &= f(x) + g(x)u \end{aligned} \tag{3.3}$$

with $f(x)$ and $g(x)$ being:

$$f(x) = \begin{bmatrix} \dot{q} \\ -D^{-1}(q)(C(q,\dot{q}) + G(q)) \end{bmatrix} \tag{3.4}$$

$$g(x) = \begin{bmatrix} 0_{5\times 4} \\ D^{-1}B \end{bmatrix} \tag{3.5}$$

Note that $D(q)$ is a positive definite matrix invertible for all $q \in \mathcal{Q}$.

3.2.2 Impact Model

The impact model is used at the double support phase when the swing foot hits the ground. There are different impact models available for modeling bipedal walking. For instance, the reaction forces between the ground and the foot are sometimes modeled with nonlinear spring-dampers in a compliant impact model [177]. However, the impact duration for common walking surfaces is very short and thus the stiffness of the corresponding differential equations makes it difficult to incorporate them into the analysis of walking gaits. Thus, we choose to use the rigid impact model from [178] to collapse the impact phase to an instant. Consequently, the impact forces are modeled by impulses, and a jump is allowed in the velocity component of the robot's state while the configuration variables remains constant throughout the impact.

The formulation of the impact model requires the dynamic model defined by generalized coordinates $q_e = [x_{st}, z_{st}, q_1, q_2, q_3, q_4, q_5]^\top$. By implementing the Lagrange method, the dynamic model during the impact phase is given by:

$$D_e(q_e)\ddot{q}_e + C_e(q_e, \dot{q}_e)\dot{q}_e + G_e(q_e) = B_e u + \delta\mathcal{F}_{imp} \tag{3.6}$$

where the matrix D_e is the (7×7) inertia matrix, C_e is the (7×1) vector of Coriolis terms and centrifugal terms, G_e is the (7×1) vector of gravity terms, B_e is the (7×4) matrix mapping the joint torques u to generalized forces, and $\delta\mathcal{F}_{imp}$ is the impulsive impact force. By integrating (3.6) over the "duration" of the impact and then calculating its limit as $\Delta t = t^+ - t^- \to 0$, we eliminate the terms $C_e(q_e, \dot{q}_e)\dot{q}_e$, $G_e(q_e)$ and $B_e u$ and obtain the equation:

$$D_e(q_e^+)\dot{q}_e^+ - D_e(q_e^-)\dot{q}_e^- = \mathcal{F}_{imp} \tag{3.7}$$

where $\mathcal{F}_{imp} = \int_{t^-}^{t^+} \delta\mathcal{F}_{imp}(\tau)d\tau$ is the integrated impulsive impact force, and the superscripts $-$ and $+$ respectively represents the state just before the impact and just after the impact. Note that there is no relabeling among q_e^-, q_e^+, $\dot{q}_e^-$ and $\dot{q}_e^+$, meaning that:

$$q_e^- = [x_{st}^-, z_{st}^-, q_1^-, q_2^-, q_3^-, q_4^-, q_5^-]^\top \qquad \dot{q}_e^- = [\dot{x}_{st}^-, \dot{z}_{st}^-, \dot{q}_1^-, \dot{q}_2^-, \dot{q}_3^-, \dot{q}_4^-, \dot{q}_5^-]^\top \tag{3.8}$$

$$q_e^+ = [x_{st}^+, z_{st}^+, q_1^+, q_2^+, q_3^+, q_4^+, q_5^+]^\top \qquad \dot{q}_e^- = [\dot{x}_{st}^+, \dot{z}_{st}^+, \dot{q}_1^+, \dot{q}_2^+, \dot{q}_3^+, \dot{q}_4^+, \dot{q}_5^+]^\top \tag{3.9}$$

By Hypothesis *HPI5*, the configuration of the robot remains unchanged during the impact, and thus $q_e^+ = q_e^-$. According to Hypothesis *HPI2*, there is no interaction between the former stance foot and the ground, and thus (3.7) can further be written as:

$$D_e(q_e^+)\dot{q}_e^+ - D_e(q_e^-)\dot{q}_e^- = J_{sw}^v(q_e^-)^\top F_{sw} \tag{3.10}$$

where $F_{sw} = [F_{sw}^x, F_{sw}^z]^\top$ represents the impact forces on the swing foot and $J_{sw}^v = \frac{\partial}{\partial q_e}[x_{sw}, z_{sw}]^\top$ with (x_{sw}, z_{sw}) being the coordinates of the swing foot. Accordingly, the expression describing the instantaneous change of the velocity of the robot during the impact can be formulated as:

$$\Pi(q_e^-)\begin{bmatrix}\dot{q}_e^+ \\ F_{sw}\end{bmatrix} = \begin{bmatrix}D_e(q_e^-)\dot{q}_e \\ 0_{2\times1}\end{bmatrix} \tag{3.11}$$

where Π is defined as:

$$\Pi(q_e^-) = \begin{bmatrix}D_e(q_e^-) & -J_{sw}^v(q_e^-)^\top \\ J_{sw}^v(q_e^-) & 0_{2\times2}\end{bmatrix} \tag{3.12}$$

Solving (3.12) yields:

$$\begin{bmatrix}\dot{q}_e^+ \\ F_{sw}\end{bmatrix} = \Pi(q_e^-)^{-1}\begin{bmatrix}D_e(q_e^-)\dot{q}_e^- \\ 0_{2\times1}\end{bmatrix} \tag{3.13}$$

Then q_6^- and $\dot{q}_6^+$ can be calculated by:

$$q_6^- = q_1^- + q_2^- + q_3^- - q_4^- - q_5^- \tag{3.14}$$

$$\dot{q}_6^+ = \dot{q}_1^+ + \dot{q}_2^+ + \dot{q}_3^+ - \dot{q}_4^+ - \dot{q}_5^+ \tag{3.15}$$

After impact, the former stance leg becomes the swing leg and vice versa, which means that the impact model must take into account the relabeling of q. Accordingly q^-, $\dot{q}^-$, q^+ and $\dot{q}^+$ are respectively given as:

$$q^- = [q_1^-, q_2^-, q_3^-, q_4^-, q_5^-]^\top \qquad \dot{q}^- = [\dot{q}_1^-, \dot{q}_2^-, \dot{q}_3^-, \dot{q}_4^-, \dot{q}_5^-]^\top \tag{3.16}$$

$$q^+ = [q_6^+, q_5^+, q_4^+, q_3^+, q_2^+]^\top \qquad \dot{q}^- = [\dot{q}_6^+, \dot{q}_5^+, \dot{q}_4^+, \dot{q}_3^+, \dot{q}_2^+]^\top \tag{3.17}$$

Accordingly, the impact model can be formulated as:

$$x^+ = \Delta(x^-) = \begin{bmatrix}\Delta_q q^- \\ \Delta_{\dot{q}}(q^-)\dot{q}^-\end{bmatrix} = \begin{bmatrix}q^+ \\ \dot{q}^+\end{bmatrix} \tag{3.18}$$

where $x^- = [q^{-\top}, \dot{q}^{-\top}]^\top$. The relabeling and sign changing incorporated by the above functions enable us to use the same swing phase model and the same impact model no matter which leg serves as the stance leg.

3.2.3 Hybrid Model

The overall model of walking is obtained by combining the swing phase model and the impact model to form a hybrid model. Assuming that the state variable vector $x(t)$ has finite left and right limits $x^-(t) = \lim_{\tau \nearrow t} x(\tau)$ and $x^+(t) = \lim_{\tau \searrow t} x(\tau)$, the hybrid model is then formulated as:

$$\Sigma : \begin{cases} \dot{x} = f(x) + g(x)u & x \notin \mathcal{S} \\ x^+ = \Delta(x^-) & x^- \in \mathcal{S} \end{cases} \tag{3.19}$$

where $S = \{(q, \dot{q}) \in TQ | z_{sw}(q) = 0, x_{sw}(q) - x_{st} > 0\}$ is the switching surface with z_{sw}, x_{sw} and x_{st} being the coordinates of the swing foot and the stance foot. The mathematical meaning of a solution of the model (3.19) is given in Section 2.3. A complete step of the robot starts with the robot in double support, ends in double support with the roles of the legs swapped, and contains only one impact event.

3.2.4 Point-foot Contact Model

The validity of the swing phase model is based on Hypothesis *HPG2* which assumes that the stance foot is firmly fixed to the ground. However, it is also possible that the stance foot slips on the ground or just rises above the ground like our stance foot does while we run. Assuming that the ground reaction force on the stance foot is $F_{st} = [F_{st}^x, F_{st}^z]^\top$, we can calculate it as a function of q, $\dot{q}$ and $\ddot{q}$ using (2.19). Since the contact is unilateral, we need to check that the vertical component of F_{st} is positive so that the bipedal robot does not jump during the single support phase, that is:

$$F_{st}^z > 0 \tag{3.20}$$

Furthermore, it is also important to make sure that the stance foot does not slide on the ground, and this can be prevented by adding the constraint:

$$\mu_{\mathrm{f}} F_{st}^z - |F_{st}^x| > 0 \tag{3.21}$$

where μ_{f} is the coefficient of friction between the foot end and the ground.

3.3 Feedback Control Design

3.3.1 Controlled Outputs

During the swing phase, the bipedal robot has four independent actuators, and thus the dimension of the outputs equals to four. The output function is defined as:

$$y = h(q) = h_0(q) - h_d \circ \theta(q) \tag{3.22}$$

where $h_0(q)$ is independent controlled quantities, $\theta(q)$ represents a strictly monotonic function of the robot's state and $h_d \circ \theta(q)$ indicates the ideal evolution of these quantities as a function of the scalar quantity $\theta(q)$ [8]. Driving the outputs y to zero forces $h_0(q)$ to track $h_d \circ \theta(q)$, and thus the posture of the robot is controlled to evolve according to the virtual constraints[1] $h_0(q) - h_d \circ \theta(q) = 0$ parameterized by

[1] The constraint is virtual because it does not arise from a physical connection among different variables but rather from the actions of a feedback controller

$\theta(q)$. This control method differs from classical trajectory tracking method because the desired evolution of $h_0(q)$ is only related to $\theta(q)$, a function of the robot's state, instead of time. As a result, the control system using these controlled outputs can be highly autonomous. For our 5-link planar robot, θ is formulated as:

$$\theta(q) = q_1 + \frac{l_f}{l_f + l_t} q_2 = \left[1, \frac{l_f}{l_f + l_t}, 0, 0, 0\right] q = c_\theta q \tag{3.23}$$

where c_θ is (1×5) constant row vector and $\theta(q)$ is the linearized angle of the virtual stance leg, which is defined as the line connecting the stance hip and the stance foot.

Intuitively, two tasks are essential for achieving bipedal walking: posture control and swing leg advancement. Posture control maintains the torso in an almost upright position, while swing leg advancement ensures a desired step length. For a 3-link compass gait robot in Figure 3.3(a), this can be achieved by enforcing the absolute torso angle $\theta_T = 0$ and the absolute angle of the bisector of virtual swing leg and virtual stance leg $\theta_{symm} = 0$. This has been done in [6] where the stability is achieved using a finite-time feedback controller. Inspired by this work, we propose, for a 5-link robot illustrated in Figure 3.3(b), the controlled outputs named "symmetry outputs" that can reflect the simplest version of posture control and swing leg advancement of a compass gait robot [121], and the corresponding outputs are defined as:

$$h_0(q) = H_0 q = [\theta_T, \theta_{symm}, q_3, q_5]^\top \tag{3.24}$$

$$\theta_{symm} = q_1 + \frac{(2l_f + l_t)q_2 - l_t q_5}{2(l_f + l_t)} + \frac{q_3 - q_4}{2} \tag{3.25}$$

$$\theta_T = q_1 + q_2 + q_3 \tag{3.26}$$

where H_0 is a (4×5) constant matrix, θ_T is also the absolute angle of the torso and θ_{symm} is the linearized absolute angle of the bisector of virtual swing leg and virtual stance leg. As for h_d, its definition is related to specific feedback designs, which will be discussed in the next section.

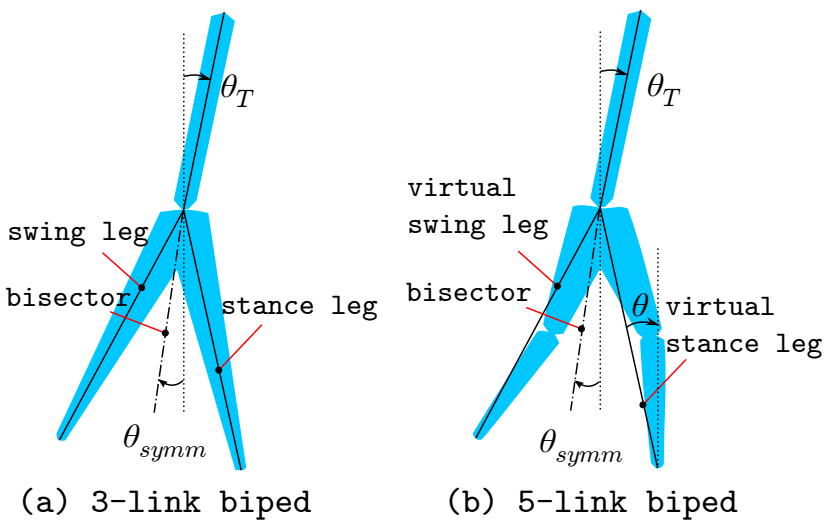

Fig. 3.3: The geometric interpretation of the controlled outputs.

3.3.2 Swing Phase Control

Since from *HPI6* the actuators have no influence during the impact phase, it is clear that the controller of the bipedal robot can only work during the swing phase. The purpose of the swing phase control is to design a nonlinear controller capable of gradually compelling the bipedal robot to evolve on a zero dynamic surface.

Note that the outputs (3.22) depend only on the configuration variables. Because of the second order nature of the robot model, the derivative of the output along solutions of (3.3) does not depend directly on the inputs. By differentiating the outputs, we have:

$$\begin{aligned}
\frac{dy}{dt} &= \frac{\partial h}{\partial x}\dot{x} \\
&= \begin{bmatrix} \frac{\partial h}{\partial q} & \frac{\partial h}{\partial \dot{q}} \end{bmatrix} \left[\underbrace{\begin{bmatrix} \dot{q} \\ D^{-1}\left[-C\dot{q} - G\right] \end{bmatrix}}_{f} + \underbrace{\begin{bmatrix} 0 \\ D^{-1}B \end{bmatrix}}_{g} u \right] \\
&= \underbrace{\begin{bmatrix} \frac{\partial h}{\partial q} & 0 \end{bmatrix} \begin{bmatrix} \dot{q} \\ D^{-1}\left[-C\dot{q} - G\right] \end{bmatrix}}_{L_f h} + \underbrace{\begin{bmatrix} \frac{\partial h}{\partial q} & 0 \end{bmatrix} \begin{bmatrix} 0 \\ D^{-1}B \end{bmatrix}}_{L_g h} u \\
&= L_f h(q, \dot{q})
\end{aligned} \tag{3.27}$$

where $L_g h = 0$. Since the outputs do not appear in the equation above, we need to differentiate the output again:

$$\begin{aligned}
\frac{d^2y}{dt} &= \begin{bmatrix} \frac{\partial}{\partial q}\left(\frac{\partial h}{\partial q}\dot{q}\right) & \frac{\partial h}{\partial q} \end{bmatrix} \left[\begin{bmatrix} \dot{q} \\ D^{-1}\left[-C\dot{q} - G\right] \end{bmatrix} + \begin{bmatrix} 0 \\ D^{-1}B \end{bmatrix} u \right] \\
&= \underbrace{\begin{bmatrix} \frac{\partial}{\partial q}\left(\frac{\partial h}{\partial q}\dot{q}\right) & \frac{\partial h}{\partial q} \end{bmatrix} \begin{bmatrix} \dot{q} \\ D^{-1}\left[-C\dot{q} - G\right] \end{bmatrix}}_{L_f^2 h} + \underbrace{\frac{\partial h}{\partial q} D^{-1} B u}_{L_g L_f h} \\
&= L_f^2 h(q, \dot{q}) + L_g L_f h(q) u
\end{aligned} \tag{3.28}$$

where matrix $L_g L_f h(q)$ is the decoupling matrix.

The equation (3.28) shows that the robot system is a MIMO system with vector relative degree $(2, \cdots, 2)$. Assume that $\widetilde{Q}$ is an open subset of Q such that for each $q \in \widetilde{Q}$, the decoupling matrix $L_g L_f h(x)$ is square and invertible. According to (2.43) and (2.44), a valid coordinate transformation $\Phi(x) = [\eta^\top, \xi^\top]^\top$of $T\widetilde{Q} = \{x = (q^\top, \dot{q}^\top)^\top | q \in \widetilde{Q}, \dot{q} \in \mathbb{R}^N\}$ is:

$$\begin{aligned}
\eta_1 &= h(q), \quad \eta_2 = L_f h(q, \dot{q}) \\
\xi_1 &= \theta(q), \quad \xi_2 = L_f \theta(q, \dot{q})
\end{aligned} \tag{3.29}$$

In these coordinates, the normal form of the system consisting of (3.3) and (3.22) becomes:

$$\begin{aligned}
\dot{\eta}_1 &= \eta_2, \quad \dot{\eta}_2 = L_f^2 h + L_g L_f h u \\
\dot{\xi}_1 &= \xi_2, \quad \dot{\xi}_2 = L_f^2 \theta + L_g L_f \theta u \\
y &= \eta_1
\end{aligned} \tag{3.30}$$

Since the columns of g in (3.5) are involutive, there exists a smooth scalar function γ such that:

$$\begin{aligned} \eta_1 &= h(q), \quad \eta_2 = L_f h(q, \dot{q}) \\ \xi_1 &= \theta(q), \quad \xi_2 = \gamma(q, \dot{q}) \end{aligned} \tag{3.31}$$

is a valid coordinate transformation with $L_g\gamma = 0$. With the point feet defined in *HPR3*, q_1 is an absolute angular coordinate as long as *HPG2* is satisfied, and all the other coordinates $(q_2, \cdots, q_5)$ during the single support phase are relative angular coordinates. As such, the hypothesis *HPR6* is guaranteed, and accordingly $\gamma(q, \dot{q})$ can be explicitly computed to be the first entry of $D(q)\dot{q}$ by applying the proof of the Frobenius theorem of [160]. As a result, (3.30) becomes:

$$\begin{aligned} \dot{\eta}_1 &= \eta_2, & \dot{\eta}_2 &= L_f^2 h(q, \dot{q}) + L_g L_f h(q) u \\ \dot{\xi}_1 &= L_f \theta(q, \dot{q}), & \dot{\xi}_2 &= L_f \gamma(q, \dot{q}) \\ y &= \eta_1 \end{aligned} \tag{3.32}$$

Enforcing the output $y \equiv 0$ causes $h(x) = 0$ and $L_f h(x) = 0$, which renders the robot system evolving on the zero dynamics manifold $\mathcal{Z}$, which is defined as:

$$\mathcal{Z} = \{x \in T\widetilde{Q} | h(x) = 0, L_f h(x) = 0\} \tag{3.33}$$

Thus the zero dynamics evolving on $\mathcal{Z}$ can be written as $\dot{z} = f_{zero}(z)$ with $f_{zero}(z)$ defined as:

$$f_{zero}(z) = f(z) + g(z)u^*(z) \in T_z\mathcal{Z}, \quad \forall z \in \mathcal{Z} \tag{3.34}$$

To achieve this, the controller can be created by combining a static state feedback controller and a linear state feedback controller. Implementing the static state feedback control law:

$$u(x) = (L_g L_f h(x))^{-1}(v_s - L_f^2 h(x)) \tag{3.35}$$

to (3.3) results in:

$$\frac{d^2 y}{dt^2} = v_s \tag{3.36}$$

Assuming K_D and K_P are (4×4) positive definite matrices and ϵ is a positive scalar, the linear state feedback control law is then chosen to be:

$$v_s = -\frac{1}{\epsilon} K_D L_f h(x) - \frac{1}{\epsilon^2} K_P h(x) \tag{3.37}$$

so that the η subsystem has the following characteristic equation:

$$\ddot{y} = -\frac{1}{\epsilon} K_D \dot{y} - \frac{1}{\epsilon^2} K_P y \tag{3.38}$$

Thus the feedback control capable of rendering $\mathcal{Z}$ forward invariant and attractive is given by:

$$u = -(L_g L_f h(x))^{-1}(L_f^2 h(x) + \frac{1}{\epsilon} K_D L_f h(x) + \frac{1}{\epsilon^2} K_P h(x)) \tag{3.39}$$

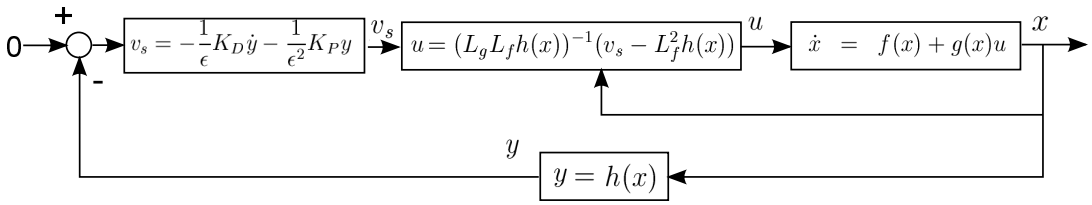

Fig. 3.4: Feedback loop of the control law that renders $\mathcal{Z}$ forward invariant and attractive.

The feedback loop diagram of the control law is illustrated in Figure 3.4. For robot system already evolving on $\mathcal{Z}$, the feedback control for keeping the system evolving on Z is:

$$u^*(x) = -(L_g L_f h(x))^{-1} L_f^2 h(x) \tag{3.40}$$

The evolution of q and $\dot{q}$ on the zero dynamics manifold can be given by:

$$q = \begin{bmatrix} H_0 \\ c_\theta \end{bmatrix}^{-1} \begin{bmatrix} h_d(\xi_1) \\ \xi_1 \end{bmatrix} \tag{3.41}$$

$$\dot{q} = \begin{bmatrix} \frac{\partial h}{\partial q} \\ \gamma_0 \end{bmatrix}^{-1} \begin{bmatrix} 0 \\ \xi_2 \end{bmatrix} \tag{3.42}$$

3.3.3 *Stability Analysis*

From Theorem 2.2, an exponentially stable periodic orbit of the hybrid zero dynamics is also an exponentially stable periodic orbit of the full-dimensional closed-loop system as long as ϵ in (3.39) is sufficiently small. Therefore, the question now is to find an exponentially stable periodic orbit of the hybrid zero dynamics.

Suppose that $\mathcal{S} \cap \mathcal{Z}$ is a smooth, one-dimensional, embedded submanifold of $T\mathcal{Q}$. If $\Delta(\mathcal{S} \cap \mathcal{Z}) \subset \mathcal{Z}$, then from [84] the nonlinear system with impulse effects:

$$\Sigma_{zero} : \begin{cases} \dot{z} = f_{zero}(z) & z^- \notin \mathcal{S} \cap \mathcal{Z}, z \in \mathcal{Z} \\ z^+ = \Delta(z^-) & z^- \in \mathcal{S} \cap \mathcal{Z} \end{cases} \tag{3.43}$$

is the hybrid zero dynamics. Using the coordinate set (3.31), the zero dynamics becomes:

$$\begin{aligned} \dot{\xi}_1 &= L_f\theta(q, \dot{q}) = \kappa_1(\xi_1)\xi_2 \\ \dot{\xi}_2 &= L_f\gamma(q, \dot{q}) = \kappa_2(\xi_1) \end{aligned} \tag{3.44}$$

where $\kappa_1(\xi_1)$ and $\kappa_2(\xi_1)$ are given by:

$$\kappa_1(\xi_1) = \frac{\partial \theta}{\partial q} \begin{bmatrix} \frac{\partial h}{\partial q} \\ \gamma_0 \end{bmatrix}^{-1} \begin{bmatrix} 0 \\ 1 \end{bmatrix} \Bigg|_Z \tag{3.45}$$

$$\kappa_2(\xi_1) = -\frac{\partial V}{\partial q_1}\Bigg|_Z \tag{3.46}$$

with $V(q)$ being the potential energy of the biped, $\gamma_0 = D_1$ (the first row of D) and $\partial V/\partial q_1 = G_1$ (the first entry of $G(q)$). By adopting the robot hypotheses *HPR1-HPR6*, the gait hypotheses HPG1-HPG6 and the impact hypotheses *HPI1-HPI6*, the

return map Δ: $(\xi_1^-, \xi_2^-) \to (\xi_1^+, \xi_2^+)$ can be explicitly calculated using the coordinate set $(\xi_1, \xi_2) = (\theta, \lambda)$, that is:

$$S \cap Z = \{(\xi_1^-, \xi_2^-) | \xi_1^- = \theta^-, \xi_2^- \in \mathbb{R}\} \tag{3.47}$$

$$\xi_1^+ = \theta^+ \tag{3.48}$$

$$\xi_2^+ = \delta_{zero} \xi_2^- \tag{3.49}$$

where δ_{zero} is a constant calculated in advance by:

$$\delta_{zero} = \gamma_0(q^+) \Delta_{\dot{q}}(q^-) \sigma_{\dot{q}}(q^-) \tag{3.50}$$

$$\sigma_{\dot{q}}(q^-) = \begin{bmatrix} \frac{\partial h}{\partial q}(q^-) \\ \gamma_0(q^-) \end{bmatrix}^{-1} \begin{bmatrix} 0 \\ 1 \end{bmatrix} \tag{3.51}$$

Since θ is defined to be monotonic, $\dot{\xi}_1$ is non-zero over any step. Therefore, the 2-dimensional dynamical system (3.44) can be equivalent to a 1-dimensional dynamical system once coordinate transformation $\zeta_2 = \frac{1}{2}(\xi_2)^2$ is adopted, yielding:

$$\frac{d\zeta_2}{d\xi_1} = \frac{\kappa_2(\xi_1)}{\kappa_1(\xi_1)} \tag{3.52}$$

For $\theta^+ \leq \xi_1 \leq \theta^-$, define:

$$V_{zero}(\xi_1) = -\int_{\theta^+}^{\xi_1} \frac{\kappa_2(\xi_1)}{\kappa_1(\xi_1)} d\xi \tag{3.53}$$

It is possible to prove that the Poincaré return map of the hybrid zero dynamics, $\rho : S \cap U \to S \cap U$ is diffeomorphic to a scalar LTI system [84], given by:

$$\rho(\zeta_2^-) = \delta_{zero}^2 \rho(\zeta_2^-) - V_{zero}(\theta^-) \tag{3.54}$$

We can determine whether a non-trivial periodic orbit of the hybrid zero dynamics exists by judging if:

$$\frac{\delta_{zero}^2}{1 - \delta_{zero}^2} V_{zero}(\theta^-) + K < 0, (\delta_{zero}^2 \neq 0) \tag{3.55}$$

where $K = \max V_{zero}(\xi_1)$ with $\theta^+ \leq \xi_1 \leq \theta^-$. Furthermore, if $0 < \delta_{zero}^2 < 1$ also holds, the periodic orbit is exponentially stable with the fixed point being:

$$\xi_1^* = c_\theta q^-, \zeta_2^* = \frac{-V_{zero}(\theta^-)}{1 - \delta_{zero}^2} \tag{3.56}$$

Given ξ_1^* and ζ_2^*, $\xi_2(\xi_1, \zeta_2^*)$ can be further calculated by:

$$\xi_2(\xi_1, \zeta_2^*) = -\sqrt{2(\delta_{zero}^2 \zeta_2^* - V_{zero}(\xi_1))} \tag{3.57}$$

and $t(\xi_2)$ can be calculated as:

$$t(\xi_2) = \int_{\theta^+}^{\theta^-} \frac{1}{\kappa_1(\xi_1)\xi_2(\xi_1, \xi_2^-)} d\xi_1 \tag{3.58}$$

Then the whole evolution of a periodic step is given by (3.40), (3.41) and (3.42).

3.4 Optimization of Walking Motion

The optimization of walking motion can be viewed as a nonlinear constrained optimization problem. As mentioned in (2.66), this involves the definition of an optimization parameter vector ϑ, an objective function $\hbar(\vartheta)$ and several scalar-valued functions $c_i(\vartheta)$ with $i \in \mathcal{E}_{set}$ or $i \in \mathcal{I}_{set}$ (note that $\mathcal{E}_{set} \cap \mathcal{I}_{set} = \emptyset$) representing respectively equality constraints or inequality constraints. From the angle of gait optimization based on hybrid zero dynamics, ϑ is used to parameterize h_d, $\hbar(\vartheta)$ is equivalent to a cost function that quantifies one particular aspect of walking gait such as energy efficiency, and $c_i(\vartheta)$ is used to ensure the validity of the walking such as the contact condition of the stance foot.

3.4.1 Parameterization of h_d

The optimization parameters we choose is based on Bézier polynomials. Following the same procedure in [8], we start by normalizing the $\theta(q)$ as:

$$s(q) = \frac{\theta(q) - \theta^+}{\theta^- - \theta^+} \tag{3.59}$$

with θ^+ being the minimum value of $\theta(q)$ and θ^- the maximum value of $\theta(q)$. Then $h_d \circ \theta(q)$ can be written as:

$$h_d \circ \theta(q) = B_Z \circ s(q) \tag{3.60}$$

where $B_Z(s) = [b_1(s), \cdots, b_4(s)]^\top$. Each $b_i(s)$ can be further defined by:

$$b_i(s) = \sum_{k=0}^{5} a_k^i \frac{5!}{k!(5-k)!} s^k (1-s)^{5-k} \tag{3.61}$$

which is a Bézier polynomial of degree 5. Group the parameters a_k^i into (4×1) vectors as $a_k = [a_k^1, \cdots, a_k^4]^\top$.

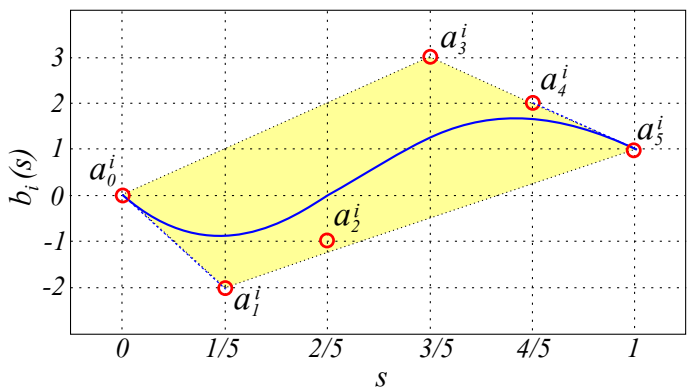

Fig. 3.5: A typical 5-degree Bézier curve.

An example of a Bézier polynomial of degree 5 is depicted in Figure 3.5. Such kind of polynomials have three useful features crucial for optimization:

1. the image of the Bézier polynomials is contained in the convex hull of the coefficients $\{(0, a_0^i), (1/5, a_1^i), \cdots, (1, a_5^i)\}$;
2. $b_i(0) = a_0^i$ and $b_i(1) = a_5^i$;
3. $(\partial b_i(s)/\partial s)|_{s=0} = 5(a_1^i - a_0^i)$ and $(\partial b_i(s)/\partial s)|_{s=1} = 5(a_5^i - a_4^i)$

The first feature implies that the polynomial does not exhibit large oscillations with small parameter variations, meaning that Bézier polynomials are numerically stable. This is crucial for running optimization program. The second two features can be used to achieve $\Delta(\mathcal{S} \cap \mathcal{Z}) \subset \mathcal{Z}$.

Assuming $\Delta(\mathcal{S} \cap \mathcal{Z}) \subset \mathcal{Z}$, we can evaluate (3.41) with given θ^+ and θ^-:

$$q^+ = H^{-1} \begin{bmatrix} a_0 \\ \theta^+ \end{bmatrix} \quad q^- = H^{-1} \begin{bmatrix} a_5 \\ \theta^- \end{bmatrix} \tag{3.62}$$

where $H = [H_0^\top, c_\theta^\top]^\top$. Note that θ^- can be calculated by the vector a_5 using $z_{sw}(q^-) = 0$. From $q^+ = \Delta_q q^-$, we can calculate the vector a_0 directly from a_5 using:

$$\begin{bmatrix} a_0 \\ \theta^+ \end{bmatrix} = H \Delta_q H^{-1} \begin{bmatrix} a_5 \\ \theta^- \end{bmatrix} \tag{3.63}$$

Evaluating $\partial h_d / \partial \theta$ at θ^+ yields:

$$\left.\frac{\partial h_d}{\partial \theta}\right|_{\theta=\theta^+} = \left.\frac{\partial B_Z}{\partial s}\frac{\partial s}{\partial \theta}\right|_{\theta=\theta^+} = \frac{5}{\theta^- - \theta^+}(a_1 - a_0) \tag{3.64}$$

Achieving $L_f h \circ \Delta(S \cap Z) = 0$ means that $\dot{q}$ must fall in the null space of $\partial h(q)/\partial q$, which is formulated as:

$$\left.\frac{\partial h(q)}{\partial q}\right|_{q=q^+} q = \left[H_0 - \frac{5}{\theta^- - \theta^+}(a_1 - a_0)c_\theta\right] \dot{q}^+ = 0 \tag{3.65}$$

Thus the vector a_1 can also be calculated using the vectors a_5 and a_4 by the equation:

$$a_1 = \frac{\theta^- - \theta^+}{5 c_\theta \dot{q}^+} H_0 \dot{q}^+ + a_0 \tag{3.66}$$

where $\dot{q}^- = \sigma_{\dot{q}}(q_0^-)$ and $\dot{q}^+ = \Delta_{\dot{q}}(q_0^-)\dot{q}^-$. Using (3.63) and (3.66), hybrid invariance is realized.

Although the parameter set $\{a_2, a_3, a_4, a_5\}$ is able to determine h_d, it is not obvious how the posture of the robot is. As such, we replace parameter vector a_5 with the postural parameter vector indicating the robot postural right before the impact. As illustrated in Figure 3.6, define the fixed coordinate frame as $o_{st}x_{st}z_{st}$, the postural parameter vector is defined as:

$$\phi_P = [\theta_T^-, x_h^-, z_h^-, x_{sw}^-]^\top \tag{3.67}$$

where (x_h^-, z_h^-) is the coordinates of the hip with reference to the frame $x_{st}z_{st}o_{st}$ and x_{sw}^- is the coordinate of the swing foot along the x_{st} axis.

Indeed, the parameter vector a_5 can be directly calculated by ϕ_P. Assuming that $z_h^- \neq 0$, we can solve a inverse kinematics problem and obtain the generalized coordinates q_1^-, q_2^-, q_3^-, q_4^-, q_5^- and q_6^- using ϕ_P by the following equations:

$$q_1^- = \arctan\left(\frac{x_h^-}{z_h^-}\right) + \arccos\left(\frac{l_t^2 + (x_h^-)^2 + (z_h^-)^2 - l_p^2}{2l_t((x_h^-)^2 + (z_h^-)^2)}\right) \tag{3.68}$$

$$q_2^- = -\pi + \arccos\left(\frac{l_p^2 + l_t^2 - (x_h^-)^2 - (z_h^-)^2}{2l_p l_t}\right) \tag{3.69}$$

$$q_3^- = \theta_T - q_1^- - q_2^- \tag{3.70}$$

$$q_6^- = \arctan\left(\frac{x_h^- - x_{sw}^-}{z_h^-}\right) + \arccos\left(\frac{l_t^2 + (x_h^- - x_{sw}^-)^2 + (z_h^-)^2 - l_p^2}{2l_t((x_h^- - x_{sw}^-)^2 + (z_h^-)^2)}\right) \tag{3.71}$$

$$q_5^- = -\pi + \arccos\left(\frac{l_p^2 + l_t^2 - (x_{sw}^- - x_h^-)^2 - (z_h^-)^2}{2l_p l_t}\right) \tag{3.72}$$

$$q_4^- = \theta_T - q_6^- - q_5^- \tag{3.73}$$

Then a_5 can be calculated by:

$$a_5 = H_0 q^- \tag{3.74}$$

where $q^- = [q_1^-, q_2^-, q_3^-, q_4^-, q_5^-]^\top$. Thus we have obtained a_5 directly from the posture parameter vector ϕ_P.

In conclusion, the parameter vector ϑ for optimization is:

$$\vartheta = [\phi_P^\top, a_2^\top, a_3^\top, a_4^\top]^\top \tag{3.75}$$

which contains 16 parameters.

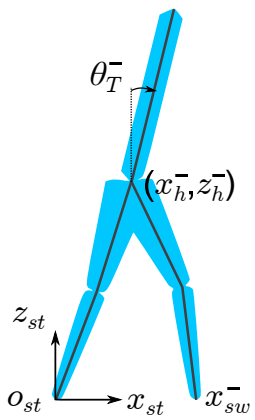

Fig. 3.6: The posture parameters of the 5-link planar biped.

3.4.2 *Optimization Criterion*

An appropriate cost function is necessary for calculating the optimization criterion. For biped robots actuated by DC motors or brushless motors, the electrical power of each motor is roughly proportional to the square of the current going through its coil, and the current is in turn proportional to the torque exerted by this motor. In

order to reflect motor energy per distance traveled, the cost function is defined as the integral of the norm of the torque for a displacement of one meter:

$$C(\vartheta) = \frac{1}{d}\int_0^{\top} \sum_{i=2}^{5} (u_i^*(t))^2 dt \tag{3.76}$$

where T is the step duration and $d = x_{sw}^-$ is the step length. To simplify the calculation, the cost function can equally be written as:

$$C(\vartheta) = \frac{1}{d}\int_{\theta^+}^{\theta^-} \frac{\sum_{i=2}^{5}(u_i^*(\xi_1,\xi_2))^2}{\kappa_1(\xi_1)\xi_2(\xi_1,\xi_2^-)} d\xi_1 \tag{3.77}$$

The validity of the cost function depends on whether there is a valid fixed point (ξ_1^*, ζ_2^*) as defined in (3.56). Indeed, there are three situations where we cannot calculate (ξ_1^*, ζ_2^*):

1. a_5 calculated by the inverse kinematics (3.68), (3.69), (3.70), (3.72), (3.73) and (3.74) contains complex numbers;
2. a_5 is valid but $\delta_{zero}^2 \geq 1$ or $\delta_{zero}^2 = 0$;
3. a_5 is valid and $0 < \delta_{zero}^2 < 1$ but $\delta_{zero}^2 V_{zero}(\theta^-)/(1-\delta_{zero}^2) + K > 0$.

Thus the objective function $\hbar(\vartheta)$ can be defined as:

$$\hbar(\vartheta) = \begin{cases} C(\vartheta) & (\xi_1^*, \zeta_2^*) \text{ is valid} \\ \text{NaN} & \text{else} \end{cases} \tag{3.78}$$

where `NaN` stands for "not a number" and $C(\vartheta)$ is calculated by (3.77).

3.4.3 *Constraints*

For ensuring the validity of the optimal walking gaits with reference to certain requirements, it is necessary to define corresponding constraints. As illustrated in Figure 3.7, these constraints include:

CP1) The torso constraint prevents the torso from leaning backward or excessively forward, i.e., $0 < \theta_T^- < \pi/4$;

CP2) The hip constraint prevents extremely low hip position, i.e., $z_h^- > 0.72\,(m)$;

CP3) The impulsive impact force given in (3.12) must be upward:

$$c_1 = -F_{sw}^z \leq 0 \tag{3.79}$$

CP4) The post-impact velocity of the swing foot is upward;

$$c_2 = -\dot{z}_{sw}^+ \leq 0 \tag{3.80}$$

CP5) The swing foot must not touch the ground prematurely:

$$c_3 = -\min_{0<s<1}(z_{sw}(s)) < 0 \tag{3.81}$$

CP6) The knees of both the swing leg and the stance leg only bend in forward direction:

$$c_4 = \max_{0\le s\le 1}(q_2(s)) \le 0 \tag{3.82}$$

$$c_5 = \max_{0\le s\le 1}(q_5(s)) \le 0 \tag{3.83}$$

CP7) The stance foot contact constraints as defined by (3.20) and (3.21):

$$c_6 = \max_{0\le s\le 1}(-F^z_{st}(s)) < 0 \tag{3.84}$$

$$c_7 = \max_{0\le s\le 1}(|F^x_{st}(s)| - \mu_{\mathrm{f}} F^z_{st}(s)) < 0 \tag{3.85}$$

CP8) The average walking speed equals to the desired speed:

$$c_8 = d/t_{step} - v_d = 0 \tag{3.86}$$

where v_d represents the desired walking speed and t_{step} is the duration of each step given by (3.58).

Among all the constraints, CP1 and CP2 are treated as the bounds of the optimization parameters ϑ, CP3-CP7 are nonlinear inequality constraints, and CP8 is nonlinear equality constraint. Accordingly, we have $\mathcal{E}_{set} = \{8\}$ and $\mathcal{I}_{set} = \{1, 2, \cdots, 7\}$. As in the case $\hbar(\vartheta)$, it is possible that we cannot calculate the constraints. In those situations, the corresponding constraints $c_i =$`NaN` for all $i \in \mathcal{I}_{set} \cup \mathcal{E}_{set}$.

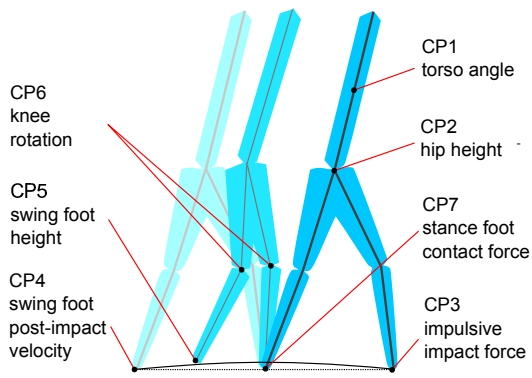

Fig. 3.7: The nonlinear inequality optimization constraints for the 5-link planar biped.

3.4.4 *Optimization Realization*

As illustrated in Figure 3.8, there are three major steps in calculating the objective function $\hbar(\vartheta)$ and the constraints $c(\vartheta)$. The equations involved in these steps are explained below:

1. Calculate the evolution of the zero dynamics. (i) Solve the inverse dynamics using (3.68), (3.69), (3.70), (3.72), (3.73) and (3.74). (ii) Parameterize h_d using (3.63), (3.66), (3.61), (3.60) and (3.59). (iii) Calculate the evolution of ξ_1 and ξ_2 using (3.50), (3.51), (3.45), (3.46), (3.53), (3.56), (3.57) and (3.58).

2. Calculate the evolution of the complete system using (3.40), (3.41), (3.42), and (3.3).

3. Calculate the cost function and the constraints using (3.77), (3.79), (3.80), (3.81), (3.82), (3.83), (3.84), (3.85) and (3.86).

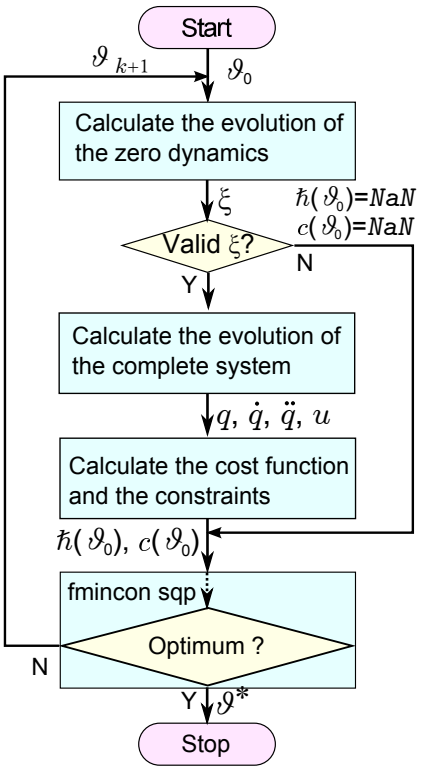

Fig. 3.8: Optimization process using `fmincon`

After the programming of $\hbar(\vartheta)$ and $c(\vartheta)$, the optimization is performed using MATLAB® Optimization toolbox. As the optimization of bipedal walking is categorized as a constrained optimization, the MATLAB® function `fmincon` (R2010b) is suited for this purpose. There are four different optimization algorithms provided by `fmincon`: `trust-region-reflective`, `interior-point`, `sqp` and `active-set`. Among them, `sqp` is chosen as our optimization method for its superiority in handling the situation where the objective function $\hbar(\vartheta)$ and the constraint function $c(\vartheta)$ cannot provide valid results due to the violation of certain requirements such as the existence of a fixed point in our case. Once these two functions return `NaN`, the `sqp` solver can attempt to evaluate at a different point. In addition, the `fmincon` function allows users to define not only an objective function and a nonlinear constraint function but also linear constraints and bounds of the optimization parameters. For the 5-link bipedal robot, the bounds of the optimization parameters are defined to prevent large lean-angle of the torso (CP1) and extremely low hip position (CP2).

The optimization process is an iterative process. As depicted in Figure 3.8, the `fmincon sqp` solver starts from a given initial parameter vector ϑ_0 and continues searching for better ϑ_k until it finds an optimum ϑ^* that satisfying stopping criterion such as KKT conditions in Section 2.4.

3.5 Results and Analysis

As the stability of the hybrid zero dynamics is well defined, we no longer need to run a simulation to prove the stability of the walking. For desired speed of 0.7 m/s, the evolution of zero dynamics is demonstrated in Figure 3.9. In addition, we also have $\zeta_2^* = 544.30$ (kgm^2/s)^2, $\delta_{zero}^2 = 0.739$, $V_{zero}(\theta^-) = -142.11$ (kgm^2/s)^2, $K = 200.32$ (kgm^2/s)^2. Assuming the constraints are satisfied, the walking motion is exponentially stable since $0 < \delta_{zero}^2 < 1$ and $\delta_{zero}^2 V_{zero}(\theta^-)/(1-\delta_{zero}^2) + K = -201.86 < 0$. The stability of the remaining optimized walking motions of the planar biped can be verified similarly.

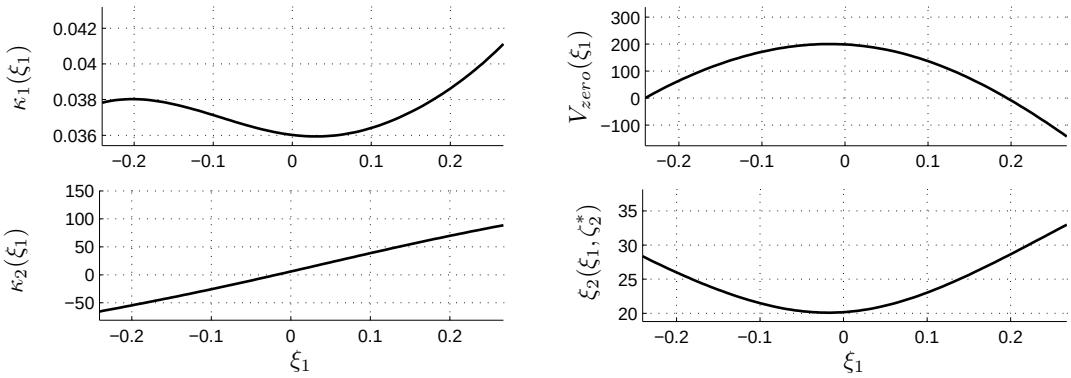

Fig. 3.9: The zero dynamics of the 5-link planar biped walking at 0.7m/s

The Froude number, commonly used to study trends in animal gait patterns, is considered when choosing the range of average walking speed for optimization. It is defined as the ratio of the centripetal force around the center of motion, the foot, and the weight of the animal walking:

$$Fr = \frac{m_b v_0^2 / l_c}{m_b g_e} = \frac{v_0^2}{g_e l_c} \tag{3.87}$$

where Fr represents the Froude number, m_b is the total mass of the entire body, l_c is the characteristic length, v_0 is the walking speed and g_e is the gravity acceleration. In analyses of bipedal walking, a walking limb is often modeled as an inverted pendulum, where the center of mass goes through a circular arc centered at the foot [179]. If the characteristic length is equal to the total leg length, then the theoretical maximum speed of walking has a Froude number of 1.0 since any higher value would theoretically result in the stance foot losing contact with the ground. For human beings, the typical transition speed from bipedal walking to running occurs with $Fr \approx 0.5$ [180]. However, the maximum Froude number of walking for the latest version of ASIMO[2] is less than 0.1. For our 5-link robot (and the 8-link 3D bipedal robot that will be studied later on), we have chosen a maximum Froude number of 0.3 for our design, which is much larger than those of most humanoid robots.

[2] For the latest version of ASIMO, the total mass equals 54kg, the maximum walking speed is 2.7km/h and its leg length is around 0.7m.

Accordingly, the maximum speed for our robot is about 1.5 m/s. Since our intention is to study dynamical walking, we do not explore all the speeds, and thus the gaits with walking speeds below 0.2 m/s are not included.

Figures 3.10 to 3.12 present some characteristics of the optimal walking as functions of the average walking speed. On the left-hand side of Figure 3.10, the energy costs of the entire robot (the black curve) and its actuators are depicted respectively, and on the right-hand side we can see the percentage of the total energy cost consumed by each actuator. At walking speed ranging from approximately 0.5 m/s to 1.5 m/s, it is obvious from the figure that the actuators of the hip joints are responsible for the most part of the robot's energy consumption. The variations of optimized posture parameters at various speeds are provided in Figure 3.11, and the step frequency and step duration at different speeds are illustrated in Figure 3.12. These values are close to the results in [115] with similar model parameters, but in this thesis we have no constraints over the maximum torques of the actuators.

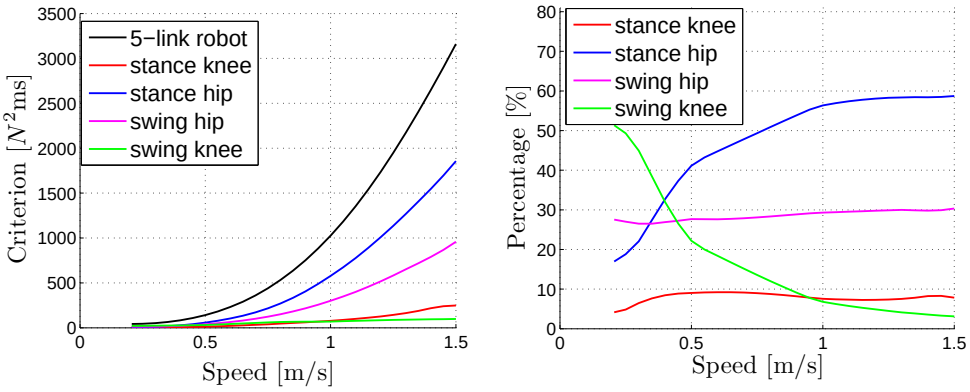

(a) The energy costs *(b)* The contribution of each actuator

Fig. 3.10: The energy cost curves of the 5-link planar biped and its actuators at different walking speeds.

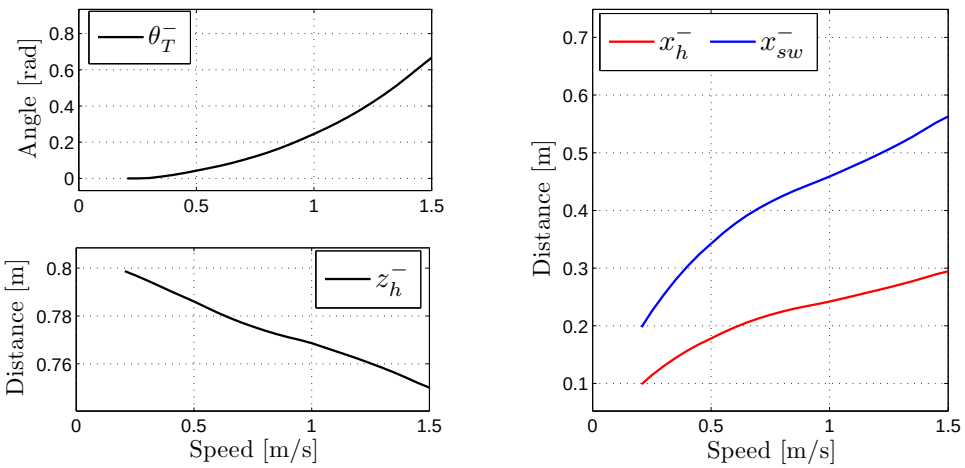

Fig. 3.11: The optimized postural parameters of the 5-link biped at different speeds.

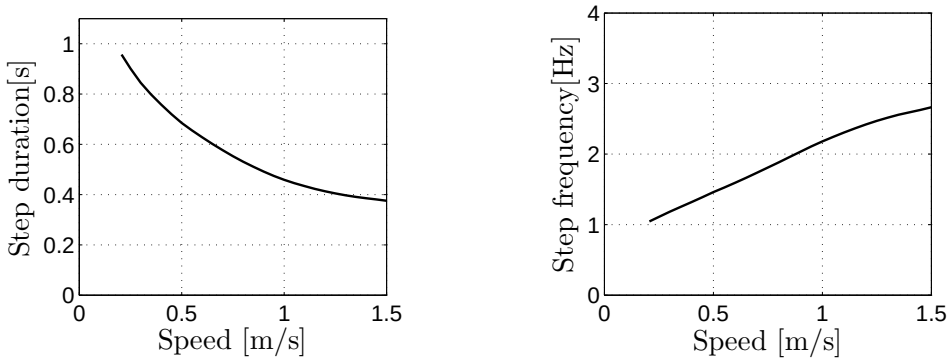

Fig. 3.12: The step duration and step frequency of the 5-link biped at different speeds.

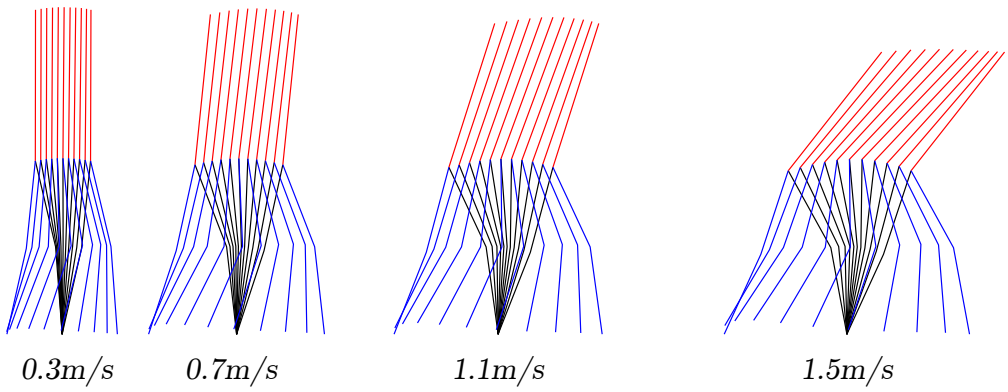

Fig. 3.13: The stick charts of the 5-link biped walking at various speeds.

The stick charts of the gaits at 0.3 m/s, 0.7 m/s, 1.1 m/s and 1.5 m/s are drawn in Figure 3.13. Among them, the detailed data for walking at 0.7 m/s and 1.5 m/s are illustrated respectively in Figures 3.14 to 3.20. In Figure 3.14, we can see that θ_T remains almost constant within a step while the variation of θ_{symm} is much more obvious. In addition, it is also interesting to note that the relation between t and θ is almost proportional, meaning that $\theta(q)$ in (3.23) is a good replacement of time in indicating the progress of the current step. As illustrated in Figure 3.16, the maximum absolute torques of the hip joints are greater than the maximum absolute torques of the knee joints for both speeds. According to Figure 3.17, the actuators of the hip joints produce roughly equal amounts of mechanical powers than the actuators of the knee joints while at high speeds the mechanical powers from the actuators of the hip joints are almost dominant. In addition, for all the actuators, the negative powers and the positive powers are close in amount, which indicates that there is a possibility of recycling negative mechanical energy and improving energy efficiency.

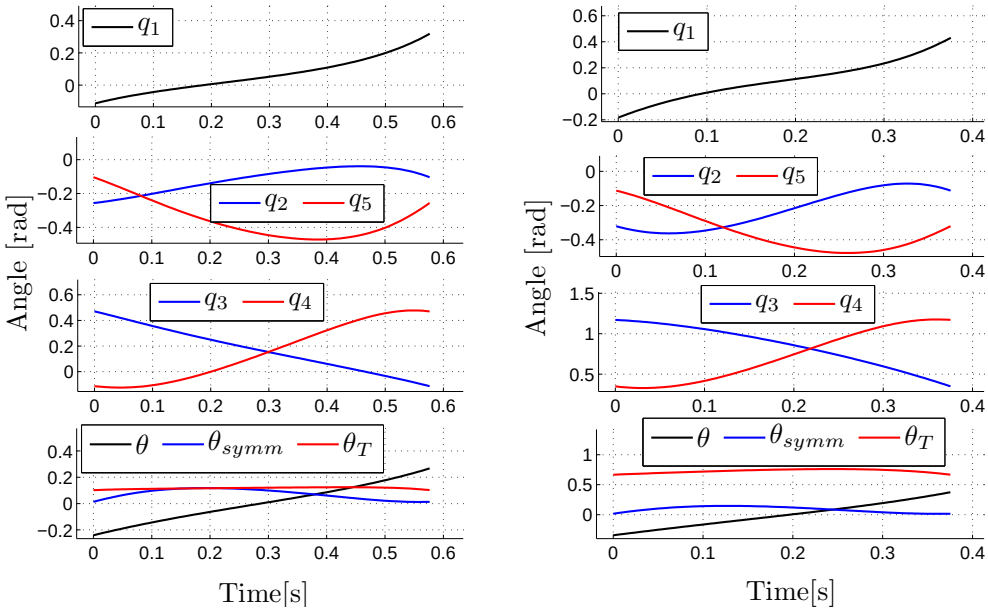

(a) **0.7** m/s (b) **1.5** m/s

Fig. 3.14: The angle curves of joints and outputs of the 5-link planar biped walking at 0.7 m/s and 1.5 m/s.

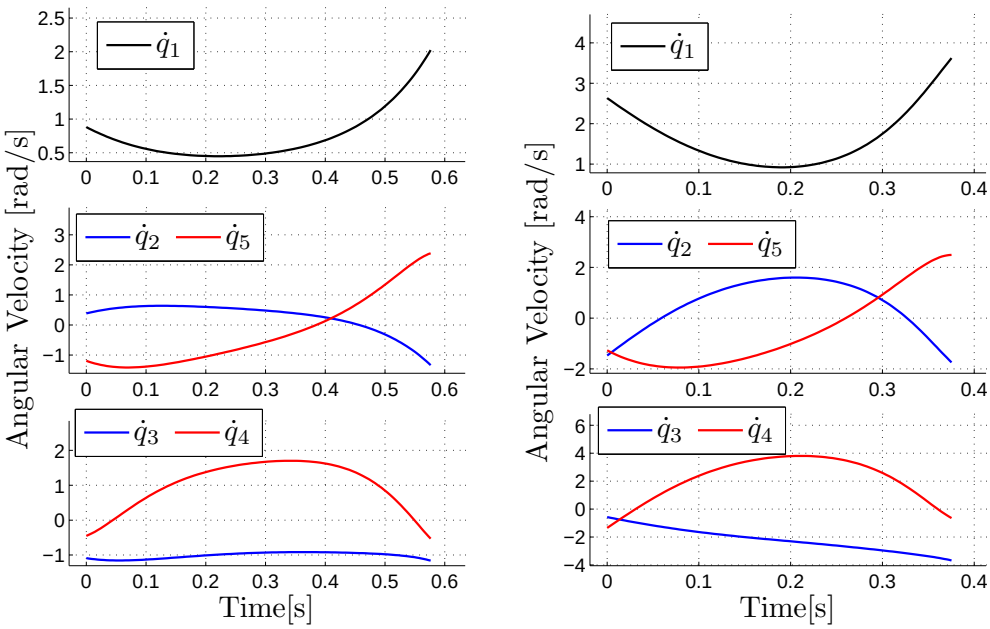

(a) **0.7** m/s (b) **1.5** m/s

Fig. 3.15: The angular velocity curves of joints of the 5-link planar biped walking at 0.7 m/s and 1.5 m/s.

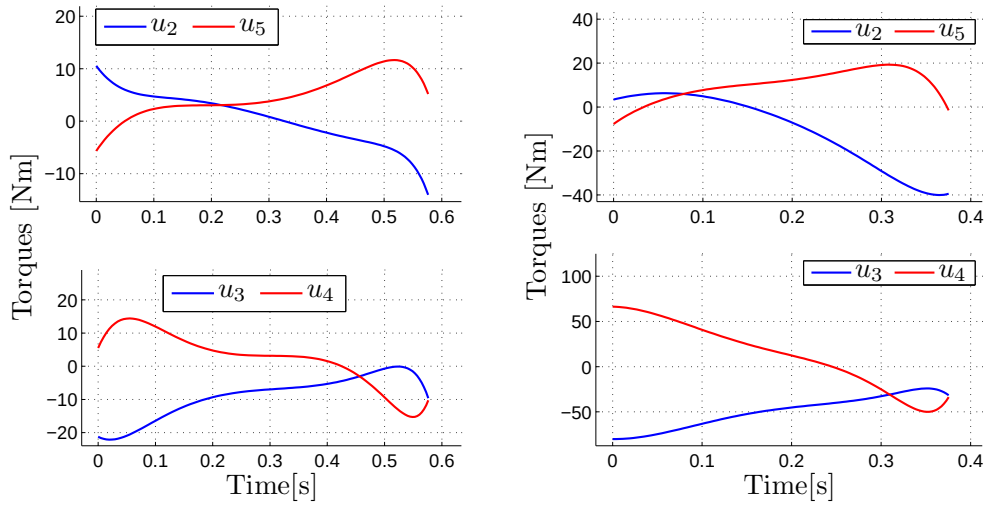

(a) **0.7** m/s (b) **1.5** m/s

Fig. 3.16: The torque curves of the actuated joints of the 5-link planar biped walking at 0.7 m/s and 1.5 m/s.

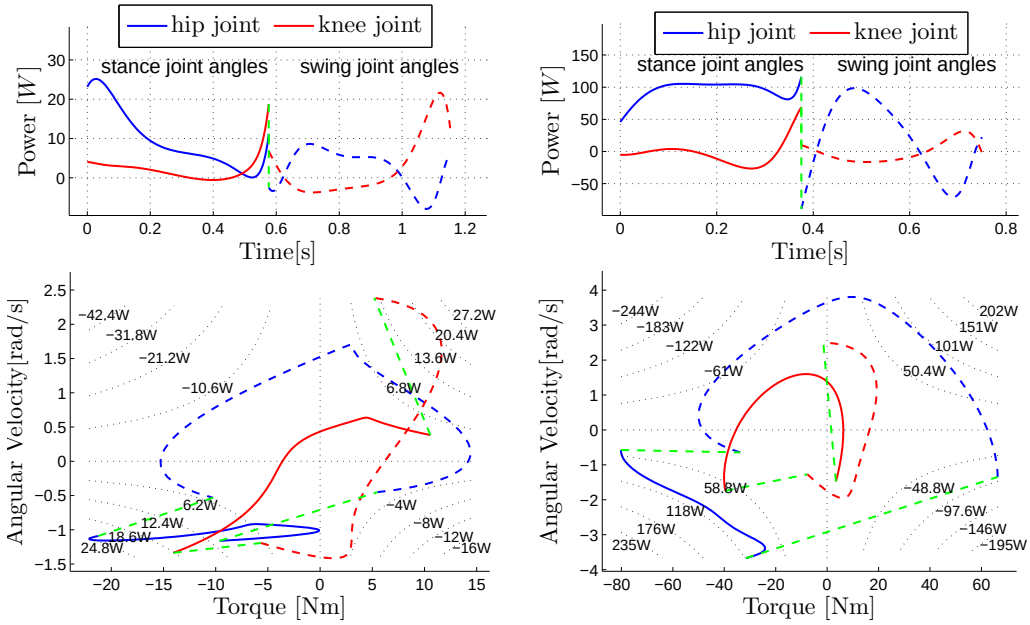

(a) **0.7** m/s (b) **1.5** m/s

Fig. 3.17: The mechanical output powers of the actuators of the 5-link planar biped walking at 0.7 m/s and 1.5 m/s (two steps) with solid lines representing stance joint angles, dashed lines representing swing joint angles, and green dashed lines representing the jumps caused by the impact

In order to verify that the stance foot does not slid within one step, the curves of the ground reaction forces are depicted in Figure 3.18. We can see clearly that F_{st}^z decreases at the end of a periodic step, especially for the speed of 1.5 m/s. For walking at 0.7 m/s, the absolute value of F_{st}^x is comparatively small compared with F_{st}^z. However, for walking at 1.5 m/s, the absolute value of F_{st}^x is almost the same with F_{st}^z at the end of a step, which means the stance foot is on the verge of sliding (in this thesis the friction coefficient $\mu_{\mathrm{f}} = 1$). All these phenomenons indicate that the margin left for the stance leg to remain contact with the ground instead of slide and take off becomes more and more limited as the walking speed increases. As for the swing foot, we can verify that it does not contact the ground before the end of step in Figure 3.20. It is also interesting to mention that the vertical coordinate of the robot's CoM depicted in the Figure 3.19 is not constant during the step, which differs from one of the key assumptions of the Linear Inverted Pendulum Model (LIPM) [48]. This also shows that the movement of the robot is highly dynamic.

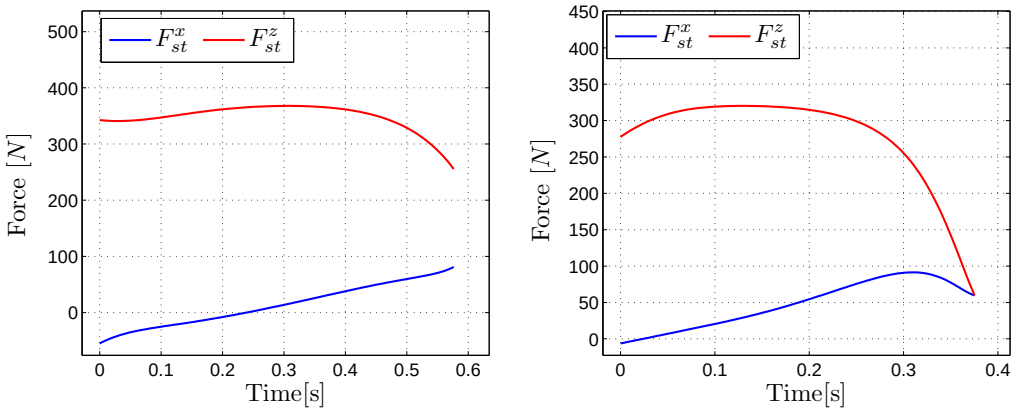

(a) **0.7** m/s (b) **1.5** m/s

Fig. 3.18: The ground reaction forces of the 5-link planar biped walking at 0.7 m/s and 1.5 m/s.

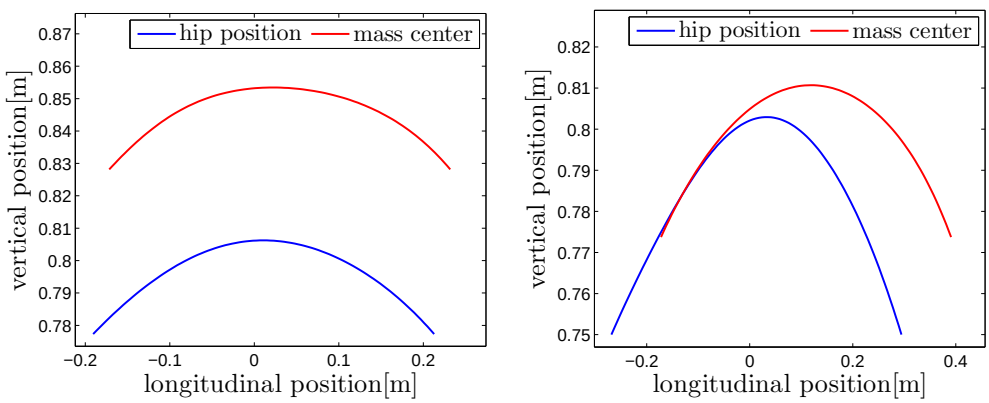

(a) **0.7** m/s (b) **1.5** m/s

Fig. 3.19: The trajectories of the hip and the CoM of the 5-link planar biped walking at 0.7 m/s and 1.5 m/s.

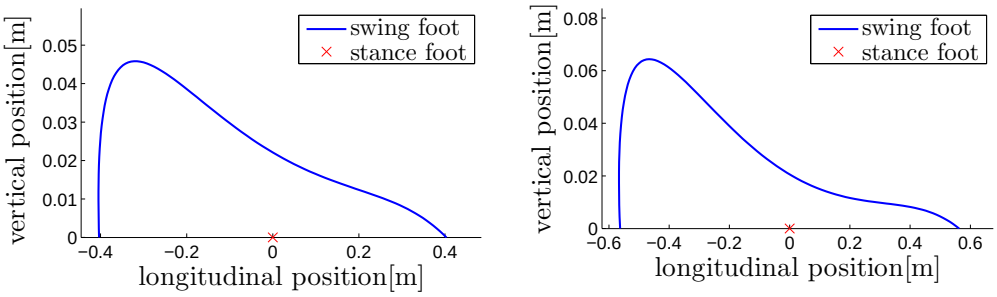

(a) **0.7** m/s *(b)* **1.5** m/s

Fig. 3.20: The trajectories of the swing foot of the 5-link planar biped walking at 0.7 m/s and 1.5 m/s.

3.6 Conclusion

In this chapter, we have discussed how to use feedback linearization and zero dynamics to achieve optimized control of planar bipedal robots with point feet. A 5-link planar biped derived from HRP-4 [172] with a torso, two thighs, two shins (with point feet) is used as an example to demonstrate the corresponding methods of modeling, controlling and optimizing. Unlike the previous work in [8], we have adopted fixed base models to achieve coherence with the models and parameters of a 8-link 3D biped in Chapter 5. The dynamic model of the robot is composed of an impact model and a swing phase model to form a hybrid model. During the swing phase, the method of feedback linearization is adopted to apply virtual constraints, which are defined by controlled output, on the joints of the robot. In this thesis, we have defined "Symmetry Output" as the controlled output to facilitate the geometric interpretation of posture control and swing leg advancement. The ideal evolution of the virtual constraints are parameterized by Bézier polynomials as functions of the normalized value of the linearized absolute angle of the virtual stance leg formed by the line connecting the hip to the feet. Thereafter, the gait stability is analyzed by a scalar LTI return map, which is a special case of Restricted Poincaré map for systems with one degree of underactuation. In order to find feasible and energy efficient gaits for our planar biped at different speeds, we have developed an optimization program using the SQP algorithm and the `fmincon` function in MATLAB®. The optimization criterion is defined based on the energy consumption of DC motors or brushless motors and the optimization constraints are used to verify the requirements of ground contact, swing foot clearance, and so on. The gait optimization is performed at different walking speeds from 0.2 m/s to 1.5 m/s. The stability and feasibility of these results are all validated. The maximum criterion is 3161 N^2ms at 1.5 m/s and the minimum criterion is 43 N^2ms at 0.2 m/s.

4. ELASTIC COUPLINGS FOR THE 5-LINK PLANAR BIPED

The work presented in this chapter focuses on exploring the superiority of adding elastic couplings (in form of hip springs) to planar bipeds using gait optimization. This is realized by adding spring constants (stiffness and unloaded positions) to the optimization parameters and optimizing gaits to obtain minimal energy cost. A similar study has been made on analyzing the contribution of elastic couplings in a 3-link biped [150] and a 5-link biped [109]. Inspired by this, we intend to study the elastic couplings in our 5-link robot. Compared with this previous research, the major differences of our work are: (i) the cost function (3.76) used in our analysis is more general and does not require detailed definition of actuators such as gear ratio and motor efficiency; (ii) the symmetry outputs are adopted in the feedback linearization. The elastic couplings are applied in the form of linear torsion springs with two different configurations: either by connecting one thigh to another or via connecting two thighs respectively to the torso. The optimization is performed by including spring constants (stiffness and unloaded positions) in the optimization parameter. Thereafter, the optimized stiffness of the torso spring is used to calculate the reference step frequency which is twice the natural frequency of a pendulum formed by the swing leg with its knee being locked. The results show that both configurations can significantly reduce the overall energy cost of our 5-link planar biped and render the step frequency to approach the reference step frequency at different walking speeds so that the robot is really walking in resonance.

This chapter is organized as follows. Section 4.1 deals with the modeling of elastic couplings and the definition of the reference step frequency of the swing leg. Section 4.2 provides detailed results concerning two different configurations of linear torsion springs. Section 4.3 provides a short discussion comparing two coupling cases and results from other research. Finally, a conclusion is given in Section 4.4.

4.1 ***Modeling of Elastic Couplings***

Since elastic components cannot produce impulses during the impact, they have no influence on the 5-link planar biped's impact model. As for the swing phase model, the equation (3.2) can now be written as:

$$D(q)\ddot{q} + C(q,\dot{q}) + G(q) = B(u + \tau_e(q)) \tag{4.1}$$

where $\tau_e = [\tau_{e2}, \tau_{e3}, \tau_{e4}, \tau_{e5}]^\top$ represents the torques generated by elastic couplings. Note that we do not add elastic couplings to the underactuated generalized coordinate q_1, and therefore the dimension of τ_e is (4×1). The value of τ_e can be calculated by (2.18). We can regard $u + \tau_e(q)$ as a whole and adjust $f_{zero}(z)$ in the

zero dynamics $\dot{z} = f_{zero}(z)$ as:

$$f_{zero} = f(z) + g(z)(u^*(z) + \tau_e(z)) \in T_z\mathcal{Z}, \quad \forall z \in \mathcal{Z} \tag{4.2}$$

Thus the static feedback control law (3.39)becomes:

$$u = -(L_g L_f h(x))^{-1}(L_f^2 h(x) + \frac{1}{\epsilon} K_D L_f h(x) + \frac{1}{\epsilon^2} K_P h(x)) - \tau_e(x) \tag{4.3}$$

with (3.40) transformed into:

$$u^*(x) = -(L_g L_f h(x))^{-1} L_f^2 h(x) - \tau_e(x) \tag{4.4}$$

The other processes of calculating zero dynamics are exactly the same as mentioned in Chapter 3, and using (4.4) we can calculate the torques of the actuators for a cyclic gait on the zero dynamics surface.

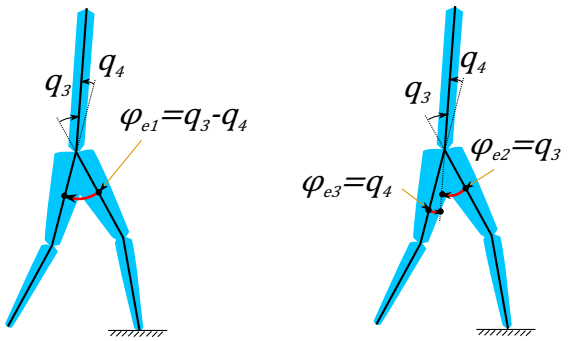

(a) 2D Coupling Case 1 (b) 2D Coupling Case 2

Fig. 4.1: 2D Coupling Cases of the 5-link planar biped.

From Figure 3.10, it is clear that for the 5-link planar biped walking at high speeds without elastic couplings, the major part of the energy consumption is caused by the actuators of the hip joints. Accordingly, it is interesting to see whether elastic couplings are capable of reducing the energy costs of these joints. As such, we propose two possible coupling cases:

2D Coupling Case I) As illustrated in Figure 4.1(a), a linear torsion spring is mounted between two thighs. Thus we have $\varphi_{e1} = q_3 - q_4$ for the deflection $\varphi_{e1} - \varphi_{e1}^*$ in (2.11) of the torsion spring. Since the robot is symmetry, we must have $\varphi_{e1}^* = 0$, and the stiffness of the torsion spring k_{e1} in (2.11) is noted as $k_{e1} = k_s$. Using (2.18), the torque vector τ_e is given by:

$$\tau_e(q) = [0, -k_s(q_3 - q_4), -k_s(q_4 - q_3), 0]^\top \tag{4.5}$$

2D Coupling Case II) As illustrated in Figure 4.1(b), two linear torsion springs are mounted respectively between the torso and the two thighs. Accordingly, we have $\varphi_{e2} = q_3$ and $\varphi_{e3} = q_4$ for the deflections $\varphi_{e2} - \varphi_{e2}^*$ and $\varphi_{e3} - \varphi_{e3}^*$ of these two springs. Because of the symmetry of the 5-link biped, the stiffness and the unloaded positions of these two springs must be the same, namely, $\varphi_{e2}^* = \varphi_{e3}^* = \varphi_s$

and $k_{e2} = k_{e3} = k_s$. By applying these two springs and using the equation (2.18), the torque vector τ_e can be calculated by:

$$\tau_e(q) = [0, -k_s(q_3 - \varphi_s), -k_s(q_4 - \varphi_s), 0]^\top \tag{4.6}$$

According to several studies on human movements [136, 137], the preferred step frequency is predictable as the resonance frequency of a force-driven harmonic oscillator. For our 5-link planar biped, we can also regard the swing leg as a compound pendulum with the hip fixed in the space and the swing knee locked in a straight position, as shown in Figure 4.2. Thus we can define the reference step frequency f^*_{step} as twice the value of the natural frequency of the swing leg:

$$f^*_{step} = \frac{1}{\pi}\sqrt{\frac{m_\mathrm{f} p_\mathrm{f} g_e + m_t(p_t + l_\mathrm{f})g_e + k_s}{I_{ah} + I_\mathrm{f} + I_t + m_\mathrm{f} p_\mathrm{f}^2 + m_t(p_t + l_\mathrm{f})^2}} \tag{4.7}$$

where I_{ah} is the rotor inertia of the hip joint, g_e is the gravity acceleration and the other notations are provided in Table 3.1.

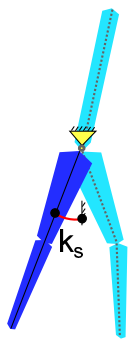

Fig. 4.2: The swing leg transformed into a compound pendulum.

4.2 Optimal Walking with Elastic Couplings

4.2.1 2D Coupling Case I

For *2D Coupling Case I*, we start with optimizing gaits with different fixed stiffness coefficient k_s at values ranging from 0 Nm/rad to 300 Nm/rad. In this way we can obtain the surface concerning the relation among the stiffness k_s, the walking speed and the energy cost (3.76) in Figure 4.3. We can draw the conclusion from this figure that, for a 5-link planar biped with a linear torsion spring mounted between two thighs, energy efficiency can be greatly improved by choosing low spring stiffness for walking at low speeds and high stiffness for walking at high speeds. The gait stick charts at different speeds (0.3 m/s, 0.7 m/s, 1.1 m/s and 1.5 m/s) with different fixed k_s are given respectively in Figure 4.5. From this figure, we can see that the robot with high spring stiffness has extremely small steps at low speeds so as to remain a high step frequency, which is not normal compared with human gaits.

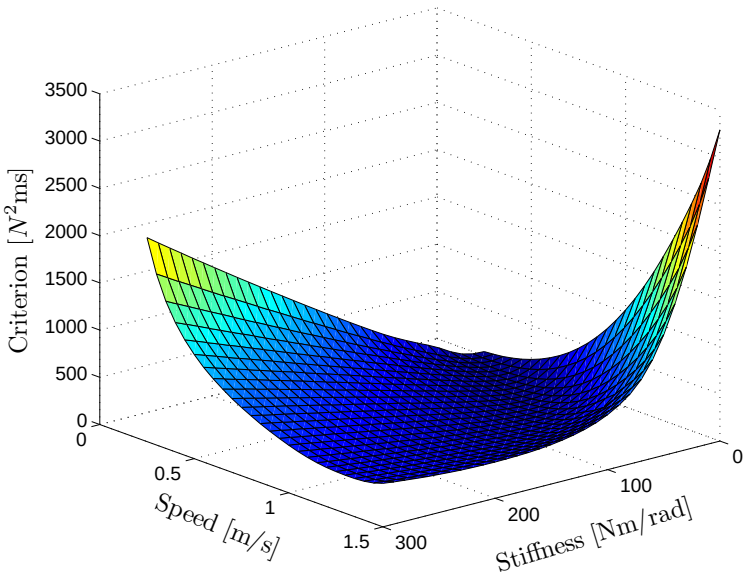

Fig. 4.3: The relation among the stiffness k_s, the walking speed and the energy cost of the 5-link planar robot for *2D Coupling Case I*

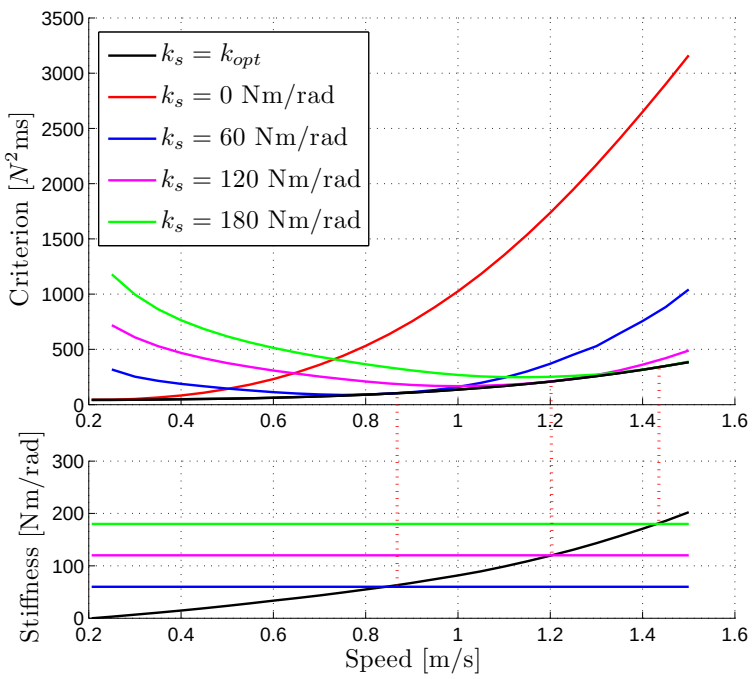

Fig. 4.4: The optimized energy cost curve with optimized k_s and the cost curves with different fixed k_s of the 5-link planar biped for *2D Coupling Case I*

In order to avoid the deficiency of fixed k_s, we can assign an optimal value k_{opt} to k_s, with k_{opt} obtained by adding k_{opt} to the optimization parameter vector ϑ (17 parameters to optimize). The corresponding results are shown in Figures 4.4, 4.7 and 4.8. We can see that the optimized cost curve with $k_s = k_{opt}$ is almost an envelop of the cost curves with fixed k_s. Compared with the other cost curves, the energy cost with $k_s = k_{opt}$ is greatly reduced for all speeds from 0.2 m/s to 1.5 m/s. In addition, the optimized stiffness k_{opt} is positively correlated with the walking speed. In comparison with previous gaits with fixed k_s, the stick charts in Figure 4.6 shows that the robot with $k_s = k_{opt}$ has normal gaits for all the speeds.

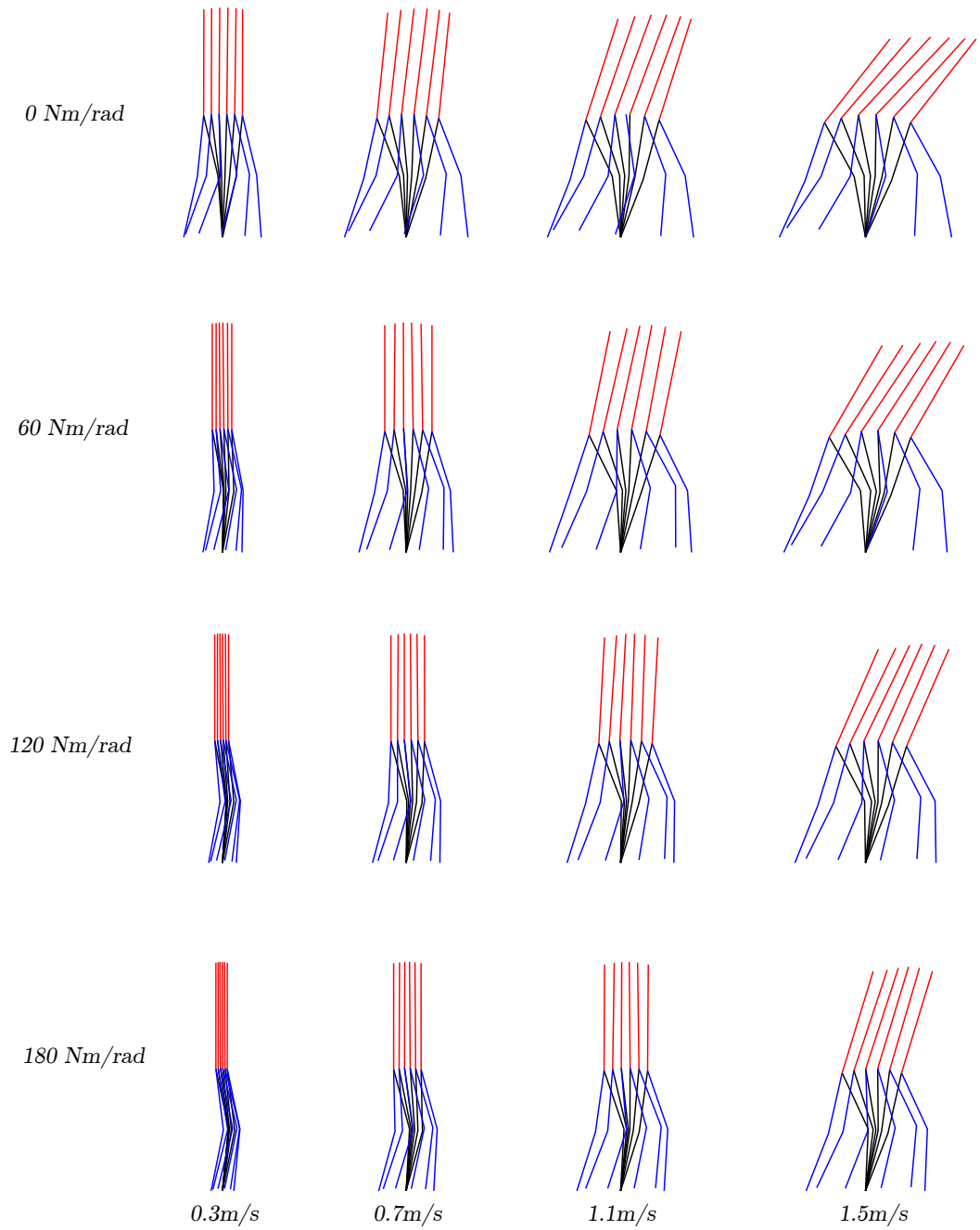

Fig. 4.5: The stick charts of the 5-link planar biped walking at different speeds for *2D Coupling Case I* with different fixed k_s

Figure 4.7 provides the energy costs of all the actuators at various speeds. The non-smoothness of these curves at 0.6 m/s is caused by the constraint *CP1* over θ_T^- for preventing the torso from leaning backward, which can be which can be confirmed in Figure 4.8. By comparing this figure with Figure 3.10, we find that, for walking at 1.5 m/s, the energy cost of the swing hip is almost 1000 N^2ms whilst this number drops significantly to less than 30 N^2ms when the torsion spring with optimized k_s is applied. A similar reduction also appears in the energy cost of the swing hip, which also drops from about 1800 N^2ms to only 180 N^2ms. In Figure 4.8, we can see that the lean angle θ_T^- of the torso at the end of a step is smaller less than the angle θ_T^- in Figure 3.11 at high speeds, which indicates that, with the elastic coupling, the robot has a more upright walking gait.

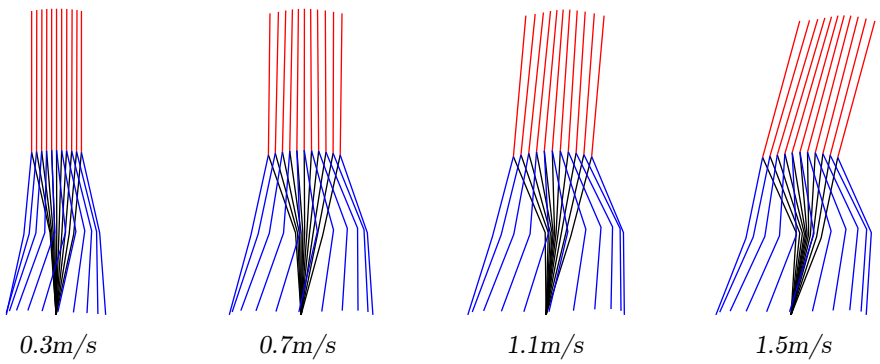

Fig. 4.6: The stick charts of the 5-link planar biped walking at different speeds for 2D Coupling Case I with $k_s = k_{opt}$

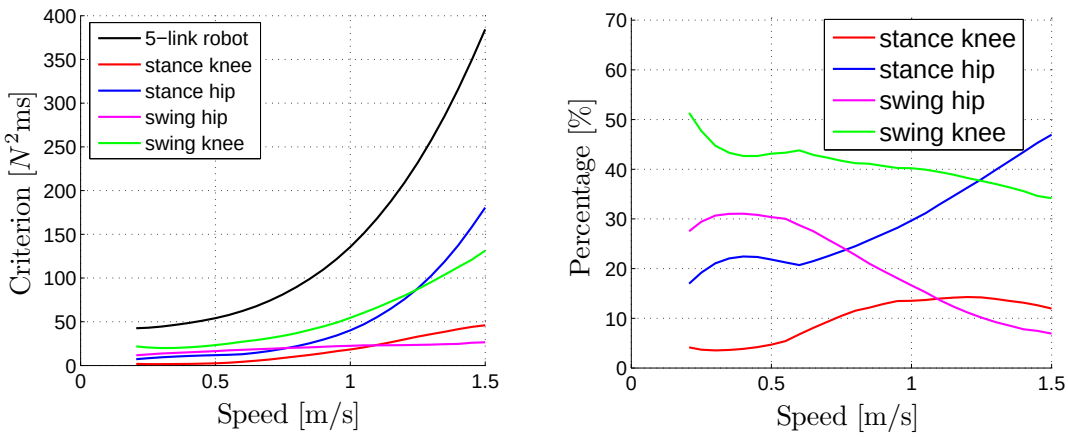

(a) The energy costs of the actuators *(b)* The contributions of the actuators

Fig. 4.7: The energy costs of the actuators of the 5-link planar biped at different walking speeds for 2D Coupling Case I with $k_s = k_{opt}$.

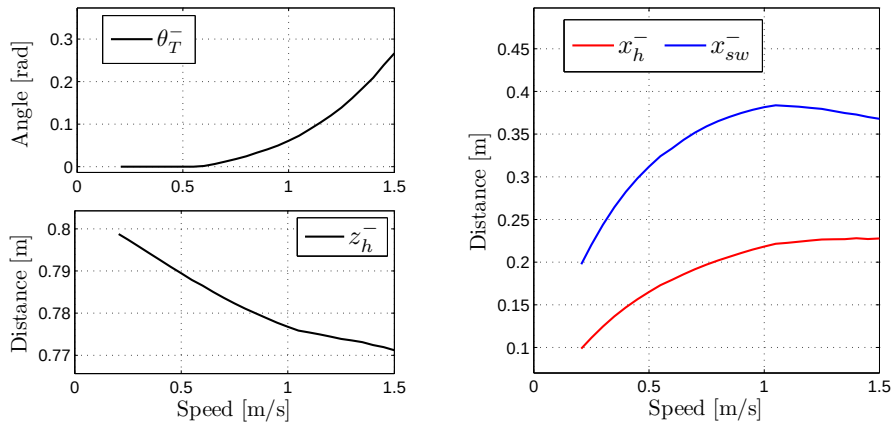

Fig. 4.8: The evolution of posture parameters at different walking speeds of the 5-link planar biped for *2D Coupling Case I* with $k_s = k_{opt}$.

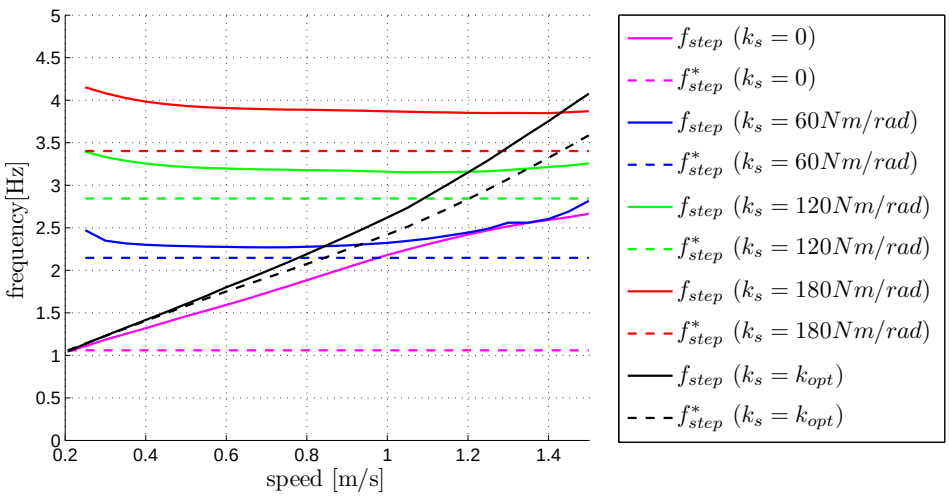

Fig. 4.9: The step frequencies and reference step frequencies of the 5-link planar robot for *2D Coupling Case I*

Indeed, the dominant purpose of adjusting the stiffness k_s is to adjust the resonance frequency of the swing leg so as to reduce energy consumption of hip joint actuators at any given walking speed. This can be verified by Figure 4.9. According to (4.7), the reference frequency f_{step} is defined as twice the number of the resonance frequency of the swing leg with locked knee. When the torsion spring is absent, i.e., $k_s = 0$, the step frequency f_{step} is only close to the reference step frequency f^*_{step} at low speeds, and the difference between the two frequencies increases significantly as the speed rises. When the torsion spring with fixed k_s is applied, the reference frequency f^*_{step} is constant and the step frequency f_{step} remains close to that constant value over a large speed range, even though the criterion in Figure 4.4 is not always satisfactory over the entire speed range and the robot has abnormal small steps in Figure 4.5 at low speeds if k_s is too high. In the case of applying the torsion spring with $k_s = k_{opt}$, k_{opt} rises as the speed increases. As a result, the reference

step frequency f^*_{step} also increases, while the real step frequency f_{step} remain close to f^*_{step}, even though the difference between these two values does gradually increase. This means that with optimized k_s, the step frequency f_{step} can remain close to the reference step frequency f^*_{step} at all speeds, which enables the bipedal robot to walk in resonance like their human counterparts with low energy consumption.

The above figures contain only general information about gaits with different hip spring stiffness k_s at different speeds. In order to delve into the detailed walking motions at 0.7 m/s and 1.5 m/s with $k_s = k_{opt}$, the curves of corresponding angles, angular velocities, actuator torques, actuator output powers and ground reaction forces are provided in Figures 4.10 to 4.14. Compared with the evolution of θ_{symm} in Figure 3.14, the curves of θ_{symm} in Figure 4.10 resembles more a sine curve. Besides, it is also observed that the amplitudes of spring torques τ_{e3} and τ_{e4} in Figure 4.12 are much larger than the corresponding actuator torques u_3 and u_4, especially for walking at 1.5 m/s.

By comparing Figure 4.13 with Figure 3.17, we can see that, although the energy criterion in (3.77) has no direct relation with mechanical power, the maximum mechanical output powers of all the actuators are greatly reduced because of the elastic coupling. An interesting phenomenon is that, the mechanical power of the hip joint actuators is mostly positive in Figure 4.13 while in Figure 3.17 the negative power of the hip joint actuators is close in amount to the positive power. These can be viewed as additional evidences supporting the fact that the 5-link bipedal robot is walking in resonance in *2D Coupling Case I* with $k_s = k_{opt}$.

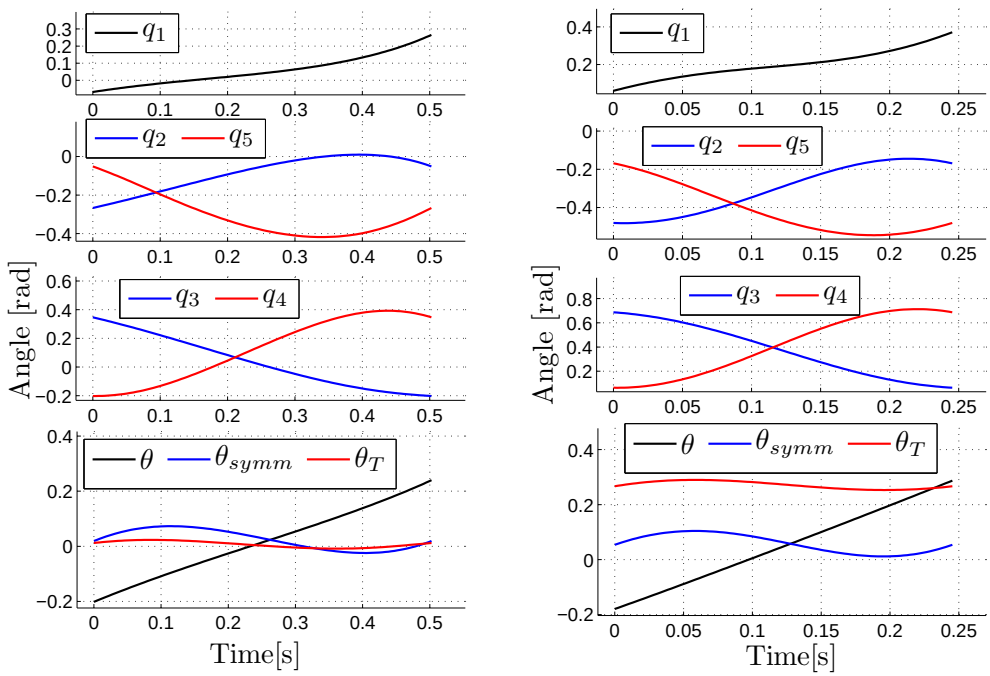

(a) **0.7** m/s (b) **1.5** m/s

Fig. 4.10: The angle curves of the joints and outputs of the 5-link planar biped walking at 0.7 m/s and 1.5 m/s for *2D Coupling Case I* with $k_s = k_{opt}$

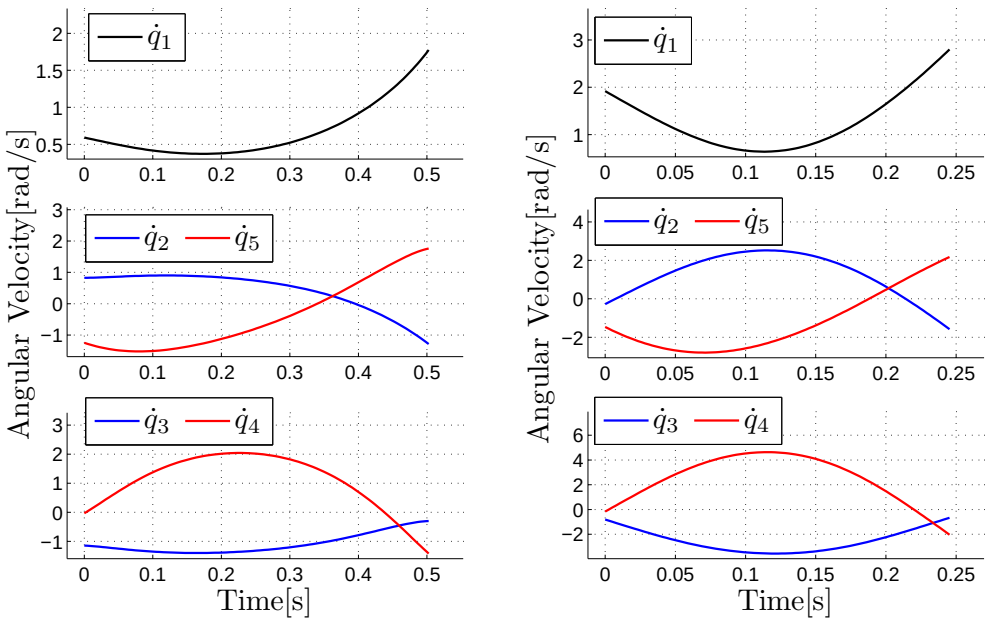

(a) **0.7** m/s (b) **1.5** m/s

Fig. 4.11: The angular velocity curves of the joints of the 5-link planar biped walking at 0.7 m/s and 1.5 m/s for *2D Coupling Case I* with $k_s = k_{opt}$.

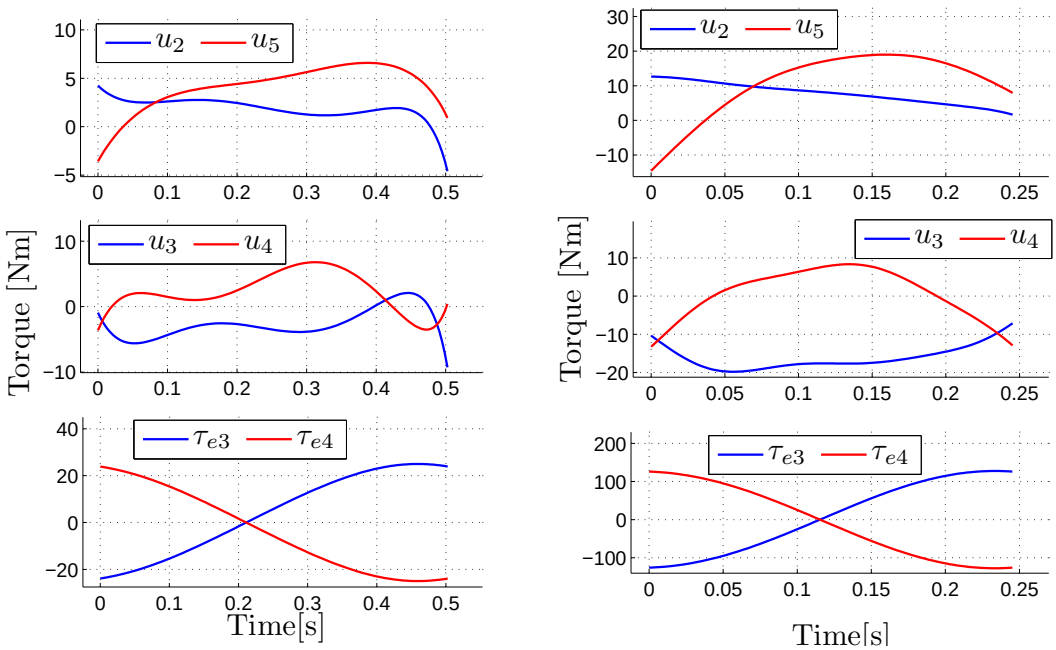

(a) **0.7** m/s (b) **1.5** m/s

Fig. 4.12: The torque curves of the actuated joints and springs of the 5-link planar biped walking at 0.7 m/s and 1.5 m/s for *2D Coupling Case I* with $k_s = k_{opt}$.

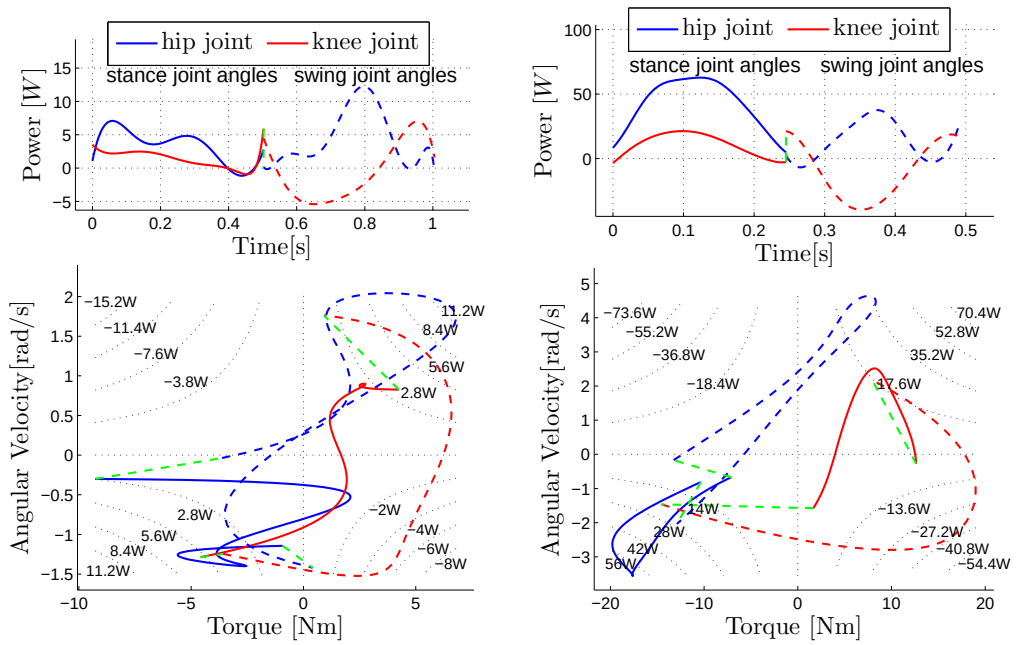

(a) **0.7** m/s (b) **1.5** m/s

Fig. 4.13: The mechanical output powers of the actuators of the 5-link planar biped walking at 0.7 m/s and 1.5 m/s (two steps) for *2D Coupling Case I* with $k_s = k_{opt}$ (Solid lines represents stance joint angles, dashed lines represents swing joint angles, and green dashed lines represents the jumps caused by the impact.)

Apart from cutting down energy consumption, the hip spring can also reduce the vertical movement of the CoM, which can be verified by comparing Figure 3.19 and Figure 4.15. As a result, the minimum value of F_{st}^z in Figure 4.14 is larger than that in Figure 3.18. In addition, the foot clearance in Figure 4.16 is around 2.5cm at both speeds, which is much smaller than the values in Figure 3.20 and close to the 1.3 cm average maximum toe clearance of human beings [181].

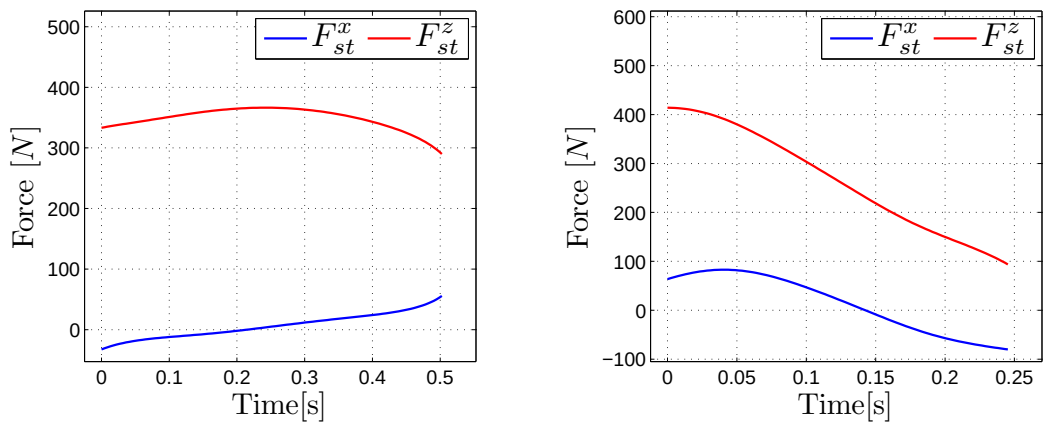

(a) **0.7** m/s (b) **1.5** m/s

Fig. 4.14: The ground reaction forces acting on the 5-link planar biped walking at 0.7 m/s and 1.5 m/s during the swing phase for *2D Coupling Case I* with $k_s = k_{opt}$.

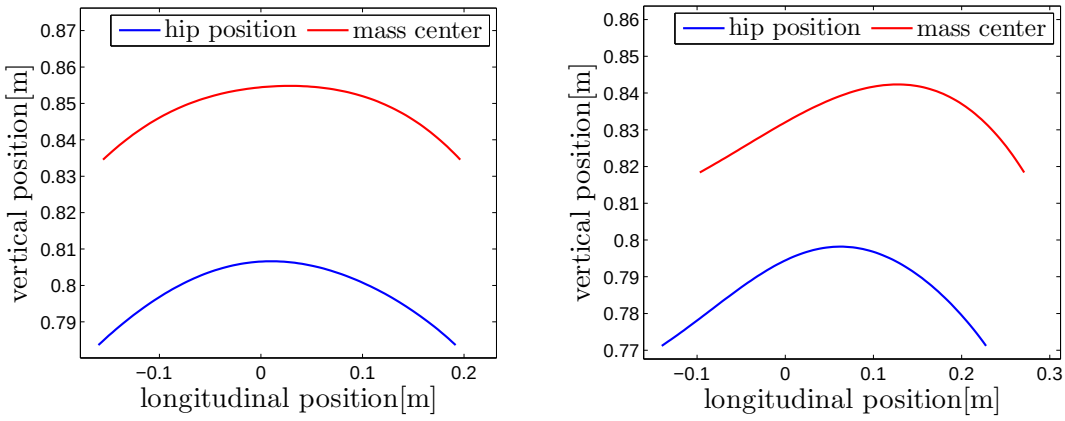

(a) **0.7** m/s (b) **1.5** m/s

Fig. 4.15: The trajectories of the hip and the CoM of the 5-link planar biped walking at 0.7 m/s and 1.5 m/s for *2D Coupling Case I* with $k_s = k_{opt}$.

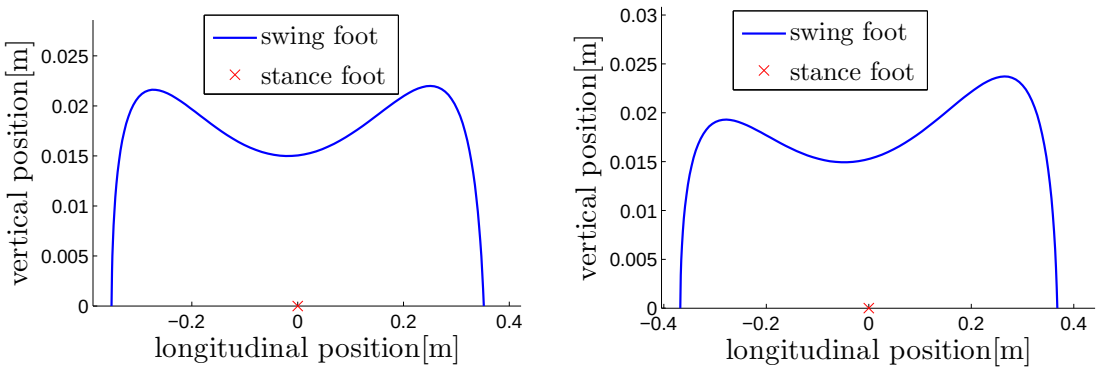

(a) **0.7** m/s (b) **1.5** m/s

Fig. 4.16: The trajectories of the swing foot of the 5-link planar biped walking at 0.7 m/s and 1.5 m/s for *2D Coupling Case I* with $k_s = k_{opt}$.

4.2.2 *2D Coupling Case II*

For *2D Coupling Case II*, there are two identical hip springs added respectively between two thighs and the torso. Accordingly we are interested in obtaining optimal values of the spring stiffness k_s and φ_s, namely, k_{opt} and φ_{opt}. This is realized by adding k_{opt} and φ_{opt} to the optimization parameter vector ϑ (18 parameters to optimize). The general results of the optimization are presented in Figures 4.17 to 4.20. As in 2D Coupling Case I, the non-smoothness of energy cost curves in Figure 4.17 is also caused by the constraint *CP1* ($\theta_T^- > 0$). By using two torsion springs connecting the torso and two thighs, it is equally possible to significantly reduce the energy cost of the 5-link planar biped (the black curve), which can be verified in Figure 4.17. At 1.5 m/s the energy cost for *2D Coupling Case II* is 329 N^2ms, which is slightly less than the energy cost 384 N^2m for *2D Coupling Case I* at the same speed. In addition, the reduction of energy cost is also due to the reduced energy costs at hip joint actuators.

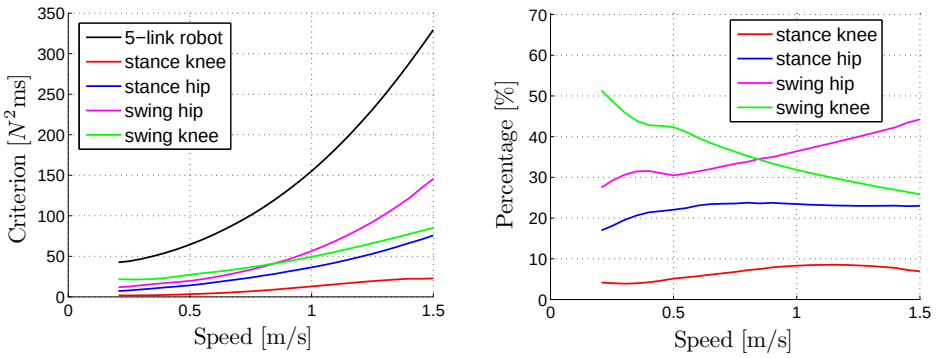

(a) energy costs of the actuators. *(b)* Contribution of the actuators.

Fig. 4.17: The energy costs of the 5-link planar biped and the actuators at different walking speeds for *2D Coupling Case II* with $k_s = k_{opt}$ and $\varphi_s = \varphi_{opt}$.

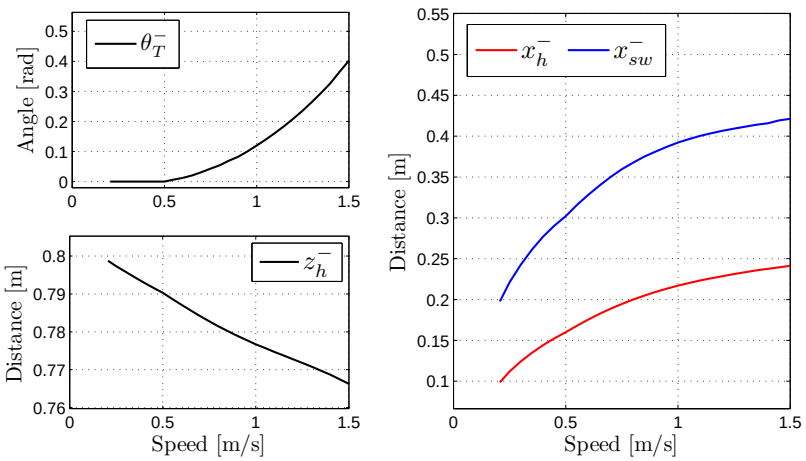

Fig. 4.18: The evolution of posture parameters of the 5-link planar biped at different walking speeds for *2D Coupling Case II* with $k_s = k_{opt}$ and $\varphi_s = \varphi_{opt}$.

In Figure 4.18, it is clear that in *2D Coupling Case II*, the robot also has a comparatively upright posture as in *2D Coupling Case I*. The gait stick charts of at different speeds (0.3 m/s, 0.7 m/s, 1.1 m/s and 1.5 m/s) are respective given in Figure 4.20. We can see that the gaits generated by *2D Coupling Case II* are also satisfactory aesthetically. In comparison with *2D Coupling Case I*, the reference frequency f^*_{step} can also be kept close to the step frequency f_{step} for all speeds using $k_s = k_{opt}$ and $\varphi_s = \varphi_{opt}$ in Figure 4.19. This indicates that *2D Coupling Case II* can also adjust the natural frequency of the swing leg to match the step frequencies at different walking speeds. In addition, it seems that the variation of unloaded position φ_{opt} with speed in Figure 4.19 is very similar to the variation of θ_T^- in Figure 4.18. Since q_3 and q_4 in (4.6) are measured in reference to the torso, this means that the unloaded positions for both hip joint springs in *2D Coupling Case II* are around the vertical position at all walking speeds, which resembles the hypothetical configuration in Figure 4.2.

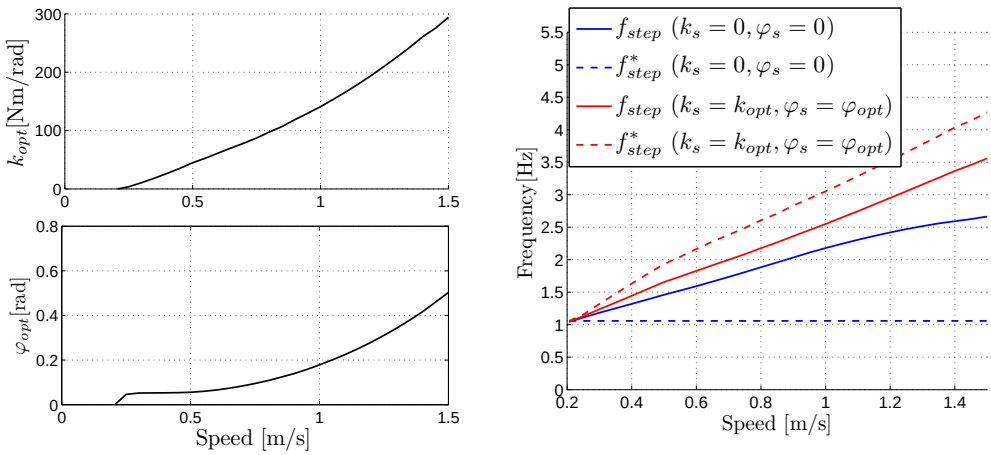

(a) The optimized stiffness k_{opt} and the optimized unloaded position φ_{opt}.

(b) The step frequency f_{step} and reference step frequency f^*_{step}.

Fig. 4.19: The stiffness k_s, unloaded position φ_s, step frequency f_{step} and reference step frequency f^*_{step} of the 5-link planar biped for *2D Coupling Case II*.

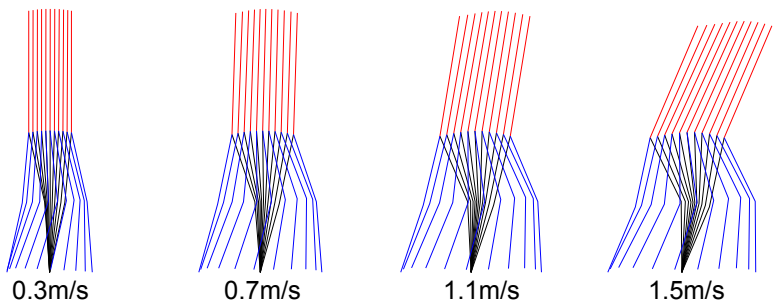

Fig. 4.20: The stick charts of the 5-link planar biped walking at different speeds for *2D Coupling Case II* with $k_s = k_{opt}$ and $\varphi_s = \varphi_{opt}$.

The detailed information of gaits at 0.7 m/s and 1.5 m/s is provided in Figures 4.21 to 4.27. These results are, to some extent, similar to the results in *2D Coupling Case I*. To begin with, the curves of θ_{symm} in Figure 4.21 also bear some resemblance to a sine curve, and it is interesting to note that the unloaded position φ_{opt} is almost in the middle of the variation range of q_3 and q_4. In addition, the amplitudes of spring torques τ_{e3} and τ_{e4} in Figure 4.23 are also much larger than the corresponding actuator torques u_3 and u_4. By comparing Figure 4.24 with Figure 4.13, we can see that, the mechanical output power of the hip joint actuators in *2D Coupling Case II* is also mostly positive. The above phenomenons indicate that 5-link bipedal robot is also walking in resonance in *2D Coupling Case II*. In Figure 4.25, it is worth mentioning that, at the walking speed 1.5 m/s, the maximum value of $|F^x_{st}|/F^z_{st}$ is smaller than the values in Figures 4.14 and 3.18, which indicates that there is more margin left for the stance foot to remain contact with the ground in *2D Coupling Case II* than the other cases mentioned before in Chapter 3 and 4. Compared with

the vertical movement of the CoM in Figure 3.19, the movement in Figure 4.26 is also smaller, and the foot clearance in Figure 4.27 is similar to that in Figure 4.16.

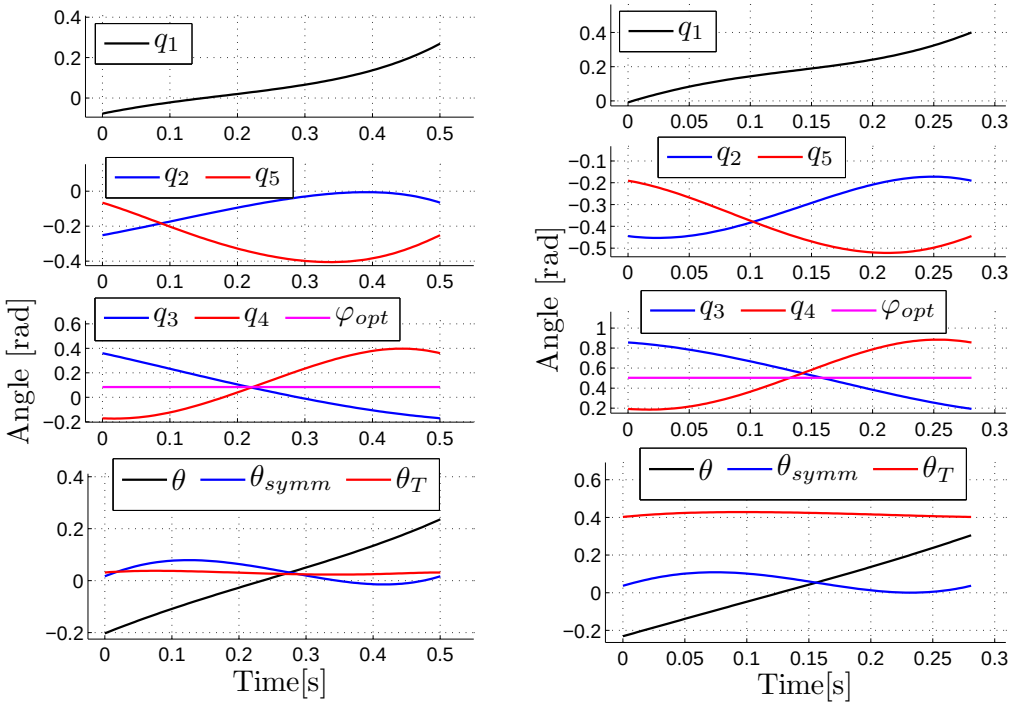

(a) **0.7** m/s (b) **1.5** m/s

Fig. 4.21: The angle curves of the joints and outputs of the 5-link planar biped walking at 0.7 m/s and 1.5 m/s for *2D Coupling Case II* with optimized k_s and φ.

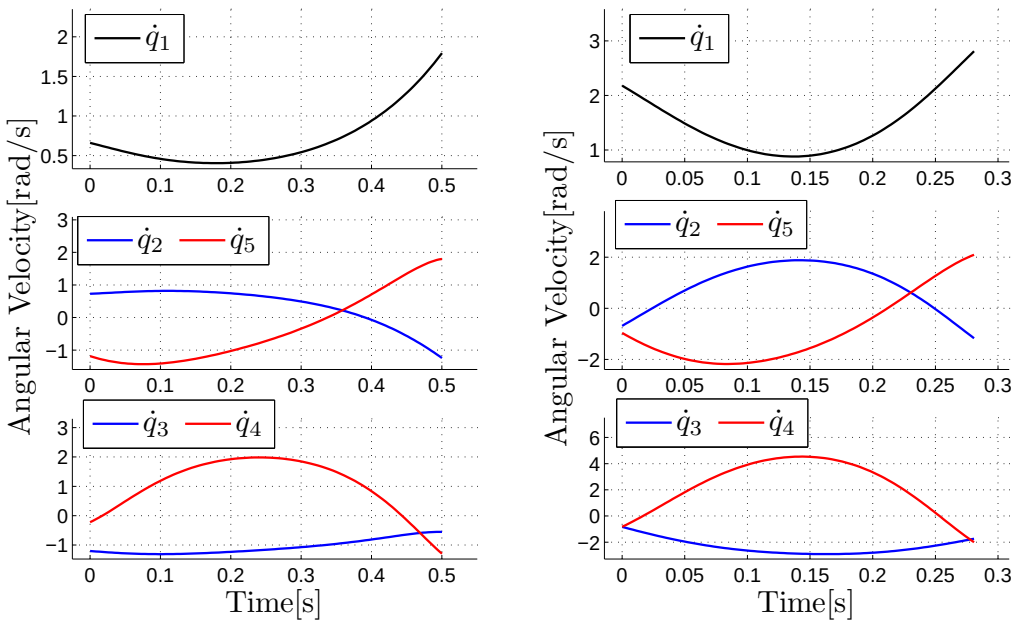

(a) **0.7** m/s (b) **1.5** m/s

Fig. 4.22: The angular velocity curves of the joints of the 5-link planar biped walking at 0.7 m/s and 1.5 m/s for *2D Coupling Case II* with $k_s = k_{opt}$ and $\varphi_s = \varphi_{opt}$.

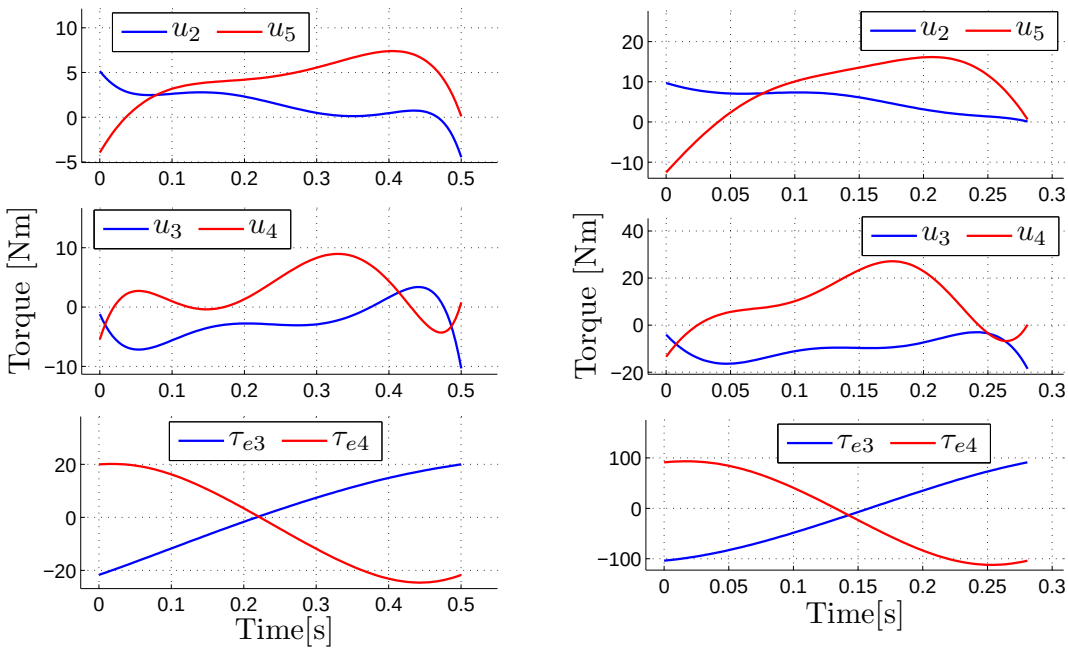

(a) **0.7** m/s (b) **1.5** m/s

Fig. 4.23: The torque curves of the joints and springs of the 5-link planar biped walking at 0.7 m/s and 1.5 m/s for *2D Coupling Case II* with $k_s = k_{opt}$ and $\varphi_s = \varphi_{opt}$.

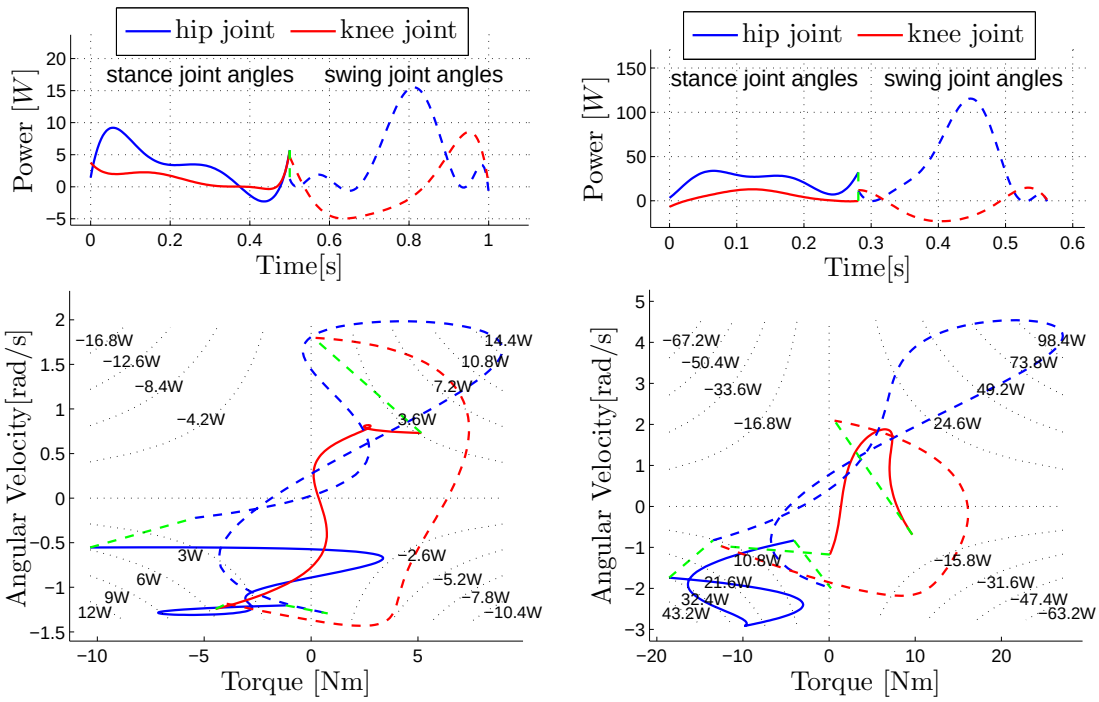

(a) **0.7** m/s (b) **1.5** m/s

Fig. 4.24: The mechanical output powers of the actuators of the 5-link planar biped walking at 0.7 m/s and 1.5 m/s (two continuous steps) for *2D Coupling Case II* with $k_s = k_{opt}$ and $\varphi_s = \varphi_{opt}$ (Solid lines represents stance joint angles, dashed lines represents swing joint angles, and green dashed lines represents the jumps caused by the impact.)

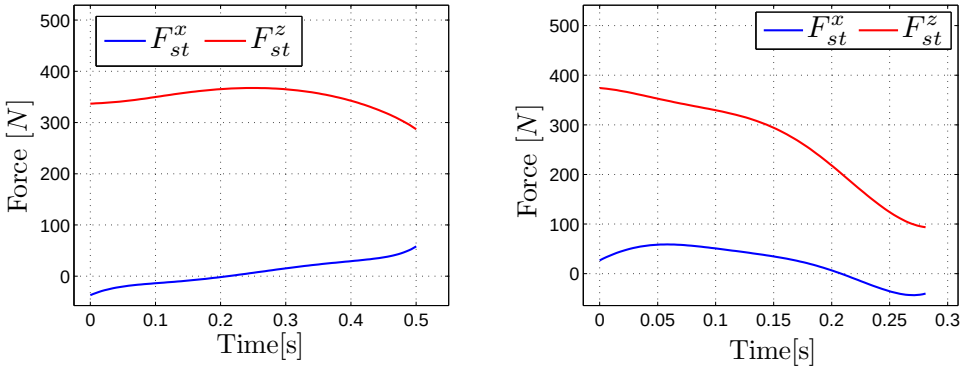

(a) **0.7** m/s (b) **1.5** m/s

Fig. 4.25: The ground reaction forces on the 5-link planar biped walking at 0.7 m/s and 1.5 m/s for *2D Coupling Case II* with $k_s = k_{opt}$ and $\varphi_s = \varphi_{opt}$.

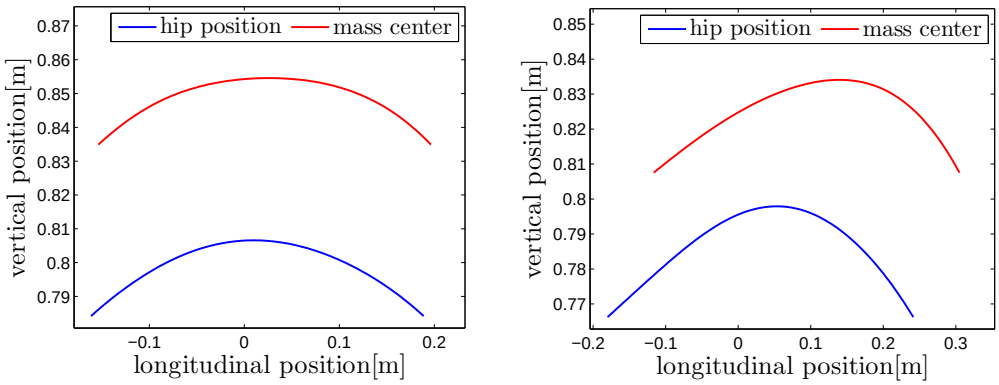

(a) **0.7** m/s (b) **1.5** m/s

Fig. 4.26: The trajectories of the hip and the CoM of the 5-link planar biped at 0.7 m/s and 1.5 m/s for *2D Coupling Case II* with $k_s = k_{opt}$ and $\varphi_s = \varphi_{opt}$.

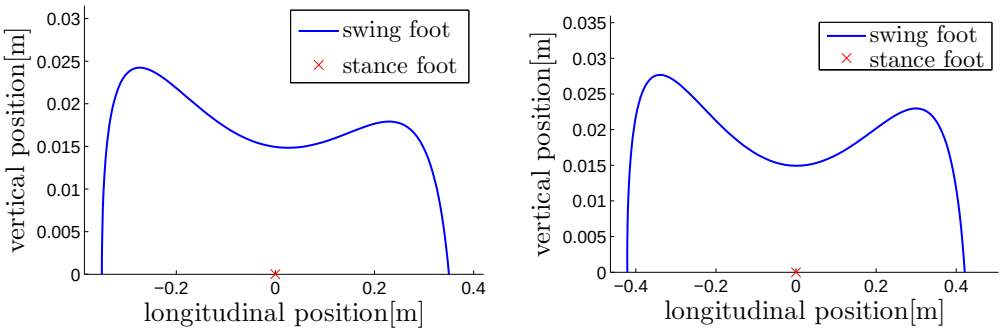

(a) **0.7** m/s (b) **1.5** m/s

Fig. 4.27: The trajectories of the swing foot of the 5-link planar biped walking at 0.7 m/s and 1.5 m/s for *2D Coupling Case II* with $k_s = k_{opt}$ and $\varphi_s = \varphi_{opt}$.

4.3 Discussion

In the previous section, we have demonstrated the appeal of adding elastic couplings in form of hip joint springs to our planar bipedal robot based on gait optimization results. In both cases, the overall energy cost is much lower than the energy cost for the same biped without elastic couplings in Chapter 3. Although *2D Coupling Case II* does provide a lower energy cost than 2D Coupling Case I, the pros and cons of these two cases make it hard to judge which one is better.

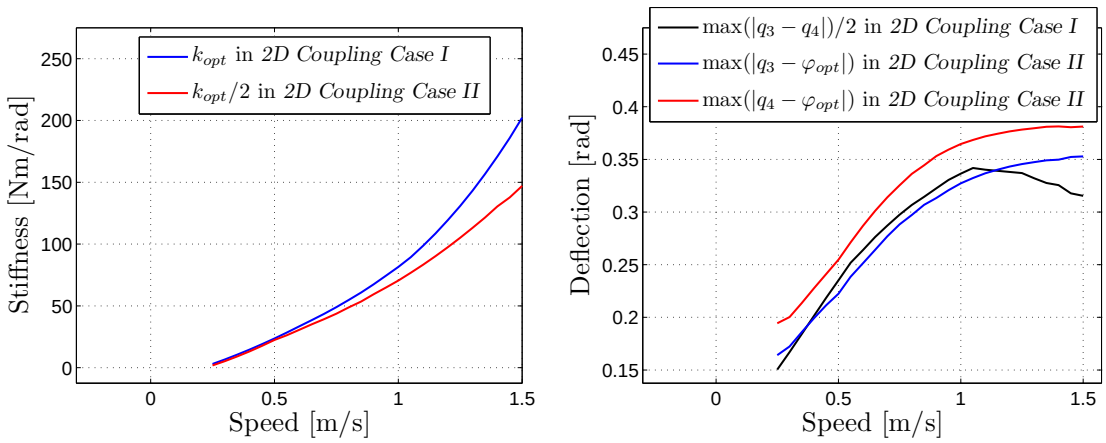

(a) spring stiffness *(b)* maximum deflection

Fig. 4.28: The comparisons of the spring stiffness and maximum deflection between *2D Coupling Case I* and *II*

Contrary to intuitive understanding, the material quantities required for manufacturing a single spring in 2D Coupling Case I and two identical springs in *2D Coupling Case II* might be quite similar. The reason behind this is simple. According to Figure 4.28, we can find that, at a given speed, the optimized spring stiffness k_{opt} for the single spring in *2D Coupling Case I* is about half the value of the stiffness of the two springs in *2D Coupling Case II*. In addition, we notice that the maximum deflections of the two springs in *2D Coupling Case II*, i.e., $\max(|q_3 - \varphi_{opt}|)$ and $\max(|q_4 - \varphi_{opt}|)$, at a given speed, are about half the value of the maximum deflection of the single spring in 2D Coupling Case I, i.e., $\max(|q_3 - q_4|)$. If the working conditions for these two cases are similar, these data suggest that we can approximately obtain the two linear springs with the stiffness a little higher than the stiffness required in *2D Coupling Case II* by equally cutting the linear spring in *2D Coupling Case I* into two pieces. The advantage of 2D Coupling Case I lies in its simplicity and reliability since it only requires a single spring with adjustable stiffness while *2D Coupling Case II* requires two springs with both adjustable stiffness and adjustable unloaded positions. However, *2D Coupling Case II* also has its advantages of keeping the torso in an upright position in the idle state and providing more margins for ground contact.

One could also be concerned with the feasibility of modifying spring stiffness and unloaded positions with power on. In fact, there are already some studies concerning tunable elastic elements. For instance, in [153, 154], a lever arm and a heart-shaped disk are respectively used to turn a linear extension spring into a linear torsion spring or a nonlinear torsion spring with adjustable spring stiffness and unloaded positions. It is also possible to to modify the spring stiffness by adjusting the pre-tension of a system with non-linear springs [156, 157]. A common problem for most of these applications is that additional actuators are required to perform the modification of spring constants, which add extra energy costs if the robot needs to change walking speed frequently. However, there are also other options for modifying spring stiffness and unloaded positions without using additional actuators. For instance, we can probably use a nonlinear stiffening spring, in which the restoring force rises more rapidly than a linear function of deflection, to replace the linear spring in *2D Coupling Case I* and *II*, since there is a positive correlation between the spring stiffness and the maximum deflection. In addition, the absolute angle of torso is also positively correlated with the optimized unloaded position and stiffness, which might inspire researchers to design certain mechanisms that can replace the additional motors.

Another interesting aspect of adding elastic couplings is that we can compare the performance of our 5-link planar biped with some unactuated or actuator-assisted dynamic biped. In Figures 4.13 and 4.24, we have mentioned that the negative power of the hip joint actuators has been great reduced by the elastic couplings in both cases. Therefore, these hip joint actuators of our robot are mainly used for injecting energy to compensate the energy lost at each impact, which is similar to the actuators in the actuator-assisted dynamic biped [66].

The periodic orbits of the 5-link biped walking at 0.7 m/s in three different cases are depicted in Figure 4.29. It is interesting to note that, for all the angles studied, the jumps of angular velocity (marked by black arrows) at the impact for both 2D Coupling Cases are much smaller than the jumps in the case where elastic couplings are absent. In Figure 4.29 (a), the absolute virtual leg angle of the biped with no elastic coupling behaves similarly to the leg angle of a actuated compass robot in [182] while the absolute virtual leg angles for two coupling cases have similar orbits with that of a passive compass biped in [183]. This suggests that the optimized gaits of actuated bipeds with elastic couplings are similar to the gaits of the passive dynamic bipeds. The orbits of the other angles can also be compared with the results in [182, 28]. It is also worth mentioning that the orbits of the relative hip joint angle for both 2D Coupling Cases resemble much more an ellipse than the orbit in the case with no coupling. This indicates that the behavior of the hip joints of the bipedal robots can be tuned to have energy efficient motions resembling rotational simple harmonic motions with the help of elastic couplings.

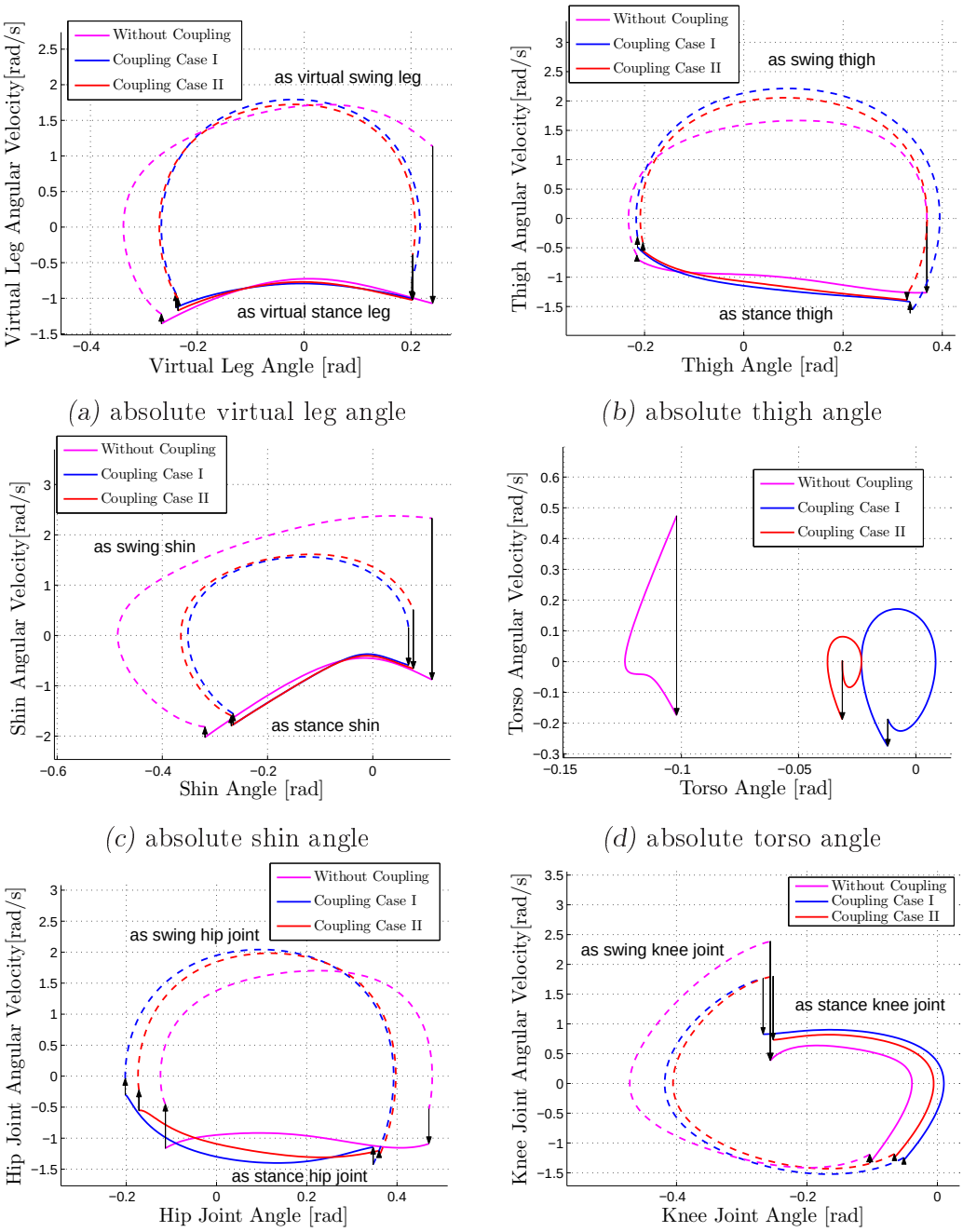

(a) absolute virtual leg angle

(b) absolute thigh angle

(c) absolute shin angle

(d) absolute torso angle

(e) relative hip joint angle

(f) relative knee joint angle

Fig. 4.29: The phase plots of the 5-link planar biped in the three different cases at 0.7 m/s. (Solid lines represent stance joint angles, dashed lines represent swing joint angles, and black arrows represent the jumps caused by the impact.)

4.4 Conclusion

In this chapter, we have discussed two cases of adding elastic couplings in form of hip joint springs to the 5-link planar biped model presented in Chapter 3. For *2D Coupling Case I*, a linear torsion spring is mounted between two thighs. For *2D Coupling Case II*, two identical linear torsion springs are installed connecting two thighs respectively to the torso. We further defined the reference step frequency, which is twice of the natural frequency of the pendulum formed by the swing leg with its knee locked in a straight position. The results for both cases are obtained using gait optimization methods in Chapter 3. In *2D Coupling Case I* et *II*, we have shown that the ideal stiffness of the hip joint spring is positively relevant to the walking speed. By adding the hip joint springs, we have greatly reduced the energy cost of the 5-link biped for the entire speed range in both cases, and the improvement is mainly due to the reduced energy costs in both hip joint actuators. In addition, the elastic couplings in both cases have also reduced negative power of the hip joint actuators. By comparing the step frequency with the reference step frequency in both cases, we have found that using the optimized stiffness (and unloaded position) we can change the natural dynamics of our planar biped so that the real step frequency can be kept close to the reference step frequency at any walking speed to ensure that the 5-link planar biped always walks in resonance. The advantages and disadvantages of these two cases are further analyzed with the suggestions of feasible ways to realize the elastic couplings in real bipedal robots, and the results from other researches including both passive dynamic bipeds and actuated dynamic bipeds have been compared with our results.

5. UNDERACTUATED 3D BIPEDAL ROBOTS WITH MASSLESS LINE FEET

This chapter focuses on modeling, controlling and optimizing an underactuated 8-link 3D bipedal robot with massless line feet, which serves as a basis for studying 3D bipeds with similar line feet and one degree of underactuation.

As mentioned in Chapter 3, the method of virtual constraints and feedback linearization in planar robots with point feet is comparatively simple. The convenience includes not only that hybrid invariance can be realized without applying a deadbeat hybrid extension [99], but also that the restricted Poincaré map is scalar, can be calculated in closed form. Nevertheless, the complexity arises significantly when one tries to extend the method to adapt the conditions of 3D robots with point feet and two or more degrees of underactuation. The only known method to achieve invariance involves using a deadbeat hybrid extension, and the corresponding restricted Poincaré map is of dimension three or higher. In addition, the asymptotic orbital stability also requires the particular choice of the virtual constraints for parameterizing the orbit. At present, there do exist some studies concerning 3D biped with point feet [91, 114]. The recent attempts to physically realize an underactuated 3D bipedal robot is presented in [39]. However, with two or more degrees of underactuation, one has to use numeric simulation instead of direct integration to create hybrid invariant manifolds, of which the stability depends on the calculation of the eigenvalues of the linearization of the restricted Poincaré map [99]. These difficulties might bring a negative effect on the numerical stability of corresponding optimization programs.

Another method to apply planar biped results to 3D bipedal robots involves functional Routhian reduction [92, 94]. The basic idea of this method is to decouple the sagittal and coronal dynamics of a 3D bipedal robot by shaping the Lagrangian of the robot system to meet the "almost-cyclic" requirement. Nevertheless, we argue that, from the standpoint of energy efficiency, motions in the sagittal plane and coronal plane are strongly coupled, and it is also questionable whether the benefit of high energy efficiency can remain once these decoupling methods are adopted. In addition, this method requires 3D bipedal robots to be fully actuated, which somehow counteracts the benefit in trying to find walking motions for underactuated planar bipedal robots. Besides, it is only possible to decouple coronal motion located at the stance ankle, thus greatly constraining the utility of the method when a 3D bipedal robot has more than one out-of-plane DOFs.

The work presented here seeks to find a compromise solution that does not require numerical simulation to determine the stability of underactuated 3D bipedal robots. Similar to the planar bipedal robot discussed in Chapter 3, the 3D bipedal

robot considered in this chapter also consists of rigid links connected via frictionless revolute joints. It is further assumed that two identical subchains named legs connect at a single pelvis (or a single torso) and that the robot model is strictly symmetric about the saggital plane. Besides, each step is also simplified into two successive phases of single support and double support. The compromise is achieved by using massless line feet different from point feet proposed in [91]. When lying flat on the ground, the line feet work as underatuated rotation axes. In this way, we can attain a scalar restricted Poincaré map for our 3D bipedal robot similar to the one of a planar biped, and thus enlarge the range of applications of the method from [84] to cover 3D bipedal walking scenarios. From the standpoint of studying optimal gaits, a similar idea was presented in [118], where a periodic 3D gait with toe rotation and one degree of underactuation is analyzed using the method in [115]. However, the control approach related to this method is different [184], and the result therein presented doesn't contain the variation of the energy criterion at different speeds. In order to avoid the complications arising from the swing foot control, we model the feet of our robot idealistically as two massless bodies with zero rotor inertiæ at the ankle joints. In this way, we can define an impact model with line contact and propose the contact constraints including a ZMP constraint and friction constraints assuming that the robot contacts the ground only at the two ends of the stance foot. These constraints can even prevent possible yaw movements of the stance line foot, which is unfortunately neglected in many previous publications [91, 114, 99]. In addition, we also adopt the symmetry outputs of planar bipeds defined in [121] to facilitate the geometric interpretation of robot movement in the sagittal plane.

For the optimization, the model parameters of our 8-link 3D robot is also estimated from the robot HRP-4 [172] by proportionally creating virtual anthropomorphic structures and then extracting model parameters from them [173, 174] as in the case of the planar biped. In addition, the cost function is also based on the energy consumption of DC or brushless motors, and the desired outputs are similarly parameterized by Bezier coefficients and postural parameters (all together 32 parameters to optimize). These parameters are further classified into two types: the 16 sagittal parameters and the 16 coronal parameters. Accordingly, the optimization is performed for two different optimization cases, namely *3D Optimization Case I* and *3D Optimization Case II* . In *3D Optimization Case I*, we directly adopt the optimized parameters from the 5-link planar biped as the sagittal parameters and optimize only the coronal parameters. In *3D Optimization Case II* , we only use the optimized parameters from the 5-link planar biped as a starting point, and all the 32 parameters are optimized. The optimization is realized by using the SQP algorithm provided by the `fmincon` function in MATLAB® optimization toolbox (R2010a).

By running optimization at different walking speeds from 0.2 m/s to 1.5 m/s, we have attained various data of optimal walking for both cases. In *3D Optimization Case I*, we find that, by optimizing only the coronal parameters we can only obtain comparatively satisfactory results (with energy cost close to that of the planar biped in Chapter 3) at high walking speeds while the coronal energy cost of the 3D biped at low speeds is abnormally high. On the contrary, the optimization results for *3D*

Optimization Case II is very similar to that of the planar biped over the entire speed range. Comparing the coronal dynamics of these two cases, it is obvious that optimizing only the coronal optimization parameters is insufficient for fully exploiting the coronal natural dynamics.

This chapter is organized as follows. Section 5.1 lists all the hypotheses concerning 3D bipedal robots with massless line feet. Section 5.2 delineates the 8-link 3D bipedal robot model treated in this chapter. Section 5.3 introduces the feedback design using optimized Hybrid Zero Dynamics (HZD) in 3D bipedal walking scenario. Section 5.4 addresses the details of the optimization program including the parameterization of holonomic constraints, the definition of the optimization criterion and constraints, and the classification of the optimization parameters. Section 5.5 presents the optimized walking data for both optimization cases with a speed ranging from 0.2 m/s to 1.5 m/s . Finally, a conclusion is given in Section 5.6.

5.1 Robot Structure and Hypotheses

The 3D bipeds considered here are bipeds with line feet and motions taking place in 3D space. The walking cycle of these robots is divided into a single support phase and a instantaneous double support phase. Similar to the hypotheses listed in Section 3.1 for the planar bipeds with point feet, the following hypotheses are defined for the 3D bipeds with massless line feet.

3D Robot Hypotheses: The planar robot is assumed to be:

HTR1) comprised of N rigid links connected by $(N-1)$ frictionless joints; each joint has at most three rotational DOFs;

HTR2) three-dimensional, with one underactuated DOF approximately in the sagittal plane;

HTR3) bipedal, with identical legs connected at a single pelvis (or a single torso), both legs are terminated by massless line feet with zero rotor inertiæ at the ankle joints, and the robot model is strictly symmetric about the saggital plane;

HTR4) underactuated at the stance line foot connecting the stance leg and the ground;

HTR5) independently actuated at the other $(N-1)$ joints.

HTR6) comprised of M DOFs, and is expressed in $(M-1)$ relative angular coordinates $(q_2, \cdots, q_M)$ plus one absolute angular coordinate q_1.

Note that the stance foot is usually approximately placed within the frontal plane. Therefore, the underactuated DOF is also approximately located in the sagittal plane.

3D Robot Gait Hypotheses: The controller of the 3D robots is required to insure robot motion satisfying the following properties:

HTG1) there are alternative phases of single support and double support, which can be equally named as the swing phase and the impact phase;

HTG2) during the single support phase, the stance foot lies on the ground, i.e., throughout each step the zero moment point(ZMP) remains inside the line segment of the stance foot and the stance foot does not slide on the ground;

HTG3) the double support phase is instantaneous and can be modeled as a rigid contact;

HTG4) in steady state, two continuous steps are plane symmetric;

HTG5) in each step, only the stance foot contacts the ground, and the swing foot starts from the position strictly behind the stance foot and lands on the position strictly in front of the stance foot with no interaction between two legs;

HTG6) walking takes place on a flat surface.

3D Robot Impact Hypotheses: An impact occurs at the double support phase when the swing foot hits the ground. The impact model for the 3D bipeds is based on the following assumptions:

HTI1) the swing foot contacts the ground horizontally with neither slipping nor rebound of the swing foot;

HTI2) at the impact, the stance foot is raised from the ground without interaction;

HTI3) the impact happens instantaneously;

HTI4) the external forces acting on the swing foot during the impact can be represented by impulses;

HTI5) there may be an instantaneous change of the velocities, but the configuration remain unchanged;

HTI6) all the actuators are not capable of generate impulses and thus they are ignored during impact.

5.2 *Dynamic Model of Walking*

This section develops a mathematical model for a 8-link 3D bipedal robot conforming to Hypotheses *HTR1-HTR6*, *HTG1-HTG6* and *HTI1-HTI6*. As illustrated in Figure 5.1, the 8-link bipedal robot is modeled as a tree structure with two identical legs and a torso all connected to a single pelvis. It is composed of eight links: a torso, a pelvis, two thighs, two shins and two line-shaped massless feet. The robot model is strictly symmetric about the sagittal plane with the ankle joints mounted along the

perpendicular bisector of the line feet. There are seven revolute joints on the robot with each hip joint having two degrees of freedom (DOF) and the other joints having one degree of freedom. The robot ankles only serve as pivots of coronal movements, and thus no yaw motion is permitted.

Like the 5-link planar robot, this robot model also uses the model parameters derived from the humanoid robot HRP-4 with the total mass of the robot being 39 kg and the total height being 1.5 m [172]. The rotor inertias are 0.8 kgm^2 for all the actuated joints except the ankle joint, and this value is the same with the rotor inertias of the planar biped. The rest of the model parameters are obtained automatically by extracting model parameters from virtual anthropomorphic structures proportionally created using the total mass and height [173, 174]. All the parameters are provided in Table 5.1. Among them, the CoMs of the thighs are measured by their distances from the hips, the CoMs of the shins are located in reference to the knees, the CoM of the pelvis is positioned by its vertical distance from the the line connecting the hips, and the CoM of the torso is defined in reference to the lumbar joint. To simplify calculation, we consider inertia matrices for all the links to be diagonal matrices written as $I_* = diag(I_{*x}, I_{*y}, I_{*z})$.

Tab. 5.1: The model parameters for the 8-link 3D biped.

Stature (m)	1.5	Foot Width l_{foot}(m)		0.15
Distance between Hips W_h(m)	0.152	Total Weight (kg)		39
Link Parameters	Thigh(f)	Shin(t)	Pelvis(p)	Torso(T)
Mass,m_*(kg)	3.936	2.227	7.882	18.793
Length,l_*(m)	0.403	0.403	0.089	0.605
Inertia,I_{*x}(m^{2}kg)	0.054	0.030	0.060	0.486
Inertia,I_{*y}(m^{2}kg)	0.054	0.030	0.040	0.418
Inertia,I_{*z}(m^{2}kg)	0	0	0.059	0.145
Center of Mass,p_*(m)	0.174	0.174	0	0.219

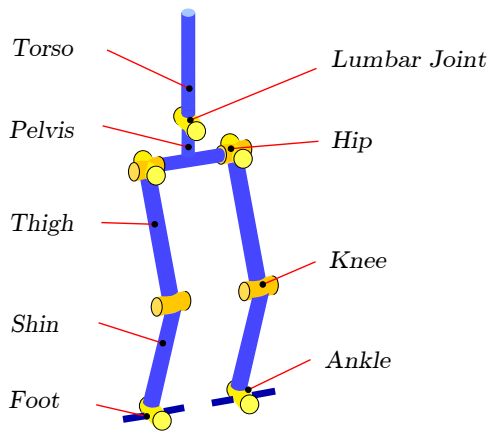

Fig. 5.1: The definitions of the joints and links of the 8-link 3D biped.

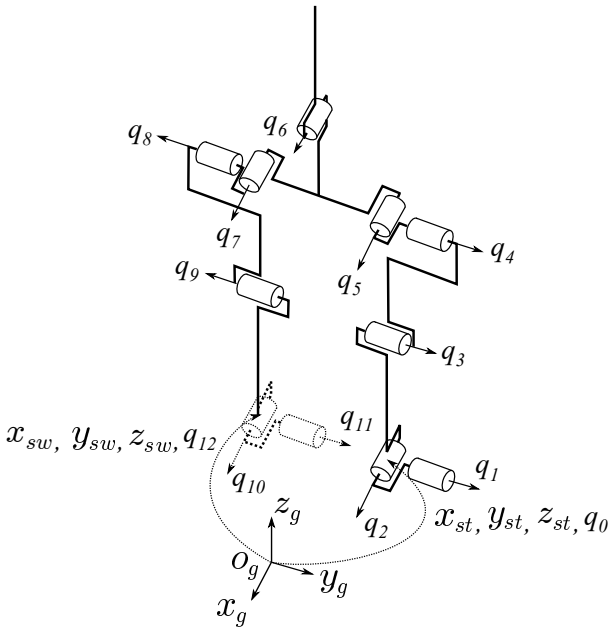

Fig. 5.2: The generalized coordinates of the 8-link 3D biped with the left foot serving as the stance foot.

Since the robot is strictly symmetric about the sagittal plane, it is possible to use a single model no matter which leg serves as the stance leg. This is achieved by relabeling previous joint angles and changing their signs when necessary. As illustrated in Figure 5.2, the coordinate frame $o_g x_g y_g z_g$ is the ground reference frame, the coordinates (x_{st}, y_{st}, z_{st}) locate the ankle joint of the stance leg, the coordinates (x_{sw}, y_{sw}, z_{sw}) locate the ankle joint of the swing leg, the angles (q_0, q_1, q_2) represent $Z-Y-X$ Euler angles of the left shin, the angles (q_{12}, q_{11}, q_{10}) represent $Z-Y-X$ Euler angles of the right shin, and $(q_3, ..., q_9)$ indicate the robot posture. When left/right foot is lying flat on the ground, q_2/q_{10} can be equally viewed as the angle of the left/right ankle joint and q_0/q_{12} is exactly the orientation of the left/right line foot with respect to the y_g axis. Here we define the generalized coordinate vector as $q_e = [x_{st}, y_{st}, z_{st}, q_0, q_1, q_2, q_3, q_4, q_5, q_6, q_7, q_8, q_9]^\top$. The angles q_{10}, q_{11} and q_{12} is useful when the swing leg and the stance leg exchange their roles at the impact, and they can be calculated by solving inverse dynamics:

$$R_{sw}(q_0, q) = \begin{bmatrix} r_{11}^{sw}(q_0, q) & r_{12}^{sw}(q_0, q) & r_{13}^{sw}(q_0, q) \\ r_{21}^{sw}(q_0, q) & r_{22}^{sw}(q_0, q) & r_{23}^{sw}(q_0, q) \\ r_{31}^{sw}(q) & r_{32}^{sw}(q) & r_{33}^{sw}(q) \end{bmatrix} \tag{5.1}$$

$$q_{11}(q) = atan2(-r_{31}^{sw}, \sqrt{(r_{32}^{sw})^2 + (r_{33}^{sw})^2}) \tag{5.2}$$

$$q_{12}(q_0, q) = atan2\left(\frac{r_{21}^{sw}}{cos(q_{11})}, \frac{r_{11}^{sw}}{cos(q_{11})}\right) \tag{5.3}$$

$$q_{10}(q) = atan2\left(\frac{r_{32}^{sw}}{cos(q_{11})}, \frac{r_{33}^{sw}}{cos(q_{11})}\right) \tag{5.4}$$

where R_{sw} is the rotation matrix of the swing shin with reference to the frame $o_g x_g y_g z_g$. Note that the angles q_{11} and q_{10} are independent of the value of q_0.

5.2.1 Swing Phase Model

The existence of two phases of the walking cycle naturally divides the dynamic model of the biped robot into a swing phase model and an impact model. Consider the left foot as the stance foot. During the single support phase, $(x_{st}, y_{st}, z_{st}, q_0)$ remains constant as long as *HTG2* is satisfied; q_2 is viewed as the joint angle of the stance ankle; and q_1 is the rotation angle about the line foot. As such, the robot has nine DOFs and eight independent actuators at this phase corresponding to the joint angles $(q_2, q_3, ..., q_9)$ leaving q_1 being underactuated.

One can use Euler-Lagrange equations to obtain the swing phase model:

$$D(q)\ddot{q} + C(q, \dot{q}) + G(q) = Bu = \begin{bmatrix} 0_{1\times 8} \\ I_{8\times 8} \end{bmatrix} u \tag{5.5}$$

where the matrix D is the (9×9) inertia matrix, C is the (9×1) vector of Coriolis and centrifugal terms, G is the (9×1) vector of gravity terms, and B is a (9×8) constant matrix mapping the (8×1) joint torque vector u to generalized forces with u written as $[u_2, ..., u_9]^\top$. For our purpose we assume that $x = [q^\top, \dot{q}^\top]^\top$ is the state variables of the robot, and the state space of the model is $T\mathcal{Q} = \{x = (q^\top, \dot{q}^\top)^\top | q \in \mathcal{Q}, \dot{q} \in \mathbb{R}^N\}$ where $\mathcal{Q}$ is a simply-connected open subset of $[-\pi, \pi)^N$ corresponding to physical realizable joint angles. Then the swing phase model can also be written in state space form:

$$\begin{aligned} \dot{x} &= \begin{bmatrix} \dot{q} \\ D^{-1}(q)[-C(q, \dot{q})\dot{q} - G(q) + Bu] \end{bmatrix} \\ &= f(x) + g(x)u \end{aligned} \tag{5.6}$$

with $f(x)$ and $g(x)$ being:

$$f(x) = \begin{bmatrix} \dot{q} \\ -D^{-1}(q)(C(q, \dot{q}) + G(q)) \end{bmatrix} \tag{5.7}$$

$$g(x) = \begin{bmatrix} 0_{9\times 8} \\ D^{-1}B \end{bmatrix} \tag{5.8}$$

Note that $D(q)$ is a positive definite matrix invertible for all $q \in \mathcal{Q}$.

5.2.2 Impact Model

As depicted in Figure 5.3, the impact model is used at the double support phase when the swing foot hits the ground. The impact is assumed to be rigid with a_{sw} and b_{sw} being the only contact points, and the double support phase lasts only an infinitesimal interval of time. Apart from modeling the instantaneous change of the robot state, the impact model also handles the switch of the robot's coordinates. Accordingly, the angles q_{10}^-, q_{11}^- and q_{12}^- need to be calculated at the impact using (5.1) to (5.4). We use "+" and "−" to indicate whether the state is just after or just before the impact. The formulation of the impact model requires the dynamic

model defined by generalized coordinates q_e. Without considering the relabeling of coordinates, we further define q_e^-, q_e^+, $\dot{q}_e^-$ and $\dot{q}_e^+$ as:

$$q_e^- = [x_{st}^-, y_{st}^-, z_{st}^-, q_0^-, q_1^-, q_2^-, q_3^-, q_4^-, q_5^-, q_6^-, q_7^-, q_8^-, q_9^-]^\top \tag{5.9}$$
$$q_e^+ = [x_{st}^+, y_{st}^+, z_{st}^+, q_0^+, q_1^+, q_2^+, q_3^+, q_4^+, q_5^+, q_6^+, q_7^+, q_8^+, q_9^+]^\top \tag{5.10}$$
$$\dot{q}_e^- = [\dot{x}_{st}^-, \dot{y}_{st}^-, \dot{z}_{st}^-, \dot{q}_0^-, \dot{q}_1^-, \dot{q}_2^-, \dot{q}_3^-, \dot{q}_4^-, \dot{q}_5^-, \dot{q}_6^-, \dot{q}_7^-, \dot{q}_8^-, \dot{q}_9^-]^\top \tag{5.11}$$
$$\dot{q}_e^+ = [\dot{x}_{st}^+, \dot{y}_{st}^+, \dot{z}_{st}^+, \dot{q}_0^+, \dot{q}_1^+, \dot{q}_2^+, \dot{q}_3^+, \dot{q}_4^+, \dot{q}_5^+, \dot{q}_6^+, \dot{q}_7^+, \dot{q}_8^+, \dot{q}_9^+]^\top \tag{5.12}$$

According to *HTG2*, $\dot{x}_{st}^-$, $\dot{y}_{st}^-$, $\dot{z}_{st}^-$ and $\dot{q}_0^-$ must equal to zero. By Hypothesis *HTI5*, the configuration of the robot remains unchanged during the impact, and thus $q_e^+ = q_e^-$. As depicted in Figure 5.3, we assume that there are only two contact points on the swing foot during the impact phase, namely a_{sw} and b_{sw}. If we define i_{sw} as the unit vector along the ankle joint q_{10} of the swing foot (which is also the perpendicular bisector of the line foot) and j_{sw} as the unit vector along the line foot, they can both be represented as functions of q_e^- by solving inverse dynamics at impact. Since the massless swing foot can transmit impulsive forces on a_{sw} and b_{sw} to the swing shin with no loss, we can replace f_{sw}^{a} and f_{sw}^{b} acting on the swing foot with a force and a torque acting on o_{sw} of the swing shin:

$$F_{sw} = f_{sw}^{\mathrm{a}} + f_{sw}^{\mathrm{b}} \tag{5.13}$$
$$\Gamma_{sw} = \frac{l_{foot} j_{sw} \times (f_{sw}^{\mathrm{b}} - f_{sw}^{\mathrm{a}})}{2} \tag{5.14}$$

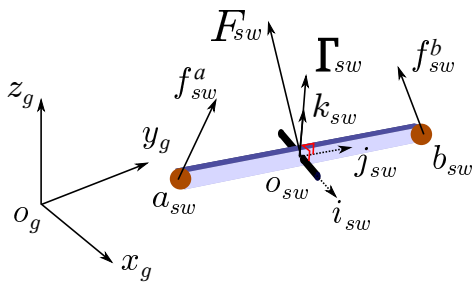

Fig. 5.3: The analysis of the swing foot of the 8-link 3D biped at the impact.

As a result, Γ_{sw} must be perpendicular to j_{sw}. According to *HTI6*, the ankle joint of the swing foot produces no impulsive torque during the impact, and accordingly Γ_{sw} is also perpendicular to i_{sw}. If we further define the unit vector k_{sw} as:

$$k_{sw}(q_e^-) = i_{sw}(q_e^-) \times j_{sw}(q_e^-) \tag{5.15}$$

Γ_{sw} can be represented by:

$$\Gamma_{sw} = k_{sw}\tau_{sw} \tag{5.16}$$

with τ_{sw} being a scalar. Thus the dynamics of the impact model are written as:

$$D_e(q_e^-)(\dot{q}_e^+ - \dot{q}_e^-) = J_{sw}^v(q_e^-)^\top F_{sw} + J_{sw}^\omega(q_e^-)^\top k_{sw}(q_e^-)\tau_{sw} \tag{5.17}$$

where the matrix D_e is the (13×13) inertia matrix, and $J_{sw}^v = \frac{\partial}{\partial q_e}[x_{sw}, y_{sw}, z_{sw}]^\top$ and $J_{sw}^\omega = \frac{\partial \omega_{sw}}{\partial \dot{q}_e}$ are the jacobian matrices with (x_{sw}, y_{sw}, z_{sw}) being the coordinates

of the o_{sw} and ω_{sw} being the angular velocity vector of the swing shin. After the impact, o_{sw} becomes fixed on the ground and ω_{sw} is:

$$\omega_{sw} = i_{sw}\dot{q}_{11}^{+} + j_{sw}\dot{q}_{10}^{+} \tag{5.18}$$

meaning that the projection of ω_{sw} on vector k_{sw} is zero, and therefore the kinematic constraints acting on the swing shin after the impact are:

$$J_{sw}^{v}(q_e^-)\dot{q}_e^+ = 0 \tag{5.19}$$

$$k_{sw}(q_e^-)^\top J_{sw}^{\omega}(q_e^-)\dot{q}_e^+ = 0 \tag{5.20}$$

By defining $J_{sw} = [J_{sw}^{\omega\top}k_{sw}, J_{sw}^{v\top}]^\top$ and $\mathscr{F}_{sw} = [\tau_{sw}, F_{sw}^\top]^\top$, the expression describing the instantaneous change of the velocity of the robot during the impact can be formulated as:

$$\Pi(q_e^-)\begin{bmatrix}\dot{q}_e^+\\ \mathscr{F}_{sw}\end{bmatrix} = \begin{bmatrix}D_e(q_e^-)\dot{q}_e^-\\ 0_{4\times1}\end{bmatrix} \tag{5.21}$$

where Π is defined as:

$$\Pi(q_e^-) = \begin{bmatrix}D_e(q_e^-) & -J_{sw}(q_e^-)^\top\\ J_{sw}(q_e^-) & 0_{4\times4}\end{bmatrix} \tag{5.22}$$

Solving (5.21) yields:

$$\begin{bmatrix}\dot{q}_e^+\\ \mathscr{F}_{sw}\end{bmatrix} = \Pi(q_e^-)^{-1}\begin{bmatrix}D_e(q_e^-)\dot{q}_e^-\\ 0_{4\times1}\end{bmatrix} \tag{5.23}$$

Then $\dot{q}_{10}^+$ and $\dot{q}_{11}^+$ can be calculated by:

$$\dot{q}_{10}^+ = i_{sw}(q_e^-)^\top J_{sw}^{\omega}(q_e^-)\dot{q}_e^+ \tag{5.24}$$

$$\dot{q}_{11}^+ = j_{sw}(q_e^-)^\top J_{sw}^{\omega}(q_e^-)\dot{q}_e^+ \tag{5.25}$$

After impact, the former stance leg becomes the swing leg and vice versa, which means that the impact model must take into account the relabeling of q. We assume that q^- and $\dot{q}^-$ represent the state before impact while q^- and $\dot{q}^-$ represent the state after impact and relabeling, and they are given by:

$$q^- = [q_1^-, q_2^-, q_3^-, q_4^-, q_5^-, q_6^-, q_7^-, q_8^-, q_9^-]^\top \tag{5.26}$$

$$\dot{q}^- = [\dot{q}_1^-, \dot{q}_2^-, \dot{q}_3^-, \dot{q}_4^-, \dot{q}_5^-, \dot{q}_6^-, \dot{q}_7^-, \dot{q}_8^-, \dot{q}_9^-]^\top \tag{5.27}$$

$$q^+ = [q_{11}^+, -q_{10}^+, q_9^+, q_8^+, q_7^+, -q_6^+, q_5^+, q_4^+, q_3^+]^\top \tag{5.28}$$

$$\dot{q}^+ = [\dot{q}_{11}^+, -\dot{q}_{10}^+, \dot{q}_9^+, \dot{q}_8^+, \dot{q}_7^+, -\dot{q}_6^+, \dot{q}_5^+, \dot{q}_4^+, \dot{q}_3^+]^\top \tag{5.29}$$

The calculation of q^+ depends only on q^-, because q_{10}^+, q_{11}^+ (equaling q_{10}^-, q_{11}^-) given by (5.2) and (5.4) are only relevant to q^-. Since $\dot{x}_{st}^-$, $\dot{y}_{st}^-$, $\dot{z}_{st}^-$ and $\dot{q}_0^-$ all equal to zero, we can prove that the calculation of $\dot{q}^+$ is only relevant to $\dot{q}^-$ and q^- by showing that the exact values of x_{st}^-, y_{st}^-, z_{st}^- and q_0^- have no influence on $\dot{q}^+$. Assume that there is a new global coordinate $\mathsf{o}_g\mathsf{x}_g\mathsf{y}_g\mathsf{z}_g$ system so that q_e is transformed into $\mathsf{q}_e = [\mathsf{x}_{st}, \mathsf{y}_{st}, \mathsf{z}_{st}, \mathsf{q}_0, \mathsf{q}_1, \cdots, \mathsf{q}_9]^\top$. Since $q_1, \cdots, q_9$ are relative angles between different links of the 3D biped, they must remain unchanged after the

coordinate transformation. Without loss of generality, we further assume that after the coordinate transformation $\mathsf{x}_{st}^-, \mathsf{y}_{st}^-, \mathsf{z}_{st}^-, \mathsf{q}_0^-$ all become zero. Thus we have:

$$\begin{aligned}
\mathsf{x}_{st} &= \cos(q_0^-)(x_{st} - x_{st}^-) + \sin(q_0^-)(y_{st} - y_{st}^-) && (5.30)\\
\mathsf{y}_{st} &= -\sin(q_0^-)(x_{st} - x_{st}^-) + \cos(q_0^-)(y_{st} - y_{st}^-) && (5.31)\\
\mathsf{z}_{st} &= z_{st} - z_{st}^- && (5.32)\\
\mathsf{q}_0 &= q_0 - q_0^- && (5.33)\\
\mathsf{q}_i &= q_i \qquad \text{for } i = 1, \cdots, 9 && (5.34)
\end{aligned}$$

Using (5.2) and (5.4), we also have $\mathsf{q}_{10} = q_{10}$ and $\mathsf{q}_{11} = q_{11}$ because of (5.34). As such, we can further obtain:

$$\begin{aligned}
\dot{\mathsf{x}}_{st} &= \cos(q_0^-)\dot{x}_{st} + \sin(q_0^-)\dot{y}_{st} && (5.35)\\
\dot{\mathsf{y}}_{st} &= -\sin(q_0^-)\dot{x}_{st} + \cos(q_0^-)\dot{y}_{st} && (5.36)\\
\dot{\mathsf{z}}_{st} &= \dot{z}_{st} && (5.37)\\
\dot{\mathsf{q}}_i &= \dot{q}_i \qquad \text{for } i = 0, \cdots, 11 && (5.38)
\end{aligned}$$

Since $\dot{x}_{st}^-$, $\dot{y}_{st}^-$, $\dot{z}_{st}^-$ and $\dot{q}_0^-$ equal to zero, we have $\mathsf{q}_e^- = [0, 0, 0, 0, q_1^-, \cdots, q_9^-]^\top$ and $\dot{\mathsf{q}}_e^- = [0, 0, 0, 0, \dot{q}_1^-, \cdots, \dot{q}_9^-]^\top$. Then we can replace q_e^- and $\dot{q}_e^-$ with q_e^- and $\dot{\mathsf{q}}_e^-$ in (5.23), (5.24) and (5.25) to obtain $\dot{\mathsf{q}}_e^+$, $\dot{\mathsf{q}}_{10}^+$, and $\dot{\mathsf{q}}_{11}^+$, in the new coordinate system $\mathsf{o}_g\mathsf{x}_g\mathsf{y}_g\mathsf{z}_g$. From (5.38), we know that $\dot{\mathsf{q}}_0^-, \cdots, \dot{\mathsf{q}}_{11}^-$ are exactly $\dot{q}_0^+, \cdots, \dot{q}_{11}^+$ in the original coordinate system $o_g x_g y_g z_g$. Since we can always find a coordinate system where x_{st}^-, y_{st}^-, z_{st}^- and q_0^- all equal to zero, we have shown that, for any q_e^- and $\dot{q}_e^-$, so far as q^- and $\dot{q}^-$ are the same, we will have the same q^+ and $\dot{q}^+$ regardless of the values of x_{st}^-, y_{st}^-, z_{st}^- and q_0^-. Thus, the impact model can be formulated as:

$$x^+ = \Delta(x^-) = \begin{bmatrix} \Delta_q q^- \\ \Delta_{\dot{q}}(q^-)\dot{q}^- \end{bmatrix} = \begin{bmatrix} q^+ \\ \dot{q}^+ \end{bmatrix} \tag{5.39}$$

where $x^- = [q^{-\top}, \dot{q}^{-\top}]^\top$. The relabeling and sign changing incorporated by the above functions enable us to use the same swing phase model and the same impact model regardless of whether right leg or left leg is chosen as the stance leg.

5.2.3 *Hybrid Model*

The overall hybrid model of walking is obtained by combining the swing phase model and the impact model to form a hybrid model formulated as:

$$\Sigma : \begin{cases} \dot{x} = f(x) + g(x)u & x \notin S \\ x^+ = \Delta(x^-) & x^- \in S \end{cases} \tag{5.40}$$

where $S = \{(q, \dot{q}) \in T\mathcal{Q} | z_{sw}(q) = 0, x_{sw}(q) - x_{st} > 0\}$ is the switching surface with z_{sw} being the height of the swing foot with reference to the ground, x_{sw} being the position of the swing ankle along the walking direction and x_{st} being the fixed position of the stance ankle.

5.2.4 *Line-foot Contact Model*

The validity of the swing phase model is based on Hypothesis *HTG2* which assumes that the stance foot is firmly fixed to the ground. Therefore, it is necessary to validate the contact condition of the stance foot. As illustrated in Fig. 5.4, we assume that there are only two contact points a_{st} and b_{st} on the stance foot. The origin o_{st} of the coordinate frame $o_{st}x_{st}y_{st}z_{st}$ coincides the stance ankle and is positioned in the middle of the line segment of the stance foot; the y_{st} axis is along the direction of the line foot; the z_{st} axis points vertically upward. Assuming that the stance foot is fixed during a step, we can decompose the net force and the net torque exerted by the ground on the stance foot center, namely Γ^x_{st}, Γ^z_{st}, F^x_{st}, F^y_{st} and F^z_{st} (Γ^y_{st} is zero because of the underactuation). All these forces and torques can be calculated as functions of q, $\dot{q}$ and $\ddot{q}$ using (2.19) and (2.22).

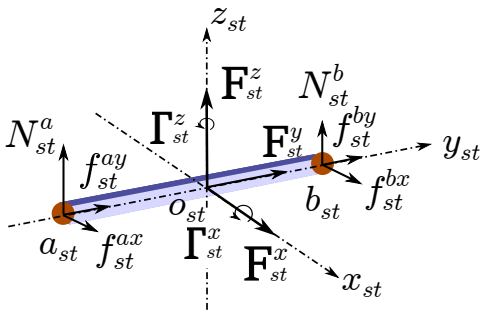

Fig. 5.4: The line-foot contact model of the 8-link 3D biped.

By solving force equilibrium equations, one can easily calculate the normal forces N^a_{st} and N^b_{st} and the decomposed forces f^{ax}_{st} and f^{bx}_{st} along the x_{st} axis.

$$N^a_{st} = \frac{F^z_{st}}{2} - \frac{\Gamma^x_{st}}{2l_{foot}} \tag{5.41}$$

$$N^b_{st} = \frac{F^z_{st}}{2} + \frac{\Gamma^x_{st}}{2l_{foot}} \tag{5.42}$$

$$f^{ax}_{st} = \frac{F^x_{st}}{2} + \frac{\Gamma^z_{st}}{2l_{foot}} \tag{5.43}$$

$$f^{bx}_{st} = \frac{F^x_{st}}{2} - \frac{\Gamma^z_{st}}{2l_{foot}} \tag{5.44}$$

Since the contact is unilateral, we need to check two inequalities concerning N^a_{st} and N^b_{st} with the form:

$$N^a_{st} > 0 \tag{5.45}$$

$$N^b_{st} > 0 \tag{5.46}$$

These equations together with *HTR4* naturally guarantees that the the position of the ZMP remains inside the interval $(-l_{foot}/2, l_{foot}/2)$ of the stance foot along the y_{st} axis throughout the single support phase, and the position of the ZMP can be calculated by:

$$p_{ZMP} = \frac{\Gamma^x_{st}}{F^z_{st}} \tag{5.47}$$

The condition imposed by the static friction can be formulated as:

$$(f_{st}^{ax})^2 + (f_{st}^{ay})^2 < (\mu N_{st}^a)^2 \tag{5.48}$$
$$(f_{st}^{bx})^2 + (f_{st}^{by})^2 < (\mu N_{st}^b)^2 \tag{5.49}$$

Nevertheless, the above equations cannot be used directly since it is impossible to calculate exact values of f_{st}^{ay} and f_{st}^{by}. Instead, we replace them with three inequalities. The first two inequalities give a necessary condition by neglecting F_y, meaning that the stance foot can no longer remain fixed if either inequality is violated.

$$|f_{st}^{ax}| < \mu N_{st}^a \tag{5.50}$$
$$|f_{st}^{bx}| < \mu N_{st}^b \tag{5.51}$$

Once these two inequalities are satisfied, the maximum absolute value of F_{st}^y is reached when the stance foot is still in equilibrium and, in the same time, maximum friction forces appear at both contact points.

$$|F_{st}^y| = |f_{st}^{ay} + f_{st}^{by}| \tag{5.52}$$
$$|f_{st}^{ay}|_{\max} = \sqrt{(\mu N_{st}^a)^2 - f_{st}^{ax2}} \tag{5.53}$$
$$|f_{st}^{by}|_{\max} = \sqrt{(\mu N_{st}^b)^2 - f_{st}^{bx2}} \tag{5.54}$$

Since $|f_{st}^{ay} + f_{st}^{by}| \leq |f_{st}^{ay}| + |f_{st}^{by}|$, the upper limit of $|F_{st}^y|$ is given by:

$$|F_{st}^y|_{\max} = \sqrt{(\mu N_{st}^a)^2 - f_{st}^{ax2}} + \sqrt{(\mu N_{st}^b)^2 - f_{st}^{bx2}} \tag{5.55}$$

Thus the third inequality shall be:

$$|F_{st}^y| < |F_{st}^y|_{\max} \tag{5.56}$$

5.3 Feedback Control Design

5.3.1 Controlled Outputs

During the swing phase, the bipedal robot has eight independent actuators, and thus the dimension of the output equals to eight. As in the case of planar bipeds, the output function for 3D bipeds is also defined as:

$$y = h(q) = h_0(q) - h_d \circ \theta(q) \tag{5.57}$$

where $h_0(q)$ indicates independent controlled quantities and $h_d \circ \theta(q)$ indicates the ideal evolution of these quantities as a function of the scalar quantity $\theta(q)$, which is a strictly monotonic function of the robot's state. For our 8-link 3D bipedal robot, θ is defined as:

$$\theta(q) = c_\theta q = q_1 + \frac{l_\mathrm{f}}{l_\mathrm{f} + l_t} q_3 \tag{5.58}$$

where c_θ is (1×9) constant row vector. If q_2 equals zero, $\theta(q)$ will be the linearized angle of the virtual stance leg. The "symmetry outputs" are also adopted in the 3D

biped [121] with the output function h_0 defined as:

$$h_0(q) = H_0 q = [\theta_T, \theta_{symm}, q_3, q_9, q_2, q_5, q_6, q_7]^\top \tag{5.59}$$

$$\theta_{symm} = q_1 + \frac{(2l_\mathrm{f} + l_t)q_3 - l_t q_9}{2(l_\mathrm{f} + l_t)} + \frac{q_4 - q_8}{2} \tag{5.60}$$

$$\theta_T = q_1 + q_3 + q_4 \tag{5.61}$$

where H_0 is a (8×9) constant matrix, θ_T reflects the behavior of the torso and θ_{symm} describes the mirror-like behavior of the virtual swing leg with regard to the virtual stance leg. If q_2, q_5, q_6 and q_7 equal zero, as illustrated in Figure 3.3(b), θ_T will be the absolute angle of the torso and θ_{symm} will be the linearized angle of the bisector of virtual swing leg and virtual stance leg with respect to the z_g axis. Actually, θ_T, θ_{symm}, q_3 and q_9 can be regarded as the sagittal outputs since they have one-to-one relations with h_0 defined in (3.24) for the planar biped, and q_2, q_5, q_6 and q_7 can be viewed as the coronal outputs. The definition of h_d is discussed right after.

5.3.2 *Swing Phase Control*

The method of explicitly constructing the zero dynamics already exists for planar bipeds. With our special ankle configuration, we can extend the usage of this method to cover the cases of 3D bipeds. Here the relevant equations previously used in Chapter 3 are briefly revisited in the context of the 8-link 3D robot configuration for logical completion. To begin with, the output $h(q)$ defined in (5.57) is purely a function of the configuration coordinates and it has all the properties of the lemma defined in [8]. Accordingly, the zero dynamics manifold is:

$$Z = \{x \in T\widetilde{Q} | h(x) = 0, L_f h(x) = 0\} \tag{5.62}$$

where $T\widetilde{Q} = \{x = (q^\top, \dot{q}^\top)^\top | q \in \widetilde{Q}, \dot{q} \in \mathbb{R}^N\}$ with $\widetilde{Q}$ being an open subset of Q such that for each $q \in \widetilde{Q}$, the decoupling matrix $L_g L_f h(x)$ is square and invertible. Using the control law similar to (3.39), we can enforce the output $y \equiv 0$, which causes $h(x) = 0$ and $L_f h(x) = 0$. By rendering the robot system evolving on Z, the applied torque vector u^* now becomes:

$$u^*(x) = -(L_g L_f h(x))^{-1} L_f^2 h(x) \tag{5.63}$$

As the columns of g in (5.8) are involutive, there exists a valid set of coordinates on Z with the form:

$$\begin{aligned} \xi_1 &= \theta(q) \\ \xi_2 &= \gamma(q, \dot{q}) \end{aligned} \tag{5.64}$$

where $\theta(q)$ is defined by (5.58) and $\gamma(q, \dot{q})$ is a smooth scalar function [160]. With the line feet defined in *HTR3*, q_1 is an absolute angular coordinate as long as *HTG2* is satisfied, and all the other coordinates $(q_2, \cdots, q_9)$ during the single support phase are relative angular coordinates. Therefore, the hypothesis *HTR6* is guaranteed, and accordingly $\gamma(q, \dot{q})$ can be explicitly computed to be the first entry of $D(q)\dot{q}$ by

applying the proof of the Frobenius theorem of [160]. The complete evolution of q and $\dot{q}$ on the zero dynamics manifold can be calculated by:

$$q = \begin{bmatrix} H_0 \\ c_\theta \end{bmatrix}^{-1} \begin{bmatrix} h_d(\xi_1) \\ \xi_1 \end{bmatrix} \tag{5.65}$$

$$\dot{q} = \begin{bmatrix} \frac{\partial h}{\partial q} \\ \gamma_0 \end{bmatrix}^{-1} \begin{bmatrix} 0 \\ \xi_2 \end{bmatrix} \tag{5.66}$$

5.3.3 Stability Analysis

Adopting the coordinate set (5.64), the zero dynamics become:

$$\begin{aligned} \dot{\xi}_1 = \quad L_f\theta(q,\dot{q}) = \quad \kappa_1(\xi_1)\xi_2 \\ \dot{\xi}_2 = \quad L_f\gamma(q,\dot{q}) = \quad \kappa_2(\xi_1) \end{aligned} \tag{5.67}$$

where $\kappa_1(\xi_1)$ and $\kappa_2(\xi_1)$ are calculated by:

$$\kappa_1(\xi_1) = \frac{\partial\theta}{\partial q} \begin{bmatrix} \frac{\partial h}{\partial q} \\ \gamma_0 \end{bmatrix}^{-1} \begin{bmatrix} 0 \\ 1 \end{bmatrix} \Bigg|_Z \tag{5.68}$$

$$\kappa_2(\xi_1) = -\frac{\partial V}{\partial q_1}\Bigg|_Z \tag{5.69}$$

with $V(q)$ being the potential energy of the biped, $\gamma_0 = D_1$ (the first row of D) and $\partial V/\partial q_1 = G_1$ (the first entry of $G(q)$).

For underatuated 3D bipedal robots with more than one degree of underactuation, the only known method to achieve hybrid invariance, i.e., $\Delta(S \cap Z) \subset Z$, is to apply a deadbeat extension, and the resulting restricted Poincaré map is of dimension three or higher [99]. These complications might impinge on the efficiency of calculating optimized gaits for 3D bipedal robot. By adopting the robot hypotheses *HTR1-HTR6*, the gait hypotheses *HTG1-HTG6* and the impact hypotheses *HTI1-HTI6*, the return map Δ: $(\xi_1^-, \xi_2^-) \to (\xi_1^+, \xi_2^+)$ can be explicitly calculated using the coordinate set $(\xi_1, \xi_2) = (\theta, \lambda)$, that is:

$$S \cap Z = \{(\xi_1^-, \xi_2^-) | \xi_1^- = \theta^-, \xi_2^- \in \mathbb{R}\} \tag{5.70}$$

$$\xi_1^+ = \theta^+ \tag{5.71}$$

$$\xi_2^+ = \delta_{zero}\xi_2^- \tag{5.72}$$

where δ_{zero} is a constant given by:

$$\delta_{zero} = \gamma_0(q^+)\Delta_{\dot{q}}(q^-)\sigma_{\dot{q}}(q^-) \tag{5.73}$$

$$\sigma_{\dot{q}}(q^-) = \begin{bmatrix} \frac{\partial h}{\partial q}(q^-) \\ \gamma_0(q^-) \end{bmatrix}^{-1} \begin{bmatrix} 0 \\ 1 \end{bmatrix} \tag{5.74}$$

Since θ is defined to be monotonic, $\dot{\xi}_1$ is non-zero over any step. Therefore, the 2-dimensional dynamical system (5.67) can be equivalent to a 1-dimensional dynamical system once coordinate transformation $\zeta_2 = \frac{1}{2}(\xi_2)^2$ is adopted, yielding:

$$\frac{d\zeta_2}{d\xi_1} = \frac{\kappa_2(\xi_1)}{\kappa_1(\xi_1)} \tag{5.75}$$

For $\theta^+ \leq \xi_1 \leq \theta^-$, define:

$$V_{zero}(\xi_1) = -\int_{\theta^+}^{\xi_1} \frac{\kappa_2(\xi_1)}{\kappa_1(\xi_1)} d\xi \tag{5.76}$$

As in the case of planar bipeds, we can determine whether a non-trivial periodic orbit of the hybrid zero dynamics exists by judging if:

$$\frac{\delta_{zero}^2}{1-\delta_{zero}^2} V_{zero}(\theta^-) + K < 0, (\delta_{zero}^2 \neq 0) \tag{5.77}$$

where $K = \max V_{zero}(\xi_1)$ with $\theta^+ \leq \xi_1 \leq \theta^-$. Furthermore, if $0 < \delta_{zero}^2 < 1$ also holds, the periodic orbit is exponentially stable with the fixed point being:

$$\xi_1^* = c_\theta q^-, \zeta_2^* = \frac{-V_{zero}(\theta^-)}{1-\delta_{zero}^2} \tag{5.78}$$

Given ξ_1^* and ζ_2^*, $\xi_2(\xi_1, \zeta_2^*)$ can be further calculated by:

$$\xi_2(\xi_1, \zeta_2^*) = -\sqrt{2(\delta_{zero}^2 \zeta_2^* - V_{zero}(\xi_1))} \tag{5.79}$$

and $t(\xi_2)$ can be calculated as:

$$t(\xi_2) = \int_{\theta^+}^{\theta^-} \frac{1}{\kappa_1(\xi_1)\xi_2(\xi_1, \xi_2^-)} d\xi_1 \tag{5.80}$$

Then the whole evolution of a periodic step is given by (5.63), (5.65) and (5.66).

5.4 Optimization of Walking Motion

The optimization of walking motion for the 8-link robot is a nonlinear constrained optimization problem involving the definition of an optimization parameter vector ϑ, an objective function $\hbar(\vartheta)$ and several scalar-valued functions $c_i(\vartheta)$ with $i \in \mathcal{E}_{set}$ or $i \in \mathcal{I}_{set}$ (note that $\mathcal{E}_{set} \cap \mathcal{I}_{set} = \emptyset$) representing respectively equality constraints or inequality constraints.

5.4.1 Parameterization of h_d

In order to parameterize h_d, we also choose Bézier polynomials of degree 5. After normalizing the $\theta(q)$ as:

$$s(q) = \frac{\theta(q) - \theta^+}{\theta^- - \theta^+} \tag{5.81}$$

with θ^+ being the minimum value of $\theta(q)$ and θ^- the maximum value of $\theta(q)$. Then $h_d \circ \theta(q)$ can be written as:

$$h_d \circ \theta(q) = B_Z \circ s(q) \tag{5.82}$$

where $B_Z(s) = [b_1(s), \cdots, b_8(s)]^\top$ with each $b_i(s)$ further defined by:

$$b_i(s) = \sum_{k=0}^{5} a_k^i \frac{5!}{k!(5-k)!} s^k (1-s)^{5-k} \tag{5.83}$$

Group the parameters a_k^i into (8×1) vectors as $a_k = [a_k^1, \cdots, a_k^8]^\top$. Enforcing $h \circ \Delta(S \cap Z) = 0$, we can calculate a_0 directly from a_5 using:

$$\begin{bmatrix} a_0 \\ \theta^+ \end{bmatrix} = H \Delta_q H^{-1} \begin{bmatrix} a_5 \\ \theta^- \end{bmatrix} \tag{5.84}$$

where $H = [H_0^\top, c_\theta^\top]^\top$. Moreover, if $L_f h \circ \Delta(S \cap Z) = 0$, a_1 can also be calculated using a_5 and a_4 by the equation:

$$a_1 = \frac{\theta^- - \theta^+}{5c\dot{q}^+} H_0 \dot{q}^+ + a_0 \tag{5.85}$$

where $\dot{q}^- = \sigma_{\dot{q}}(q_0^-)$ and $\dot{q}^+ = \Delta_{\dot{q}}(q_0^-)\dot{q}^-$. Using (5.84) and (5.85), hybrid invariance is realized [8].

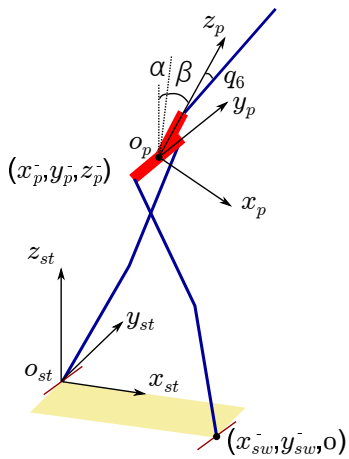

Fig. 5.5: The posture parameters of the 8-link 3D biped with the pelvis marked in red

Although the parameter set $\{a_2, a_3, a_4, a_5\}$ is able to determine h_d, it is not obvious how the posture of the robot is. Therefore, we replace parameter vector a_5 with the postural parameter vector indicating the robot postural right before the impact. As illustrated in Figure 5.5, define the fixed coordinate frame as $o_{st}x_{st}y_{st}z_{st}$ with z_{st} axis pointing vertically upward and the origin o_{st} located at the midpoint of the stance line foot. Then place the moving frame on the pelvis $o_p x_p y_p z_p$ with the y_p axis going through two hips, z_p axis pointing towards the lumbar joint and the origin o_p placed at middle of two hips. Assuming that the orientations of the frame $o_p x_p y_p z_p$ and the frame $o_{st}x_{st}y_{st}z_{st}$ are initially the same, we can define α as the rotation about the x_p axis of the moving frame and β as the rotation about the rotated y_p axis of the moving frame. Represent o_p in the fixed frame $o_{st}x_{st}y_{st}z_{st}$ as (x_p^-, y_p^-, z_p^-) and the swing foot center as $(x_{sw}^-, y_{sw}^-, 0)$, the postural parameter vector is then given by:

$$\phi_P = [q_6^-, \alpha, \beta, x_p^-, y_p^-, z_p^-, x_{sw}^-, y_{sw}^-]^\top \tag{5.86}$$

In order to obtain all the angles $(q_0^-, q_1^-, ..., q_{12}^-)$, we need to solve a problem of inverse kinematics depicted in Figure 5.6. We start by analyzing the swing leg. The first step is to calculate unit vectors of the axes x_p and y_p, which are noted as n_{px}

and n_{py} respectively.

$$n_{px} = [\cos(\beta), \sin(\alpha)\sin(\beta), -\cos(\alpha)\sin(\beta)]^\top \quad (5.87)$$
$$n_{py} = [0, \cos(\alpha), \sin(\alpha)] \quad (5.88)$$

Then we can calculate the vector of the virtual swing leg l_{sw} as:

$$l_{sw} = [x_{sw}^- - x_p, 0.5W_h\cos(\alpha) - y_p + y_{sw}^-, 0.5W_h\sin(\alpha) - z_p]^\top \quad (5.89)$$

where W_h is the distance between two hip joints. If the angles $q_0, \cdots, q_7$ are fixed, the swing leg can only move in a plane. Since n_{px} is parallel to the rotation axis of q_7, we can calculate the unit normal vector of the swing leg plane using:

$$n_{swl} = (l_{sw} \times n_{px})/|l_{sw}| \quad (5.90)$$

If $q_7 = 0$, n_{swl} is equal to $-n_{py}$. Therefore q_7 can be viewed as the angle between $-n_{py}$ and n_{swl}, and thus we have:

$$q_7 = \arcsin(n_{px}^\top(n_{swl} \times n_{py})) \quad (5.91)$$

Then q_8 and q_9 can be easily obtained by:

$$q_8 = \pi/2 - \arccos(l_{sw}^\top n_{px}/|l_{sw}|) + \arccos((|l_{sw}|^2 + l_f^2 - l_t^2))/(2l_f|l_{sw}|)) \quad (5.92)$$
$$q_9 = -\pi + \arccos((l_t^2 + l_f^2 - |l_{sw}|^2))/(2l_t l_f)) \quad (5.93)$$

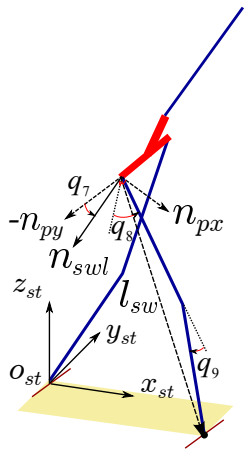

Fig. 5.6: The inverse kinematics of the 8-link 3D biped.

The method for calculating angles for the stance leg is similar, and the corresponding equations are listed below:

$$l_{st} = [-x_p, -0.5W_h\cos(\alpha) - y_p, -0.5W_h\sin(\alpha) - z_p]^\top \quad (5.94)$$
$$n_{stl} = (l_{st} \times n_{px})/|l_{st}| \quad (5.95)$$
$$q_5 = -\arcsin(n_{px}^\top(n_{stl} \times n_{py})) \quad (5.96)$$
$$q_4 = \pi/2 - \arccos(l_{st}^\top n_{px}/|l_{st}|) + \arccos((|l_{st}|^2 + l_f^2 - l_t^2))/(2l_f|l_{st}|)) \quad (5.97)$$
$$q_3 = -\pi + \arccos((l_t^2 + l_f^2 - |l_{st}|^2))/(2l_t l_f)) \quad (5.98)$$

Once α, β, q_3, q_4, q_5, q_7, q_8 and q_9 has been obtained, we can calculate q_0, q_1, q_2, q_{10}, q_{11} and q_{12} using following equations:

$$R_{sw}(\alpha, \beta, q_7, q_8, q_9) = \begin{bmatrix} r_{11}^{sw} & r_{12}^{sw} & r_{13}^{sw} \\ r_{21}^{sw} & r_{22}^{sw} & r_{23}^{sw} \\ r_{31}^{sw} & r_{32}^{sw} & r_{33}^{sw} \end{bmatrix} \tag{5.99}$$

$$q_{11}^{-}((\alpha, \beta, q_7, q_8, q_9) = atan2(-r_{31}^{sw}, \sqrt{(r_{32}^{sw})^2 + (r_{33}^{sw})^2}) \tag{5.100}$$

$$q_{12}^{-}((\alpha, \beta, q_7, q_8, q_9) = atan2\left(\frac{r_{21}^{sw}}{cos(q_{11}^{-})}, \frac{r_{11}^{sw}}{cos(q_{11}^{-})}\right) \tag{5.101}$$

$$q_{10}^{-}((\alpha, \beta, q_7, q_8, q_9) = atan2\left(\frac{r_{32}^{sw}}{cos(q_{11}^{-})}, \frac{r_{33}^{sw}}{cos(q_{11}^{-})}\right) \tag{5.102}$$

$$R_{st}(\alpha, \beta, q_3, q_4, q_5) = \begin{bmatrix} r_{11}^{st} & r_{12}^{st} & r_{13}^{st} \\ r_{21}^{st} & r_{22}^{st} & r_{23}^{st} \\ r_{31}^{st} & r_{32}^{st} & r_{33}^{st} \end{bmatrix} \tag{5.103}$$

$$q_{1}^{-}(\alpha, \beta, q_3, q_4, q_5) = atan2(-r_{31}^{st}, \sqrt{(r_{32}^{st})^2 + (r_{33}^{st})^2}) \tag{5.104}$$

$$q_{0}^{-}(\alpha, \beta, q_3, q_4, q_5) = atan2\left(\frac{r_{21}^{st}}{cos(q_{1}^{-})}, \frac{r_{11}^{st}}{cos(q_{1}^{-})}\right) \tag{5.105}$$

$$q_{2}^{-}(\alpha, \beta, q_3, q_4, q_5) = atan2\left(\frac{r_{32}^{st}}{cos(q_{1}^{-})}, \frac{r_{33}^{st}}{cos(q_{1}^{-})}\right) \tag{5.106}$$

Then a_5 can be calculated by:

$$a_5 = H_0 q^{-} \tag{5.107}$$

It is important to note that q_0^- and q_{12}^- given by (5.101) and (5.105) do not satisfy the equation $q_0^- = -q_{12}^-$. This suggests that there is a deviation between the walking direction and the x_{st} axis, and therefore x_{sw}^- is not the step size of each step. The deviation angle θ_d and the step size d can be given by:

$$\theta_d = (q_0^- + q_{12}^-)/2 \tag{5.108}$$

$$d = x_{sw}^- \cos(\theta_d) + y_{sw}^- \sin(\theta_d) \tag{5.109}$$

Notice that θ_d is usually very small and therefore the difference between x_{sw}^- and d is also trivial, but it is still necessary to calculate the accurate step size so as to ensure the accuracy of the average walking speed and the energy cost.

Thus, the complete parameter set for optimization is $\{\phi_P, a_2, a_3, a_4\}$, which contains 32 parameters. However, further study revealed that it is possible to classify these optimization parameters into 16 sagittal parameters and 16 coronal parameters. First of all, for the posture parameters ϕ_P, β, x_p^-, z_p^- and x_{sw}^- are counted as sagittal parameters while q_6^-, α, y_p^- and y_{sw}^- are regarded as coronal parameters. Since the first four entries of h_0 are sagittal outputs, the parameters a_2^1, a_2^2, a_2^3, a_2^4, a_3^1, a_3^2, a_3^3, a_3^4, a_4^1, a_4^2, a_4^3, a_4^4 are counted also as sagittal outputs, and the rest parameters a_2^5, a_2^6, a_2^7, a_2^8, a_3^5, a_3^6, a_3^7, a_3^8, a_4^5, a_4^6, a_4^7, a_4^8 are coronal parameters as the last four entries of h_0 are coronal outputs.

5.4.2 Optimization Criterion

As in the case of the 5-link planar biped, the cost function is defined as the integral of the norm of the torque for a displacement of one meter, and the simplified form is written as:

$$C(\vartheta) = \frac{1}{d}\int_{\theta^+}^{\theta^-} \frac{\sum_{i=2}^{9}(u_i^*(\xi_1,\xi_2))^2}{\kappa_1(\xi_1)\xi_2(\xi_1,\xi_2^-)} d\xi_1 \tag{5.110}$$

where T is the step duration and d is the step length given by (5.109). The validity of the cost function depends on whether there is a valid fixed point (ξ_1^*, ζ_2^*) as defined in (5.78). As in the case of the planar biped, there are three situations where we cannot calculate (ξ_1^*, ζ_2^*) for the 3D biped:

1. a_5 calculated by the inverse kinematics (5.87) to (5.107) contains complex numbers;
2. a_5 is valid but $\delta_{zero}^2 \geq 1$ or $\delta_{zero}^2 = 0$;
3. a_5 is valid and $0 < \delta_{zero}^2 < 1$ but $\delta_{zero}^2 V_{zero}(\theta^-)/(1-\delta_{zero}^2) + K > 0$.

Accordingly, the objective function $\hbar(\vartheta)$ can be defined as:

$$\hbar(\vartheta) = \begin{cases} C(\vartheta) & (\xi_1^*, \zeta_2^*)\text{is valid} \\ \text{NaN} & \text{else} \end{cases} \tag{5.111}$$

where `NaN` stands for "not a number" and $C(\vartheta)$ is calculated by (5.110).

5.4.3 Constraints

For ensuring the validity of the optimal walking trajectory with reference to certain requirements, it is necessary to define corresponding constraints including:

CT1) The pelvis constraint and torso constraint prevent large lean-angles of the torso and the pelvis, i.e., $-\pi/15\,(rad) < \alpha^- < \pi/15\,(rad)$, $0 < \beta^- < \pi/4\,(rad)$ and $-\pi/36\,(rad) < q_6^- < \pi/36\,(rad)$;

CT2) The pelvis constraint prevents extremely low pelvis position, i.e., $z_p^- > 0.72\,(m)$;

CT3) The vertical component F_{sw}^z of impulsive impact force given in (5.23) must be upward:

$$c_1 = -F_{sw}^z < 0 \tag{5.112}$$

CT4) The post-impact velocity of the swing foot is upward;

$$c_2 = -\dot{z}_{sw}^+ < 0 \tag{5.113}$$

CT5) The swing foot must not touch the ground prematurely:

$$c_3 = -\min_{0<s<1}(z_{sw}(s)) < 0 \tag{5.114}$$

CT6) The swing leg and the stance leg have no interaction during the step:

$$c_4 = \max_{0\leq s\leq 1}(-\sin(\theta_d)x_{sw}(s) + \cos(\theta_d)y_{sw}(s) + 0.6l_{foot}) < 0 \tag{5.115}$$

CT7) The knees of both the swing leg and the stance leg only bend in forward direction:

$$c_5 = \max_{0\leq s\leq 1}(q_3(s)) \leq 0 \tag{5.116}$$

$$c_6 = \max_{0\leq s\leq 1}(q_9(s)) \leq 0 \tag{5.117}$$

CT8) The stance foot contact constraints as defined by (5.45), (5.46), (5.50), (5.51) and (5.56):

$$c_7 = -N_{st}^a < 0 \tag{5.118}$$

$$c_8 = -N_{st}^b < 0 \tag{5.119}$$

$$c_9 = |f_{st}^{ax}| - \mu N_{st}^a < 0 \tag{5.120}$$

$$c_{10} = |f_{st}^{bx}| - \mu N_{st}^b < 0 \tag{5.121}$$

$$c_{11} = |F_{st}^y| - |F_{st}^y|_{\max} < 0 \tag{5.122}$$

CT9) The average walking speed equals to the desired speed:

$$c_{12} = d/T - v_d = 0 \tag{5.123}$$

where v_d represents the desired speed.

Among all the constraints, *CT1* and *CT2* are treated as the bounds of the optimization parameters ϑ, *CT3-CT8* are nonlinear inequality constraints, and *CT9* is nonlinear equality constraint. Accordingly, we have $\mathcal{E}_{set} = \{12\}$ and $\mathcal{I}_{set} = \{1, 2, \cdots, 11\}$. As in the case $\hbar(\vartheta)$, it is possible that we cannot calculate the constraints. In those situations, $c_i =$`NaN` for all $i \in \mathcal{I}_{set} \cup \mathcal{E}_{set}$.

5.4.4 Optimization Realization

The optimization of the 8-link 3D biped also uses the SQP algorithm and the processes of optimization has already been explained in Section 3.4.4. For the 3D biped, the three major steps in calculating the objective function $\hbar(\vartheta)$ and the constraints $c(\vartheta)$ are given below:

1. Calculate the evolution of the zero dynamics. (1) Solve the inverse dynamics using equations (5.87) to (5.107). (2) Parameterize h_d using (5.84), (5.85), (5.83), (5.82) and (5.81). (3) Calculate the evolution of ξ_1 and ξ_2 using (5.73), (5.74), (5.68), (5.69), (5.76), (5.78) and (5.79) and (5.80).

2. Calculate the evolution of the complete system by calculating (5.63), (5.65), (5.66), and (5.6).

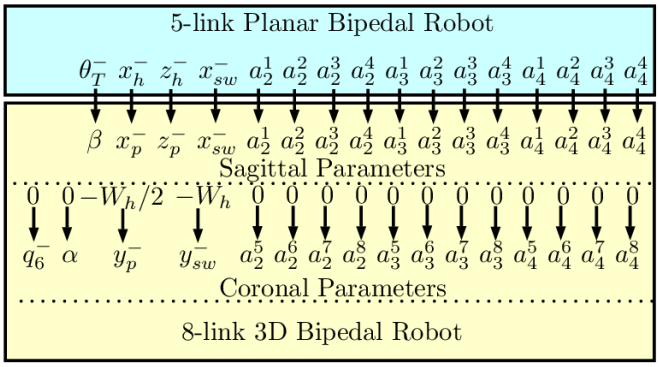

Fig. 5.7: The starting point ϑ_0 for optimizing the 8-link 3D biped

3. Calculate the objective function using the equation (5.111) and all the constraints using (5.112) to (5.123).

For optimization, a feasible starting point ϑ_0 is crucial. In our case, a feasible starting point requires that a valid fixed point (ξ_1^*, ζ_2^*) defined in (5.78) does exist for the given parameters even though the walking motion can be invalid in terms of ground reaction forces, ZMP range, etc. One benefit of dividing the optimization parameters into two groups lies in the convenience of creating the starting point for optimization. Since both the 3D biped and the planar biped use model parameters derived from the robot HRP-4, we can actually use the optimized parameters from the planar biped to form the starting point for optimizing the 3D biped. The details are illustrated in Figure 5.7. By directly using the optimized parameters of the planar biped as the sagittal parameters of the 3D biped and assigning constants in Figure 5.7 to the coronal parameters, we can obtain a starting point for the optimization program.

Another benefit of dividing the optimization parameters is that we can choose to optimize only the coronal parameters while using the optimized parameters from the planar biped as the sagittal parameters. In this way, there are only 16 parameters to optimize.

5.5 Results And Analysis

In this section, we start from analyzing the starting point formed by the method explained in Section 5.4.4. After that, two cases of optimization are given in detail:

3D Optimization Case I) Optimize only the 16 coronal parameters while using the optimized parameters of the 5-link planar biped as the sagittal parameters. Thus, the parameter vector ϑ is:

$$\vartheta = [\beta, x_p^-, z_p^-, x_{sw}^-, a_2^1, a_2^2, a_2^3, a_2^4, a_3^1, a_3^2, a_3^3, a_3^4, a_4^1, a_4^2, a_4^3, a_4^4]^\top \tag{5.124}$$

3D Optimization Case II) Optimize all the 32 parameters with the parameter vector ϑ being:

$$\vartheta = [\phi_P^\top, a_2^\top, a_3^\top, a_4^\top]^\top \tag{5.125}$$

5.5.1 Analysis of the Starting Point

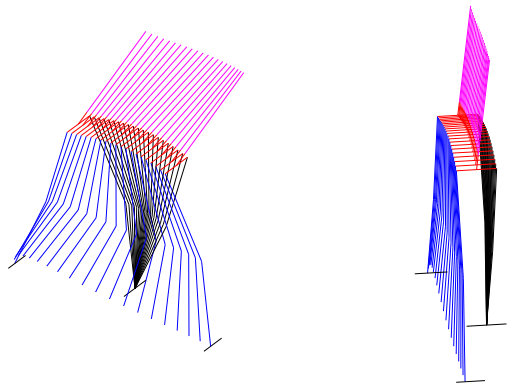

Fig. 5.8: The stick chart of the 3D biped by directly applying the optimized parameters of the planar biped walking at 1.5m/s.

By applying the starting point composed of coronal parameters given in Figure 5.7 and sagittal parameters equaling the optimized parameters of the 5-link planar biped walking at 1.5 m/s, we have, in Figure 5.8, the stick chart of the 8-link 3D biped of which the coronal motion is almost completely suppressed. In addition, we also have $\zeta_2^* = 1904$ (kgm^2/s)^2, $\delta_{zero}^2 = 0.610$, $V_{zero}(\theta^-) = -742.4$ (kgm^2/s)^2, $K = 192.1$ (kgm^2/s)^2. If we do not consider the contact condition of the stance foot, the walking motion generated by the starting point is exponentially stable since $0 < \delta_{zero}^2 < 1$ and $\delta_{zero}^2 V_{zero}(\theta^-)/(1-\delta_{zero}^2) + K = -1295 < 0$.

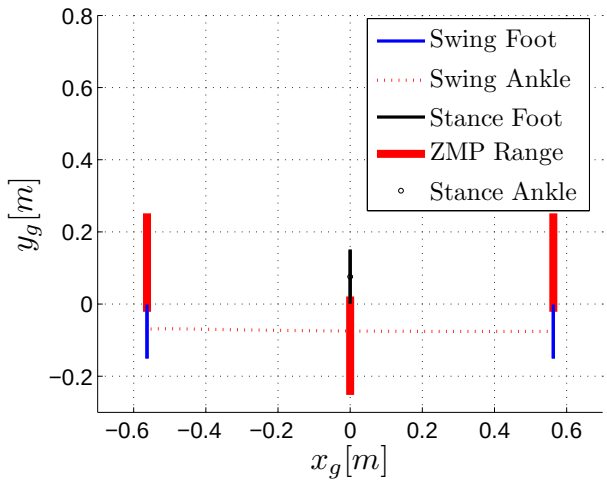

Fig. 5.9: The ZMP range of the 3D biped by directly applying the optimized parameters of the planar biped walking at 1.5m/s.

However, the walking motion thus generated is not practical since almost all the contact conditions of the stance foot are violated. The most obvious one is shown in Figure 5.9 where the required ZMP range is outside the range of the line segment of the stance foot. In addition, the energy cost of this walking motion is 4893 N^2ms, which is much larger than 3161 N^{2}ms in Figure 3.10 consumed by the corresponding planar biped.

5.5.2 3D Optimization Case I

For *3D Optimization Case I*, the sagittal parameters of the 3D biped are exactly the optimized parameters of the planar biped at respective speeds required by the speed constraint *CT9*. Thus the remaining parameters to be optimized are all coronal parameters. The stability can be analyzed similarly. For walking at $0.7m/s$, the evolution of zero dynamics is shown in Figure 5.10. In addition, we have $\zeta_2^* = 595.32$ $(\text{kgm}^2/\text{s})^2$, $\delta_{zero}^2 = 0.719$, $V_{zero}(\theta^-) = -167.6$ $(\text{kgm}^2/\text{s})^2$, $K = 202.9$ $(\text{kgm}^2/\text{s})^2$. Assuming the constraints are satisfied, the walking motion is exponentially stable since $0 < \delta_{zero}^2 < 1$ and $\delta_{zero}^2 V_{zero}(\theta^-)/(1-\delta_{zero}^2) + K = -224.8 < 0$. The stability of the remaining optimized gaits of the 3D biped can be validated in the same manner.

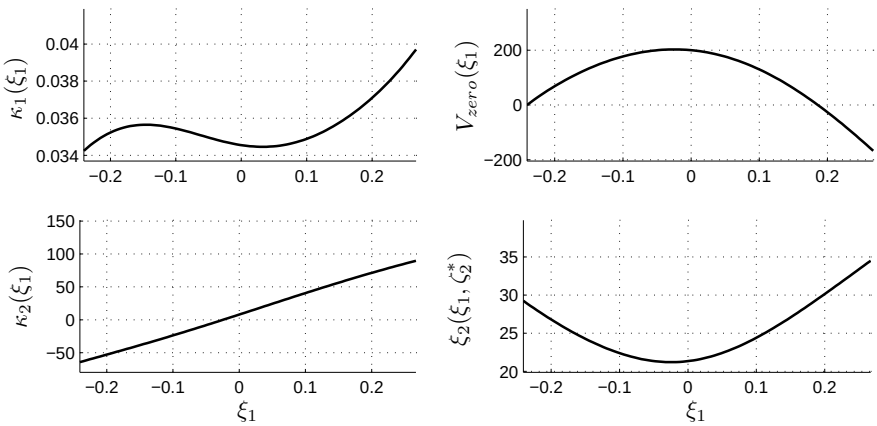

Fig. 5.10: The evolution of the zero dynamics of the 8-link 3D biped walking at $0.7m/s$ for *3D Optimization Case I*.

Ideally, one would expect that the sagittal motion and the coronal motion can be decoupled and this simplified optimization may as well provide energy efficient walking motions. However, the energy cost curves in Figure 5.11 seem disappointing. Compared with the energy cost of the planar biped in Figure 3.10, the energy cost of the 3D biped is much higher for low speeds. By combining the energy cost caused by u_3, u_4, u_8, u_9 as the sagittal energy cost and considering the remaining energy cost as the coronal energy cost, we might understand why optimizing only the coronal parameters is insufficient for obtaining energy efficient walking motions. From Figure 5.11, we can see that the sagittal cost in *3D Optimization Case I* is almost the same with the energy cost of the planar biped throughout the entire speed range while the coronal cost exhibit approximately quadratic growth as the speed decreases. Furthermore, the energy costs at low speeds from the actuators of the coronal DOF of the stance hip and the lumber joint are abnormally high, which means the 3D biped wastes much energy in supporting the pelvis and regulating ZMP while this could have been done more efficiently by exploiting the robot's natural dynamics in the coronal plane. This result also shows that the motions of 3D bipeds in the sagittal plane and the coronal plane are strongly coupled and that the decoupling methods that enforcing the ideal motions obtained from corresponding planar bipeds might no longer be energy efficient.

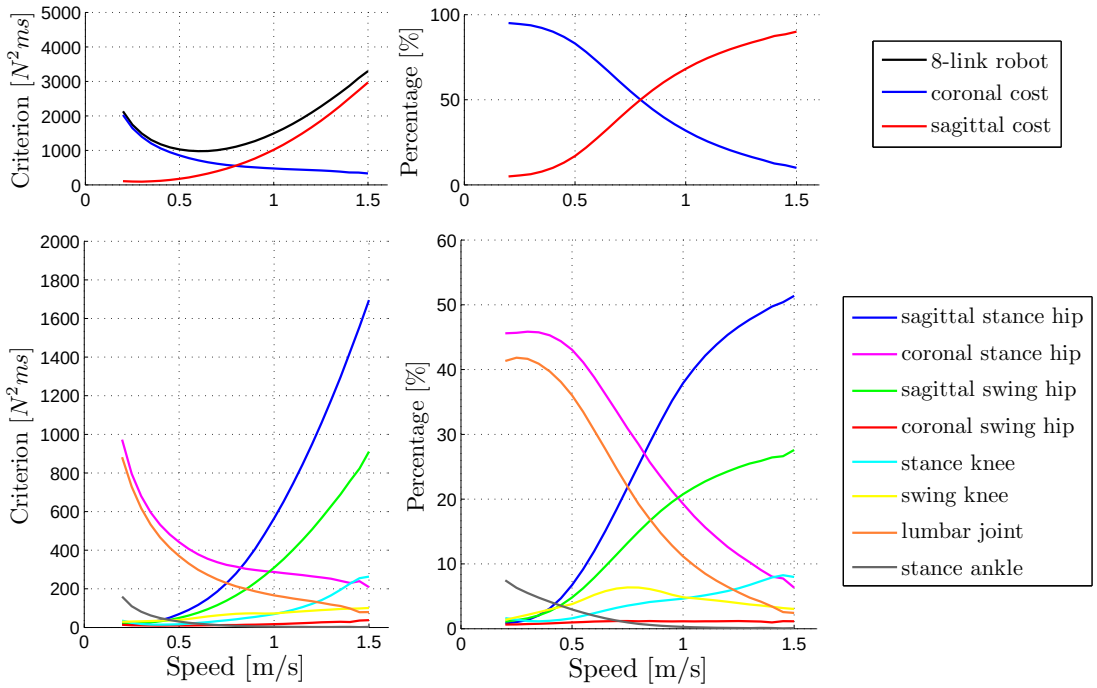

Fig. 5.11: The energy costs of the 8-link 3D biped and its actuators and the percentages of contribution at different speeds for *3D Optimization Case I*

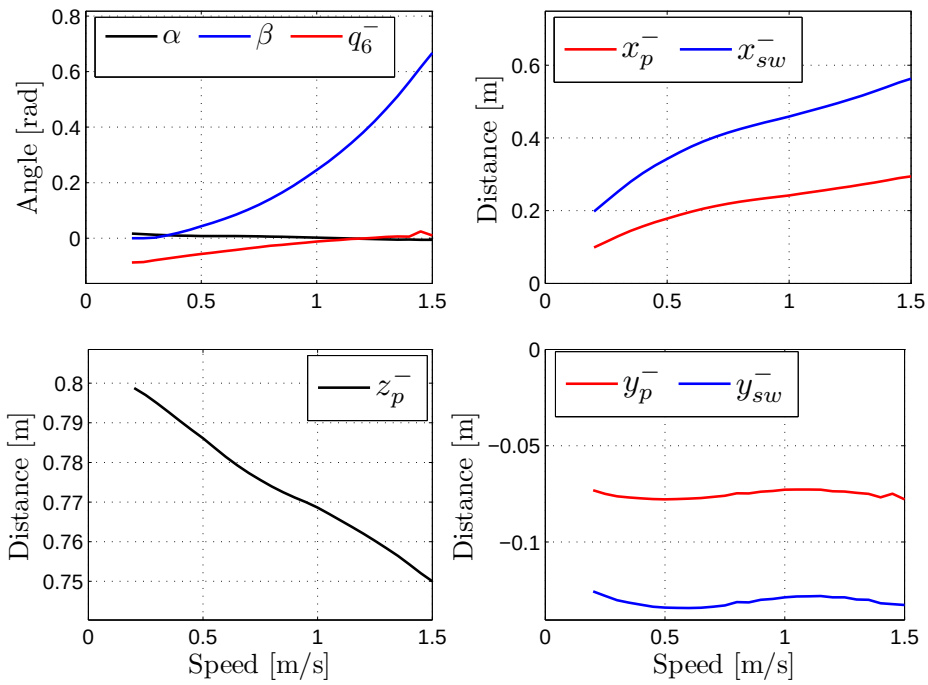

Fig. 5.12: The optimized posture parameters of the 8-link 3D biped at different speeds for *3D Optimization Case I* with the stance ankle being the origin and the sagittal parameters being the same with the parameters shown in Figure 3.11

The variation of posture parameters at different speeds is demonstrated in Figure 5.12, and we can see that the variation ranges of the coronal parameters y_p^-, y_{sw}^- and α are quite limited. This is due to the fact that the coronal posture parameters and the sagittal posture parameters are coupled, and fixing one of them will limit the variation range of the other. According to Figure 5.7, the sagittal parameter x_{sw}^- are exactly the optimized parameter x_{sw}^- of the 5-link planar biped and, because θ_d in the equation (5.109) is usually very small, the optimized step length d of the 3D biped in *3D Optimization Case I* at a given speed is then very close to the step length x_{sw}^- of the planar biped at the same speed. Accordingly, the evolution of step frequency and step duration in Figure 5.13 is almost the same with the one in Figure 3.12.

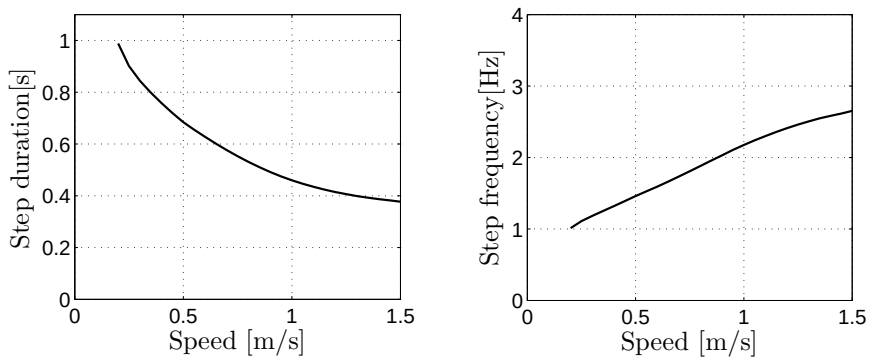

Fig. 5.13: The step duration and step frequency of the 8-link 3D biped at different speeds for *3D Optimization Case I*

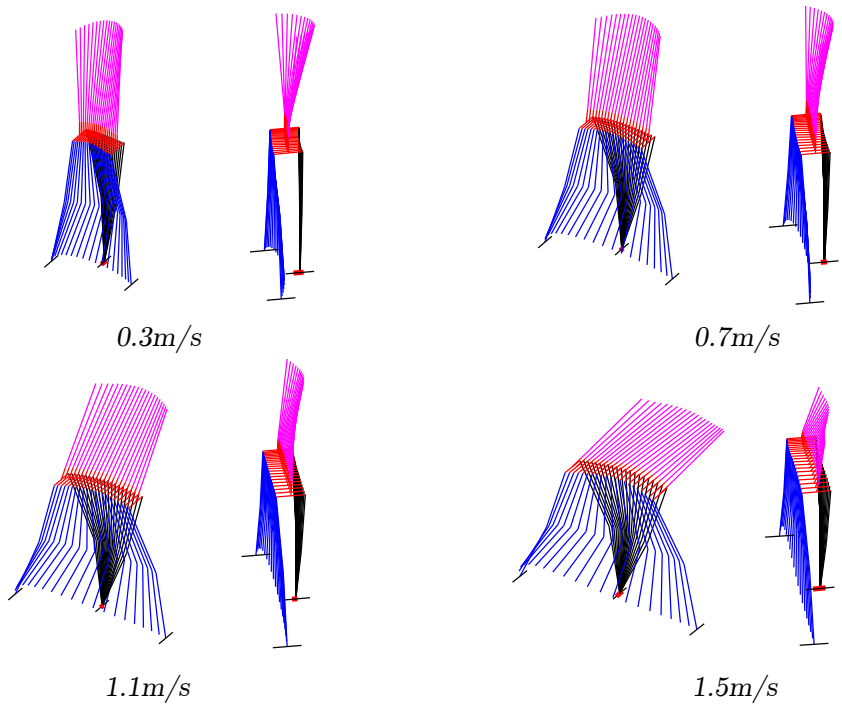

Fig. 5.14: The stick charts of the 8-link 3D biped walking at various speeds for *3D Optimization Case I*

The stick charts of the 3D biped walking at 0.3 m/s, 0.7 m/s, 1.1 m/s and 1.5 m/s are drawn in Figure 5.14. The predominant impression we can get from this figure is that the 3D biped seems to have large torso swings at low speeds. The detailed data of walking motions are illustrated respectively from Figures 5.15 to 5.21. By comparing Figure 3.14 and Figure 5.15, it is obvious that the evolution of all the sagittal angles and outputs of the 3D biped is very close to the evolution of corresponding angles and outputs of the planar biped. In addition, the sagittal trajectories of the COMs and the swing ankle of the 3D biped in Figures 5.20 and 5.21 are almost identical to the sagittal trajectories the COMs and the swing foot of the 5-link biped in Figures 3.19 and 3.20. It is interesting to note that in Figures 5.15 and 5.16 that the movements of the coronal hip joints described by q_5, $\dot{q}_5$, q_7, $\dot{q}_7$ are quite small compared with the movements of the other joints. According to Figure 5.18, the negative powers and the negative energy caused by the hip joint actuators cannot be neglected. As mentioned above, the walking trajectories generated here can satisfy the contact constraints defined by a comprehensive line foot contact model. This can be verified in Figure 5.19 using equations (5.45), (5.46), (5.50), (5.51) and (5.56). It is interesting to note that the range of p_{ZMP} in Figure 5.21 is much smaller than the size of the line foot and at $1.5m/s$ the margin left between $|F_{st}^y|_{max}$ and $|F_{st}^y|$ is almost zero. Therefore we can conclude that the purpose of having comparatively long line feet is mainly for restraining yaw movement.

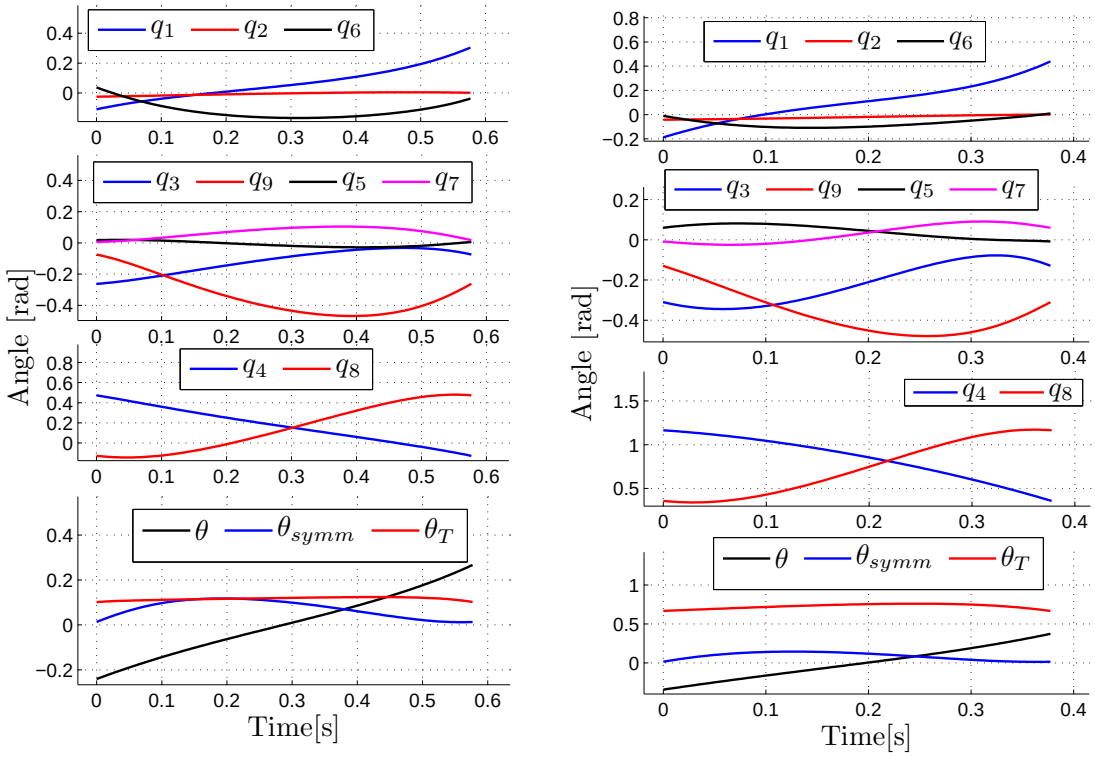

(a) **0.7** m/s (b) **1.5** m/s

Fig. 5.15: The angle charts of the joints and outputs of the 8-link 3D biped walking at 0.7 m/s and 1.5 m/s for *3D Optimization Case I*

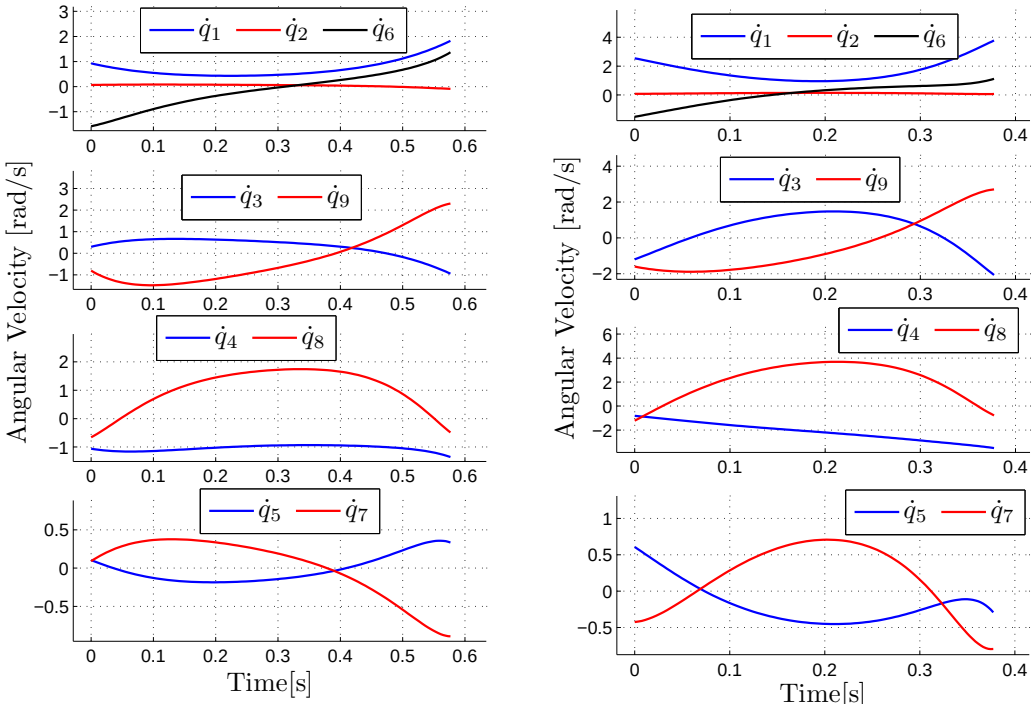

(a) **0.7 m/s** (b) **1.5 m/s**

Fig. 5.16: The angular velocity charts of the joints of the 8-link 3D biped walking at 0.7 m/s and 1.5 m/s for *3D Optimization Case I*

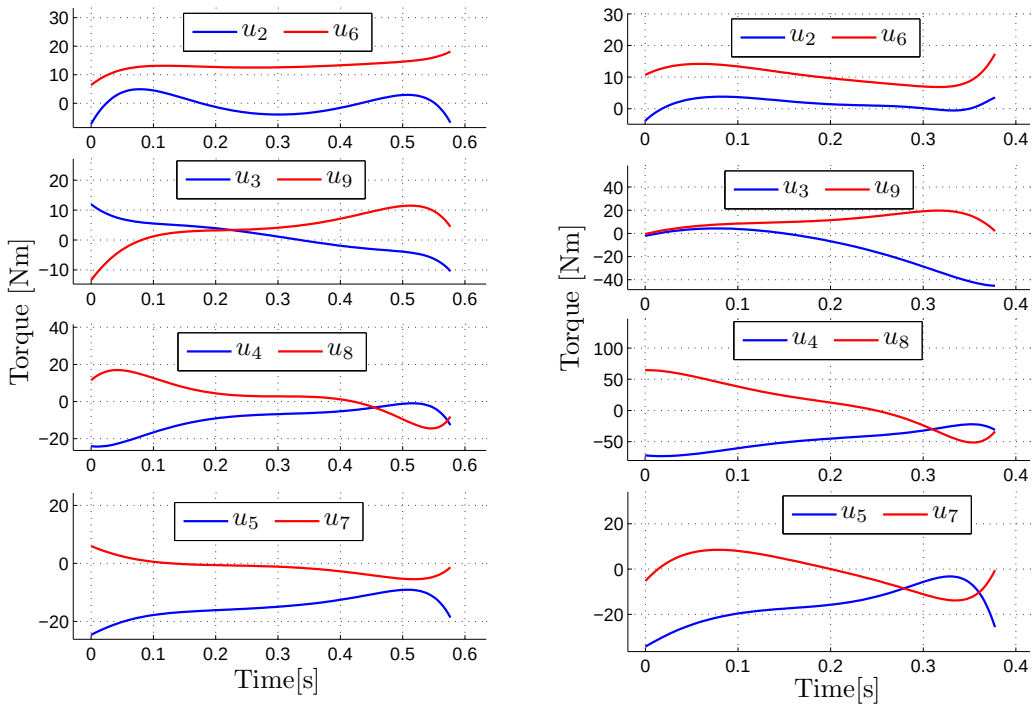

(a) **0.7 m/s** (b) **1.5 m/s**

Fig. 5.17: The torque charts of the actuators of the 8-link 3D biped walking at 0.7 m/s and 1.5 m/s for *3D Optimization Case I*

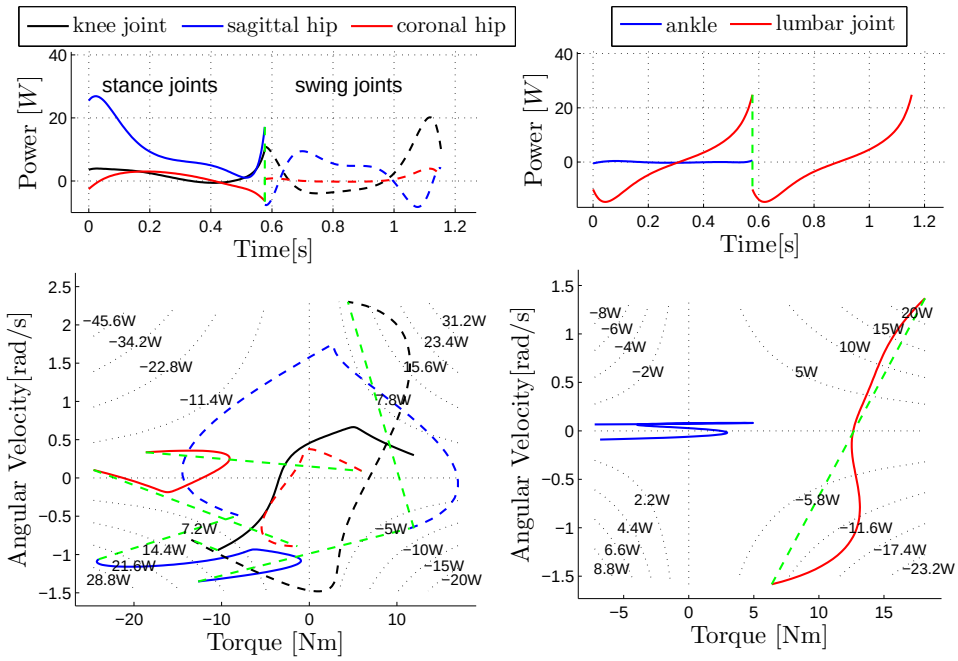

(a) **0.7m/s**

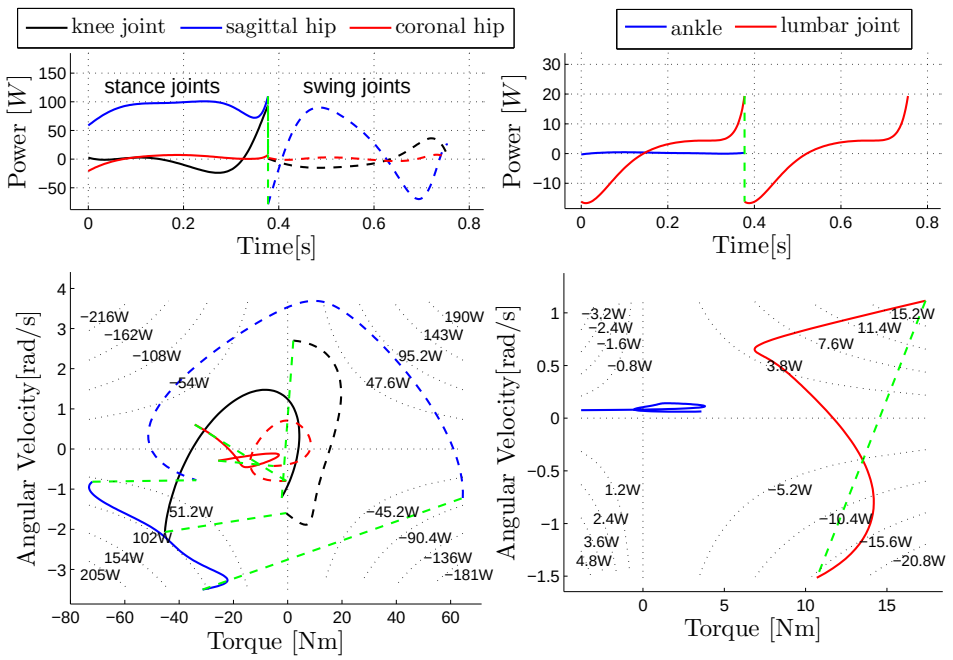

(b) **1.5m/s**

Fig. 5.18: The mechanical output powers of the actuators of the 8-link 3D biped walking at 0.7 m/s and 1.5 m/s (two steps) for *3D Optimization Case I* (Dashed lines represent swing joint angles, and green dashed lines represent the jumps caused by the impact. On the left side, solid lines represent stance joint angles.)

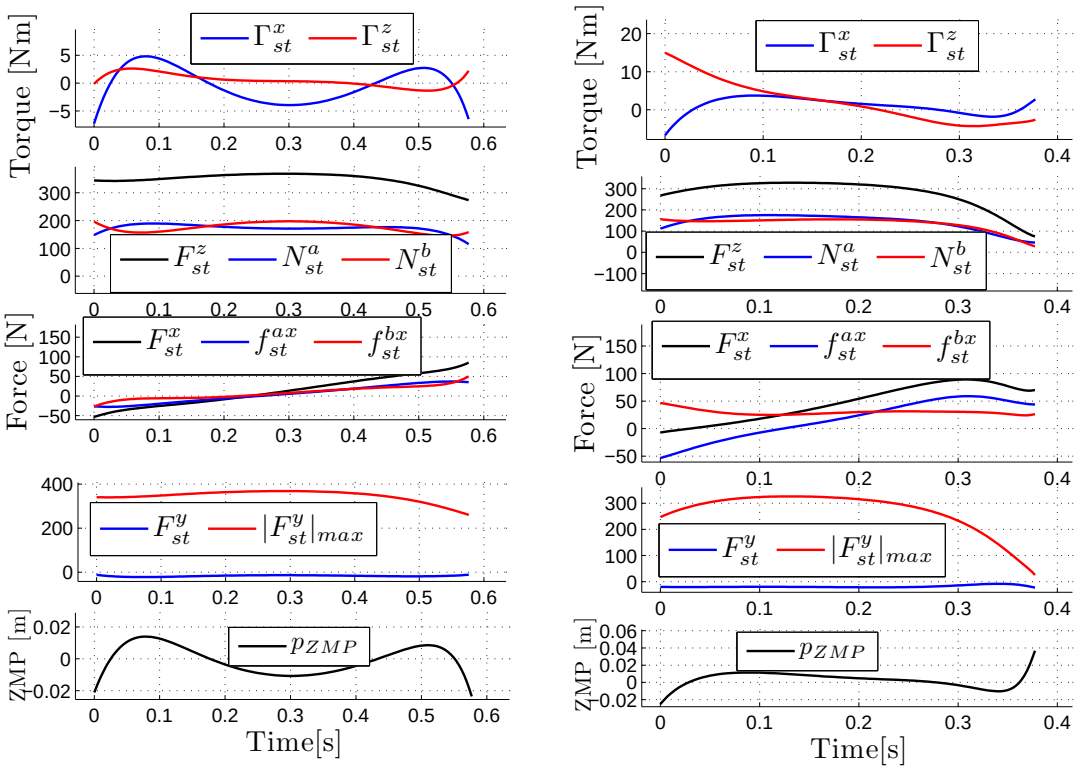

(a) **0.7 m/s** (b) **1.5 m/s**

Fig. 5.19: The ground reaction forces and torques of the 8-link 3D biped walking at 0.7 m/s and 1.5 m/s for *3D Optimization Case I*

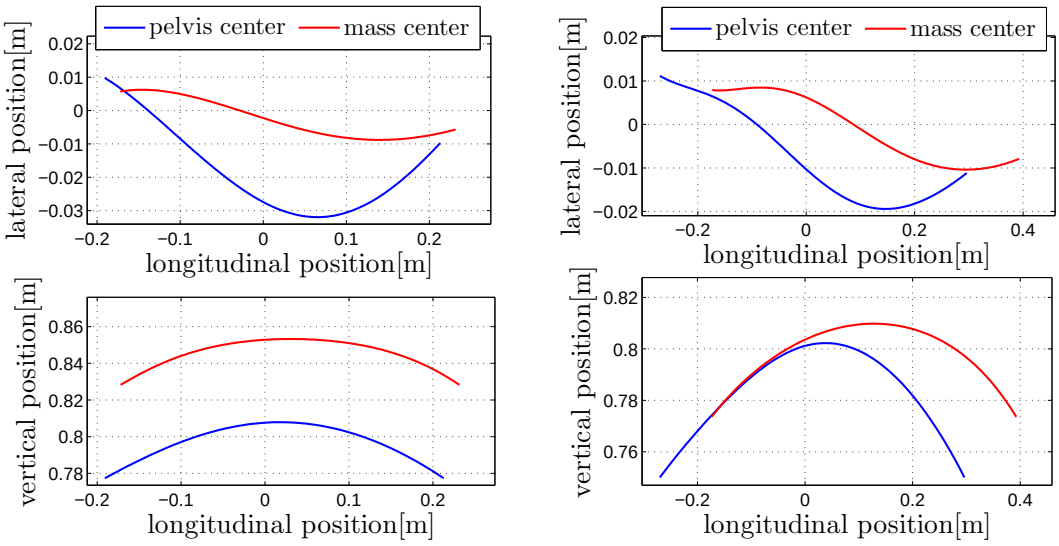

(a) **0.7 m/s** (b) **1.5 m/s**

Fig. 5.20: The trajectories of the pelvis center and the CoM of the 8-link 3D biped walking at 0.7 m/s and 1.5 m/s for *3D Optimization Case I*.

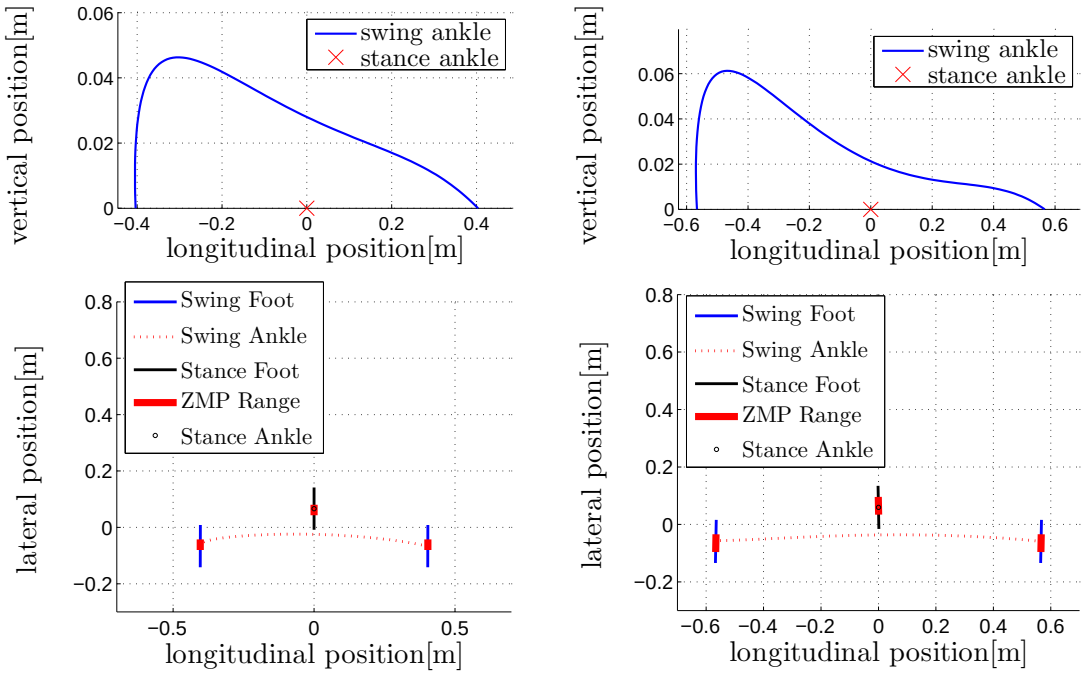

(a) **0.7** m/s (b) **1.5** m/s

Fig. 5.21: The trajectories of the swing ankle and the footprint of the 8-link 3D biped walking at 0.7 m/s and 1.5 m/s for *3D Optimization Case I*

5.5.3 *3D Optimization Case II*

For *3D Optimization Case II* , both the sagittal parameters and coronal parameters are optimized for obtaining energy efficient walking motions. The superiority of optimizing all the parameters is obvious. As demonstrated in Figure 5.22, the energy cost of the 3D biped at high speeds (3155 N^2ms at 1.5 m/s) in *3D Optimization Case II* is very close to the energy cost of the planar biped in Figure 3.10 (3161 N^2ms at 1.5 m/s). Although the energy cost of the 3D biped at low speeds (239 N^2ms at 0.3 m/s) is higher than the energy cost of the planar biped without couplings at the same speeds (52 N^2ms at 0.3 m/s), it is much lower than the value in *3D Optimization Case I* (1484 N^2ms at 0.3 m/s). Furthermore, when it comes to the sagittal energy cost, the value for the 3D biped at high speeds in *3D Optimization Case II* (2700 N^2ms at 1.5 m/s) is lower than the corresponding values for the same biped in *3D Optimization Case I* (2970 N^2ms at 1.5 m/s). This shows that the motions in the sagittal plane and the coronal plane are highly coupled, and by properly distributing energy cost in these two planes, a 3D bipedal robot can greatly reduce its energy consumption and lower the requirements of the actuators (such as peak torques). Despite the difference between two optimization cases, the percentages of the sagittal energy cost and the coronal energy cost at different speeds are very similar in Figures 5.11 and 5.22.

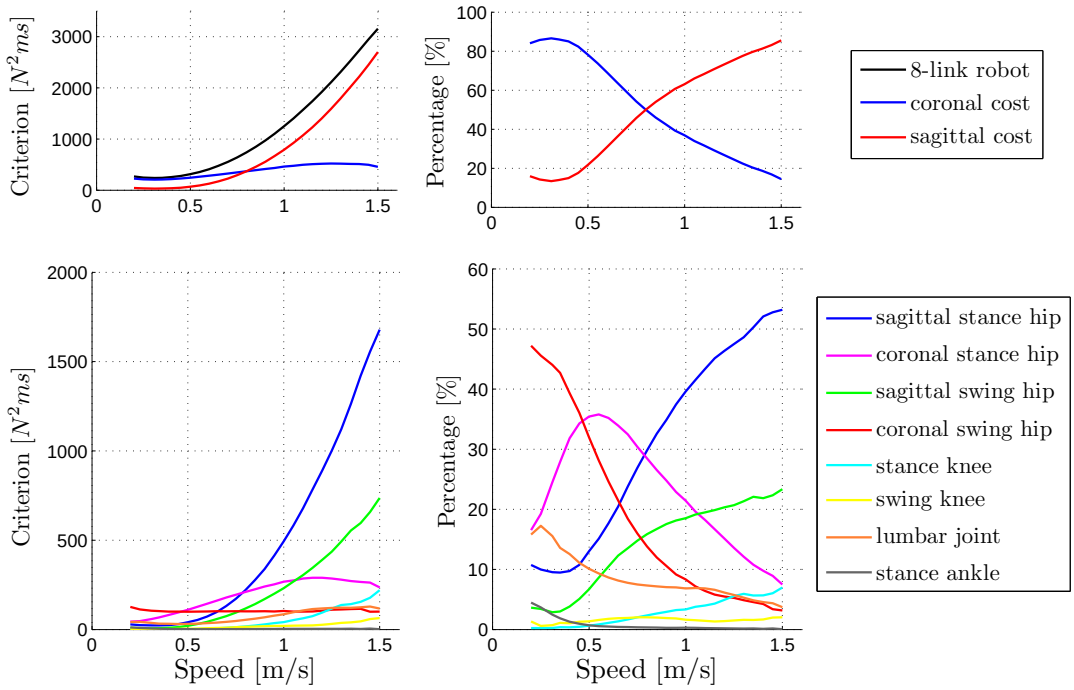

Fig. 5.22: The energy costs of the 8-link 3D biped and its actuators and the percentages of contribution at different speeds for *3D Optimization Case II*

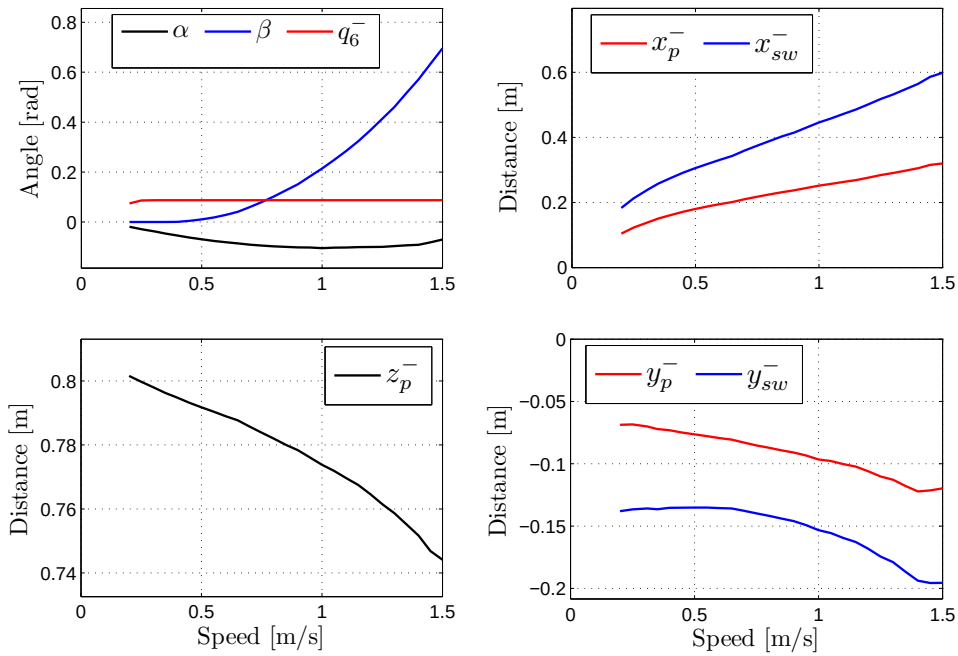

Fig. 5.23: The optimized posture parameters of the 8-link 3D biped at different speeds for *3D Optimization Case II* with the stance ankle being the origin.

The variation of the optimized posture parameters at different speeds is given in Figure 5.23, and it is interesting to note that the angle q_6^- of the lumbar joint at the end of each step is bounded by the upper-limit of the constraint *CT1* (i.e., $-\pi/36\,\text{rad} < q_6^- < \pi/36\,\text{rad}$). Comparing the step duration in Figures 5.24 and 3.12, we find that, at low speeds, the planar biped (without elastic couplings) obviously takes larger step than the 3D biped does. Besides, it is also worth mentioning that the lateral distance between the stance foot and the swing foot ankles at the end of each step has a positive correlation with the walking speeds, which seems awkward compared with the gaits of human beings at different speeds.

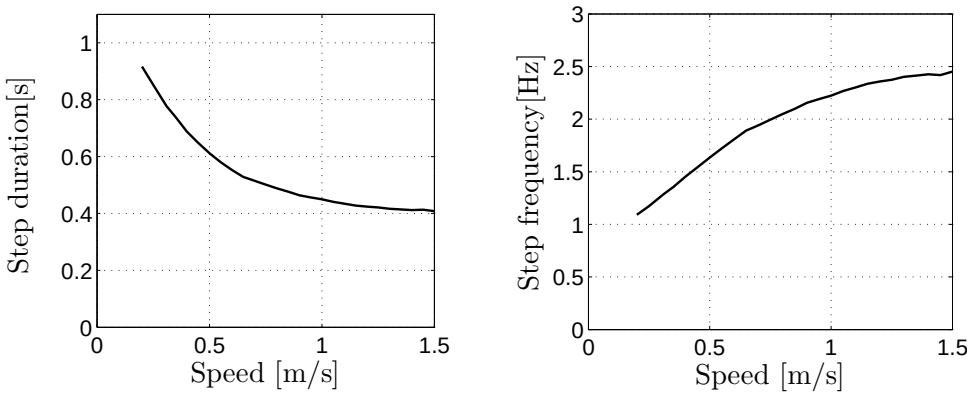

Fig. 5.24: The step duration and step frequency of the 8-link 3D biped at different speeds for *3D Optimization Case II*

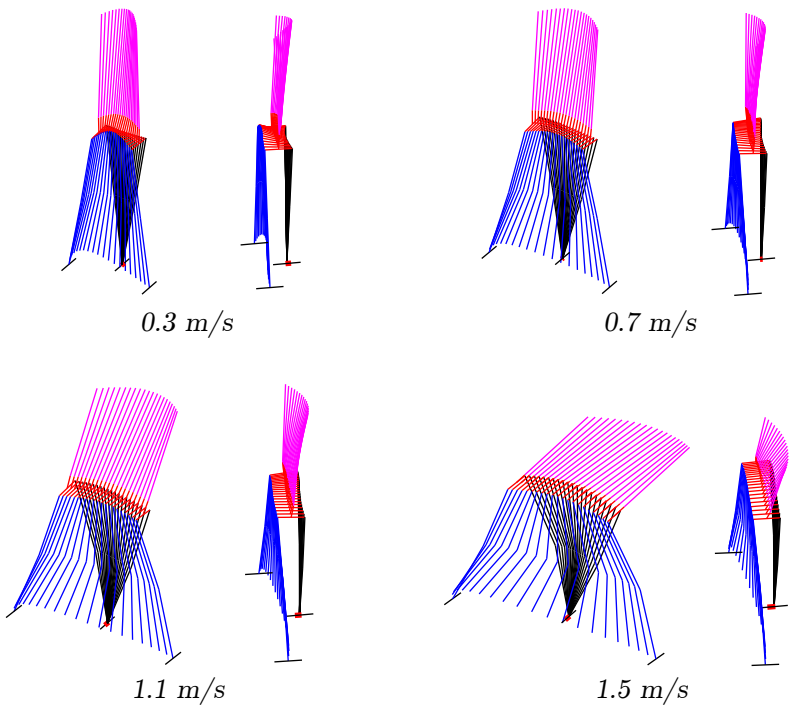

Fig. 5.25: The stick charts of the 8-link 3D biped walking at various speeds for *3D Optimization Case II*

The stick charts of the gaits of the 3D biped at 0.3 m/s, 0.7 m/s, 1.1 m/s and 1.5 m/s are drawn in Figure 5.25. Compared with Figure 5.14, the amplitude of the lateral movement of the torso is much smaller in Figure 5.25. The detailed data concerning the gaits at $0.7m/s$ and 1.5 m/s are illustrated respectively in Figures 5.26 to 5.32.

In Figures 5.15 and 5.26, we can see that the angle θ defined in (5.58) is almost a linear function of time. This indicate θ is a good replacement of time in synchronizing the movements of different joints. By comparison, at the walking speed 0.7 m/s, q_6 and $\dot{q}_6$, in Figures 5.26 and 5.27 seem to evolve in the opposite directions of the evolution of q_6 and $\dot{q}_6$ in Figures 5.15 and 5.16. In addition, the movements of the coronal hip joints in *3D Optimization Case II* described by q_5, $\dot{q}_5$, q_7 and $\dot{q}_7$ are much more obvious than those in *3D Optimization Case I* . This suggests that, in *3D Optimization Case II* , the 3D biped is capable of using proper movements of the coronal hip joints to avoid large movement of the torso and reduce energy cost.

By studying Figures 5.27, 5.28 and 5.29, we can find that, at 0.7 m/s, mechanical energy is mostly consumed by the coronal hip actuator on the stance leg, while at 1.5 m/s the sagittal hip actuator on the stance leg consumes most mechanical energy. In addition, the negative powers and the negative energy caused by the hip joint actuators cannot be neglected.

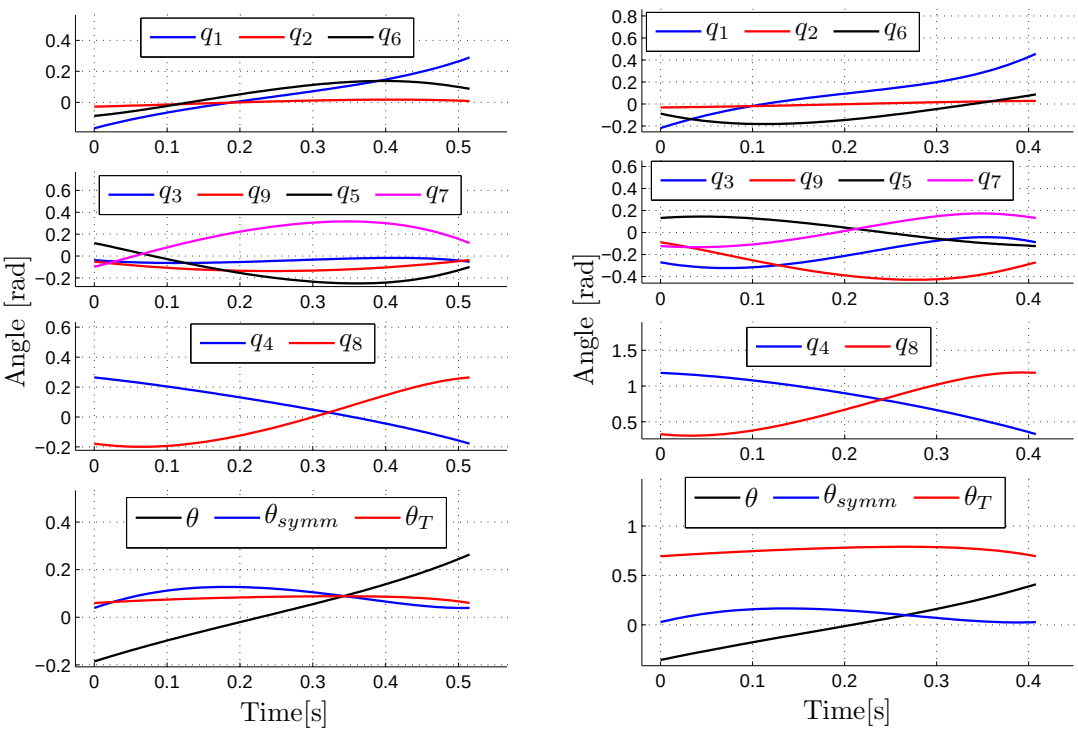

(a) **0.7** m/s (b) **1.5** m/s

Fig. 5.26: The angle charts of the joints and outputs of the 8-link 3D biped walking at 0.7 m/s and 1.5 m/s for *3D Optimization Case II*

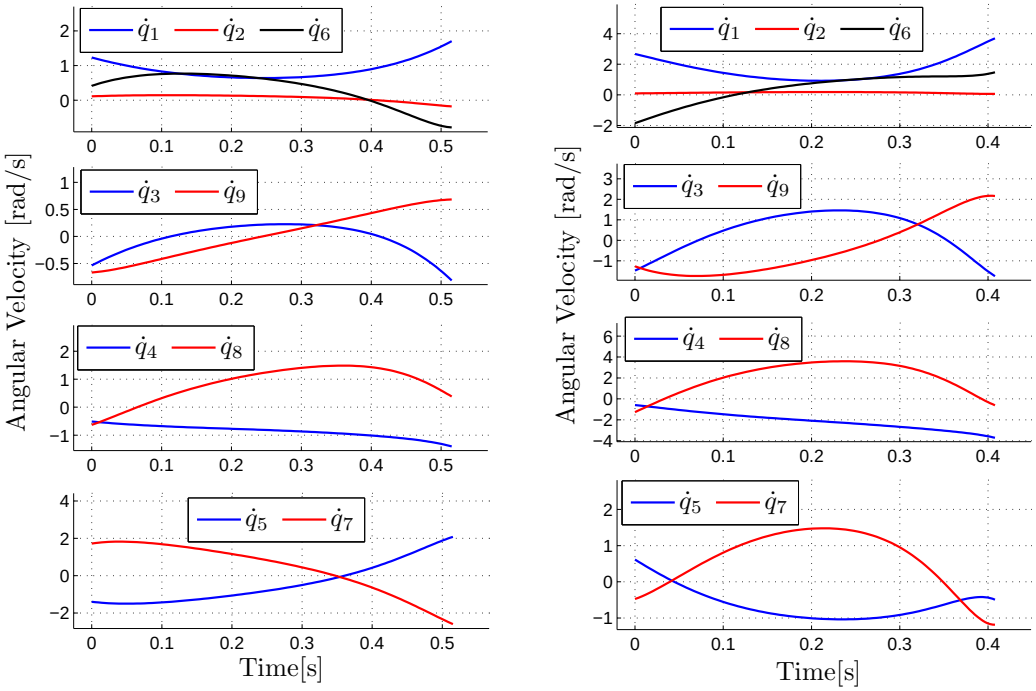

(a) **0.7** m/s (b) **1.5** m/s

Fig. 5.27: The angular velocity charts of the joints of the 8-link 3D biped walking at 0.7 m/s and 1.5 m/s for *3D Optimization Case II*

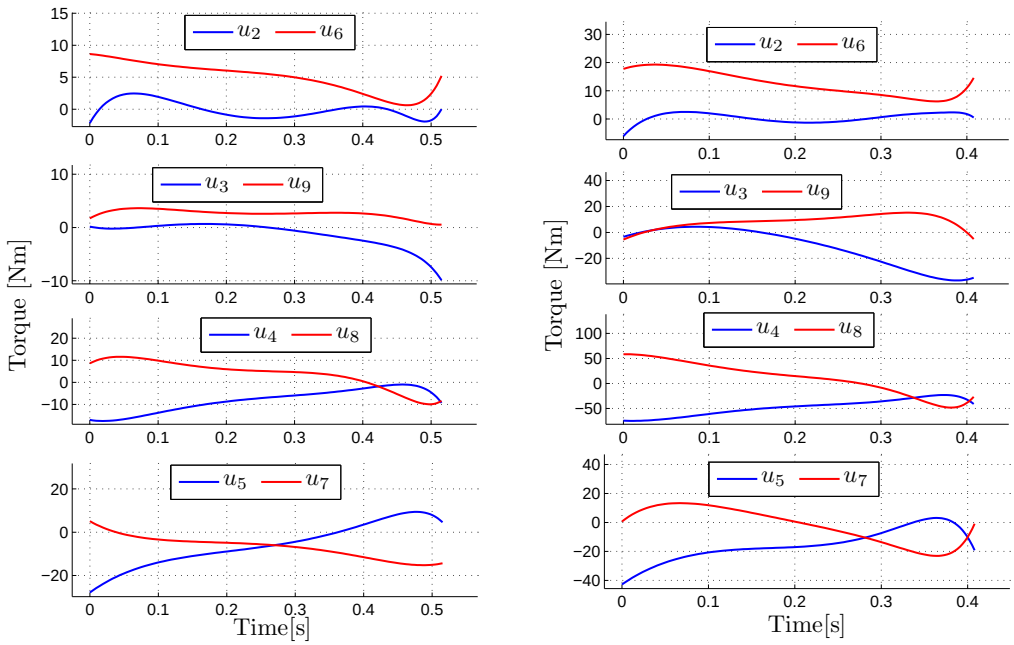

(a) **0.7** m/s (b) **1.5** m/s

Fig. 5.28: The torque charts of the actuators of the 8-link 3D biped walking at 0.7 m/s and 1.5 m/s for *3D Optimization Case II*

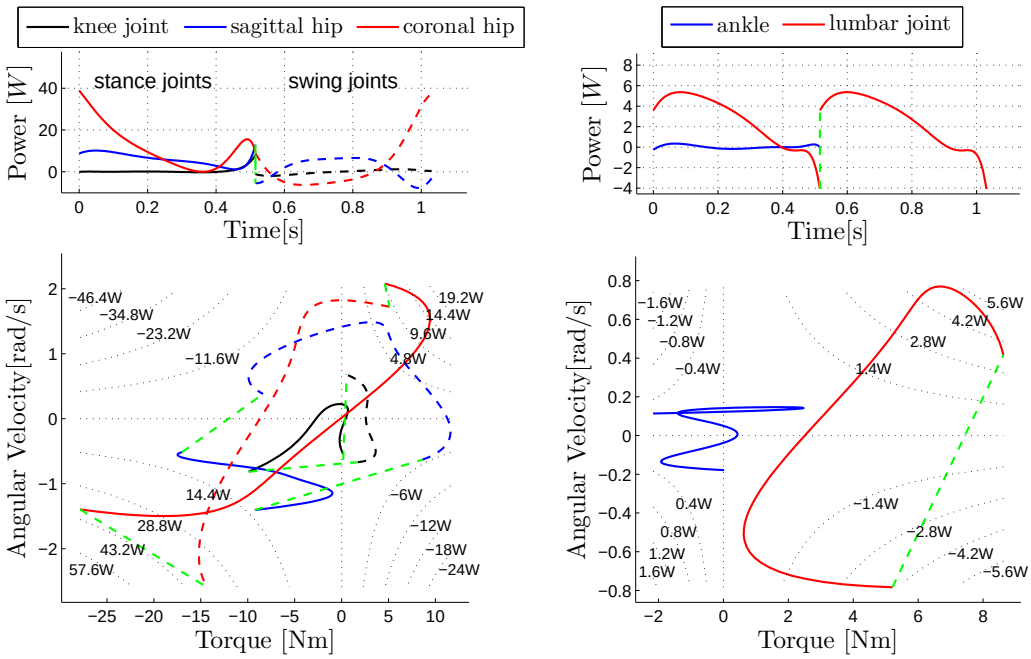

(a) **0.7** m/s

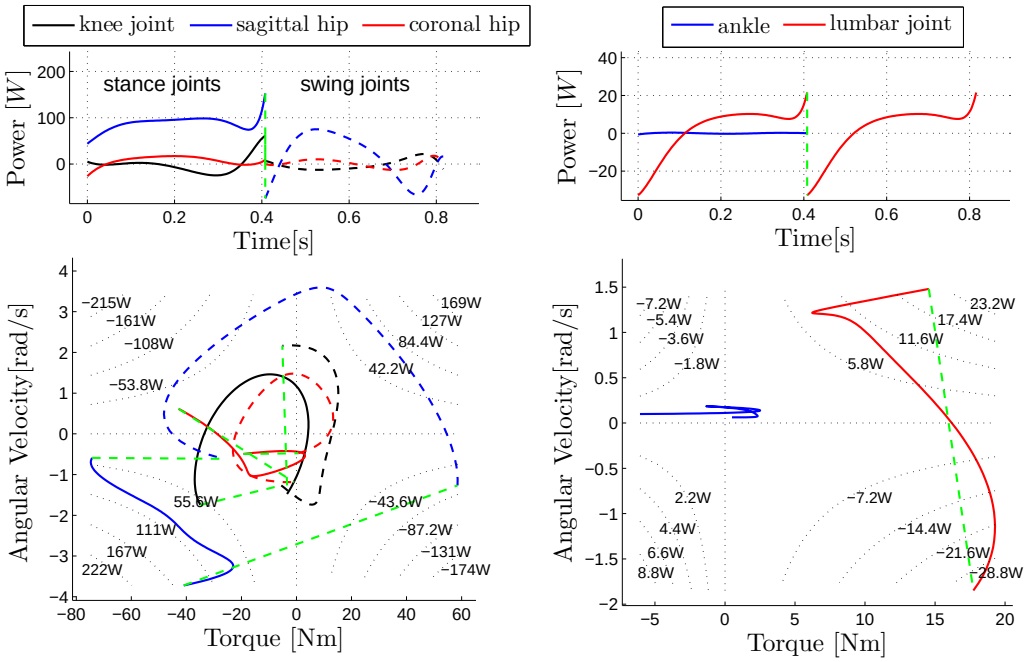

(b) **1.5** m/s

Fig. 5.29: The mechanical output powers of the actuators of the 8-link 3D biped walking at 0.7 m/s and 1.5 m/s (two steps) for *3D Optimization Case II* (Dashed lines represent swing joint angles, and green dashed lines represent the jumps caused by the impact. On the left side, solid lines represent stance joint angles.)

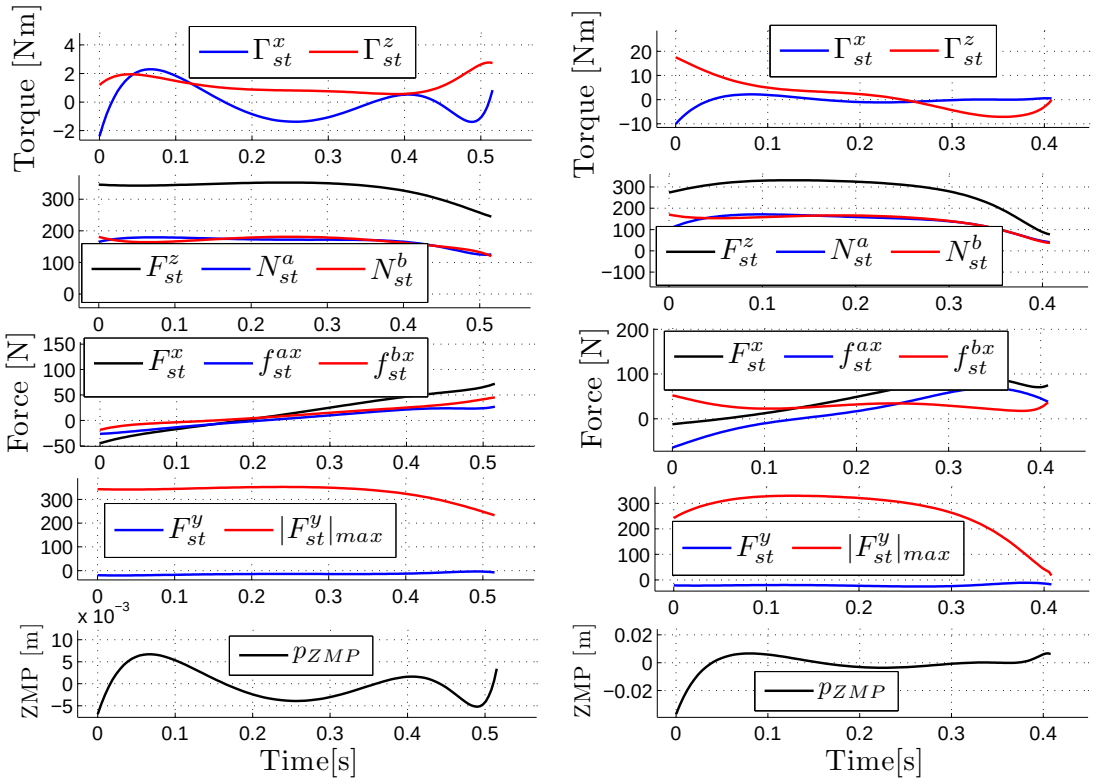

(a) **0.7** m/s (b) **1.5** m/s

Fig. 5.30: The ground reaction forces, torques and the ZMP curves of the 8-link 3D biped walking at 0.7 m/s and 1.5 m/s for *3D Optimization Case II*

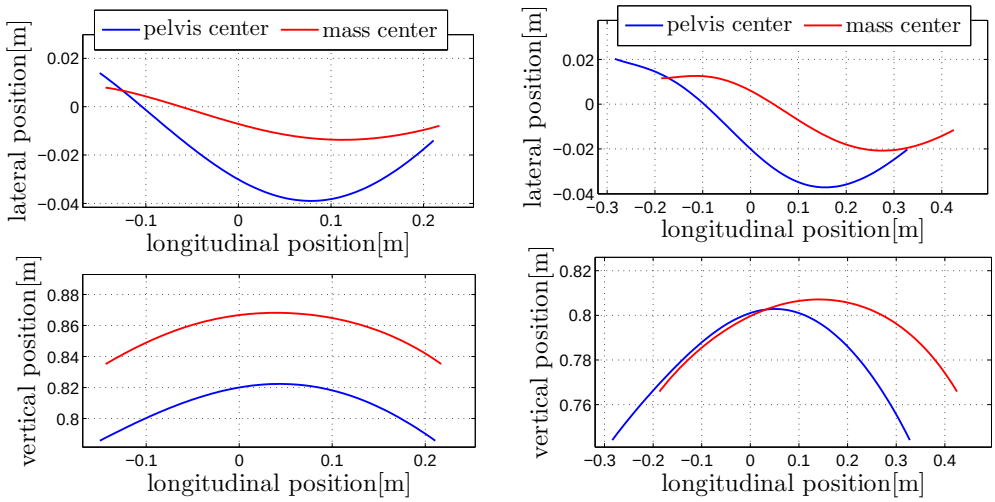

(a) **0.7** m/s (b) **1.5** m/s

Fig. 5.31: The trajectories of the pelvis center and the CoM of the 8-link 3D biped walking at 0.7 m/s and 1.5 m/s for *3D Optimization Case II*

The ground contact of the gaits can be verified in Figure 5.30. It is interesting to note that the range of p_{ZMP} in (5.32) is much smaller than the size of the line foot and at 1.5 m/s the margin left between $|F^y_{st}|_{max}$ and $|F^y_{st}|$ is almost zero.

The trajectories of the CoM and pelvis center of the 3D biped are depicted in

Figure 5.31. By comparing Figure 5.31 with Figure 5.20 for *3D Optimization Case I*, we find that the lateral movements of the pelvis center and CoM in *3D Optimization Case II* is much larger. The trajectories of the swing ankle and the foot prints of the 3D biped are provided in Figure 5.32. The foot clearance for both speeds is above 5 cm, which is comparatively large compared with the 1.3 cm average maximum toe clearance of human beings [181].

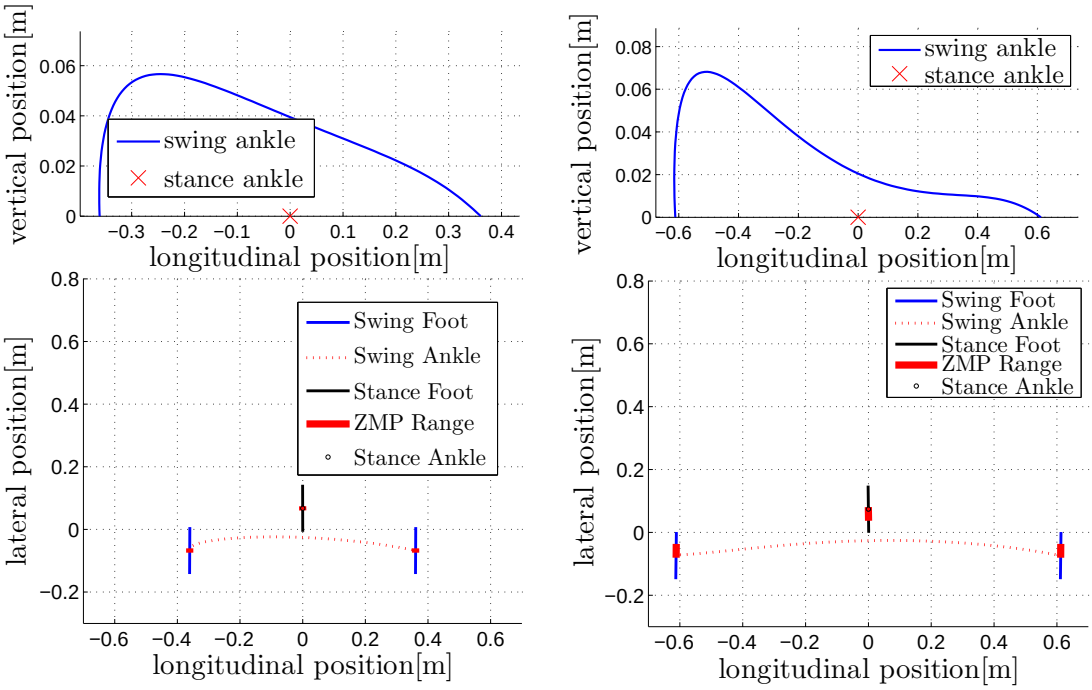

(a) **0.7** m/s (b) **1.5** m/s

Fig. 5.32: The trajectories of the swing ankle and the footprint of the 8-link 3D biped walking at 0.7 m/s and 1.5 m/s for *3D Optimization Case II*

5.6 Conclusion

In this chapter, we have extended the application range of the method of applying feedback linearization and achieving hybrid invariance in [8] for planar bipeds to tackle the problem of 3D bipedal walking. An 8-link 3D planar biped derived from HRP-4 [172] with a torso, two thighs, two shins and two massless line feet is used as an example to demonstrate the corresponding methods of modeling, controlling and optimizing. Like the 5-link planar biped in Chapter 3, the dynamic model of the 3D biped is also composed of an impact model and a swing phase model to form a hybrid model. In particular, we have developed a line-foot contact model to ensure validity of the swing phase model and a line-foot impact model to realize instantaneous status transition at the impact.

During the swing phase, the method of feedback linearization is adopted to apply virtual constraints defined by "Symmetry Output" in Chapter 3. By adopting the line foot configuration with one degree of underactuation, we can achieve hybrid

invariance in closed form and perform the stability analysis on a scalar LTI return map as in the case of the planar biped in Chapter 3.

The ideal evolution of the virtual constraints are parameterized by Bézier polynomials of order 5 as functions of the normalized value of the linearized absolute angle of the virtual stance leg. In addition we have replace some of the Bézier parameters with posture parameters to facilitate the geometric interpretation of walking gaits. A inverse dynamic model is provided to create a mapping between the posture parameters and Bézier parameters. The optimization parameters are further divided into coronal parameters and sagittal parameters, and the optimized parameters from the planar biped are used as the starting point for the optimization of the 3D biped. The objective function and optimization constraints are similarly defined as in the case of the planar biped. Particularly, the optimization constraints include the constraint from the line-foot contact model to prevent yaw movement and a constraint to avoid interference of two legs. Thereafter, the optimization is performed following the same procedures in Chapter 3.

There are two optimization cases discussed in this chapter, namely *3D Optimization Case I* and *3D Optimization Case II* . In 3D Optimization Case I, we optimize only the 16 coronal parameters and use the optimized parameters from the 5-link planar biped as the sagittal parameters. In *3D Optimization Case II* , we optimize all the 32 parameters. By comparing these two cases, we find that optimizing only the coronal parameters is only comparatively effective at high speeds while optimizing all the parameters can provide gaits with similar energy cost to the planar biped (without elastic couplings) at the entire speed range with the minimum energy cost being $238\,\mathrm{N^2ms}$ at $0.3\,\mathrm{m/s}$ and the maximum energy cost being $3155\,\mathrm{N^2ms}$ at $1.5\,\mathrm{m/s}$.

6. ELASTIC COUPLINGS FOR UNDERACTUATED 3D BIPEDAL ROBOTS

The work presented in this chapter focuses on exploring the superiority of adding elastic couplings (in form of hip joint springs) to 3D bipeds using gait optimization. As in the case of the planar biped in Chapter 4, this is realized by adding spring constants to the optimization parameters and searching optimal gaits at different speeds with minimal energy cost. There are three coupling cases discussed in this chapter, namely, *3D Coupling Case I*, *II* and *III*. In *3D Coupling Case I*, a torsion spring is added to connect the movements of two thighs in the sagittal plane. In *3D Coupling Case II*, two torsion springs are used to build connections between the movements of two thighs and the movement of the pelvis in the coronal plane. In *3D Coupling Case III*, the ideas of the first two cases are combined, and three torsion springs are installed in both the sagittal plane and the coronal plane. The results of gait optimization indicate that, compared with the hip joint springs in the coronal plane, the hip joint spring in the sagittal plane plays a much more important role in saving energy, but the best option is to add springs in both the sagittal plane and the coronal plane.

This chapter proceeds as follows. Section 6.1 deals with the modeling of elastic couplings. Section 6.2 provides detailed results concerning three different configurations of hip joint springs. Section 6.3 provides a short discussion comparing the three coupling cases. Finally, a conclusion is given in Section 6.4.

6.1 Modeling of Elastic Couplings

Since elastic components cannot produce impulses during the impact, they have no influence on the 8-link 3D biped's impact model. As for the swing phase model, the equation (5.5) can now be written as:

$$D(q)\ddot{q} + C(q,\dot{q}) + G(q) = B(u + \tau_e(q)) \tag{6.1}$$

where $\tau_e = [\tau_{e2}, \tau_{e3}, \tau_{e4}, \tau_{e5}, \tau_{e6}, \tau_{e7}, \tau_{e8}, \tau_{e9}]^\top$ is the torque vector generated by elastic couplings. The torques of each actuator for a cyclic gait on the zero dynamic surface is obtained by subtracting τ_e from (5.63):

$$u^*(x) = -(L_g L_f h(x))^{-1} L_f^2 h(x) - \tau_e(x) \tag{6.2}$$

We can see in Figure 5.22 that, in the case where no elastic coupling is available, the dominant part of the energy cost of the 8-link 3D biped is caused by the coronal hip joint actuators at low speeds and by the sagittal hip joint actuators at high

speeds. As such, it would be interesting to add elastic couplings to these hip joints, and we propose three elastic coupling cases for our 3D bipedal robot in Figure 5.2:

3D Coupling Case I) As illustrated in Figure 6.1(a), a linear torsion spring is mounted in the sagittal plane to build a connection between two thighs with the deflection $\varphi_{e1} - \varphi_{e1}^*$ in (2.11) given by $\varphi_{e1} = q_4 - q_8$ and $\varphi_{e1}^* = 0$ (because of the symmetry of the 3D biped). Replacing k_{e1} in (2.18) with optimized stiffness k_{opt1}, the torque vector τ_e of the sagittal hip joint spring is then given by:

$$\tau_e(q) = [0, 0, -k_{opt1}(q_4 - q_8), 0, 0, 0, -k_{opt1}(q_8 - q_4), 0]^\top \tag{6.3}$$

3D Coupling Case II) As illustrated in Figure 6.1(b), two linear torsion springs are mounted in the coronal plane connecting the two thighs respectively to the pelvis. Accordingly, we have $\varphi_{e2} = q_5$ and $\varphi_{e3} = q_7$ for the deflections $\varphi_{e2} - \varphi_{e2}^*$ and $\varphi_{e3} - \varphi_{e3}^*$ in (2.11) of these two springs. Because of the symmetry of the 8-link 3D biped, the stiffness of these two springs must be the same, namely, $k_{e2} = k_{e3}$. Out of consideration for reducing the number of optimization parameters, we further assume that the release positions for these two springs are zero, i.e., $\varphi_{e2}^* = \varphi_{e3}^* = 0$. Replacing k_{e2} and k_{e3} with optimized stiffness k_{opt2} and using (2.18), the torque vector τ_e is then given by:

$$\tau_e(q) = [0, 0, 0, -k_{opt2}\, q_5, 0, -k_{opt2}\, q_7, 0, 0]^\top \tag{6.4}$$

3D Coupling Case III) In this case, a torsion spring is added in the sagittal plane in the same way as for *3D Coupling Case I*, and two linear torsion springs are added in the coronal plane in the same way as for *3D Coupling Case II*. Using (2.18), the torque vector τ_e is given by:

$$\begin{aligned}\tau_e(q) =& [0, 0, -k_{opt1}(q_4 - q_8), -k_{opt2}\, q_5, \\ & 0, -k_{opt2}\, q_7, -k_{opt1}(q_8 - q_4), 0]^\top\end{aligned} \tag{6.5}$$

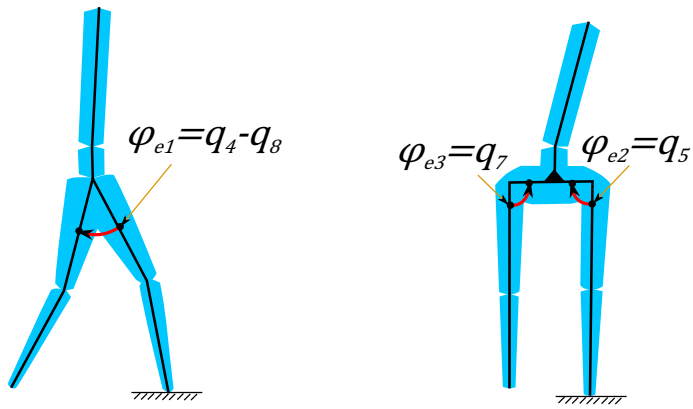

(a) Coupling Case I (b) Coupling Case II

Fig. 6.1: Coupling cases of the 8-link 3D biped

6.2 Optimal Walking with Elastic Couplings

6.2.1 3D Coupling Case I

According to the cost curves shown in Figure 6.2, the energy cost of the entire 8-link bipedal robot is greatly reduced for speeds ranging from 0.6 m/s to 1.5 m/s compared with the overall energy cost in Figure 5.22 without elastic couplings. For a wide range of speeds from 0.35 m/s to 1.0 m/s the energy cost is around 200 N^2ms. At 1.5 m/s, the overall energy cost is 475 N^2ms while the corresponding value without elastic couplings is 3155 N^2ms in *3D Optimization Case II* of Chapter 5. Despite the obvious improvement in energy efficiency at high speeds, there is few improvement for the energy cost at low speeds. At the lowest speed, the coronal cost (the energy cost of the joint actuators in the coronal plane) is very close to the overall cost and the sagittal cost is almost negligible.

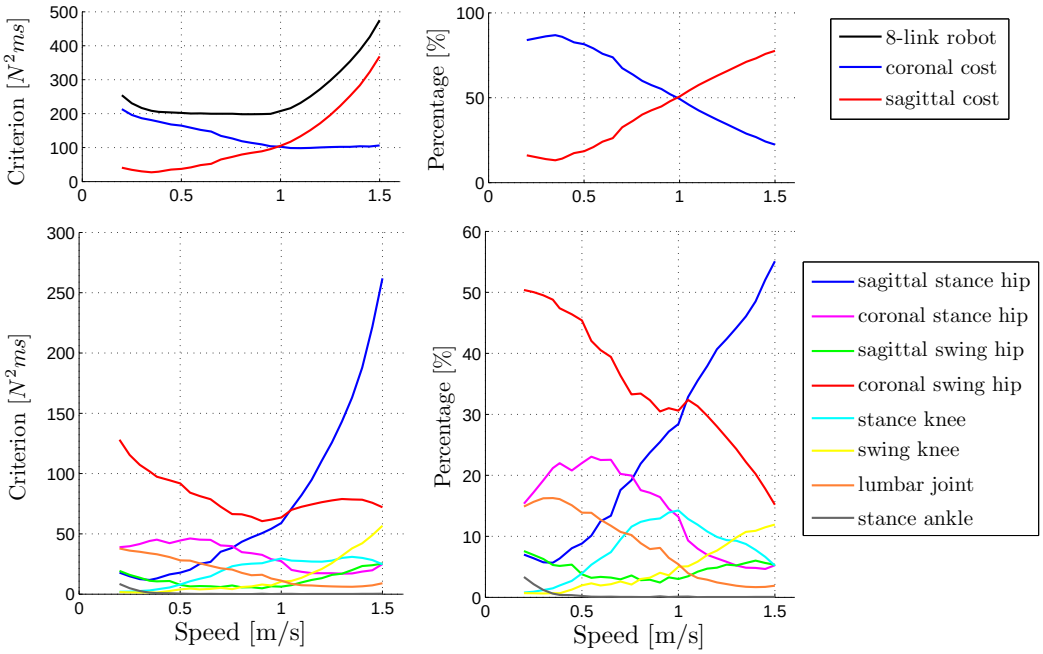

Fig. 6.2: The energy costs and percentages of contribution of the 8-link 3D biped and its actuators at different speeds for *3D Coupling Case I*

The evolution of the posture parameters (defined in Figure 5.5) at different speeds is provided in Figure 6.3. Compared with Figures 4.7 and 4.8, the variations of the optimized posture parameters and actuator energy costs for the 3D biped is not as smooth as those for the planar biped. This indicates that the results so far obtained for our 3D biped are sub-optimal, which is quite normal for gait optimization of 3D bipeds [114, 123]. However, it is still possible to see the general tendency of these variations without using any interpolations. In comparison with the gaits in Figure 5.25 for *3D Optimization Case II* where elastic couplings are absent, the gaits for *3D Coupling Case I* is featured with smaller steps and more upright torso positions. These phenomenons can be verified in Figures 6.3 and 6.5. As for the spring stiffness k_{opt1}, we can see in Figure 6.4 that k_{opt1} has a positive correlation with the walking

speed, but it does seem to reach a saturation point at high speeds. The most likely explanation for the saturation is the limited margins left for remaining ground contact at high speeds (Figure 6.21).

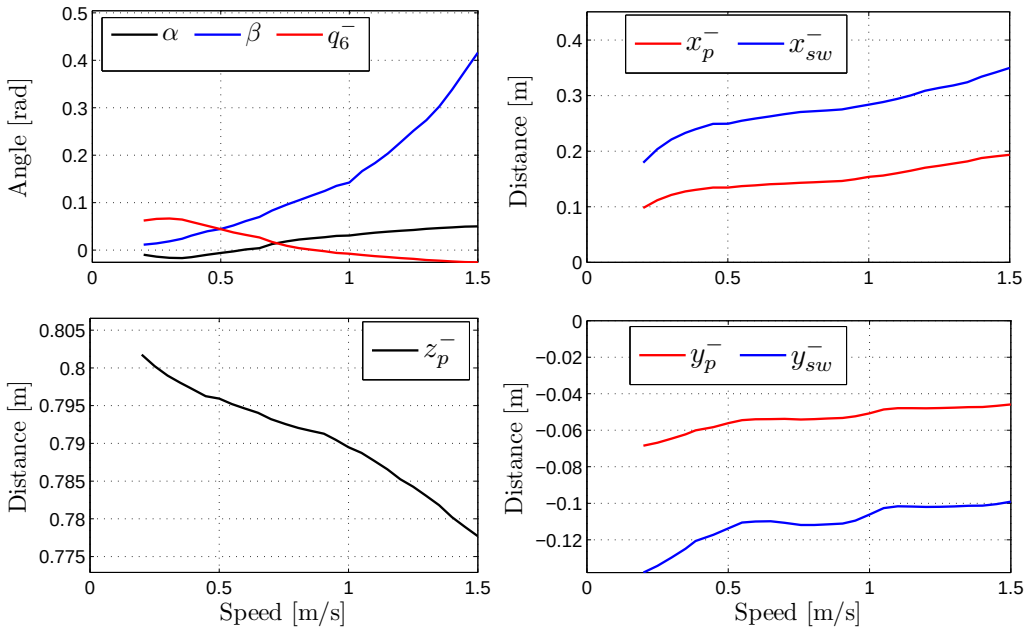

Fig. 6.3: The optimized posture parameters of the 8-link 3D biped at different speeds for *3D Coupling Case I* with the stance ankle being the origin.

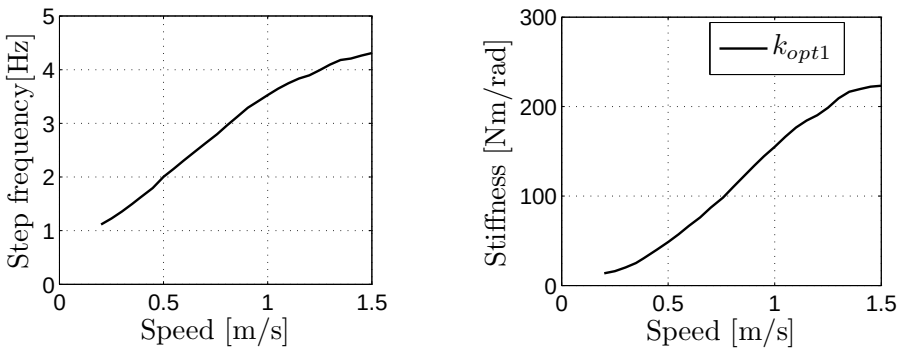

Fig. 6.4: The step frequency and the spring stiffness of the 8-link 3D biped at different speeds for *3D Coupling Case I*.

The stick charts of the 3D biped walking at 0.3 m/s, 0.7 m/s, 1.1 m/s, and 1.5 m/s is depicted in Figure 6.5, and the detailed information is provided from Figures 6.6 to 6.12. Apart from having more upright gaits than the 3D biped with no coupling in Figure 5.25 of *3D Optimization Case II*, the 3D biped in *3D Coupling Case I* also has a smaller lateral movement of the torso and the CoM, which can be equally verified by comparing Figures 6.6, 6.7 and 6.11 with Figures 5.26, 5.27 and 5.31. In addition, the lateral distance between the stance foot and the swing foot are also shorter at high speeds compared with *3D Optimization Case II*.

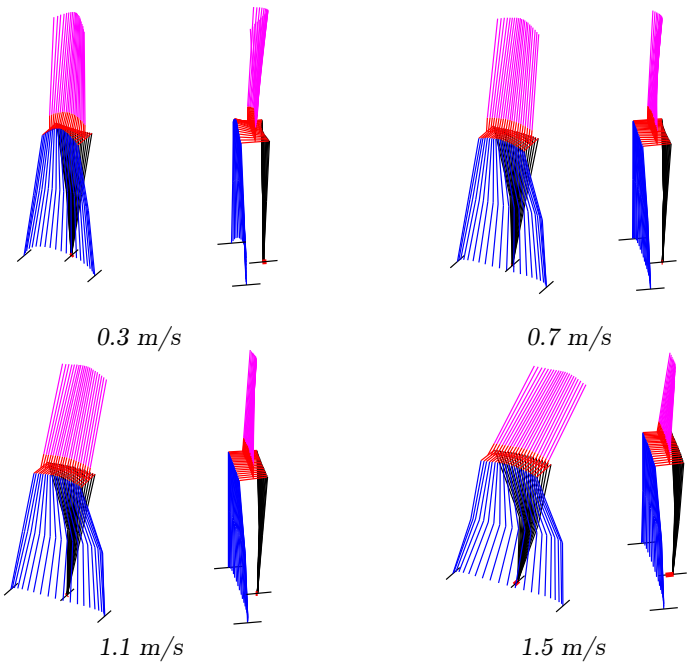

Fig. 6.5: The stick charts of the 8-link 3D biped walking at various speeds for *3D Coupling Case I*

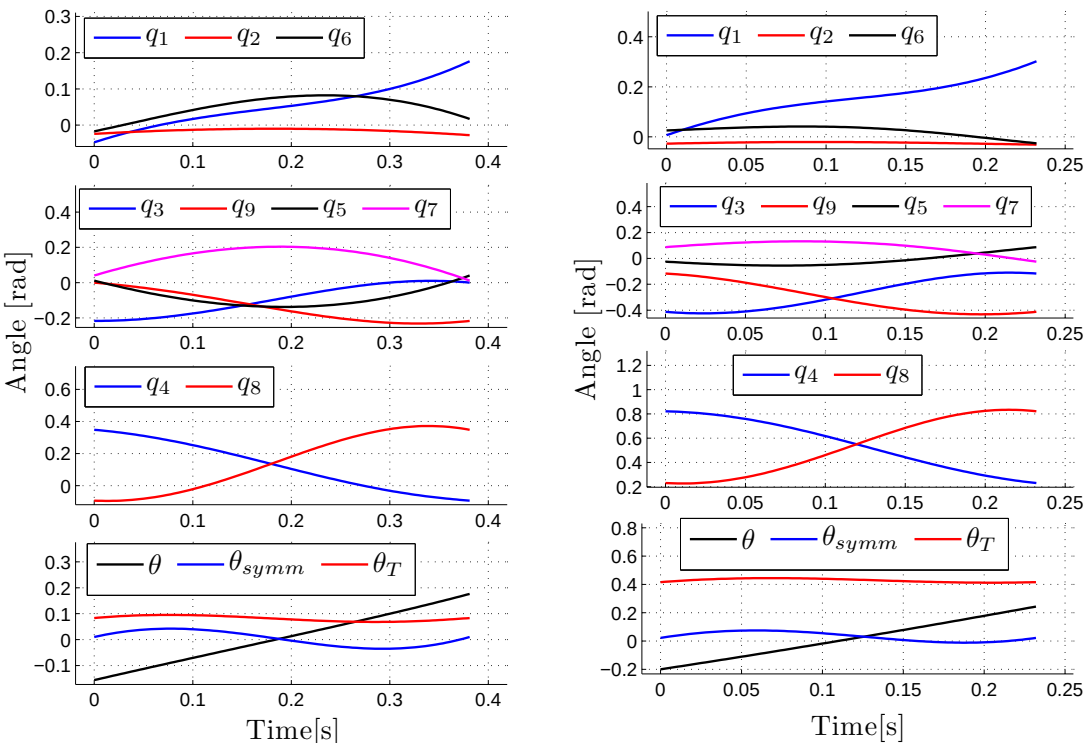

(a) **0.7** m/s (b) **1.5** m/s

Fig. 6.6: The angle charts of the joints and output variables of the 8-link 3D biped walking at 0.7 m/s and 1.5 m/s for *3D Coupling Case I*

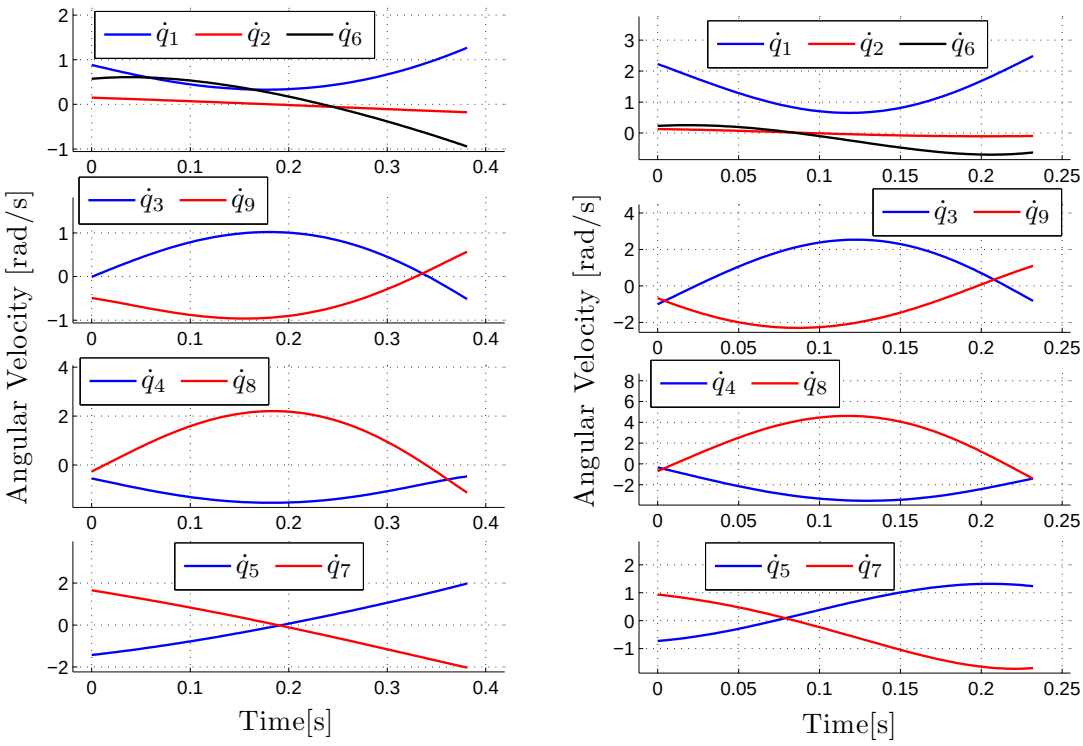

(a) **0.7** m/s (b) **1.5** m/s

Fig. 6.7: The angular velocity charts of the joints of the 8-link 3D biped walking at 0.7 m/s and 1.5 m/s for *3D Coupling Case I*

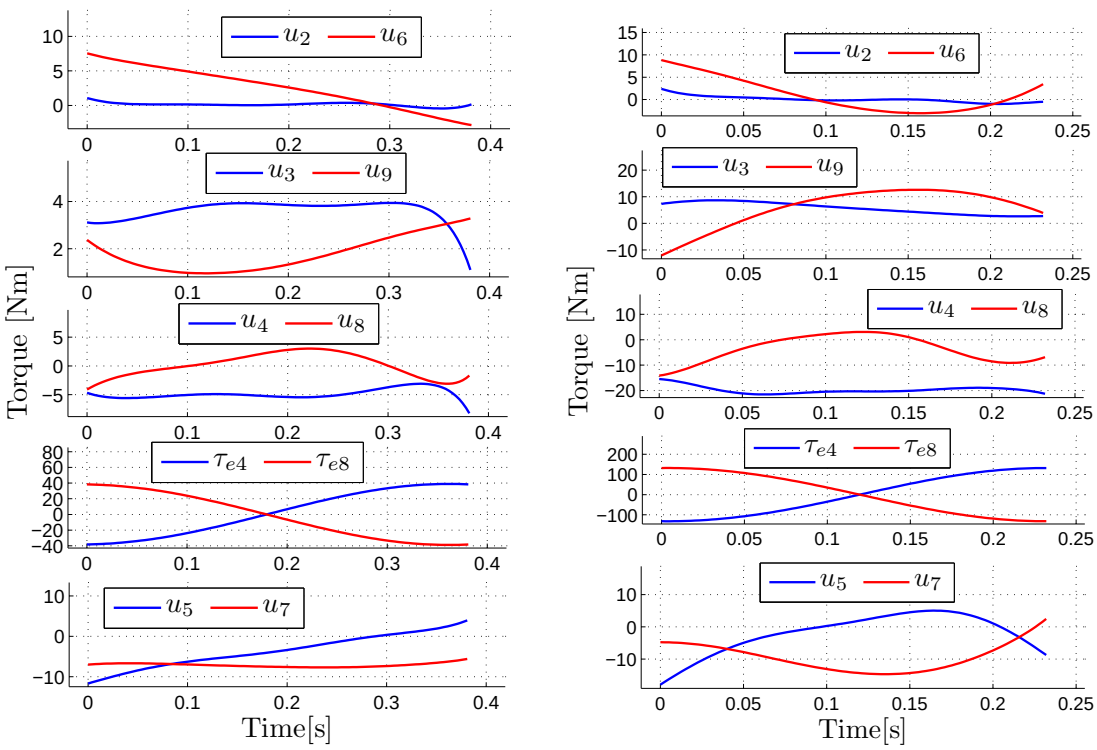

(a) **0.7** m/s (b) **1.5** m/s

Fig. 6.8: The torque charts of the actuators of the 8-link 3D biped walking at 0.7 m/s and 1.5 m/s for *3D Coupling Case I*

Compared with Figure 5.29 of *3D Optimization Case II*, the negative power and energy consumed by the sagittal hip joints in *3D Coupling Case I* are much smaller.

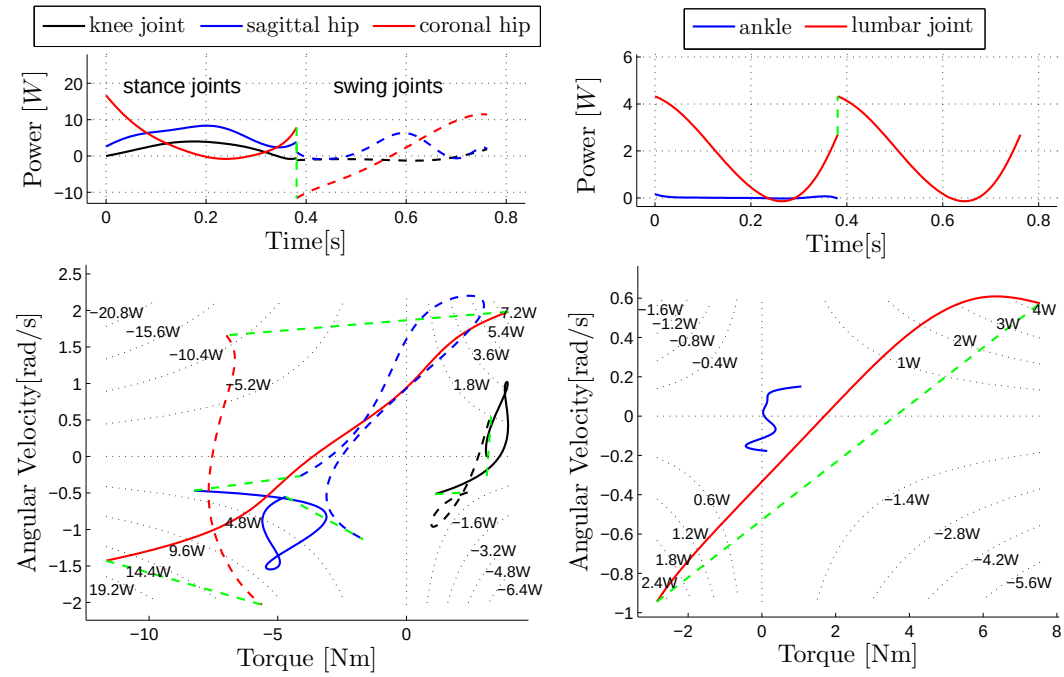

(a) **0.7** m/s

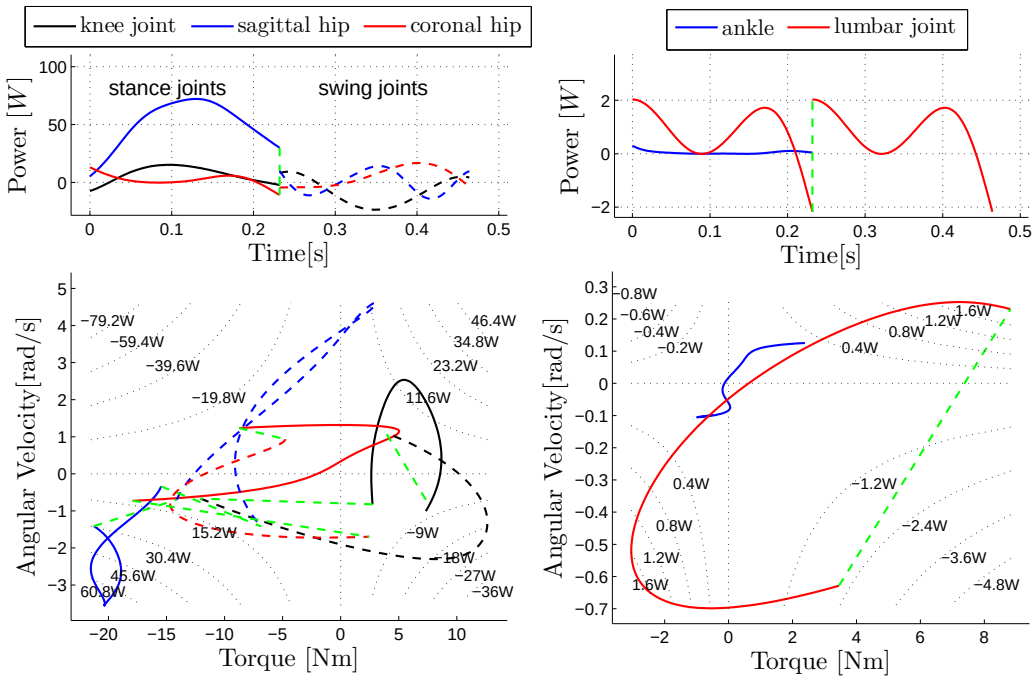

(b) **1.5** m/s

Fig. 6.9: The mechanical output powers of the actuators of the 8-link 3D biped walking at 0.7 m/s and 1.5 m/s (two steps) for *3D Coupling Case I* (Dashed lines represent swing joint angles, and green dashed lines represent the jumps caused by the impact. On the left side, solid lines represent stance joint angles.)

In Figure 6.10, we can verify the ground contact constraints using equations (5.45), (5.46), (5.50), (5.51) and (5.56) defined in *CT8*.

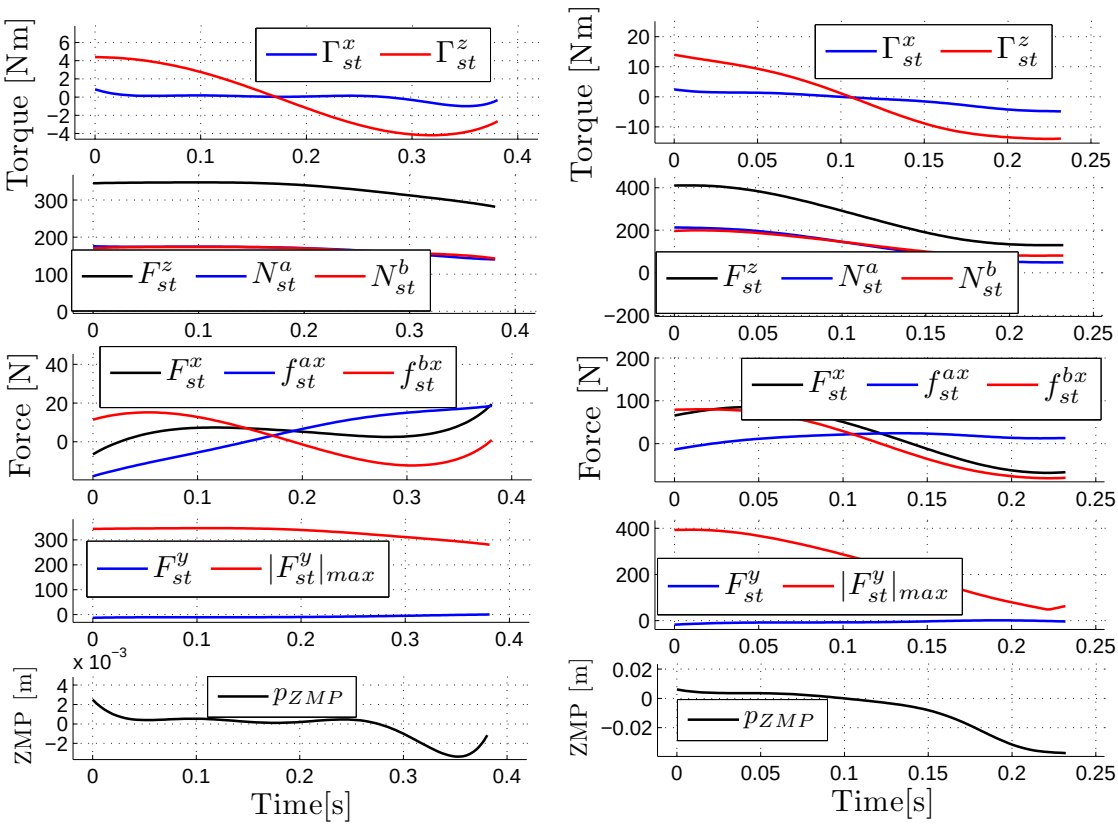

(a) **0.7** m/s (b) **1.5** m/s

Fig. 6.10: The ground reaction forces and torques of the 8-link 3D biped walking at 0.7 m/s and 1.5 m/s for *3D Coupling Case I*

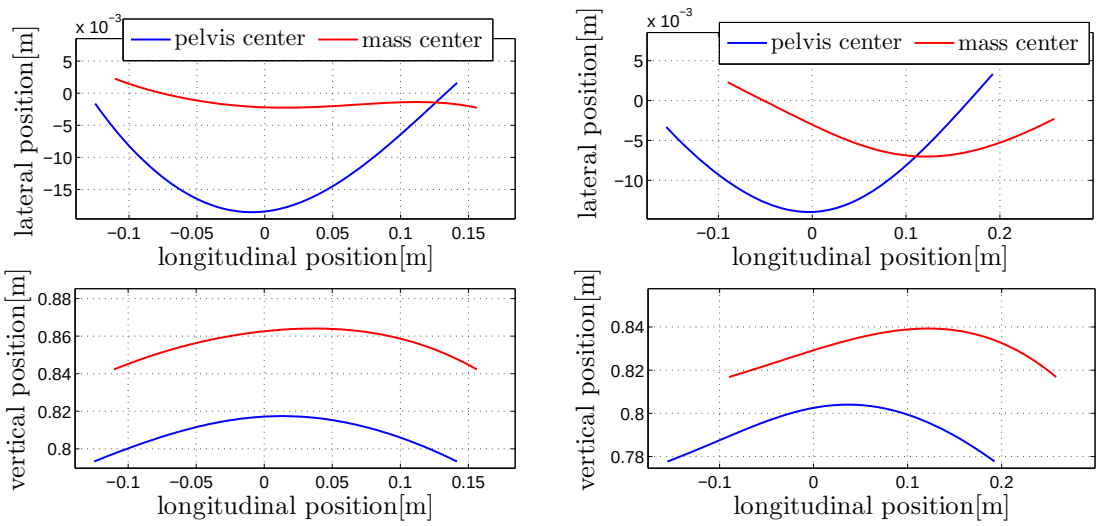

(a) **0.7** m/s (b) **1.5** m/s

Fig. 6.11: The trajectories of the pelvis center and the CoM of the 8-link 3D biped walking at 0.7 m/s and 1.5 m/s for *3D Coupling Case I*

Compared with Figure 5.32 of *3D Optimization Case II*, the maximum foot clearance in *3D Coupling Case I* are smaller.

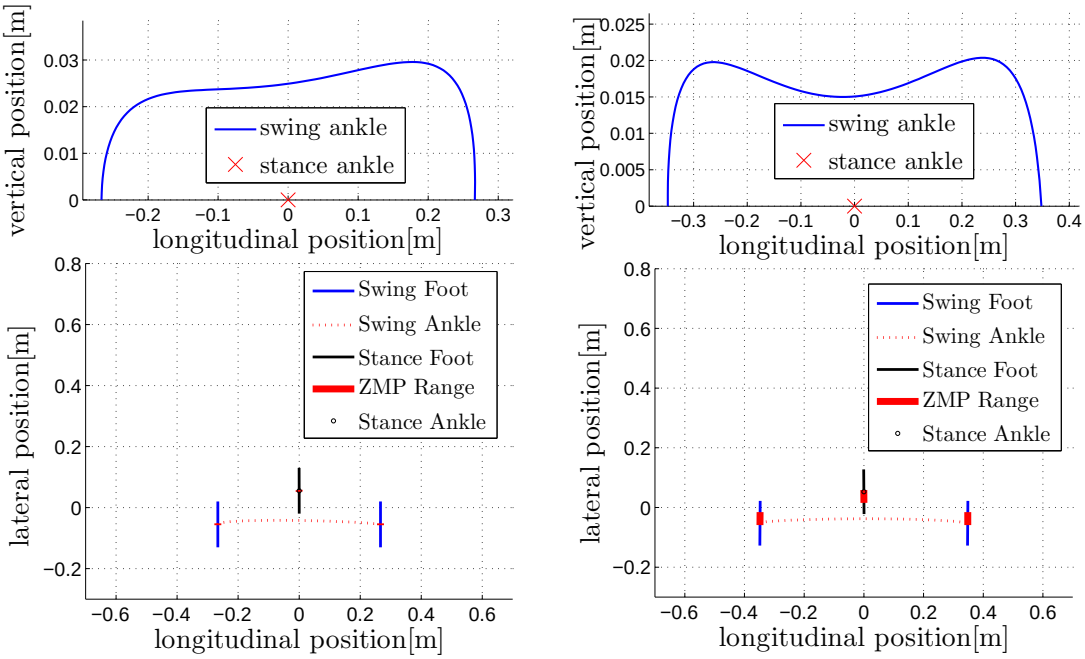

(a) **0.7** m/s (b) **1.5** m/s

Fig. 6.12: The trajectories of the swing ankle and the footprint of the 8-link 3D biped walking at 0.7 m/s and 1.5 m/s for *3D Coupling Case I*

6.2.2 *3D Coupling Case II*

The cost curves of *3D Coupling Case II* are given in Figure 6.13. Although the overall energy cost does decrease at the entire speed range compared with the cost in *3D Optimization Case II* (Figure 5.22), the reduction is much smaller at high speeds than that in *3D Coupling Case I*. This means that *3D Coupling Case II* should not be considered first when designing 3D bipedal robots walking at high speeds. However, at low speeds, *3D Coupling Case II* is better than *3D Coupling Case I* with the minimum overall energy cost equaling only 131 N^2ms while the corresponding values are about 200 N^2ms in *3D Coupling Case I* and 238 N^2ms in *3D Optimization Case II*. The possible explanation for this phenomenon is that, as shown already in Figures 5.11, 5.22 and 6.2, the coronal energy cost accounts for the major energy cost of our 3D biped at low speeds in different cases, and thus adding couplings to the coronal plane is naturally more effective for low speeds than for high speeds.

The variations of the posture parameters at different speeds are provided in Figure 6.14. It is interesting to note that there seem to be "turning points" on the cost curves of the actuators and on the coordinates y_p^- and y_{sw}^- around the speed 1.0 m/s. This is caused by the boundaries of α (to avoid a large lean angle of the torso in the coronal plane) and β (to avoid the torso from leaning backward) in the optimization constraint *CT1*.

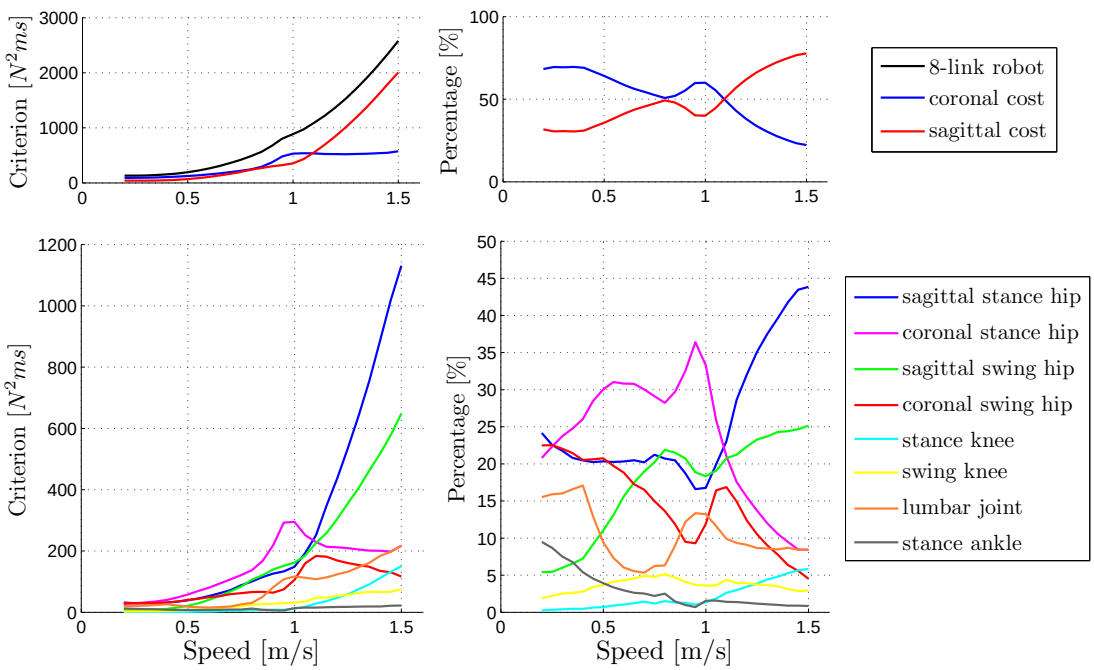

Fig. 6.13: The energy costs of the 8-link 3D biped and its actuators at different speeds for *3D Coupling Case II*

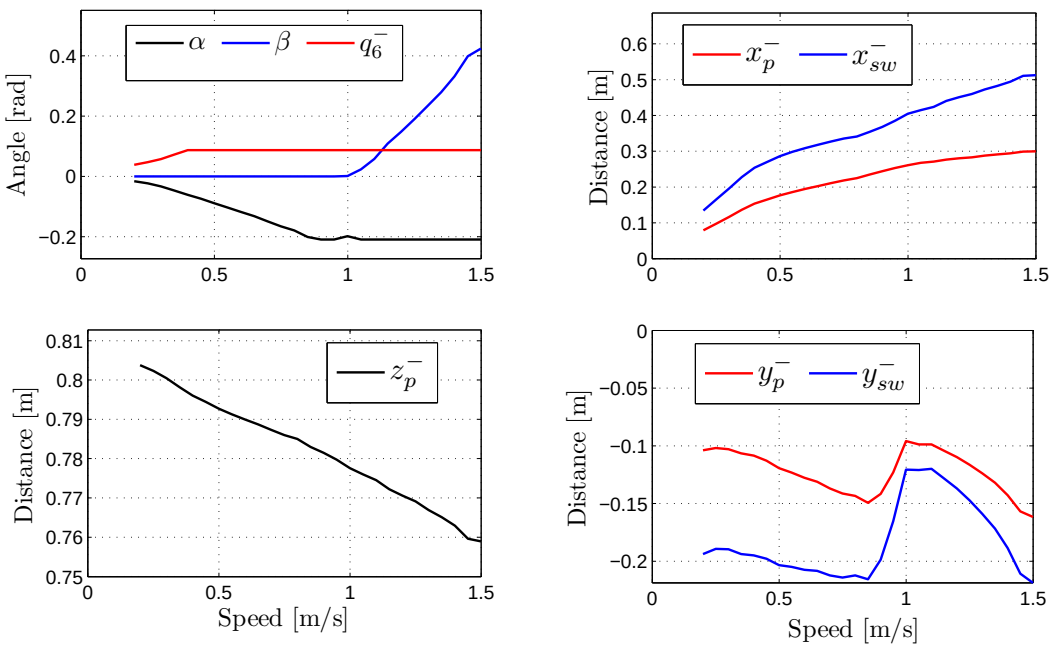

Fig. 6.14: The optimized posture parameters of the 8-link 3D biped at different speeds for *3D Coupling Case II* with the stance ankle being the origin

The spring stiffness k_{opt2} and step frequency at different speeds are illustrated in Figure 6.15. At low speeds, the optimized step frequency in *3D Coupling Case II* is higher than the values in *3D Coupling Case I* and *Optimization Case II* while, at the high speeds, the step frequency is lower than the value in *3D Coupling Case I* but higher than the value in *3D Optimization Case II*. As for the spring stiffness k_{opt2}, we can see that, like k_{opt1} of the sagittal hip joint spring in *3D Coupling Case I*, k_{opt2} also has an almost positive correlation with the walking speed, but the saturation happens at a much lower speed and at high speeds k_{opt2} even drops a bit. As in the Coupling Case I, the saturation is also related to the ground contact conditions.

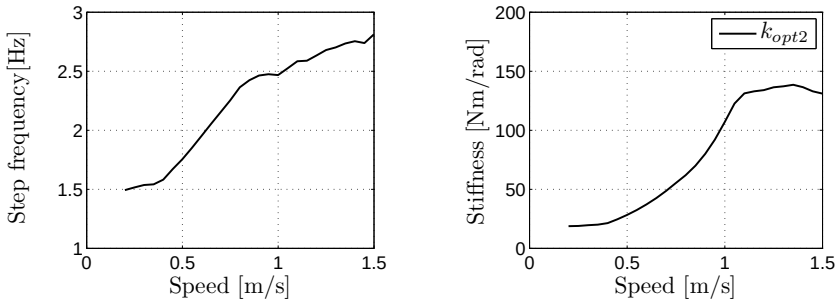

Fig. 6.15: The step frequency and the spring stiffness of the 8-link 3D biped at different speeds for *3D Coupling Case II*

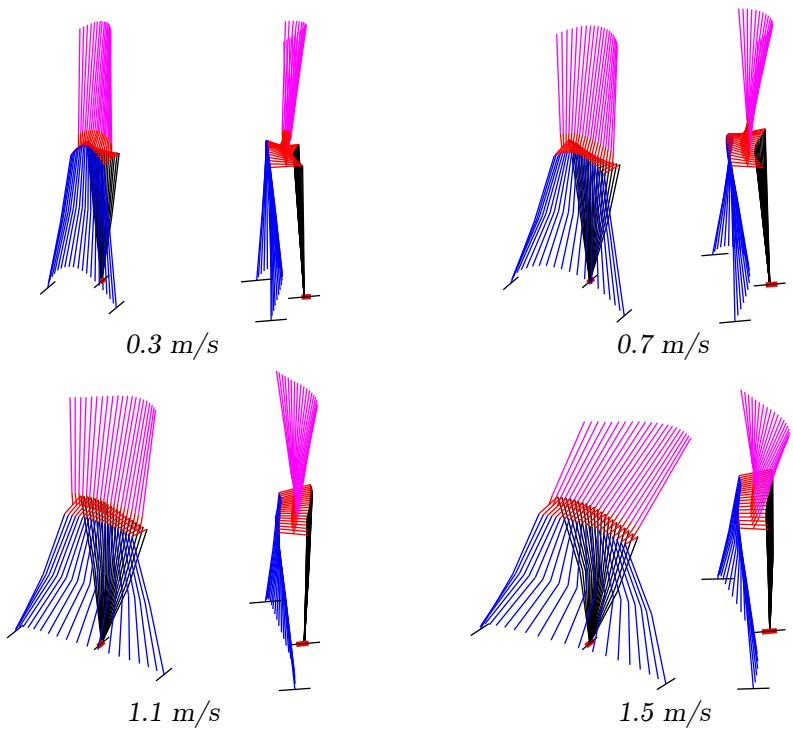

Fig. 6.16: The stick charts of the 8-link 3D biped walking at various speeds for *3D Coupling Case II*

The stick charts of the 8-link 3D biped walking at 0.3 m/s, 0.7 m/s, 1.1 m/s and 1.5 m/s are illustrated in Figure 6.16, and the detailed information concerning the gaits at 0.7 m/s and 1.5 m/s are provided from Figures 6.17 to 6.23. It is obvious that the extent of the movement of the 3D bipedal robot in the coronal plane (such as the swing of the torso) is much larger than those in Figures 6.5 and 5.25. This is also shown by the fact that the variation ranges of q_5, $\dot{q}_5$, q_6, $\dot{q}_6$, q_7 and $\dot{q}_7$ are much larger in Figures 6.17 and 6.18 than in Figures 6.6, 6.7, 5.26 and 5.27 for *3D Optimization Case II* and *3D Coupling Case I*.

By comparing Figure 6.8 with Figure 6.19, we can find that the maximum absolute values of the torques u_4 and u_8 in *3D Coupling Case I* are much smaller than those in *3D Coupling Case II*, especially at the speed 1.5 m/s. According to the mechanical power charts in Figures 6.20, the negative power and energy of the sagittal hip joints are of the same order of magnitude as the positive power and energy. These all suggest that it is possible to further reduce the energy cost by adding elastic couplings to the sagittal plane.

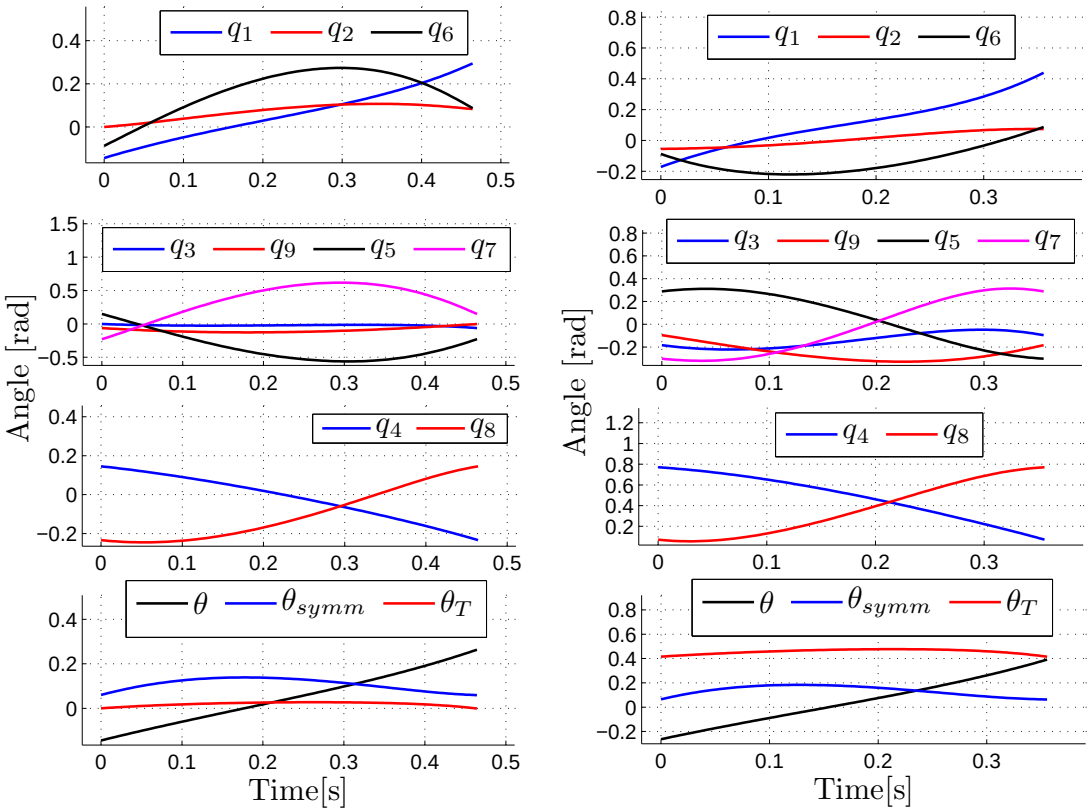

(a) **0.7** m/s (b) **1.5** m/s

Fig. 6.17: The angle charts of the joints and output variables of the 8-link 3D biped walking at 0.7 m/s and 1.5 m/s for *3D Coupling Case II*

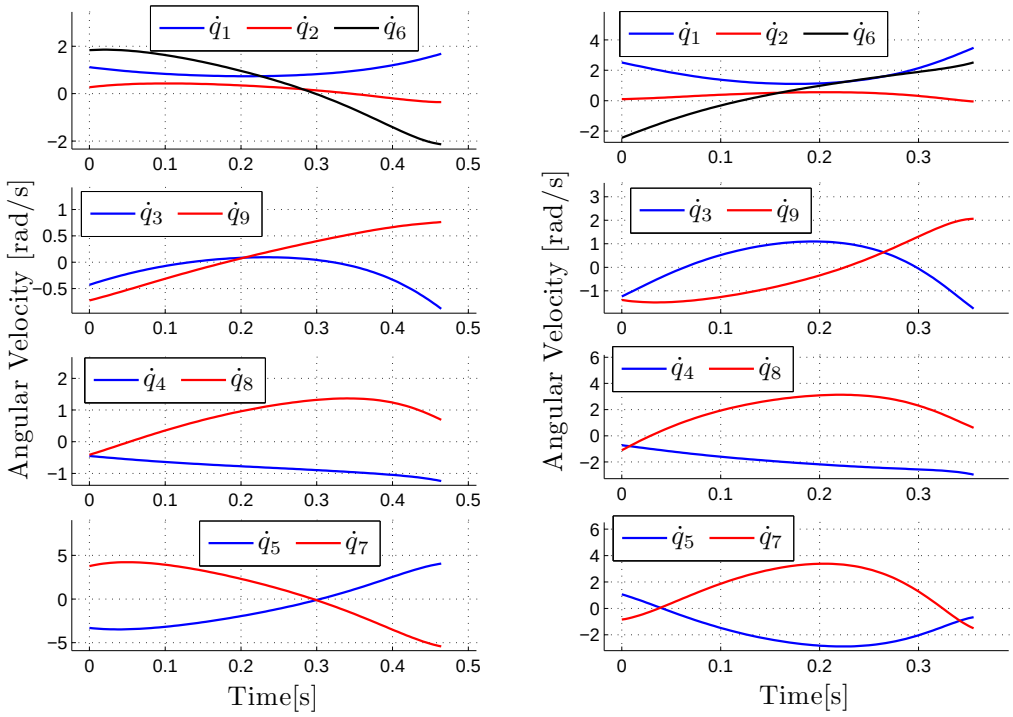

(a) **0.7** m/s (b) **1.5** m/s

Fig. 6.18: The angular velocity charts of the joints of the 8-link 3D biped walking at 0.7 m/s and 1.5 m/s for *3D Coupling Case II*

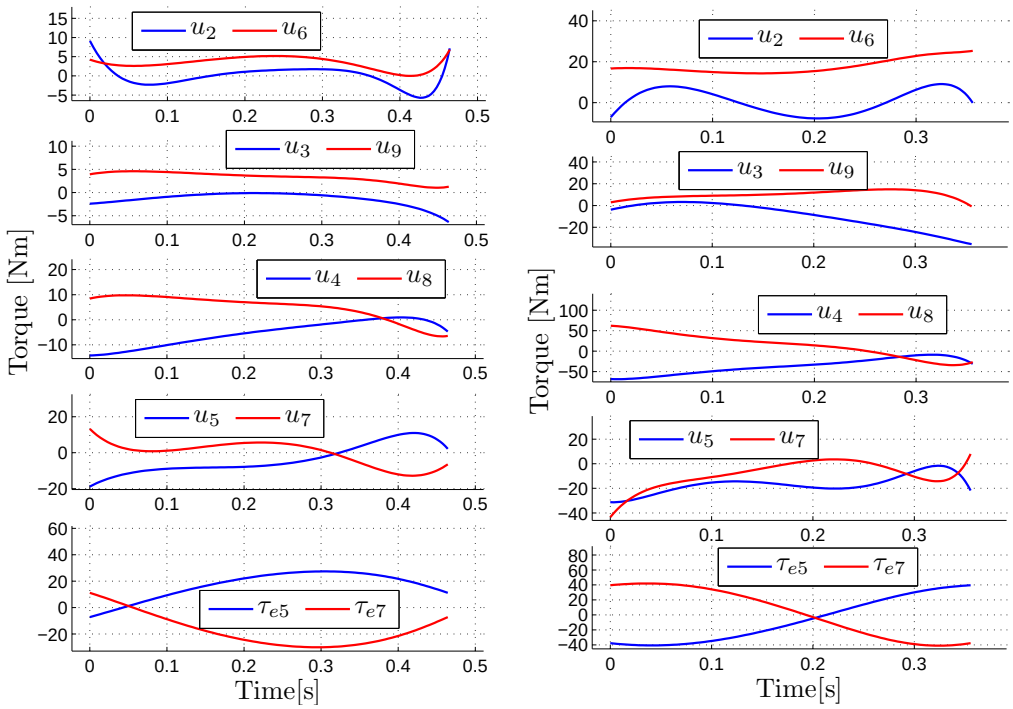

(a) **0.7** m/s (b) **1.5** m/s

Fig. 6.19: The torque charts of the actuators of the 8-link 3D biped walking at 0.7 m/s and 1.5 m/s for *3D Coupling Case II*

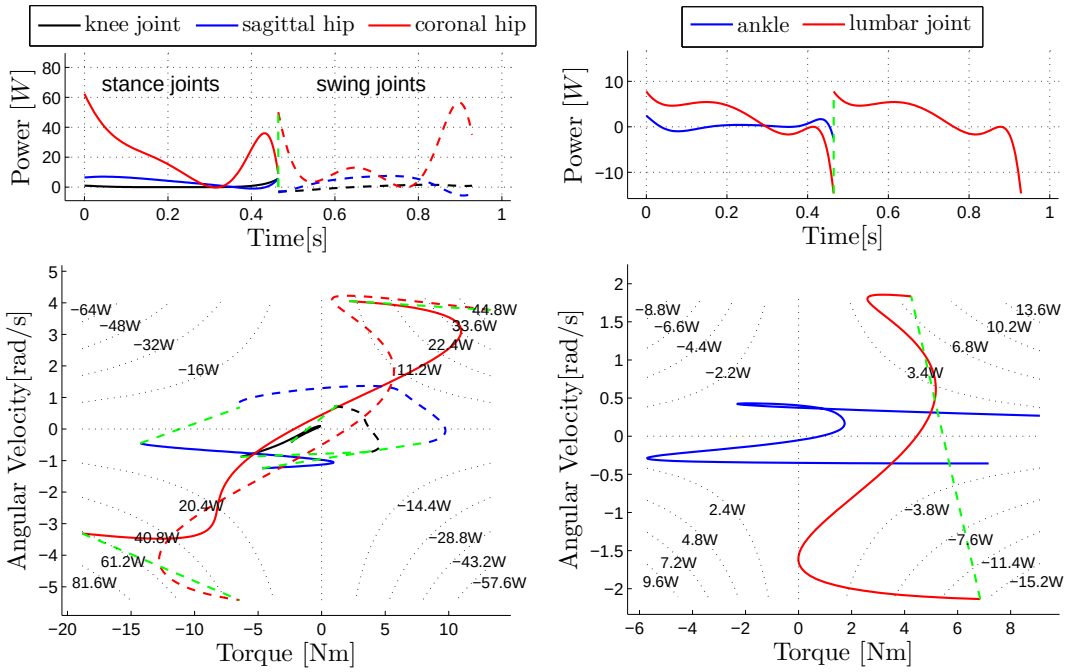

(a) **0.7** m/s

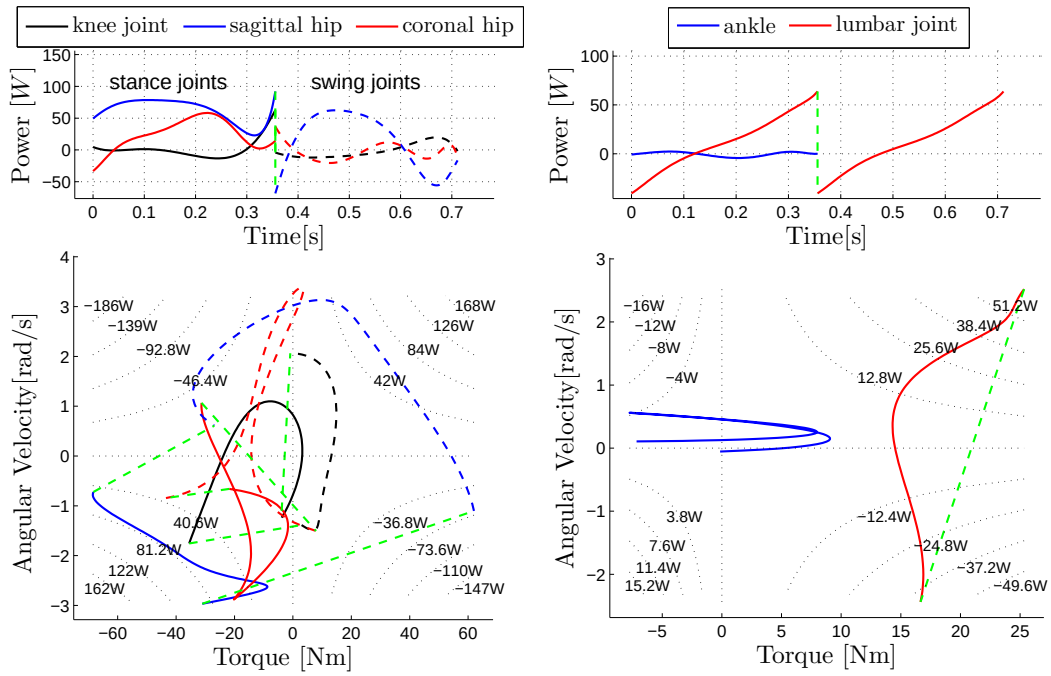

(b) **1.5** m/s

Fig. 6.20: The mechanical output powers of the actuators of the 8-link 3D biped walking at 0.7 m/s and 1.5 m/s (two steps) for *3D Coupling Case II* (Dashed lines represent swing joint angles, and green dashed lines represent the jumps caused by the impact. On the left side, solid lines represent stance joint angles.)

Compared with the ZMP range at 0.7 m/s and 1.5 m/s in the previous cases of our 3D biped, the required ZMP range in Figure 6.21 is larger, and this is possibly due to the large movement of the CoM in Figure 6.22.

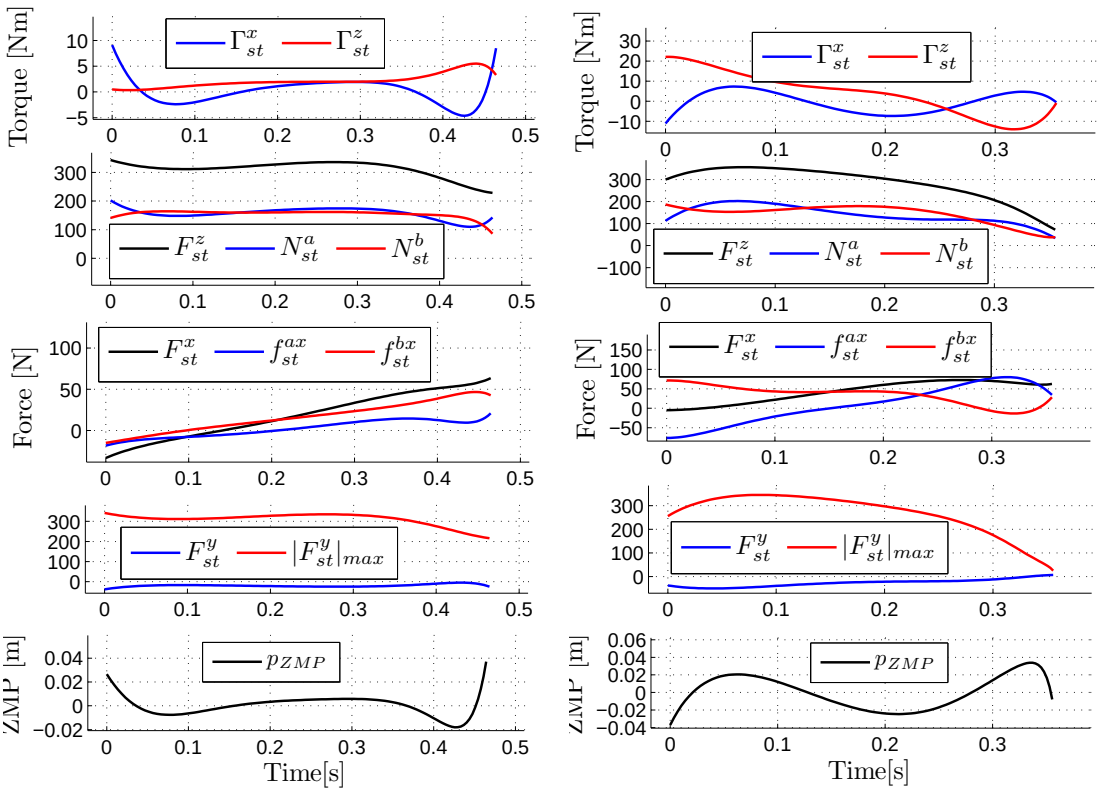

(a) **0.7** m/s (b) **1.5** m/s

Fig. 6.21: The ground reaction forces and torques of the 8-link 3D biped walking at 0.7 m/s and 1.5 m/s for *3D Coupling Case II*

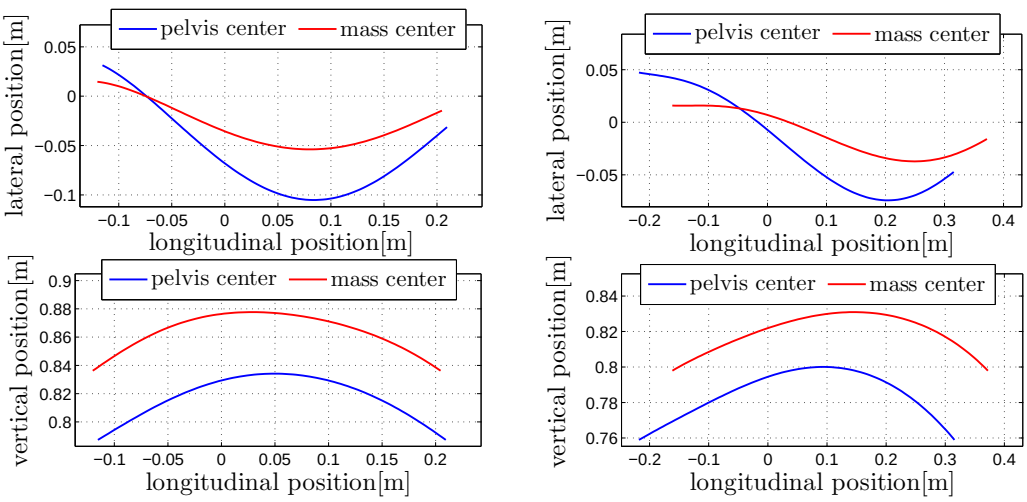

(a) **0.7** m/s (b) **1.5** m/s

Fig. 6.22: The trajectories of the pelvis center and the CoM of the 8-link 3D biped walking at 0.7 m/s and 1.5 m/s for *3D Coupling Case II*

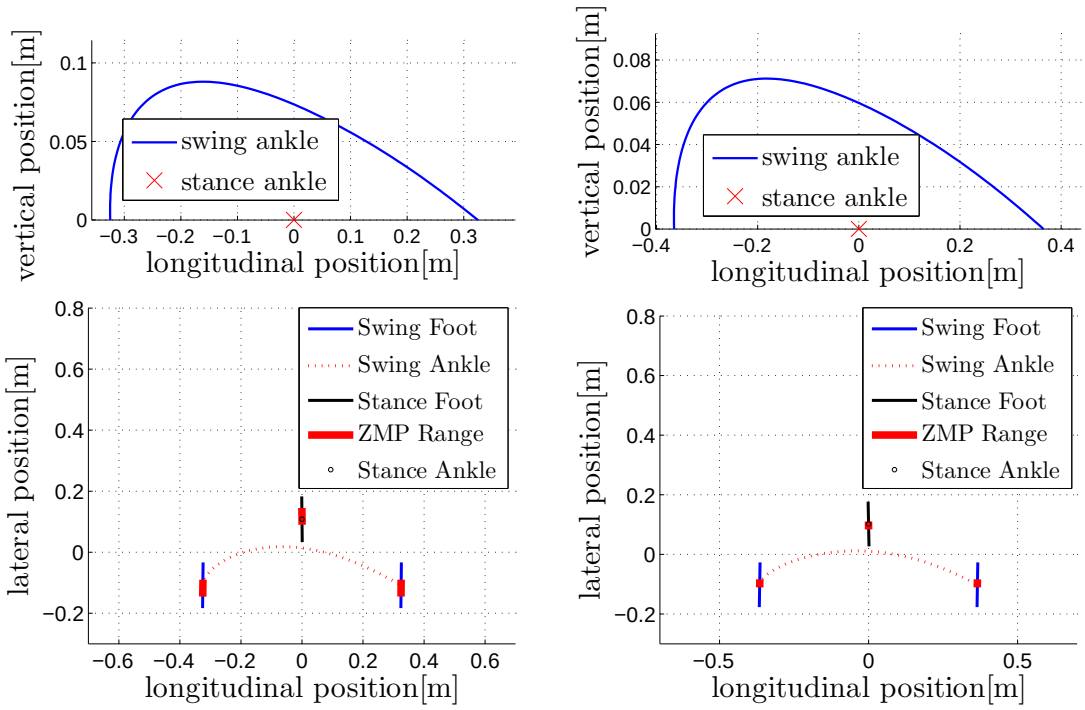

(a) **0.7** m/s (b) **1.5** m/s

Fig. 6.23: The trajectories of the swing ankle and the footprint of the 8-link 3D biped walking at 0.7 m/s and 1.5 m/s for *3D Coupling Case II*

6.2.3 *3D Coupling Case III*

The cost curves of *3D Coupling Case III* are given in Figure 6.24. Compared with all the other cases illustrated in Figures 5.22, 6.2 and 6.13, the overall energy cost of the 8-link 3D bipedal robot is lowest in *3D Coupling Case III*. Not only the maximum energy cost at 1.5 m/s drops to only 367 N^2ms, but for a wide speed range from 0.35 m/s to 0.8 m/s the energy cost is only around 75 N^2ms. This means that we can achieve highly energy efficient gaits in 3D bipedal robots simply by adding hip joint springs to both the sagittal plane and the coronal plane.

The variations of the posture parameters at different speeds are provided in Figure 6.25. By observing the variation of the posture parameter y_{sw}^- at different speeds, we can find that the 3D robot tends to have a short lateral distance between its feet at high speeds and a long lateral distance between its feet at low speeds. This conforms to our intuitive understanding about the difference between strolling and race walking. This phenomenon is also observed in *3D Coupling Case I* (Figure 6.3) but in *3D Optimization Case II* (Figure 5.23) the tendency is reversed, suggesting that the gaits of our 3D biped are quite different from the gaits of human beings when there is no elastic coupling. Another interesting point is that the maximum lean angle β of the pelvis in the sagittal plane is only about 0.4 rad in *3D Coupling Case I*, *II*, and *III* while for *3D Optimization Case I* and *II* the maximum β is above 0.6 rad. This suggests that the 3D biped can have more upright postures during walking with the help of elastic couplings in the hip joints.

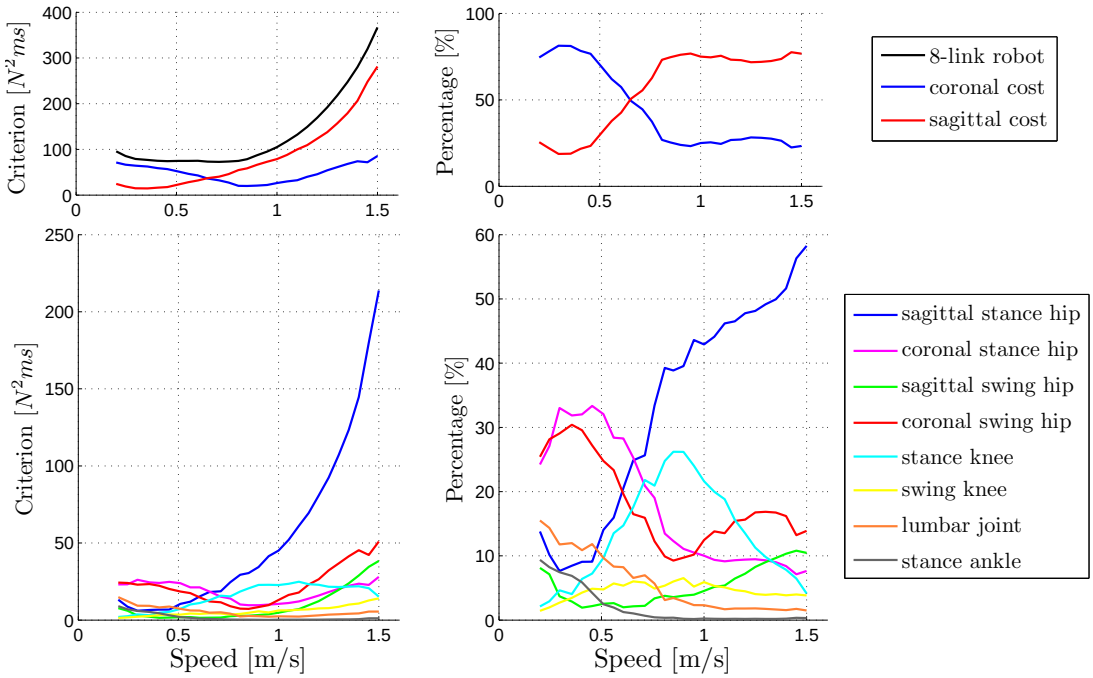

Fig. 6.24: The energy costs and percentages of contribution of the 8-link 3D biped and its actuators at different speeds for *3D Coupling Case III*

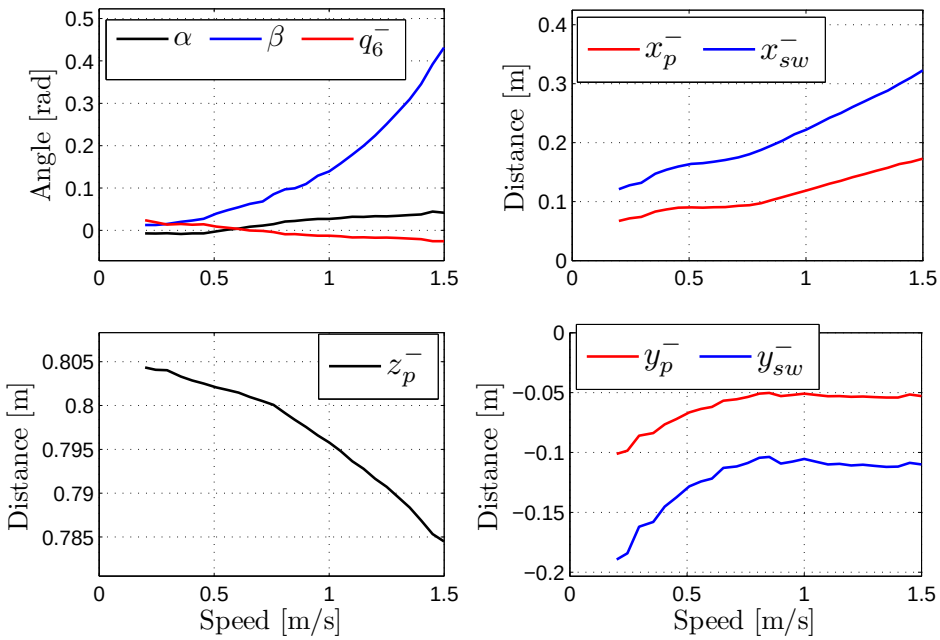

Fig. 6.25: The optimized posture parameters of the 8-link 3D biped at different speeds for *3D Coupling Case III* with the stance ankle being the origin

The optimized spring stiffness k_{opt1} and k_{opt2} are illustrated in Figure 6.26. We can see that both of them have positive correlations with the walking speed at low speeds and are saturated at high speeds, which conforms to the previous conclusions

from Figure 6.4 and Figure 6.15 in *3D Coupling Case I* and *II*. In addition, the curves of k_{opt1} and k_{opt2} in *3D Coupling Case III* are respectively close to the curve of k_{opt1} in *3D Coupling Case I* and the curve of k_{opt2} in *3D Coupling Case II*.

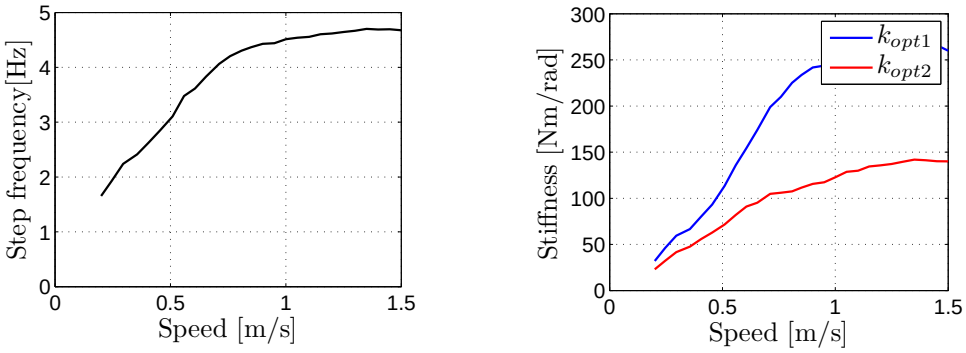

Fig. 6.26: The step frequency and the spring stiffness of the 8-link 3D biped at different speeds for *3D Coupling Case III*

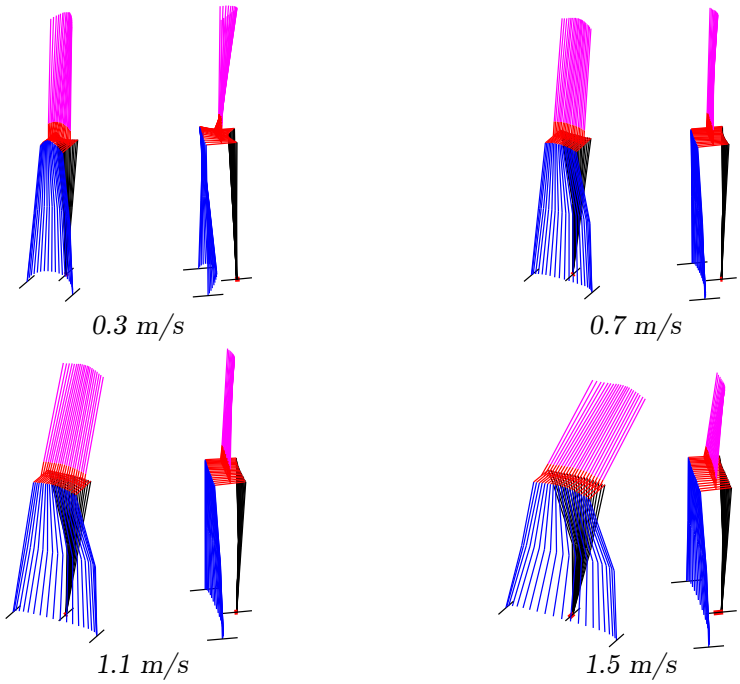

Fig. 6.27: The stick charts of the 8-link 3D biped walking at various speeds for *3D Coupling Case III*

The stick charts of the 3D biped walking at 0.3 m/s, 0.7 m/s, 1.1 m/s and 1.5 m/s are given in Figure 6.27. We can see that, compared with the other 3D gaits so far obtained in Figure 5.25 (*3D Optimization Case II*), 6.5 (*3D Coupling Case I*) and 6.16 (*3D Coupling Case II*), the optimized gaits in *3D Coupling Case III* bear a stronger resemblance to human gaits, which is is mainly demonstrated by more upright torso positions and a milder lateral motion of the swing leg.

For the walking speed 0.7 m/s and 1.5 m/s, the detailed information is provided in Figures 6.28 to 6.34. The angle charts and angular velocity charts in Figures 6.28

and 6.29 are similar to the angle charts in Figures 6.6 and 6.7 for *3D Coupling Case I*, but they are quite different from the angle charts in Figures 6.17 and 6.18 for *3D Coupling Case II*, especially for q_5, $\dot{q}_5$, q_6, $\dot{q}_6$, q_7 and $\dot{q}_7$ at $1.5m/s$. This is caused by the large lateral movements of our 3D biped in *3D Coupling Case II*. In addition, the curves of the output variable θ_{symm} in *3D Coupling Case I* and *III* resembles more a sine curve than the curves of θ_{symm} in *3D Coupling Case II* and *3D Optimization Case I* and *II*. This suggests that θ_{symm} is a good indicator of whether our biped is walking in resonance in the sagittal plane.

According to Figure 6.30, the torques τ_{e4} and τ_{e8} generated by the elastic couplings in *3D Coupling Case III* are much larger than the torques u_4 and u_8 of the corresponding actuators related to the couplings. This also applies to *3D Coupling Case I* (Figure 6.8), but in *3D Coupling Case II* (Figure 6.19), the magnitudes of u_5, u_7 are quite close to the magnitudes of τ_{e5}, τ_{e7}.

The effectiveness of the elastic couplings in *3D Coupling Case III* can be further verified by the mechanical output powers of the 3D biped's actuators in Figure 6.31. In *3D Coupling Case I* and *II* (Figures 6.9 and 6.20), there are always sagittal hip joint actuators or coronal hip joint actuators that produce a nonnegligible amount of negative mechanical energy, but in *3D Coupling Case III* the negative mechanical energy produced by all the hip joint actuators is much less than the corresponding positive mechanical energy.

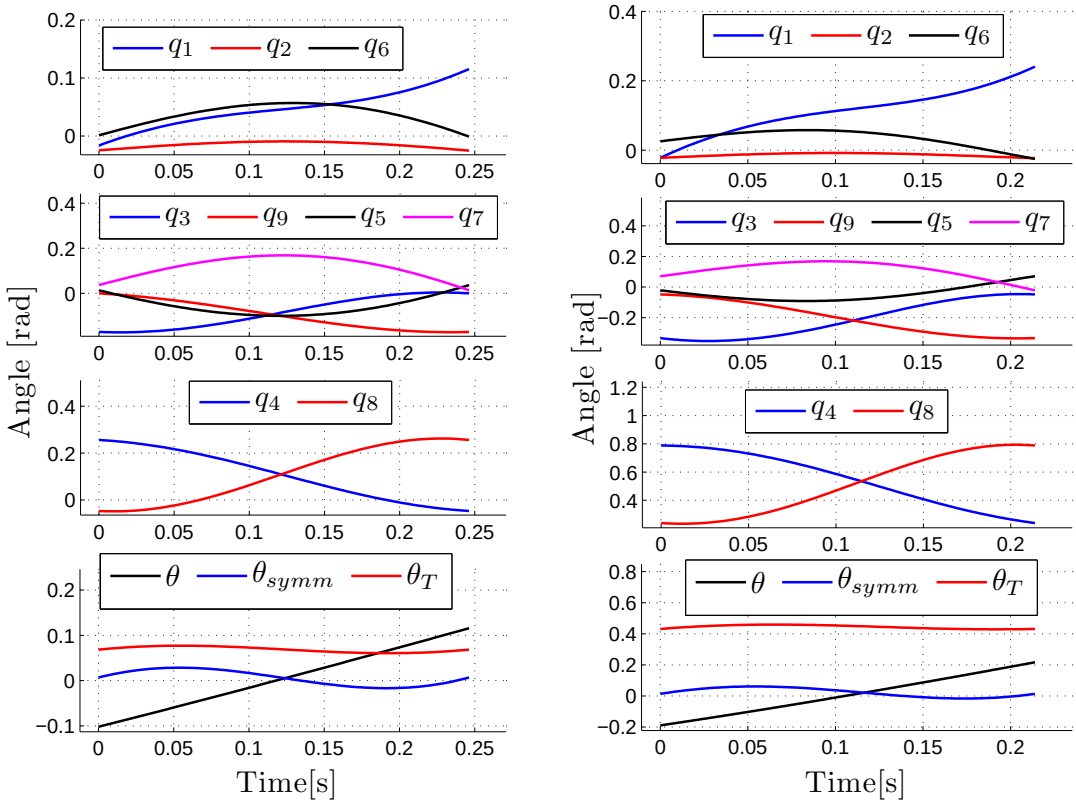

(a) **0.7** m/s (b) **1.5** m/s

Fig. 6.28: The angle charts of the joints and output variables of the 8-link 3D biped walking at 0.7 m/s and 1.5 m/s for *3D Coupling Case III*

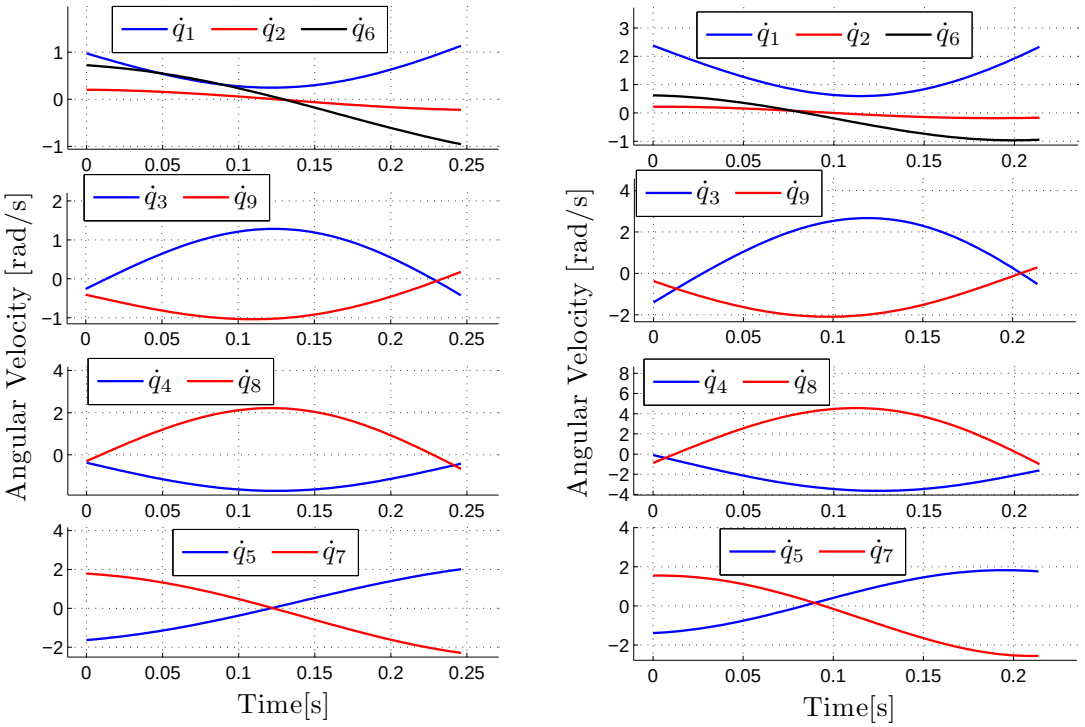

(a) **0.7** m/s (b) **1.5** m/s

Fig. 6.29: The angular velocity charts of the joints of the 8-link 3D biped walking at 0.7 m/s and 1.5 m/s for *3D Coupling Case III*

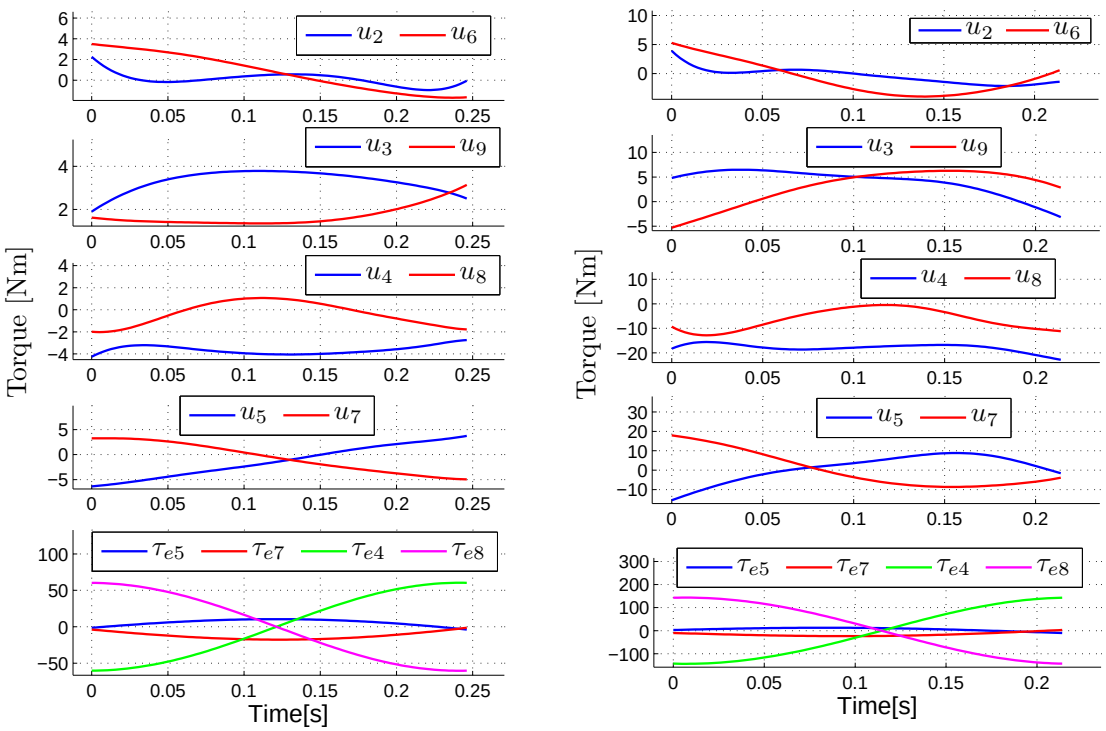

(a) **0.7** m/s (b) **1.5** m/s

Fig. 6.30: The torque charts of the actuators of the 8-link 3D biped walking at 0.7 m/s and 1.5 m/s for *3D Coupling Case III*

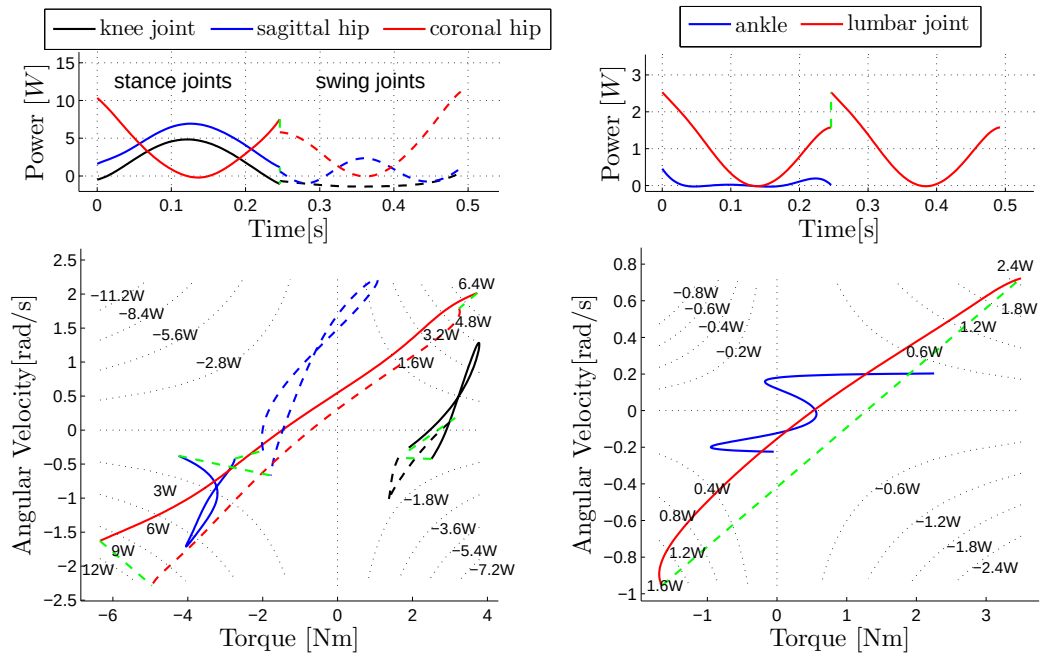

(a) **0.7** m/s

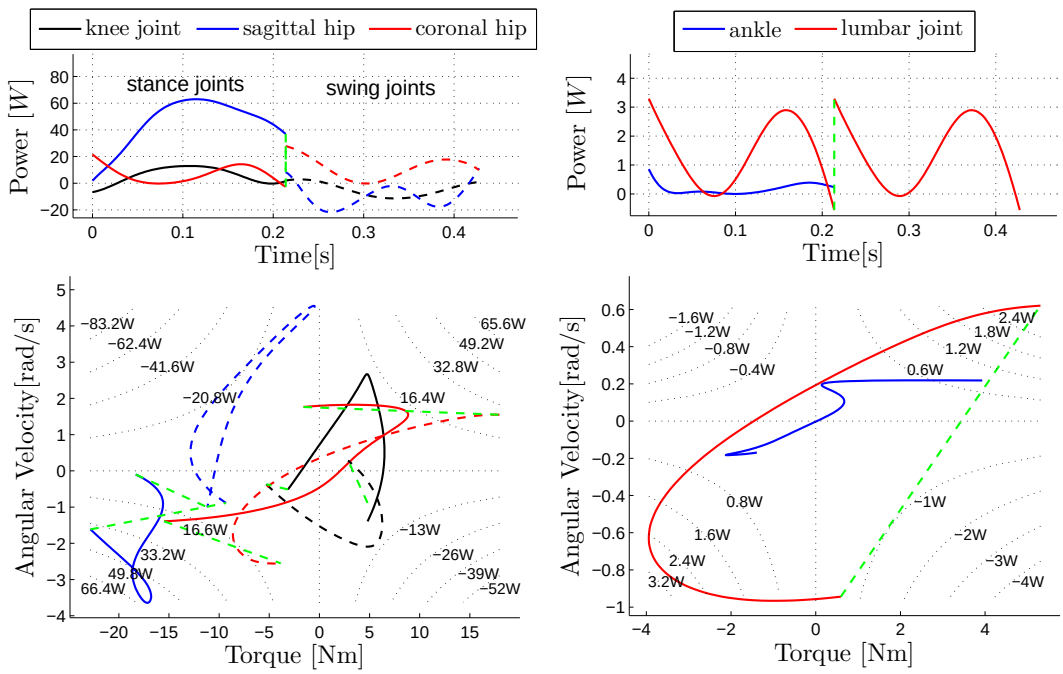

(b) **1.5** m/s

Fig. 6.31: The mechanical output powers of the actuators of the 8-link 3D biped walking at 0.7 m/s and 1.5 m/s (two steps) for *3D Coupling Case III* (Dashed lines represent swing joint angles, and green dashed lines represent the jumps caused by the impact. On the left side, solid lines represent stance joint angles.)

The range of ZMP positions in Figure 6.32 is similar to those in Figure 6.10 for *3D Coupling Case I* and in Figure 5.30 for *3D Optimization Case II*. However, in Figure 6.21 for *3D Coupling Case II*, the required ZMP range is the largest at 0.7 m/s and 1.5 m/s among all the gait optimization cases of the 3D biped (*3D Coupling Case I, II, III* and *3D Optimization Case I, II*). This means that the negative influence on the ZMP range in *3D Coupling Case II* can be avoided by adding elastic couplings in the sagittal plane.

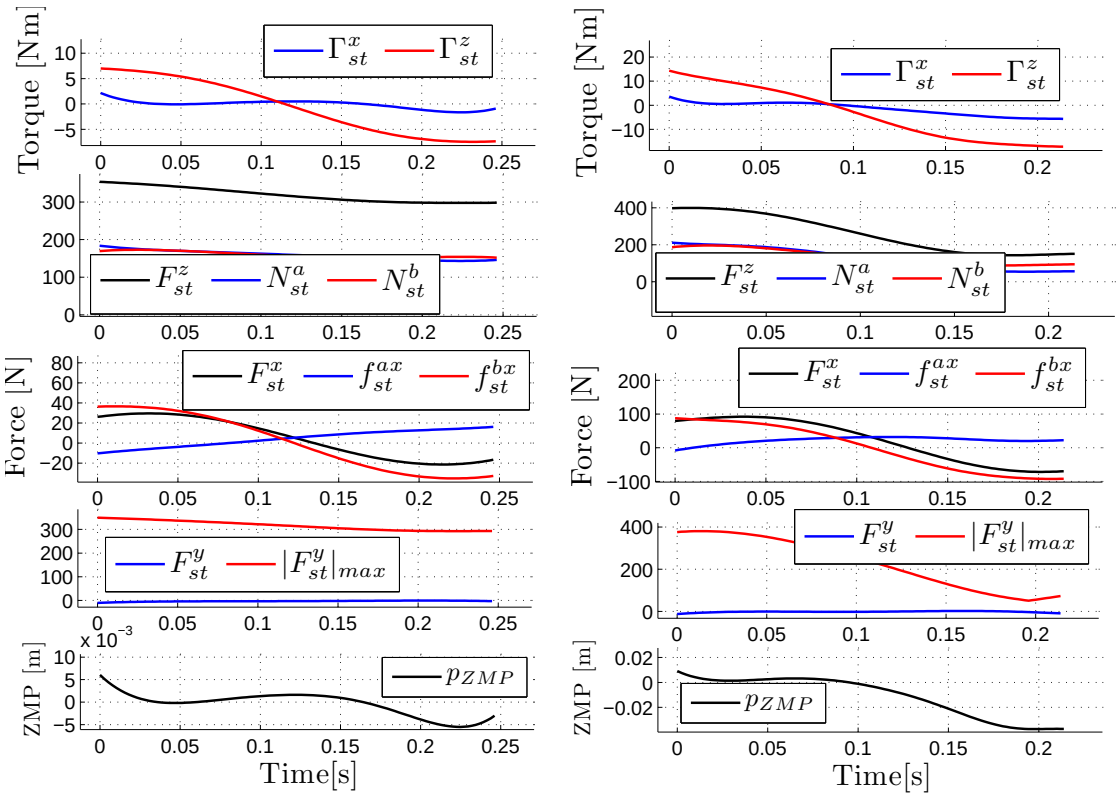

(a) **0.7** m/s (b) **1.5** m/s

Fig. 6.32: The ground reaction forces and torques of the 8-link 3D biped walking at 0.7 m/s and 1.5 m/s for *3D Coupling Case III*

By comparing the trajectory of the robot's CoM in Figure 6.33 with those in Figure 6.11 (*3D Coupling Case I*) and 6.22 (*3D Coupling Case II*), we can see that the magnitudes of both lateral motion and vertical motion of the CoM are similar in *3D Coupling Case I* and *III*. However, in *3D Coupling Case II*, the movement of the robot's CoM is much larger, which is probably related to the large ZMP range in Figure 6.21.

The footprints and the trajectories of the swing ankle are illustrated in Figure 6.34. Compared with the foot clearance for all the other cases of our 3D biped depicted respectively in Figures 5.21, 5.32, 6.12 and 6.23, the maximum foot clearance in *3D Coupling Case III* is less than 2 *cm* at both walking speeds 0.7 m/s and 1.5 m/s, and this value is very close to the 1.3 *cm* average maximum toe clearance for humans [181].

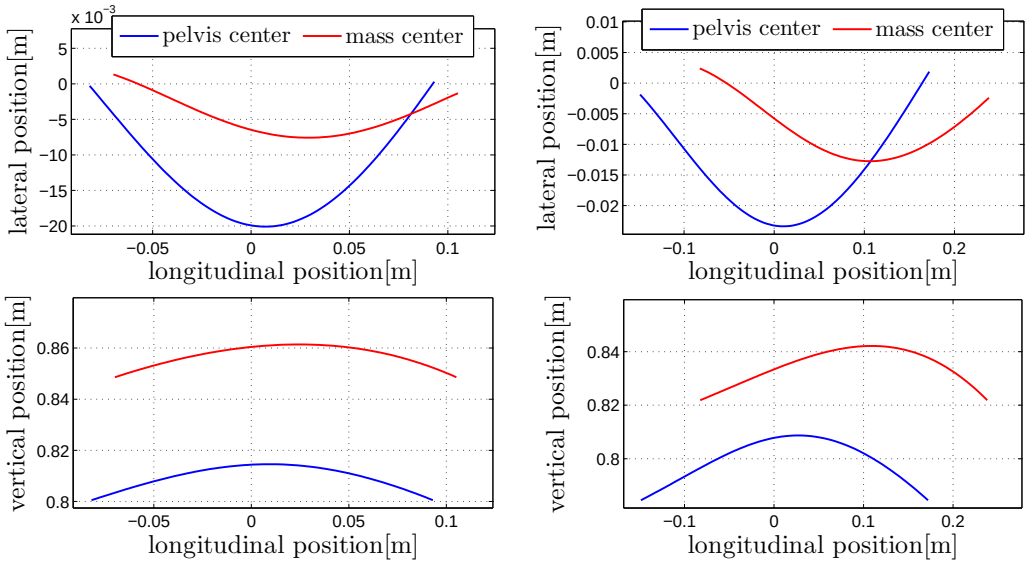

(a) **0.7** m/s (b) **1.5** m/s

Fig. 6.33: The trajectories of the pelvis center and the CoM of the 8-link 3D biped walking at 0.7 m/s and 1.5 m/s for *3D Coupling Case III*

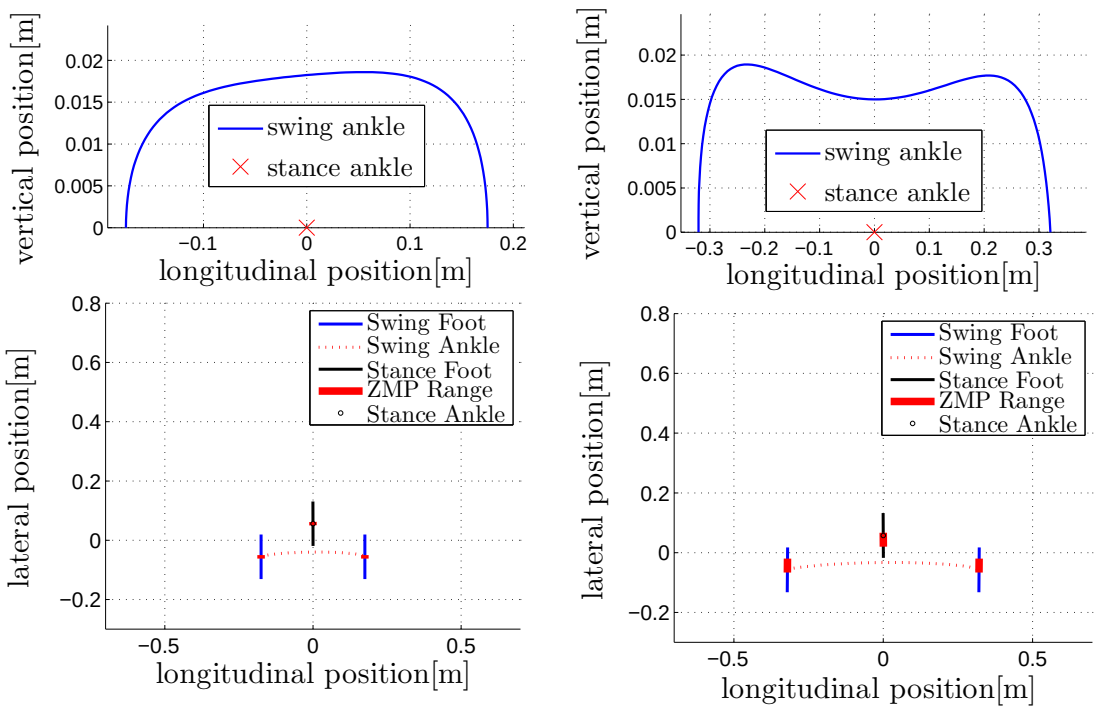

(a) **0.7** m/s (b) **1.5** m/s

Fig. 6.34: The trajectories of the swing ankle and the footprint of the 8-link 3D biped walking at 0.7 m/s and 1.5 m/s for *3D Coupling Case III*

6.3 Discussion

In the previous section, we have demonstrated the appeal of adding elastic couplings in form of hip joint springs to our 3D bipedal robot based on gait optimization results. It is interesting to make comparisons between all the optimization cases for our 3D biped and planar biped.

When it comes to the overall energy cost, *3D Coupling Case III* undoubtedly provide the best solution among *3D Coupling Case I, II, III* and *3D Optimization Case I, II*, but the energy cost in *3D Coupling Case I* is also satisfactory. The shortcomings of *3D Coupling Case III* is that it requires two more linear torsion springs with adjustable stiffness than *3D Coupling Case I*, which might have a negative influence on the 3D biped's reliability. Therefore, one needs to consider all the possible trade-offs to make a wise choice between *3D Coupling Case I* and *III*. One thing for sure is that, *3D Coupling Case II* is never the wise choice for designing a 3D biped with a walking speed above 0.5 m/s not only because it only provides a limited reduction in the energy cost, but also because it has negative features like excessive coronal motions and a limited margin for maintaining ground contact.

As for the feasibility of modifying spring constants, the situation is similar to that of our planar biped. In order to avoid using additional actuators as in [153, 154, 156, 157], we can consider several options. For realizing a 3D biped with three linear torsion springs in *3D Coupling Case III*, we can probably use linear torsion springs with fixed stiffness for all the walking speeds above 1 m/s, since there are obvious saturations of k_{opt1} and k_{opt2} for the speed range between 1 m/s and 1.5 m/s in Figure 6.26. In addition, we can also use an nonlinear stiffening spring as proposed in Chapter 4 to replace the sagittal hip joint spring in *3D Coupling Case I* and *III*, because the variation range of the deflection $q_4 - q_8$ is positively correlated with the step size (which is close to x_{sw}^- in Figures 6.3 and 6.25), and the latter is positively correlated with the walking speed and k_{opt1}.

The periodic orbits of all the relative joint angles of the 8-link 3D biped walking at 0.7 m/s in five different cases are depicted in Figure 6.35. For all the relative joint angles studied, the jumps of angular velocity (marked by black arrows) at the impact in *3D Coupling Case I* and *III* (especially *Case III*) are smaller than those in *3D Coupling Case II* and *3D Optimization Case I* and *II*. Except for the angle of the ankle, the orbits of all the other relative joint angles in *3D Coupling Case I* and *III* are much closer to ellipses than the orbits in the other cases in Figure 6.35. For the relative joint angles in the coronal plane in Figure 6.35 (b), (d) and (e), the maximum variation range appears in *3D Coupling Case II*, which probably caused the limited margin left for ZMP positions in Figure 6.21. By comparing Figure 6.35 (c) with 4.29 (f), we can find that, the variation ranges of the relative knee joint angle of our 3D biped for all cases expect *3D Optimization Case I* (where sagittal optimization parameters directly come from the optimized parameters of our planar biped with no coupling) are generally smaller than those of our planar biped. This means that our 3D biped has straight-legged gaits, and the most possible explanation is that the additional coronal joints of the 3D biped can also ensure foot clearance like the knee joints do for both planar and 3D bipeds.

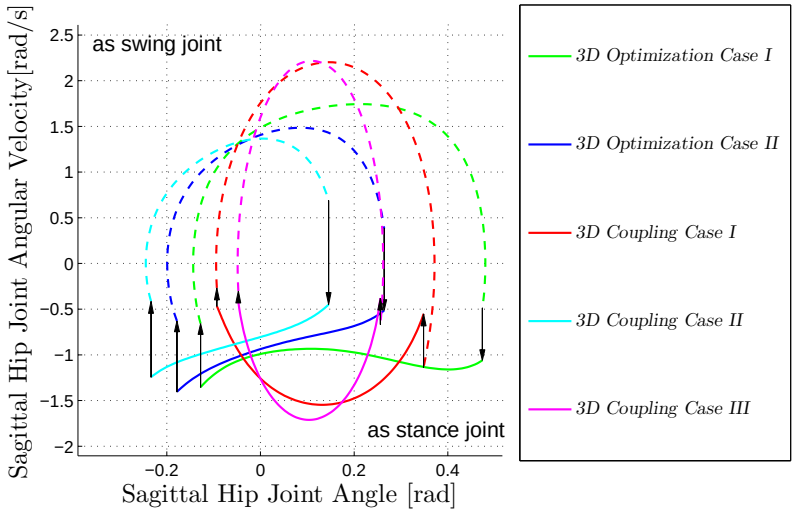

(a) relative sagittal hip joint angle

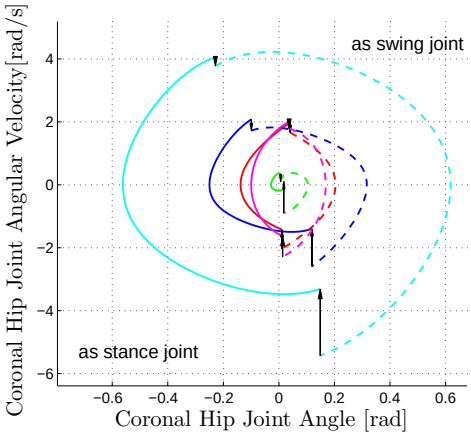

(b) relative coronal hip joint angle

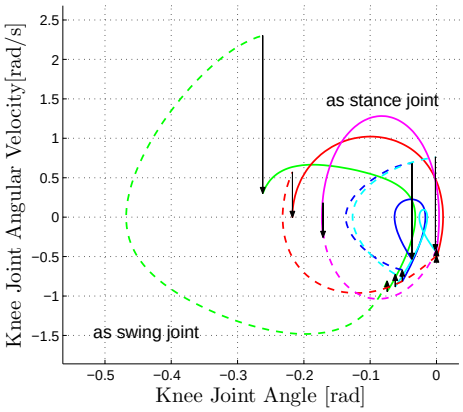

(c) relative knee joint angle

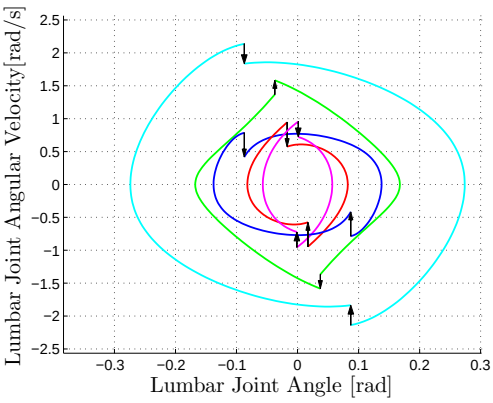

(d) relative lumbar joint angle

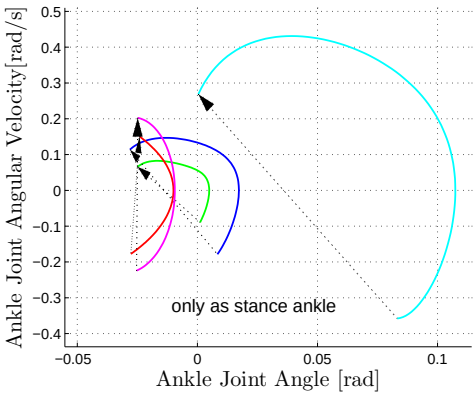

(e) relative ankle joint angle

Fig. 6.35: The phase plots of the 8-link 3D biped in three different cases at 0.7 m/s (Solid lines represent stance joint angles except for the lumber joint, dashed lines represent swing joint angles, and black arrows represent the jumps caused by the impact. Note that the evolution of the swing ankle during the step is unknown.)

6.4 Conclusion

In this chapter, we have discussed three cases of adding elastic couplings in form of hip joint springs to the 8-link 3D biped model introduced in Chapter 5. In *3D Coupling Case I*, a torsion spring is added to connect the movements of two thighs in the sagittal plane. In *3D Coupling Case II*, two torsion springs are used to build connections between the movements of two thighs and the movement of the pelvis in the coronal plane. In *3D Coupling Case III*, the ideas of the first two cases are combined, and three torsion springs are installed in both the sagittal plane and the coronal plane. By adding spring constants to the optimization parameters, we have obtained results for all three cases using gait optimization methods in Chapter 5. The elastic couplings in all three cases have reduced negative mechanical power and energy of the corresponding hip joint actuators that are coupled with torsion springs. Among these three coupling cases, *3D Coupling Case III* has the lowest energy cost over the entire speed range with the energy cost ranging from 74.3 N^2ms to 367 N^2ms. The second best option is *3D Coupling Case I*, which has an energy cost from 198 N^2ms to 475 N^2ms. As for *3D Coupling Case II*, it has a energy cost ranging from 132 N^2ms to 2579 N^2ms. *3D Coupling Case II* is only worth considering for designing a 3D biped with a walking speed below 0.5 m/s, but for high speeds it has the problems of excessive lateral movements and large ZMP ranges. According to the gait optimization results at the walking speeds 0.7 m/s and 1.5 m/s, *3D Coupling Case I* and *III* both have the advantages of comparatively small ZMP ranges and small maximum foot clearances that are close to the average maximum foot clearance of human beings. Besides, the phase plots of the relative joint angles of these two cases (especially *3D Coupling Case III*) are featured with smaller jumps and more resemblance to ellipses than the other cases of our 3D biped do, which can be viewed as a sign indicating that the 3D biped is walking efficiently in resonance. The other advantages and disadvantages of these two cases require further consideration from designers that attempt to design a 3D bipedal robot.

7. CONCLUSIONS AND FUTURE WORK

7.1 Conclusions

Compared with human beings, current bipedal robots are usually less efficient due to mainly two reasons: (1) conservative control strategies of bipedal robots support only quasi-static walking motions whilst a moving human body has no need to remain static equilibrium; (2) human beings have natural elastic components such as muscles, tendons and ligaments for recycling energy whist elastic couplings are ignored by many bipedal robots. Accordingly, the aim of this study is three-fold: (1) to exploit natural dynamics of bipedal walking by improving control strategies, (2) to realize optimization of periodic bipedal locomotion, and (3) to compare the contributions of different configurations of elastic couplings.

There are two types of bipedal robots studied in this thesis: planar bipeds with point feet and 3D bipeds with massless line feet approximately parallel to the coronal plane. These two types of robots are modeled respectively by a 5-link robot with a torso, two thighs and two shins and a 8-link robot with a torso, a pelvis, two thighs, two shins, and two massless line feet. In reference to the humanoid robot HRP-4, the total mass is 39 kg and the total statue is 1.5 m for both models. Using these two variables, we can generate virtual anthropomorphic structures, from which the other model parameters can be obtained [173, 174].

For the walking, we suppose that each step is composed of a single support phase and an instantaneous double support phase. These two phases are connected by a rigid impact to form a hybrid model. During the single support phase, both robots have one degree of underactuation. Using the control method based on virtual constraints and feedback linearization, we can study the complete hybrid model by its two dimensional, invariant sub-dynamics named hybrid zero dynamics. In this way, the exponential stability of the complete hybrid model is equivalent to the exponential stability of the hybrid zero dynamics, of which the Poincaré map is diffeomorphic to a scalar LTI system that can be calculated in closed form. Previously, this method mainly applied to planar bipeds [8], and now we demonstrate its applicability for 3D bipeds by changing point feet into massless line feet. Compared with 3D bipedal robots with point feet and two or more degrees of underactuation, 3D bipedal robots with line feet and one degree of underactuation are much simpler, although one corresponding shortcoming is that the ZMP is now required to be within the range of the line foot segment. In addition, we adopt the controlled output named "symmetry output" to facilitate geometric interpretation of posture control and swing leg advancement.

For the gait optimization, we use postural parameters and Bézier polynomials of

order 5 to define the desired outputs. The numbers of parameters to be optimized without considering elastic couplings are 16 for the 5-link robot and 32 for the 8-link robot. For the 8-link biped, the 32 parameters are further divided into 16 sagittal parameters and 16 coronal parameters, and accordingly there are two optimization cases, namely, *3D Optimization Case I* and *II*. In *3D Optimization Case I*, we directly adopt the optimized parameters from the 5-link planar biped as the sagittal parameters and optimize only the coronal parameters. In *3D Optimization Case II* , we only use the optimized parameters from the 5-link planar biped as a starting point, and all the 32 parameters are optimized.

The gait optimization for both robots use `fmincon` function in MATLAB® optimization toolbox (R2010a) with the algorithm being the SQP (Sequential Quadratic Programming) algorithm and the objective function defined based on the energy consumption of DC or brushless motors. As for the optimization constraints, both robots has constraints for ground contact, swing foot clearance, posture requirements and average walking speeds. For our 3D biped, we defined a line-foot contact model with the assumption that there are only two contact points on the stance foot. Unlike most contact models of bipedal robots, this model can even prevent possible yaw movements of the stance line foot. For both biped, the average walking speed is the only equality constraint, and the numbers of inequality constraints are 7 for the 5-link robot and 11 for the 8-link robot.

As for elastic couplings, they are added to both the planar biped and the 3D biped in form of linear torsion springs. For the planar biped, there are two coupling cases, namely, *2D Coupling Case I* and *II*. In *2D Coupling Case I*, a linear torsion spring is mounted between two thighs. In *2D Coupling Case II*, two linear torsion springs are installed connecting two thighs respectively to the torso. For the 3D biped, there are three coupling cases, namely *3D Coupling Case I*, *II* and *III*. In *3D Coupling Case I*, a torsion spring is added to connect the movements of two thighs in the sagittal plane. In *3D Coupling Case II*, two torsion springs are used to build connections between the movements of two thighs and the movement of the pelvis in the coronal plane. In *3D Coupling Case III*, the ideas of *3D Coupling Case I* and *II* are combined, and three torsion springs are installed in both the sagittal plane and the coronal plane. The optimized gaits with elastic couplings are obtained by adding spring constants (stiffness and unloaded positions) to optimization parameters. In all cases, the walking speeds investigated are in the range from 0.2 m/s to 1.5 m/s, and the stability and validity of optimized periodic gaits are checked numerically.

The most important optimization results are briefly summarized below. For the planar biped without elastic couplings, the energy cost ranges from 42.6 N^2ms (at 0.2 m/s) to 3161 N^2ms (at 1.5 m/s). By applying two different configurations of torsion springs to the hip joints, the maximum cost drops respectively to 384 N^2ms for *2D Coupling Case I* and 329 N^2ms for *2D Coupling Case II*, meaning that both spring configurations can significantly reduce the energy cost of the planar biped. In both cases, the gaits of the planar biped are more upright than those in the case with no coupling, and the step frequency is shown to be positively relevant and close

to the reference step frequency, which is twice the value of the natural frequency of the pendulum formed by the swing leg.

For the 3D biped without elastic couplings, *3D Optimization Case II* outperforms *Case I* with the energy cost ranges from 239 N^2ms (at 0.3 m/s) to 3155 N^2ms (at 1.5 m/s). *3D Optimization Case I* is only effective at high speeds with the maximum energy cost being 3300 N^2ms (at 1.5 m/s), but the minimum energy cost is 975 N^2ms (at 0.6 m/s). This indicates that the coronal dynamics and sagittal dynamics of our 3D biped are highly coupled, especially at low speeds. By adding elastic couplings to the sagittal hip joints, the maximum energy cost is reduced to 475 N^2ms in *3D Coupling Case I*, and for a wide range of speeds from 0.35 m/s to 1.0 m/s the energy cost is around 200 N^2ms. On the other hand, the effect of adding elastic couplings to the coronal hip joints in *3D Coupling Case II* is comparatively limited, with the maximum energy cost being 2579 N^2ms. However, the minimum energy cost in *3D Coupling Case II* is reduced to 132 N^2ms, which is smaller than the minimum energy cost 198 N^2ms in *3D Coupling Case I*. The lowest energy cost is obtained by *3D Coupling Case III*, of which the maximum energy cost is 367 N^2ms. In addition, for a wide speed range from 0.35 m/s to 0.8 m/s the energy cost is only around 75 N^2ms. These data suggest that, for our 3D biped, the elastic couplings in the sagittal plane play a central role in saving energy and that the elastic couplings in the coronal plane cannot be neglected if we wish to reduce the energy cost even further. Apart from the benefit of energy efficiency, *3D Coupling Case I* and III also have gaits that are more similar to human gaits (featured with upright postures, mild lateral movements and small maximum swing foot clearance) than the gaits in the other cases of our 3D biped.

7.2 Future Work

After three years of research, resulting in this thesis, some questions concerning dynamic walking and elastic couplings of both 2D and 3D bipeds have been answered. However, these answers also led to many new questions and ideas that are appealing for future research.

- **Additional DoFs:** Among many possible ways of adding DoFs to our 3D biped, we would prefer to add one rotational DoF to each hip joint so that these hip joints can have yaw movements. The reasons for adding these two additional DoFs include: (1) to reduce the lateral swing and impact shock of our 3D biped through the yaw rotation of hip joints; (2) to design control laws for steering; (3) to study optimal gaits of 3D bipeds walking in circles with different radiuses.

- **Different mechanical and electrical designs:** For instance, we can add features like rolling knees, swinging arms, toe rotations, nonlinear springs and so on. In this thesis, we have studied theoretical appeals of adding elastic couplings parallel to the corresponding actuators. In practice, it is of great

interest to find elastic actuators with potential for realizing the theoretical reduction of energy cost in real humanoid robots.

- **Control system robustness:** Although the ZMP position are considered in the gait optimization for our 3D biped, there is no regulation of ZMP in our control law. As a result, our 3D biped might not remain stable if there were large lateral disturbances. Therefore, we are interested in improving the robustness of our 3D biped against these disturbances by testing different controlled outputs and enhancing our control methods.

- **Optimization algorithm:** In this thesis, we use the SQP algorithm to realize gait optimization. According to our experience, the optimization programs based on the SQP algorithm are highly satisfactory at finding optimal gaits for our planar biped. However, the performance of these programs deteriorates when we need to find optimal gaits for our 3D biped. As such, we are thinking of testing other optimization algorithms to make gait optimization more efficient for 3D bipeds.

- **Foot mass:** Out of consideration for simplifying dynamic model and reducing optimization parameters, we have made the assumption that the line feet of our 3D biped are massless. However, our method also has the potential to be utilized in controlling and optimizing the gaits of bipedal robots with feet that have mass and contact surfaces. This can be done by considering the rotational DoF about the stance line foot as another DoF of the stance ankle joint, but in doing so it is necessary to study swing foot control.

8. RÉSUMÉ EN FRANÇAIS : OPTIMISATION DE LA MARCHE D'UN ROBOT BIPÈDE 3D À 8 CORPS

8.1 ***Introduction***

Comme d'autres robots à pattes, les robots bipèdes sont susceptibles de surpasser les machines à roues grâce à leur aptitudes de se déplacer sur différents types de terrains. En outre, des études en biomécanique ont montré que, la stature bipède a permis à l'homme de parcourir de longs trajets avec une grande efficacité energétique, ce qui a facilité sa survie. Cependant, comparés aux êtres humains, la plupart des robots bipèdes actionnés consomment beaucoup d'énergie. Cela limite énormément leur utilisation.

Motivation

Avant ce projet de recherche, Dr. Mathieu Hobon a déjà étudié la modélisation et l'optimisation de la marche d'un robot bipède avec un tronc, deux cuisses, deux tibias, et deux pieds. Ce robot a deux genoux roulants de cinématique similaire à celle d'êtres humains. Les résultats de simulation ont démontré les avantages apportés par ces genoux par rapport aux genoux à liaison rotoïde [3, 4]. Sur la base des résultats obtenus en optimisation de la marche de ce robot, l'objectif de départ pour notre projet de recherche est triple: (1) introduire davantage de degrés de liberté, de corps et de structures dans un robot bipède, (2) étudier les allures de marche optimales dans un espace tridimensionnel avec des méthodes de commande correspondantes, et (3) comparer les résultats d'optimisation du robot bipède 2D à ceux du robot bipède 3D.

Ce travail de recherche s'est inspiré des résultats obtenues sur le robot bipède RABBIT localisé à Grenoble, en France [5] et des travaux pionniers dans [6, 7]. Le robot RABBIT est sous-actionné et donc la méthode ZMP ne s'applique pas pour sa commande. Sa commande se fonde sur la linéarisation par retour d'état et la dynamique des zéros hybride [8]. Les résultats expérimentaux [5] et les résultats d'optimisation [8] ont clairement démontré la possibilité d'atteindre des allures dynamiques 2D. Comme les résultats correspondants d'optimisation concernant des robots bipèdes dans un espace tridimensionnel sont relativement rares, nous nous sommes fixés comme objectif l'optimisation des allures de marche 3D.

Développements actuels des robots bipèdes

L'histoire moderne concernant des robots bipèdes a débuté dans les années 1960. Les acquis majeurs sont venus de trois continents: l'Asie, l'Amérique du Nord et l'Europe.

En Asie, Ichiro Kato et son équipe ont ouvert la voie vers les études de la robotique bipède à l'université Waseda en construisant le robot WL-1 en 1967. Dans les quelques années suivantes, ils ont construit les robots WL-3, WABOT-1, etc [9]. À cette époque, la performance des robots bipèdes était évaluée en fonction de la durée de chaque pas. Par exemple, le robot WL-5 met 45 secondes pour chaque pas, alors que sa version ultérieure WL10-RD a réussi à diminuer cette durée à 1,3 secondes [10]. Le dernier né des robots bipèdes à Waseda est le WABIAN-2. Il a 41 degrés de liberté et ses articulations sont similaires à celles des humains [11, 12]. À côté de l'université Waseda, les entreprises japonaises comme Honda et Kawada sont également renommées pour leurs robots bipèdes de pointe tels que le robot ASIMO [13] et le robot HRP-4 [22]. Malgré la position de leader du Japon en terme de robotique humanoïde, d'autres pays d'Asie comme la Corée du Sud et la Chine ont rattrapé leur retard au cours des dernières années, KHR-3 en Corée du Sud [23] et BHR-2 en Chine [24] méritent d'être mentionnés.

En Europe, beaucoup de pays participent à des projets de recherche sur les robots bipèdes. Conçu et fabriqué en Allemagne, le robot LOLA, avec une vitesse de marche supérieure à $0,83\,\mathrm{m/s}$, est peut-être le plus impressionnant robot humanoïde en Europe. Les caractéristiques distinctives de LOLA incluent la structure cinématique redondante (chaque jambe a 7 degrés de liberté) et sa construction légère (55 kg pour une taille de $1,80\,\mathrm{m}$) [25]. En France, le robot RABBIT est un robot bipède 2D à 5 corps avec des pieds ponctuels. Ce robot est important dans l'histoire des robots bipèdes car il est sous-actionné et est capable de marcher à $1,0\,\mathrm{m/s}$ sans utiliser les méthodes de contrôle fondées sur le ZMP (Zero Moment Point) [5]. D'autres robots bipèdes européens sont intéressants: le robot italienne iCub caractérisé par ses logiciels ouverts et sa capacité cognitive [31, 32], le robot belge LUCY caractérisé par ses muscles artificiels pneumatiques [33] et le robot néerlandais Dribbel caractérisé par son mécanisme de verrouillage sur les genoux.

En Amérique du Nord, Marc Raibert est le premier chercheur qui a réalisé une percée remarquable sur des robots à pattes. Il a conçu une série des robots sautillants avec une, deux ou quatre jambes. La version bipède fabriquée en 1989 peut même faire un saut périlleux [34]. Dans les années 1960, McGeer a entrepris un travail de pionnier concernant la conception des robots bipèdes passifs. Il a réussi à fabriquer un robot compas passif et un robot bipède passif avec des genoux [35]. En outre, il a aussi diffusé parmi les roboticiens l'application de la méthode de Poincaré pour analyser la stabilité orbitale. Ensuite, Steven H. Collins et son équipe ont réussi à réaliser un robot bipède passif en 3D avec l'aide des bras en contre-balancement [36]. En référence au robot RABBIT, MABEL et ATRIAS ont été conçus et fabriqués à l'université du Michigan et à l'université d'État de l'Oregon. MABEL est encore un robot bipède 2D, mais il peut courir à $3\,m/s$ et a des composants élastiques [37, 38].

ATRIAS est un prototype de robot bipède sous-actionné de même taille que l'être humain. Il peut marcher et courir dans un espace tridimensionnel [39, 40].

Méthodes de contrôle de la marche bipède

On peut distinguer trois types de marche: (1) la marche quasi-statique actionnée, (2) la marche dynamique non actionnée ou assistée, et (3) la marche dynamique actionnée. Cette classification n'est peut être pas exhaustive et les frontières entre ces trois types pourraient ne pas être décisives non plus mais elle représente néanmoins certaines des orientations de recherche dominantes de la marche bipède.

Beaucoup de robots humanoïdes de nos jours tels que HRP-4 [20] et Honda ASIMO [13] ont attiré l'attention du public sur leur importante intégration de technologies de pointe et leur intelligence artificielle étonnante, mais fondamentalement, la marche bipède qu'ils ont montrée n'est pas tout à fait dynamique, surtout en comparaison à la marche humaine. En fait, la dynamique de ces robots est limitée par des conditions d'équilibre fondées sur le ZMP [44]. La condition ZMP stipule que tant que le ZMP d'un robot reste contenu dans le polygone de sustentation, le robot ne tombe pas. Pour les chercheurs qui étudient la marche quasi-statique, cette condition doit toujours être respectée malgré le fait que pour la marche dynamique, la condition de ZMP est parfois violée à chaque pas durant un certain temps. Du fait de sa simplicité, le ZMP a plusieurs variantes - qui incluent le FRI (Foot Rotation Index) [45] et le CoP (Center of Pressure) [46]. Historiquement, la condition ZMP est étroitement liée à plusieurs simplifications basées sur des modèles de pendules inverses tels que le modèle linéaire du pendule inversé (LIPM), le LIPM avec la compensation de gravité [51] et le LIPM avec trois masses (3MLIPM) [52]. Les exemples de réussite mettant en œuvre cette méthode sont: HRP-4 [20], ASIMO [13], LOLA [25], BIP-2000 [29], Hubo [23], BHR-2 [24], etc. Malgré ces progrès remarquables, les limites inhérentes à l'adoption de cette simplification sont de plus en plus reconnues. En plus de limiter l'efficacité énergétique, les allures conçues à l'aide de cette méthode nécessitent des mises au point, donc le succès sur un robot n'est pas entièrement transférable sur un autre. Par ailleurs, la condition de ZMP n'est pas suffisante pour assurer la stabilité asymptotique des allures périodiques [50].

La marche dynamique non actionnée se réfère à la marche effectuée par des robots bipèdes passifs. Ces robots bipèdes ne disposent pas d'actionneurs et donc leur locomotion est purement due à l'interaction entre leur structure mécanique et l'environnement. Ceci rend la locomotion des robots passifs dynamique et économe en énergie. Dans les études en simulation des robots bipèdes passifs, la stabilité des allures est vérifiée par l'estimation des valeurs propres de la linéarisation jacobienne de l'application de Poincaré, mais ce test de stabilité n'a aucun lien avec des allures passives. Les travaux pionniers dans cette voie sont présentés dans [63, 35], [36], et [64, 65]. La marche dynamique assistée est réalisée par l'ajout d'un ensemble réduit d'actionneurs à des robots bipèdes passifs afin que la perte d'énergie puisse être compensée. Un bon exemple est le robot fabriqué à l'université de technologie de Delft aux Pays-Bas. Ce robot est caractérisé par ses actionneurs pneumatiques

appelés muscle de McKibben [67]. Les caractéristiques de stabilité de ce robot ont été analysées dans [69] et le rejet de perturbation a été étudié dans [70]. Le défaut majeur des robots dynamiques non actionnés ou assistés est leur autonomie limitée. Ainsi, il est impossible pour ces robots de monter des escaliers, de tourner ou de courir.

La marche dynamique actionnée est difficile à réaliser parce qu'elle est non linéaire, théoriquement instable et multi-entrées multi-sorties (MIMO). En plus, la dynamique correspondante est hybride et variant dans le temps. Afin d'améliorer l'efficacité énergétique, il est nécessaire de faire usage d'un moment balistique et d'énergie potentielle de gravité. Ainsi, les méthodes basées sur la méthode du ZMP sont en général incapables de produire des allures dynamiques.

Ces dernières années, beaucoup de chercheurs ont étudié les systèmes hybrides dans lesquels la dynamique continue et un événement discret sont étroitement liés [6, 77, 78]. Les difficultés concernant les systèmes hybrides comprennent les stratégies liées à leur grande dimension [79], l'analyse de la stabilité [80], la recherche du contrôle optimal [81], etc. Les travaux de Grizzle et al. [6] portent sur un robot bipède 2D à 3 corps avec un degré de sous-actionnement et des pieds ponctuels et ont proposé l'idée de réaliser une allure asymptotiquement stable en utilisant des techniques de la dynamique des zéros et un contrôleur en temps fini. Cette méthode a aussi été mis en œuvre dans un robot bipède 2D à 5 corps [7], et des extensions de cette méthode peuvent être trouvés dans [82, 5].

Pour les robots bipèdes 2D, les principaux avantages de cette méthode sont: premièrement, l'invariance hybride peut être facilement réalisée; deuxièmement, la stabilité peut être validée en calculant l'application scalaire restreinte de Poincaré à forme fermée [84]. Par conséquent, l'optimisation peut être effectuée directement sur les paramètres de la commande par rapport à certains critères d'optimisation et donc une allure dynamique et une commande correspondante peuvent être déterminés en même temps. La validation expérimentale de la dynamique des zéros hybride a été obtenue sur les robots RABBIT [5, 85] et MABEL [37].

Par rapport aux travaux sur les robots bipèdes 2D, l'étude de la dynamique des zéros et des contraintes virtuelles n'en sont qu'à leurs débuts pour les robots bipèdes 3D. Dans les travaux de Chevallereau et al. [91], la marche asymptotiquement stable d'un robot bipède 3D à 5 corps est réalisée en utilisant trois stratégies: une condition de stabilité, un contrôleur basé sur des évènements et une sélection de sorties appropriées. La stabilité des allures est évaluée en calculant l'application tridimensionnelle de Poincaré. Parmi ces trois stratégies, l'idée de concevoir des contrôleurs basés sur des événements discrets a été étendue à la commande d'un robot bipède 3D nommé Atrias [40, 39].

Une autre approche intéressante pour étendre la méthode de la dynamique des zéros hybride et des contraintes virtuelles est appelée la réduction de la fonction routhienne. Cette méthode est très utile pour la marche quasi-tridimensionnelle réalisée durant l'expérimentation [94] et en simulation [92, 93]. L'idée de base est de découpler la dynamique frontale et sagittale d'un robot bipède 3D afin que les méthodes de commande des robots bipèdes 2D puissent être appliquées à des robots

bipèdes 3D. La principale limite de cette méthode réside dans le fait qu'elle ne peut découpler les degrés de liberté dans le plan frontal que pour les chevilles. En outre, les robots bipèdes 3D doivent être pleinement actionnés afin que cette méthode soit efficace. Ceci élimine les avantages des méthodes de commande synthétisées pour les robots bipèdes 2D sous-actionnés. Enfin et surtout, il n'est pas certain que l'efficacité énergétique subsiste après la réduction de la fonction routhienne.

Malgré ces efforts, il reste encore de nombreux défis à relever. L'un des défis consiste à rechercher des allures optimales associées à l'application des contraintes virtuelles. En effet, il s'agit de savoir si la fonction de coût de la consommation d'énergie est vraiment minimisée. Cependant, la complexité de l'obtention des allures optimales augmente considérablement quand on essaie d'optimiser des allures de robots bipèdes 3D avec deux ou plusieurs degrés de sous-actionnement. En outre, les conditions de stabilité asymptotique dépendent du choix spécifique des contraintes virtuelles [99, 91]. Ces difficultés pourraient influencer négativement la qualité des allures optimisées.

D'autres méthodes pour réaliser la marche dynamique actionnée sont également disponibles, y compris le contrôle d'un modèle virtuel [72], le calcul des couples de contrôle dépendant de l'état des éléments passifs virtuels [73, 74], et l'application des techniques d'apprentissage automatique comme un réseau neuronal [75, 76].

Allures optimales des robots bipèdes

Un des principaux défis de la locomotion bipède est de trouver des paramètres optimaux de contrôle qui satisfont certaines conditions comme la vitesse de mouvement tout en minimisant l'énergie nécessaire pour effectuer la marche. En raison des corrélations imprévisibles entre les paramètres de la marche, l'optimisation de la marche est un problème ouvert dont les résultats analytiques sont rares et seulement limités à quelques cas simples [100]. Dans la plupart des cas, la résolution numérique est la seule option. Certaines des premières tentatives datent des années 1970 [101]. En général, la recherche des allures optimales se ramène à un problème d'optimisation sous contraintes qui consiste à sélectionner des paramètres à optimiser, des fonctions objectifs, des algorithmes et des contraintes.

Tout d'abord, le choix des paramètres à optimiser n'est pas unique. Des coordonnées cartésiennes et des coordonnées articulaires peuvent toutes être utilisées pour paramétrer les allures de marche. Par exemple, dans les premiers travaux [102], des couples constants par morceaux sont choisis comme paramètres d'optimisation. Cependant, lorsque les couples sont traités comme des courbes paramétrées à optimiser, il est nécessaire de résoudre le problème dynamique inverse afin de trouver les coordonnées articulaires correspondantes et vérifier si les allures générées sont cycliques. Au début de la robotique bipède, les coordonnées cartésiennes de la hanche et du pied oscillant ainsi que l'angle du tronc ont été utilisés comme paramètres à optimiser [103], mais l'inconvénient de cette méthode est la nécessité d'inverser le modèle géométrique pour définir les trajectoires de référence des articulations. En raison de ce problème, les chercheurs utilisent aujourd'hui des coordonnées articulaires dont l'évolution peut être définie par des polynômes [103], des fonctions splines

cubiques [104], des courbes de Bézier [84], des développements en série de Fourier [105], des fonctions canoniques de la marche humaine [106, 107].

Il existe également de multiples critères énergétiques. Au lieu d'utiliser l'énergie mécanique [65], le coût de l'énergie peut également être défini comme l'intégrale de la valeur absolue du travail des forces et des couple extérieures [108]. Cependant, cette définition n'a pas de relation directe avec la consommation d'énergie des actionneurs en particulier. Une fonction coût plus courante est donnée dans [102] où le coût est défini comme l'intégrale de la norme 2 du couple pour un déplacement unitaire. Cette définition est basée sur le fait que, pour des moteurs à courant continu (ou des moteurs synchrones à aimants permanents), la plus grande partie de la consommation d'énergie est due à l'effet Joule dans les bobinages.

La plupart des algorithmes pour l'optimisation de la marche peuvent être classés en deux catégories: les méthodes du gradient et les méthodes de recherche directe. La différence entre les deux dépend de la nécessité du calcul des dérivés. Dans les travaux remarquables de Cabodevila et Abba [110], trois méthodes de recherche directe sont testées pour la recherche des allures optimales, y compris la méthode de Nelder-Mead, la méthode génétique et le recuit simulé. Les applications supplémentaires de ces méthodes peuvent être trouvées dans [4, 111, 112]. Bien que ces méthodes soient très flexibles en raison de leur bonne tolérance au bruit, elles sont coûteuses en temps de calcul. Afin d'augmenter la vitesse de convergence, plusieurs chercheurs ont essayé des méthodes du gradient telles que la méthode de programmation quadratique séquentielle (SQP) [84, 113, 114, 115], la méthode du lagrangien augmenté [116], et la méthode des points intérieurs [117]. Parmi eux, la méthode la plus courante est la méthode SQP, qui a été utilisé dans l'optimisation des allures pour les robots bipèdes 2D [84, 113, 115] et les robots bipèdes 3D [114, 118]. D'autres algorithmes disponibles comprennent l'algorithme de tir [102], l'algorithme d'essaim particulaire [119], etc.

Les contraintes pour l'optimisation des allures sont imposées par des conditions telles que les limitations articulaires, la stabilité des allures, le contact unilatéral avec le sol, la vitesse moyenne de marche, la périodicité, etc. Pour l'optimisation traditionnelle de la marche basée sur les trajectoires en boucle ouverte, la vérification de la stabilité n'est pas incluse dans le processus d'optimisation. Toutefois, pour les robots bipèdes avec un degré de sous-actionnement, il est possible de vérifier la stabilité en remplaçant le temps avec un paramètre scalaire dans les trajectoires articulaires [115] ou en utilisant la méthode des contraintes virtuelles [84]. Un sous-produit positif de ces méthodes est que la contrainte de la périodicité n'est plus nécessaire. Une autre contrainte intéressante est la contrainte de frottement pour le pied d'appui. Pour la plupart des études sur les allures optimales des robots bipèdes 3D [114], la possibilité de rotation en lacet du pied d'appui n'est pas prise en compte dans leur modèle de contact. Ce problème est difficile à aborder car le calcul de la répartition de pression au sol est difficile et coûteux en temps. Dans cette thèse, nous allons développer un modèle simplifié qui peut inclure cette contrainte (Section 5.2.4).

En raison de la puissance limitée de calcul, presque toutes les premières tentatives

d'optimisation de la marche bipède sont menées sur les modèles 2D, et certains utilisent même des simplifications de modèle dynamique [102]. Jusqu'à maintenant, différents cas d'allures ont été étudiés, y compris la rotation des pieds [120], des pieds ponctuels [115], le tronc en deux parties [121], des genoux roulants [3], et des bras mobiles [122]. Compte tenu de l'évolution des ressources informatiques, il y a de plus en plus de résultats d'optimisation des allures obtenus pour des modèles de robots bipèdes 3D [114]. Les cas étudiés comprennent des pieds ponctuels [123], la rotation des orteils [118], des bras mobiles [124], etc. Cependant, en comparaison avec les cas 2D, les résultats de l'optimisation pour les robots bipèdes 3D sont limités en quantité et qualité. Par exemple, dans la plupart des cas, on doit utiliser des méthodes d'interpolation pour illustrer la variation du coût de l'énergie en fonction de la vitesse moyenne de marche [123], et dans certains autres cas, des résultats sont fournis pour une seule vitesse de marche [124]. En outre, il y a peu d'études qui évaluent la relation entre les optimisations des robots bipèdes 2D et des robots bipèdes 3D. Ces problèmes seront abordés par la suite dans cette thèse.

Couplages élastiques

Lorsqu'il s'agit d'améliorer l'efficacité énergétique, par analogie avec les muscles et les tendons chez l'Homme, des couplages élastiques représentent une option attrayante. Cela vaut non seulement pour les robots bipèdes mais également pour tous les robots à pattes [125, 126, 127, 128]. En fait, la plupart des systèmes biologiques possède des muscles et des tendons qui assurent la fluidité de la marche ainsi que le stockage d'énergie [129]. Selon [130], ces structures élastiques dans les systèmes biologiques à pattes ont principalement trois objectifs: (1) agir comme un coussin élastique pour amortir les chocs; (2) fonctionner comme une échasse sauteuse pour rediriger le mouvement vertical du centre de masse; (3) servir de ressorts de rappel pour stocker l'énergie pendant la redirection de la jambe mobile. En exploitant pleinement la dynamique naturelle et des composants élastiques conformément à (2) et (3), les systèmes biologiques comme les humains, peuvent se déplacer en mode de résonance à faible consommation d'énergie [131, 132]. Étant donné que des mouvements efficaces de marche ont longtemps été recherchés par de nombreux roboticiens, il devrait être intéressant d'appliquer cette approche bio-inspirée à la conception de robots bipèdes.

En effet, l'application de composants élastiques dans des robots bipèdes remonte aux années 80 où Marc Raibert et son équipe ont construit un robot bipède 2D capable de courir. Ce robot est équipé de ressorts pneumatiques pour le recyclage d'énergie du mouvement vertical du centre de masse [133]. Des méthodes similaires ont également été appliquées au robot bipède MABEL [37]. Cependant, ces exemples utilisent des couplages élastiques seulement comme des échasses sauteuses.

Pour la marche bipède, le mouvement vertical du centre de masse est assez limité. Donc dans ce cas le but principal des couplages élastiques est d'accélérer ou de ralentir le mouvement pendulaire de la jambe mobile, ce qui est également observée chez l'homme [136, 137]. Néanmoins, des couplages élastiques agissant comme des ressorts de rappel ont seulement été utilisés pour améliorer la course dynamique

[138, 139]. Ce n'est que plus tard que des couplages élastiques ont été appliqués sous forme d'un ressort au niveau des hanches à un robot bipède passif pour stabiliser le mouvement latéral [70]. Par la suite, les recherches dans cette direction ont retenu l'attention de roboticiens. Par exemple, des ressorts de hanche ont commencé à être utilisé pour ajuster la fréquence de pas [140] et pour estimer la relation entre la vitesse de marche et la longueur de pas [141]. Selon [142], la perte d'énergie lors de l'impact est la principale cause la consommation d'énergie métabolique pour la marche humaine. Certains chercheurs ont également tenté d'utiliser des couplages élastiques pour réaliser des robots bipèdes passifs avec des allures sans impact et sans aucune consommation d'énergie [64, 65]. En plus d'influencer la fréquence de pas et l'efficacité énergétique, des ressorts de hanche sont également utilisés pour empêcher des robots bipèdes passifs de tomber vers l'avant [140]. Une étude révèle que la posture droite pour des robots bipèdes passifs est possible uniquement avec des ressorts correctement installés au niveau des articulations des hanches [144].

En dépit de ces progrès, ces études ne sont valables que pour des robots bipèdes passifs dans un environnement hautement contrôlé. Pour des robots bipèdes actionnés, certains chercheurs ont tenté d'appliquer des forces virtuelles générées par des ressorts virtuelles et des amortisseurs virtuels [73, 72]. Cependant, il n'est pas certain que des composants passifs virtuelles puissent être remplacés par des composants physiques pour le recyclage d'énergie. En outre, il est coûteux en temps d'évaluer le critère d'énergie à une vitesse donnée parce que le manque de condition de périodicité dans ces méthodes obligent les chercheurs à simuler des dizaines de pas pour obtenir la vitesse moyenne et le critère moyen d'énergie. Il y a aussi quelques robots bipèdes flexibles qui utilisent des approches heuristiques [145, 146], mais les résultats expérimentaux ainsi obtenus ne peuvent pas vraiment démontrer les avantages des composants élastiques parce que des approches heuristiques ne peuvent pas exploiter pleinement la dynamique naturelle des robots bipèdes. Tout bien considéré, il semble que l'optimisation d'un pas périodique est une approche viable dans l'analyse de l'avantage de l'ajout de composants élastiques aux robots bipèdes.

Actuellement, les recherches dans cette voie sont principalement limitées à des robots bipèdes 2D. En utilisant les trajectoires de référence comme fonctions du temps, les allures optimales d'un robot bipède sans genoux et à 3 corps ont déjà été présentées [147, 148]. Néanmoins, les robots bipèdes sans genoux sont loin d'être des robots humanoïdes. Des études similaires ont également été menées sur un robot bipède à 7 corps composé d'un tronc, deux cuisses, deux tibias et deux pieds [149]. Dans ce cas, des ressorts sont ajoutés aux articulations des hanches, des genoux et des chevilles. Cependant, le modèle de transition sans impact au cours de la phase instantanée de double appui ne peut pas représenter la situation de la marche chez l'homme ou chez les robots bipèdes. En dehors de toutes ces lacunes, tous les résultats de l'optimisation pour les exemples ci-dessus sont obtenues grâce à l'optimisation des paramètres des trajectoires de référence comme fonctions du temps, et donc la condition de stabilité n'est pas considérée dans ces méthodes. Afin d'assurer la stabilité des allures optimisés, de récentes études fondées sur la

linéarisation par retour d'état et les contraintes virtuelles ont été menées sur les couplages élastiques d'un robot bipède 2D à 3 corps [150] et d'un robot bipède 2D à 5 corps [109]. Bien que les résultats livrés par cette étude couvrent différentes combinaisons de ressorts, cette étude s'est limitée aux robots bipèdes 2D, et en plus, la définition du critère est trop dépendante des caractéristiques des actionneurs pour être comparée avec d'autres résultats.

Bien que les résultats présentés dans ce mémoire ne sont que théoriques, il y a déjà quelques études publiées concernant la réalisation des couplages élastiques dans des robots bipèdes physiques avec des méthodes de contrôle viables [151, 152]. Afin d'améliorer l'efficacité énergétique de robots bipèdes à des vitesses différentes, certains chercheurs ont étudié les moyens possibles pour modifier des raideurs de ressort et des positions de repos pendant le fonctionnement des robots. Jusqu'à présent, certains actionneurs élastiques ont déjà été développés, tels que le MACCEPA [153, 154] et le Jack Spring™ [155] qui permet le réglage de position de repos d'un élément élastique en série. Une autre méthode consiste à modifier des raideurs par réglage des pré-tensions de ressorts non-linéaires. Cette approche a été utilisée dans le VSSEA (actionneurs élastiques en série avec des raideurs variables) [156] et le AMASC [157]. En conclusion, sur la base des progrès technologiques, il est intéressant d'étudier l'avantage d'ajouter des couplages élastiques à des articulations de hanche à la fois pour des robots bipèdes 2D et pour des robots bipèdes 3D.

Contributions de cette thèse

Les contributions de cette thèse sont:

1. L'extension de la méthode de contrôle [84] à des scénarios 3D.
2. Le modèle d'impact et le modèle de contact pour les robots bipèdes 3D avec des pieds sans masse à contact linéique.
3. Les sorties symétriques pour atteindre une meilleure interpolation géométrique de la commande de la posture et de la jambe mobile.
4. La comparaison des allures optimisés entre un robot bipède 2D et un robot bipède 3D avec les mêmes paramètres de modèle dans le plan sagittal.
5. La méthode d'utilisation des paramètres optimisés d'un robot bipède 2D comme initialisation ou comme paramètres sagittaux pour faciliter le processus d'optimisation du robot bipède 3D correspondant.
6. Les études détaillées concernant les couplages élastiques au niveau des articulation de hanche à la fois pour des robots bipèdes 2D et pour des robots bipèdes 3D.

8.2 Méthodologie

Ce chapitre permet d'introduire les outils théoriques concernant la mécanique lagrangienne, la linéarisation par retour d'état, la stabilité des systèmes hybrides et l'optimisation numérique. Les applications de ces théories dans les chapitres suivants comprennent : (1) la génération des modèles dynamiques pour différents robots bipèdes, (2) l'application d'une loi de commande non linéaire en utilisant des contraintes virtuelles, (3) l'analyse de la stabilité des allures données, et (4) l'obtention des allures optimisées avec une haute efficacité énergétique ou selon d'autres critères quadratiques satisfaisants.

Mécanique lagrangienne

L'approche Euler-Lagrange a été largement appliquée après sa découverte dans les années 1750 par Euler et Lagrange pendant leurs études du problème tautochrone. Comparé à l'approche Newton-Euler, elle est capable de traiter un robot à plusieurs corps dans son ensemble au lieu de considérer chaque corps de ce robot à tour de rôle. En utilisant l'approche Euler-Lagrange, on peut obtenir les modèles dynamiques d'une manière simple.

Si le robot est constitué de corps rigides et de composants élastiques idéaux qui ne peuvent exercer que des forces conservatives, les équations de Lagrange peuvent être définis comme dans (2.2). Afin de calculer le lagrangien $\mathcal{L}$, on a besoin de connaître l'énergie cinétique $\mathcal{K}$, l'énergie potentielle gravitationnelle $\mathcal{V}_g$ et l'énergie potentielle élastique $\mathcal{V}_e$. Ces variables peuvent être calculées par les équations (2.8), (2.10) et (2.12). Les équations de Lagrange peuvent ensuite être écrites sous la forme matricielle comme dans (2.13). Les moments d'inertie des rotors des moteurs sont également pris en compte dans l'équation (2.16). Les équations supplémentaires pour calculer les forces extérieures et les couples externes sont données dans (2.19) et (2.22).

Linéarisation par retour d'état

La linéarisation par retour d'état est une approche courante pour contrôler des systèmes non linéaires. L'idée principale de cette méthode est de transformer algébriquement des systèmes non linéaires en des systèmes linéaires équivalents de sorte que ces systèmes non linéaires peuvent également utiliser des méthodes linéaires de contrôle [160]. Cette procédure comporte deux opérations : la transformation non linéaire de coordonnées et le retour d'état non linéaire [165]. La condition préalable pour cette approche est que la transformation de coordonnées soit un difféomorphisme. En d'autres termes, la transformation ne doit pas seulement être réversible, mais cette transformation et sa réciproque doivent être lisses [160].

Après la linéarisation par retour d'état, un système non linéaire défini par les équations (2.25) et (2.26) est maintenant linéaire et peut être représenté par les équations (2.27) et (2.28). La linéarisation entrée-sortie est l'une des approches pour réaliser la linéarisation par retour d'état. L'objectif de cette approche est de linéariser l'application entre l'entrée transformée v_s et la sortie y [161]. Ainsi, on

peut utiliser un contrôleur linéaire pour le modèle entrée-sortie linéarisée. Le sous-système qui n'est pas linéarisé s'écrit comme dans l'équation (2.29). Dans certains cas, on peut atteindre les objectifs de contrôle par l'adoption d'une loi de commande non linéaire par retour d'état statique sous la forme (2.30).

En fonction du nombre des entrées et des sorties, les systèmes de commande peuvent être classés en deux types: les systèmes SISO (possédant une seule entrée et une seule sortie) et les systèmes MIMO (possédant plusieurs entrées et plusieurs sorties). Dans ces deux cas, les processus sont similaires. Premièrement, des systèmes non linéaires sont transformés en des formes normales données par l'équation (2.35) pour des systèmes SISO et par l'équation (2.45) pour des systèmes MIMO. En utilisant la loi de commande non linéaire par retour d'état statique de (2.36) et (2.49) pour ces deux types de systèmes, l'application entre l'entrée v_s et la sortie y est linéarisée. Puis la loi de commande linéaire par retour d'état est définie dans les équations (2.37) et (2.52) pour stabiliser le sous-système défini par η. En choisissant les paramètres appropriés κ_i, les variables d'état η tendent exponentiellement vers zéro, et l'équation (2.29) est transformée en l'équation (2.39) lorsque $t \to \infty$. L'équation (2.39) est connue sous le nom de la dynamique des zéros.

Stabilité des systèmes hybrides

Les systèmes hybrides sont des systèmes dynamiques constitués de processus continus interagissant avec ou supervisés par des processus discrets. Les systèmes impulsionnels sont une classe spéciale de systèmes hybrides. Ils sont composés d'une équation différentielle ordinaire, d'une surface de commutation, et d'une loi de réinitialisation. Pour la marche bipède, nous nous sommes principalement intéressés à déterminer l'existence et la stabilité des orbites périodiques de ces systèmes. Dans ce but, la méthode classique consiste à appliquer l'idée de l'application de Poincaré. La méthode de la section de Poincaré peut fournir les conditions nécessaires et suffisantes pour l'existence et la stabilité des orbites périodiques, mais il est impossible de déterminer analytiquement des applications de Poincaré pour un système robotique typique. En outre, les méthodes numériques disponibles d'estimation des valeurs propres sont généralement complexes. Pour cette raison, l'application restreinte de Poincaré est étudiée pour simplifier l'analyse de stabilité.

En utilisant des lois de commande par retour d'état comme celle définie dans (2.53), le système non linéaire déjà défini dans (2.25) peut être considéré comme un système autonome non linéaire (2.55) dans l'espace d'état $\mathcal{X}$. Pour des systèmes impulsionnels, nous pouvons définir une surface $\mathcal{S} \subset \mathcal{X}$ de co-dimension 1 sur laquelle le système autonome subit une transition discrète. Ainsi, un système autonome impulsionnel peut être représenté par Σ avec sa définition dans (2.56). Selon [83], le système autonome (2.56) est de classe C^1 si les hypothèses *HSH1-HSH5* (de la page 44) sont satisfaites. Un emsemble $\mathcal{O} \subset \mathcal{X}$ est une orbite périodiques du système (2.56) si $\mathcal{O} = \{\varphi(t) | t \geq t_0\}$ pour certaines solutions périodiques $\varphi(t)$ de (2.56). Si une solution périodique subit un événement d'impact, l'orbite périodique correspondante $\mathcal{O}$ n'est pas fermée, et sa clôture est représentée par $\bar{\mathcal{O}}$.

En système dynamique, une application de Poincaré, nommée en l'honneur de

Henri Poincaré, est une application définissant l'intersection d'une orbite périodique dans l'espace d'état d'un système dynamique avec un certain sous-espace de dimension moindre, appelé la section de Poincaré, transverse au flux du système. Pour l'étude des orbites périodiques avec des événements d'impact, il est naturel de choisir $\mathcal{S}$ comme la section de Poincaré. Ensuite, l'application de Poincaré $P : \mathcal{S} \to \mathcal{S}$ est définie comme dans (2.3.2).

Théorème 2.1: Si un système (2.56) est de classe C^1 et s'il a une orbite périodique $\mathcal{O}$ avec un singleton $x^* = \bar{\mathcal{O}} \cap \mathcal{S}$ et $L_f H(x^*) \neq 0$, alors les propositions suivantes sont équivalentes :

1. Le point fixe x^* de P est exponentiellement stable ;
2. L'orbite périodique $\mathcal{O}$ est exponentiellement stable.

La preuve de ce théorème est fournie dans [83]. Grâce à ce théorème, nous pouvons maintenant vérifier la stabilité exponentielle des orbites en linéarisant P au voisinage de x^* et calculer les valeurs propres correspondantes.

Considérons un système hybride Σ^ϵ (2.59) qui dépend d'un paramètre réel $\epsilon > 0$, et supposons que les hypothèses *HSH1-HSH5* sont satisfaites. Nous pouvons aussi supposer que les hypothèses structurelles *HS1-HS6* sont également satisfaites. Sur la base de ces hypothèses, l'évolution du système Σ^ϵ peut être limitée à la variété $\mathcal{Z}$, qui crée un système $\Sigma_{\mathcal{Z}}$ avec la dynamique restreinte (2.62). L'invariance de $\mathcal{Z}$ donne $P^\epsilon(\mathcal{S} \cap \mathcal{Z}) \subset \mathcal{S} \cap \mathcal{Z}$. Par conséquent, l'application restreinte de Poincaré, $\rho : \mathcal{S} \cap \mathcal{Z} \to \mathcal{S} \cap \mathcal{Z}$, est définie par (2.65).

Théorème 2.2: D'après les hypothèses *HSH1-HSH5* et *HS1-HS6*, il existe une variable $\bar{\epsilon} > 0$ telle que pour $0 < \epsilon < \bar{\epsilon}$ les propositions suivantes sont équivalentes :

1. Le point fixe x^* de ρ est exponentiellement stable ;
2. Le point fixe x^* de P^ϵ est exponentiellement stable.

La preuve de ce théorème est fournie dans [83]. Ce théorème montre que, pour un réel ϵ strictement positif, suffisamment petit, une orbite périodique exponentiellement stable de la dynamique restreinte est aussi une orbite périodique exponentiellement stable du modèle de pleine dimension.

Optimisation paramétrique

L'optimisation est une méthode importante dans les sciences de la décision et dans l'analyse des systèmes physiques. Afin de réaliser une optimisation, nous devons tout d'abord connaître l'objectif qui est une mesure quantitative de la performance du système étudié. L'objectif dépend alors de certains paramètres du système. Selon que les paramètres sont continus ou discrets, l'optimisation se subdivise en deux types : l'optimisation discrète et l'optimisation continue. Dans cette thèse, l'optimisation qui nous intéresse est continue. Selon qu'il y a des contraintes ou non sur les paramètres à optimiser, l'optimisation continue peut encore se subdiviser en deux types : l'optimisation continue sous contraintes et l'optimisation continue sans contrainte. Dans notre travail, nous nous concentrons uniquement sur l'optimisation continue sous contraintes en utilisant la programmation quadratique séquentielle.

Du point de vue mathématique, le but de l'optimisation sous contraintes est de

minimiser une fonction objectif soumise à des contraintes sur ses paramètres. Quand il s'agit de l'optimisation sous contraintes, l'approche générale consiste à transformer le problème en un sous-problème plus facile à résoudre. Le sous-problème est alors utilisé de façon itérative dans des algorithmes d'optimisation. Les premières approches d'optimisation nécessitent de convertir un problème sous contraintes en un problème fondamental sans contrainte en utilisant la technique de pénalisation. De cette façon, le problème sous contraintes est résolu en résolvant une suite de problèmes sans contraintes. Aujourd'hui, ces méthodes sont considérées comme inefficaces, et elles sont remplacées par les méthodes consistant à résoudre les équations de Karush-Kuhn-Tucker [162].

Pour les problèmes de programmation non linéaire (2.66), il existe trois types de conditions d'optimalité : (1) les conditions nécessaires du premier ordre, (2) les conditions nécessaires du second ordre, (3) les conditions suffisantes du second ordre. Les équations pour ces conditions sont fournies dans (2.69), (2.75) et (2.76). Dans l'optimisation sous contraintes, nous sommes souvent confrontés aux objectifs contradictoires de diminuer la fonction objectif et ceux de satisfaire les contraintes. Par conséquent, une fonction de mérite est définie dans (2.77) pour mesurer l'équilibre entre ces deux objectifs.

La programmation quadratique séquentielle est une des méthodes les plus efficaces pour l'optimisation sous contraintes non linéaires. La méthode est basée sur les travaux décrits dans [168, 169, 170]. Compte tenu de la description du problème dans (2.66), l'idée principale de SQP est de formuler un sous-problème de programmation quadratique (2.78) basé sur une approximation quadratique de la fonction de Lagrange (2.68).

Le principal avantage de l'application de cet algorithme pour générer des allures est sa robustesse vis-à-vis des résultats invalides. Au cours de ses itérations, l'algorithme SQP peut tenter de faire un pas qui échoue. Cela se produit lorsque la fonction objectif ou la fonction des contraintes non linéaires ne peut pas fournir des valeurs valides. Dans ce cas, l'algorithme tente de faire un pas plus petit.

Conclusion

Quatre fondements de la commande optimisée de la marche bipède ont été abordés dans ce chapitre. D'abord l'approche Euler-Lagrange et les équations supplémentaires pour calculer les forces extérieures et les couples externes sont donnés pour établir les modèles dynamiques des robots bipèdes avec des corps rigides, des ressorts idéaux, des actionneurs rotatifs et des structures non parallèles. Ensuite, la méthode de la linéarisation par retour d'état a été introduite pour réaliser la commande non linéaire des robots bipèdes et pour forcer le système du robot à évoluer sur la surface de la dynamique des zéros. Pour les robots bipèdes étudiés ici, il est commode de réaliser l'invariance hybride et de créer ainsi la dynamique des zéros hybride. Par la suite, la stabilité des allures cycliques peut être assurée par le calcul de l'application restreinte de Poincaré. Enfin, les concepts généraux de l'optimisation paramétrique et de la méthode de la programmation quadratique séquentielle ont été expliqués brièvement, et ils seront plus tard utilisés pour le calcul des allures optimisées.

8.3 Robot bipède 2D avec des pieds ponctuels

Ce chapitre se concentre sur la modélisation, l'optimisation et la commande d'un robot bipède 2D sous-actionné à 5 corps avec des pieds ponctuels. Ces concepts et ces méthodes sont fondamentaux pour le développement des robots 2D qui satisfont les hypothèses définies ci-après.

Structure et Hypothèses pour les robots 2D

Un robot bipède 2D est un robot effectuant des mouvements que dans le plan sagittal. Il se compose de deux sous-chaînes cinématiques appelées jambes et une autre sous-chaîne appelée tronc, toutes ces sous-chaînes sont reliées à un point commun nommé la hanche. Quand une seule des deux jambes est en contact avec le sol, cette jambe en appui est appelée la jambe de support et l'autre est appelée la jambe mobile. Un pied est défini comme l'extrémité d'une jambe. La phase de simple appui est définie comme la phase de locomotion où un seul des deux pieds est en contact avec le sol. Inversement, la phase de double appui est la phase où les deux pieds sont en contact avec le sol. La marche est alors considérée comme une succession de phases alternées de simple appui et de double appui. Forts de ces définitions, nous pouvons réexaminer les hypothèses proposées à l'origine dans [84] et les reformuler dans le contexte de notre robot.

Hypothèses pour les robots bipèdes 2D : Le robot bipède 2D est supposé être :

HPR1) composé de N corps rigides reliés par $(N-1)$ articulations sans frottement à liaison pivot et chaque corps a une masse non nulle ;

HPR2) à deux dimensions, en mouvement uniquement dans le plan sagittal ;

HPR3) bipède, avec deux jambes symétriques reliées à un point commun appelé hanche et les deux jambes ont des pieds ponctuels ;

HPR4) sous-actionné au pied de support reliant la jambe de support et le sol ;

HPR5) actionné de façon autonome pour les autres $(N-1)$ articulations ;

HPR6) exprimé par $(N-1)$ coordonnées angulaires relatives $(q_2, \cdots, q_N)$ et une coordonnée angulaire absolue q_1 tel que représentées sur la figure 3.2.

Les propriétés du robot sont indépendantes du choix des coordonnées et l'hypothèse *HPR6* est utilisée seulement pour faciliter le calcul de la dynamique des zéros. L'idée de concevoir ce type de robots a commencé il y a près de deux décennies quand un robot bipède 2D appelé RABBIT a été construit à Grenoble [5]. Au fil des années, des robots similaires ont été construits tels que le robot AMBER [106] et le robot MABEL [171].

Hypothèses pour les allures de marche 2D : Le contrôleur du robot doit assurer les propriétés suivantes :

HPG1) il existe en alternance des phases de simple appui et de double appui;

HPG2) pendant la phase de simple appui, le pied de support est placé sur le sol et ne glisse pas ;

HPG3) la phase de double appui est instantanée et peut être modélisée par un impact rigide ;

HPG4) à l'état stationnaire, deux pas continus sont symétriques ;

HPG5) pendant chaque pas, seul le pied de support est en contact avec le sol, et le pied mobile décolle du sol derrière le pied de support et atterrit devant celui-ci ;

HPG6) la marche a lieu sur une surface horizontale.

Hypothèses pour des impacts 2D : Un impact apparaît pendant la phase de double appui quand le pied mobile touche le sol. Le modèle d'impact est basé sur les hypothèses suivantes :

HPI1) l'impact apparaît quand le pied mobile touche le sol sans rebond ni glissement ;

HPI2) à l'impact, le pied de support décolle du sol sans interaction avec celui-ci ;

HPI3) l'impact est instantané ;

HPI4) les forces externes agissant sur le pied mobile à l'impact peuvent être représentées par des impulsions ;

HPI5) il peut y avoir un changement instantané de vitesses, mais la configuration reste inchangée ;

HPI6) tous les actionneurs ne sont pas capables de générer des impulsions et donc ils sont ignorés à l'impact.

Modèle dynamique de la marche

Dans cette section, nous développons un modèle mathématique pour un robot bipède à 5 corps, tout en se conformant aux hypothèses *HPR1-HPR6*, *HPG1-HPG6* et *HPI1-HPI6*. Comme l'illustre la figure 3.1, le robot 2D analysé dans ce chapitre est composé de cinq corps : un tronc, deux cuisses et deux tibias. L'extrémité de chaque tibia est considéré comme un pied ponctuel. Le vecteur des coordonnées généralisées décrivant les mouvements du robot est $q_e = [x_{st}, z_{st}, q_1, q_2, q_3, q_4, q_5]^\top$. Il contient deux coordonnées (x_{st}, z_{st}) dans le système de coordonnées $o_g x_g z_g$ pour décrire la position du pied de support et un vecteur des angles $q = [q_1, q_2, q_3, q_4, q_5]^\top$ pour décrire l'orientation des corps du robot. Étant donné le vecteur q, l'angle absolu du tibia mobile q_6 est donné dans (3.1). Cet angle est utilisé avec (x_{sw}, z_{sw}) pour calculer le modèle d'impact.

En référence aux données du robot humanoïde HRP-4, notre robot a une masse totale de 39 kg et une taille totale de 1,5 m [172]. Les moments d'inertie des rotors des actionneurs ramenés sur le côté articulaire sont de 0,8 kgm^2. Le reste des paramètres du modèle est calculé à partir de structures anthropomorphiques virtuelles générées automatiquement par la masse totale et la taille totale [173, 174]. Tous les autres paramètres sont indiqués dans le tableau 3.1.

Le modèle de la phase de simple appui est utilisé pour simuler le comportement du robot bipède lorsque l'un des deux pieds est en contact avec le sol. Comme les allures sont supposées être symétriques selon l'hypothèse *HPG4*, nous pouvons toujours utiliser le même modèle de la phase de simple appui, peu importe lequel des deux pieds est le pied de support. La permutation des jambes peut être traitée par le modèle de double appui.

Pendant la phase de simple appui, on note $\mathcal{Q}$ l'espace de dimension 5 de configuration du robot, $q \in \mathcal{Q}$ le vecteur des coordonnées articulaires généralisées, $x = [q^\top, \dot{q}^\top]^\top$ la variable d'état du robot, et $\mathcal{TQ} = \{x = (q^\top, \dot{q}^\top)^\top | q \in \mathcal{Q}, \dot{q} \in \mathbb{R}^N\}$ l'espace d'état. Le modèle de la phase de simple appui peut être écrit sous forme d'espace d'état (3.3). La formulation du modèle de double appui exige le modèle dynamique utilisant le vecteur des coordonnées généralisées q_e, les équations permettant de calculer ce modèle sont données par (3.6) à (3.18). Le modèle global de la marche est obtenu en combinant les modèles de la phase de simple appui et celui de la phase de double appui pour former un modèle hybride défini par (3.19). La validité du modèle de la phase de simple appui est basée sur l'hypothèse *HPG2* qui suppose que le pied de support est fixe par rapport au sol. Pour vérifier cette condition, on note $F_{st} = [F_{st}^x, F_{st}^z]^\top$ la force de réaction du sol, et le modèle de contact est donné par (3.20) et (3.21).

Conception de la commande par retour d'état

Pendant la phase de simple appui, le robot bipède a quatre actionneurs indépendants. Ainsi, les sorties sont quadridimensionnels et sont définies comme $y = h(q) = h_0(q) - h_d \circ \theta(q)$ où $h_0(q)$ représente les variables contrôlées indépendantes, $\theta(q)$ représente une fonction strictement monotone de l'état du robot, et $h_d \circ \theta(q)$ indique l'évolution idéale de ces variables en fonction de la variable scalaire $\theta(q)$ [8]. En rendant la variable y égale à zéro, les variables $h_0(q)$ sont forcées de suivre l'évolution idéale de $h_d \circ \theta(q)$. Ainsi, la posture du robot est contrôlée pour évoluer en fonction des contraintes virtuelles $h_0(q) - h_d \circ \theta(q) = 0$ paramétrées par $\theta(q)$. Cette méthode de commande est différente des méthodes classiques fondées sur le suivi de trajectoires parce que l'évolution idéale de $h_d \circ \theta(q)$ est seulement liée à $\theta(q)$ et non au temps. En conséquence, les systèmes de commande correspondants peuvent être très autonomes.

Pour notre robot bipède 2D, $\theta(q)$ est l'angle linéarisé de la jambe virtuelle de support, qui est définie comme la ligne reliant la hanche et le pied d'appui (voir figure 3.3). En général, deux tâches sont essentielles pour la réalisation de la marche bipède : la commande de posture et l'avancement de la jambe mobile. La commande de posture maintient le tronc dans une position presque verticale, et l'avancement

de la jambe mobile assure une longueur souhaitée de pas. Inspirés par les travaux de [6], nous proposons pour notre robot 2D sur la figure 3.3(b) les sorties contrôlées appelées "sorties symétriques" données par l'équation (3.24) [121].

Le contrôleur du robot ne fonctionne que pendant la phase de simple appui. Le but de la commande de cette phase est de contraindre progressivement le robot bipède à évoluer sur une surface de la dynamique des zéros. Pour atteindre cet objectif, le contrôleur peut être créé en combinant un contrôleur non linéaire par retour d'état statique (3.35) et un contrôleur linéaire par retour d'état (3.37).

Selon le théorème 2.2, la stabilité exponentielle de l'orbite périodique du système en boucle fermée est équivalente à celle de l'orbite périodique de la dynamique des zéros tant qu'une loi de commande comme (3.39) est appliquée. Pour notre robot 2D, le système de la dynamique des zéros défini par (3.44) est bidimensionnel et il peut être équivalent à un système dynamique unidimensionnel (3.52) en utilisant une transformation de coordonnées. Ainsi, l'application de Poincaré de la dynamique des zéros $\rho : S \cap U \to S \cap U$ est difféomorphe à un système LTI scalaire (3.54) dont la stabilité peut être facilement vérifiée.

Optimisation des allures de marche

L'optimisation des allures de marche peut être considérée comme un problème d'optimisation non lineaire sous contraintes. Comme mentionné dans (2.66), il est nécessaire de définir des paramètres à optimiser, une fonction objectif et plusieurs fonctions scalaires représentant respectivement des contraintes d'égalité et des contraintes d'inégalité.

Afin de paramétrer h_d défini par (3.22), nous avons choisi d'utiliser des courbes de Bézier d'ordre 5. Pour chaque courbe, il y a six paramètres a_1^i, a_2^i, ..., a_6^i. Étant donné que la dimension de h_d est égale à 4, nous pouvons regrouper les paramètres a_k^i dans les vecteurs $a_k = [a_k^1, \cdots, a_k^4]$ de taille (4×1). Par la réalisation de l'invariance hybride $\Delta(\mathcal{S} \cap \mathcal{Z}) \subset \mathcal{Z}$, nous pouvons calculer les vecteurs a_0 et a_1 à partir des vecteurs a_2, a_3, a_4 et a_5. Ainsi, l'ensemble des paramètres $\{a_2, a_3, a_4, a_5\}$ est suffisant pour définir h_d. Afin de faciliter l'optimisation de la marche, nous remplaçons a_5 par le vecteur des paramètres de posture ϕ_P pour représenter plus clairement la posture du robot. Au total, l'ensemble des paramètres à optimiser est $\{\phi_P, a_3, a_4, a_5\}$.

Quand il s'agit des robots bipèdes actionnés par des moteurs à courant continu ou des moteurs synchrones sans balais, la puissance électrique de chaque moteur est approximativement proportionnelle au carré du courant d'alimentation, et le courant est à son tour proportionnel au couple exercé par ce moteur. Afin d'exprimer la consommation d'énergie du moteur par mètre parcouru, la fonction coût est ainsi définie comme l'intégrale du carré du couple pour un déplacement unitaire.

Afin d'assurer la validité des allures optimales de marche, il est nécessaire de définir certaines contraintes. Comme illustré sur la figure 3.7, ces contraintes sont :

CP1) Le tronc ne peut pas se pencher en arrière ou se pencher excessivement en avant ;

CP2) La position de la hanche ne peut pas être trop basse ;

CP3) La force impulsionnelle d'impact définie par (3.12) doit être vers le haut ;

CP4) La vitesse du pied oscillant après l'impact doit être vers le haut ;

CP5) Le pied mobile ne doit pas toucher le sol prématurément ;

CP6) Les genoux se plient vers l'avant ;

CP7) Les conditions de contact (3.20) et (3.21) doivent être satisfaites ;

CP8) La vitesse moyenne de marche est égale à la vitesse désirée.

Comme illustré sur la figure 3.8, il existe trois étapes importantes dans les calculs de la fonction objectif et des contraintes. Les équations utilisées dans ces étapes sont énumérées ci-dessous :

1. Calculer l'évolution de la dynamique des zéros. (i) Résoudre la dynamique inverse en utilisant (3.68), (3.69), (3.70), (3.72), (3.73) et (3.74). (ii) Paramétrer h_d par (3.63), (3.66), (3.61), (3.60) et (3.59). (iii) Calculer l'évolution de ξ_1 et de ξ_2 en utilisant (3.50), (3.51), (3.45), (3.46), (3.53), (3.56), (3.57) et (3.58).

2. Calculer l'évolution du système complet en utilisant (3.40), (3.41), (3.42), et (3.3).

3. Calculer la fonction coût et les contraintes en utilisant (3.77), (3.79), (3.80), (3.81), (3.82), (3.83), (3.84), (3.85) et (3.86).

L'optimisation est réalisée par la toolbox d'optimisation de MATLAB®. Le problème étant classé comme une optimisation sous contraintes, la fonction `fmincon` de MATLAB® (R2010b) est adaptée à cet effet. Il y a quatre algorithmes disponibles : `trust-region-reflective`, `interior-point`, `sqp` et `active-set`. Nous avons choisi `sqp` comme algorithme d'optimisation. Notre choix est motivé par sa supériorité dans les situations où la fonction objectif et les contraintes ne peuvent pas fournir de valeurs correctes.

Analyse des résultats

Le nombre de Froude est considéré dans le choix de la gamme de la vitesse moyenne de marche. Pour l'être humain, la transition de la marche à la course se produit lorsque le nombre de Froude $Fr \approx 0{,}5$ [180]. Cependant, le nombre maximum de Froude pour la marche de la dernière version du robot ASIMO est de moins de 0,1. Dans cette thèse, nous avons choisi 0,3 comme le nombre maximum de Froude. Nous ne voulons pas étudier des allures à faible vitesse. Ainsi, notre plage de vitesse de marche est choisie comprise entre 0,2 m/s et 1,5 m/s.

Les coûts d'énergie consommée par le robot et ses actionneurs sont représentés sur la figure 3.10. Il est évident que les actionneurs des articulations des hanches sont responsables de la majeure partie de la consommation d'énergie du robot. La représentation des allures aux vitesses 0,3 m/s, 0,7 m/s, 1,1 m/s et 1,5 m/s est fournie sur la figure 3.13. Les données détaillées pour la marche à 0,7 m/s et 1,5 m/s sont

données sur les figures 3.14 à 3.20. Il est intéressant de noter que la relation entre t et θ est presque linéaire, ce qui signifie que $\theta(q)$ dans (3.23) est un substitut judicieux du temps pour indiquer la progression à chaque pas. Selon la figure 3.17, l'énergie mécanique consommée par les actionneurs des articulations des hanches est à peu près équivalente à celle consommée par les actionneurs des articulations des genoux. Mais à grande vitesse, l'énergie mécanique consommée par les hanches est plus significative. En outre, pour tous les actionneurs, les puissances négatives ne peuvent pas être négligées, ce qui indique qu'il y a une possibilité de recycler l'énergie mécanique négative et par conséquent d'améliorer l'efficacité énergétique.

Afin de vérifier que le pied de support ne glisse pas pendant la phase de simple appui, les courbes des forces de réaction du sol sont représentées sur la figure 3.18. Nous pouvons voir clairement que F_{st}^z diminue à la fin d'un pas, en particulier pour la vitesse 1,5 m/s. À 0,7 m/s, la valeur absolue de F_{st}^x est relativement faible par rapport à F_{st}^z. Cependant, pour la marche à 1,5 m/s, la valeur absolue de F_{st}^x est presque équivalente à celle de F_{st}^z à la fin d'un pas, ce qui signifie que le pied de support est sur le point de glisser (le coefficient de frottement $\mu_{\mathrm{f}} = 1$). Tous ces phénomènes indiquent que, le pied d'appui a de plus en plus tendance à décoller ou glisser lorsque la vitesse de marche augmente.

Conclusion

Dans ce chapitre, nous avons discuté de la façon d'utiliser la linéarisation par retour d'état et la dynamique des zéros pour réaliser la commande optimale d'un robot bipède 2D avec un tronc, deux cuisses, deux tibias et deux pieds ponctuels. Les paramètres du modèle de notre robot sont dérivés du robot HRP-4 [172]. Le modèle de la marche est obtenu en combinant les modèles de la phase de simple appui et de la phase de double appui pour former un modèle hybride. Pendant la phase de simple appui, la méthode de la linéarisation par retour d'état est adoptée pour appliquer des contraintes virtuelles définies par des sorties contrôlées. Dans cette thèse, nous avons défini les "sorties symétriques" comme les sorties contrôlées pour faciliter l'interprétation géométrique de la commande de la posture et de l'avancement de la jambe mobile. L'évolution idéale des contraintes virtuelles est paramétrée par des courbes de Bézier en fonction de la valeur normalisée de l'angle absolu linéarisé de la jambe virtuelle de support. Par la suite, la stabilité de marche est analysée par une application LTI scalaire. Afin d'obtenir des allures optimales de marche pour notre bipède 2D à des vitesses différentes, nous avons développé un programme d'optimisation en utilisant l'algorithme SQP et la fonction `fmincon` de MATLAB®. La fonction objectif est définie en fonction de la consommation d'énergie des moteurs à courant continu ou des motors synchrones à aimants permanents. Des contraintes d'optimisation sont utilisées pour vérifier les exigences pour le contact avec le sol, l'avancement du pied, etc. L'optimisation de la marche est effectuée pour des vitesses de 0,2 m/s à 1,5 m/s. La stabilité et la faisabilité de ces résultats sont validées. La valeur maximale du critère est 3161 $\mathrm{N^2ms}$ à 1,5 m/s et la valeur minimale est 43 $\mathrm{N^2ms}$ à 0,2 m/s.

8.4 Couplages élastiques pour le robot 2D

Les travaux présentés dans ce chapitre portent sur l'exploration des avantages de l'ajout de couplages élastiques (sous forme de ressorts au niveau des hanches) à des robots bipèdes 2D. Ceci est réalisé par l'addition des paramètres des couplages aux paramètres d'optimisation et par l'optimisation de la marche avec une faible consommation d'énergie. Une étude similaire a été faite sur l'analyse de la contribution des couplages élastiques sur un robot bipède à 3 corps [150] et une autre étude sur un robot à 5 corps [109]. Inspirés par ces deux études, nous avons l'intention d'étudier l'utilisation des couplages élastiques sur notre robot à 5 corps. En comparaison avec l'étude précédente, les différences importantes de nos travaux sont : (i) la fonction coût (3.76) utilisée dans notre analyse ne nécessite pas de définition détaillée des actionneurs tels que des rapports de vitesse et des efficacités de moteur; (ii) les sorties symétriques sont adoptées dans la linéarisation par retour d'état. Les couplages élastiques sont appliqués sous la forme de ressorts de torsion linéaires avec deux différentes configurations: soit en connectant une cuisse à l'autre, soit en reliant chacune des cuisses au tronc. Après l'optimisation des allures de marche, les raideurs optimisées des ressorts sont utilisées pour calculer la fréquence de référence de pas qui est égale à deux fois la fréquence propre du pendule formé par la jambe mobile avec son genou verrouillé. Les résultats montrent que les deux configurations peuvent réduire considérablement le critère d'énergie de notre robot bipède 2D et forcer la fréquence de pas à se rapprocher de la fréquence de référence de pas afin que le robot puisse marcher en résonance.

Modèle des couplages élastiques

Étant donné que des composants élastiques ne peuvent pas produire des impulsions de couple lors de l'impact, ils n'ont aucune influence sur le modèle de l'impact. Quant au modèle de la phase de simple appui, l'équation (3.2) peut être écrite comme (4.1). Ainsi, la loi de commande non linéaire par retour d'état statique (3.39) devient (4.3). Les autres procédés pour calculer la dynamique des zéros sont mentionnés dans le chapitre 3, et en utilisant (4.4), nous pouvons calculer les couples des actionneurs du robot évoluant sur la variété de la dynamique des zéros.

La figure 3.10 montre que, pour notre robot bipède 2D marchant à grande vitesse sans couplages élastiques, la majeure partie de la consommation d'énergie est dûe aux actionneurs des articulations de hanche. En conséquence, il est intéressant de voir si les couplages élastiques peuvent réduire les critères énergétiques de ces articulations. Nous proposons donc deux configurations :

Couplage 2D Cas I) Comme illustré sur la figure 4.1(a), un ressort linéaire de torsion est monté entre les deux cuisses. Ainsi, nous avons $\varphi_{e1} = q_3 - q_4$ pour la déviation $\varphi_{e1} - \varphi_{e1}^*$ dans (2.11) du ressort. Étant donné que le robot est symétrique, nous avons $\varphi_{e1}^* = 0$, et la raideur du ressort de torsion k_{e1} dans (2.11) est notée $k_{e1} = k_s$. En utilisant (2.18), le vecteur des couples τ_e est donné par (4.5).

Couplage 2D Cas II) Comme illustré sur la figure 4.1(b), deux ressorts linéaires de

torsion sont montés respectivement entre le tronc et les deux cuisses. Ainsi, nous avons $\varphi_{e2} = q_3$ et $\varphi_{e3} = q_4$ pour les déviations $\varphi_{e2} - \varphi^*_{e2}$ et $\varphi_{e3} - \varphi^*_{e3}$ de ces ressorts. En raison de la symétrie du robot, les raideurs et les positions de repos de ces deux ressorts doivent être les mêmes, à savoir $\varphi^*_{e2} = \varphi^*_{e3} = \varphi_s$ et $k_{e2} = k_{e3} = k_s$. En appliquant ces deux ressorts et en utilisant l'équation (2.18), le vecteur des couples τ_e peut être calculé par (4.6).

Selon plusieurs études sur des allures de marche humaine [136, 137], la fréquence préférée de pas est sensiblement égale à la fréquence de résonance d'un oscillateur harmonique entraîné par des forces. Pour notre robot bipède 2D, nous pouvons aussi considérer la jambe mobile comme un pendule pesant composé avec la hanche fixée dans l'espace et le genou oscillant verrouillé dans une position droite, comme illustré sur la figure 4.2. Ainsi, nous pouvons définir la fréquence de référence de pas f^*_{step} comme deux fois la valeur de la fréquence naturelle d'oscillation de la jambe mobile (4.7).

Allures optimales de marche avec des couplages élastiques

Dans le couplage 2D Cas I, nous commençons par l'optimisation des allures avec les raideurs fixées k_s allant de 0 Nm/rad à 300 Nm/rad. De cette façon, nous pouvons obtenir la surface sur la figure 4.3 reliant la raideur k_s, la vitesse de marche et le critère d'énergie (3.76). Nous pouvons conclure que pour un robot bipède 2D à 5 corps avec un ressort linéaire de torsion monté entre ses deux cuisses, l'efficacité énergétique peut être grandement améliorée en choisissant une raideur faible pour marcher à basse vitesse et une raideur importante à grande vitesse. La représentation des allures de marche du robot aux vitesses 0,3 m/s, 0,7 m/s, 1,1 m/s et 1,5 m/s est fournie sur la figure 4.5. A partir de cette figure, nous pouvons voir que le robot, avec une grande raideur du ressort, a une petite taille de pas et vice versa.

Afin d'éviter l'inconvénient d'avoir la raideur k_s fixe, nous pouvons attribuer une valeur optimale k_{opt} à k_s et ajouter k_{opt} au vecteur des paramètres d'optimisation ϑ. Les résultats correspondants d'optimisation sont représentés sur les figures 4.4, 4.7 et 4.8. Par rapport aux autres courbes du critère, le critère d'énergie avec $k_s = k_{opt}$ est considérablement réduit pour toutes les vitesses de 0,2 m/s à 1,5 m/s. En outre, la raideur optimisée k_{opt} est positivement corrélée avec la vitesse de marche. En comparaison avec les allures précédentes avec la raideur k_s fixe, les allures avec $k_s = k_{opt}$ ont des tailles de pas "normales" à toutes les vitesses.

Les critères énergétiques du robot et de ses actionneurs avec $k_s = k_{opt}$ sont représentés sur la figure 4.4. En comparant cette figure avec la figure 3.10, nous constatons que le critère d'énergie de la hanche mobile sans couplages à 1,5 m/s est presque de 1000 N^2ms alors que cette valeur diminue à moins de 30 N^2ms lorsque le ressort de torsion avec la raideur k_s optimisée est appliquée. De même, le critère de la hanche de support est réduit de 1800 N^2ms à 180 N^2ms. En effet, l'objectif principal de réglage de la raideur k_s est d'ajuster la fréquence de résonance de la jambe mobile afin de réduire les critères énergétiques des actionneurs de hanche à toutes les vitesses. Comme illustré sur la figure 4.9, la fréquence de pas avec la raideur k_s optimisée peut rester proche de la fréquence de référence f^*_{step}, ce qui

permet au robot bipède de marcher en résonance avec une faible consommation d'énergie.

Les courbes des angles, des vitesses angulaires, des couples, des puissances des actionneurs et des forces de réaction au sol sont fournies sur les figures 4.10 à 4.14. Il est intéressant de noter que les courbes de θ_{symm} sur la figure 4.10 présentent une similitude avec une courbe sinusoïdale. Nous pouvons constater que les amplitudes des couples des ressorts τ_{e3} et τ_{e4} sur la figure 4.12 sont plus grandes que celles des couples des actionneurs correspondants u_3 et u_4, surtout à la vitesse 1,5 m/s.

En comparant la figure 4.13 et la figure 3.17, nous pouvons voir que, bien que le critère d'énergie dans l'équation (3.77) n'a aucun lien avec la puissance mécanique, les puissances mécaniques maximales de tous les actionneurs ont nettement diminué en raison des couplages élastiques. Un phénomène intéressant est que les puissances mécaniques des actionneurs de hanche sont majoritairement positives sur la figure 4.13, alors que sur la figure 3.17 les puissances négatives sont proches des puissances positives en termes d'amplitudes.

En dehors de la réduction de la consommation d'énergie, le ressort de hanche peut également réduire le mouvement vertical du centre de masse, ce qui peut être vérifié en comparant la figure 3.19 et la figure 4.15. En outre, la hauteur maximale du pied mobile sur la figure 4.16 est d'environ 2,5 cm, elle est beaucoup plus petite que la valeur sur la figure 3.20.

Dans le couplage 2D Cas II, deux ressorts identiques sont ajoutés respectivement entre les deux cuisses et le tronc. Nous sommes intéressés par la recherche des valeurs optimales de la raideur k_s et la position au repos φ_s, c'est à dire k_{opt} et φ_{opt}. Les résultats généraux de l'optimisation sont présentés sur les figures 4.17 à 4.20. En utilisant deux ressorts de torsion reliant le tronc et deux cuisses, il est également possible de réduire considérablement le critère d'énergie, comme illustré sur la figure 4.17. À la vitesse de 1,5 m/s, le critère d'énergie dans le couplage 2D Cas II est de 329 N^2ms. La réduction du critère d'énergie est également due à la réduction des critères énergétiques des actionneurs de hanche.

La représentation des allures à les vitesses 0,3 m/s, 0,7 m/s, 1,1 m/s et 1,5 m/s est fournie sur la figure 4.20. Nous pouvons voir que les allures dans le couplage 2D Cas II sont également satisfaisantes esthétiquement. En comparaison avec le couplage 2D Cas I, la fréquence de référence f^*_{step} est également proche de la fréquence de pas f_{step} sur la figure 4.19 à toutes les vitesses en utilisant $k_s = k_{opt}$ et $\varphi_s = \varphi_{opt}$. Ceci indique que les ressorts dans le couplage 2D Cas II peuvent également régler la fréquence de pas proche de la fréquence de référence à des vitesses différentes.

L'information détaillée aux vitesses 0,7 m/s et 1,5 m/s est fournie sur les figures 4.21 à 4.27. Ces résultats sont, dans une certaine mesure, similaires aux résultats pour le couplage 2D Cas I. Pour commencer, les courbes de θ_{symm} sur la figure 4.21 présentent également une similitude avec une courbe sinusoïdale. En outre, la position au repos φ_{opt} est presque au milieu de la fourchette de variation de q_3 et q_4. Ceci est étroitement liée à la définition de la fréquence de référence sur la figure 4.2. De plus, les amplitudes des couples des ressorts τ_{e3} et τ_{e4} sur la figure 4.23 sont aussi beaucoup plus grandes que celles des couples des actionneurs correspondants u_3 et

u_4. En comparant les figures 4.24 et 4.13, nous pouvons voir que, les puissances mécaniques des actionneurs de hanche sont aussi majoritairement positives. Les phénomènes décrits ci-dessus indiquent que le robot marche aussi en résonance avec le couplage 2D Cas II. Comme illustré sur la figure 4.25, à la vitesse 1,5 m/s, la valeur maximale de $|F_{st}^x|/F_{st}^z$ est plus petite que les valeurs sur les figures 4.14 et 3.18, ce qui indique qu'il y a plus de marge pour le pied de support de rester en contact avec le sol sans glisser dans le couplage 2D Cas II que dans les autres cas. En comparaison avec le mouvement vertical du centre de masse sur la figure 3.19, le mouvement sur la figure 4.26 est plus petit. En outre, la hauteur maximale du pied libre sur la figure 4.27 est similaire à la valeur sur la figure 4.16.

Discussion

Dans la partie précédente, on a démontré les avantages de l'ajout des couplages élastiques sous la forme de ressorts de torsion aux hanches de notre robot bipède 2D. Dans les deux cas, les critères énergétiques sont beaucoup plus petits que ceux dans le cas sans couplage traité au chapitre 3. Bien que le critère d'énergie dans le couplage 2D Cas II est plus petit que celui dans le couplage 2D Cas I, il n'est pas toujours simple de savoir quel cas est le mieux. Cela dépend sûrement de l'objectif spécifique.

Contrairement à ce que l'on pourrait penser, la quantité nécessaire de matériaux pour la fabrication d'un seul ressort dans le coulage 2D Cas I est similaire à celle pour la fabrication de deux ressorts dans le couplage 2D Cas II. Les avantages du couplage 2D Cas I résident dans sa simplicité et sa fiabilité parce qu'il ne nécessite qu'un seul ressort. Cependant, le couplage 2D Cas II a les avantages d'une position verticale du tronc dans l'état de repos et de la plus grande marge pour le pied de support de rester fixe par rapport au sol.

On peut s'interroger sur la modification de la raideur du ressort et la position de repos sous tension. En fait, il y a déjà quelques études concernant des composants élastiques accordables. Par exemple, il est possible de modifier la raideur par réglage des pré-tensions des ressorts non linéaires [156, 157]. Un problème commun pour la plupart de ces applications est que des actionneurs supplémentaires sont nécessaires pour effectuer la modification. Cependant, il y a aussi d'autres options pour modifier les raideurs et les positions de repos sans utiliser des actionneurs supplémentaires. Par exemple, au lieu d'utiliser un ressort linéaire, nous pouvons probablement utiliser un ressort non linéaire dont la raideur est corrélée positivement avec la force de rappel parce que la déviation maximale est aussi corrélée positivement avec la raideur.

Un autre aspect intéressant est que nous pouvons comparer la performance de notre robot avec celle des robots bipèdes passifs et des robots bipèdes assistés par des actionneurs. Sur les figures 4.13 et 4.24, nous avons mentionné que les puissances négatives des actionneurs de hanche sont considérablement réduites par les couplages élastiques dans les deux cas. Par conséquent, ces actionneurs de hanche dans notre robot sont principalement utilisés pour compenser l'énergie perdue à chaque impact, ce qui est similaire aux robots dynamiques assistés par des actionneurs [66].

Les orbites périodiques de notre robot 2D marchant à la vitesse 0,7 m/s sont illustrées sur la figure 4.29. Il est intéressant de noter que, pour tous les angles étudiés, les sauts de vitesses angulaires (marqués par les flèches noires) à l'impact avec les couplages élastiques sont beaucoup plus petits que les sauts dans le cas sans couplages. Comme montré sur la figure 4.29 (a), l'angle absolu de la jambe virtuelle de notre robot 2D sans couplages se comporte de façon similaire à l'angle absolu de la jambe d'un robot actionné à trois corps dans [182] lorsque cet angle de notre robot 2D avec les couplages ont des orbites similaires à celles de l'angle absolu de la jambe d'un robot passif à trois corps [183]. Ceci suggère que les allures optimisées des robots bipèdes actionnés avec des couplages élastiques sont similaires aux allures des robots bipèdes dynamiques passifs.

Conclusion

Dans ce chapitre, nous avons discuté deux cas d'ajout de couplages élastiques sous forme de ressorts de torsion aux hanches du robot présenté dans le chapitre 3. Dans le couplage 2D Cas I, un ressort linéaire de torsion est monté entre les deux cuisses. Dans le couplage 2D Cas II, deux ressorts linéaires de torsion sont installés pour relier les mouvements des deux cuisses au mouvement du tronc. Nous avons défini la fréquence de référence de pas comme deux fois la fréquence naturelle du pendule formé par la jambe mobile avec son genou bloqué dans une position droite. Les résultats pour les deux cas sont obtenues en utilisant les méthodes d'optimisation du chapitre 3. Dans les couplages 2D Cas I et II, nous avons montré que la raideur idéale du ressort de hanche est positivement corrélée à la vitesse de marche. En utilisant les couplages, nous avons considérablement réduit le critère d'énergie à toutes les vitesses étudiées dans les deux cas. En outre, les couplages élastiques dans les deux cas ont également réduit les puissances négatives des actionneurs de hanche. En comparant la fréquence de pas et la fréquence de référence de pas, nous avons constaté que nous pouvons changer la dynamique naturelle de notre bipède 2D en utilisant la raideur optimisée (et la position de repos optimisée) afin de réduire la consommation d'énergie. Les avantages et les inconvénients de ces deux cas sont analysés en détail avec des suggestions sur les solutions possibles pour réaliser les couplages élastiques. Les résultats d'autres chercheurs ont été comparés à nos résultats.

8.5 Robot bipède 3D avec des pieds à contact linéique

Ce chapitre se concentre sur la modélisation, l'optimisation et la commande d'un robot bipède 3D sous-actionné à 8 corps avec des pieds sans masse à contact linéique. Ces concepts et ces méthodes sont fondamentaux pour le développement des robots 3D qui satisfont les hypothèses définies ci-après.

Structure et Hypothèses pour les robots 3D

Les robots bipèdes 3D considérés ici sont des robots avec des pieds à contact linéique et des mouvements qui ont lieu dans l'espace 3D. La phase de marche de ces robots est divisée en une phase de simple appui et une autre phase instantanée de double appui. Les hypothèses suivantes sont définies pour les robots bipèdes 3D avec des pieds sans masse à contact linéique.

Hypothèses pour les robots bipèdes 3D : Le robot bipède 3D de la figure 5.1 est supposé être :

HTR1) composé de N corps rigides reliés par $(N-1)$ articulations sans frottement à liaison pivot et un degré de sous-actionnement approximativement dans le plan sagittal ;

HTR2) à trois dimensions, en mouvement dans l'espace 3D ;

HTR3) bipède, avec deux jambes symétriques reliées à un seul bassin (ou un seul tronc) ; toutes les deux jambes ont des pieds sans masse à contact linéique ; et le modèle du robot est strictement symétrique par rapport au plan sagittal ;

HTR4) sous-actionné au pied de support à contact linéique reliant la jambe de support et le sol ;

HTR5) actionné de façon autonome pour les $(N-1)$ articulations ;

HTR6) constitué de M degrés de liberté, et est exprimé par $(M-1)$ coordonnées angulaires relatives $(q_2, \cdots, q_M)$ et une coordonnée angulaire absolue q_1.

Hypothèses pour les allures de marche 3D : Le contrôleur 3D doit avoir les propriétés suivantes :

HTG1) il y a des phases en alternance de simple appui et de double appui ;

HTG2) pendant la phase de simple appui, le pied d'appui est placé sur le sol, c'est à dire que le ZMP reste à l'intérieur du segment de ligne du pied d'appui et que le pied d'appui ne glisse pas ;

HTG3) la phase de double appui est instantanée et peut être modélisée comme un impact entre deux corps rigides ;

HTG4) à l'état stationnaire, deux pas continus sont symétriques ;

HTG5) pendant chaque pas, seul le pied de support est en contact avec le sol, et le pied mobile décolle du sol derrière le pied de support et atterrit devant celui-ci sans collision entre les deux jambes ni avec le sol ;

HTG6) la marche a lieu sur une surface horizontale.

Hypothèses pour des impacts 3D : Un impact apparaît pendant la phase de double appui quand le pied mobile touche le sol. Le modèle d'impact pour les robots bipèdes 3D est basé sur les hypothèses suivantes :

HTI1) l'impact apparaît quand le pied mobile touche le sol et ce pied ne glisse ni ne rebondit ;

HTI2) à l'impact, le pied de support décolle du sol sans interaction ;

HTI3) l'impact est instantané ;

HTI4) les forces externes agissant sur le pied mobile à l'impact peuvent être représentées par des impulsions ;

HTI5) il peut y avoir un changement instantané de vitesses, mais la configuration de position reste inchangée ;

HTI6) tous les actionneurs ne sont pas capables de générer des couples impulsionnels et donc ils sont ignorés à l'impact.

Modèle dynamique de la marche

Dans cette partie, nous développons un modèle mathématique pour un robot bipède 3D à 8 corps, tout en se conformant aux hypothèses *HTR1-HTR6*, *HTG1-HTG6* et *HTI1-HTI6*. Comme l'illustre la figure 5.1, le robot 3D est composé de huit corps : un tronc, un bassin, deux cuisses, deux tibias, deux pied sans masse à contact linéique. Le modèle du robot est strictement symétrique par rapport au plan sagittal avec les articulations des chevilles montées le long des bissectrices perpendiculaires des pieds. Le robot dispose de sept articulations rotoïdes; chaque articulation de hanche comporte deux degrés de liberté et les autres articulations ont un degré de liberté. Les chevilles du robot servent seulement comme les axes de rotation pour les mouvements dans le plan frontal, et la rotation en lacet du tibia de support n'est pas possible.

Comme dans les cas du robot 2D, ce modèle du robot utilise aussi les paramètres calculés à partir du robot humanoïde HRP-4. Notre robot a une masse totale de 39 kg et une taille totale de 1,5 m [172]. Les moments d'inertie des rotors des actionneurs ramenés sur le coté articulaire sont de 0,8 kgm^2. Le reste des paramètres est calculé à partir des structures anthropomorphiques virtuelles générées automatiquement par la masse totale et la taille totale [173, 174]. Tous les autres paramètres sont indiqués dans le tableau 5.1.

Étant donné que le robot est strictement symétrique par rapport au plan sagittal, il est possible d'utiliser un seul modèle quelle que soit la jambe de support. Ceci

est réalisé en changeant le système de coordonnées généralisées. Comme illustré sur la figure 5.2, le système de coordonnées cartésiennes $o_g x_g y_g z_g$ est placé sur le sol; les coordonnées (x_{st}, y_{st}, z_{st}) localisent la position de la cheville de support; les coordonnées (x_{sw}, y_{sw}, z_{sw}) localisent la position de la cheville mobile; les angles (q_0, q_1, q_2) représentent les angles d'Euler $Z-Y-X$ du tibia gauche; les angles (q_{12}, q_{11}, q_{10}) représentent les angles d'Euler $Z-Y-X$ du pied droit par rapport au tibia; et les angles ($q_3, ..., q_9$) indiquent la posture du robot. Lorsque le pied gauche/droit repose à plat sur le sol, q_2/q_{10} peut être aussi considéré comme l'angle de l'articulation de la cheville gauche/droite et q_0/q_{12} est l'orientation du pied gauche/droite par rapport à l'axe y_g. Le vecteur des coordonnées généralisées décrivant les mouvements du robot est $q_e = [x_{st}, y_{st}, z_{st}, q_0, q_1, q_2, q_3, q_4, q_5, q_6, q_7, q_8, q_9]^\top$. Les angles q_{10}, q_{11} et q_{12} sont utiles lorsque la jambe mobile et la jambe de support échangent leurs rôles à l'impact.

L'existence de deux phases de la marche divise le modèle dynamique du robot 3D en deux parties : un modèle de simple appui et un modèle de double appui. Pendant la phase de simple appui, on note $\mathcal{Q}$ l'espace de configuration du robot de dimension 9, $q \in \mathcal{Q}$ le vecteur des coordonnées généralisées, $x = [q^\top, \dot{q}^\top]^\top$ les variables d'état du robot, et $\mathcal{TQ} = \{x = (q^\top, \dot{q}^\top)^\top | q \in \mathcal{Q}, \dot{q} \in \mathbb{R}^N\}$ l'espace d'état. Le modèle de la phase de simple appui peut être écrit sous forme d'espace d'état (5.6). La formulation du modèle de double appui exige le modèle dynamique en utilisant le vecteur des coordonnées généralisées q_e, les équations permettant de calculer ce modèle sont données par (5.9) à (5.39). Le modèle global de la marche est obtenu en combinant le modèle de la phase de simple appui et celui de la phase de double appui pour former un modèle hybride défini par (5.40).

La validité du modèle de la phase de simple appui est basée sur l'hypothèse *HTG2* qui suppose que le pied de support est fixe par rapport au sol. Comme illustré sur la figure 5.4, on suppose qu'il n'y a que deux points de contact a_{st} et b_{st} sur le pied de support. On peut décomposer la force et le couple agissant sur le pied d'appui en plusieurs composantes : Γ^x_{st}, Γ^z_{st}, F^x_{st}, F^y_{st} et F^z_{st} (le couple Γ^y_{st} est égal à zéro en raison du sous-actionnement de la cheville). Toutes ces forces et ces couples peuvent être calculés en fonction de q, $\dot{q}$ et $\ddot{q}$ en utilisant les équations (2.19) et (2.22). En résolvant les équations d'équilibre statique, on peut facilement calculer les composantes verticales N^a_{st} et N^b_{st} et les composantes f^{ax}_{st} et f^{bx}_{st} le long de l'axe x_{st}. Ensuite, nous devons vérifier deux inégalités (5.45) et (5.46) concernant N^a_{st} et N^b_{st} car le contact est unilatérale. Étant donné qu'il est impossible de calculer les forces f^{ay}_{st} et f^{by}_{st}, nous utilisons trois inégalités (5.50), (5.51) et (5.56) pour remplacer les conditions (5.48) et (5.49) de frottement statique. De cette façon, l'hypothèse *HTG2* peut être vérifiée par les cinq inégalités (5.45), (5.46), (5.50), (5.51) et (5.56).

Conception de la commande par retour d'état

Pendant la phase de simple appui, le robot bipède a huit actionneurs indépendants. Ainsi, les sorties sont à 8 dimensions et sont définies comme $y = h(q) = h_0(q) - h_d \circ \theta(q)$ où $h_0(q)$ représente les variables contrôlées indépendantes, $\theta(q)$ représente une fonction strictement monotone de l'état du robot, et $h_d \circ \theta(q)$ indique l'évolution

idéale de ces variables en fonction de la variable scalaire $\theta(q)$ [8]. Comme dans le cas de notre robot 2D, nous proposons pour notre robot 3D les "sorties symétriques" données par l'équation (5.59).

Le but de la commande pendant la phase de simple appui est de contraindre progressivement le robot bipède à évoluer sur une surface de la dynamique des zéros. À cet effet, le contrôleur est similaire à celui défini dans (3.39) et le vecteur des couples des actionneurs u^* est donné par (5.63).

Pour les robots bipèdes 3D avec plus d'un degré de sous-actionnement, la seule méthode connue pour obtenir l'invariance hybride est d'appliquer une extension deadbeat, et la dimension correspondante de l'application restreinte de Poincaré est supérieure à trois [99]. Ces complications pourraient nuire à la performance des algorithmes d'optimisation. Étant donné que notre robot 3D ne dispose que d'un degré de sous-actionnement, le système de la dynamique des zéros dans (5.67) est bidimensionnel et il peut être équivalent à un système dynamique unidimensionnel dans (5.75) en utilisant une transformation de coordonnées. Ainsi, l'application de Poincaré de la dynamique des zéros est difféomorphe à un système LTI scalaire dont la stabilité peut être facilement vérifiée.

Optimisation des allures de marche

L'optimisation des allures de marche peut être considérée comme un problème d'optimisation non linéaire sous contraintes. Ainsi, il est nécessaire de définir des paramètres à optimiser, une fonction objectif et plusieurs fonctions de contraintes.

Afin de paramétrer la sortie h_d, nous avons choisi d'utiliser des courbes de Bézier d'ordre 5. Pour chaque courbe, il y a six paramètres a_1^i, a_2^i, ..., a_6^i. Étant donné que la dimension de h_d est égale à 8, nous pouvons regrouper les paramètres a_k^i dans des vecteurs $a_k = [a_k^1, \cdots, a_k^8]$ de dimension (8×1). Par la réalisation de l'invariance hybride $\Delta(\mathcal{S} \cap \mathcal{Z}) \subset \mathcal{Z}$, nous pouvons calculer les vecteurs a_0, a_1 à partir des vecteurs a_2, a_3, a_4, a_5. Ainsi, l'ensemble de paramètres $\{a_2, a_3, a_4, a_5\}$ est suffisant pour définir h_d.

Afin de mieux représenter la posture du robot 3D, nous pouvons remplacer a_5 par le vecteur ϕ_P des paramètres de posture. Comme illustré sur la figure 5.5, on définit $o_{st}x_{st}y_{st}z_{st}$ comme le système fixe avec l'axe z_{st} pointant verticalement vers le haut et l'origine o_{st} au milieu du pied d'appui. Ensuite, on définit $o_px_py_pz_p$ comme le système mobile avec l'axe y_p passant par les deux hanches, l'axe z_p pointant vers l'articulation lombaire et l'origine o_p au milieu des deux hanches. En supposant que les orientations du système $o_px_py_pz_p$ et du système $o_{st}x_{st}y_{st}z_{st}$ coïncident initialement, nous pouvons définir α comme la rotation autour de l'axe x_p du système mobile et β comme la rotation autour de l'axe y_p du système mobile. En représentant le point o_p comme (x_p^-, y_p^-, z_p^-) et la cheville mobile comme $(x_{sw}^-, y_{sw}^-, 0)$, le vecteur des paramètres posturals est donné par $\phi_P = [q_6^-, \alpha, \beta, x_p^-, y_p^-, z_p^-, x_{sw}^-, y_{sw}^-]^\top$.

Nous pouvons calculer le vecteur a_5 à partir du vecteur ϕ_P en résolvant le modèle géométrique inverse avec les équations (5.87) à (5.107). En outre, la déviation de la direction de marche et la longueur de pas sont données par (5.108) et (5.109). Le vecteur complet à optimiser est $\{\phi_P, a_2, a_3, a_4\}$. Il comprend 32 paramètres à

optimiser. En plus, nous pouvons classer ces paramètres en 16 paramètres sagittaux (comprenant ϕ_P, β, x_p^-, z_p^- x_{sw}^-, a_2^1, a_2^2, a_2^3, a_2^4, a_3^1, a_3^2, a_3^3, a_3^4, a_4^1, a_4^2, a_4^3, a_4^4) et 16 paramètres frontaux (comprenant q_6^-, α, y_p^-, y_{sw}^-, a_2^5, a_2^6, a_2^7, a_2^8, a_3^5, a_3^6, a_3^7, a_3^8, a_4^5, a_4^6, a_4^7, a_4^8).

Comme dans le cas de notre robot 2D, la fonction coût pour notre robot 3D est définie comme l'intégrale du carré des couples pour un déplacement unitaire. Afin d'assurer la validité des allures optimales, il est nécessaire de définir les contraintes suivantes :

CT1) Le tronc et le bassin ne doivent pas se pencher excessivement ;

CT2) La position du bassin ne peut pas être trop basse ;

CT3) La force impulsionnelle définie par (5.23) doit être vers le haut ;

CT4) La vitesse du pied oscillant après l'impact doit être vers le haut ;

CT5) Le pied mobile ne doit pas toucher le sol prématurément ;

CT6) La jambe mobile et la jambe de support ne se touchent pas ;

CT7) Les genoux se plient vers l'avant ;

CT8) Les conditions de contact (5.45), (5.46), (5.50), (5.51) et (5.56) doivent être satisfaites ;

CT9) La vitesse moyenne de marche est égale à la vitesse désirée.

Comme illustré sur la figure 3.8, il existe aussi trois étapes importantes dans les calculs de la fonction objectif et des contraintes pour notre robot 3D. Les équations utilisées dans ces étapes sont énumérées ci-dessous :

1. Calculer l'évolution de la dynamique des zéros. (i) Résoudre la dynamique inverse en utilisant les équations (5.87) à (5.107). (ii) Paramétrer h_d par (5.84), (5.85), (5.83), (5.82) et (5.81). (iii) Calculer l'évolution de ξ_1 et de ξ_2 en utilisant (5.73), (5.74), (5.68), (5.69), (5.76), (5.78), (5.79) et (5.80).

2. Calculer l'évolution du système en utilisant (5.63), (5.65), (5.66), et (5.6).

3. Calculer la fonction coût et les contraintes en utilisant l'équation (5.111) et les équations (5.112) à (5.123).

Pour l'optimisation, une initialisation ϑ_0 du vecteur des paramètres à optimiser est essentielle. Étant donné que notre robot 2D et notre robot 3D ont tous les deux des paramètres issus du robot HRP-4, nous pouvons utiliser les paramètres optimisés des allures de notre bipède 2D comme initialisation pour optimiser notre bipède 3D. Les détails sont illustrés sur la figure 5.7. En utilisant directement les paramètres optimisés du bipède 2D comme les paramètres sagittaux du bipède 3D et en attribuant des constantes sur la figure 5.7 aux paramètres frontaux, nous pouvons

obtenir cette initialisation. En plus, nous pouvons aussi choisir d'optimiser uniquement les paramètres frontaux. De cette façon, il ne reste plus que 16 paramètres à optimiser. Les algorithmes d'optimisation sont similaires à ceux utilisés pour notre robot 2D.

Analyse des résultats

En appliquant l'initialisation sur la figure 5.7 à la vitesse de 1,5 m/s, nous avons sur la figure 5.8 la représentation de l'allure du robot 3D. Selon cette figure, nous pouvons constater que le mouvement frontal du robot est presque éliminé. Bien que l'allure est stable en calculant l'application scalaire restreinte de Poincaré, elle n'est pas pratique puisque presque toutes les conditions de contact sont violées, comme illustré sur la figure 5.9. En outre, le critère d'énergie 4893 N^2ms pour le point de départ est beaucoup plus grand que le critère de 3161 N^2ms sur la figure 3.10 pour notre robot 2D.

Afin d'obtenir des allures optimisées, nous allons étudier deux cas d'optimisation pour notre robot 3D :

Optimisation 3D Cas I) Dans ce cas, nous n'optimisons que les 16 paramètres frontaux tout en utilisant les paramètres optimisés de notre robot 2D comme paramètres sagittaux.

Optimisation 3D Cas II) Dans ce cas, nous optimisons tous les 32 paramètres.

Idéalement, on pense que le mouvement sagittal et le mouvement frontal peuvent être découplés et que la méthode simplifiée d'optimisation dans l'optimisation 3D Cas I peut également fournir les allures optimisées avec une faible consommation d'énergie. Cependant, les courbes du critère d'énergie sur la figure 5.11 sont décevantes. En comparaison avec le critère d'énergie de notre robot 2D sur la figure 3.10, le critère d'énergie de notre robot 3D est beaucoup plus élevé aux basses vitesses. Afin d'obtenir une compréhension plus profonde, nous pouvons combiner les critères d'énergie causées par les couples u_3, u_4, u_8 et u_9 dans un critère sagittal et les énergies restantes dans un critère frontal. Comme montré sur la figure 5.11, nous pouvons voir que le critère sagittal dans l'optimisation 3D Cas I est proche du critère de notre robot 2D à toutes les vitesses lorsque le critère frontal diminue quadratiquement avec la vitesse. En outre, les critères énergétiques des actionneurs frontaux sont anormalement élevés, ce qui indique que les mouvements du robot bipède 3D dans le plan sagittal et le plan frontal sont fortement couplés.

La variation des paramètres de posture à des vitesses différentes est démontrée sur la figure 5.12. Selon cette figure, nous pouvons voir que la variation des paramètres frontaux y_p^-, y_{sw}^- et α est assez limitée. En comparant la figure 3.14 et la figure 5.15, il est évident que l'évolution de tous les angles sagittaux et des sorties sagittales est très proche de l'évolution des angles et des sorties pour notre robot 2D. Selon la figure 5.18, les puissances négatives causées par les actionneurs de hanche ne peuvent être négligés. Comme mentionné ci-dessus, les allures optimisées satisfont aux conditions du contact au sol. Cela peut être vérifié sur la figure en utilisant les équations (5.45), (5.46), (5.50), (5.51) et (5.56). Il est intéressant de noter que la plage de la variation de p_{ZMP} sur la figure 5.21 est inférieure à la

taille des pieds alors qu'à la vitesse 1,5 m/s, la différence entre $|F_{st}^y|_{max}$ et $|F_{st}^y|$ est presque nulle. Nous pouvons donc conclure que le but principal d'avoir des pieds relativement longs est de limiter le lacet du pied de support.

Dans l'optimisation 3D Cas II, les paramètres sagittaux et les paramètres frontaux sont tous optimisés. L'efficacité de la méthode est évidente. Comme montré sur la figure 5.22, le critère d'énergie de notre robot 3D à des vitesses élevées (3155 N^2ms à 1,5 m/s) est très proche du critère de notre robot 2D sans couplages élastiques sur la figure 3.10 (3161 N^2ms à 1,5 m/s). Bien que le critère d'énergie du robot bipède 3D à basse vitesse (239 N^2ms à 0,3 m/s) est plus élevé que celui du robot bipède 2D sans couplages à la même vitesse (52 N^2ms à 0,3 m/s), il est bien inférieure au critère correspondant dans 3DO Cas I (1484 N^2ms à 0,3 m/s). En outre, quand il s'agit du critère sagittal, les valeurs pour notre robot 3D à des vitesses élevées dans l'optimisation 3D Cas II (2700 N^2ms à 1,5m/s) sont inférieures aux valeurs correspondantes dans l'optimisation 3D Cas I (2970 N^2ms à 1,5 m/s). Cela indique que, en distribuant le critère aux actionneurs dans les deux plans, nous pouvons réduire davantage le critère d'énergie. Malgré la différence entre les deux cas d'optimisation, les pourcentages du critère sagittal et du critère frontal sont proches sur les figures 5.11 et 5.22. Selon la figure 5.23, la distance latérale entre la cheville mobile et la cheville de support a une corrélation positive avec la vitesse, ce qui est contraire à ce qu'on trouve pour les allures humaines.

La représentation des allures aux vitesses 0,3 m/s, 0,7 m/s, 1,1 m/s et 1,5 m/s est fournie sur la figure 5.25. Par rapport à la figure 5.14, l'amplitude du mouvement latéral du tronc est beaucoup plus faible sur la figure 5.25. Sur les figures 5.15 et 5.26, nous pouvons voir que la relation entre t et θ est presque linéaire, ce qui signifie que $\theta(q)$ est un bon substitut du temps pour représenter la progression du robot au cours de chaque pas. En plus, les mouvements des articulations frontales de hanche dans l'optimisation 3D Cas II décrits par q_5, $\dot{q}_5$, q_7 et $\dot{q}_7$ sont beaucoup plus amples que ceux dans l'optimisation 3D Cas I. Ceci suggère que le robot bipède 3D est capable d'utiliser les mouvements propres des articulations coronales de hanche pour éviter un grand mouvement du tronc et pour réduire le critère d'énergie. Selon les figures 5.27, 5.28 et 5.29, nous pouvons constater qu'à la vitesse 0,7 m/s, l'énergie mécanique est surtout consommée par les actionneurs frontaux de hanche, lorsque les actionneurs sagittals de hanche consomment plus d'énergie mécanique à la vitesse 1,5 m/s.

Le contact avec le sol peut être vérifié sur la figure 5.30. Il est intéressant de noter que la plage de variation de p_{ZMP} est beaucoup plus petite que la largeur du pied. Les trajectoires des centres de masse et du bassin sont représentées sur la figure 5.31. En comparant cette figure avec la figure 5.20 dans l'optimisation 3D Cas I, nous constatons que les mouvements latéraux des centres de masse et du bassin dans l'optimisation 3D Cas II sont plus grands que ceux dans l'optimisation 3D Cas I. Les trajectoires de la cheville mobile sont fournies sur la figure 5.32. La hauteur maximale du levée de la cheville est supérieure à 5 cm. Cette valeur est plus grande que la valeur moyenne de 1,3 cm chez l'Homme [181].

Conclusion

Dans ce chapitre, nous avons étendu la méthode de la génération des allures cycliques de marche appliquée aux robots 2D avec un seul degré de sous-actionnement à des scénarios 3D en utilisant des pieds sans masse à contact linéique. Un robot bipède 3D à 8 corps est utilisé comme un exemple. Ce robot a un tronc, un bassin, deux cuisses, deux tibias, deux pieds sans masse à contact linéique. Les paramètres dynamiques du modèle de ce robot sont dérivés du robot HRP-4 [172]. Le modèle de la marche est obtenu en combinant les modèles de la phase de simple appui et de la phase de double appui pour former un modèle hybride. En particulier, nous avons proposé un modèle de contact pour des robots avec des pieds à contact linéique essentiellement dans le plan frontal. Ce modèle nous permet de considérer la possibilité de la rotation en lacet du pied d'appui en supposant que la réaction du sol est appliquée seulement aux deux extrémités du pied.

Pendant la phase de simple appui, la méthode de la linéarisation par retour d'état est adoptée pour appliquer des contraintes virtuelles. En choisissant des robots 3D avec des pieds à contact linéique et un degré de sous-actionnement, nous pouvons atteindre l'invariance hybride analytiquement. Par la suite, la stabilité de marche est analysée par une application LTI scalaire. L'évolution idéale des contraintes virtuelles est paramétrée par des courbes de Bézier d'ordre 5. En plus, nous remplaçons certains des paramètres de Bézier par les paramètres de posture afin de faciliter l'optimisation de la marche. Un modèle de la dynamique inverse est fourni pour créer une application entre les paramètres de posture et les paramètres correspondants de Bézier. Les paramètres d'optimisation sont classés en 16 paramètres sagittaux et 16 paramètres frontaux. Une initialisation est obtenue en utilisant directement les paramètres optimisés des allures de notre robot 2D comme les paramètres sagittaux et en attribuant les constantes par défaut aux paramètres frontaux. La fonction objectif et la fonction de coût sont similaires à celles du cas 2D. Pour notre robot 3D, il existe deux contraintes supplémentaires : les contraintes du pied d'appui et la contrainte pour éviter une collision entre les deux jambes. Par la suite, l'optimisation est effectuée suivant les mêmes procédures que dans le chapitre 3.

Deux cas d'optimisation des allures de marche 3D ont été étudiés : l'optimisation 3D Cas I et l'optimisation 3D Cas II. Dans l'optimisation 3D Cas I, nous n'optimisons que les 16 paramètres frontaux et utilisons les paramètres optimisés des allures de notre robot bipède 2D pour les paramètres sagittaux. Dans l'optimisation 3D Cas II, nous optimisons tous les 32 paramètres. En comparant ces deux cas, nous constatons que l'optimisation simplifiée dans l'optimisation 3D Cas I est seulement efficace à grande vitesse. Dans l'optimisation 3D Cas II, la courbe du coût est semblable à celle de notre robot 2D sans couplage. La valeur maximale du coût est de 3155 N^2ms à 1,5 m/s et la valeur minimale est de 238 N^2ms à 0,3 m/s.

8.6 Couplages élastiques pour le robot 3D

Les travaux présentés dans ce chapitre portent sur l'exploration des avantages de l'ajout de couplages élastiques sous forme de ressorts de torsion au niveau des hanches à des robots bipèdes 3D. Comme dans les cas de couplages élastiques du robot 2D, ceci est réalisé par l'addition des paramètres de couplages aux paramètres d'optimisation et par l'optimisation de la marche. Les couplages élastiques sont appliqués sous la forme de ressorts linéaires de torsion avec trois différentes configurations. Dans le premier cas, un ressort est introduit entre les deux cuisses dans le plan sagittal. Dans le second cas, deux ressorts linéaires sont introduits respectivement entre le bassin et chacune des cuisses dans le plan frontal. Dans le troisième cas, tous les ressorts des deux premiers cas sont introduits. Les résultats montrent l'intérêt de mettre des couplages élastiques dans le plan sagittal, l'ajout de ressorts dans le plan frontal permet de réduire un peu plus la consommation énergétique.

Modèle des couplages élastiques

Étant donné que des composants élastiques ne peuvent pas produire des forces impulsionnelles lors de l'impact, ils n'ont aucune influence sur le modèle de l'impact. Quand au modèle de la phase de simple appui, l'équation (5.5) peut être écrite en (6.1). En utilisant (5.63), nous pouvons calculer les couples des actionneurs du robot évoluant sur la variété de la dynamique des zéros.

La figure 5.22 montre que, pour notre robot bipède 3D, la majeure partie de la consommation d'énergie est dûe aux actionneurs frontaux des articulations de hanche à faible vitesse et aux actionneurs sagittaux des articulations de hanche à grande vitesse. En conséquence, il est intéressant de voir si les couplages élastiques peuvent réduire les critères énergétiques de ces articulations. Nous proposons donc trois configurations:

Couplage 3D Cas I) Comme illustré sur la figure 6.1(a), un ressort linéaire de torsion est monté entre les deux cuisses dans le plan sagittal. Ainsi, nous avons $\varphi_{e1} = q_4 - q_8$ pour la déviation $\varphi_{e1} - \varphi^*_{e1}$ dans l'équation (2.11) du ressort. Étant donné que le robot est symétrique, nous avons $\varphi^*_{e1} = 0$, et la raideur k_{e1} est remplacée par k_{opt1}. Le vecteur des couples τ_e est donné par l'équation (6.3).

Couplage 3D Cas II) Comme illustré sur la figure 6.1(b) deux ressorts linéaires de torsion sont montés respectivement entre le bassin et chacune des cuisses dans le plan frontal. Ainsi, nous avons $\varphi_{e2} = q_5$ et $\varphi_{e3} = q_7$ pour les déviations $\varphi_{e2} - \varphi^*_{e2}$ et $\varphi_{e3} - \varphi^*_{e3}$ des ressorts. Étant donné que le robot 3D est symétrique, nous avons $k_{e2} = k_{e3}$. Nous supposons que les positions de repos de ces deux ressorts sont nulles, $\varphi^*_{e2} = \varphi^*_{e3} = 0$. Les raideurs k_{e2} et k_{e3} sont remplacées par k_{opt2}. En utilisant l'équation (2.18), le vecteur des couples τ_e est donné par l'équation (6.4).

Couplage 3D Cas III) Dans ce cas, un ressort est introduit dans le plan sagittal de la même manière que dans le couplage 3D Cas I, et deux ressorts sont ajoutés dans le plan frontal de la même manière que dans le couplage 3D Cas II. En utilisant l'équation (2.18), le vecteur des couples τ_e est donné par l'équation (6.5).

Allures optimales de marche avec des couplages élastiques

Selon la figure 6.2, le coût global d'énergie est beaucoup plus faible aux vitesses de 0,6 m/s à 1,5 m/s dans le couplage 3D Cas I que dans l'optimisation 3D Cas II (sans couplage) sur la figure 5.22. Pour une grande plage de vitesse de 0,35 m/s à 1 m/s, le coût de l'énergie est d'environ 200 N^2ms. À 1, 5 m/s, le coût de l'énergie est 475 N^2ms alors que la valeur correspondante sans couplage élastique est 3155 N^2ms dans l'optimisation 3D Cas II. Malgré la réduction évidente du coût de l'énergie à grande vitesse, il y a peu de réduction pour le coût de l'énergie à faible vitesse. À la vitesse la plus basse, le coût de l'énergie des actionneurs dans le plan frontal est très proche du coût global et le coût de l'énergie des actionneurs dans le plan sagittal est presque négligeable.

Les variations des paramètres de la posture à des vitesses différentes sont fournies sur la figure 6.3. En comparaison avec les allures de marche sur la figure 5.25 dans l'optimisation 3D Cas II sans couplage, les allures dans le couplage 3D Cas I sont décrites avec des pas plus petits et une position du tronc plus verticale. Quant à la raideur k_{opt1}, nous pouvons voir sur la figure 6.4 qu'elle augmente avec la vitesse de marche, mais elle atteind un point de saturation à grande vitesse. L'explication la plus probable de cette saturation sont les marges limitées pour les conditions de contact au sol sur la figure 6.21.

Les évolutions des allures aux vitesses 0,3 m/s, 0,7 m/s, 1,1 m/s et 1,5 m/s sont fournies sur la figure 6.5. Les informations détaillées concernant les allures à 0,7 m/s et 1,5 m/s sont fournies sur les figures 6.6 à 6.12. Dans le couplage 3D Cas I, les mouvements latéraux du tronc et du centre de masse sont plus petits que ceux de l'optimisation 3D Cas II. En outre, la distance latérale entre le pied d'appui et le pied mobile est plus courte que celle de l'optimisation 3D Cas II. Les puissances mécaniques sont illustrées sur la figure 6.9. Il est évident que les puissances négatives dans le couplage 3D Cas I sont plus grandes que celles dans l'optimisation 3D Cas II sur la figure 5.29. Sur la figure 6.10, nous pouvons vérifier les contraintes de contact en utilisant les équations (5.45), (5.46), (5.50), (5.51) et (5.56).

Dans le couplage 3D Cas II (avec des couplages), les courbes des coûts d'énergie sont données sur la figure 6.13. Bien que le coût global d'énergie diminue à toutes les vitesses par rapport au coût de l'optimisation 3D Cas II (sans couplage) sur la figure 5.22, la réduction est beaucoup plus petite à grande vitesse que celle dans le couplage 3D Cas I. Cela suggère que, à grande vitesse, les couplages dans le plan frontal sont moins efficaces pour la réduction de la consommation d'énergie que les couplages dans le plan sagittal. Cependant, à basse vitesse, le coût minimum d'énergie de 131 N^2ms dans le couplage 3D Cas II est plus faible que le coût de 200 N^2ms dans le couplage 3D Cas I. La variation de la raideur à des vitesses différentes est fournie sur la figure 6.15. Comme la raideur k_{opt1} dans le couplage 3D Cas I, la raideur k_{opt2} augmente aussi avec la vitesse de marche, mais la saturation arrive à une vitesse plus faible et à grande vitesse la raideur k_{opt2} diminue même un peu.

Les évolutions des allures à des vitesses différentes sont fournies sur la figure 6.16. Les informations détaillées concernant les allures à 0,7 m/s et 1,5 m/s sont fournies sur les figures 6.17 à 6.23. Il est évident que les mouvements du robot bipède 3D

dans le plan frontal sont plus grands que ceux sur les figures 6.5 et 5.25 dans le couplage 3D Cas I et l'optimisation 3D Cas II. En comparant la figure 6.8 à la figure 6.19, nous pouvons constater que les valeurs absolues maximales des couples u_4 et u_8 dans le couplage 3D Cas I sont plus petits que celles dans le couplage 3D Cas II, en particulier à la vitesse 1,5 m/s. Selon les courbes des puissances mécaniques sur la figure 6.20, les amplitudes des puissances négatives des articulations de la hanche dans le plan sagittal sont proches de celles des puissances positives. En conséquence, il est possible de réduire encore le coût de l'énergie par l'ajout des couplages élastiques dans le plan sagittal.

Dans le couplage 3D Cas III, les courbes des coûts d'énergie sont données sur la figure 6.24. En comparaison avec les autres coûts d'énergie sur les figures 5.22, 6.2 et 6.13, le coût d'énergie du robot bipède 3D est la plus faible dans le couplage 3D Cas III. Le coût maximal d'énergie est 367 N^2ms à 1,5 m/s, et pour une grande plage de vitesse de 0,35 m/s à 0,8 m/s le coût de l'énergie est seulement autour de 75 N^2ms. Cela signifie que nous pouvons améliorer l'efficacité énergétique de notre robot 3D en ajoutant des couplages élastiques dans les deux plans.

Les évolutions des allures à des vitesses différentes sont fournies sur la figure 6.27. Les variations des paramètres de la posture à des vitesses différentes sont fournies sur la figure 6.25. En observant la variation du paramètre y_{sw}^{-}, nous pouvons voir que le robot 3D a une faible distance latérale entre les pieds à grande vitesse et une grande distance latérale à faible vitesse. Cela est conforme à notre compréhension intuitive concernant la différence entre une promenade et une marche athlétique. Ce phénomène est également observé dans le couplage 3D Cas I, mais dans l'optimisation 3D Cas II la relation est inverse, ce qui suggère que les allures de marche de notre robot bipède 3D sont différentes des allures humaines quand il n'y a pas de couplage élastique. Un autre point intéressant est que l'angle β du bassin dans le plan sagittal est plus petit dans les couplages 3D Cas I, II et III que celui dans les optimisation 3D Cas I et II. Ceci suggère que le robot bipède 3D peut avoir des postures plus droites lors de la marche à l'aide des couplages élastiques au niveau des articulations de hanche. La variation des raideurs k_{opt1} et k_{opt2} en fonction de la vitesse est fournie sur la figure 6.26. Les deux raideurs augmentent avec la vitesse de marche, mais elles atteignent un point de saturation à grande vitesse.

Les évolutions des allures à des vitesses différentes sont fournies sur la figure 6.27. Nous pouvons voir que les allures optimisées de marche dans le couplage 3D Cas III sont plus près des allures humaines que celles dans les autres cas 3D, ce qui est principalement démontré par la position du tronc plus verticale et le mouvement latéral de la jambe mobile plus petit. Les informations détaillées concernant les allures à 0,7 m/s et 1,5 m/s sont fournies sur les figures 6.28 à 6.34.

Selon la figure 6.30, les amplitudes des couples τ_{e4} et τ_{e8} générés par les couplages élastiques dans le couplage 3D Cas III sont beaucoup plus grandes que celles des couples u_4 et u_8 des actionneurs correspondants. Cela vaut aussi dans le couplage 3D Cas I, alors que dans le couplage 3D Cas II, les amplitudes des couples u_5 et u_7 sont proches de celles des couples τ_{e5} et τ_{e7}. L'efficacité des couplages élastiques dans le couplage 3D Cas III peut être vérifiée par les puissances mécaniques des

actionneurs dans la figure 6.31. Dans les couplages 3D Cas I et II (figures 6.9 et 6.20), les amplitudes des puissances négatives des actionneurs de hanche ne sont pas négligeables par rapport aux puissances positives correspondantes, mais dans le couplage 3D Cas III, les amplitudes des puissances négatives des actionneurs de hanche sont beaucoup plus petites que les puissances positives correspondantes. Ceci suggère que l'objectif principal des actionneurs de hanche dans le couplage 3D Cas III est de compenser la perte d'énergie.

La plage de la position du ZMP sur la figure 6.32 est proche de celle sur la figure 6.10 dans le couplage 3D Cas I et de celle sur la figure 5.30 dans l'optimisation 3D Cas II. Cependant, sur la figure 6.21 dans le couplage 3D Cas II, la plage de variation de la position du ZMP est la plus importante par rapport à celles dans les autres cas 3D. Cela signifie que l'influence négative sur la plage de la position du ZMP dans le couplage 3D Cas II peut être évitée en ajoutant des couplages élastiques dans le plan sagittal. En comparant les trajectoires du centre de masse sur les figure 6.11, 6.22 et 6.33, nous pouvons voir que les amplitudes des mouvements latérals et verticals du centre de masse sont similaires dans les couplages 3D Cas I et III. Les mouvements du centre de masse sont beaucoup plus grands dans le couplage 3D Cas II, ce qui est probablement lié à la large plage du ZMP sur la figure 6.21. La hauteur maximale du pied mobile sur la figure 6.34 est de moins de 2 cm aux deux vitesses 0,7 m/s et 1,5 m/s, et ces valeurs sont très proches de la valeur moyenne de 1,3 cm chez l'Homme [181].

Discussion

Dans la partie précédente, nous avons démontré les avantages de l'ajout de couplages élastiques de type ressorts de torsion aux hanches à notre robot bipède 3D. Il est intéressant de faire des comparaisons entre tous les cas de couplage 3D.

Lorsqu'il s'agit du coût de l'énergie, le couplage 3D Cas III fournit sans doute la meilleure solution et le couplage 3D Cas I est également satisfaisant. L'inconvénient du 3DC Cas III par rapport au 3DC Cas I est que deux ressorts supplémentaires sont nécessaires, ce qui est plus difficile à réaliser. Une chose est sûre, le couplage 3D Cas II n'est jamais le choix judicieux non seulement parce que la réduction du coût de l'énergie est limitée, mais aussi parce qu'il a des caractéristiques négatives comme des mouvements frontaux excessifs.

Quant à la possibilité de modifier les constantes de ressort, nous pouvons envisager plusieurs options pour éviter d'utiliser des actionneurs supplémentaires comme dans [153, 154, 156, 157]. Dans le couplage 3D Cas III, nous pouvons probablement utiliser des ressorts linéaires avec les raideurs fixes aux vitesses supérieures à $1\,m/s$ car il y a des saturations évidentes de k_{opt1} et de k_{opt2}. En outre, nous pouvons également utiliser les ressorts non-linéaires, cela a été proposé au chapitre 4.

Les orbites périodiques de tous les angles relatifs du robot 3D sont fournies dans la figure 6.35. Pour tous les angles relatifs des articulations, les sauts des vitesses angulaires (indiqués par des flèches noires) pendant la phase de double appui dans les couplages 3D Cas I et III sont plus petits que ceux dans le couplage 3D Cas II et dans l'optimisations 3D Cas I et II. En comparant les figures 6.35 (c) et 4.29

(f), nous pouvons voir que, dans tous les cas 3D sauf l'optimisation 3D Cas I, les plages des variations des angles relatifs de genou sont plus petites que celles dans les cas 2D. Cela signifie que notre robot bipède 3D a des allures avec des jambes plus droites.

Conclusion

Dans ce chapitre, nous avons envisagé trois cas d'ajout de couplages élastiques sous forme de ressorts aux hanches au robot 3D présentés dans le chapitre 5. Dans le couplage 3D Cas I, un ressort linéaire de torsion est introduit entre les deux cuisses dans le plan sagittal. Dans le couplage 3D Cas II, deux ressorts linéaires de torsion sont introduits respectivement entre le bassin et chacune des cuisses dans le plan frontal. Dans le couplage 3D Cas III, tous les ressorts dans les deux premiers cas sont introduits. Les résultats pour les trois cas sont obtenus en utilisant les méthodes d'optimisation énoncées dans le chapitre 5. Le couplage 3D Cas III a le coût de l'énergie le plus bas pour toutes les vitesses de 0,2 m/s à 1,5 m/s, et le coût de l'énergie varie de $74,3\,N^2ms$ à 367 N^2ms. La deuxième option est le couplage 3D Cas I. Dans ce cas, nous avons un coût de l'énergie variant de 198 N^2ms à 475 N^2ms. Dans le couplage 3D Cas II, le coût de l'énergie varie de 132 N^2ms à 2579 N^2ms. Ce cas est seulement utile pour la conception d'un robot bipède 3D avec une vitesse de marche de moins de $0,5$ m/s. À partir les résultats de l'optimisation de la marche aux vitesses de 0,7 m/s et 1,5 m/s, les couplages 3D Cas I et III ont une petite plage de variation du ZMP. De plus, ces deux cas ont les sauts de vitesses angulaires plus petits que le couplage 3D Cas II, ce qui peut être considéré comme un signe indiquant que le robot bipède 3D marche efficacement en résonance.

8.7 Conclusion et perspectives

Conclusion

Des études en biomécanique ont montré que, la stature bipède a permis à l'homme de parcourir de longs trajets avec une grande efficacité energétique, ce qui a facilité sa survie. Nous pouvons alors nous demander s'il est possible d'arriver à la même efficacité pour les robots humanoïdes. En effet, l'homme a des allures de marche très dynamiques alors que la plupart des robots humanoïdes marchent maladroitement. En outre, le corps humain possède des muscles et des tendons qui assurent la fluidité de ses mouvements ainsi que le recyclage de l'énergie, mais les composants élastiques sont encore rarement utilisés dans les robots humanoïdes. D'un point de vue général, cette étude traite principalement du sujet de la commande des robots bipèdes, de l'optimisation des allures et des couplages élastiques.

Deux robots bipèdes sont étudiés : un robot 2D avec des pieds ponctuels et un robot 3D avec des pieds sans masse à contact linéique. En référence au robot humanoïde HRP-4, la masse totale est 39 kg et la taille est 1,5 m pour les deux modèles. En utilisant ces deux variables, nous pouvons générer des structures anthropomorphiques virtuelles, à partir desquelles les autres paramètres du modèle peuvent être obtenus [173, 174]. Pour les allures de marche, nous supposons que pour chaque pas il y a deux phases alternées de simple appui et de double appui. Ces deux phases sont séparées par un impact rigide. Pendant la phase de simple appui, les deux robots considérés ont un seul degré de sous-actionnement.

En utilisant la méthode basée sur les contraintes virtuelles et la linéarisation par retour d'état, nous pouvons étudier le modèle hybride d'un robot par son sous-système de la dynamique des zéros. Si la dynamique des zéros est invariante après l'impact, la stabilité de ce sous-système est équivalente à celle de l'ensemble du système. Pour les robots avec un degré de sous-actionnement, cette application est scalaire, en conséquence, nous pouvons facilement vérifier la stabilité. Cette méthode a été appliquée principalement aux robots 2D. Nous avons étendu cette méthode à des scénarios 3D en utilisant des pieds sans masse à contact linéique. En comparaison avec les robots bipèdes 3D avec des pieds ponctuels et deux ou plusieurs degrés de sous-actionnement, les robots avec des pieds à contact linéique et un degré de sous-actionnement sont beaucoup plus simples, bien que la position du ZMP doit rester à l'intérieur du pied d'appui. En plus, nous avons utilisé les sorties symétriques pour obtenir une bonne interprétation géométrique de la commande de marche.

Pour l'optimisation des allures de marche, nous utilisons des paramètres de la posture et des paramètres des courbes de Bézier d'ordre 5 pour définir les sorties souhaitées. Le nombre de paramètres à optimiser sans couplages élastiques est de 16 pour le robot 2D et de 32 pour le robot 3D. Pour le robot 3D, les 32 paramètres sont ensuite divisés en 16 paramètres sagittaux et 16 paramètres frontaux. Deux cas d'optimisation 3D sont proposés. Dans l'optimisation 3D Cas I, nous n'optimisons que les 16 paramètres frontaux tout en utilisant les paramètres optimisés de notre robot 2D comme paramètres sagittaux. Dans l'optimisation 3D Cas II, nous utilisons

les paramètres optimisés de notre robot 2D pour créer une initialisation et optimisons tous les 32 paramètres.

L'optimisation des allures de marche pour les deux robots est réalisée par la fonction `fmincon` de la toolbox d'optimisation de MATLAB® (R2010b). Nous avons choisi la méthode d'optimisation `sqp`. La fonction objectif est définie comme l'intégrale du carré des couples pour un déplacement unitaire. Quant aux contraintes d'optimisation, les deux robots ont des contraintes de contact, de la position du pied mobile, de la vitesse moyenne de marche, etc. Pour notre robot 3D, nous avons défini un modèle de contact avec des pieds à contact linéique en supposant que la réaction du sol est appliquée seulement aux deux extrémités du pied. Ce modèle nous permet de vérifier la possibilité de rotation en lacet du pied d'appui. Pour les deux robots bipèdes, la vitesse moyenne de marche est la seule contrainte d'égalité. Les nombres de contraintes d'inégalité sont de 7 pour le robot 2D et de 11 pour le robot 3D.

Quant aux couplages élastiques, ils sont introduits sur le robot 2D/3D sous forme de ressorts linéaires de torsion. Pour le robot 2D, nous proposons deux configurations de couplages élastiques. Dans le couplage 2D Cas I, un ressort linéaire de torsion est monté entre les deux cuisses. Dans le couplage 2D Cas II, deux ressorts sont montés respectivement entre le tronc et chacune des cuisses. Pour le robot 3D, nous proposons trois configurations de couplages élastiques. Dans le couplage 3D Cas I, un ressort linéaire est introduit entre les deux cuisses dans le plan sagittal. Dans le couplage 3D Cas II, deux ressorts linéaires sont introduits respectivement entre le bassin et chacune des cuisses dans le plan frontal. Dans le couplage 3D Cas III, tous les ressorts des deux premiers cas sont introduits.

Les allures optimisées avec des couplages élastiques sont obtenues en incluant des raideurs et des positions de repos dans les paramètres à optimiser. Dans tous les cas, les vitesses de marche étudiés vont de 0,2 m/s à 1,5 m/s. La stabilité et la validité des allures sont vérifiées numériquement.

Les résultats de l'optimisation les plus importants sont brièvement résumés ci-dessous. Pour le robot 2D sans couplage élastique, le coût de l'énergie varie de 42,6 N^2ms (à 0,2 m/s) à 3161 N^2ms (à 1,5 m/s). En appliquant les deux configurations de couplages élastiques, le coût maximal diminue à 384 N^2ms dans le 2DC Cas I et à 329 N^2ms dans le 2DC Cas II. Ceci signifie que les deux configurations peuvent considérablement réduire le coût de l'énergie du robot 2D. Dans les deux cas de couplage élastique, le tronc du robot est plus proche de la verticale que dans le cas sans couplage, et la fréquence de pas est proche de la fréquence de référence de pas, qui est définie comme deux fois la fréquence propre de la jambe mobile avec le genou verrouillé dans une position droite.

Pour le robot 3D sans couplage élastique, l'optimisation 3D Cas II est mieux que l'optimisation 3D Cas I avec un coût de l'énergie de 239 N^2ms (à 0,3 m/s) à 3155 N^2ms (à 1,5 m/s). l'optimisation 3D Cas I est efficace seulement à grande vitesse avec un coût de l'énergie de 975 N^2ms (à 0,6 m/s) à 3300 N^2ms (à 1,5 m/s). Cela suggère que, à basse vitesse, les mouvements sagittaux et les mouvements frontaux sont fortement couplés. En ajoutant des couplages élastiques dans le plan sagittal, le coût maximal de l'énergie est réduit à 475 N^2ms et aux vitesses

de 0,35 m/s à 1 m/s le coût de l'énergie est d'environ 200 N^2ms. D'autre part, l'effet de l'ajout de couplages élastiques dans le plan frontal est relativement limité et le coût maximal de l'énergie est de 2579 N^2ms. Cependant, le coût minimal de l'énergie dans le couplage 3D Cas II diminue à 132 N^2ms et cette valeur est plus petite que la valeur 198 N^2ms dans le couplage 3D Cas I. Le coût de l'énergie le plus bas est obtenu dans le couplage 3D Cas III. Dans ce cas, le coût maximal de l'énergie est seulement de 367 N^2ms. En plus, aux vitesses de 0,35 m/s à 0,8 m/s le coût de l'énergie est autour de 75 N^2ms. Ces données indiquent que les couplages dans le plan sagittal sont beaucoup plus importants que ceux dans le plan frontal et que la meilleure option est d'ajouter des couplages élastiques dans les deux plans.

Perspectives

Après trois années de recherche, nous avons répondu à quelques questions concernant la marche dynamique et les couplages élastiques pour des robots bipèdes 2D/3D. Toutefois, ces réponses posent de nouvelles questions pour des recherches futures.

D'abord, nous proposons de faire des expériences sur un robot réel afin d'expérimenter nos propositions et d'évaluer leur robustesse.

Il est possible de vérifier les résultats avec des couplages élastiques en utilisant une commande d'impédance sur les axes concernés.

On pourra aussi faire des comparaisons entre nos résultats et des données de la marche humaine. Il serait également intéressant d'essayer d'autres sorties, ce qui nous permettra de connaître les avantages et les inconvénients des sorties symétriques.

Nous pouvons aussi tenir compte de la masse des pieds de notre robot 3D et de concevoir une loi de commande pour des robots avec des pieds avec masse à contact linéique dans le plan sagittal.

Enfin, on pourra ajouter des degrés de liberté en lacet, surtout au niveau des hanches et des chevilles.

BIBLIOGRAPHY

[1] W. R. Leonard and M. L. Robertson, "Energetic efficiency of human bipedality." *American Journal of Physical Anthropology*, vol. 97, no. 3, pp. 335–338, 1995.

[2] M. Hobon, *Modélisation et optimisation de la marche d'un robot bipède avec genoux anthropomorphiques.* Laboratoire de Conception Fabrication Commande, Ecole Doctorale Sciences des Métiers de l'Ingénieur - SMI (Paris), 2012.

[3] M. Hobon, N. Lakbakbi-Elyaaqoubi, and G. Abba, "Gait optimization of a rolling knee biped at low walking speeds," in *ICINCO 2013 - Proceedings of the 10th International Conference on Informatics in Control, Automation and Robotics*, vol. 2, Reykjavík, Iceland, 2013, pp. 207–214.

[4] M. Hobon, N. Lakbakbi-Elyaaqoubi, and G. Abba, "Quasi optimal sagittal gait of a biped robot with a new structure of knee joint," *Robotics and Autonomous Systems*, vol. 62, no. 4, pp. 436–445, 2014.

[5] C. Chevallereau, G. Abba, Y. Aoustin, F. Plestan, E. R. Westervelt, C. Canudas-de Wit, and J. W. Grizzle, "Rabbit: a testbed for advanced control theory," *Control Systems, IEEE*, vol. 23, no. 5, pp. 57–79, Oct 2003.

[6] J. W. Grizzle, G. Abba, and F. Plestan, "Asymptotically stable walking for biped robots: Analysis via systems with impulse effects," *IEEE Transactions on Automatic Control*, vol. 46, no. 1, pp. 51–64, 2001.

[7] F. Plestan, J. W. Grizzle, E. R. Westervelt, and G. Abba, "Stable walking of a 7-dof biped robot," *IEEE Transactions on Robotics and Automation*, vol. 19, no. 4, pp. 653–668, 2003.

[8] E. R. Westervelt, J. W. Grizzle, C. Chevallereau, J. H. Choi, and B. Morris, *Feedback Control of Dynamic Bipedal Robot Locomotion*, 1st ed. Boca Raton, FL, USA: CRC press, 2007, vol. 28.

[9] H. O. Lim and A. Takanishi, "Biped walking robots created at waseda university: Wl and wabian family," *Royal Society of London Philosophical Transactions Series A*, vol. 365, pp. 49–64, Jan. 2007.

[10] A. Takanishi, M. Ishida, Y. Yamazaki, and I. Kato, "Realization of dynamic walking by the biped walking robot WL-10RD," in *1985 International Conference on Advanced Robotics*, Tokyo, Japan, 1985, pp. 459–466.

[11] A. M. M. Omer, R. Ghorbani, H. O. Lim, and A. Takanishi, "Semi-passive dynamic walking for biped walking robot using controllable joint stiffness based on dynamic simulation," in *IEEE/ASME International Conference on Advanced Intelligent Mechatronics, AIM*, Singapore, 2009, pp. 1600–1605.

[12] K. Hashimoto, K. Hattori, T. Otani, H. O. Lim, and A. Takanishi, "Foot placement modification for a biped humanoid robot with narrow feet," *The Scientific World Journal*, vol. 2014, pp. 1–9, 2014.

[13] Y. Sakagami, R. Watanabe, C. Aoyama, S. Matsunaga, N. Higaki, and K. Fujimura, "The intelligent asimo: System overview and integration," in *IEEE International Conference on Intelligent Robots and Systems*, vol. 3, Lausanne, Switzerland, 2002, pp. 2478–2483.

[14] K. Hirai, M. Hirose, Y. Haikawa, and T. Takenaka, "The development of honda humanoid robot," in *Proceedings of the 1998 IEEE International Conference on Robotics and Automation*, vol. 2, Lueven, Belgium, May 1998, pp. 1321–1326 vol.2.

[15] K. Kaneko, F. Kanehiro, S. Kajita, K. Yokoyama, K. Akachi, T. Kawasaki, S. Ota, and T. Isozumi, "Design of prototype humanoid robotics platform for hrp," in *IEEE/RSJ 2002 International Conference on Intelligent Robots and Systems*, vol. 3, Lausanne, Switzerland, 2002, pp. 2431–2436.

[16] F. Kanehiro, K. Kaneko, K. Fujiwara, K. Harada, S. Kajita, K. Yokoi, H. Hirukawa, K. Akachi, and T. Isozumi, "The first humanoid robot that has the same size as a human and that can lie down and get up," in *IEEE International Conference on Robotics and Automation*, Taipei, Taiwan, 2003, pp. 1633–1639.

[17] S. Kajita, F. Kanehiro, K. Kaneko, K. Fujiwara, K. Yokoi, and H. Hirukawa, "A realtime pattern generator for biped walking," in *Proceedings of the 2002 IEEE International Conference on Robotics and Automation*, vol. 1, Washington, DC, USA, 2002, pp. 31–37.

[18] S. Kajita, T. Nagasaki, K. Kaneko, K. Yokoi, and K. Tanie, "A hop towards running humanoid biped," in *Proceedings of the 2004 IEEE International Conference on Robotics and Automation*, vol. 1, New Orleans, LA USA, April 2004, pp. 629–635.

[19] K. Kaneko, K. Harada, F. Kanehiro, G. Miyamori, and K. Akachi, "Humanoid robot HRP-3," in *2008 IEEE/RSJ International Conference on Intelligent Robots and Systems*, Nice, France, Sept 2008, pp. 2471–2478.

[20] K. Kaneko, F. Kanehiro, M. Morisawa, K. Akachi, G. Miyamori, A. Hayashi, and N. Kanehira, "Humanoid robot HRP-4 - humanoid robotics platform with lightweight and slim body," in *2011 IEEE/RSJ International Conference on Intelligent Robots and Systems (IROS)*, San Francisco, California, USA, Sept 2011, pp. 4400–4407.

[21] E. Yoshida, C. Esteves, T. Sakaguchi, J. P. Laumond, and K. Yokoi, "Smooth collision avoidance: Practical issues in dynamic humanoid motion," in *2006 IEEE/RSJ International Conference on Intelligent Robots and Systems*, Beijing, China, Oct 2006, pp. 827–832.

[22] C. Santacruz and Y. Nakamura, "Analytical real-time pattern generation for trajectory modification and footstep replanning of humanoid robots," in *2012 IEEE/RSJ International Conference on Intelligent Robots and Systems (IROS)*, Vilamoura, Portugal, Oct 2012, pp. 2095–2100.

[23] M. A. Ali, H. A. Park, and C. S. G. Lee, "Closed-form inverse kinematic joint solution for humanoid robots," in *2010 IEEE/RSJ International Conference on Intelligent Robots and Systems (IROS)*, Taipei, Taiwan, Oct 2010, pp. 704–709.

[24] P. Zhaoqin, Y. F., Z. T., and Q. H., "Online walking pattern generation and system software of humanoid bhr-2," in *2006 IEEE/RSJ International Conference on Intelligent Robots and Systems*, Beijing, China, Oct 2006, pp. 5471–5476.

[25] V. Favot, M. Schwienbacher, T. Buschmann, S. Lohmeier, and H. Ulbrich, "The humanoid robot lola - experimental results," in *AIP Conference Proceedings*, vol. 1281, Rhodes, Greece, 2010, pp. 398–401.

[26] C. Ott, A. Dietrich, and M. Roa, "Torque-based multi-task and balancing control for humanoid robots," in *2014 11th International Conference on Ubiquitous Robots and Ambient Intelligence (URAI)*, Kuala Lumpur, Malaysia, 2014, pp. 143–144.

[27] C. Ott, C. Baumgärtner, J. Mayr, M. Fuchs, R. Burger, D. Lee, O. Eiberger, A. Albu-Schäffer, M. Grebenstein, and G. Hirzinger, "Development of a biped robot with torque controlled joints," in *2010 10th IEEE-RAS International Conference on Humanoid Robots*, Nashville, TN, USA, 2010, pp. 167–173.

[28] A. D. Ames, "Human-inspired control of bipedal walking robots," *IEEE Transactions on Automatic Control*, vol. 59, no. 5, pp. 1115–1130, May 2014.

[29] C. Azevedo, N. Andreff, and S. Arias, "Bipedal walking: From gait design to experimental analysis," *Mechatronics*, vol. 14, no. 6, pp. 639–665, 2004.

[30] P. Sardain, M. Rostami, E. Thomas, and G. Bessonnet, "Biped robots: Correlations between technological design and dynamic behavior," *Control Engineering Practice*, vol. 7, no. 3, pp. 401 – 411, 1999.

[31] A. Droniou, S. Ivaldi, V. Padois, and O. Sigaud, "Autonomous online learning of velocity kinematics on the iCub: A comparative study," in *IEEE International Conference on Intelligent Robots and Systems*, Vila Moura, Algave, Portugal, 2012, pp. 3577–3582.

[32] S. M. Nguyen, S. Ivaldi, N. Lyubova, A. Droniou, D. Gerardeaux-Viret, D. Filliat, V. Padois, O. Sigaud, and P. Y. Oudeyer, "Learning to recognize objects through curiosity-driven manipulation with the iCub humanoid robot," in *Electronic Conference Proceedings of 2013 IEEE 3rd Joint International Conference on Development and Learning and Epigenetic Robotics (ICDL)*, Osaka, Japan, 2013.

[33] B. Vanderborght, B. Verrelst, R. Van Ham, J. Vermeulen, and D. Lefeber, "Dynamic control of a bipedal walking robot actuated with pneumatic artificial muscles," in *Proceedings - IEEE International Conference on Robotics and Automation*, vol. 2005, Barcelona, Spain, 2005, pp. 1–6.

[34] M. H. Raibert, *Legged Robots That Balance.* Cambridge, MA, USA: Massachusetts Institute of Technology, 1986.

[35] T. McGeer, "Passive walking with knees," in *Proceedings of the 1990 IEEE International Conference on Robotics and Automation*, vol. 3, Cincinnati, OH, USA, 1990, pp. 1640–1645.

[36] S. H. Collins, M. Wisse, and A. Ruina, "A three-dimensional passive-dynamic walking robot with two legs and knees," *International Journal of Robotics Research*, vol. 20, no. 7, pp. 607–615, 2001.

[37] K. Sreenath, H. W. Park, I. Poulakakis, and J. W. Grizzle, "Design and experimental implementation of a compliant hybrid zero dynamics controller for walking on mabel," in *Proceedings of the IEEE Conference on Decision and Control*, Orlando, Florida, USA, 2010, pp. 280–287.

[38] K. Sreenath, H. W. Park, I. Poulakakis, and J. W. Grizzle, "Embedding active force control within the compliant hybrid zero dynamics to achieve stable, fast running on mabel," *International Journal of Robotics Research*, vol. 32, no. 3, pp. 324–345, 2013.

[39] K. Akbari-Hamed and J. W. Grizzle, "Event-based stabilization of periodic orbits for underactuated 3-D bipedal robots with left-right symmetry," *IEEE Trans. Robot.*, vol. 30, no. 2, pp. 365–381, Apr. 2014.

[40] A. Ramezani and J. W. Grizzle, "Atrias 2.0, a new 3D bipedal robotic walker and runner," in *Adaptive Mobile Robotics - Proceedings of the 15th International Conference on Climbing and Walking Robots and the Support Technologies for Mobile Machines (CLAWAR)*, Homewood, Alabama, USA, 2012, pp. 467–474.

[41] J. Pratt and B. Krupp, "Design of a bipedal walking robot," in *Proceedings of SPIE - The International Society for Optical Engineering*, vol. 6962, Marseille, France, 2008, pp. 1–13.

[42] J. Rebula, F. Cañnas, J. Pratt, and A. Goswami, "Learning capture points for humanoid push recovery," in *Proceedings of the 2007 7th IEEE-RAS International Conference on Humanoid Robots*, Pittsburgh, PA, USA, 2008, pp. 65–72.

[43] R. Playter, K. Blankespoor, J. Bondaryk, A. Rizzi, A. Saunders, and M. Raibert, "Building man and beast at boston dynamics," in *2012 AUVSI Unmanned Systems North America Conference*, vol. 2, Las Vegas, NV, USA, 2012, pp. 1041–1046.

[44] M. Vukobratović, B. Borovac, and V. Potkonjak, "ZMP: A review of some basic misunderstandings," *International Journal of Humanoid Robotics*, vol. 3, no. 2, pp. 153–175, 2006.

[45] A. Goswami, "Postural stability of biped robots and the foot-rotation indicator (FRI) point," *International Journal of Robotics Research*, vol. 18, no. 6, pp. 523–533, 1999.

[46] P. Sardain and G. Bessonnet, "Forces acting on a biped robot. center of pressure - zero moment point," *IEEE Transactions on Systems, Man, and Cybernetics Part A:Systems and Humans.*, vol. 34, no. 5, pp. 630–637, 2004.

[47] S. Cotton, A. P. Murray, and P. Fraisse, "Estimation of the center of mass: From humanoid robots to human beings," *IEEE/ASME Transactions on Mechatronics*, vol. 14, no. 6, pp. 707–712, 2009.

[48] S. Kajita and K. Tani, "Study of dynamic biped locomotion on rugged terrain-theory and basic experiment," in *Fifth International Conference on Advanced Robotics, 'Robots in Unstructured Environments', 91 ICAR.*, vol. 1, Pisa, Italy, June 1991, pp. 741–746.

[49] A. D. Kuo, "Choosing your steps carefully," *Robotics Automation Magazine, IEEE*, vol. 14, no. 2, pp. 18–29, June 2007.

[50] J. H. Choi and J. W. Grizzle, "Planar bipedal walking with foot rotation," in *American Control Conference, 2005. Proceedings of the 2005*, vol. 7, Portland, June 2005, pp. 4909–4916.

[51] J. H. Park and K. Kim, "Biped robot walking using gravity-compensated inverted pendulum mode and computed torque control," in *Proceedings of the 1998 IEEE International Conference on Robotics and Automation*, vol. 4, Leuven, Belgium, May 1998, pp. 3528–3533.

[52] D. Galdeano, A. Chemori, S. Krut, and P. Fraisse, "Optimal pattern generator for dynamic walking in humanoid robotics," in *2013 10th International Multi-Conference on Systems, Signals and Devices (SSD)*, Hammamet, Tunisia, 2013, pp. 1–6.

[53] J. E. Pratt and S. V. Drakunov, "Derivation and application of a conserved orbital energy for the inverted pendulum bipedal walking model," in *2007 IEEE International Conference on Robotics and Automation*, Rome, Italy, April 2007, pp. 4653–4660.

[54] B. J. Stephens and C. G. Atkeson, "Push recovery by stepping for humanoid robots with force controlled joints," in *2010 10th IEEE-RAS International Conference on Humanoid Robots*, Nashville, TN, USA, Dec 2010, pp. 52–59.

[55] T. Takenaka, T. Matsumoto, and T. Yoshiike, "Real time motion generation and control for biped robot -3rd report: Dynamics error compensation," in *2009 IEEE/RSJ International Conference on Intelligent Robots and Systems (IROS)*, St. Louis, MO, USA, Oct 2009, pp. 1594–1600.

[56] J. Pratt, J. Carff, S. Drakunov, and A. Goswami, "Capture point: A step toward humanoid push recovery," in *2006 6th IEEE-RAS International Conference on Humanoid Robots*, Genoa, Italy, Dec 2006, pp. 200–207.

[57] J. E. Pratt, T. Koolen, T. de Boer, J. Rebula, s. Cotton, J. Carff, M. Johnson, and P. Neuhaus, "Capturability-based analysis and control of legged locomotion, part 2: Application to m2v2, a lower body humanoid," *The International Journal of Robotics Research*, vol. 31, no. 10, pp. 1117–1133, 2012.

[58] M. Krause, J. Englsberger, P. B. Wieber, and C. Ott, "Stabilization of the capture point dynamics for bipedal walking based on model predictive control," in *IFAC Proceedings Volumes (IFAC-PapersOnline)*, Dubrovnik, Croatia, 2012, pp. 165–171.

[59] S. Lengagne, N. Ramdani, and P. Fraisse, "Planning and fast replanning safe motions for humanoid robots," *IEEE Transactions on Robotics*, vol. 27, no. 6, pp. 1095–1106, 2011.

[60] A. Ibanez, P. Bidaud, and V. Padois, "Emergence of humanoid walking behaviors from mixed-integer model predictive control," in *2014 IEEE/RSJ International Conference on Intelligent Robots and Systems (IROS)*, Chicago, Illinois, USA, Sept 2014, pp. 4014–4021.

[61] A. Ibanez, P. Bidaud, and V. Padois, "A distributed model predictive control approach for robust postural stability of a humanoid robot," in *Proceedings - IEEE International Conference on Robotics and Automation*, Hong Kong, China, 2014, pp. 202–209.

[62] D. Galdeano, A. Chemori, S. Krut, and P. Fraisse, "Task-based whole-body control of humanoid robots with zmp regulation, real-time application to a squat-like motion," in *2014 IEEE 11th International Multi-Conference on Systems, Signals and Devices (SSD)*, Barcelona, Spain, 2014.

[63] T. McGeer, "Passive dynamic walking," *Int. J. Rob. Res.*, vol. 9, no. 2, pp. 62–82, Mar 1990.

[64] J. Rouhollah, L. F. Louis, H. Aren, and M. Ranjan, "Energy-conserving gaits for point-foot planar bipeds: a five-dof case study," in *ASME 2013 Dynamic Systems and Control Conference*, San Diego, California, USA, 2013.

[65] M. Gomes and A. Ruina, "Walking model with no energy cost," *Phys. Rev. E*, vol. 83, no. 3, pp. 35–39, Mar 2011.

[66] S. H. Collins and A. Ruina, "A bipedal walking robot with efficient and human-like gait," in *Proceedings of the 2005 IEEE International Conference on Robotics and Automation (ICRA)*, vol. 2005, Barcelona, Spain, April 2005, pp. 1983–1988.

[67] R. Q. Van Der Linde, "Design, analysis, and control of a low power joint for walking robots, by phasic activation of McKibben muscles," *IEEE Transactions on Robotics and Automation*, vol. 15, no. 4, pp. 599–604, 1999.

[68] S. H. Collins, A. Ruina, R. Tedrake, and M. Wisse, "Efficient bipedal robots based on passive-dynamic walkers," *Science*, vol. 307, no. 5712, pp. 1082–1085, 2005.

[69] M. Wisse, A. L. Schwab, R. Q. van der Linde, and F. C. T. van der Helm, "How to keep from falling forward: Elementary swing leg action for passive dynamic walkers," *IEEE Transactions on Robotics*, vol. 21, no. 3, pp. 393–401, 2005.

[70] A. D. Kuo, "Stabilization of lateral motion in passive dynamic walking," *International Journal of Robotics Research*, vol. 18, no. 9, pp. 917–930, 1999.

[71] T. Geng, B. Porr, and F. Wörgötter, "A reflexive neural network for dynamic biped walking control," *Neural Computation*, vol. 18, no. 5, pp. 1156–1196, 2006.

[72] J. Pratt, C. M. Chew, A. Torres, P. Dilworth, and G. Pratt, "Virtual model control: an intuitive approach for bipedal locomotion," *International Journal of Robotics Research*, vol. 20, no. 2, pp. 129–143, 2001.

[73] D. J. Braun and M. Goldfarb, "A control approach for actuated dynamic walking in biped robots," *IEEE Transactions on Robotics*, vol. 25, no. 6, pp. 1292–1303, 2009.

[74] D. J. Braun, J. E. Mitchell, and M. Goldfarb, "Actuated dynamic walking in a seven-link biped robot," *IEEE/ASME Transactions on Mechatronics*, vol. 17, no. 1, pp. 147–156, 2012.

[75] C. Sabourin and O. Bruneau, "Robustness of the dynamic walk of a biped robot subjected to disturbing external forces by using CMAC neural networks," *Robotics and Autonomous Systems*, vol. 51, no. 2-3, pp. 81–89, 2005.

[76] T. Geng, B. Porr, and F. Wörgötter, "Fast biped walking with a sensor-driven neuronal controller and real-time online learning," *International Journal of Robotics Research*, vol. 25, no. 3, pp. 243–259, 2006.

[77] U. Serres, J. C. Vivalda, and P. Riedinger, "On the convergence of linear switched systems," *IEEE Transactions on Automatic Control*, vol. 56, no. 2, pp. 320–332, 2011.

[78] F. Zhu and P. J. Antsaklis, "Optimal control of hybrid switched systems: A brief survey," *Discrete Event Dynamic Systems: Theory and Applications*, vol. 25, no. 3, pp. 345–364, 2015.

[79] C. Iung and P. Riedinger, "Optimal control in hybrid systems," in *2nd IFAC Conference on Analysis and Design of Hybrid Systems*, vol. 2, no. 1, Alghero, Italy, 2006, pp. 4–5.

[80] J. Daafouz, P. Riedinger, and C. Iung, "Stability analysis and control synthesis for switched systems: A switched lyapunov function approach," *IEEE Transactions on Automatic Control*, vol. 47, no. 11, pp. 1883–1887, 2002.

[81] D. Patino, P. Riedinger, and C. Iung, "Practical optimal state feedback control law for continuous-time switched affine systems with cyclic steady state," *International Journal of Control*, vol. 82, no. 7, pp. 1357–1376, 2009.

[82] E. R. Westervelt, J. W. Grizzle, and D. E. Koditschek, "Hybrid zero dynamics of planar biped walkers," *IEEE Transactions on Automatic Control*, vol. 48, no. 1, pp. 42–56, Jan 2003.

[83] B. Morris and J. W. Grizzle, "A restricted poincaré map for determining exponentially stable periodic orbits in systems with impulse effects: Application to bipedal robots," in *44th IEEE Conference on Decision and Control and European Control Conference*, Seville, Spain, Dec 2005, pp. 4199–4206.

[84] E. R. Westervelt and J. W. Grizzle, "Design of asymptotically stable walking for a 5-link planar biped walker via optimization," in *Proceedings - IEEE International Conference on Robotics and Automation*, vol. 3, Washington, DC, USA, 2002, pp. 3117–3122.

[85] E. R. Westervelt, G. Buche, and J. W. Grizzle, "Experimental validation of a framework for the design of controllers that induce stable walking in planar bipeds," *International Journal of Robotics Research*, vol. 23, no. 6, pp. 559–582, 2004.

[86] R. W. Sinnet and A. D. Ames, "2D bipedal walking with knees and feet: a hybrid control approach," in *Proceedings of the IEEE Conference on Decision and Control*, Shanghai, China, 2009, pp. 3200–3207.

[87] C. Chevallereau, D. Djoudi, and J. W. Grizzle, "Stable bipedal walking with foot rotation through direct regulation of the zero moment point," *IEEE Transactions on Robotics*, vol. 24, no. 2, pp. 390–401, 2008.

[88] J. H. Choi and J. W. Grizzle, "Feedback control of an underactuated planar bipedal robot with impulsive foot action," *Robotica*, vol. 23, no. 5, pp. 567–580, 2005.

[89] K. Galloway, K. Sreenath, A. D. Ames, and J. W. Grizzle, "Torque saturation in bipedal robotic walking through control Lyapunov function-based quadratic programs," *Access, IEEE*, vol. 3, pp. 323–332, 2015.

[90] K. Akbari-Hamed, B. G. Buss, and J. W. Grizzle, "Continuous-time controllers for stabilizing periodic orbits of hybrid systems: Application to an underactuated 3d bipedal robot," Los Angeles, California, USA, 2014, pp. 1507–1513.

[91] C. Chevallereau, J. W. Grizzle, and C.-. L. Shih, "Asymptotically stable walking of a five-link underactuated 3-D bipedal robot," *IEEE Trans. Robot.*, vol. 25, no. 1, pp. 37–50, Feb. 2009.

[92] A. D. Ames, R. D. Gregg, and M. W. Spong, "A geometric approach to three-dimensional hipped bipedal robotic walking," in *Proceedings of the IEEE Conference on Decision and Control*, New Orleans, LA, USA, 2007, pp. 5123–5130.

[93] A. D. Ames, R. W. Sinnet, and E. D. B. Wendel, "Three-dimensional kneed bipedal walking: A hybrid geometric approach," *Lecture Notes in Computer Science (including subseries Lecture Notes in Artificial Intelligence and Lecture Notes in Bioinformatics)*, vol. 5469, pp. 16–30, 2009.

[94] R. W. Sinnet and A. D. Ames, "Extending two-dimensional human-inspired bipedal robotic walking to three dimensions through geometric reduction," in *Proceedings of the American Control Conference*, Montreal, QC, Canada, 2012, pp. 4831–4836.

[95] T. Wang and C. Chevallereau, "A new control law for a 3D biped robot based on regulation of the zero moment point and joint path," in *2010 10th IEEE-RAS International Conference on Humanoid Robots, Humanoids 2010*, Nashville, TN, USA, 2010, pp. 27–32.

[96] T. Wang, C. Chevallereau, and C. F. Rengifo, "Walking and steering control for a 3D biped robot considering ground contact and stability," *Robotics and Autonomous Systems*, vol. 60, no. 7, pp. 962–977, 2012.

[97] T. Wang, C. Chevallereau, and D. Tlalolini, "Stable walking control of a 3D biped robot with foot rotation," *Robotica*, vol. 32, no. 4, pp. 551–570, 2014.

[98] P. W. M. van Zutven, *Control and Identification of Bipedal Humanoid Robots: Stability Analysis and Experiments.* PhD Thesis, Eindhoven University of Technology, 2014.

[99] J. W. Grizzle, C. Chevallereau, R. W. Sinnet, and A. Ames, "Models, feedback control, and open problems of 3D bipedal robotic walking," *Automatica*, vol. 50, no. 8, pp. 1955–1988, 2014.

[100] C. Francois and C. Samson, "Running with constant energy," in *Proceedings - IEEE International Conference on Robotics and Automation*, vol. 1, no. 1, San Diego, CA, USA, 1994, pp. 131–136.

[101] C. K. Chow and D. H. Jacobson, "Studies of human locomotion via optimal programming," *Mathematical Biosciences*, vol. 10, no. 3-4, pp. 239–306, 1971.

[102] L. Roussel, C. Canudas-de Wit, and A. Goswami, "Generation of energy optimal complete gait cycles for biped robots," in *Proceedings - IEEE International Conference on Robotics and Automation*, vol. 3, Leuven, Belgium, 1998, pp. 2036–2041.

[103] P. Channon, S. Hopkins, and D. Pham, "Simulation and optimization of gait for a bipedal robot," *Mathematical and Computer Modelling*, vol. 14, no. C, pp. 463–467, 1990.

[104] A. A. Thant and K. K. Aye, "Application of cubic spline interpolation to walking patterns of biped robot," *World Academy of Science, Engineering and Technology*, vol. 38, pp. 27–34, 2009.

[105] G. Cabodevila, N. Chaillet, and G. Abba, "Energy-minimized gait for a biped robot," in *Autonome Mobile Systeme 1995*, ser. Informatik aktuell, R. Dillmann, U. Rembold, and T. Lüth, Eds. Springer Berlin Heidelberg, 1995, pp. 90–99.

[106] A. D. Ames, "First steps toward underactuated human-inspired bipedal robotic walking," in *Proceedings - IEEE International Conference on Robotics and Automation*, Saint Paul, MN, USA, 2012, pp. 1011–1017.

[107] R. W. Sinnet, M. J. Powell, R. P. Shah, and A. D. Ames, "A human-inspired hybrid control approach to bipedal robotic walking," in *IFAC Proceedings Volumes (IFAC-PapersOnline)*, vol. 18, no. 1, Milan, Italy, 2011, pp. 6904–6911.

[108] A. M. Formal'sky, "Locomotion of anthropomorphic mechanisms," Moscow, Nauka, 1982.

[109] F. Bauer, *Optimierung der Energieeffizienz zweibeiniger Roboter durch elastische Kopplungen*, ser. Schriftenreihe des Instituts fuer Technische Mechanik, Karlsruher Institut fuer Technologie. Karlsruher Institut für Technologie, 2014.

[110] G. Cabodevila and A. Gabriel, "Quasi optimal gait for a biped robot using genetic algorithm," in *Proceedings of the IEEE International Conference on Systems, Man and Cybernetics*, vol. 4, Hyatt Orlando, Orlando, Florida, USA, 1997, pp. 3960–3965.

[111] J. G. Kim, S. H. Choi, and K. H. Park, "Optimal gait control for a biped locomotion using genetic algorithm," *Lecture Notes in Computer Science (including subseries Lecture Notes in Artificial Intelligence and Lecture Notes in Bioinformatics)*, vol. 3046 LNCS, no. PART 4, pp. 29–38, 2004.

[112] G. Dip, V. Prahlad, and P. D. Kien, "Genetic algorithm-based optimal bipedal walking gait synthesis considering tradeoff between stability margin and speed," *Robotica*, vol. 27, no. 3, pp. 355–365, 2009.

[113] C. Chevallereau and Y. Aoustin, "Optimal reference trajectories for walking and running of a biped robot," *Robotica*, vol. 19, no. 5, pp. 557–569, 2001.

[114] D. Tlalolini, Y. Aoustin, and C. Chevallereau, "Design of a walking cyclic gait with single support phases and impacts for the locomotor system of a thirteen-link 3D biped using the parametric optimization," *Multibody System Dynamics*, vol. 23, no. 1, pp. 33–56, Jan. 2010.

[115] D. Djoudi, C. Chevallereau, and Y. Aoustin, "Optimal reference motions for walking of a biped robot," in *Proceedings - IEEE International Conference on Robotics and Automation*, vol. 2005, Barcelona, Spain, 2005, pp. 2002–2007.

[116] A. Khoukhi, "An integrated approach to multi-objective gait planning for bipedal robots," *International Journal of Vehicle Autonomous Systems*, vol. 7, no. 1-2, pp. 96–117, 2009.

[117] K. J. Russcher, *Optimization of Bipedal Walker Gaits with Constant Knee Stiffness.* MS Report, University of Twente, November 2014.

[118] D. Tlalolini, C. Chevallereau, and Y. Aoustin, "Human-like walking: optimal motion of a bipedal robot with toe-rotation motion," *IEEE/ASME Transactions on Mechatronics*, vol. 16, no. 2, pp. 310–320, April 2011.

[119] N. Rokbani, E. H. B. Boussada, and A. M. Alimi, "Particle swarm optimization for humanoid walking-gaits generation," in *Advances in Mobile Robotics - Proceedings of the 11th International Conference on Climbing and Walking Robots and the Support Technologies for Mobile Machines (CLAWAR)*, Coimbra, Portugal, 2008, pp. 744–751.

[120] D. Tlalolini, C. Chevallereau, and Y. Aoustin, "Optimal reference motions with rotation of the feet for a biped," in *2008 Proceedings of the ASME International Design Engineering Technical Conferences and Computers and Information in Engineering Conference, DETC 2008*, vol. 2, no. PART B, Boston, Massachusetts, USA, 2009, pp. 1027–1036.

[121] Z. Chen, N. Lakbakbi-Elyaaqoubi, and G. Abba, "Optimal walking of an underactuated planar biped with segmented torso," in *ICINCO*, no. 2, Vienna, Austria, 2014, pp. 213–220.

[122] B. Kaddar, Y. Aoustin, and C. Chevallereau, "Arms swing effects on a walking planar biped," in *ASME 2012 11th Biennial Conference on Engineering Systems Design and Analysis*, vol. 3, Nantes, France, 2012, pp. 293–301.

[123] A. Ramezani, J. W. Hurst, K. Akbari-Hamed, and J. W. Grizzle, "Performance analysis and feedback control of ATRIAS, a three-dimensional bipedal robot," *ASME. J. Dyn. Sys., Meas., Control.*, vol. 136, no. 2, pp. 37–45, 2013.

[124] Y. Aoustin and A. M. Formalskii, "3D walking biped: Optimal swing of the arms," *Multibody System Dynamics*, vol. 32, no. 1, pp. 55–66, 2014.

[125] U. Scarfogliero, C. Stefanini, and P. Dario, "The use of compliant joints and elastic energy storage in bio-inspired legged robots," *Mechanism and Machine Theory*, vol. 44, no. 3, pp. 580–590, 2009.

[126] L. Bai, W.-J. Ge, X.-H. Chen, and X.-Y. Meng, "Hopping capabilities of a bio-inspired and mininally actuated hopping robot," in *2011 International Conference on Electronics, Communications and Control, ICECC 2011 - Proceedings*, Ningbo, Zhejiang, China, 2011, pp. 1485–1489.

[127] E. Kljuno, J. J. Zhu, R. L. Williams II, and S. M. Reilly, "A biomimetic elastic cable driven quadruped robot - the RoboCat," in *ASME 2011 International Mechanical Engineering Congress and Exposition, IMECE 2011*, vol. 2, Washington, DC, USA, 2011, pp. 759–769.

[128] J. L. Pusey, J. M. Duperret, G. C. Haynes, R. Knopf, and D. E. Koditschek, "Free-standing leaping experiments with a power-autonomous, elastic-spined quadruped," in *Proceedings of SPIE - The International Society for Optical Engineering*, vol. 8741, Baltimore, Maryland, USA, 2013, pp. 352–359.

[129] R. Blickhan, A. Seyfarth, H. Geyer, S. Grimmer, H. Wagner, and M. Günther, "Intelligence by mechanics," *Philosophical Transactions of the Royal Society A: Mathematical, Physical and Engineering Sciences*, vol. 365, no. 1850, pp. 199–220, 2007.

[130] R. M. Alexander, "Three uses for springs in legged locomotion," *Int. J. Rob. Res.*, vol. 9, no. 2, pp. 53–61, March 1990.

[131] S. Kim and S. Park, "Leg stiffness increases with speed to modulate gait frequency and propulsion energy," *Journal of Biomechanics*, vol. 44, no. 7, pp. 1253–1258, 2011.

[132] B. K. Ahlborn and R. W. Blake, "Walking and running at resonance," *Zoology*, vol. 105, no. 2, pp. 165–174, 2002.

[133] J. Hodgins, J. Koechling, and M. H. Raibert, "Running experiments with a planar biped." in *Third International Symposium. MIT Press Series in Artificial Intelligence*, Gouvieux, France, 1986, pp. 349–355.

[134] R. J. Full and D. E. Koditschek, "Templates and anchors: Neuromechanical hypotheses of legged locomotion on land," *Journal of Experimental Biology*, vol. 202, no. 23, pp. 3325–3332, 1999.

[135] T. Yang, E. R. Westervelt, J. P. Schmiedeler, and R. A. Bockbrader, "Design and control of a planar bipedal robot ernie with parallel knee compliance," *Autonomous Robots*, vol. 25, no. 4, pp. 317–330, 2008.

[136] K. G. Holt, J. Hamill, and R. O. Andres, "The force-driven harmonic oscillator as a model for human locomotion," *Human Movement Science*, vol. 9, no. 1, pp. 55 – 68, 1990.

[137] K. G. Holt, J. Hamill, and R. O. Andres, "Predicting the minimal energy costs of human walking," *Med Sci Sports Exerc*, vol. 23, no. 4, pp. 491–498, 1991.

[138] T. McGeer, "Passive bipedal running," *Proceedings of the Royal Society B: Biological Sciences*, vol. 240, no. 1297, pp. 107–134, 1990.

[139] M. Ahmadi and M. Buehler, "Control strategy for stable passive running," in *IEEE International Conference on Intelligent Robots and Systems*, vol. 3, Pittsburgh, USA, 1995, pp. 152–157.

[140] M. Wisse, D. G. E. Hobbelen, and A. L. Schwab, "Adding an upper body to passive dynamic walking robots by means of a bisecting hip mechanism," *IEEE Transactions on Robotics*, vol. 23, no. 1, pp. 112–123, Feb 2007.

[141] A. D. Kuo, "A simple model of bipedal walking predicts the preferred speed-step length relationship," *Journal of Biomechanical Engineering*, vol. 123, no. 3, pp. 264–269, 2001.

[142] J. M. Donelan, R. Kram, and A. D. Kuo, "Mechanical work for step-to-step transitions is a major determinant of the metabolic cost of human walking," *Journal of Experimental Biology*, vol. 205, no. 23, pp. 3717–3727, 2002.

[143] J. C. Dean and A. D. Kuo, "Elastic coupling of limb joints enables faster bipedal walking," *Journal of the Royal Society Interface*, vol. 6, no. 35, pp. 561–573, 2009.

[144] E. Borzova and Y. Hurmuzlu, "Passively walking five-link robot," *Automatica*, vol. 40, no. 4, pp. 621 – 629, 2004.

[145] H. Dallali, P. Kormushev, Z. Li, and D. Caldwell, "On global optimization of walking gaits for the compliant humanoid robot, coman using reinforcement learning," *Cybernetics and Information Technologies*, vol. 12, no. 3, pp. 39–52, 2012.

[146] B. Lim, M. Lee, J. Kim, J. Lee, J. Park, K. Seo, and K. Roh, "Control design to achieve dynamic walking on a bipedal robot with compliance," in *Proceedings - IEEE International Conference on Robotics and Automation*, St Paul, MN, USA, 2012, pp. 79–84.

[147] V. Duindam and S. Stramigioli, "Optimization of mass and stiffness distribution for efficient bipedal walking," in *Proceedings of the International Symposium on Nonlinear Theory and Its Applications*, Bruges, Belgium, 2005, pp. 114–117.

[148] T. Narukawa, M. Takahashi, and K. Yoshida, "Efficient walking with optimization for a planar biped walker with a torso by hip actuators and springs," *Robotica*, vol. 29, no. 4, pp. 641–648, 7 2011.

[149] A. Haq, Y. Aoustin, and C. Chevallereau, "Compliant joints increase the energy efficiency of bipedal robot," in *Proceedings of the 14th International Conference on Climbing and Walking Robots and the Support Technologies for Mobile Machines (CLAWAR)*, Paris, France, 2011, pp. 539–546.

[150] F. Bauer, A. Fidlin, and W. Seemann, "Energy efficient bipedal robots walking in resonance," *ZAMM - Journal of Applied Mathematics and Mechanics*, vol. 94, no. 11, pp. 968–973, 2014.

[151] P. A. Bhounsule, J. Cortell, and A. Ruina, "Design and control of ranger: An energy-efficient, dynamic walking robot," in *Adaptive Mobile Robotics - Proceedings of the 15th International Conference on Climbing and Walking Robots and the Support Technologies for Mobile Machines (CLAWAR)*, Homewood, Alabama, USA, 2012, pp. 441–448.

[152] K. Sreenath, H. W. Park, I. Poulakakis, and J. W. Grizzle, "A compliant hybrid zero dynamics controller for stable, efficient and fast bipedal walking on mabel," *International Journal of Robotics Research*, vol. 30, no. 9, pp. 1170–1193, 2011.

[153] R. Van Ham, B. Vanderborght, M. Van Damme, B. Verrelst, and D. Lefeber, "Maccepa: the mechanically adjustable compliance and controllable equilibrium position actuator for 'controlled passive walking'," in *Proceedings of the 2006 IEEE International Conference on Robotics and Automation*, Orlando, Florida, USA, May 2006, pp. 2195–2200.

[154] B. Vanderborght, N. G. Tsagarakis, C. Semini, R. V. Ham, and D. G. Caldwell, "MACCEPA 2.0: Adjustable compliant actuator with stiffening characteristic for energy efficient hopping," Kobe, Japan, 2009, pp. 544–549.

[155] K. W. Hollander, T. G. Sugar, and D. E. Herring, "Adjustable robotic tendon using a 'jack spring' trade;," in *9th International Conference on Rehabilitation Robotics (ICORR 2005)*, Chicago, Illinois, USA, June 2005, pp. 113–118.

[156] I. Thorson, M. Svinin, S. Hosoe, F. Asano, and K. Taji, "Design considerations for a variable stiffness actuator in a robot that walks and runs," in *ROBOMECH*, 2007, pp. 332–336.

[157] J. W. Hurst, J. E. Chestnutt, and A. A. Rizzi, "An actuator with physically variable stiffness for highly dynamic legged locomotion," in *Proceedings of the 2004 IEEE International Conference on Robotics and Automation (ICRA)*, vol. 5, New Orleans, LA, USA, April 2004, pp. 4662–4667 Vol.5.

[158] G. Mathijssen, R. Furnemont, B. Brackx, R. Van Ham, D. Lefeber, and B. Vanderborght, "Design of a novel intermittent self-closing mechanism for a maccepa-based series-parallel elastic actuator (spea)," in *2014 IEEE/RSJ International Conference on Intelligent Robots and Systems (IROS 2014)*, Chicago, Illinois, USA, Sept 2014, pp. 2809–2814.

[159] B. Siciliano and O. Khatib, *Springer Handbook of Robotics*, ser. Gale virtual reference library. Springer, 2008. [Online]. Available: https://books.google.fr/books?id=Xpgi5gSuBxsC

[160] A. Isidori, *Nonlinear Control Systems*, 3rd ed. London, UK: Springer Science-Business Media, 1995, vol. 1.

[161] H. K. Khalil and J. W. Grizzle, *Nonlinear systems*. Prentice hall New Jersey, 1996, vol. 3.

[162] J. Nocedal and S. J. Wright, *Numerical Optimization*, 2nd ed. New York, USA: Springer, 2006.

[163] J. E. Marsden and T. S. Ratiu, *Introduction to Mechanics and Symmetry: A Basic Exposition of Classical Mechanical Systems*, ser. Texts in Applied Mathematics. Springer, 1999. [Online]. Available: http://books.google.fr/books?id=I2gH9ZIs-3AC

[164] M. W. Spong, S. Hutchinson, and M. Vidyasagar, *Robot Modeling and Control*. Wiley New York, 2006, vol. 3.

[165] M. A. Henson and D. E. Seborg, *Nonlinear Process Control*. Upper Saddle River, NJ, USA: Prentice-Hall, Inc., 1997.

[166] H. K. Khalil, *Nonlinear Systems*. Prentice Hall, 2002.

[167] T. S. Parker and L. O. Chua, *Practical Numerical Algorithms for Chaotic Systems*. New York, USA: Springer-Verlag New York, Inc., 1989.

[168] M. J. D. Powell and Y. Yuan, "A recursive quadratic programming algorithm that uses differentiable exact penalty functions," *Mathematical Programming*, vol. 35, no. 3, pp. 265–278, 1986.

[169] S. P. Han, "A globally convergent method for nonlinear programming," *Journal of Optimization Theory and Applications*, vol. 22, no. 3, pp. 297–309, 1977.

[170] M. J. D. Powell, "A fast algorithm for nonlinearly constrained optimization calculations," *Numerical Analysis*, vol. 630, pp. 144–157, 1978.

[171] H.-W. Park, K. Sreenath, J. W. Hurst, and J. W. Grizzle, "Identification of a bipedal robot with a compliant drivetrain," *IEEE Control Systems Magazine*, vol. 31, no. 2, pp. 63–88, April 2011.

[172] S. Kajita, M. Morisawa, K. Miura, S. Nakaoka, K. Harada, K. Kaneko, F. Kanehiro, and K. Yokoi, "Biped walking stabilization based on linear inverted pendulum tracking," in *IEEE/RSJ 2010 International Conference on Intelligent Robots and Systems, IROS 2010 - Conference Proceedings*, Taipei, Taiwan, 2010, pp. 4489–4496.

[173] F. Gravez, O. Bruneau, and F. Ben Ouezdou, "Analytical and automatic modeling of digital humanoids," *I. J. Humanoid Robotics*, vol. 2, no. 3, pp. 337–359, Sept. 2005.

[174] D. W. Seward, A. Bradshaw, and F. Margrave, "The anatomy of a humanoid robot," *Robotica*, vol. 14, no. 4, pp. 437–443, July 1996.

[175] J. P. Ferreira, M. M. Crisostomo, and A. P. Coimbra, "Adaptive pd controller modeled via support vector regression for a biped robot," *IEEE Transactions on Control Systems Technology*, vol. 21, no. 3, pp. 941–949, 2013.

[176] L. Yang, C. M. Chew, Y. Zheng, and A. N. Poo, "Truncated fourier series formulation for bipedal walking balance control," *Robotica*, vol. 28, no. 1, pp. 81–96, 2010.

[177] D. W. Marhefka and D. E. Orin, "Simulation of contact using a nonlinear damping model," in *Proceedings of the 1996 IEEE International Conference on Robotics and Automation*, vol. 2, Apr 1996, pp. 1662–1668.

[178] C.-L. Shih and W. A. Gruver, "Control of a biped robot in the double-support phase," *IEEE Transactions on Systems, Man and Cybernetics*, vol. 22, no. 4, pp. 729–735, Jul 1992.

[179] C. L. Vaughan and M. J. O'Malley, "Froude and the contribution of naval architecture to our understanding of bipedal locomotion," *Gait and Posture*, vol. 21, no. 3, pp. 350–362, 2005.

[180] R. M. Alexander, "Optimization and gaits in the locomotion of vertebrates," *Physiological Reviews*, vol. 69, no. 4, pp. 1199–1227, 1989.

[181] D. A. Winter, "Foot trajectory in human gait: A precise and multifactorial motor control task," *Physical Therapy*, vol. 72, no. 1, pp. 45–56, 1992.

[182] C. Chevallereau, G. Bessonnet, G. Abba, and Y. Aoustin, *Bipedal Robots: Modeling, Design and Walking Synthesis*, ser. ISTE. Wiley, 2010. [Online]. Available: https://books.google.fr/books?id=mRgkUk41F6oC

[183] A. Goswami, B. Espiau, and A. Keramane, "Limit cycles and their stability in a passive bipedal gait," in *Proceedings - IEEE International Conference on Robotics and Automation*, vol. 1, Minneapolis, MN, USA, 1996, pp. 246–251.

[184] C. Chevallereau, A. Formal'sky, and D. Djoudi, "Tracking a joint path for the walk of an underactuated biped," *Robotica*, vol. 22, no. 1, pp. 15–28, 2004.

APPENDIX

A. SUPPLEMENTARY CHARTS FOR CHAPTER 3

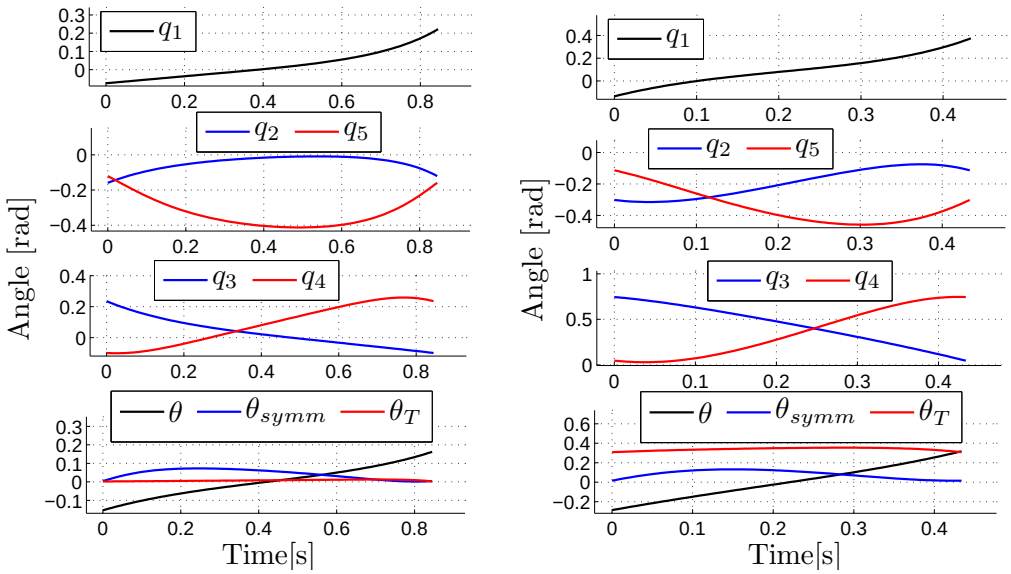

(a) **0.3 m/s** (b) **1.1 m/s**

Fig. A.1: The angle curves of joints and outputs of the 5-link planar biped walking at $0.3\,m/s$ and $1.1\,m/s$.

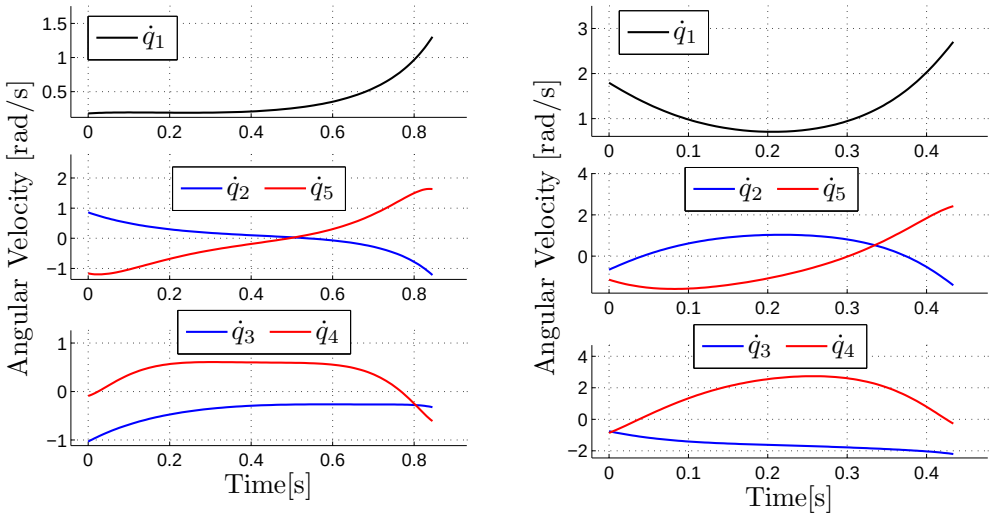

(a) **0.3 m/s** (b) **1.1 m/s**

Fig. A.2: The angular velocity curves of joints of the 5-link planar biped walking at $0.3\,m/s$ and $1.1\,m/s$.

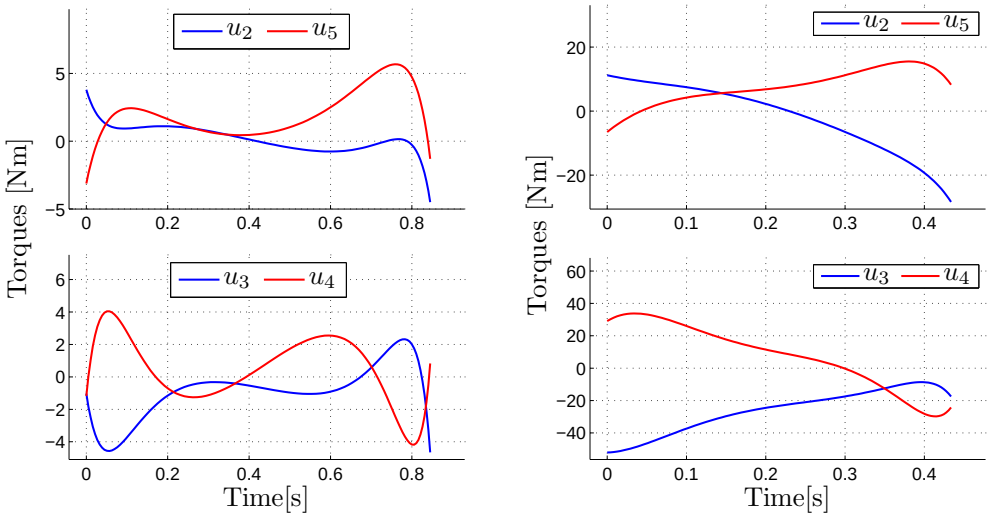

(a) **0.3 m/s** (b) **1.1 m/s**

Fig. A.3: The torque curves of the actuated joints of the 5-link planar biped walking at $0.3\,m/s$ and $1.1\,m/s$.

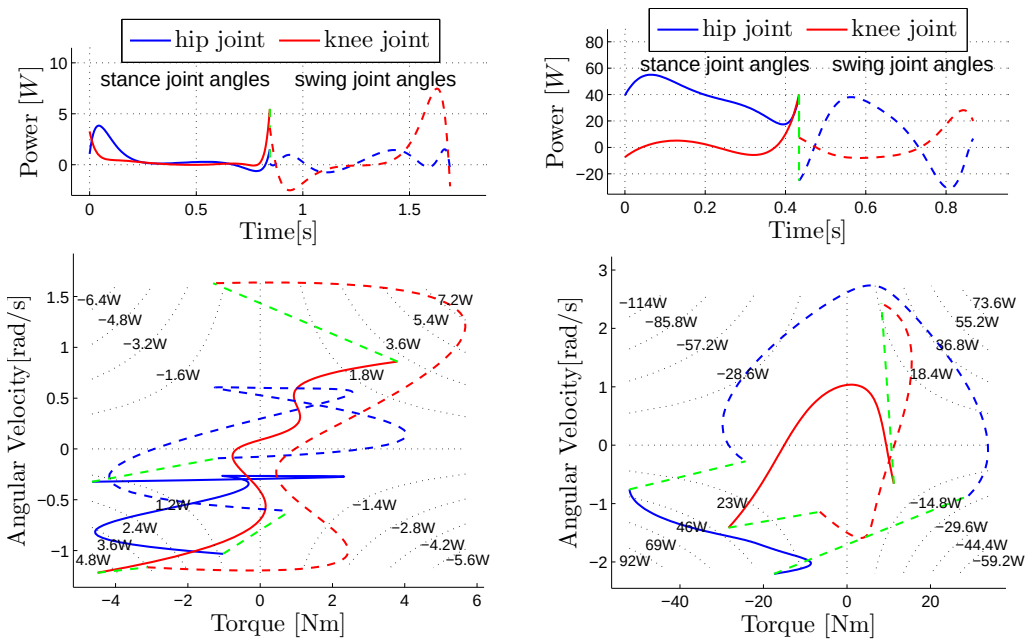

(a) **0.3 m/s** (b) **1.1 m/s**

Fig. A.4: The mechanical output powers of the actuators of the 5-link planar biped walking at $0.3\,m/s$ and $1.1\,m/s$ (two steps) with solid lines representing stance joint angles, dashed lines representing swing joint angles, and green dashed lines representing the jumps caused by the impact

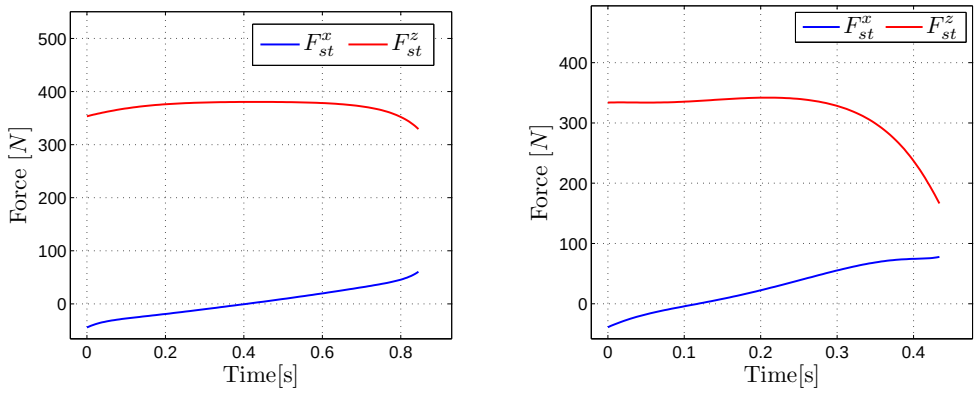

(a) **0.3 m/s** (b) **1.1 m/s**

Fig. A.5: The ground reaction forces of the 5-link planar biped walking at $0.3\,m/s$ and $1.1\,m/s$.

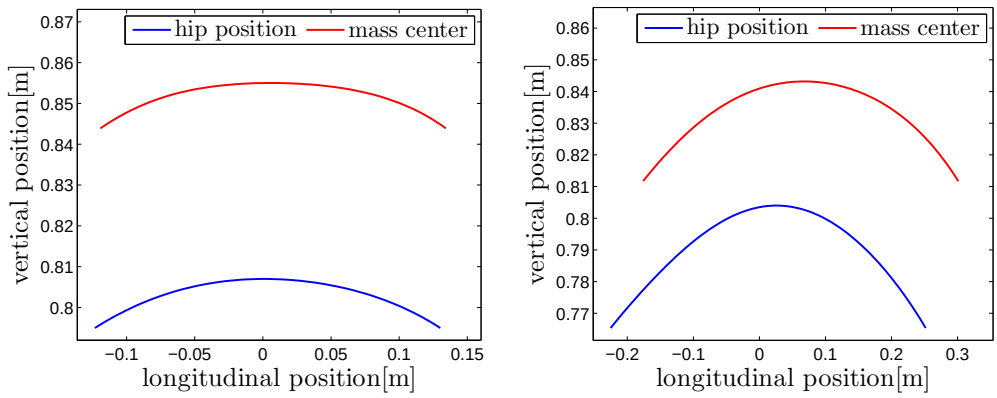

(a) **0.3 m/s** (b) **1.1 m/s**

Fig. A.6: The trajectories of the hip and the CoM of the 5-link planar biped walking at $0.3\,m/s$ and $1.1\,m/s$.

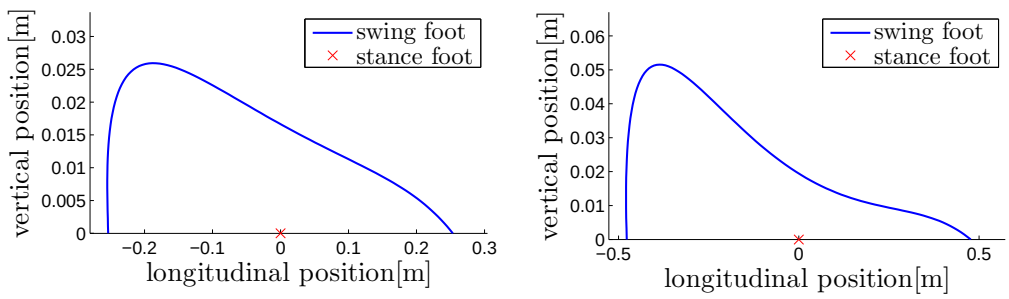

(a) **0.3 m/s** (b) **1.1 m/s**

Fig. A.7: The trajectories of the swing foot of the 5-link planar biped walking at $0.3\,m/s$ and $1.1\,m/s$.

B. SUPPLEMENTARY CHARTS FOR CHAPTER 4

B.1 ***2D Coupling Case I***

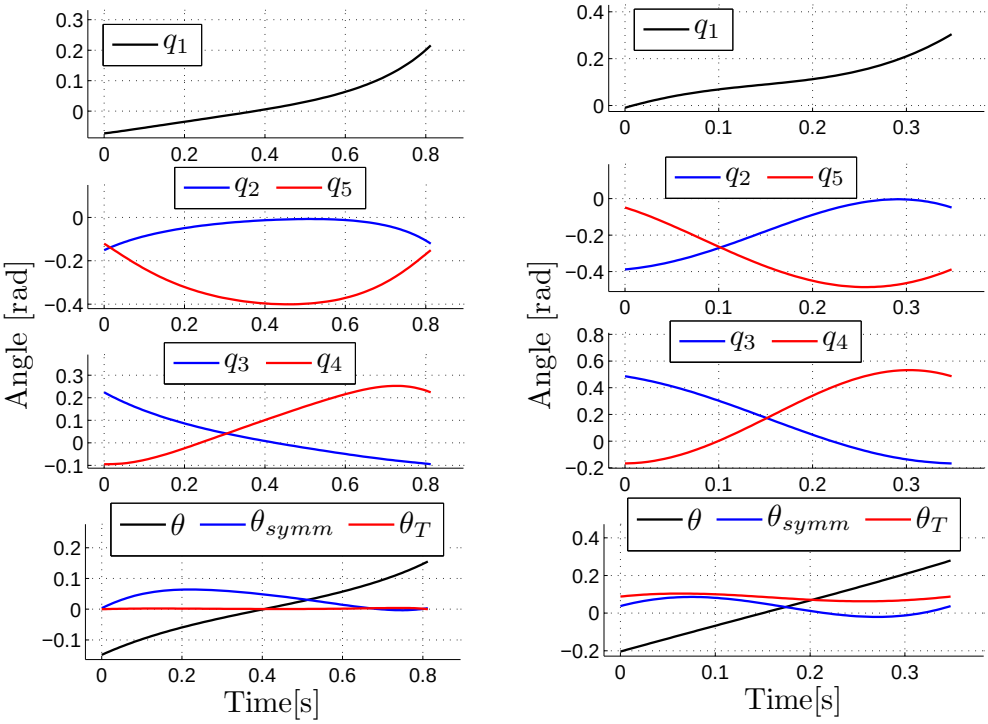

(a) **0.3 m/s** *(b)* **1.1 m/s**

Fig. B.1: The angle curves of the joints and outputs of the 5-link planar biped walking at $0.3\,m/s$ and $1.1\,m/s$ for *2D Coupling Case I* with $k_s = k_{opt}$

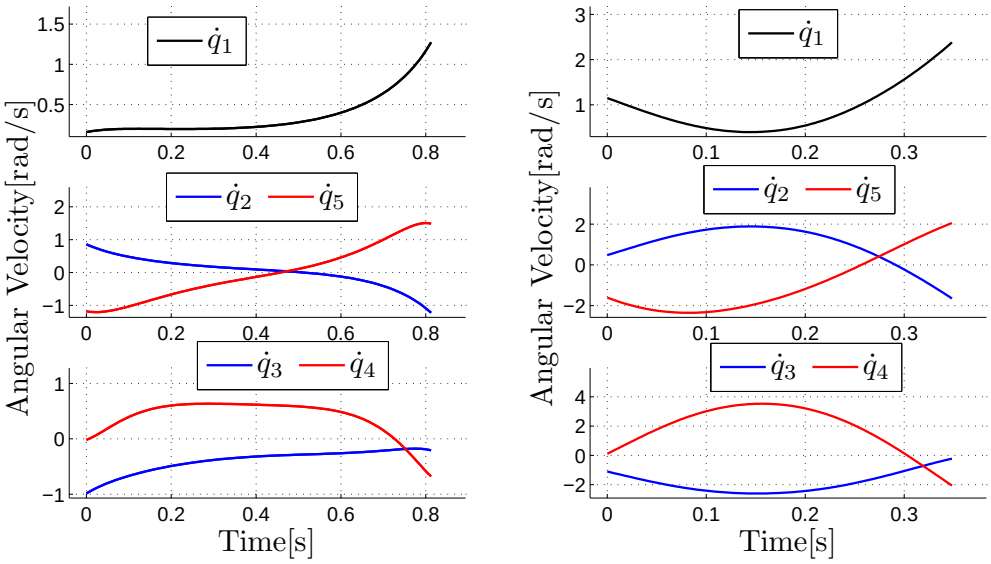

(a) **0.3 m/s** (b) **1.1 m/s**

Fig. B.2: The angular velocity curves of the joints of the 5-link planar biped walking at $0.3\,m/s$ and $1.1\,m/s$ for *2D Coupling Case I* with $k_s = k_{opt}$.

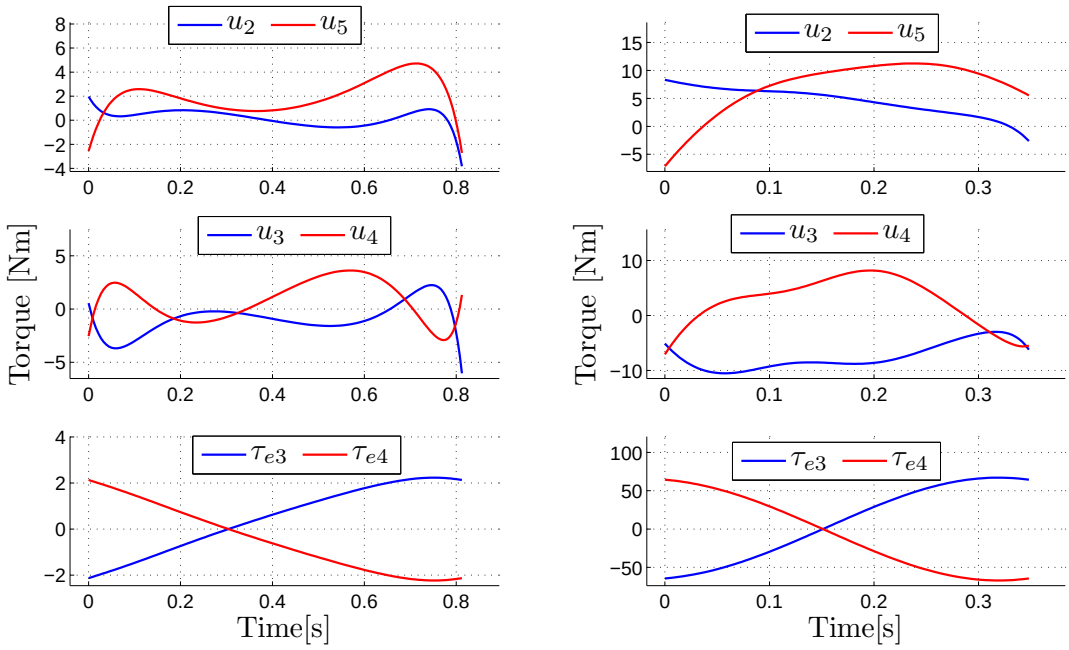

(a) **0.3 m/s** (b) **1.1 m/s**

Fig. B.3: The torque curves of the actuated joints and springs of the 5-link planar biped walking at $0.3\,m/s$ and $1.1\,m/s$ for *2D Coupling Case I* with $k_s = k_{opt}$.

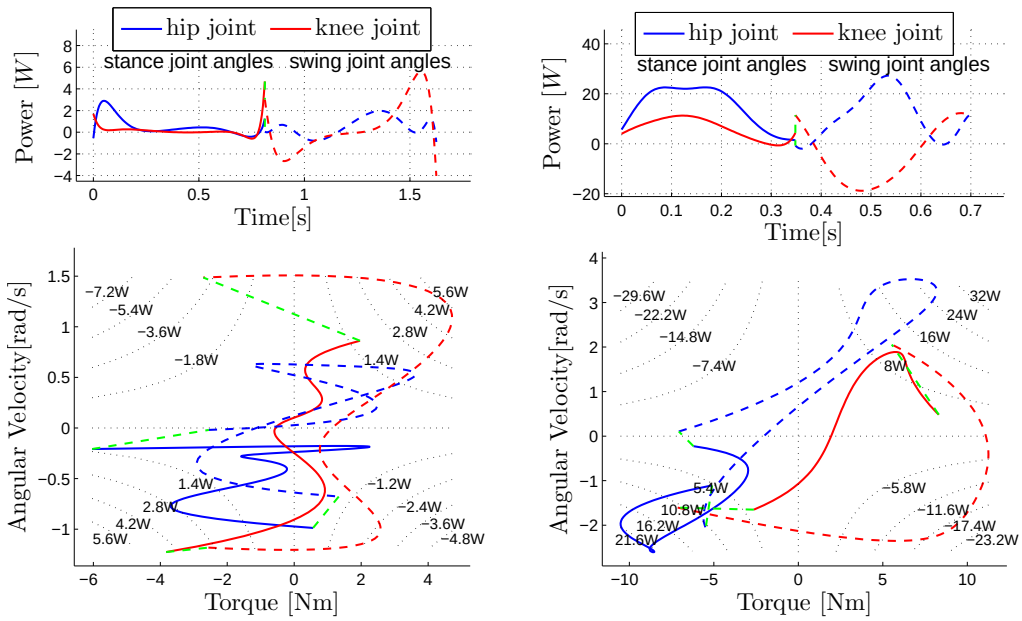

(a) **0.3 m/s** (b) **1.1 m/s**

Fig. B.4: The mechanical output powers of the actuators of the 5-link planar biped walking at $0.3\,m/s$ and $1.1\,m/s$ (two steps) for *2D Coupling Case I* with $k_s = k_{opt}$ (Solid lines represent stance joint angles, dashed lines represent swing joint angles, and green dashed lines represent the jumps caused by the impact.)

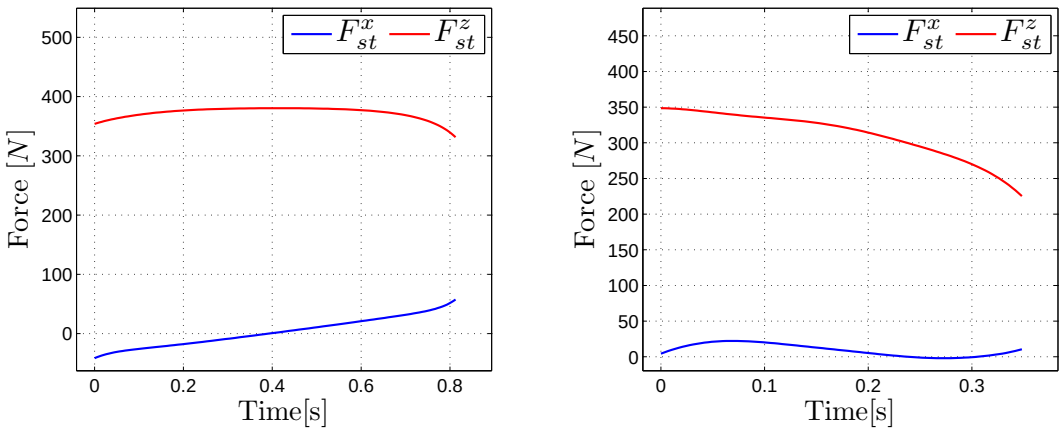

(a) **0.3 m/s** (b) **1.1 m/s**

Fig. B.5: The ground reaction forces acting on the 5-link planar biped walking at $0.3\,m/s$ and $1.1\,m/s$ during the swing phase for *2D Coupling Case I* with $k_s = k_{opt}$.

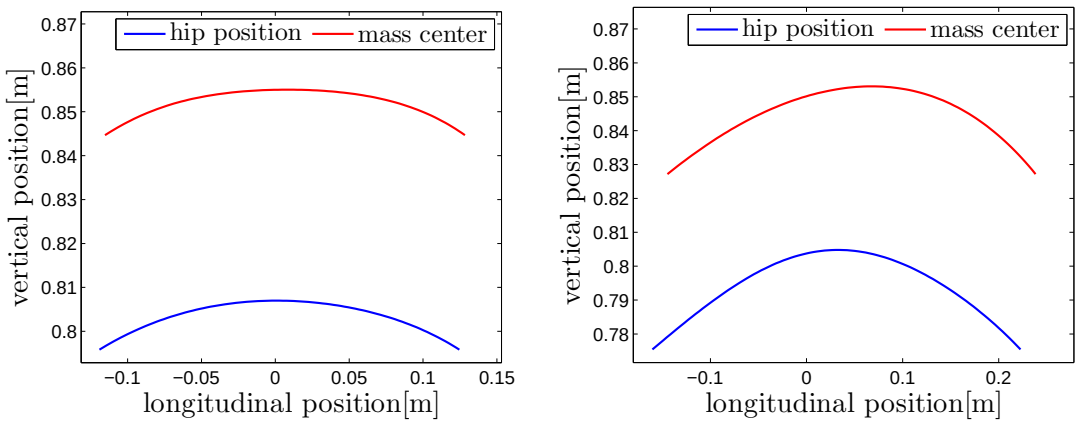

(a) **0.3 m/s** (b) **1.1 m/s**

Fig. B.6: The trajectories of the hip and the CoM of the 5-link planar biped walking at $0.3\,m/s$ and $1.1\,m/s$ for *2D Coupling Case I* with $k_s = k_{opt}$.

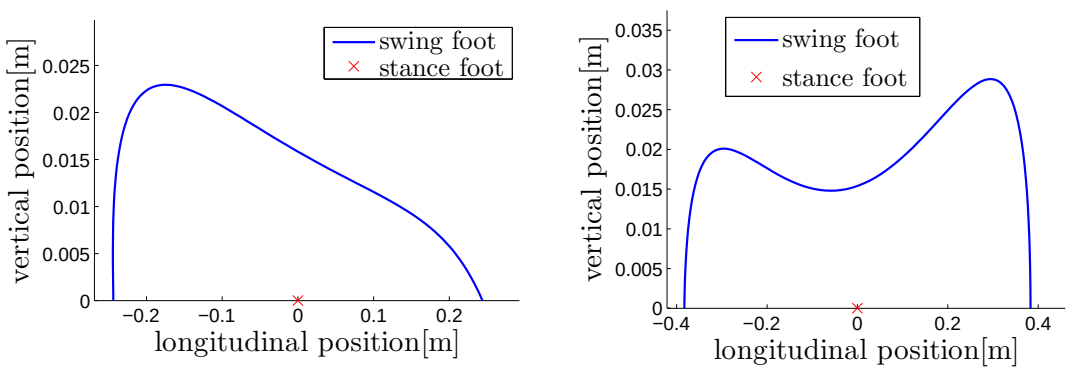

(a) **0.3 m/s** (b) **1.1 m/s**

Fig. B.7: The trajectories of the swing foot of the 5-link planar biped walking at $0.3\,m/s$ and $1.1\,m/s$ for *2D Coupling Case I* with $k_s = k_{opt}$.

B.2 2D Coupling Case II

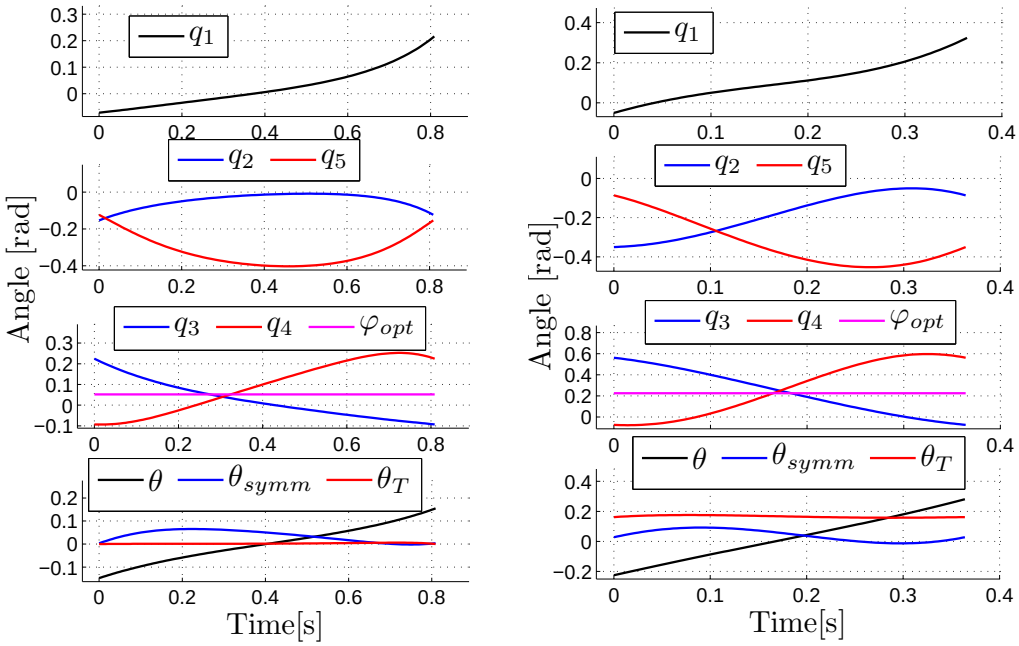

(a) **0.3 m/s** (b) **1.1 m/s**

Fig. B.8: The angle curves of the joints and outputs of the 5-link planar biped walking at $0.3\,m/s$ and $1.1\,m/s$ for *2D Coupling Case II* with optimized k_s and φ.

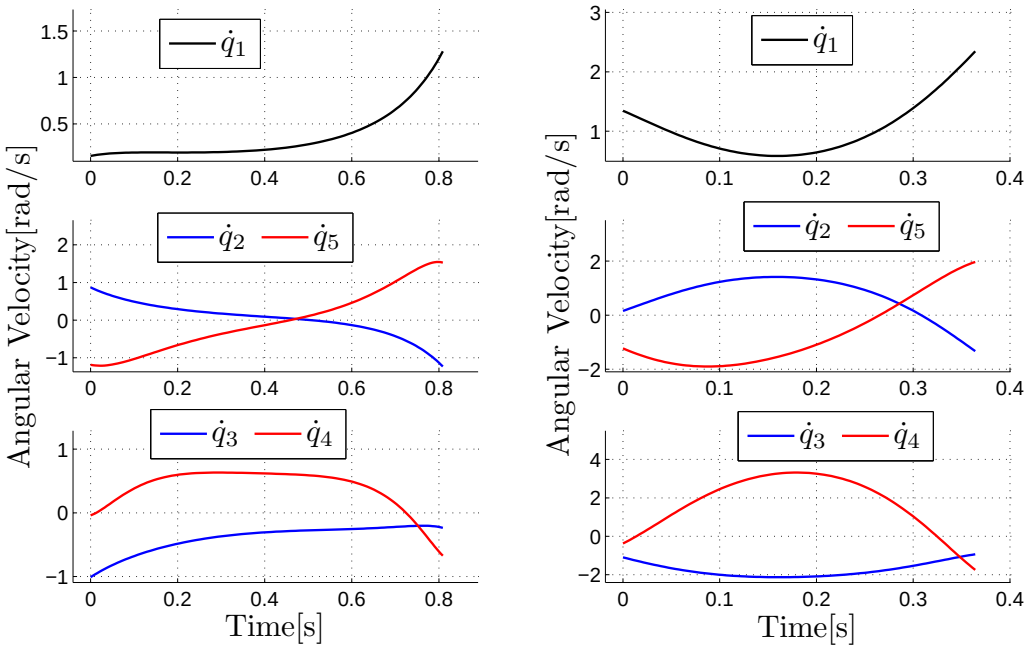

(a) **0.3 m/s** (b) **1.1 m/s**

Fig. B.9: The angular velocity curves of the joints of the 5-link planar biped walking at $0.3\,m/s$ and $1.1\,m/s$ for *2D Coupling Case II* with $k_s = k_{opt}$ and $\varphi_s = \varphi_{opt}$.

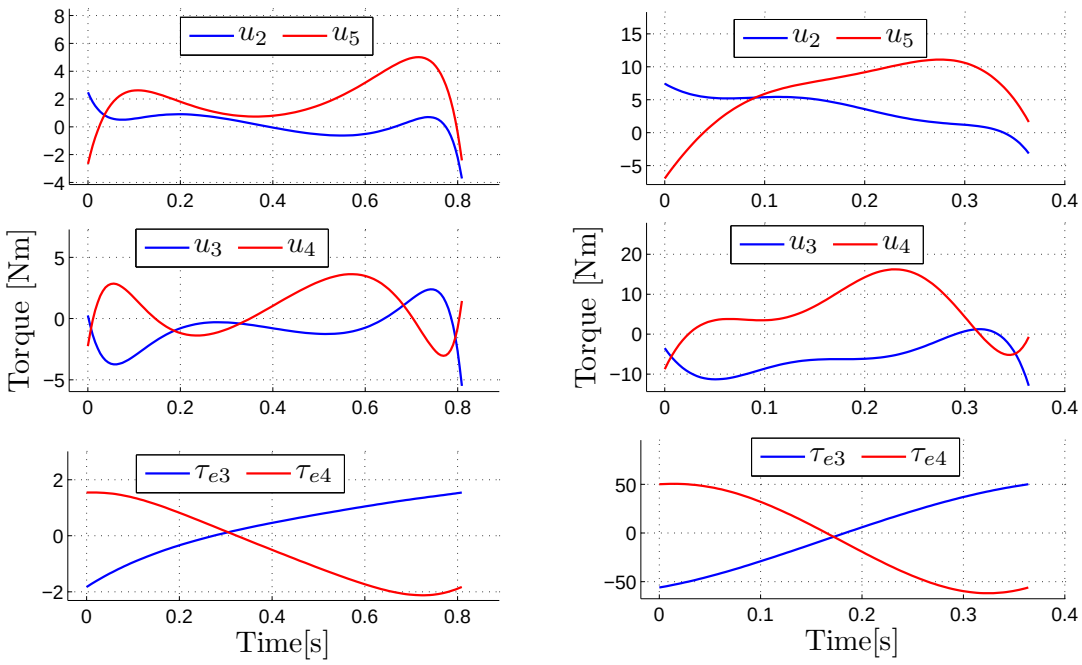

(a) **0.3 m/s** (b) **1.1 m/s**

Fig. B.10: The torque curves of the joints and springs of the 5-link planar biped walking at $0.3\,m/s$ and $1.1\,m/s$ for *2D Coupling Case II* with $k_s = k_{opt}$ and $\varphi_s = \varphi_{opt}$.

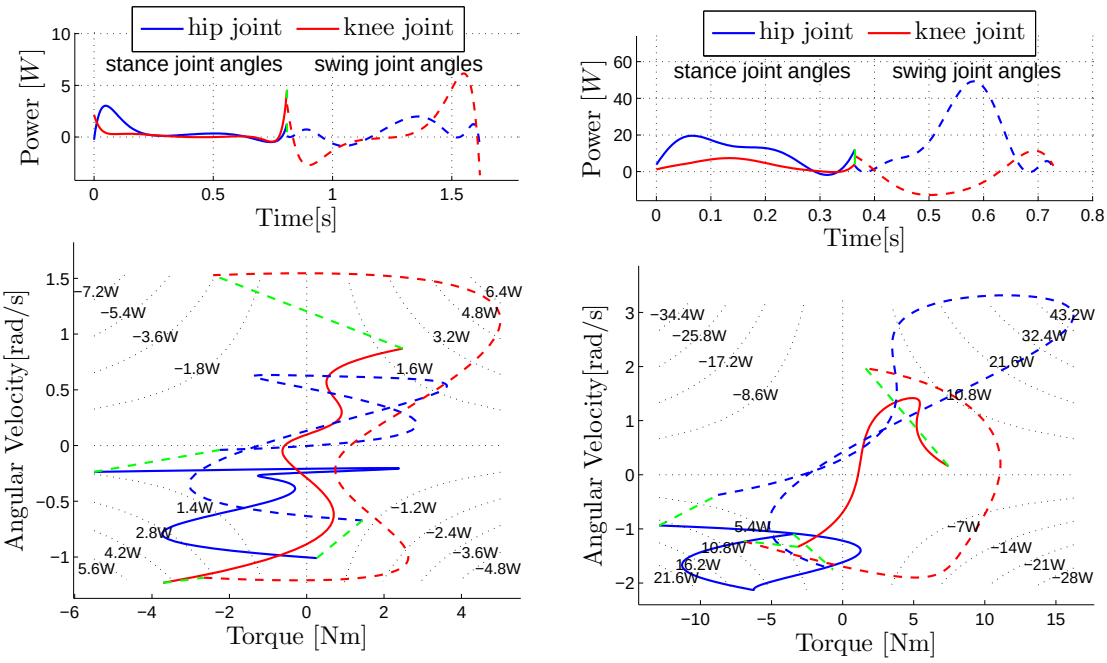

(a) **0.3 m/s** (b) **1.1 m/s**

Fig. B.11: The mechanical output powers of the actuators of the 5-link planar biped walking at $0.3\,m/s$ and $1.1\,m/s$ (two continuous steps) for *2D Coupling Case II* with $k_s = k_{opt}$ and $\varphi_s = \varphi_{opt}$ (Solid lines represent stance joint angles, dashed lines represent swing joint angles, and green dashed lines represent the jumps caused by the impact.)

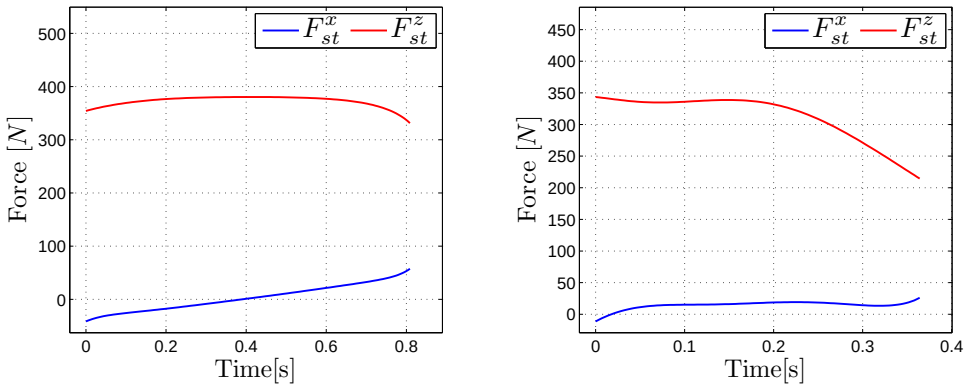

(a) **0.3 m/s** (b) **1.1 m/s**

Fig. B.12: The ground reaction forces on the 5-link planar biped walking at $0.3\,m/s$ and $1.1\,m/s$ for *2D Coupling Case II* with $k_s = k_{opt}$ and $\varphi_s = \varphi_{opt}$.

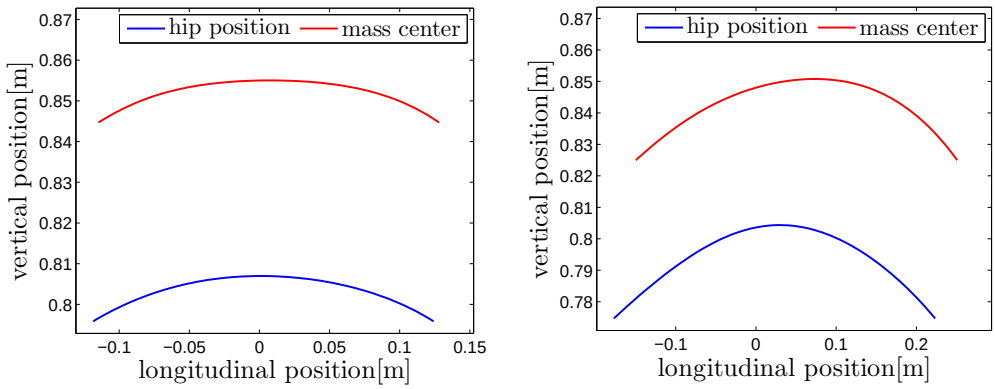

(a) **0.3 m/s** (b) **1.1 m/s**

Fig. B.13: The trajectories of the hip and the CoM of the 5-link planar biped at $0.3\,m/s$ and $1.1\,m/s$ for *2D Coupling Case II* with $k_s = k_{opt}$ and $\varphi_s = \varphi_{opt}$.

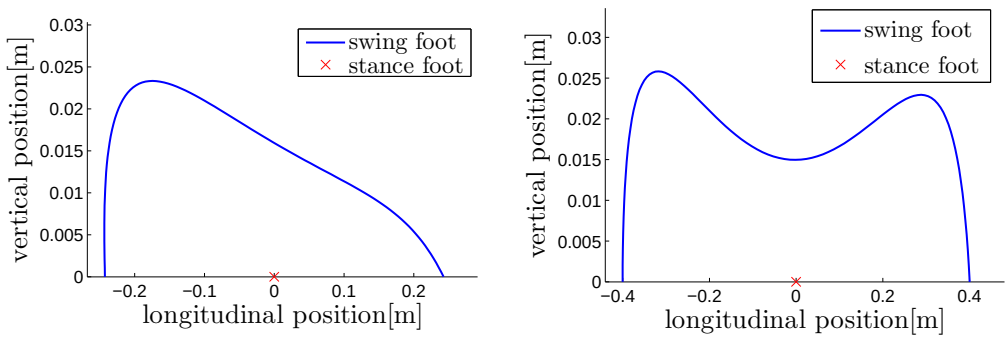

(a) **0.3 m/s** (b) **1.1 m/s**

Fig. B.14: The trajectories of the swing foot of the 5-link planar biped walking at $0.3\,m/s$ and $1.1\,m/s$ for *2D Coupling Case II* with $k_s = k_{opt}$ and $\varphi_s = \varphi_{opt}$.

C. SUPPLEMENTARY CHARTS FOR CHAPTER 5

C.1 *3D Optimization Case I*

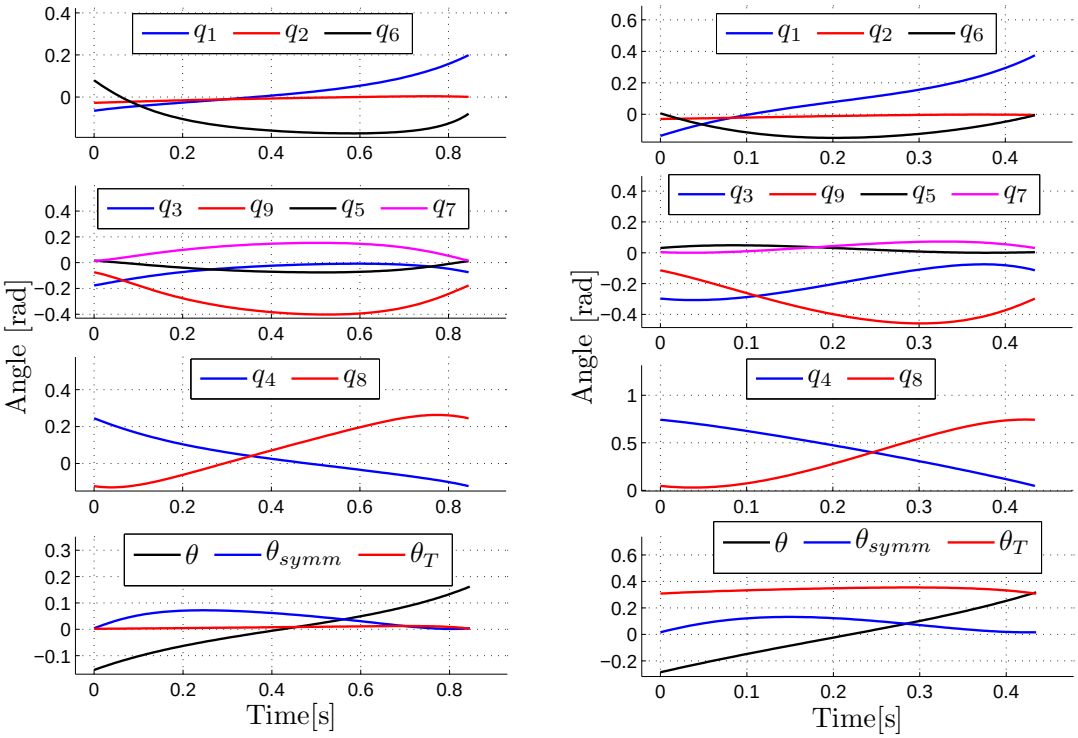

(a) **0.3 m/s** (b) **1.1 m/s**

Fig. C.1: The angle charts of the joints and outputs of the 8-link 3D biped walking at $0.3\,m/s$ and $1.1\,m/s$ for *3D Optimization Case I*

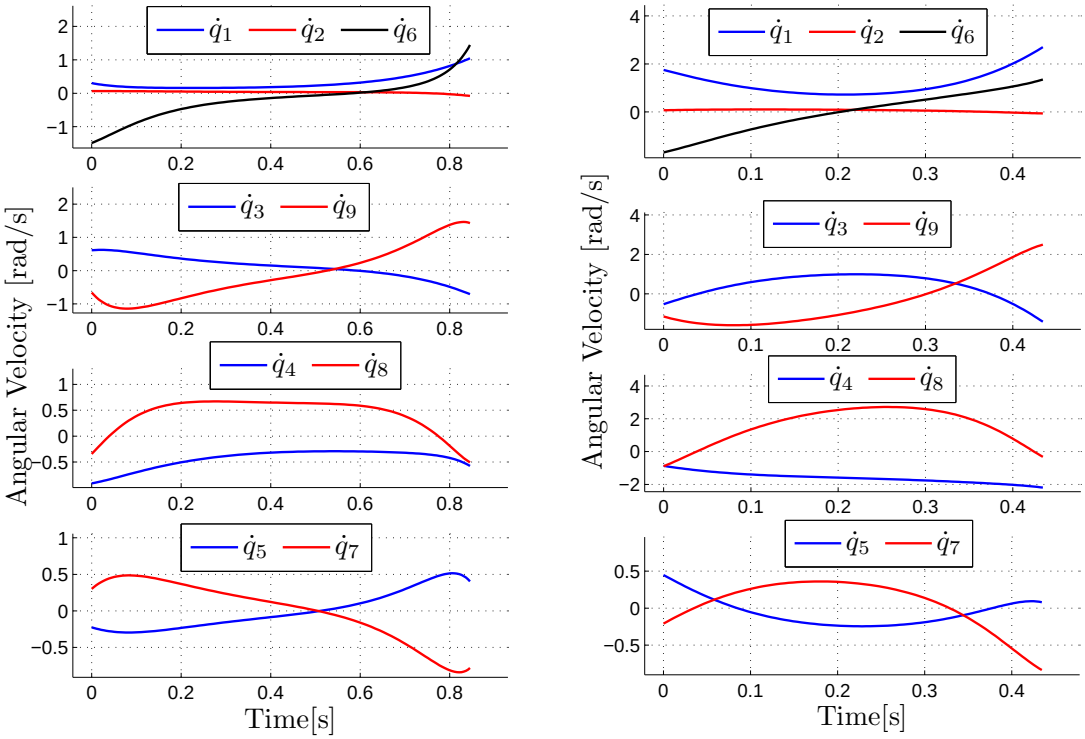

(a) **0.3 m/s** (b) **1.1 m/s**

Fig. C.2: The angular velocity charts of the joints of the 8-link 3D biped walking at 0.3 m/s and 1.1 m/s for *3D Optimization Case I*

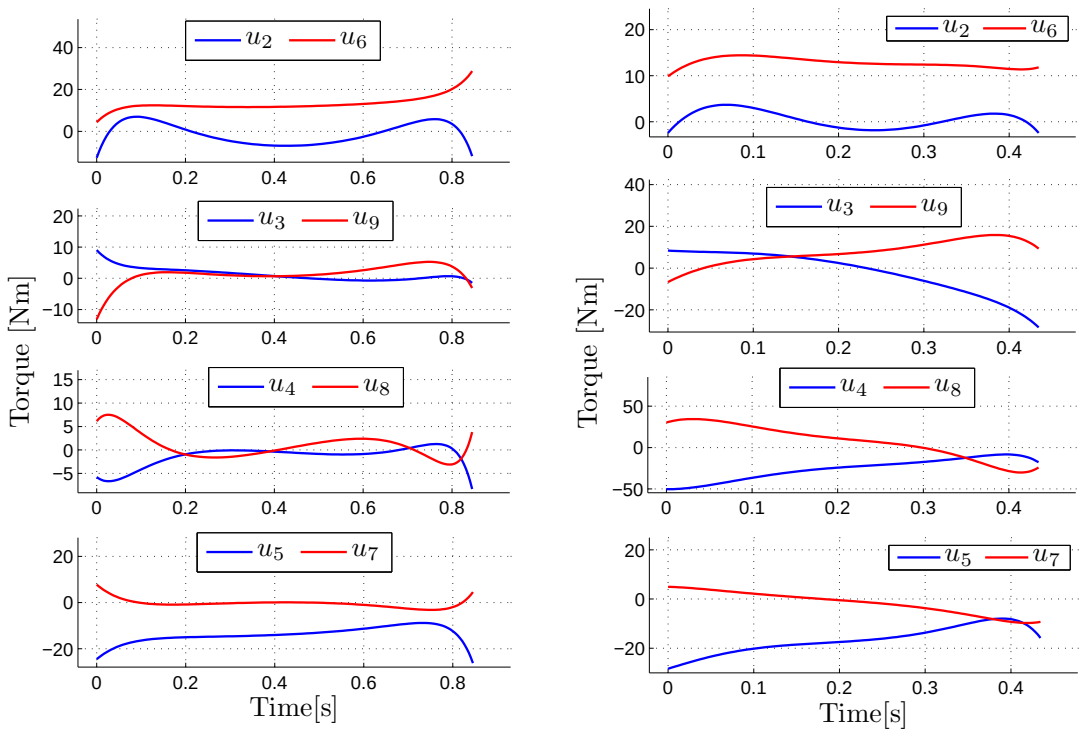

(a) **0.3 m/s** (b) **1.1 m/s**

Fig. C.3: The torque charts of the actuators of the 8-link 3D biped walking at 0.3 m/s and 1.1 m/s for *3D Optimization Case I*

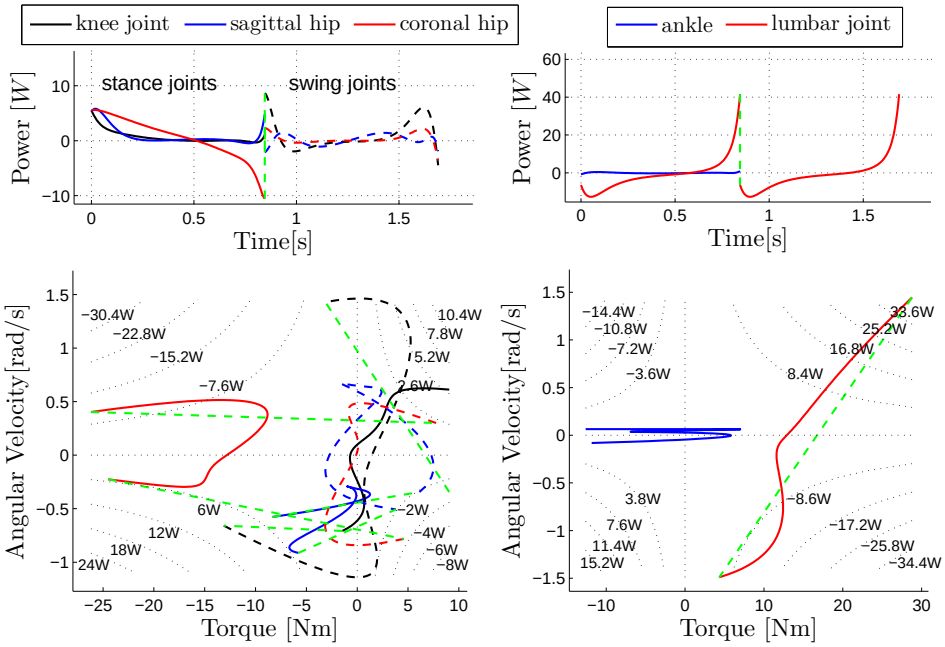

(a) **0.3 m/s**

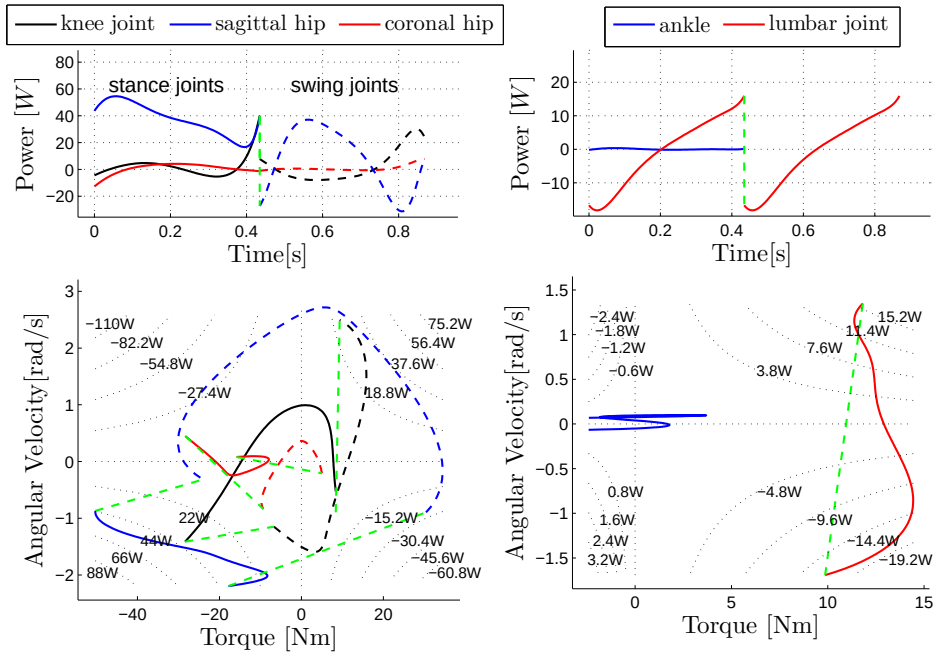

(b) **1.1 m/s**

Fig. C.4: The mechanical output powers of the actuators of the 8-link 3D biped walking at 0.3 m/s and 1.1 m/s (two steps) for *3D Optimization Case I* (Dashed lines represent swing joint angles, and green dashed lines represent the jumps caused by the impact. On the left side, solid lines represent stance joint angles.)

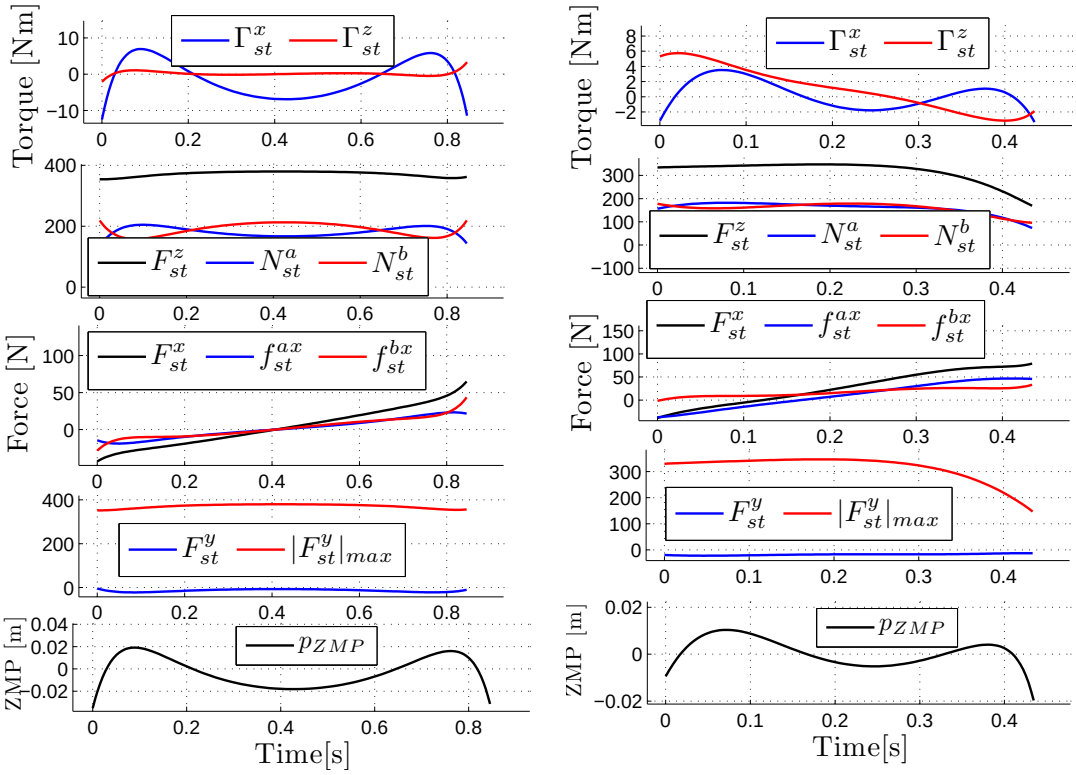

(a) **0.3 m/s** (b) **1.1 m/s**

Fig. C.5: The ground reaction forces and torques of the 8-link 3D biped walking at 0.3 m/s and 1.1 m/s for *3D Optimization Case I*

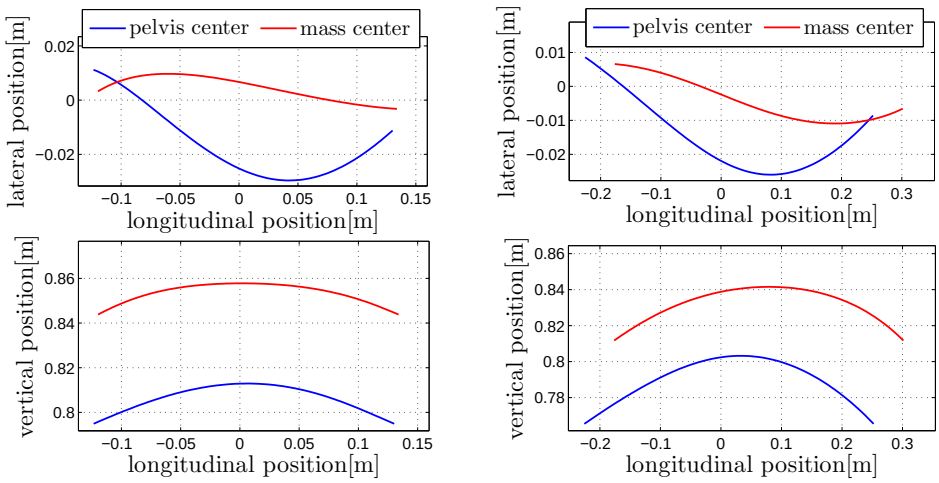

(a) **0.3 m/s** (b) **1.1 m/s**

Fig. C.6: The trajectories of the pelvis center and the CoM of the 8-link 3D biped walking at 0.3 m/s and 1.1 m/s for *3D Optimization Case I.*

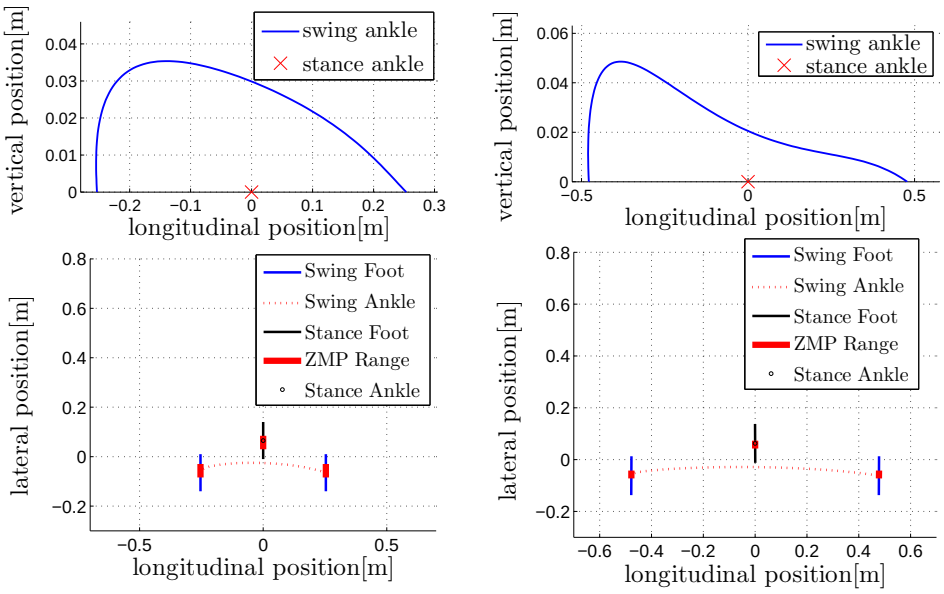

(a) **0.3 m/s** (b) **1.1 m/s**

Fig. C.7: The trajectories of the swing ankle and the footprint of the 8-link 3D biped walking at 0.3 m/s and 1.1 m/s for *3D Optimization Case I*

C.2 3D Optimization Case II

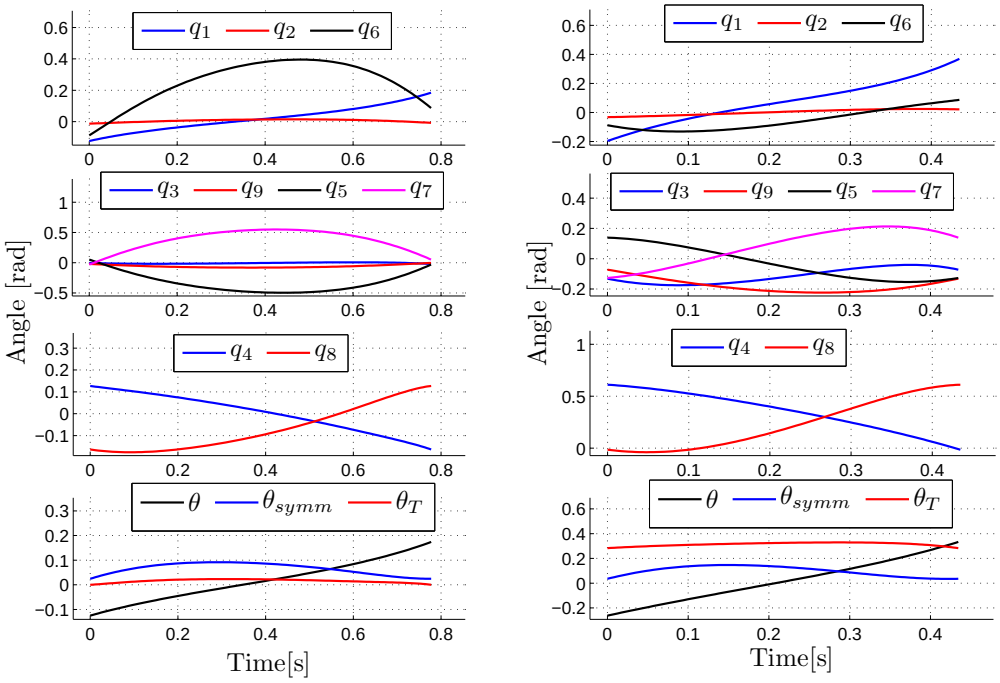

(a) **0.3 m/s** (b) **1.1 m/s**

Fig. C.8: The angle charts of the joints and outputs of the 8-link 3D biped walking at 0.3 m/s and 1.1 m/s for *3D Optimization Case II*

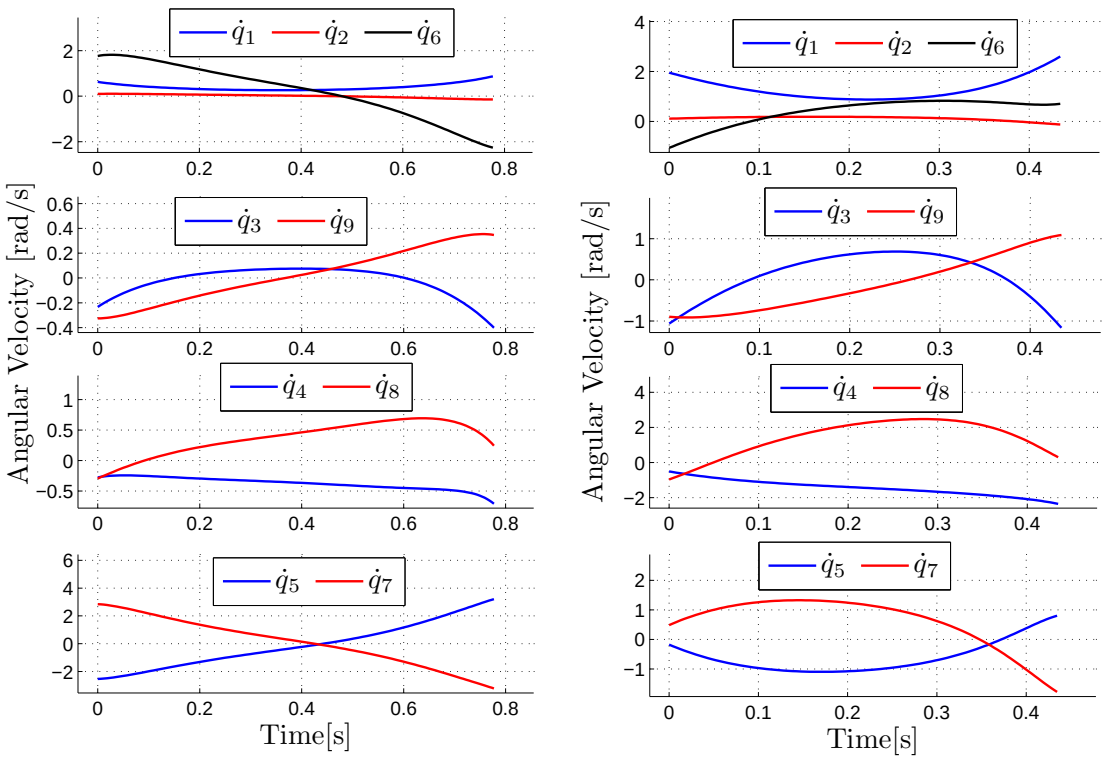

(a) **0.3 m/s** (b) **1.1 m/s**

Fig. C.9: The angular velocity charts of the joints of the 8-link 3D biped walking at 0.3 m/s and 1.1 m/s for *3D Optimization Case II*

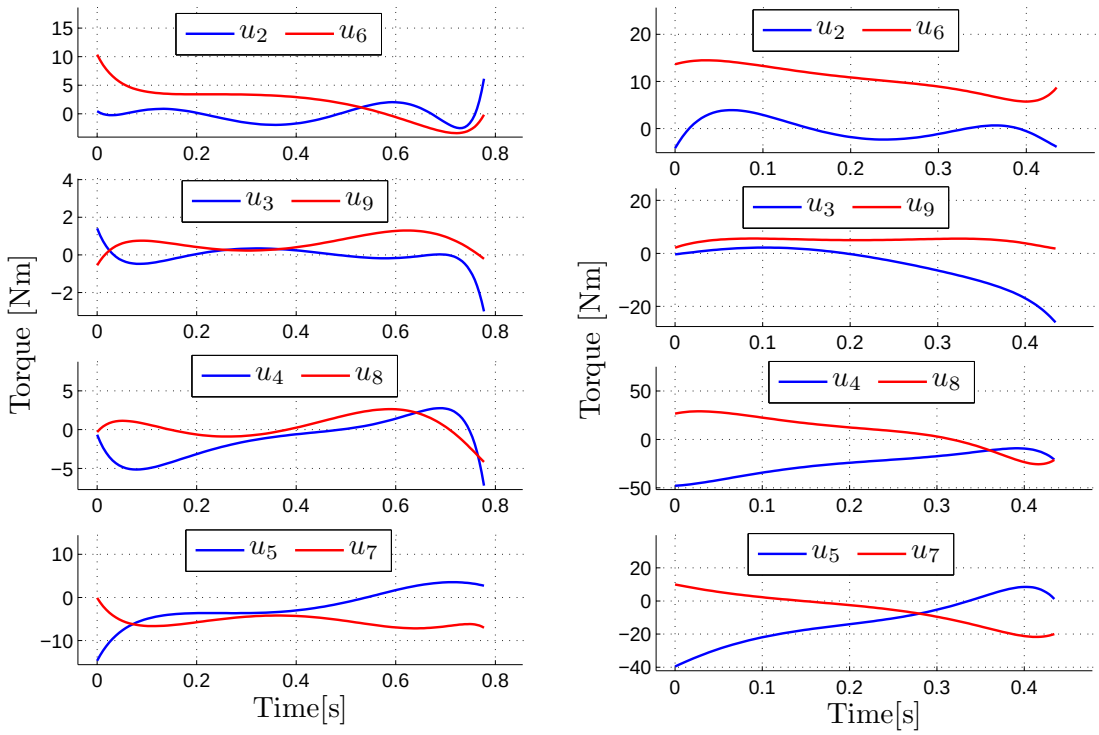

(a) **0.3 m/s** (b) **1.1 m/s**

Fig. C.10: The torque charts of the actuators of the 8-link 3D biped walking at 0.3 m/s and 1.1 m/s for *3D Optimization Case II*

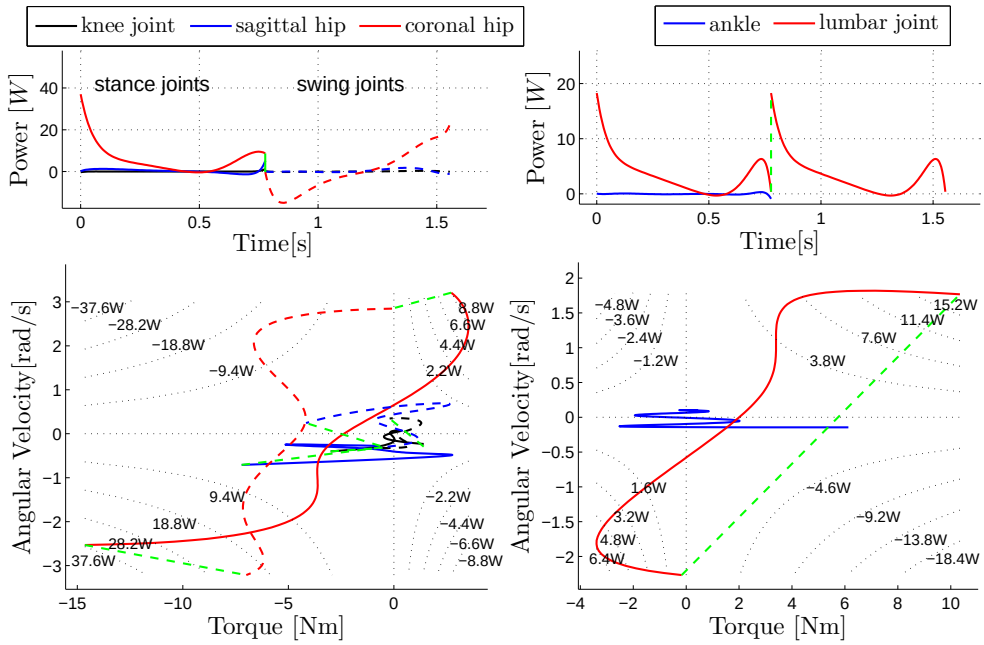

(a) **0.3 m/s**

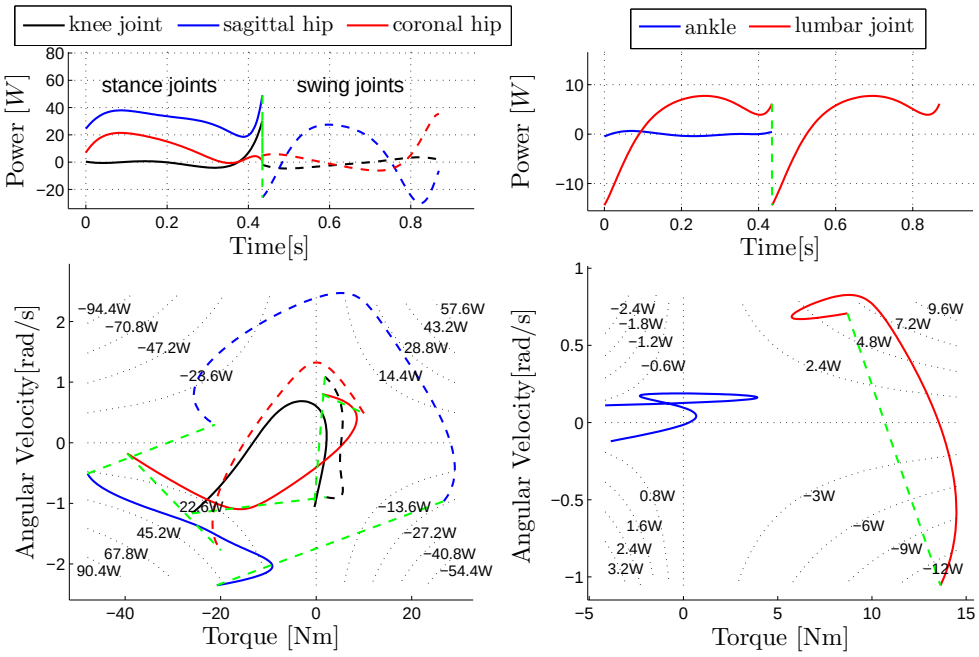

(b) **1.1 m/s**

Fig. C.11: The mechanical output powers of the actuators of the 8-link 3D biped walking at 0.3 m/s and 1.1 m/s (two steps) for *3D Optimization Case II* (Dashed lines represent swing joint angles, and green dashed lines represent the jumps caused by the impact. On the left side, solid lines represent stance joint angles.)

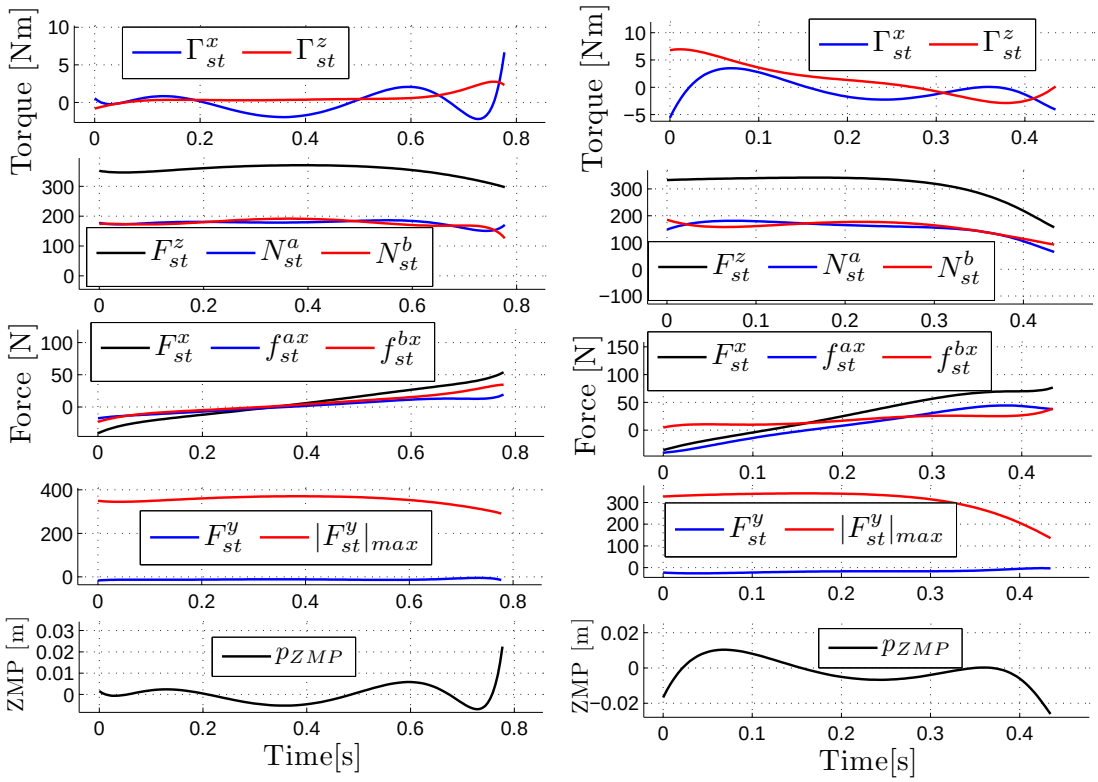

(a) **0.3 m/s** (b) **1.1 m/s**

Fig. C.12: The ground reaction forces and torques of the 8-link 3D biped walking at 0.3 m/s and 1.1 m/s for *3D Optimization Case II*

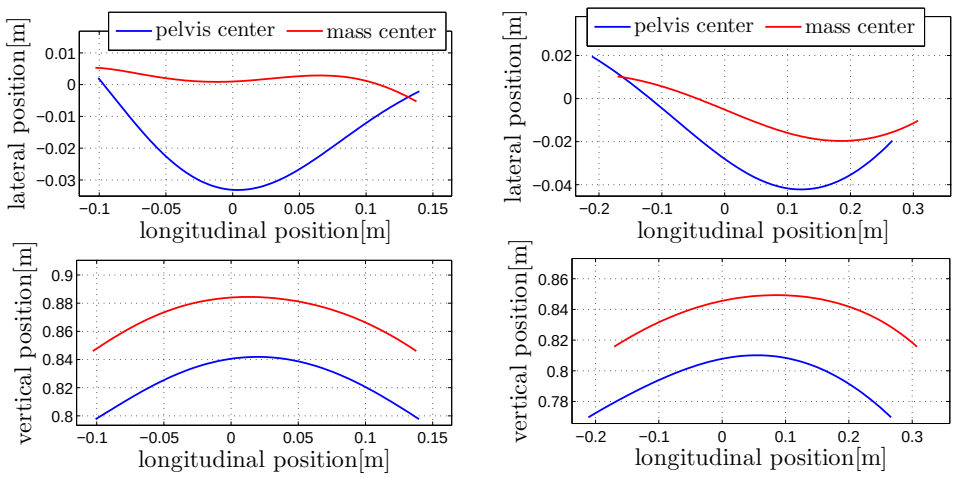

(a) **0.3 m/s** (b) **1.1 m/s**

Fig. C.13: The trajectories of the pelvis center and the CoM of the 8-link 3D biped walking at 0.3 m/s and 1.1 m/s for *3D Optimization Case II*.

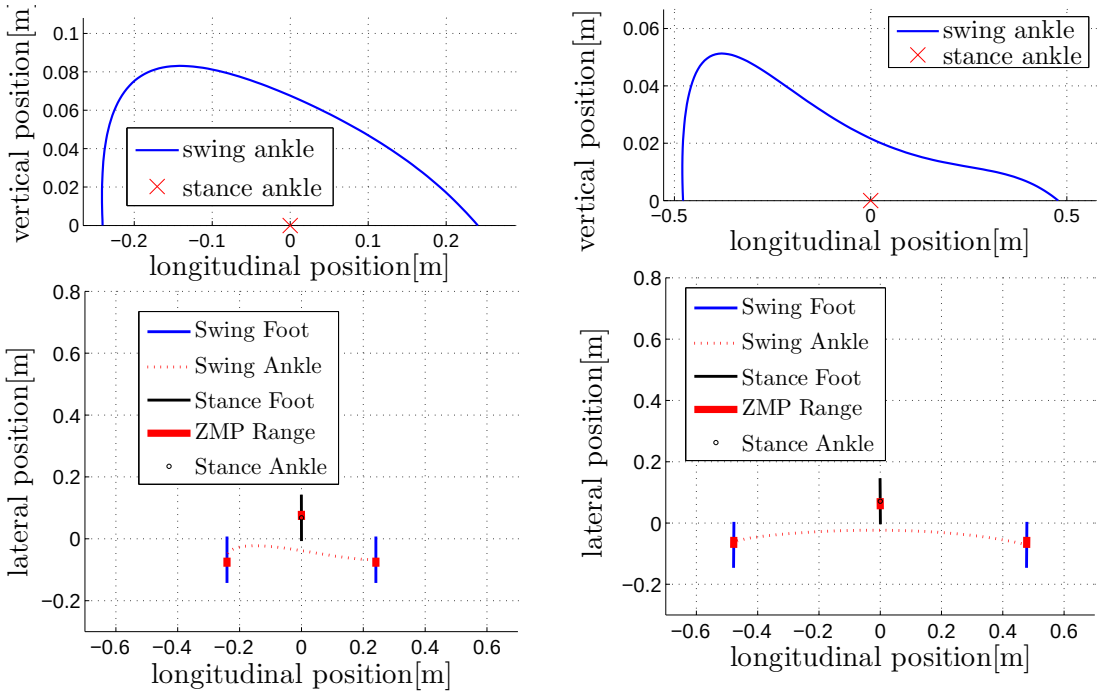

(a) **0.3 m/s** (b) **1.1 m/s**

Fig. C.14: The trajectories of the swing ankle and the footprint of the 8-link 3D biped walking at $0.3\,m/s$ and $1.1\,m/s$ for *3D Optimization Case II*

D. SUPPLEMENTARY CHARTS FOR CHAPTER 6

D.1 *3D Coupling Case I*

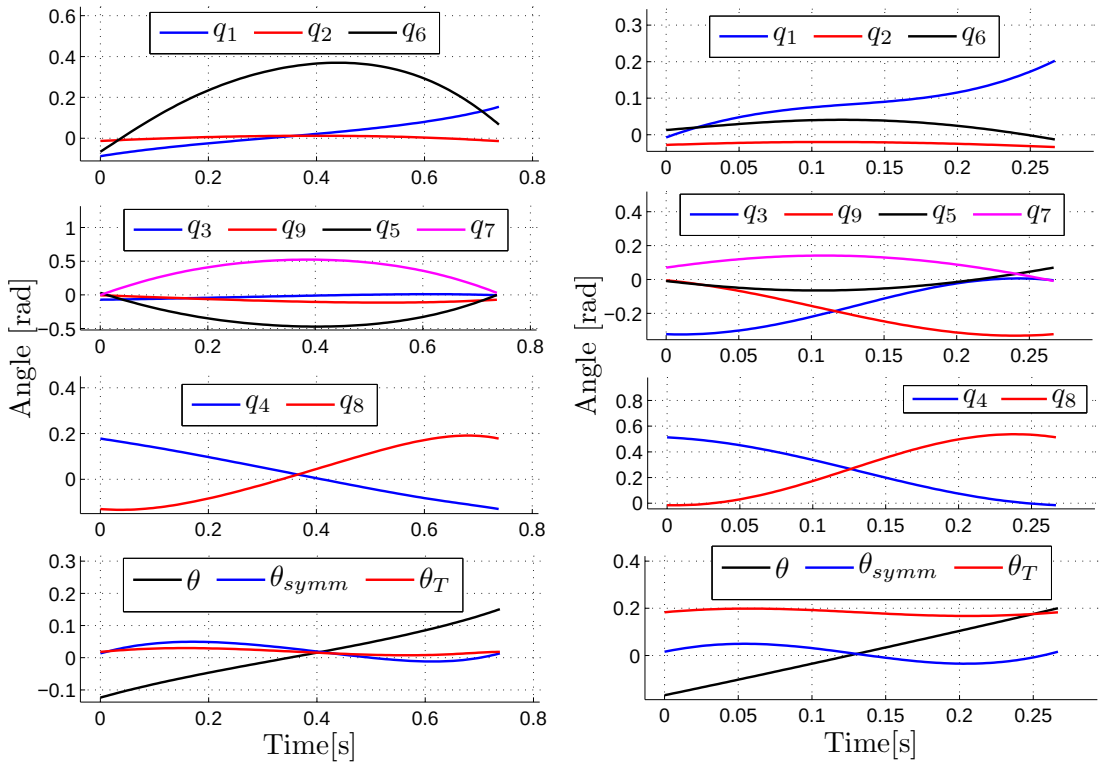

(a) **0.3 m/s** (b) **1.1 m/s**

Fig. D.1: The angle charts of the joints and output variables of the 8-link 3D biped walking at $0.3\,m/s$ and $1.1\,m/s$ for *3D Coupling Case I*

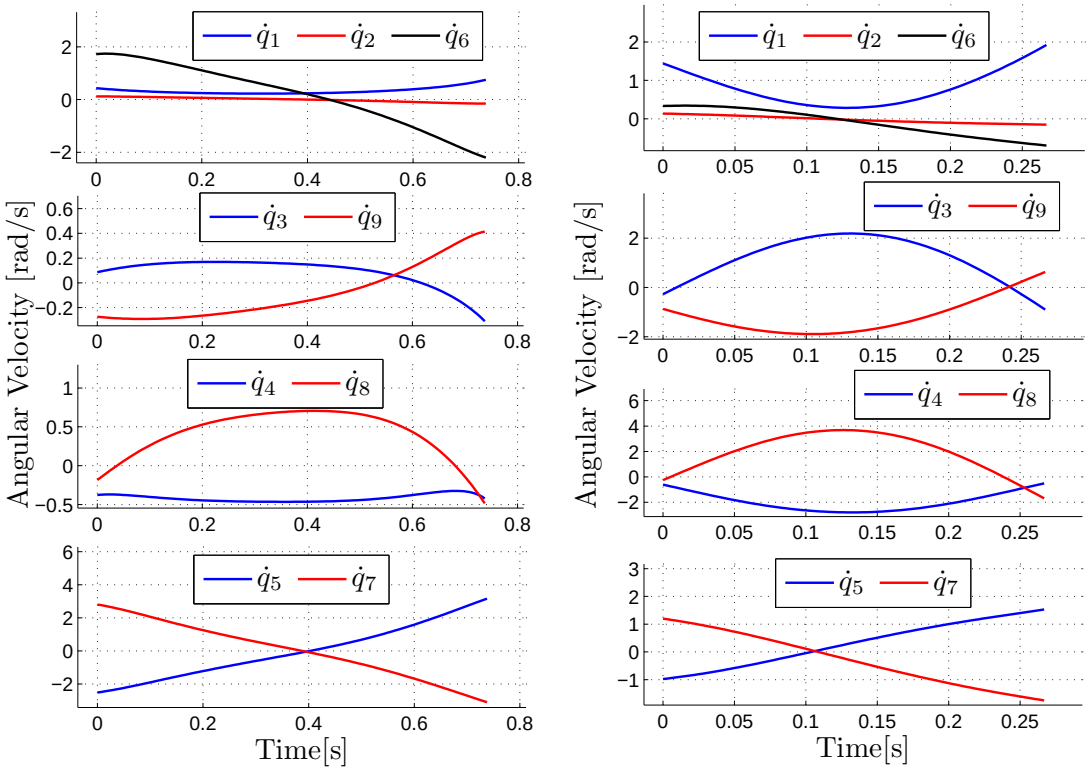

(a) **0.3 m/s** (b) **1.1 m/s**

Fig. D.2: The angular velocity charts of the joints of the 8-link 3D biped walking at $0.3\,m/s$ and $1.1\,m/s$ for *3D Coupling Case I*

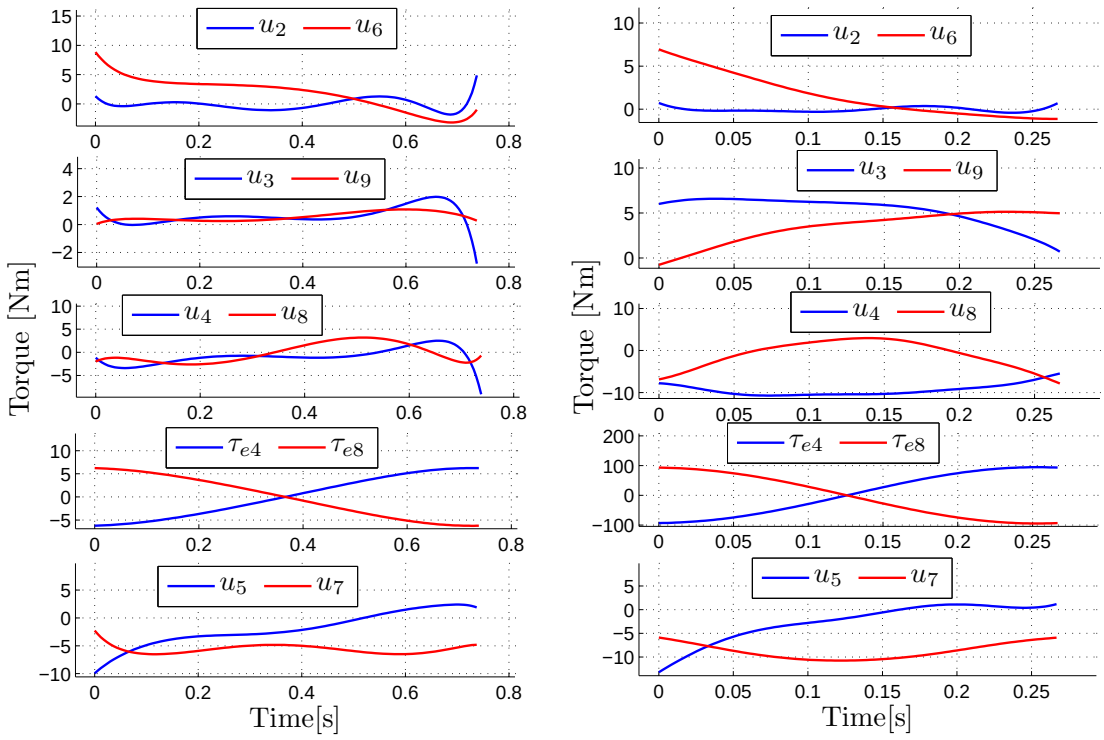

(a) **0.3 m/s** (b) **1.1 m/s**

Fig. D.3: The torque charts of the actuators of the 8-link 3D biped walking at $0.3\,m/s$ and $1.1\,m/s$ for *3D Coupling Case I*

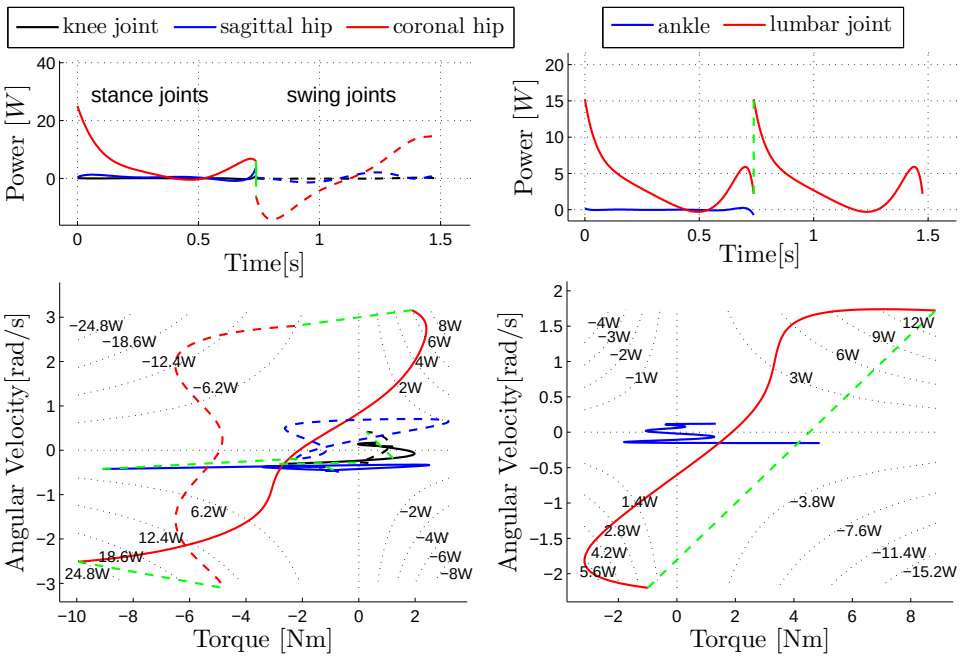

(a) **0.3 m/s**

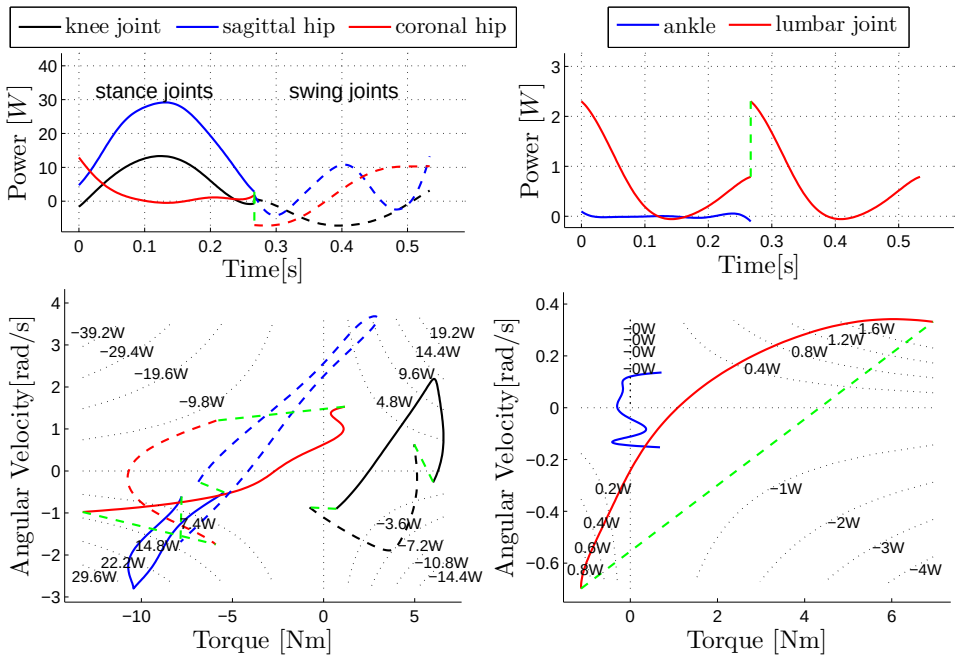

(b) **1.1 m/s**

Fig. D.4: The mechanical output powers of the actuators of the 8-link 3D biped walking at $0.3\,m/s$ and $1.1\,m/s$ (two steps) for *3D Coupling Case I* (Dashed lines represent swing joint angles, and green dashed lines represent the jumps caused by the impact. On the left side, solid lines represent stance joint angles.)

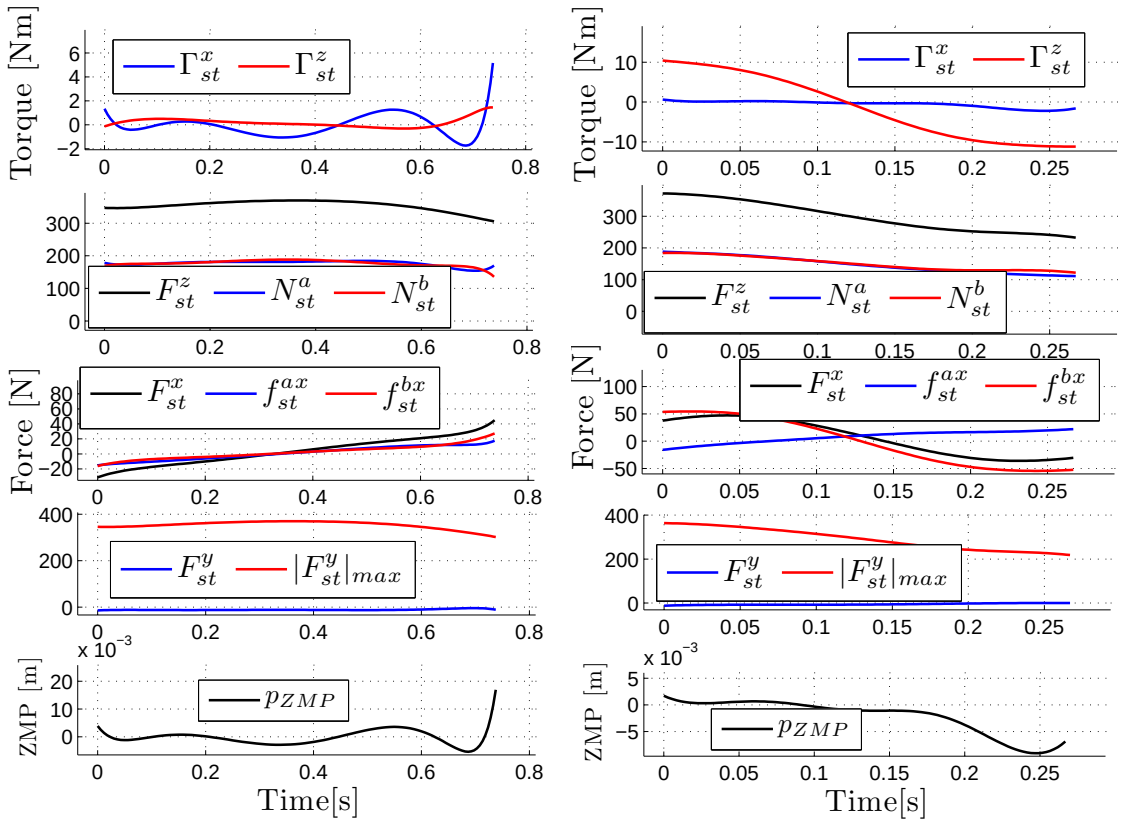

(a) **0.3 m/s** (b) **1.1 m/s**

Fig. D.5: The ground reaction forces and torques of the 8-link 3D biped walking at 0.3 m/s and 1.1 m/s for *3D Coupling Case I*

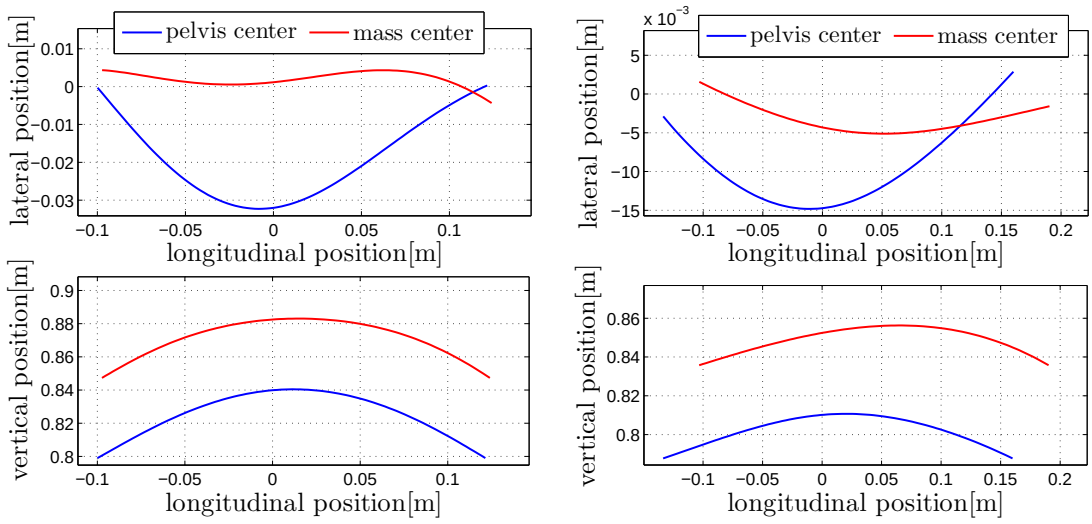

(a) **0.3 m/s** (b) **1.1 m/s**

Fig. D.6: The trajectories of the pelvis center and the CoM of the 8-link 3D biped walking at 0.3m/s and 1.1m/s for *3D Coupling Case I*

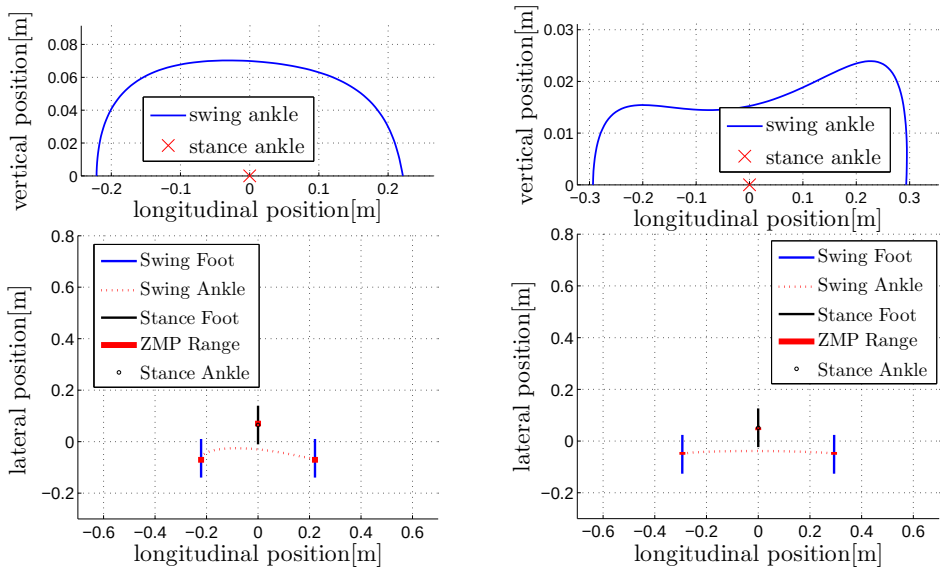

(a) **0.3 m/s** (b) **1.1 m/s**

Fig. D.7: The trajectories of the swing ankle and the footprint of the 8-link 3D biped walking at $0.3\,m/s$ and $1.1\,m/s$ for *3D Coupling Case I*

D.2 *3D Coupling Case II*

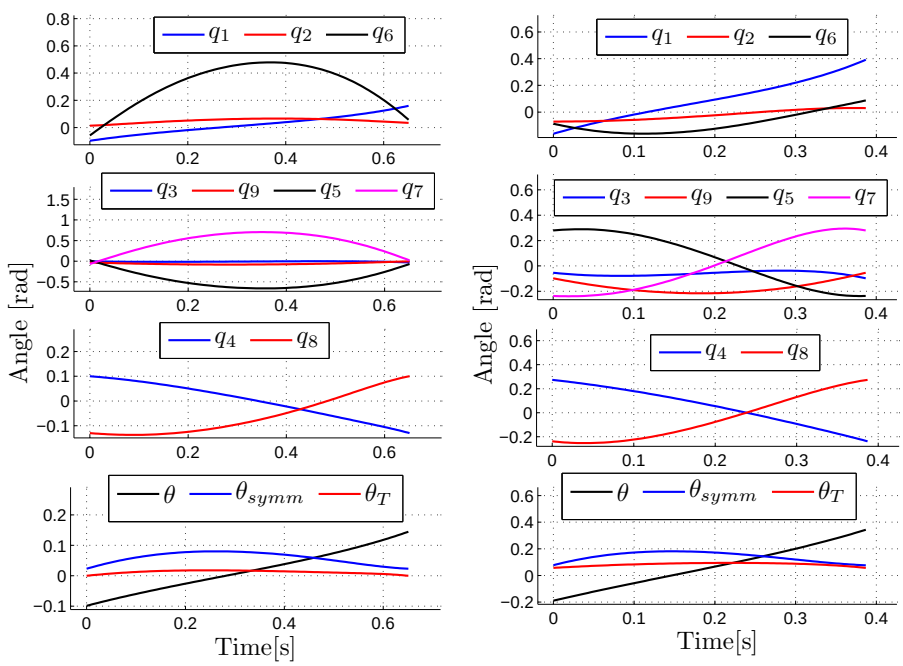

(a) **0.3 m/s** (b) **1.1 m/s**

Fig. D.8: The angle charts of the joints and output variables of the 8-link 3D biped walking at $0.3\,m/s$ and $1.1\,m/s$ for *3D Coupling Case II*

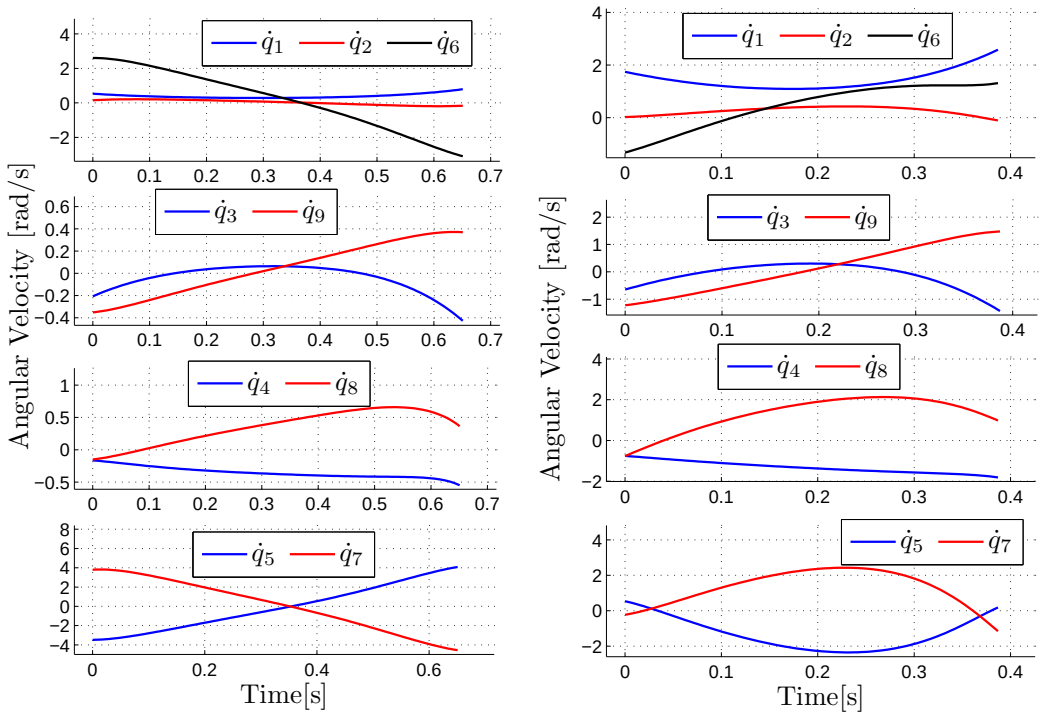

(a) **0.3 m/s** (b) **1.1 m/s**

Fig. D.9: The angular velocity charts of the joints of the 8-link 3D biped walking at 0.3 m/s and 1.1 m/s for *3D Coupling Case II*

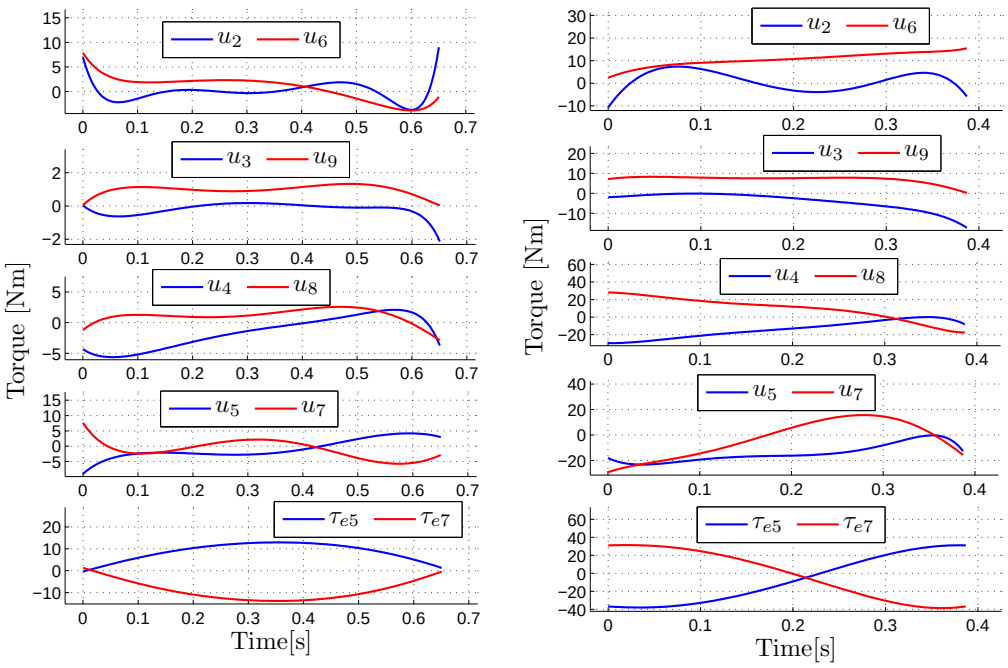

(a) **0.3 m/s** (b) **1.1 m/s**

Fig. D.10: The torque charts of the actuators of the 8-link 3D biped walking at 0.3 m/s and 1.1 m/s for *3D Coupling Case II*

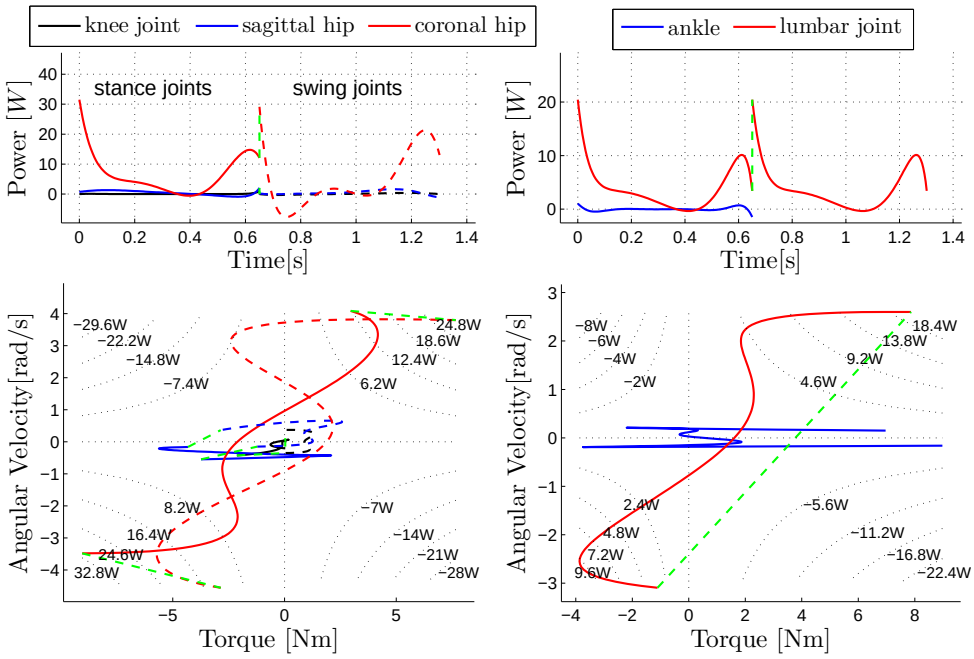

(a) **0.3 m/s**

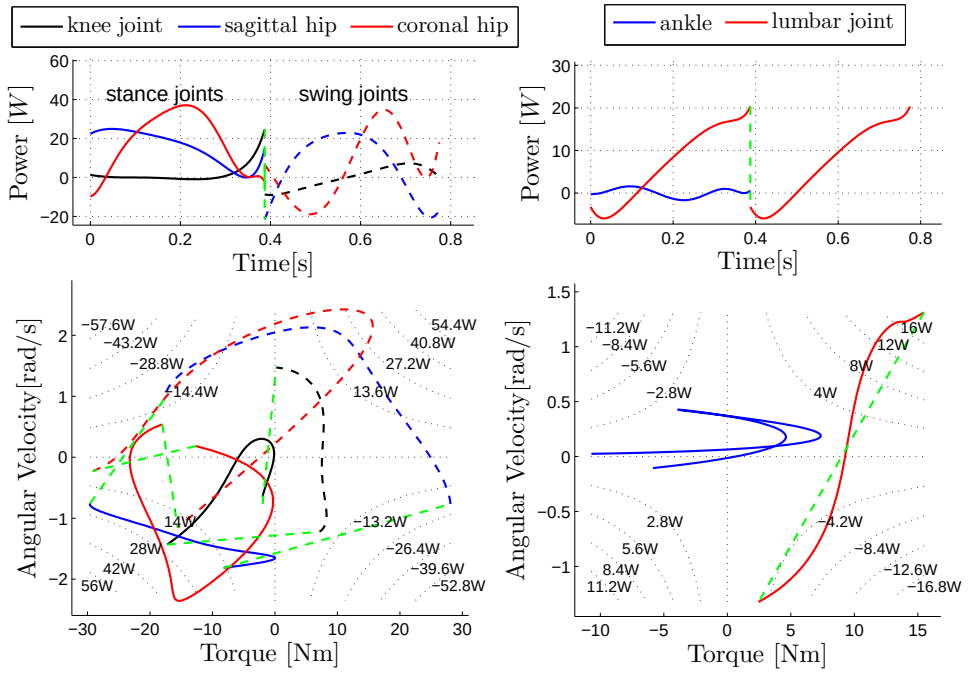

(b) **1.1 m/s**

Fig. D.11: The mechanical output powers of the actuators of the 8-link 3D biped walking at $0.3\,m/s$ and $1.1\,m/s$ (two steps) for *3D Coupling Case II* (Dashed lines represent swing joint angles, and green dashed lines represent the jumps caused by the impact. On the left side, solid lines represent stance joint angles.)

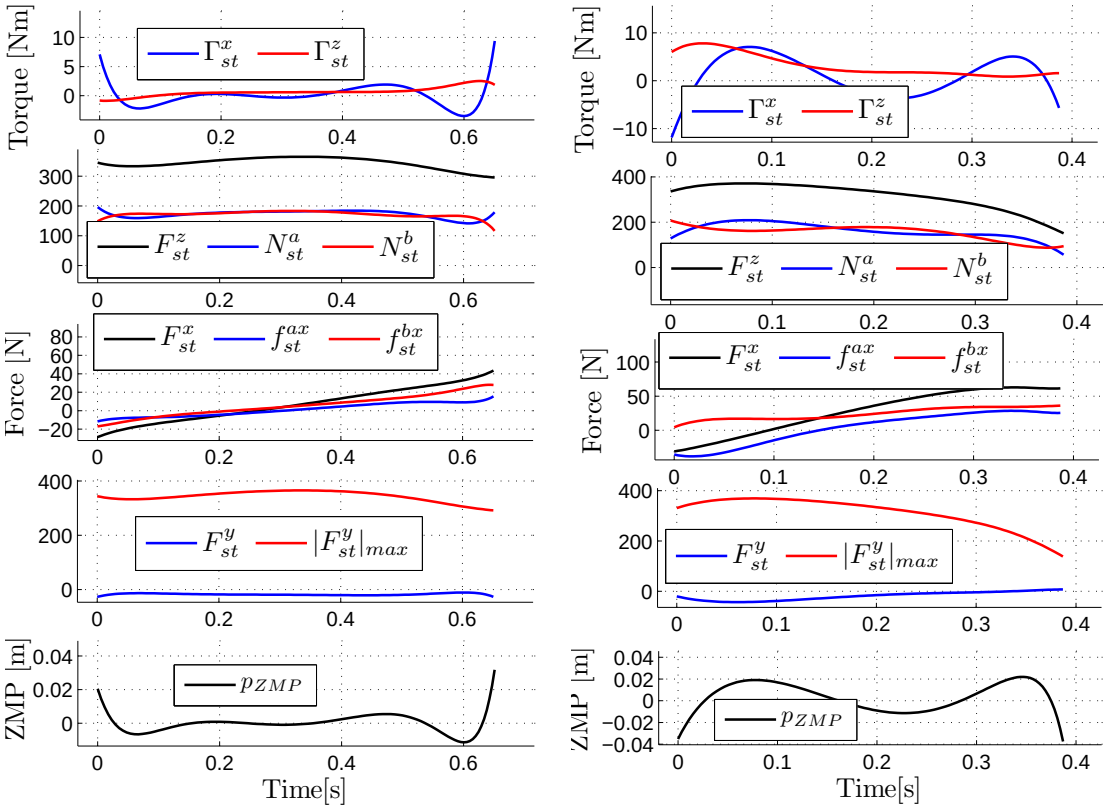

(a) **0.3 m/s** (b) **1.1 m/s**

Fig. D.12: The ground reaction forces and torques of the 8-link 3D biped walking at 0.3 m/s and 1.1 m/s for *3D Coupling Case II*

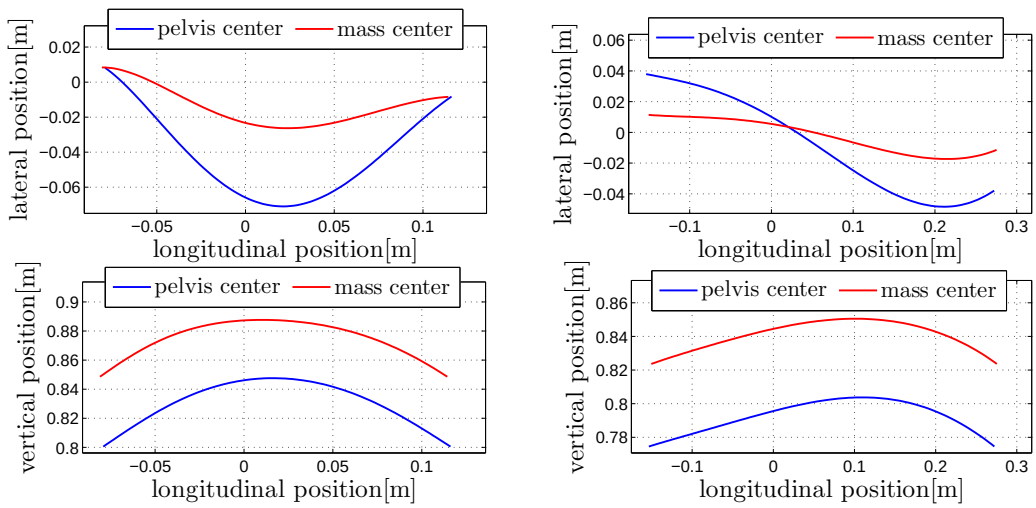

(a) **0.3 m/s** (b) **1.1 m/s**

Fig. D.13: The trajectories of the pelvis center and the CoM of the 8-link 3D biped walking at 0.3 m/s and 1.1 m/s for *3D Coupling Case II*

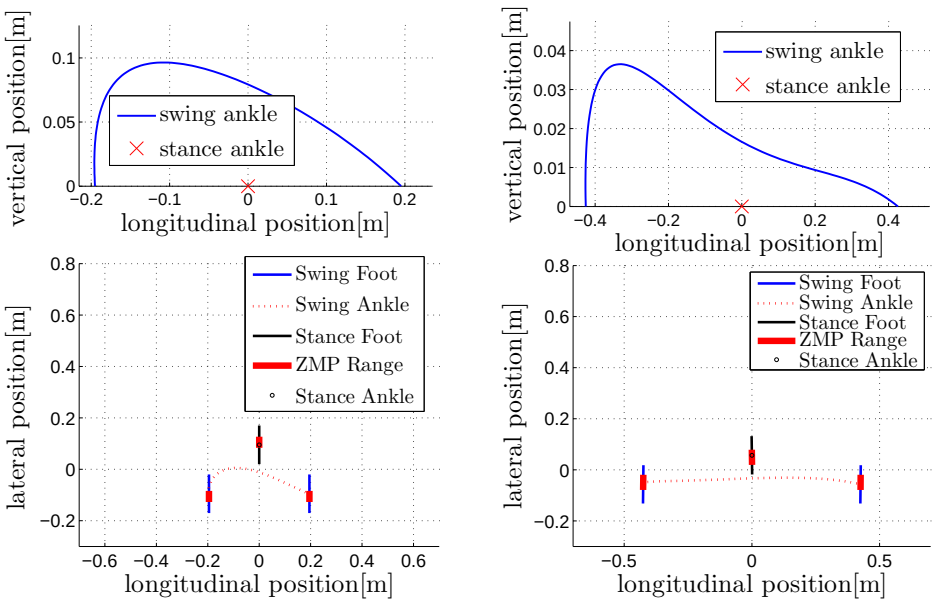

(a) **0.3 m/s** (b) **1.1 m/s**

Fig. D.14: The trajectories of the swing ankle and the footprint of the 8-link 3D biped walking at 0.3 m/s and 1.1 m/s for *3D Coupling Case II*

D.3 3D Coupling Case III

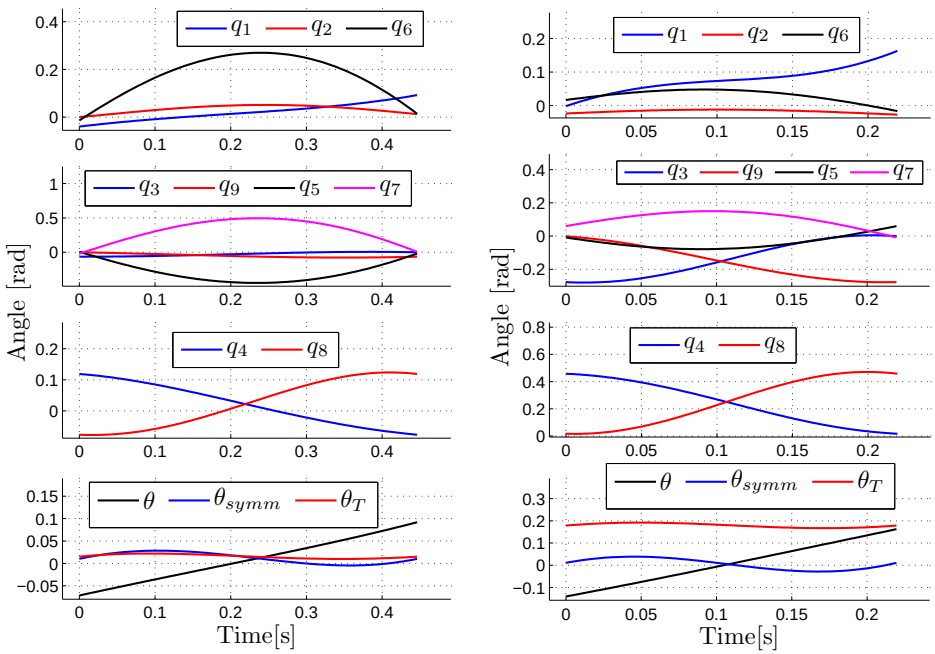

(a) **0.3 m/s** (b) **1.1 m/s**

Fig. D.15: The angle charts of the joints and output variables of the 8-link 3D biped walking at 0.3 m/s and 1.1 m/s for *3D Coupling Case III*

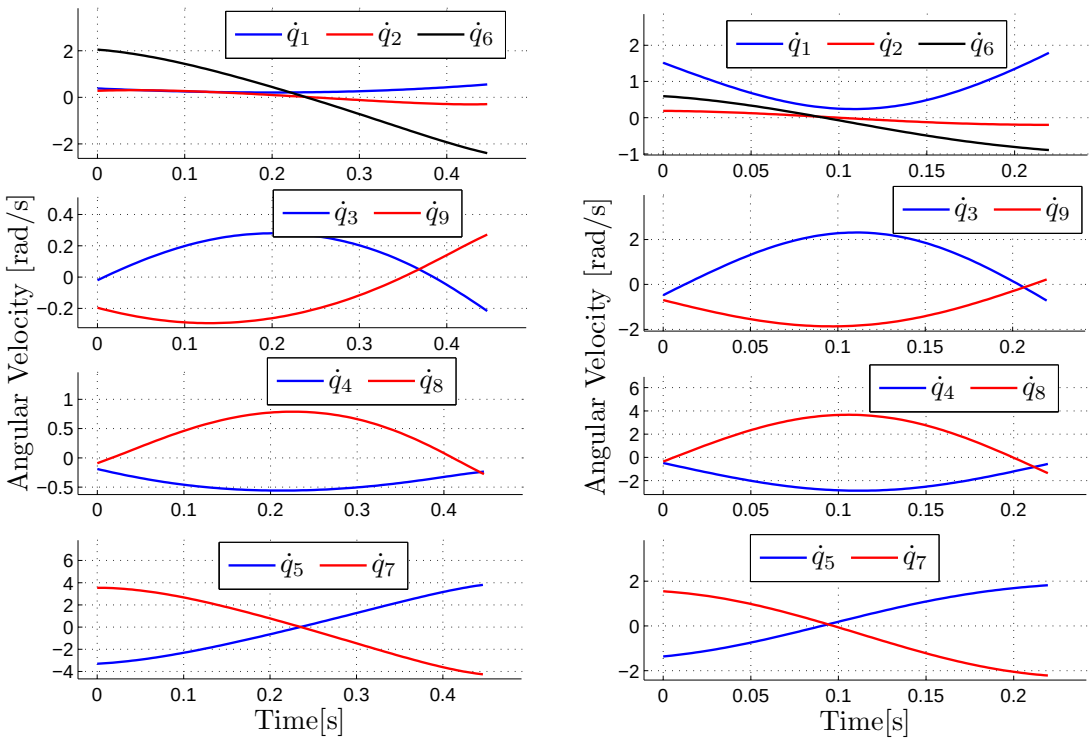

(a) **0.3 m/s** (b) **1.1 m/s**

Fig. D.16: The angular velocity charts of the joints of the 8-link 3D biped walking at $0.3\,m/s$ and $1.1\,m/s$ for *3D Coupling Case III*

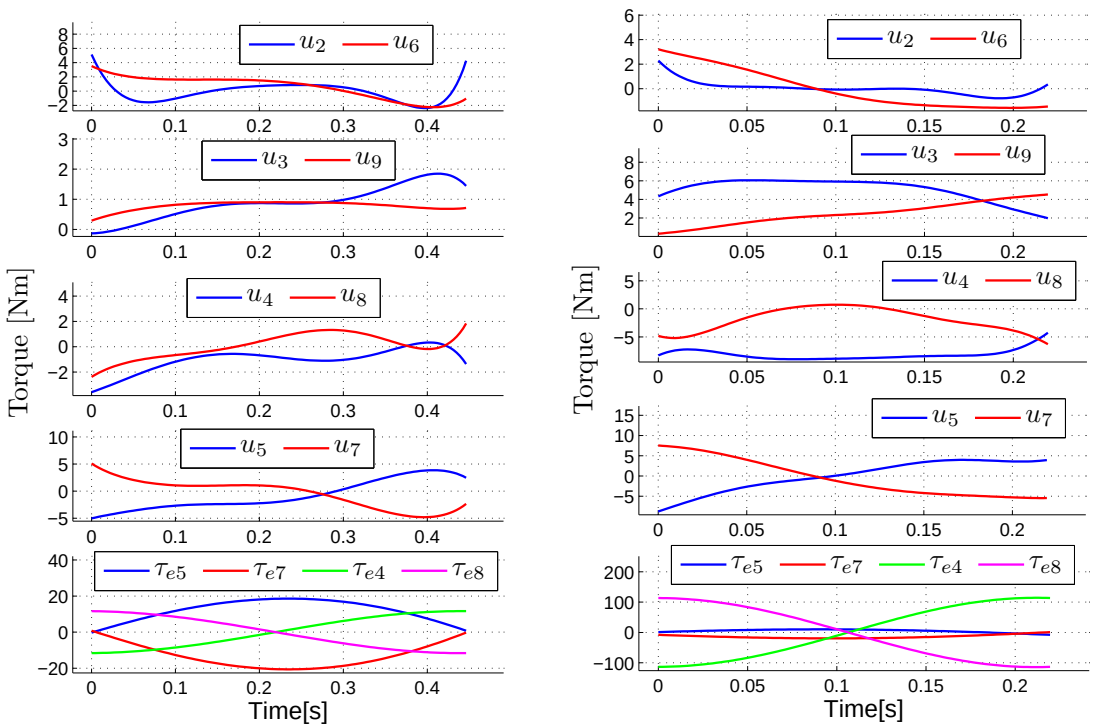

(a) **0.3 m/s** (b) **1.1 m/s**

Fig. D.17: The torque charts of the actuators of the 8-link 3D biped walking at $0.3\,m/s$ and $1.1\,m/s$ for *3D Coupling Case III*

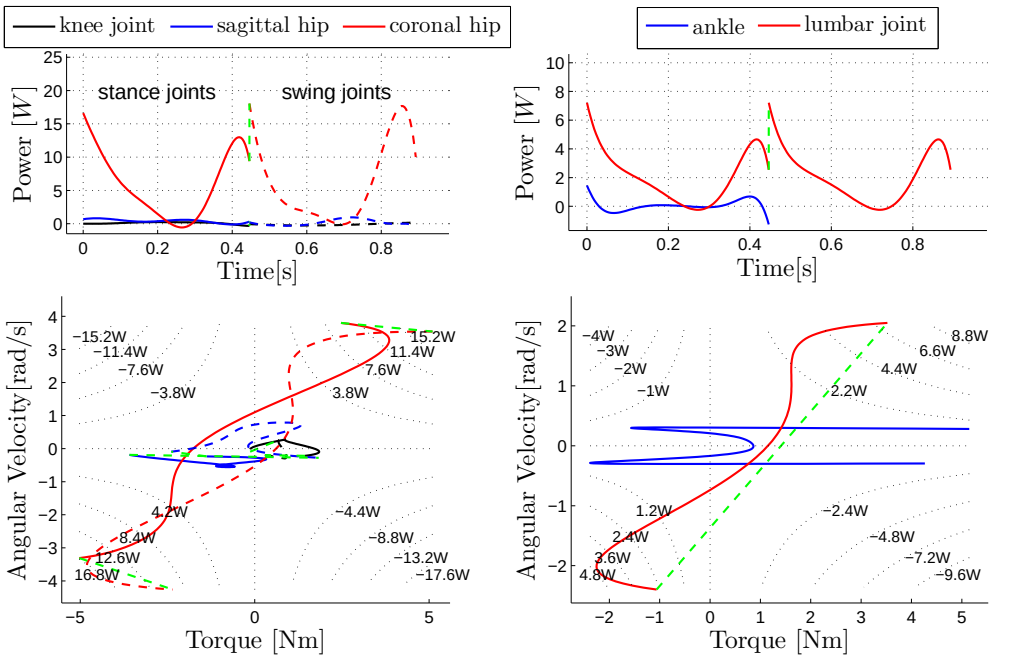

(a) **0.3 m/s**

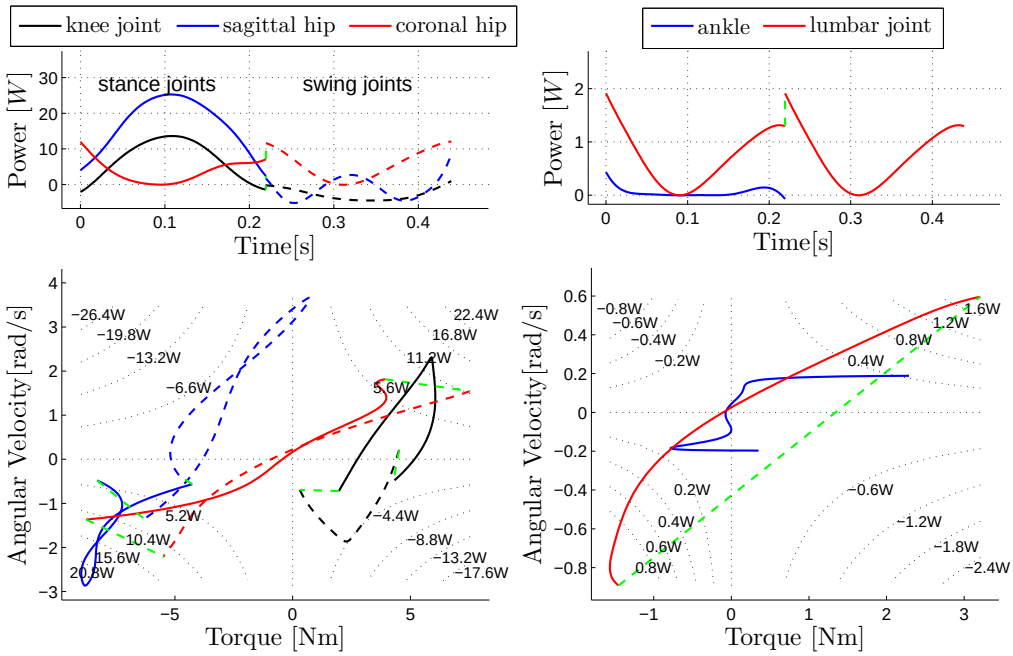

(b) **1.1 m/s**

Fig. D.18: The mechanical output powers of the actuators of the 8-link 3D biped walking at $0.3\,m/s$ and $1.1\,m/s$ (two steps) for *3D Coupling Case III* (Dashed lines represent swing joint angles, and green dashed lines represent the jumps caused by the impact. On the left side, solid lines represent stance joint angles.)

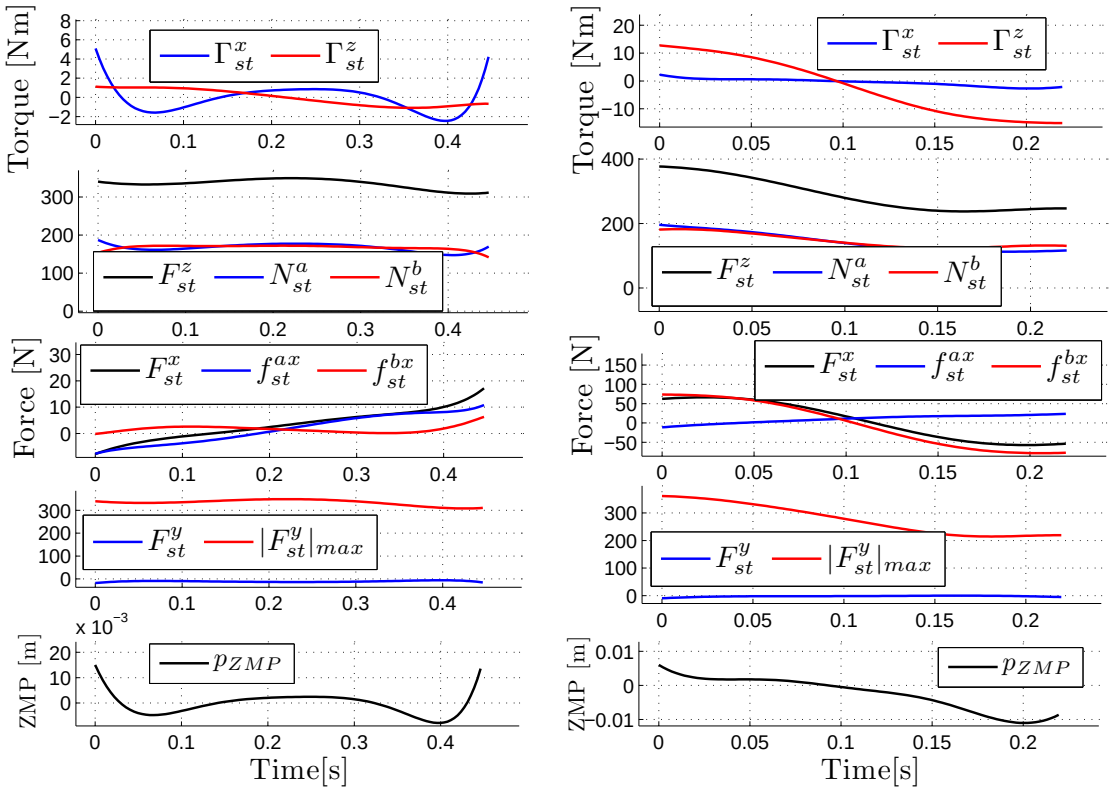

(a) **0.3 m/s** (b) **1.1 m/s**

Fig. D.19: The ground reaction forces and torques of the 8-link 3D biped walking at $0.3\,m/s$ and $1.1\,m/s$ for *3D Coupling Case III*

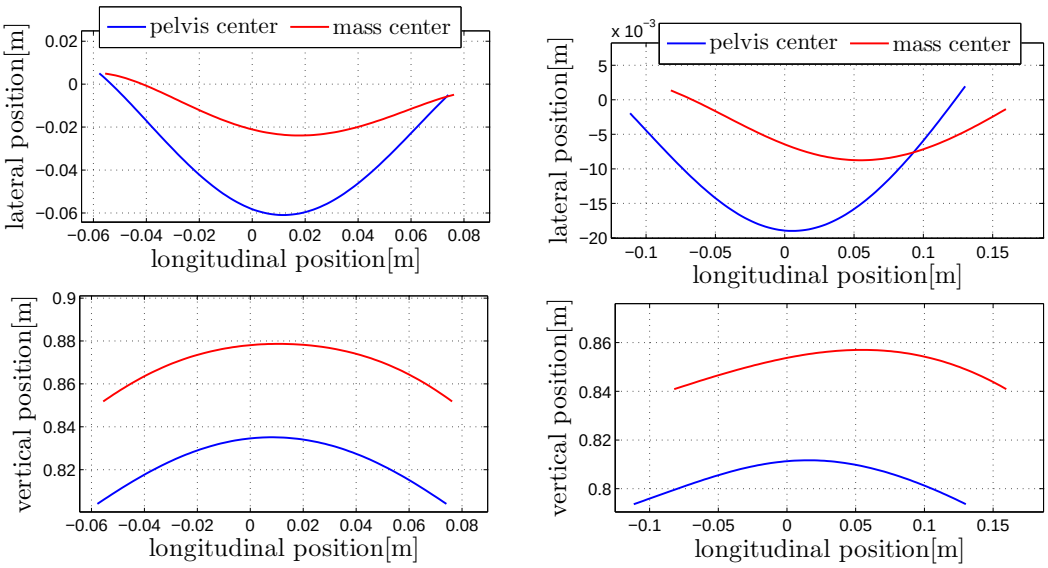

(a) **0.3 m/s** (b) **1.1 m/s**

Fig. D.20: The trajectories of the pelvis center and the CoM of the 8-link 3D biped walking at $0.3\,m/s$ and $1.1\,m/s$ for *3D Coupling Case III*

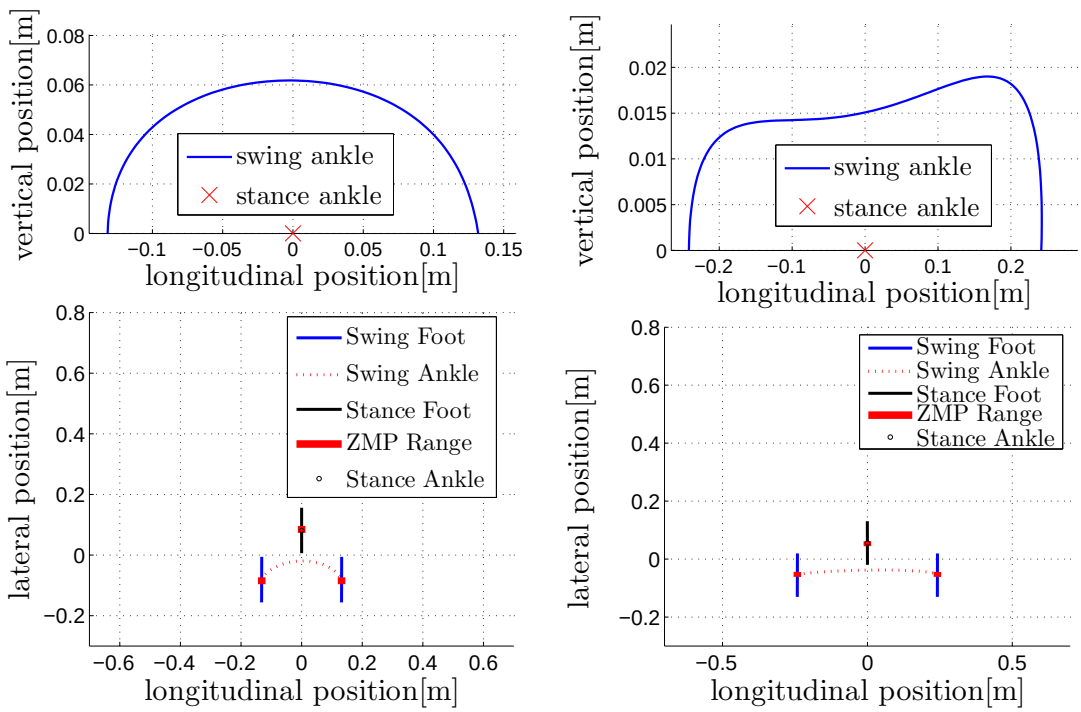

(a) **0.3 m/s** (b) **1.1 m/s**

Fig. D.21: The trajectories of the swing ankle and the footprint of the 8-link 3D biped walking at $0.3\,m/s$ and $1.1\,m/s$ for *3D Coupling Case III*

OPTIMISATION DE LA MARCHE D'UN ROBOT BIPÈDE 3D À 8 CORPS

RÉSUMÉ : D'un point de vue énergétique, les robots marcheurs sont moins performants que les humains. Face à ce défi, cette thèse propose une approche pour contrôler et optimiser les allures de marche des robots bipèdes à la fois en 2D et 3D en considérant les fréquences propres du robot et par ajout de ressorts. L'étude porte essentiellement sur un robot bipède 2D à 5 corps et des pieds ponctuels ainsi qu'un robot bipède 3D à 8 corps avec des pieds sans masse à contact linéique. La commande en boucle fermée considérée est basée sur la méthode des contraintes virtuelles et la linéarisation par retour d'état. Suite à des études précédentes, la stabilité du robot bipède 2D est vérifiée par une section de Poincaré unidimensionnelle et étendue au robot bipède 3D à contact linéique avec le sol. L'optimisation est effectuée en utilisant la programmation quadratique séquentielle. Les paramètres optimisés incluent des coefficients de polynômes de Bézier et des paramètres posturaux. Des contraintes d'optimisation sont imposées pour assurer la validité de l'allure de marche. Pour le robot bipède 2D, deux configurations différentes de ressorts placés aux hanches sont étudiées. Ces deux configurations ont permis de réduire le coût énergétique. Pour le robot bipède 3D, les paramètres d'optimisation sont séparés en deux parties : ceux décrivant le mouvement dans le plan sagittal et ceux du plan frontal. Les résultats de l'optimisation montrent que ces deux types de paramètres doivent être optimisés. Ensuite, des ressorts sont ajoutés respectivement par rapport au plan sagittal, par rapport au plan frontal puis dans les deux plans. Les résultats montrent que l'ajout des ressorts dans le plan sagittal permet de réduire significativement le coût énergétique et que l'association de ressorts dans le plan frontal améliore encore plus la consommation d'énergie.

Mots clés : robot bipède 3D, marche optimale, commande non linéaire, robot sous-actionné, optimisation paramétrique.

OPTIMIZED WALKING OF AN 8-LINK 3D BIPEDAL ROBOT

ABSTRACT: From an energy standpoint, walking robots are less efficient than humans. In facing this challenge, this study aims to provide an approach for controlling and optimizing the gaits of both 2D and 3D bipedal robots with consideration for exploiting natural dynamics and elastic couplings. A 5-link 2D biped with point feet and an 8-link 3D biped with massless line feet are studied. The control method is based on virtual constraints and feedback linearization. Following previous studies, the stability of the 2D biped is verified by computing scalar Poincaré map in closed form, and now this method also applies to the 3D biped because of its line-foot configuration. The optimization is performed using sequential quadratic programming. The optimization parameters include postural parameters and Bézier coefficients, and the optimization constraints are used to ensure gait validity. For the 2D biped, two different configurations of hip joint springs are investigated and both configurations successfully reduce the energy cost. For the 3D biped, the optimization parameters are further divided into sagittal parameters and coronal parameters, and the optimization results indicate that both these parameters should be optimized. After that, hip joint springs are added respectively to the sagittal plane, the coronal plane and both these planes. The results demonstrate that the elastic couplings in the sagittal plane should be considered first and that the additional couplings in the coronal plane reduce the energy cost even further.

Keywords : 3D bipedal robot, optimal walking, nonlinear control, underactuated robot, parametric optimization.

ARTS ET MÉTIERS ParisTech

ParisTech
INSTITUT DES SCIENCES ET TECHNOLOGIES
PARIS INSTITUTE OF TECHNOLOGY